TECHNISCHE UNIVERSITÄT MÜNCHEN
Physik-Department
Institut für Theoretische Physik
Lehrstuhl Univ.-Prof. Dr. Peter Vogl

Quantum transport in semiconductor nanostructures

Tillmann Christoph Kubis

Vollständiger Abdruck der von der Fakultät für Physik der Technischen Universität München zur Erlangung des akademischen Grades eines

Doktors der Naturwissenschaften (Dr. rer. nat.)

genehmigten Dissertation.

Vorsitzender:	Univ.-Prof. Dr. Gerhard Abstreiter
Prüfer der Dissertation:	1. Univ.-Prof. Dr. Peter Vogl 2. Univ.-Prof. Dr. Wilhelm Zwerger

Die Dissertation wurde am 8.9.2009 bei der Technischen Universität München eingereicht und durch die Fakultät für Physik am 29.10.2009 angenommen.

Für meinen Vater

Wir sehen uns wieder, wenn sich der Kreis schließt.

Contents

Zusammenfassung

Das Hauptanliegen dieser Arbeit ist die theoretische Beschreibung des stationären Ladungs- und Spintransports in mesoskopischen Halbleiterbauelementen unter dem Einfluss von Phononen und Defekten. Bekanntermaßen stellt die Nichtgleichgewichtsgreensfunktionsmethode (NEGF) eine sehr allgemeine und umfassende Beschreibung genau solcher Transportprobleme dar. Allerdings sind Lehrbücher zu dieser Theorie kaum erhältlich, auch wenn die NEGF Methode bereits in den 1960ern eingeführt worden ist. Aus diesem Grund beginnen wir diese Dissertation mit einer Einführung in die Grundlagen der NEGF Methode und leiten ihre wichtigsten Gleichungen und Näherungen explizit her. Dabei folgen wir grundlegenden Arbeiten auf dem Gebiet der NEGF Methode und ergänzen lediglich einige kleinere Ableitungen die in der Literatur nur selten ausgeführt werden.

Obschon die NEGF Methode bereits häufig auf numerische Transportprobleme angewandt worden ist, enthalten alle Arbeiten auf diesem Gebiet eine nicht geringe Anzahl von Näherungen deren Auswirkungen auf die Ergebnisse und deren Gültigkeitsbereich selten bekannt sind. Daher vermeiden wir die meisten der üblichen Näherungen und implementieren im zweiten Teil dieser Dissertation die NEGF Methode so akkurat wie numerisch möglich. Hierfür leiten wir einige neue Streuselbstenergien her und entwickeln ein neues selbstadaptives Gitter für die Diskretisierung der Greensfunktionen und Selbstenergien. Die wichtigsten Neuerungen unserer Implementierung der NEGF Methode betreffen allerdings die Impuls- und Energieerhaltung bei inkohärenten Streuungen, das paulische Ausschlussprinzip, die Stromerhaltung im und außerhalb des Bauteils und die reflexionslose Propagation über die offenen Bauteilgrenzen hinweg. Unsere ungewöhnlich getreue Implementierung der NEGF Methode ermöglicht es uns, die meisten der in der Literatur üblichen Näherungen zu analysieren und numerische Artefakte, die sich aus diesen Näherungen ergeben, aufzudecken. Wir verwenden unsere numerische Implementierung der NEGF Methode auch um den stationären Elektronentransport in THz Quantenkaskadenlasern zu berechnen. Dabei beantworten wir einige kontrovers diskutierte Fragestellungen über die Natur des Ladungstransports in derartigen Bauteilen. Im Gegensatz zu Ergebnissen früherer vereinfachender Arbeiten zeigen wir, dass der Ladungstransport in Quantenkaskadenlasern von der angelegten Bauteilspannung abhängt und sich von rein kohärentem bis hin zu vollständig inkohärentem Transport verändern lässt. Wir stellen außerdem fest, dass die elastische Streuung an rauen Grenzflächen eine der effizientesten Streumechanismen in THz Quantenkaskadenlasern ist und erheblichen Einfluss auf die Laserleistung hat. Bisher ist diese Streuung in der Literatur weitestgehend unterschätzt worden. Alle bisherigen theoretischen Modelle in der Literatur berechnen den Transport in Quantenkaskadenlasern mit periodischen (oder feldperiodischen) Randbedingungen. Dank der von uns überarbeiteten offenen Randbedingungen können wir aber Quantenkaskadenlaser als offene Bauteile betrachten. Daher können wir zeigen wie sich Ladungsverteilungen im Quantenkaskadenlaser ausbilden, die entweder nur noch kommensurabel, oder sogar inkommensurabel zur Periodizität des Quantenkaskadenlasers

sind. Dieser Effekt führt zu effizienten nichtstrahlenden Übergängen zwischen den Laserniveaus und ist – wegen der üblichen periodischen Randbedingungen – bisher in der Literatur komplett übersehen worden. Schließlich schlagen wir neue THz Quantenkaskadenlaser vor, die Laserlicht besser verstärken, eine geringere thermische Belastung haben und widerstandsfähiger gegenüber Wachstumsfehlern sind.

Der dritte Teil dieser Dissertation behandelt den Spintransport in zweidimensionalen Halbleiterheterostrukturen. Es ist üblich die Spinbahnwechselwirkung in diesen Bauteilen mit einem Model für die Einhüllende der elektronischen Wellenfunktion (EFT) zu nähern, obwohl dieses Näherungsmodell bekanntermaßen die Spinaufspaltung in Halbleiterbauelementen falsch wiedergibt. Aus diesem Grund wenden wir die NEGF Methode sowohl in der üblichen EFT-Darstellung als auch in einem mikroskopisch atomaren „tight-binding“ Modell an. Das letztere Model behandelt die Spinbahnwechselwirkung nicht perturbativ und geht daher weit über die näherungsweise EFT-Darstellung hinaus. Wir zeigen, dass die Ergebnisse des numerisch effizienteren EFT-Models qualitativ mit den Vorhersagen des äußerst aufwendigen „tight-binding“ Modells übereinstimmen. Das ermöglicht es uns die Spinpolarisation propagierender und gebundener Ladungsträger in zweidimensionalen Halbleiterbauelementen komplexer Geometrie zu untersuchen. So zeigen wir, dass die Spinpolarisation des intrinsischen Spin-Halleffekts nicht von Phononen auf gebundene Ladungsträger übertragen werden kann. Wir zeigen allerdings auch, dass die Interferenzen teilweise gebundener Ladungsträger die lokale Spinpolarisation erheblich verstärken können und Polarisationen bis zu 100 % erreichbar sind. Schließlich schlagen wir nichtmagnetische Halbleiterbauelemente mit drei bzw. vier Kontakten vor, die den Spin der Ladungsträger effizient polarisieren.

Abstract

The main objective of this thesis is to theoretically predict the stationary charge and spin transport in mesoscopic semiconductor quantum devices in the presence of phonons and device imperfections. It is well known that the nonequilibrium Green's function method (NEGF) is a very general and all-inclusive scheme for the description of exactly this kind of transport problem. Although the NEGF formalism has been derived in the 1960's, textbooks about this formalism are still rare to find. Therefore, we introduce the NEGF formalism, its fundamental equations and approximations in the first part of this thesis. Thereby, we extract ideas of several seminal contributions on NEGF in literature and augment this by some minor derivations that are hard to find.

Although the NEGF method has often been numerically implemented on transport problems, all current work in literature is based on a significant number of approximations with often unknown influence on the results and unknown validity limits. Therefore, we avoid most of the common approximations and implement in the second part of this thesis the NEGF formalism as exact as numerically feasible. For this purpose, we derive several new scattering self-energies and introduce new self-adaptive discretizations for the Green's functions and self-energies. The most important improvements of our NEGF implementation, however, affect the momentum and energy conservation during incoherent scattering, the Pauli blocking, the current conservation within and beyond the device and the reflectionless propagation through open device boundaries. Our uncommonly accurate implementation of the NEGF method allows us to analyze and assess most of the common approximations and to unveil numerical artifacts that have plagued previous approximate implementations in literature. Furthermore, we apply our numerical implementation of the NEGF method on the stationary electron transport in THz quantum cascade lasers (QCLs) and answer several controversially discussed questions on the nature of transport in this type of nanodevices. In contrast to previous approximate approaches, we show that the nature of transport in QCLs is sensitive to the applied bias voltage and can be tuned from the coherent to the incoherent regime. We point out that the elastic scattering at rough interfaces is among the most efficient incoherent scattering mechanisms in THz-QCLs and significantly influences the laser performance. Up to now, this has been utterly underestimated in approximate studies of THz-QCLs with direct optical transitions. All current theoretical models apply periodic (or field-periodic) boundary conditions on the transport in QCLs. Our revision of the open boundary conditions allows us to consider the QCL as an open quantum devices, instead. In this way, we illustrate that charge distributions in QCLs can develop periodicities that are only commensurable or even incommensurable with the QCL periodicity. This effect leads to efficient non-radiative transitions between the laser levels and is - due to the common periodic boundary conditions - completely missed in literature. We also propose several novel THz-QCLs with larger optical gain, lower thermal load and a higher resistivity against growth imperfections.

The third part of this thesis is dedicated to the spin transport in two-dimensional semiconductor heterostructures. It is common to apply an approximate envelope function model (EFT) for the spin-orbit interaction in such devices, in spite of the well-known fact that EFT calculations typically incorrectly predict the spin-splitting in semiconductor heterostructures. For this reason, we represent the NEGF method in the EFT model as well as in a microscopic atomistic tight binding model. In the later model, the spin-orbit interaction is treated nonperturbatively going far beyond the approximate EFT model. We show that the numerically efficient EFT model yields results that qualitatively agree with predictions of the numerically very demanding microscopic model. This allows us to study the spin polarization of propagating and confined carriers in two-dimensional semiconductor devices of complex geometries. We show that the spin polarization generated by the intrinsic spin-Hall effect cannot be significantly mediated by phonons into confined states. However, we demonstrate that the interferences of partially confined carriers can significantly enhance the local spin polarization to values of almost 100 %. We finally propose three and four terminal devices that act as efficient all-semiconductor nonmagnetic spin polarizers.

Introduction

State of the art semiconductor technology allows for the fabrication of semiconductor nanodevices on very short length scales. In recent scientific studies many types of semiconductor nanodevices have been presented with dimensions of 10 nm and smaller [1–3]. Even the commercial mass production of nanodevices has reached 45 nm length scale and the International Technology Roadmap for Semiconductors predicts a shrinkage of this scale below 10 nm during the next decade [4].

At these length scales, however, the transport is dominated by quantum mechanics such as interferences, quantum confinement and coherent tunneling. These effects complicate any intuitive explanation of the device properties. A thourough understanding of the electronic structure, the optical properties and the transport physics in nanometer scaled devices necessarily requires for a theoretical model. Since these devices are never free of imperfections, any charge carrier faces incoherent scattering. This is particularly true when the device temperatures exceed the temperature of liquid Helium and a significant number of phonons disrupt the coherent propagation. Therefore, a realistic model for the transport in semiconductor nanodevices has to treat carrier confinement, tunneling, quantum interferences and incoherent scattering on an equal footing.

It is well established that the nonequilibrium Green's function theory (NEGF) is a most general scheme for the prediction of coherent and incoherent quantum transport. Since its introduction in the 1960's, this formalism has been successfully applied on a great variety of transport problems. However, there is still only a rather limited number of textbooks about the NEGF formalism [5, 6] while most books about many particle physics concentrate on *equilibrium* Green's functions and add only some sections concerning the *nonequilibrium* Green's functions [7–10]. For this reason, we begin this thesis with a brief introduction to the NEGF formalism. Thereby, we start with the very fundamental definition of the one particle propagator and the time evolution of operators in the Heisenberg picture. We derive all the remaining expressions in this thesis from these two fundamental equations. The time dependence of the nonequilibrium Green's functions is particularly complicated when many particle interactions are taken into account. We present the common technique of transforming the Green's functions into the interaction picture and to approximate the transformation operators in a series expansion. In this way, we introduce the concept of scattering self-energies, a diagram technique and the corresponding Feynman rules. For illustrative reasons and for later reference, we end the first part of the thesis with the derivation of general self-energies describing the scattering of electrons with phonons and charged impurities.

Unfortunately, the NEGF formalism is too complicated to allow for *analytical* solutions for the transport in arbitrary nanodevices in the presence of incoherent scattering. Even *numerical* implementations of NEGF on realistic devices require for simplifying approximations. Due to the system's complexity, the effect of the common approximations on the results in realistic

devices is often hard to distinguish from intrinsic properties of the devices. The most failsafe way to assess these common approximations is to implement the NEGF formalism as exactly as possible and to apply the approximations only for comparison. For this purpose, we limit our considerations in the second part of this thesis to the comprehensible problem of stationary vertical transport in a single conduction band of layered semiconductor heterostructures. This transport problem has already been described frequently within the NEGF formalism. However, this has always been done with many approximations that we have to avoid and in order to assess them later on. Therefore, we first have to revise the common implementation of the NEGF method on vertical transport. In order to include all relevant incoherent scattering mechanisms, we derive several new scattering self-energies and prepare those self-energies that are given in literature for a numerically efficient implementation. The nice agreement of the resulting scattering rates with known analytical results of Fermi's golden rule illustrates the validity of our approximations. We calculate all scattering self-energies in the self-consistent Born approximation. This self-consistency increases the numerical load significantly, but we show that it is inevitable for the current conservation. Many approximations in the NEGF literature affect the semi-infinite leads that are implemented via open boundary conditions. We revise the approximations for the lead density of states and develop novel self-consistent models for the lead electron distribution and the electric fields at the lead/device boundaries. We also present numerical details of our implementation that are essential for a numerical efficient solution of the nonequilibrium Green's functions.

With this comparatively exact treatment of vertical transport, we are able to unveil artificial interferences that arise from common approximations of the lead density of states. We agree with findings in literature that the current density in the leads may only be ignored, when the device current density is very small. Nevertheless, the current in the leads can be modelled with a shifted Fermi distribution. In contrast to common models in literature, we find that the shift k_D of the lead Fermi distribution is not in general directly proportional to the current density. In particular, we show a superlinear increase of k_D for moderate current densities. We also consider common approximations concerning the scattering self-energies. We identify the validity limits for the neglect of the Pauli blocking and the exclusion of non-local scattering events. We also illustrate artifacts of the approximation of momentum and energy independent scattering self-energies. In particular, we find that the carrier thermalization in the wide-spread Büttiker probe scattering model is notoriously overestimated.

The vertical charge transport in THz quantum cascade lasers (THz-QCLs) has been frequently modelled within the NEGF formalism. All of the quantum cascade laser (QCL) studies in literature have implemented the NEGF formalism with periodic boundary conditions. These boundary conditions seem to be very appealing, since a typical QCL consists of several hundreds of periodically repeated semiconductor layers. However, non-periodic phenomena are thereby completely missed. Furthermore, periodic solutions of the Green's functions in a biased QCL essentially require for sufficient energy dissipation that thermalize the carrier distribution within each QCL period. A selective exclusion of one or several dissipation mechanisms that would clarify the relative importance of the various transport mechanisms is impossible if periodic boundary conditions are applied. Therefore, we apply the NEGF formalism on QCLs with open boundary conditions. Our revision of the common lead model (mentioned above) allows us to include an infinite number of QCL periods within the semi-infinite leads and to consider the QCL as an open quantum device. We calculate the electronic transport of a recently fabricated resonant phonon THz-QCL and find an excellent agreement with experimental results for the current-voltage characteristics, the optical gain as well as the laser performance as a

function of the heat sink temperature and the doping density. This comparison has been done in close cooperation with the experimental group of professor Karl Unterrainer at the Technische Universität Wien (Vienna, Austria) that fabricates and characterizes the THz-QCLs. We analyze in detail the transport properties of the resonant phonon THz-QCL and answer several controversially discussed questions. We find that the balance between coherent and incoherent transport critically depends on the applied bias voltage. By selectively turning on and off individual scattering mechanisms, we identify scattering at rough interfaces to dramatically reduce the occupation inversion and the optical gain. This is in contrast to previous suggestions of approximate studies in literature, but it is in agreement with experimental findings. We show that thermal backfilling and thermally activated phonon emission of electrons in the upper laser level are the dominant mechanisms that determine the maximum operating temperature of the QCL. Most notably, however, we find electron distributions that deviate from the QCL periodicity. In particular, we show that an incomplete thermalization in typical resonant phonon QCLs generates periodic electron distributions with a periodicity length that is - depending on the applied bias per period - commensurable or incommensurable with the QCL geometry. This effect allows non-radiative transitions between the laser levels in a large portion of the QCL periods and significantly worsens the performance of state of the art THz-QCLs. Due to the widespread periodic boundary conditions, this effect has been completely missed in literature. The experience we gain from these results allow us to propose several improved THz-QCL designs. We show how to modify present QCL designs in order to suppress the coherent leakage of the upper laser level and thereby to reduce the threshold current density. We show that this coherent leakage is particularly small in the "indirect pump"resonant phonon THz-QCLs proposed by Yaminishi *et al.* [11]. We propose in a cooperation with professor Kaz Hirakawa at the University of Tokyo (Tokyo, Japan) a four level "indirect pump"THz-QCL that exhibits a much larger optical gain than the common resonant phonon design. Furthermore, we propose a THz-QCL with a non-local photon transition. We agree with suggestions in literature, that non-radiative losses in QCLs with such "diagonal"optical transitions are much less likely. In particular, we find this novel QCL to be comparably insensitive to rough interfaces. Finally, we propose a novel double resonant phonon design that pins the electron distribution to the QCL geometry. In the latter design, the QCL periodicity is restored and non-radiative losses are efficiently suppressed.

In the last part of this thesis, we implement the NEGF formalism on the spin transport in two- and three-dimensional semiconductor heterostructures. The purpose of this part is first to demonstrate the applicability of our implementation of NEGF on systems of higher dimensionality and complexity. Second, we want to enlight several aspects of the spin-orbit interaction in semiconductor nanodevices. This interaction is known to give rise to the so-called spin-Hall effect, i.e. the spin accumulation on the lateral surfaces of a current-carrying sample. Since its recent experimental verification [12, 13], this effect has attracted great interest, because it is a promising candidate for efficient all-semiconductor spin polarizers. In order to analyze this and related effects, we implement the NEGF formalism in a common two-band envelope function approach. This continuum approach approximates the spin-orbit interaction with a interaction potential that is linear in the propagation momentum. Since band structure calculations have shown that such approximate continuum models may fail to describe the spin-orbit interaction, we additionally implement the NEGF formalism in a microscopic relativistic tight binding model. We extend the lead model of the previous part of this thesis to two- and three-dimensional, continuum and microscopic transport problems in order to guarantee reflectionless lead/device transitions. We also derive a novel self-energy for the inelastic scattering

with acoustic phonons in the self-consistent Born approximation. The particular symmetry of this self-energy allows for a numerically efficient, *self-consistent* inclusion of *inelastic* scattering in a two-dimensional transport problem. Up to now, either scattering in terms of the Büttiker probe model or only elastic scattering has been included in two-dimensional NEGF calculations. We compare the spin polarization in a quantum wire resulting from microscopic and approximate continuum calculations. We find that the commonly applied efficient two-band model gives indeed correct qualitative predictions of the spin-Hall effect in nanodevices. We show that interferences of carriers in semiconductor nanodevices in the presence of a finite spin-orbit interaction can yield spin polarization up to almost 100 %. However, this effect is strongly correlated with an efficient propagation and cannot be used to polarize the spin of confined carriers. Accordingly, we show that phonons cannot significantly mediate the spin polarization from propagating to confined carriers. Finally, we propose two new nanodevices that act as efficient non-magnetic all-semiconductor spin polarizers.

Part I

Introduction to nonequilibrium Green's functions theory

The first part of this thesis is meant to give a brief introduction in the nonequilibrium Green's function formalism that has been simultaneously developed by Schwinger [14], Kadanoff and Baym [5] as well as the Keldysh [15] in the 1960s. In order to combine conciseness as well as readability, we thereby combine several different studies in literature. Of course, we do not present a complete summary of the nonequilibrium Green's function theory, since this is far beyond the scope of this thesis. However, the major purpose of this introduction is to present a complete derivation of all transport equations that are relevant for this thesis - starting from the definition of the one-particle propagator. This brief introduction might be in particular useful for readers that are completely unfamiliar with the nonequilibrium Green's function theory. However, there is no "new"information given in this part of the thesis and we have to refer to the cited literature and textbooks about many-particle physics for more thorough presentations of this formalism. Nevertheless, we require several of the equations derived here in later parts of this thesis.

We start with the definition of the Green's function in the Heisenberg picture and transform it into the interaction picture. Thereby, we introduce the common notation of contour ordered Green's functions. We show that any many-particle interaction potential involves many-particle Green's functions in the equation of motion of one-particle Green's functions. In order to gain a closed set of differential equations of motion for the one-particle Green's function, we introduce the common concept of scattering self-energies.

The time evolution of the one-particle Green's function in the presence of many-particle interactions is very complex. Thus we have to perform a perturbation expansion with respect to the many-particle interaction. It is very common to define additional Green's functions by parts of the contour ordered Green's function and to perform the perturbation expansion for those additional Green's functions. Unfortunately, there is no unique notation for these additional Green's functions in literature. For this reason, we introduce the most common notation as well as the notation that is most suited for the perturbation expansion. We exemplify the perturbation expansion in linear order and introduce a diagrammatic technique and Feynman rules for the expansion in arbitrary order. In this way, we introduce the self-consistent Born approximation and derive the differential Dyson equations. We end our introduction in the nonequilibrium Green's function formalism with the derivation of two scattering self-energies that are frequently applied in this thesis.

Chapter 1

Contour ordered nonequilibrium Green's function

1.1 Introduction

We introduce in the Heisenberg picture the fundamental definition of one-particle Green's functions in arbitrary nonequilibrium systems. Since the time dependence of operators in the Heisenberg picture becomes complicated when many-particle interactions and transient effects are present, we transform the Green's function into the interaction picture. Such transformations do not simplify the Green's function per se, but they allow for consistent perturbation expansions of the Green's function in later chapters. However, these transformations involve complicated contour integrals. We derive fundamental symmetry relations that allow to simplify and approximate the complicated integration contours with the simple Keldysh contour.

Starting from its definition, we derive the equation of motion for an arbitrary fermionic Green's function. We show that any many-particle interaction involves many-particle Green's functions in the equation of motion of the one-particle Green's function. In order to reduce the complexity of the equations, we follow the common approach and approximate the many-particle Green's functions with products of one-particle Green's functions. In this way, we introduce the concept of self-energies and gain a closed and complete system of differential equations for the one-particle Green's function.

1.2 Propagator in different pictures

1.2.1 Definition in the Heisenberg picture

Propagators are often called Green's functions. This stems from the fact that the propagator can be viewed as the solution of a specific differential equation. In this thesis, we do not differ between the terms "propagator"and "Green's function", since most of the differential equations in this thesis are indeed solved by the propagator. Therefore, we define the one-particle "Green's function"G with the particle operators $(\hat{\psi},\hat{\psi}^{\dagger})$ in the Heisenberg picture (denoted with subindex $\mathcal{H}$)

$$G\left(\vec{x}_1,t_1;\vec{x}_2,t_2\right)\equiv -i\left\langle \phi\left|\hat{T}\left[\hat{\psi}_{\mathcal{H}}\left(\vec{x}_1,t_1\right)\hat{\psi}^{\dagger}_{\mathcal{H}}\left(\vec{x}_2,t_2\right)\right]\right|\phi\right\rangle/\hbar. \tag{1.2.1}$$

This is the expectation value of an operator that first adds a single particle at position $\vec{x}_2$ and at the time t_2 to the system in state ϕ and then removes a single particle at position $\vec{x}_1$ and at time t_1 so that we finally end up with the system back in the state ϕ. Therefore, the Green's function is closely related to the propagation of a particle between the points $\vec{x}_1$ and $\vec{x}_2$ during the time interval $[t_1, t_2]$. The causality of this process enters the formula with the time ordering operator $\hat{T}$, which orders operators of later times to the left. At finite temperatures and with many particles in the system, the state ϕ is unknown and this expectation value is given from statistics

$$G\left(\vec{x}_1, t_1; \vec{x}_2, t_2\right) = -\frac{i}{\hbar} \operatorname{Tr}\left\{\hat{\rho}_{\mathcal{H}}\left(\hat{H}\right) \hat{T}\left[\hat{\psi}_{\mathcal{H}}\left(\vec{x}_1, t_1\right) \hat{\psi}^{\dagger}_{\mathcal{H}}\left(\vec{x}_2, t_2\right)\right]\right\}, \tag{1.2.2}$$

with the density matrix $\hat{\rho}$ of the canonical ensemble

$$\hat{\rho}_{\mathcal{H}}\left(\hat{h}\right) = \frac{\exp\left(-\beta \hat{h}\right)}{\operatorname{Tr} \exp\left(-\beta \hat{h}\right)}. \tag{1.2.3}$$

Here, β is the inverse product of temperature T and Boltzmann constant k_B

$$\beta = \left(k_B T\right)^{-1} \tag{1.2.4}$$

and the $\operatorname{Tr}\left(\hat{O}\right)$ denotes the trace over the expectation values of an arbitrary operator $\hat{O}$ with respect to a complete set of system states $|\phi_n\rangle$

$$\operatorname{Tr}\left(\hat{O}\right) \equiv \sum_n \left\langle \phi_n | \hat{O} | \phi_n \right\rangle. \tag{1.2.5}$$

1.2.2 Transformation into the interaction picture

We separate the system's Hamilton operator $\hat{H}(t)$ into time independent $(\hat{h})$ and time dependent $(\hat{H}'(t))$ contributions

$$\hat{H}(t) = \hat{h} + \hat{H}'(t). \tag{1.2.6}$$

For example, interactions with external time-dependent disturbances such as oscillating electric fields are included in $\hat{H}'(t)$. We can simplify the time dependence of any operator, if we transform the operators from the Heisenberg picture into the interaction picture [16]

$$\hat{O}_{\mathcal{H}}(t) = \hat{u}^{\dagger}(t, t_0)\, \hat{O}_{\hat{h}}(t)\, \hat{u}(t, t_0). \tag{1.2.7}$$

Here, the index $\hat{h}$ denotes the time evolution of an operator in the interaction picture with respect to the time independent part of the system's Hamilton operator $\hat{h}$. When we assume the time dependent perturbation $\hat{H}'(t)$ to vanish for times prior to t_0, the unitary transformation $\hat{u}(t, t_0)$ reads

$$\hat{u}(t, t_0) = \hat{T} \exp\left(-\frac{i}{\hbar} \int_{t_0}^{t} \hat{H}'_{\hat{h}}(t')\, \mathrm{d}t'\right), \tag{1.2.8}$$

with the time dependent part of the Hamiltonian evolving due to $\hat{h}$

$$\hat{H}'_{\hat{h}}(t) = \exp\left(\frac{i}{\hbar} \hat{h}\,(t - t_0)\right) \hat{H}'(t) \exp\left(-\frac{i}{\hbar} \hat{h}\,(t - t_0)\right). \tag{1.2.9}$$

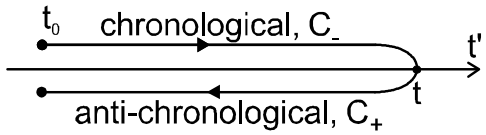

Figure 1.2.1: Contour for the transformation integral from Heisenberg to interaction picture. The perturbing part of the Hamiltonian, $\hat{H}_i(t)$ vanishes for times earlier than t_0. The small shift of the two contour branches are only meant to clarify the integration direction ($t' \in \mathbb{R}$).

The time ordering operator $\hat{T}$ orders operators at later times to the left, whereas its Hermitian conjugated $\hat{T}^\dagger$ orders operators at later times to the right

$$\hat{T}\left(\hat{\psi}(\vec{x}_1,t_1)\,\hat{\psi}^\dagger(\vec{x}_2,t_2)\right) = \begin{cases} \hat{\psi}(\vec{x}_1,t_1)\,\hat{\psi}^\dagger(\vec{x}_2,t_2)\,, \text{ for } t_1 > t_2 \\ \mp\hat{\psi}^\dagger(\vec{x}_2,t_2)\,\hat{\psi}(\vec{x}_1,t_1)\,, \text{ for } t_2 > t_1 \end{cases}. \tag{1.2.10}$$

Upper signs refer to fermions, lower signs to bosons. It is common (see e.g. [6]) to merge the two transformation integrals in Eq. (1.2.7) into an integral along the contour C (see Fig. 1.2.1)

$$\hat{O}_{\mathcal{H}} = \hat{T}_C \exp\left(-\frac{i}{\hbar}\int_C \hat{H}'_{\hat{h}}(t')\,\mathrm{d}t'\right)\hat{O}_h(t)\,. \tag{1.2.11}$$

Depending on the integration direction, the contour branches are called chronological (C_-) or anti-chronological (C_+). It is important to note that the small shift of the contour branches up- and downwards from the time axis is only meant to clarify the integration direction. Thus, the time variables are still real entities ($t \in \mathbb{R}$). The time ordering operator on the contour $\hat{T}_C$ is a piecewise composition of $\hat{T}$ and $\hat{T}^\dagger$

$$\hat{T}_C\hat{a}(t) \equiv \begin{cases} \hat{T}\hat{a}(t)\,, \forall t \in C_- \\ \hat{T}^\dagger\hat{a}(t)\,, \forall t \in C_+ \end{cases}. \tag{1.2.12}$$

Apart from one-particle contributions that we denote with $\hat{H}_0$, the time independent operator $\hat{h}$ may still contain sophisticated many body interactions ($\hat{H}^i$) that complicate the time dependence of all operators

$$\hat{h} = \hat{H}_0 + \hat{H}^i. \tag{1.2.13}$$

Therefore, it is useful to transform all operators again into the interaction picture, but now with respect to these many body interactions $\hat{H}^i$. Consequently, the time development of the interaction part of the Hamilton operator reads in the interaction picture

$$\hat{H}^i_{\hat{H}_0}(t) = \exp\left(\frac{i}{\hbar}\hat{H}_0(t-t_0)\right)\hat{H}^i\exp\left(-\frac{i}{\hbar}\hat{H}_0(t-t_0)\right). \tag{1.2.14}$$

We assume the time dependent part of the Hamiltonian ($\hat{H}_{\hat{h}}(t)$) to oscillate too rapidly to affect the system's density matrix ρ. However, we can not assume the density matrix to be independent of the many body interactions ($\hat{H}^i$), because the time t_0 at which these interactions "have set in"is $t_0 \to -\infty$. In order to separate all terms containing $\hat{H}^i$ in the transformation formulas, Rammer and Smith [17] have rewritten the statistical operator into an integral over imaginary times

$$\exp\left(-\beta\hat{h}\right) = \exp\left(-\beta\hat{H}_0\right)\hat{T}^*\exp\left(-\frac{i}{\hbar}\int_{t_0}^{t_0-i\hbar\beta}\hat{H}^i_{\hat{H}_0}(t')\,\mathrm{d}t'\right), \tag{1.2.15}$$

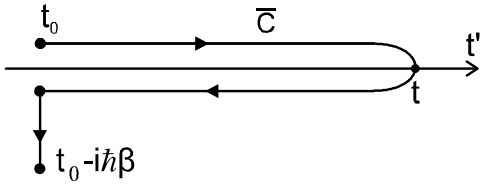

Figure 1.2.2: Combined contour for the transformation integral into interaction picture. The small shift of the two contour branches are only meant to clarify the integration direction. Apart from the section $[t_0; t_0 - i\hbar\beta]$, all time values on the contour are real ($t' \in \mathbb{R}$).

where $\hat{T}^*$ orders operators with larger imaginary times to the left. Thus, when the Green's function at finite temperatures (Eq. (1.2.2)) is transformed into the interaction picture, its formula is modified by the integrals given in Eqs. (1.2.11) and (1.2.15). The two transformation integrals and the integral of the last equation can be merged into an integral along the contour $\bar{C}$ (compare with Fig. 1.2.2), when we define a combined time ordering operator $\hat{T}_{\bar{C}}$ on this new contour

$$\hat{T}_{\bar{C}} \equiv \begin{cases} \hat{T}_C, \ \forall\ t \in C \\ \hat{T}^*, \ \text{elsewhere} \end{cases} . \tag{1.2.16}$$

In summary, the contour ordered nonequilibrium Green's function at finite temperatures reads in the interaction picture

$$G\left(\vec{x}_1, t_1; \vec{x}_2, t_2\right) = -\frac{i}{\hbar} \frac{\mathrm{Tr}\left\{\exp\left(-\beta\hat{H}_0\right)\left[\hat{S}_{\bar{C}}\hat{S}_C\hat{T}\left(\hat{\psi}_{\hat{H}_0}\left(\vec{x}_1, t_1\right)\hat{\psi}^\dagger_{\hat{H}_0}\left(\vec{x}_2, t_2\right)\right)\right]\right\}}{\mathrm{Tr}\left\{\exp\left(-\beta\hat{H}_0\right)\hat{S}_{\bar{C}}\hat{S}_C\right\}}, \tag{1.2.17}$$

with the transformation with respect to the interaction Hamiltonian

$$\hat{S}_{\bar{C}} = \hat{T}_{\bar{C}} \exp\left(-\frac{i}{\hbar}\int_{\bar{C}} \hat{H}^i_{\hat{H}_0}\left(t'\right) \mathrm{d}t'\right) \tag{1.2.18}$$

and the transformation with respect to the time dependent part of the Hamiltonian

$$\hat{S}_C = \hat{T}_C \exp\left(-\frac{i}{\hbar}\int_{C} \hat{H}'_{\hat{H}_0}\left(t'\right) \mathrm{d}t'\right). \tag{1.2.19}$$

1.3 Keldysh contour

In this work, we are primarily interested in stationary phenomena. Therefore all transients are assumed to have died out and we apply the limit $t_0 \to -\infty$ as is frequently done in literature [6, 17, 18]. This allows us to simplify the transformation contour we have introduced in the preceding section. The contribution of the integral along the finite distance $[t_0, t_0 - i\beta\hbar]$ in Fig. 1.2.2 is negligible compared to the infinite integral over the rest of $\bar{C}$. Then, the two transformation contours C (Fig. 1.2.1) and $\bar{C}$ (Fig. 1.2.2) coincide and the two transformation integrals can be merged into one*

$$\hat{S}_{C,\mathrm{total}} = \hat{T}_C \exp\left(-\frac{i}{\hbar}\int_{C} \left(\hat{H}^i_{\hat{H}_0}\left(t'\right) + \hat{H}'_{\hat{H}_0}\left(t'\right)\right) \mathrm{d}t'\right). \tag{1.3.1}$$

*In stationary problems, the explicitly time dependent Hamiltonian $\hat{H}'\left(t\right)$ vanishes.

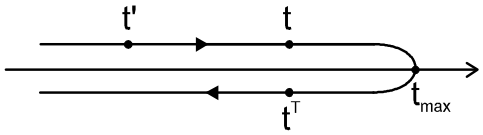

Figure 1.3.1: Contour for the transformation integral into interaction picture under the assumption $t_0 \to -\infty$. t^T marks the opposing time of t and $t_{\max}$ the maximum of $|t|$ on the contour. The small shift of the two contour branches are only meant to clarify the integration direction ($t \in \mathbb{R}$).

In order to simplify the contour further, we follow Danielewicz [19] and derive a symmetry relation. Let us assume $t > t'$. When we define t^T to equal t but to lie on the opposing contour branch (see Fig. 1.3.1), then* $t^T > t'$ and the time ordering operator $\hat{T}$ orders the particle operators of the time arguments t^T and t' in the same way as the operators at the times t and t'. Therefore we get the symmetry relation

$$G\left(\vec{x}, t; \vec{x}', t'\right) = G\left(\vec{x}, t^T; \vec{x}', t'\right). \tag{1.3.2}$$

The same relation holds for the second time argument of the Green's function, when $t' > t$. Therefore, when we increase the transformation contour so that the maximum value of all times on the contour $t_{\max}$ exceeds t, additional contributions of the Green's function appear in the transformation integral. These additional terms enter the formulas twice, once for the chronological branch, i.e. an integral from t to $t_{\max}$ and once for the anti-chronological branch, i.e. an integral from $t_{\max}$ to t^T. Since the two branches have opposite integration orientations but equal integrands (see Eq. (1.3.2)), these additional contributions cancel each other. Therefore, we may expand the contour C into the Keldysh contour, i.e. to shift $t_{\max} \to \infty$ (see Fig. 1.3.2). Finally, the nonequilibrium Green's function given on the Keldysh contour reads

$$G\left(\vec{x}_1, t_1; \vec{x}_2, t_2\right) = -\frac{i}{\hbar} \frac{\mathrm{Tr}\left[\exp\left(-\beta \hat{H}_0\right) \hat{S}_{C,\mathrm{total}} \hat{T}\left(\hat{\psi}_{\hat{H}_0}\left(\vec{x}_1, t_1\right) \hat{\psi}^{\dagger}_{\hat{H}_0}\left(\vec{x}_2, t_2\right)\right)\right]}{\mathrm{Tr}\left[\exp\left(-\beta \hat{H}_0\right) \hat{S}_{C,\mathrm{total}}\right]}. \tag{1.3.3}$$

We can abbreviate the trace over the statistical operator with

$$\langle \ldots \rangle \equiv \frac{\mathrm{Tr}\left[\exp\left(-\beta \hat{H}_0\right) \ldots\right]}{\mathrm{Tr} \exp\left(-\beta \hat{H}_0\right)} \tag{1.3.4}$$

and get for the Keldysh contour ordered Green's function

$$G\left(\vec{x}_1, t_1; \vec{x}_2, t_2\right) = -\frac{i}{\hbar} \left\langle \hat{S}_{C,\mathrm{total}} \hat{T}\left(\hat{\psi}_{\hat{H}_0}\left(\vec{x}_1, t_1\right) \hat{\psi}^{\dagger}_{\hat{H}_0}\left(\vec{x}_2, t_2\right)\right)\right\rangle. \tag{1.3.5}$$

We can follow the common approach (see e.g. [6]) and commute the time ordering operator $\hat{T}$ with the transformation $\hat{S}_{C,\mathrm{total}}$ in the last equation. For this purpose, we have to replace $\hat{T}$ with the contour ordered time ordering operator $\hat{T}_C$ and keep in mind that this time ordering operator

*Please not again that all time variables are real ($t \in \mathbb{R}$). The shift into the complex plain in the figures is only meant to highlight the integration direction.

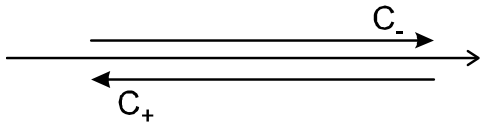

Figure 1.3.2: The Keldysh contour for the transformaion into interaction picture. The small shift of the two contour branches are only meant to clarify the integration direction.

acts only on the particle operators at times t_1 and t_2, irrespective whether the transformation operator $\hat{S}_{C,\text{total}}$ is written to the left or right of $\hat{T}_C$. In this way, we can define the contour ordered Green's function in the Heisenberg picture

$$G\left(\vec{x}_1,t_1;\vec{x}_2,t_2\right)=-\frac{i}{\hbar}\left\langle \hat{T}_C\left[\hat{\psi}_{\mathcal{H}}\left(\vec{x}_1,t_1\right)\hat{\psi}^{\dagger}_{\mathcal{H}}\left(\vec{x}_2,t_2\right)\right]\right\rangle . \tag{1.3.6}$$

1.4 Equations of motion of fermionic Green's functions

1.4.1 Many-particle Green's functions

In this thesis, we assume the bosons to stay in thermal equilibrium and to maintain a density of states corresponding to homogeneous systems. In addition, we assume the density matrix of the system to change so slowly with time that we may neglect its time derivative. Therefore, we concentrate in the following on the propagation of a single fermion. When we take the derivative of the fermionic Green's function with respect to either propagation time, we get [5]

$$i\hbar\partial_{t_1}G\left(\vec{x}_1,t_1;\vec{x}_2,t_2\right)=\delta_C\left(\vec{x}_1,t_1;\vec{x}_2,t_2\right)+\frac{-i}{\hbar}\left\langle \hat{T}_C\left(i\hbar\partial_{t_1}\hat{\psi}_{\mathcal{H}}\left(\vec{x}_1,t_1\right)\right)\hat{\psi}^{\dagger}_{\mathcal{H}}\left(\vec{x}_2,t_2\right)\right\rangle \tag{1.4.1}$$

and

$$-i\hbar\partial_{t_2}G\left(\vec{x}_1,t_1;\vec{x}_2,t_2\right)=\delta_C\left(\vec{x}_1,t_1;\vec{x}_2,t_2\right)+\frac{-i}{\hbar}\left\langle \hat{T}_C\hat{\psi}_{\mathcal{H}}\left(\vec{x}_1,t_1\right)\left(-i\hbar\partial_{t_2}\hat{\psi}^{\dagger}_{\mathcal{H}}\left(\vec{x}_2,t_2\right)\right)\right\rangle \tag{1.4.2}$$

with δ_C, the δ-distribution defined on the Keldysh contour

$$\delta_C\left(\vec{x}_1,t_1;\vec{x}_2,t_2\right)\equiv\begin{cases}\delta\left(\vec{x}_1-\vec{x}_2\right)\delta\left(t_1-t_2\right),\ \forall t_1,t_2\in C_-\\ -\delta\left(\vec{x}_1-\vec{x}_2\right)\delta\left(t_1-t_2\right),\ \forall t_1,t_2\in C_+\\ 0,\ \text{elsewhere}\end{cases}. \tag{1.4.3}$$

Hereby, the δ-distribution originates from the commutation of the time derivative with the ordering operator $\hat{T}_C$. In order to derive the Dyson equations, let us consider a general Hamilton operator that includes arbitrary one- and two-particle interaction potentials

$$\begin{aligned}\hat{H} &= \int_C \mathrm{d}\vec{x}\mathrm{d}t\hat{\psi}^{\dagger}_{\mathcal{H}}\left(\vec{x},t\right)\left[H_0\left(\vec{x},t\right)+U\left(\vec{x},t\right)\right]\hat{\psi}_{\mathcal{H}}\left(\vec{x},t\right)+\frac{1}{2}\int_C \mathrm{d}\vec{x}_1\mathrm{d}t_1\mathrm{d}\vec{x}_2\mathrm{d}t_2\left[\hat{\psi}^{\dagger}_{\mathcal{H}}\left(\vec{x}_1,t_1\right)\hat{\psi}^{\dagger}_{\mathcal{H}}\left(\vec{x}_2,t_2\right)\right.\\ &\left.\times W\left(\vec{x}_1,t_1;\vec{x}_2,t_2\right)\hat{\psi}_{\mathcal{H}}\left(\vec{x}_2,t_2\right)\hat{\psi}_{\mathcal{H}}\left(\vec{x}_1,t_1\right)\right].\end{aligned} \tag{1.4.4}$$

Here, H_0 and U represent the free-particle Hamiltonian and a single-particle potential, respectively. We also consider a two-particle interaction potential given by W. Since the time

dependence of the particle operators is given in the interaction picture, the time integrals of H_0, U and W are taken along the Keldysh contour C. With the help of the fermionic anticommutator rules

$$\begin{aligned}\left[\hat{\psi}\left(\vec{x}_1,t_1\right),\hat{\psi}\left(\vec{x}_2,t_2\right)\right]_+ &= \left[\hat{\psi}^\dagger\left(\vec{x}_1,t_1\right),\hat{\psi}^\dagger\left(\vec{x}_2,t_2\right)\right]_+ = 0\\ \left[\hat{\psi}\left(\vec{x}_1,t_1\right),\hat{\psi}^\dagger\left(\vec{x}_2,t_2\right)\right]_+ &= \delta\left(\vec{x}_1-\vec{x}_2\right)\delta\left(t_1-t_2\right)\end{aligned} \tag{1.4.5}$$

the derivatives of the particle operators with respect to time are given by the Heisenberg equation

$$\begin{aligned}i\hbar\partial_t\hat{\psi}_{\mathcal{H}}\left(\vec{x}_1,t_1\right) &= \left[\hat{\psi}_{\mathcal{H}}\left(\vec{x}_1,t_1\right),\hat{H}\right]_-\\ &= \left[H_0\left(\vec{x}_1,t_1\right)+U\left(\vec{x}_1,t_1\right)\right]\hat{\psi}_{\mathcal{H}}\left(\vec{x}_1,t_1\right)+\int_C \mathrm{d}\vec{x}_2\mathrm{d}t_2\left[W\left(\vec{x}_1,t_1;\vec{x}_2,t_2\right)\hat{\psi}^\dagger_{\mathcal{H}}\left(\vec{x}_2,t_2\right)\right.\\ &\quad\left.\times\hat{\psi}_{\mathcal{H}}\left(\vec{x}_2,t_2\right)\hat{\psi}_{\mathcal{H}}\left(\vec{x}_1,t_1\right)\right]\end{aligned} \tag{1.4.6}$$

and

$$\begin{aligned}&-i\hbar\partial_t\hat{\psi}^\dagger_{\mathcal{H}}\left(\vec{x}_2,t_2\right)\\ =\ &\left[\hat{\psi}^\dagger_{\mathcal{H}}\left(\vec{x}_2,t_2\right),\hat{H}\right]_-\\ =\ &\left[H_0\left(\vec{x}_2,t_2\right)+U\left(\vec{x}_2,t_2\right)\right]\hat{\psi}_{\mathcal{H}}\left(\vec{x}_2,t_2\right)+\int_C \mathrm{d}\vec{x}_2\mathrm{d}t_2\left[W\left(\vec{x}_1,t_1;\vec{x}_2,t_2\right)\hat{\psi}^\dagger_{\mathcal{H}}\left(\vec{x}_2,t_2\right)\right.\\ &\left.\times\hat{\psi}_{\mathcal{H}}\left(\vec{x}_2,t_2\right)\hat{\psi}_{\mathcal{H}}\left(\vec{x}_2,t_2\right)\right].\end{aligned} \tag{1.4.7}$$

We set these results into the derivatives of the fermionic Green's function and get

$$\begin{aligned}&i\hbar\partial_{t_1}G\left(\vec{x}_1,t_1;\vec{x}_2,t_2\right)\\ =\ &\delta_C\left(\vec{x}_1,t_1;\vec{x}_2,t_2\right)+\left[H_0\left(\vec{x}_1,t_1\right)+U\left(\vec{x}_1,t_1\right)\right]G\left(\vec{x}_1,t_1;\vec{x}_2,t_2\right)\\ &-i\hbar\lim_{\substack{\vec{x}_3\to\vec{x}_4\\ t_3\to t_4}}\int_C \mathrm{d}\vec{x}_4\mathrm{d}t_4 W\left(\vec{x}_1,t_1;\vec{x}_3,t_3\right)G_2\left(\vec{x}_1,t_1;\vec{x}_4,t_4;\vec{x}_2,t_2;\vec{x}_3,t_3\right)\end{aligned} \tag{1.4.8}$$

and

$$\begin{aligned}&-i\hbar\partial_{t_2}G\left(\vec{x}_1,t_1;\vec{x}_2,t_2\right)\\ =\ &\delta_C\left(\vec{x}_1,t_1;\vec{x}_2,t_2\right)+G\left(\vec{x}_1,t_1;\vec{x}_2,t_2\right)\left[H_0\left(\vec{x}_2,t_2\right)+U\left(\vec{x}_2,t_2\right)\right]\\ &-i\hbar\lim_{\substack{\vec{x}_3\to\vec{x}_4\\ t_3\to t_4}}\int_C \mathrm{d}\vec{x}_4\mathrm{d}t_4 G_2\left(\vec{x}_1,t_1;\vec{x}_4,t_4;\vec{x}_2,t_2;\vec{x}_3,t_3\right)W\left(\vec{x}_2,t_2;\vec{x}_3,t_3\right).\end{aligned} \tag{1.4.9}$$

Here, we have introduced the two-particle fermionic Green's function [5]

$$\begin{aligned}&G_2\left(\vec{x}_1,t_1;\vec{x}_4,t_4;\vec{x}_2,t_2;\vec{x}_3,t_3\right)\\ \equiv\ &-\left\langle\hat{T}_C\left(\hat{\psi}_{\mathcal{H}}\left(\vec{x}_1,t_1\right)\hat{\psi}_{\mathcal{H}}\left(\vec{x}_4,t_4\right)\hat{\psi}^\dagger_{\mathcal{H}}\left(\vec{x}_3,t_3\right)\hat{\psi}^\dagger_{\mathcal{H}}\left(\vec{x}_2,t_2\right)\right)\right\rangle/\hbar^2.\end{aligned} \tag{1.4.10}$$

In a similar fashion, three- and more-particle interactions involve three- and more-particle Green's functions in the equation of motion of the one-particle Green's function. Analogously to this, the equation of motion of the two-particle Green's function evolving under the influence of a two- (or many-) particle interaction potential introduces Green's functions of even more particles (see [5]).

1.4.2 Self-energies

We have seen in the preceding section that an exact solution of the one-particle propagation (facing at least two-particle interactions) would require for the knowledge of Green's functions that describe the correlated propagation of arbitrary many particles. In order to keep the complexity of our equations manageable, we have to approximate the correlated propagation of two particles and limit our equations to single-particle Green's functions. We may do so, because the major focus of this work is the transport of electrons in semiconductor heterostructures. Here, typical electron densities are not large enough that three particle scattering events or correlations between several two-particle scattering events play a crucial role. Furthermore, particle-particle correlations are not expected to influence the charge transport or the resonant states in the devices significantly, in contrast to e.g. exciton-exciton correlations in faintly doped quantum wells or superconductivity in metals at low temperatures. In the Hartree-Fock approximation, i.e. in lowest order in W, this two particle Green's function is approximated by

$$\begin{aligned} & G_2\left(\vec{x}_1,t_1;\vec{x}_4,t_4;\vec{x}_2,t_2;\vec{x}_3,t_3\right) \\ \approx\ & G\left(\vec{x}_1,t_1;\vec{x}_2,t_2\right)G\left(\vec{x}_4,t_4;\vec{x}_3,t_3\right)-G\left(\vec{x}_1,t_1;\vec{x}_3,t_3\right)G\left(\vec{x}_4,t_4;\vec{x}_2,t_2\right). \end{aligned} \tag{1.4.11}$$

The first term (Hartree term) on the right side of the last equation describes the independent propagation of two fermions with origins $(\vec{x}_3,t_3)$ and $(\vec{x}_2,t_2)$ to the target points $(\vec{x}_1,t_1)$ and $(\vec{x}_4,t_4)$. Since fermions are indistinguishable particles, we have also to take into account a propagation with flipped coordinates, which gives the second term (Fock term). The asymmetry of fermionic wave functions under particle exchange gives the negative sign of the Fock term. This approximation simplifies the time derivatives of the fermionic one-particle Green's function to

$$\begin{aligned} i\hbar\partial_{t_1}G\left(\vec{x}_1,t_1;\vec{x}_2,t_2\right) &= \delta_C\left(\vec{x}_1,t_1;\vec{x}_2,t_2\right)+\left[H_0\left(\vec{x}_1,t_1\right)+U\left(\vec{x}_1,t_1\right)\right]G\left(\vec{x}_1,t_1;\vec{x}_2,t_2\right) \\ &\quad -i\hbar\lim_{\substack{\vec{x}_3\to\vec{x}_4\\ t_3\to t_4}}\int_C \mathrm{d}\vec{x}_4\mathrm{d}t_4 W\left(\vec{x}_1,t_1;\vec{x}_4,t_4\right)\left[G\left(\vec{x}_1,t_1;\vec{x}_2,t_2\right)G\left(\vec{x}_4,t_4;\vec{x}_3,t_3\right)\right. \\ &\quad \left.-G\left(\vec{x}_1,t_1;\vec{x}_3,t_3\right)G\left(\vec{x}_4,t_4;\vec{x}_2,t_2\right)\right] \end{aligned} \tag{1.4.12}$$

and

$$\begin{aligned} -i\hbar\partial_{t_2}G\left(\vec{x}_1,t_1;\vec{x}_2,t_2\right) &= \delta_C\left(\vec{x}_1,t_1;\vec{x}_2,t_2\right)+G\left(\vec{x}_1,t_1;\vec{x}_2,t_2\right)\left[H_0\left(\vec{x}_2,t_2\right)+U\left(\vec{x}_2,t_2\right)\right] \\ &\quad -i\hbar\lim_{\substack{\vec{x}_3\to\vec{x}_4\\ t_3\to t_4}}\int_C \mathrm{d}\vec{x}_4\mathrm{d}t_4 W\left(\vec{x}_2,t_2;\vec{x}_4,t_4\right)\left[G\left(\vec{x}_1,t_1;\vec{x}_2,t_2\right)G\left(\vec{x}_4,t_4;\vec{x}_3,t_3\right)\right. \\ &\quad \left.-G\left(\vec{x}_1,t_1;\vec{x}_3,t_3\right)G\left(\vec{x}_4,t_4;\vec{x}_2,t_2\right)\right]. \end{aligned} \tag{1.4.13}$$

Kadanoff and Baym have shown in [5] that any approximation of the two-particle Green's function has to obey two conditions in order to guarantee the particle number-, momentum-, and energy-conservation laws, which we repeat here for later reference:

1. The one-particle Green's function $G\left(\vec{x}_1,t_1;\vec{x}_2,t_2\right)$ solves the Eqs. (1.4.12) and (1.4.13).
2. The (approximated) two-particle Green's function is symmetric with respect to a twofold coordinate exchange

$$G_2\left(\vec{x}_1,t_1;\vec{x}_4,t_4;\vec{x}_2,t_2;\vec{x}_3,t_3\right)=G_2\left(\vec{x}_4,t_4;\vec{x}_1,t_1;\vec{x}_3,t_3;\vec{x}_2,t_2\right). \tag{1.4.14}$$

Kadanoff and Baym also exemplified that the Hartree-Fock approximation Eq. (1.4.11) fulfills these requirements. However, we stress here for later reference, that the approximate products in Eq. (1.4.11) involve one particle Green's functions of the same kind, i.e. according to the same Hamilton operator. We will explicitly elaborate in Sec. 3.5.7 that approximating the two particle Green's function in Eq. (1.4.11) with one-particle Green's functions of different scattering environment* violates current conservation. It is common to abbreviate the interaction integrals of the respective last two lines of these equations with the definition of a fermionic self-energy Σ

$$\begin{aligned}\Sigma\left(\vec{x}_1,t_1;\vec{x}_2,t_2\right) \equiv & -i\hbar\delta\left(\vec{x}_1-\vec{x}_2\right)\delta\left(t_1-t_2\right)\int_C \mathrm{d}\vec{x}_3\mathrm{d}t_3 W\left(\vec{x}_1,t_1;\vec{x}_3,t_3\right)G\left(\vec{x}_3,t_3;\vec{x}_3,t_3\right)\\ & +i\hbar W\left(\vec{x}_1,t_1;\vec{x}_2,t_2\right)G\left(\vec{x}_1,t_1;\vec{x}_2,t_2\right). \end{aligned} \tag{1.4.15}$$

Now, the equations of motion of the fermionic one-particle Green's function can be rewritten to the common differential formulation of the Dyson equations

$$\begin{aligned}i\hbar\partial_{t_1}G\left(\vec{x}_1,t_1;\vec{x}_2,t_2\right) = & \delta_C\left(\vec{x}_1,t_1;\vec{x}_2,t_2\right)+\left[H_0\left(\vec{x}_1,t_1\right)+U\left(\vec{x}_1,t_1\right)\right]G\left(\vec{x}_1,t_1;\vec{x}_2,t_2\right)\\ & +\lim_{\substack{\vec{x}_3\to\vec{x}_4\\ t_3\to t_4}}\int_C \mathrm{d}\vec{x}_4\mathrm{d}t_4\Sigma\left(\vec{x}_1,t_1;\vec{x}_3,t_3\right)G\left(\vec{x}_4,t_4;\vec{x}_2,t_2\right) \end{aligned} \tag{1.4.16}$$

and

$$\begin{aligned}-i\hbar\partial_{t_2}G\left(\vec{x}_1,t_1;\vec{x}_2,t_2\right) = & \delta_C\left(\vec{x}_1,t_1;\vec{x}_2,t_2\right)+G\left(\vec{x}_1,t_1;\vec{x}_2,t_2\right)\left[H_0\left(\vec{x}_2,t_2\right)+U\left(\vec{x}_2,t_2\right)\right]\\ & +\lim_{\substack{\vec{x}_3\to\vec{x}_4\\ t_3\to t_4}}\int_C \mathrm{d}\vec{x}_4\mathrm{d}t_4 G\left(\vec{x}_1,t_1;\vec{x}_3,t_3\right)\Sigma\left(\vec{x}_4,t_4;\vec{x}_2,t_2\right). \end{aligned} \tag{1.4.17}$$

When we compare the last equations with the Schrödinger equation (considering the Green's functions as wave functions), it is obvious that the real part of the self-energy Σ shifts the eigenenergies, whereas the imaginary part causes a damping in the states' time evolution and thereby limits the state life time.

By introducing self-energies, the two-particle Green's functions are approximated with products of one-particle Green's functions. Physically, this means that we neglect correlations in the propagation of two (and many) particles. Such an approximation cannot be applied in systems of high particle densities or in transport problems with focus on correlation effects such as entanglement. Our major focus in this thesis, however, is the transport of electrons and holes in semiconductor nanodevices. In these systems, the particle density as well as the dephasing length are in a regime, where correlated transport may be neglected.

*As is done in the first order Born and single Born approximation.

Chapter 2

Piecewise defined Green's functions

2.1 Introduction

Calculations with the contour ordered Green's function of the last chapter are rarely found in literature, because it is cumbersome to implement certain identities on a transformation contour. Furthermore, the transformation into the interaction picture is only the first step towards a perturbation expansion of the Green's function with respect to interaction potentials. Thus, it is common to define piecewise defined Green's functions that agree with the contour ordered one for specific constellations of the time arguments. In this chapter, we introduce these piecewise defined Green's functions and derive their equations of motion. Unfortunately, the notation of these new Green's functions is ambiguous in literature and the most common notation is not the best suited one for the perturbation expansion. For this reason, we present the Green's functions and self-energies in two notations. We use the notation of Lifschitz and Pitajewski [8] in the perturbation expansion and Feynman graphs, because this notation is best suited for this purpose. For convenience however, we translate all results into the most widespread notation of Kadanoff and Baym [5]. We also give translation tables to avoid confusions.

We perform the diagrammatic expansion of the transformation into the interaction picture and derive the differential equations of motion for all piecewise defined Green's functions. Thereby, we introduce the concept of scattering self-energies in the self-consistent Born approximation. We end this chapter with the derivation of two scattering self-energies representing the scattering of electrons with bulk phonons and at charged impurities. In this way, we give two illustrative examples for the perturbation expansion in the diagram technique and we derive fundamental formulas for scattering self-energies. We will specify these formulas when we implement phonon and impurity scattering on concrete systems in later chapters.

2.2 Definitions and notations

2.2.1 Introduction

Many different definitions of Green's functions can be found in literature. Those definitions differ either with respect to the constellation of the two time coordinates of the Green's function or simply by notation. We introduce in this section the probably most common definition of six Green's functions as special cases of the contour ordered Green's function. Thereby, we

choose a notation that is frequently used in literature. However, we also present the rather uncommon notation of Lifschitz and Pitajewski [8], since this notation is most convenient for the perturbation expansion of later sections. For later reference, we also introduce general formulas for the spectral function, the particle density and the probability current density.

2.2.2 Common notation and linear dependencies

The contour ordered Green's function that we have defined in the preceding chapter can be subdivided into four different constellations of its two time coordinates. Unfortunately, there is no unique notation in literature for the resulting four subclasses of Green's functions. Probably the most frequently used notation reads (see Fig. 1.3.2 for the contour branches $C_\pm$)

$$G\left(\vec{x}_1,t_1;\vec{x}_2,t_2\right)=\begin{cases} G^C\left(\vec{x}_1,t_1;\vec{x}_2,t_2\right),\ \forall\ t_1,t_2\in C_- \\ G^<\left(\vec{x}_1,t_1;\vec{x}_2,t_2\right),\ \forall\ t_1\in C_-,t_2\in C_+ \\ G^>\left(\vec{x}_1,t_1;\vec{x}_2,t_2\right),\ \forall\ t_1\in C_+,t_2\in C_- \\ G^{AC}\left(\vec{x}_1,t_1;\vec{x}_2,t_2\right),\ \forall\ t_1,t_2\in C_+ \end{cases}. \tag{2.2.1}$$

Here, G^C is the causal Green's function*

$$\begin{aligned} G^C\left(\vec{x}_1,t_1;\vec{x}_2,t_2\right) &= -\frac{i}{\hbar}\theta\left(t_1-t_2\right)\left\langle\hat{\psi}_{\mathcal{H}}\left(\vec{x}_1,t_1\right)\hat{\psi}^\dagger_{\mathcal{H}}\left(\vec{x}_2,t_2\right)\right\rangle \\ &\quad \pm\frac{i}{\hbar}\theta\left(t_2-t_1\right)\left\langle\hat{\psi}^\dagger_{\mathcal{H}}\left(\vec{x}_2,t_2\right)\hat{\psi}_{\mathcal{H}}\left(\vec{x}_1,t_1\right)\right\rangle, \end{aligned} \tag{2.2.2}$$

the anticausal Green's function is given by G^{AC}

$$\begin{aligned} G^{AC}\left(\vec{x}_1,t_1;\vec{x}_2,t_2\right) &= -\frac{i}{\hbar}\theta\left(t_2-t_1\right)\left\langle\hat{\psi}_{\mathcal{H}}\left(\vec{x}_1,t_1\right)\hat{\psi}^\dagger_{\mathcal{H}}\left(\vec{x}_2,t_2\right)\right\rangle \\ &\quad \pm\frac{i}{\hbar}\theta\left(t_1-t_2\right)\left\langle\hat{\psi}^\dagger_{\mathcal{H}}\left(\vec{x}_2,t_2\right)\hat{\psi}_{\mathcal{H}}\left(\vec{x}_1,t_1\right)\right\rangle, \end{aligned} \tag{2.2.3}$$

and the correlation functions $G^<$ and $G^>$ are often called the lesser and greater Green's functions, respectively. The effect of the time ordering operator on the contour in the formulas of $G^<$ and $G^>$ is obvious and we can write for these Green's functions

$$G^<\left(\vec{x}_1,t_1;\vec{x}_2,t_2\right)=\pm\frac{i}{\hbar}\left\langle\hat{\psi}^\dagger_{\mathcal{H}}\left(\vec{x}_2,t_2\right)\hat{\psi}_{\mathcal{H}}\left(\vec{x}_1,t_1\right)\right\rangle \tag{2.2.4}$$

and

$$G^>\left(\vec{x}_1,t_1;\vec{x}_2,t_2\right)=-\frac{i}{\hbar}\left\langle\hat{\psi}_{\mathcal{H}}\left(\vec{x}_1,t_1\right)\hat{\psi}^\dagger_{\mathcal{H}}\left(\vec{x}_2,t_2\right)\right\rangle. \tag{2.2.5}$$

The lesser Green's function $G^<$ is closely related to the density operator whereas the greater Green's function $G^>$ contains information about the empty states. Consequently, the expectation value of the particle density operator is given by

$$\left\langle\hat{n}\left(\vec{x}_1,t_1\right)\right\rangle=\pm\frac{\hbar}{i}\lim_{t_2\to t_1}\lim_{\vec{x}_2\to\vec{x}_1}G^<\left(\vec{x}_1,t_1;\vec{x}_2,t_2\right), \tag{2.2.6}$$

whereas the probability current density is given by (see e.g. [9, 10])

$$\left\langle\hat{j}\left(\vec{x}_1,t_1\right)\right\rangle=\lim_{t_2\to t_1}\lim_{\vec{x}_2\to\vec{x}_1}i\hbar\hat{v}G^<\left(\vec{x}_1,t_1;\vec{x}_2,t_2\right) \tag{2.2.7}$$

*Please mind that upper signs refer to fermions, lower signs to bosons.

with the velocity operator

$$\hat{v} = \frac{i}{\hbar}\left[\hat{H}, \hat{x}\right]_- . \tag{2.2.8}$$

When the Hamilton operator does not contain spatial derivative operators except for the squared momentum operator, the probability current density reads

$$\langle \hat{j}(\vec{x}_1, t_1)\rangle = -\lim_{t_2\to t_1}\lim_{\vec{x}_2\to\vec{x}_1}\frac{\hbar^2}{2m}\left(\nabla_{\vec{x}_1} - \nabla_{\vec{x}_2}\right) G^<(\vec{x}_1, t_1; \vec{x}_2, t_2) . \tag{2.2.9}$$

It is easy to see from Eqs. (2.2.2)-(2.2.5) that only three of those four Green's functions are linearly independent

$$G^C(\vec{x}_1, t_1; \vec{x}_2, t_2) + G^{AC}(\vec{x}_1, t_1; \vec{x}_2, t_2) = G^<(\vec{x}_1, t_1; \vec{x}_2, t_2) + G^>(\vec{x}_1, t_1; \vec{x}_2, t_2) . \tag{2.2.10}$$

Apart from the these four Green's functions, it is common in literature to additionally define the retarded (G^R) and the advanced (G^A) Green's functions

$$\begin{aligned} G^R(\vec{x}_1, t_1; \vec{x}_2, t_2) &\equiv \theta(t_1 - t_2)\left[G^>(\vec{x}_1, t_1; \vec{x}_2, t_2) - G^<(\vec{x}_1, t_1; \vec{x}_2, t_2)\right] \\ &= G^>(\vec{x}_1, t_1; \vec{x}_2, t_2) - G^{AC}(\vec{x}_1, t_1; \vec{x}_2, t_2) \\ &= G^C(\vec{x}_1, t_1; \vec{x}_2, t_2) - G^<(\vec{x}_1, t_1; \vec{x}_2, t_2) , \end{aligned} \tag{2.2.11}$$

$$\begin{aligned} G^A(\vec{x}_1, t_1; \vec{x}_2, t_2) &\equiv \theta(t_2 - t_1)\left[G^<(\vec{x}_1, t_1; \vec{x}_2, t_2) - G^>(\vec{x}_1, t_1; \vec{x}_2, t_2)\right] \\ &= G^<(\vec{x}_1, t_1; \vec{x}_2, t_2) - G^{AC}(\vec{x}_1, t_1; \vec{x}_2, t_2) \\ &= G^C(\vec{x}_1, t_1; \vec{x}_2, t_2) - G^>(\vec{x}_1, t_1; \vec{x}_2, t_2) . \end{aligned} \tag{2.2.12}$$

The difference of these Green's functions is commonly termed the spectral function A

$$\begin{aligned} A(\vec{x}_1, t_1; \vec{x}_2, t_2) &= iG^R(\vec{x}_1, t_1; \vec{x}_2, t_2) - iG^{R\dagger}(\vec{x}_1, t_1; \vec{x}_2, t_2) \\ &= iG^>(\vec{x}_1, t_1; \vec{x}_2, t_2) - iG^<(\vec{x}_1, t_1; \vec{x}_2, t_2) . \end{aligned} \tag{2.2.13}$$

In the stationary case, we can Fourier transform the Green's functions with respect to the difference of the propagation times $(t_1 - t_2)$ into the energy (E) domain. Then, we get an additional relation between the time ordered Green's functions

$$G^C(\vec{x}_1, \vec{x}_2, E) = -\left[G^{AC}(\vec{x}_1, \vec{x}_2, E)\right]^\dagger . \tag{2.2.14}$$

In this case, it is sufficient to know two of the piecewise defined Green's functions in order to determine the total propagator. In this thesis, we choose to explicitly calculate (as is typically done in literature) the retarded and the lesser Green's functions.

In equilibrium, an additional equation holds, given by the fluctuation-dissipation theorem (see e.g. [6])

$$G^<(\vec{x}_1, \vec{x}_2, E) = if(E, \mu) A(\vec{x}_1, \vec{x}_2, E) . \tag{2.2.15}$$

Here, the lesser Green's function is a product of the spectral function and - in the case of Fermions - the Fermi distribution f

$$f(E, \mu) = \left[\exp\left(\beta(E - \mu)\right) + 1\right]^{-1} . \tag{2.2.16}$$

Therefore, in equilibrium the knowledge of a single Green's function, typically G^R, is sufficient to determine the total contour ordered Green's function. When we compare Eq. (2.2.15) with the definition of the particle density (Eq. (2.2.6)), we can identify the spectral function A at equal coordinates to be proportional to the local density of states.

2.2.3 Notation of Lifschitz and Pitajewski

We will stick as often as possible to the common notation, just because it is most widespread in literature. Unfortunately, this notation is inconvenient for the purpose of the diagram technique which we use in section 2.3 to derive a perturbation expansion for transport problems including incoherent scattering. The notation of Lifschitz and Pitajewski [8] is most suited for the diagram technique and we will use it when we derive the perturbation expansion. Therefore, we add here a translation rule between the common notation and the notation of Lifschitz and Pitajewski. This second notation can be easily understood, when we write a coordinate that lies on the contour branch C_+ or C_- with a superscript of the corresponding sign

$$t_1 = t_1^{\pm}, \text{ if } t_1 \in C_{\pm}. \tag{2.2.17}$$

Instead of keeping these superscripts near the time coordinates in the variables of the Green's functions, Lifschitz and Pitajewski attach them to the symbol "G"in an appropriate order

$$\begin{aligned}
G^{--}(\vec{x}_1,t_1;\vec{x}_2,t_2) &\equiv G^{C}(\vec{x}_1,t_1;\vec{x}_2,t_2) = G(\vec{x}_1,t_1;\vec{x}_2,t_2)\,,\ \forall\, t_1,t_2 \in C_-,\\
G^{-+}(\vec{x}_1,t_1;\vec{x}_2,t_2) &\equiv G^{<}(\vec{x}_1,t_1;\vec{x}_2,t_2) = G(\vec{x}_1,t_1;\vec{x}_2,t_2)\,,\ \forall\, t_1 \in C_-, t_2 \in C_+,\\
G^{+-}(\vec{x}_1,t_1;\vec{x}_2,t_2) &\equiv G^{>}(\vec{x}_1,t_1;\vec{x}_2,t_2) = G(\vec{x}_1,t_1;\vec{x}_2,t_2)\,,\ \forall\, t_1 \in C_+, t_2 \in C_-,\\
G^{++}(\vec{x}_1,t_1;\vec{x}_2,t_2) &\equiv G^{AC}(\vec{x}_1,t_1;\vec{x}_2,t_2) = G(\vec{x}_1,t_1;\vec{x}_2,t_2)\,,\ \forall\, t_1,t_2 \in C_+.
\end{aligned} \tag{2.2.18}$$

2.3 Perturbation expansion and Feynman rules

2.3.1 Introduction

The exact time development of the Green's functions in systems with many-particle interactions is typically unsolvable. For this reason, it is common to transform the Green's functions into the interaction representation and to approximate this transformation with an incomplete series expansion.

We start this section with the lowest nontrivial order of this series expansion and show that particle operators that originate from the approximated transformation can be contracted to Green's functions of various time ordering. The complexity of the involved equations motivates the introduction of a diagrammatic technique. We introduce pictograms for all relevant functions of the perturbation expansion and summarize the (adapted) Feynman rules. These rules allow us to present the Green's function of an infinite series expansion in a concise manner. In this way, we introduce the self-consistent Born approximation for the self-energies and derive the differential form of the Dyson equation for the six commonly considered Green's functions. For completeness, we end this section with the analytical formulas for these six free-particle Green's functions.

2.3.2 Linear order

In the following sections, we will stick to the notation of Lifschitz and Pitajewski that we have introduced in the preceding paragraph, because it is most suitable for the perturbation expansion of the contour ordered Green's function of the interaction picture. In order to derive this expansion, let us assume for simplicity that the two-particle interaction potential $\hat{W}$ of Eq. (1.4.4) is the only time dependent part of the system's Hamilton operator. Thus, we

transform the contour ordered Green's functions with respect to $\hat{W}$ into the interaction picture (see chapter 1.2.2). The time dependence of this operator is given by the remaining time independent part $\hat{H}_0$ of the Hamilton

$$\hat{W}_{\hat{H}_0}(t_1) = \frac{1}{2}\int \mathrm{d}\vec{x}_1\mathrm{d}\vec{x}_2\mathrm{d}t_2 \hat{\psi}^\dagger_{\hat{H}_0}(\vec{x}_1,t_1)\,\hat{\psi}^\dagger_{\hat{H}_0}(\vec{x}_2,t_2)\,W(\vec{x}_1,t_1;\vec{x}_2,t_2)\,\hat{\psi}_{\hat{H}_0}(\vec{x}_2,t_2)\,\hat{\psi}_{\hat{H}_0}(\vec{x}_1,t_1)\,. \tag{2.3.1}$$

Actually, we have already implemented a perturbation expansion of the scattered transport, when we approximated the two particle Green's function in Eq. (1.4.11). This has led us to the definition of the self-energy in Eq. (1.4.15). There, we have motivated the terms of the lowest order by simple physical considerations. However, the expansion of the propagation problem to higher orders in the interaction potential requires for a systematic expansion rule. Thus, instead of considering the interaction potential W explicitly in the equation of motion of the one particle Green's function and approximating the two-particle Green's function (as done in chapter 1.4), we expand the unitary transformation into the interaction picture. Here, this unitary transformation operator is defined on the Keldysh contour

$$\hat{S}_{C,\mathrm{total}} = \hat{T}_C \exp\left(-\frac{i}{\hbar}\int_C \hat{W}_{\hat{H}_0}(t)\,\mathrm{d}t\right). \tag{2.3.2}$$

We have introduced this contour as the composition of two integration paths in the preceding chapter, because this shortens the equations of motion and is a widespread scheme in literature. However, it is easier to expand the transformation operator $\hat{S}$, when it is defined on the real axis. Therefore, we redivide the unitary transformation $\hat{S}_{C,\mathrm{total}}$ in the two originally separated operators with integrals along the two parts of the Keldysh contour C_- and C_+ (see Fig. 1.3.2)

$$\hat{S}_{C_-} = \hat{T}\exp\left(-\frac{i}{\hbar}\int_{-\infty}^{\infty}\hat{W}_{\hat{H}_0}(t)\,\mathrm{d}t\right), \tag{2.3.3}$$

$$\hat{S}_{C_+} = \hat{T}^\dagger\exp\left(\frac{i}{\hbar}\int_{-\infty}^{\infty}\hat{W}^\dagger_{\hat{H}_0}(t)\,\mathrm{d}t\right). \tag{2.3.4}$$

Now, we get a formula for the contour ordered Green's function in the shape of Eq. (1.2.7)

$$G(\vec{x}_1,t_1;\vec{x}_2,t_2) = -\frac{i}{\hbar}\left\langle \hat{S}_{C_+}\hat{T}\left(\hat{\psi}_{\hat{H}_0}(\vec{x}_1,t_1)\,\hat{\psi}^\dagger_{\hat{H}_0}(\vec{x}_2,t_2)\,\hat{S}_{C_-}\right)\right\rangle. \tag{2.3.5}$$

In order to shorten the upcoming equations, we abbreviate the multi dimensional coordinates and related integrals with

$$\begin{aligned}(1) &\equiv (\vec{x}_1,t_1)\,,\\ (1;2) &\equiv (\vec{x}_1,t_1;\vec{x}_2,t_2)\,,\\ \int \mathrm{d}1\mathrm{d}2 &\equiv \int \mathrm{d}\vec{x}_1\mathrm{d}t_1\mathrm{d}\vec{x}_2\mathrm{d}t_2.\end{aligned}$$

Whenever the absolute value of the interaction potential W is small enough, we may expand the exponential operators $\hat{S}_{C_-}$ and $\hat{S}_{C_+}$ in a series. When we apply such a series expansion on

G, equation (2.3.5) reads* in linear order of W

$$\begin{aligned}
&2\hbar^2 G(1;2) = 2\hbar^2 G_0(1;2) \\
&+\left\langle \hat{T}^\dagger \left(\int \mathrm{d3d4} \hat{\psi}^\dagger_{\hat{H}_0}(3)\, \hat{\psi}^\dagger_{\hat{H}_0}(4)\, W^*(3;4)\, \hat{\psi}_{\hat{H}_0}(4)\, \hat{\psi}_{\hat{H}_0}(3) \right) \hat{T} \left(\hat{\psi}_{\hat{H}_0}(1)\, \hat{\psi}^\dagger_{\hat{H}_0}(2) \right) \right\rangle \\
&-\left\langle \hat{T} \left(\hat{\psi}_{\hat{H}_0}(1)\, \hat{\psi}^\dagger_{\hat{H}_0}(2) \right) \hat{T} \left(\int \mathrm{d3d4} \hat{\psi}^\dagger_{\hat{H}_0}(3)\, \hat{\psi}^\dagger_{\hat{H}_0}(4)\, W(3;4)\, \hat{\psi}_{\hat{H}_0}(4)\, \hat{\psi}_{\hat{H}_0}(3) \right) \right\rangle, \quad (2.3.6)
\end{aligned}$$

with G_0, the free-particle Green's function, i.e. the Green's function that solves Eqs. (1.4.12) and (1.4.13) with vanishing W. Our next step is to simplify the expectation values in the last equation with products of one particle Green's functions. This can be done with Wick's theorem [9]

$$T\left(\hat{U}\hat{V}\hat{W}\ldots\hat{X}\hat{Y}\hat{Z}\right) = N\left(\hat{U}\hat{V}\hat{W}\ldots\hat{X}\hat{Y}\hat{Z}\right) + N\,(\text{sum over all possible pairs of contractions}). \quad (2.3.7)$$

Here, $T\left(\hat{U}\hat{V}\hat{W}\ldots\hat{X}\hat{Y}\hat{Z}\right)$ is a time-ordered and $N\left(\hat{U}\hat{V}\hat{W}\ldots\hat{X}\hat{Y}\hat{Z}\right)$ a normal-ordered product of operators. As has been mentioned by Lifschitz and Pitajewski [8], the expectation values of normal-ordered products given in Eq. (1.3.4) vanish. Therefore, the time-ordered products in Eq. (2.3.6) equal the sum of all possible pairwise contractions of operators. Since only those expectation values of pairwise contractions do not vanish that contain both, a creation as well as a destruction operator, the summands on the right side of Eq. (2.3.6) are products of one-particle Green's functions. We show in the appendix that any contraction that leads to Green's functions of the coordinates $(1;2)$ represent so-called vacuum terms that vanish exactly (see Appendix A). The remaining summands in Eq. (2.3.6) are the following contractions (marked with lines)

$$-\frac{i}{\hbar}\left\langle \hat{T}^\dagger\left(\frac{1}{2}\frac{i}{\hbar}\int \mathrm{d3d4}\overbrace{\hat{\psi}^\dagger_{\hat{H}_0}(3)\,\hat{\psi}^\dagger_{\hat{H}_0}(4)\,W^*(3;4)\,\hat{\psi}_{\hat{H}_0}(4)\,\hat{\psi}_{\hat{H}_0}(3)}\right)\hat{T}\left(\hat{\psi}_{\hat{H}_0}(1)\,\hat{\psi}^\dagger_{\hat{H}_0}(2)\right)\right\rangle,$$

$$-\frac{i}{\hbar}\left\langle \hat{T}^\dagger\left(\frac{1}{2}\frac{i}{\hbar}\int \mathrm{d3d4}\overbrace{\hat{\psi}^\dagger_{\hat{H}_0}(3)\,\hat{\psi}^\dagger_{\hat{H}_0}(4)\,W^*(3;4)\,\hat{\psi}_{\hat{H}_0}(4)}\,\hat{\psi}_{\hat{H}_0}(3)\right)\hat{T}\left(\hat{\psi}_{\hat{H}_0}(1)\,\hat{\psi}^\dagger_{\hat{H}_0}(2)\right)\right\rangle,$$

$$-\frac{i}{\hbar}\left\langle \hat{T}\left(\overbrace{\hat{\psi}_{\hat{H}_0}(1)\,\hat{\psi}^\dagger_{\hat{H}_0}(2)}\right)\hat{T}\left(\frac{1}{2}\frac{-i}{\hbar}\int \mathrm{d3d4}\overbrace{\hat{\psi}^\dagger_{\hat{H}_0}(3)}\,\overbrace{\hat{\psi}^\dagger_{\hat{H}_0}(4)\,W(3;4)\,\hat{\psi}_{\hat{H}_0}(4)}\,\hat{\psi}_{\hat{H}_0}(3)\right)\right\rangle,$$

$$-\frac{i}{\hbar}\left\langle \hat{T}\left(\overbrace{\hat{\psi}_{\hat{H}_0}(1)\,\hat{\psi}^\dagger_{\hat{H}_0}(2)}\right)\hat{T}\left(\frac{1}{2}\frac{-i}{\hbar}\int \mathrm{d3d4}\overbrace{\hat{\psi}^\dagger_{\hat{H}_0}(3)}\,\overbrace{\hat{\psi}^\dagger_{\hat{H}_0}(4)\,W(3;4)\,\hat{\psi}_{\hat{H}_0}(4)}\,\hat{\psi}_{\hat{H}_0}(3)\right)\right\rangle$$

and the same terms again, but with the coordinates 3 and 4 interchanged.

Let us consider fermionic operators and assume the interaction potential W to be instantaneous, i.e.

$$W(3;4) = W(\vec{x}_3, t_3; \vec{x}_4, t_4)\,\delta(t_3 - t_4). \quad (2.3.8)$$

Then, both interaction times t_3 and t_4 in Eq. (2.3.6) lie on the same branch of the transformation contour, i.e. either on C_- or C_+. In the case of $t_1, t_2 \in C_-$ we can rewrite Eq. (2.3.6) after

*We use the symmetry of the interaction potential, i.e. $W(3;4) = W(4;3)$.

permuting the operators using the anticommutator rules in Eqs. (1.4.5)

$$\begin{aligned} G^{--}(1;2) &= G_0^{--}(1;2) \\ &\quad -i\int \mathrm{d3d4}iG_0^{-+}(1;3)\, i\hbar W^*(3;4)\, iG_0^{++}(3;4)\, iG_0^{+-}(4;2) \\ &\quad -i(-1)\int \mathrm{d3d4}iG_0^{-+}(1;3)\, i\hbar W^*(3;4)\, iG_0^{++}(4;4)\, iG_0^{+-}(3;2) \\ &\quad -i\int \mathrm{d3d4}iG_0^{--}(1;3)\,(-i\hbar)\, W(3;4)\, iG_0^{--}(3;4)\, iG_0^{--}(4;2) \\ &\quad -i(-1)\int \mathrm{d3d4}iG_0^{--}(1;3)\,(-i\hbar)\, W(3;4)\, iG_0^{--}(4;4)\, iG_0^{--}(3;2)\,. \end{aligned} \tag{2.3.9}$$

The time ordering of the each one-particle Green's function in this equation is given by the limited scope of the respective time ordering operator. Particle operators that are ordered in opposite time orientations, can only contract into G_0^{-+} or G_0^{+-} Green's functions, for instance. Equation (2.3.9) contains Green's functions with two equal coordinates ($G_0^{++}(4;4)$ and $G_0^{--}(4;4)$). The effect of the time ordering operator $\hat{T}$ is undefined at equal propagation times. However, it is obvious (see [9]) that these terms arise from the interaction Hamiltonian in the second quantization. In the representation of Eq. (2.3.1), particle destruction operators are always positioned to the right of creation operators. Since this order is not changed by $\hat{T}$, Green's functions at equal times in Eq. (2.3.9) have to be interpreted as

$$\begin{aligned} G_0(4;4) &= \lim_{t_4'\to t_4+} -\frac{i}{\hbar}\left\langle \hat{T}\left(\hat{\psi}_{\hat{H}_0}(\vec{x}_4,t_4)\,\hat{\psi}^\dagger_{\hat{H}_0}(\vec{x}_4,t_4')\right)\right\rangle \\ &= \frac{i}{\hbar}\left\langle \hat{\psi}^\dagger_{\hat{H}_0}(\vec{x}_4,t_4)\,\hat{\psi}_{\hat{H}_0}(\vec{x}_4,t_4)\right\rangle \\ &= G_0^{-+}(4;4)\,. \end{aligned} \tag{2.3.10}$$

2.3.3 Diagram technique

The complexity of Eq. (2.3.9) and similar equations for the three remaining constellations of (t_1,t_2) motivate the introduction of diagrammatic technique. Such a technique is in particular important, when terms of higher order than linear in W have to be taken into account. For this reason, we follow the common approaches in literature and introduce pictograms for the frequently appearing elements in the equations for the Green's function. For completeness, we summarize the Feynman rules for these pictograms at the end of this paragraph.

We associate solid lines with free-particle Green's functions and place the propagation coordinates at the respective end of the line

$$\begin{aligned} iG_0^{--}(1;2) &= \text{1- 2-}, \\ iG_0^{+-}(1;2) &= \text{1+ 2-}, \\ iG_0^{-+}(1;2) &= \text{1- 2+}, \\ iG_0^{++}(1;2) &= \text{1+ 2+}. \end{aligned}$$

Each sign indicates whether the propagation coordinate is placed on the chronological ($-$) or antichronological ($+$) branch of the transformation contour. Since our two particle interaction

potential W is instantaneous, its coordinates have always equal sign. We represent interaction potentials with dashed lines

$$i\hbar W^{*}(1;2) \;=\; \text{1+} \;\text{ - - - - - - - - - - - - }\; \text{2+}$$

$$-i\hbar W(1;2) \;=\; \text{1-} \;\text{ - - - - - - - - - - - - }\; \text{2-}.$$

Finally, we depict the exact Green's functions with thick solid lines. In this way, Eq. (2.3.9) reads in diagrammatic form

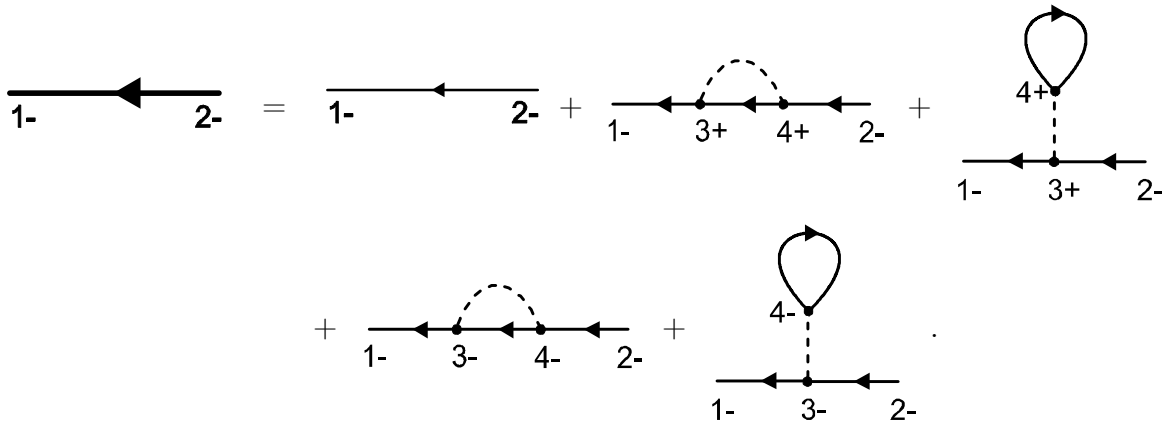

We can use the following Feynman rules [9, 19] to derive the equations of motion of the remaining Green's functions:

1. Draw all topologically distinct (irreducible) diagrams, i.e. diagrams that can not be separated into fragments by dividing one solid line into two parts. Hereby, consider all permutations of the signs at the coordinates. The sequence of solid lines runs from $2\pm$ to $1\pm$ in the equation of motion for $G^{\pm\pm}(1;2)$.

2. A solid line from $3\pm$ to $4\pm$ represents the free particle Green's function $iG_0^{\pm\pm}(3;4)$ (see above), a thick solid line depicts an exact Green's function $iG^{\pm\pm}(3;4)$. Graphs of self-energies, i.e. segments of diagrams for $G^{\pm\pm}(1;2)$ represent $-i\Sigma^{\pm\pm}$.

3. Each dashed line represents an interaction potential. When the considered interaction is instantaneous, such a dashed line between $3\pm$ and $4\pm$ equals a factor of $-i\hbar W(3;4)\,\delta_C(t_3,t_4)$ (δ-distribution on the contour, see Eq.(1.4.3)).

4. Any solid line that forms a loop (e.g. from $4\pm$ to $4\pm$) corresponds to $-iG_0^{-+}$ in the case of fermions and iG_0^{-+} for bosons.

5. One particle potentials U are included with a sign due to the respective vertex. Negative coordinates at such vertices stand for the factor $-iU$. Positive signs give a factor of iU^{*}.

6. Integrate each diagrammatic term over all coordinates at its vertices. These integrals run over the total considered space and the total Keldysh contour.

2.3.4 Expanded equations of motion - infinite order

We have already introduced the self-energy for the interaction potential W in linear approximation (see Eq. (1.4.15)). When we compare the definition of the self-energy Σ on the contour Eq. (1.4.15) with Eq. (2.3.9), we can give expressions for the piecewise defined self-energies in linear order in W:

$$
\begin{aligned}
-i\Sigma^{--}(3;4) \;=\; & \\
&= (-1)\,\delta(3-4)\int \mathrm{d}4'\,(-i\hbar)\,W(3;4')\,iG_0^{-+}(4';4') \\
&\quad +(-i\hbar)\,W(3;4)\,iG_0^{--}(3;4)\,,
\end{aligned}
\tag{2.3.11}
$$

$$
\begin{aligned}
-i\Sigma^{++}(3;4) \;=\; & \\
&= (-1)\,\delta(3-4)\int \mathrm{d}4' i\hbar W^{*}(3;4')\,iG_0^{-+}(4';4') \\
&\quad +i\hbar W^{*}(3;4)\,iG_0^{++}(3;4)\,.
\end{aligned}
\tag{2.3.12}
$$

All Green's functions given in these self-energies are free-particle Green's functions. Thus, the self-energies are calculated in the single-Born approximation. When we replace the solid lines in these self-energies with thick lines, i.e. when we replace the free particle Green's function G_0 with fully scattered Green's functions G, we perform an infinite series of these interaction graphs. Then, the self-energies are calculated in the self-consistent Born approximation. Physically, this means that any propagator in the upper diagrams faces the same interaction potential W. Thereby, we take into account feynman graphs with an infinite series of interaction lines lying in parallel to each other, i.e. graphs of the self-energy of the kind

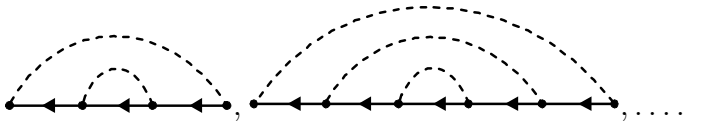

(2.3.13)

The infinite series of consecutive scattering events, i.e. graphs of the shape

(2.3.14)

can be accounted for, when we additionally replace the rightmost or the leftmost free particle Green's functions of the interaction terms in Eq. (2.3.9) with fully scattered Green's functions (G instead of G_0). In this way*, we get from Eq. (2.3.9) the integral form of the Dyson equation

*We will show in Sec. 3.5.7 that the inclusion of this infinite series of scattering events is necessary for a conserved current.

for $G^{--}(1;2)$

$$\begin{aligned} G^{--}(1;2) &= G_0^{--}(1;2) + \int \mathrm{d3d4} G_0^{--}(1;3)\,\Sigma^{--}(3;4)\,G^{--}(4;2) \\ &\quad + \int \mathrm{d3d4} G_0^{-+}(1;3)\,\Sigma^{++}(3;4)\,G^{+-}(4;2) \\ &\quad + \int \mathrm{d3d4} G_0^{--}(1;3)\,\Sigma^{-+}(3;4)\,G^{+-}(4;2) \\ &\quad + \int \mathrm{d3d4} G_0^{-+}(1;3)\,\Sigma^{+-}(3;4)\,G^{--}(4;2)\,. \end{aligned} \tag{2.3.15}$$

The self-energies of the last line (Σ^{-+} and Σ^{+-}) vanish in linear order for instantaneous interactions. Terms including these self-energies are only given for completeness. The first nonvanishing graphs of Σ^{-+} are of second order

$-i\Sigma^{-+}(3;4)$

$=$ 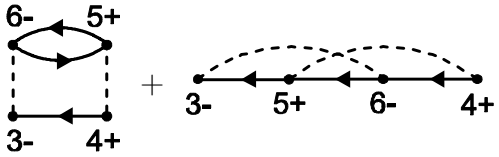

$+\ldots$

$$\begin{aligned} &= \int \mathrm{d6d5} iG_0^{-+}(3;4)\,(-i\hbar)\,W(3;6)\,i\hbar W(4;5)\,iG_0^{-+}(6;5)\,iG_0^{+-}(5;6) \\ &\quad + \int \mathrm{d6d5} iG_0^{-+}(3;5)\,(-i\hbar)\,W(3;6)\,i\hbar W(4;5)\,iG_0^{+-}(5;6)\,iG_0^{-+}(6;4) + \ldots . \end{aligned} \tag{2.3.16}$$

Similar to Lifschitz and Pitajewski [8] we define matrices of piecewise defined Green's functions and self-energies, respectively

$$\mathbf{G}(1;2) \equiv \begin{pmatrix} G^{--}(1;2) & G^{-+}(1;2) \\ G^{+-}(1;2) & G^{++}(1;2) \end{pmatrix}, \tag{2.3.17}$$

$$\mathbf{\Sigma}(1;2) \equiv \begin{pmatrix} \Sigma^{--}(1;2) & \Sigma^{-+}(1;2) \\ \Sigma^{+-}(1;2) & \Sigma^{++}(1;2) \end{pmatrix}. \tag{2.3.18}$$

Then, Eq. (2.3.15) and results of analogous calculations for the three remaining Green's functions can be summarized into a single matrix shaped equation

$$\mathbf{G}(1;2) = \mathbf{G}_0(1;2) + \int \mathrm{d3d4} \mathbf{G}_0(1;3)\,\mathbf{\Sigma}(3;4)\,\mathbf{G}(4;2)\ . \tag{2.3.19}$$

In contrast to the translation rules given in Eqs. (2.2.18), the self-energies of this notation translate with mixed signs to the more common one

$$\begin{aligned} \Sigma^{--}(\vec{x}_1,t_1;\vec{x}_2,t_2) &\equiv \Sigma^{C}(\vec{x}_1,t_1;\vec{x}_2,t_2) \\ \Sigma^{-+}(\vec{x}_1,t_1;\vec{x}_2,t_2) &\equiv -\Sigma^{<}(\vec{x}_1,t_1;\vec{x}_2,t_2) \\ \Sigma^{+-}(\vec{x}_1,t_1;\vec{x}_2,t_2) &\equiv -\Sigma^{>}(\vec{x}_1,t_1;\vec{x}_2,t_2) \\ \Sigma^{++}(\vec{x}_1,t_1;\vec{x}_2,t_2) &\equiv \Sigma^{AC}(\vec{x}_1,t_1;\vec{x}_2,t_2)\,. \end{aligned} \tag{2.3.20}$$

Lifschitz and Pitajewski [8] define the operator

$$\hat{G}_0^{-1}(1) = i\hbar\partial_{t_1} - \hat{H}_0(\vec{x}_1) - U(\vec{x}_1)\,\hat{1} \tag{2.3.21}$$

and get straightforwardly the differential Dyson equation for the free Green's functions in matrix shape

$$\hat{G}_0^{-1}(1)\,\mathbf{G}_0(1;2) = \boldsymbol{\sigma}_z\delta(1-2)\,. \tag{2.3.22}$$

The delta distribution multiplied with the Pauli matrix

$$\sigma_z = \begin{pmatrix} 1 & 0 \\ 0 & -1 \end{pmatrix} \tag{2.3.23}$$

equals the contour ordered delta distribution δ_C of Eq. (1.4.3). When we multiply both sides of Eq. (2.3.19) with $\hat{G}_0^{-1}(1)$ from the left, we get the differential Dyson equation Eq. (1.4.8) in the new matrix shape

$$\hat{G}_0^{-1}(1)\,\mathbf{G}(1;2) = \boldsymbol{\sigma}_z\delta(1-2) + \int \mathrm{d}3\boldsymbol{\sigma}_z\boldsymbol{\Sigma}(1;3)\,\mathbf{G}(3;2)\,. \tag{2.3.24}$$

Equivalently to our derivations in the exact diagram technique we can consider the right most (instead of the left most) solid line to be a free particle Green's function. Then, analogously to the derivation given above, the resulting equation can be multiplied with $\hat{G}_0^{-1}(2)$ from the right and we get the second differential Dyson equation Eq. (1.4.9)

$$\hat{G}_0^{-1}(2)^*\,\mathbf{G}(1;2) = \boldsymbol{\sigma}_z\delta(1-2) + \int \mathrm{d}3\mathbf{G}(1;3)\,\boldsymbol{\Sigma}(3;2)\,\boldsymbol{\sigma}_z. \tag{2.3.25}$$

It is important to note, that these results are given with integrals along the real axis instead of contour integrals. This allows us to specify the differential equations of motion for almost all Green's functions:

$$\hat{G}_0^{-1}(1)\,G^{--}(1;2) = \delta(1-2) + \int \mathrm{d}3\left(\Sigma^{--}(1;3)\,G^{--}(3;2) + \Sigma^{-+}(1;3)\,G^{+-}(3;2)\right), \tag{2.3.26}$$

$$\hat{G}_0^{-1}(1)\,G^{++}(1;2) = -\delta(1-2) - \int \mathrm{d}3\left(\Sigma^{++}(1;3)\,G^{++}(3;2) + \Sigma^{+-}(1;3)\,G^{-+}(3;2)\right), \tag{2.3.27}$$

$$\hat{G}_0^{-1}(1)\,G^{-+}(1;2) = \int \mathrm{d}3\left(\Sigma^{--}(1;3)\,G^{-+}(3;2) + \Sigma^{-+}(1;3)\,G^{++}(3;2)\right), \tag{2.3.28}$$

$$\hat{G}_0^{-1}(1)\,G^{+-}(1;2) = -\int \mathrm{d}3\left(\Sigma^{+-}(1;3)\,G^{--}(3;2) + \Sigma^{++}(1;3)\,G^{+-}(3;2)\right). \tag{2.3.29}$$

For the purpose of completeness, we derive the linear dependence of the self-energies in the appendix (see appendix B)

$$\Sigma^{--}(1;2) + \Sigma^{++}(1;2) = -\Sigma^{+-}(1;2) - \Sigma^{-+}(1;2)\,. \tag{2.3.30}$$

It is common to define retarded and advanced self-energies

$$\Sigma^{R}(1;2) \equiv \Sigma^{--}(1;2) + \Sigma^{-+}(1;2) = -\Sigma^{++}(1;2) - \Sigma^{+-}(1;2)\,, \tag{2.3.31}$$

$$\Sigma^{A}(1;2) \equiv \Sigma^{--}(1;2) + \Sigma^{+-}(1;2) = -\Sigma^{++}(1;2) - \Sigma^{-+}(1;2)\,. \tag{2.3.32}$$

When we combine the equations of motion of G^{--}, G^{+-} and G^{-+}, we get the equations of motion for the retarded and advanced Green's functions

$$\begin{aligned}\hat{G}_0^{-1}(1)\,G^R(1;2) &= \delta(1-2)+\int \mathrm{d}3\left[\Sigma^{--}(1;3)\,G^{--}(3;2)+\Sigma^{-+}(1;3)\,G^{+-}(3;2)\right.\\ &\quad\left.-\Sigma^{--}(1;3)\,G^{-+}(3;2)-\Sigma^{-+}(1;3)\,G^{++}(3;2)\right]\\ &= \delta(1-2)+\int \mathrm{d}3\Sigma^R(1;3)\,G^R(3;2)\,, \end{aligned} \tag{2.3.33}$$

$$\begin{aligned}\hat{G}_0^{-1}(1)\,G^A(1;2) &= \delta(1-2)+\int \mathrm{d}3\left[\Sigma^{--}(1;3)\,G^{--}(3;2)+\Sigma^{-+}(1;3)\,G^{+-}(3;2)\right.\\ &\quad\left.+\Sigma^{+-}(1;3)\,G^{--}(3;2)+\Sigma^{++}(1;3)\,G^{+-}(3;2)\right]\\ &= \delta(1-2)+\int \mathrm{d}3\Sigma^A(1;3)\,G^A(3;2)\,. \end{aligned} \tag{2.3.34}$$

We have already mentioned previously that the knowledge of two Green's functions is sufficient to determine all physics in a stationary situation (see chapter 2.2). All the numerical calculations of the remaining parts of this thesis deal with stationary problems and solve for the lesser and retarded Green's function. Therefore, we have to rewrite the equation of motion for G^{-+} $(=G^<)$, so that only retarded and lesser functions enter the formula*

$$\begin{aligned}\hat{G}_0^{-1}(1)\,G^{-+}(1;2) &= \int \mathrm{d}3\left(\Sigma^{--}(1;3)\,G^{-+}(3;2)+\Sigma^{-+}(1;3)\,G^{++}(3;2)\right)\\ &= \int \mathrm{d}3\left(\Sigma^R(1;3)\,G^{-+}(3;2)-\Sigma^{-+}(1;3)\,G^{R\dagger}(3;2)\right). \end{aligned} \tag{2.3.35}$$

Translated into the more common notation, the formula for the lesser Green's function reads

$$\hat{G}_0^{-1}(1)\,G^<(1;2)=\int \mathrm{d}3\left(\Sigma^R(1;3)\,G^<(3;2)+\Sigma^<(1;3)\,G^{R\dagger}(3;2)\right). \tag{2.3.36}$$

The last equation can be simplified using Eq. (2.3.33) to the most common shape of the Keldysh equation

$$G^<(1;2)=\int \mathrm{d}3\mathrm{d}4 G^R(1;3)\,\Sigma^<(3;4)\,G^{R\dagger}(4;2)\,. \tag{2.3.37}$$

An alternative way in literature to derive these equations is often termed the Langreth theorem [6, 20, 21]. Utilizing the Langreth theorem, we can summarize the equations of motion for all Green's functions

$$G(1;2)=G_0(1;2)+\int \mathrm{d}3\mathrm{d}4 G_0(1;3)\,\Sigma(3;4)\,G(4;2)\,. \tag{2.3.38}$$

2.3.5 Noninteracting particles Green's functions

Particles in homogeneous systems are considered free when they do not interact with other particles ($\Sigma=0$) and are not affected by external potentials (such as electric fields). Therefore the equations of motion for the free-particle Green's functions $\mathbf{G}_0$ are very simple

$$\hat{G}_0^{-1}(1)\,\mathbf{G}_0(1;2)=\boldsymbol{\sigma}_z\delta(1-2)\,, \tag{2.3.39}$$

*Please mind that in the stationary case $G^A=G^{R\dagger}$.

with

$$\hat{G}_0^{-1}(1) = i\hbar\partial_{t_1} - \hat{H}_0(\vec{x}_1). \tag{2.3.40}$$

We utilize the identities

$$\left\langle \hat{\psi}_{\vec{k}}^{\dagger}\hat{\psi}_{\vec{k}} \right\rangle = n_{\vec{k}} \tag{2.3.41}$$

$$\left\langle \hat{\psi}_{\vec{k}}\hat{\psi}_{\vec{k}}^{\dagger} \right\rangle = 1 \mp n_{\vec{k}} \tag{2.3.42}$$

with $n_{\vec{k}}$ the number of particles with momentum $\vec{k}$ and Fourier transform the Green's functions into frequency ω and momentum $\vec{k}$ space. Then, we get for particles with a dispersion relation $\varepsilon\left(\vec{k}\right)$ (see any many particle textbook)

$$\begin{aligned}
G_0^{-+}\left(\omega,\vec{k}\right) &= \pm 2\pi i n_{\vec{k}}\delta\left(\omega - \varepsilon\left(\vec{k}\right)/\hbar\right)/\hbar, \\
G_0^{+-}\left(\omega,\vec{k}\right) &= -2\pi i\left(1 \mp n_{\vec{k}}\right)\delta\left(\omega - \varepsilon\left(\vec{k}\right)/\hbar\right)/\hbar, \\
G_0^{--}\left(\omega,\vec{k}\right) &= -G_0^{++}\left(\omega,\vec{k}\right)^* = \Pr\frac{1}{\hbar\omega - \varepsilon\left(\vec{k}\right)} + i\pi\left(\pm 2n_{\vec{k}} - 1\right)\delta\left(\omega - \varepsilon\left(\vec{k}\right)/\hbar\right)/\hbar, \\
G_0^{R}\left(\omega,\vec{k}\right) &= G_0^{A}\left(\omega,\vec{k}\right)^* = \lim_{\eta\to 0+}\left(\hbar\omega - \varepsilon\left(\vec{k}\right) + i\eta\right)^{-1} \\
&= \Pr\frac{1}{\hbar\omega - \varepsilon\left(\vec{k}\right)} - i\pi\delta\left(\omega - \varepsilon\left(\vec{k}\right)/\hbar\right)/\hbar.
\end{aligned} \tag{2.3.43}$$

2.4 Examples of electronic self-energies

2.4.1 Introduction

In this section, we derive two scattering self-energies in the self-consistent Born approximation, i.e. scattering at charged impurities and scattering with any kind of bulk phonon. We present the derivations in detail for two purposes. First, we want to give illustrative examples for the diagram technique that we have introduced in the preceding section. Second, we have to specify the scattering self-energies in later chapters and therefore derive their fundamental shape for later reference.

Emission and absorption of phonons are an inelastic scattering mechanisms that - in general - are capable to change the energy dependent distribution of electrons. We derive the prerequisite for phonon self-energies that needs to be fulfilled in order to get Fermi distributions for electrons in equilibrium: The phonons have to be distributed according to the Bose distribution.

2.4.2 Scattering on phonons

We approximate the phonons of semiconductor heterostructures with the bulk dispersion of the respective predominant material and denote their propagators with D. The interaction potential is well known in literature (see e.g. [22])

$$\hat{H}'(\vec{x},t) = \hat{U}(\vec{x},t) = \hat{\psi}_{\hat{H}_0}^{\dagger}(\vec{x},t)\frac{1}{\sqrt{V}}\sum_{\vec{q}} U_q \mathrm{e}^{i\vec{q}\cdot\vec{x}}\left(\hat{a}_{\vec{q}}(t) + \hat{a}_{-\vec{q}}^{\dagger}(t)\right)\hat{\psi}_{\hat{H}_0}(\vec{x},t). \tag{2.4.1}$$

Here, the operators $\hat{a}_{\vec{q}}(t)$ and $\hat{a}^\dagger_{\vec{q}}(t)$ create and destroy a phonon with wave number $\vec{q}$ at the time t, respectively. In this model, different types of phonons (e.g. polar optical or acoustic) differ only in the interaction potential U_q. We consider the phonons to be in thermal equilibrium and to remain completely unaffected by the interaction with the electrons. Therefore, the portion of the unperturbed system's Hamilton operator $\hat{h}$ that acts on phonons reads

$$\hat{h}_{\text{phonon}} = \sum_{\vec{q}} \hbar\omega_q \left(\hat{n}_{\vec{q}} + \frac{1}{2}\right), \tag{2.4.2}$$

with ω_q, the phonon frequency and $\hat{n}_{\vec{q}}$, the phonon number operator. It is straightforward to derive the time evolution of the phonon operators under this Hamiltonian

$$\hat{a}_{\vec{q}}(t) = \mathrm{e}^{-i\omega_q t}\hat{a}_{\vec{q}}, \tag{2.4.3}$$

$$\hat{a}^\dagger_{\vec{q}}(t) = \mathrm{e}^{i\omega_q t}\hat{a}^\dagger_{\vec{q}}. \tag{2.4.4}$$

Since a sum of a phonon creation and a destruction operator enters the formula of the perturbing potential, any term in a perturbation expansion of the Green's function that is of odd order in $\hat{U}$ changes the total number of phonons in the system. This would be in contradiction to the equilibrium situation of the phonon bath so that such terms have to vanish. The only terms that are conform with the approximation of an equilibrium phonon bath create/destroy phonons with wave number $\vec{q}$ at one coordinate and destroy/create phonons of the same wave number at a second coordinate. This is exactly the definition of phonon Green's functions in momentum representation. However, creating a phonon with wave vector $\vec{q}$ or annihilating a phonon with wave vector $-\vec{q}$ is the same process. Consequently, the phonon Green's function is not defined with the phonon particle operators $\hat{a}_{\vec{q}}$ and $\hat{a}^\dagger_{\vec{q}}$, but with the raising ($\hat{A}^\dagger_{\vec{q}}$) and lowering ($\hat{A}_{\vec{q}}$) operators

$$\hat{A}^\dagger_{-\vec{q}}(t) = \hat{A}_{\vec{q}}(t) = \mathrm{e}^{-i\omega_q t}\hat{a}_{\vec{q}} + \mathrm{e}^{i\omega_q t}\hat{a}^\dagger_{-\vec{q}}. \tag{2.4.5}$$

Therefore, the phonon Green's functions differ from the otherwise general results in Eq. (2.3.43). For example, the free phonon correlation function D_0^{-+} is a sum of two contractions. Obviously, it contains two terms that introduce the phonon density n_q (see e.g. [10])

$$i\hbar D_0^{-+}(\vec{q},\omega) = i\hbar D_0^{+-}(-\vec{q},-\omega) = 2\pi n_q \delta(\omega-\omega_q) + 2\pi(1+n_q)\,\delta(\omega+\omega_q). \tag{2.4.6}$$

Since the phonons are assumed to be unaffected by the scattering with electrons, D_0 depends only on the difference of the two time coordinates (but not on their sum) and it is transformed into the frequency domain ω. The causal phonon Green's function can be directly derived from its definition Eq. (2.2.2) (see appendix C.1)

$$\begin{aligned} & i\hbar D_0^{--}(\vec{q},\omega) \\ = \;& i\hbar \int \mathrm{d}(t_2-t_1)\,\mathrm{e}^{-i\omega(t_2-t_1)}\left[\theta(t_1-t_2)\,D_0^{+-}(\vec{q},t_1-t_2) + \theta(t_2-t_1)\,D_0^{-+}(\vec{q},t_1-t_2)\right] \\ = \;& i\lim_{\varepsilon\to 0}\frac{1}{\omega-\omega_q+i\varepsilon} - i\lim_{\varepsilon\to 0}\frac{1}{\omega+\omega_q+i\varepsilon} + 2\pi(1+n_q)\,\delta(\omega+\omega_q) + 2\pi n_q\delta(\omega-\omega_q) \end{aligned} \tag{2.4.7}$$

The phonons enter the electronic equations of motion via the potential $\hat{U}$ given in Eq. (2.4.1). From the electronic point of view, $\hat{U}$ is a one particle potential (in contrast to $\hat{W}$ in Eq. (2.3.1)). Only the phonon operators of expansion terms of *second* order in $\hat{U}$ can be contracted to phonon

Green's functions (see above) whereas $\hat{W}$ introduces already in *first* order enough operators for an additional Green's functions (see Sec. 2.3.2). This difference results in a "missing"factor of $\hbar$. Therefore we slightly modify the Feynman rules given in chapter 2.3.3 and include $\hbar$ in the pictogram of D, i.e. a curly phonon line represents the factor $i\hbar D^{\pm\pm}$ instead of $iD^{\pm\pm}$. It is also common (see e.g. [23]) to add the interaction potentials U_q represented by vertices. We have introduced the phonon Green's functions and the phonon-electron interaction potentials in the frequency and momentum representation. Therefore, we include a four dimensional Fourier transformation in the pictograms of the interaction lines

$$\frac{1}{(2\pi)^4}\int \mathrm{d}\vec{q}\mathrm{d}\omega \mathrm{e}^{i\vec{q}\cdot(\vec{x}_1-\vec{x}_2)}\mathrm{e}^{-i\omega(t_2-t_1)} iU_q^* iU_q^* i\hbar D_0^{++}(\vec{q};\omega) = \quad 1+ \quad 2+ \,,$$

$$\frac{1}{(2\pi)^4}\int \mathrm{d}\vec{q}\mathrm{d}\omega \mathrm{e}^{i\vec{q}\cdot(\vec{x}_1-\vec{x}_2)}\mathrm{e}^{-i\omega(t_2-t_1)} (-iU_q)\, iU_q^* i\hbar D_0^{-+}(\vec{q};\omega) = \quad 1- \quad 2+ \,,\ldots.$$

With these diagrams, the pictorial version of the equation of motion of $G^{--}(1;2)$ up to first nonvanishing (i.e. second) order in $\hat{U}$ reads

1- 2- = 1- 2- + 1- 3+ 4+ 2- + 1- 3+ 4- 2-

+ 1- 3- 4- 2- + 1- 3- 4+ 2- .

Here we can see another important difference to the instantaneous two particle interaction $\hat{W}$. The time coordinates at the two interaction points may differ and so may the signs at the two vertices (3 and 4) differ, too. Therefore, we get already in this order contributions to correlation self-energies

$$-i\Sigma^{+-}(3;4) = \quad 3+ \quad 4- \,,$$

$$-i\Sigma^{-+}(3;4) = \quad 3- \quad 4+ \,.$$

Since we need $\Sigma^{<}(\vec{x}_3,\vec{x}_4,\omega)$ in next chapters, we Fourier transform the last pictorial equation and use Eq. (2.4.6)

$$\begin{aligned}
& -i\Sigma^{-+}(\vec{x}_3,\vec{x}_4,\omega) \\
= \;& i\Sigma^{<}(\vec{x}_3,\vec{x}_4,\omega) \\
= \;& \frac{1}{(2\pi)^3}\int \mathrm{d}\vec{q}\mathrm{d}(t_4-t_3)(-iU_q)\left(iU_q^*\right)\mathrm{e}^{i\vec{q}\cdot(\vec{x}_3-\vec{x}_4)}\mathrm{e}^{i\omega(t_4-t_3)} iG_0^{-+}(\vec{x}_3,t_3;\vec{x}_4,t_4)\, i\hbar D_0^{-+}(\vec{q};t_3,t_4) \\
= \;& \frac{i}{(2\pi)^3}\int \mathrm{d}\vec{q}\,|U_q|^2\,\mathrm{e}^{i\vec{q}\cdot(\vec{x}_3-\vec{x}_4)}\left[n_q G_0^{<}(\vec{x}_3,\vec{x}_4,\omega-\omega_q)+(1+n_q)\,G_0^{<}(\vec{x}_3,\vec{x}_4,\omega+\omega_q)\right]. \quad (2.4.8)
\end{aligned}$$

In order to derive the formula for the retarded self-energy, we need $\Sigma^{--}(\vec{x}_3,\vec{x}_4,\omega)$ (see Eq. (C.2.4))

and get with the definition of the retarded self-energy Eq. (2.3.31)

$$\begin{aligned}
& -i\Sigma^R\left(\vec{x}_3,\vec{x}_4,\omega\right) \\
= \; & -i\left(\Sigma^{--}\left(\vec{x}_3,\vec{x}_4,\omega\right)+\Sigma^{-+}\left(\vec{x}_3,\vec{x}_4,\omega\right)\right) \\
= \; & -\frac{i}{(2\pi)^3}\int \mathrm{d}\vec{q}|U_q|^2\,\mathrm{e}^{i\vec{q}\cdot(\vec{x}_1-\vec{x}_2)}\left[n_q G_0^R\left(\vec{x}_3,\vec{x}_4,\omega+\omega_q\right)+\left(1+n_q\right)G_0^R\left(\vec{x}_3,\vec{x}_4,\omega-\omega_q\right)\right] \\
& -\frac{i}{(2\pi)^3}\int \mathrm{d}\vec{q}|U_q|^2\,\mathrm{e}^{i\vec{q}\cdot(\vec{x}_3-\vec{x}_4)}\left[\frac{1}{2}G_0^<\left(\vec{x}_3,\vec{x}_4,\omega-\omega_q\right)-\frac{1}{2}G_0^<\left(\vec{x}_3,\vec{x}_4,\omega+\omega_q\right)\right] \\
& -\frac{1}{(2\pi)^4}\int \mathrm{d}\omega'\int \mathrm{d}\vec{q}|U_q|^2\,\mathrm{e}^{i\vec{q}\cdot(\vec{x}_1-\vec{x}_2)}G_0^<\left(\vec{x}_3,\vec{x}_4,\omega-\omega'\right)\mathrm{Pr}\left(\frac{1}{\omega'+\omega_q}-\frac{1}{\omega'-\omega_q}\right). \qquad (2.4.9)
\end{aligned}$$

These two self-energies are given in the single Born approximation, since they depend on the free-particle Green's function G_0. We can extend these self-energies to the self-consistent Born approximation by simply replacing the free fermionic Green's functions G_0 with the exact one G (see Sec. 2.3.4). We will show in detail in Sec. 3.5.7 that the self-consistent Born approximation conserves the current - in contrast to the single Born approximation. However, we can see this already here, when we recall that the two-fold scattering with phonons actually gives us a two particle Green's function G_2 in the equation of motion of G. We have approximated this two particle Green's function with a product of one particle Green's functions in Eq. (1.4.11) and merged one of those one particle Green's functions with the interaction potential into the self-energy. The remaining one particle Green's function given in that product enters the Dyson equation explicitly. One of the prerequisites that such an approximation obeys the conservation laws is given in Eq. (1.4.14), i.e. the symmetry of the approximated two particle Green's function under exchange of the propagation coordinates. When the Green's function in the self-energy formula does not match the Green's function that is explicitly given in the Dyson equation (as is the case in the single Born approximation), Eq. (1.4.14) can obviously not be fulfilled.

Fluctuation-Dissipation-Theorem in the presence of phonons

We have seen in Eq. (2.2.15) that in equilibrium, the lesser Green's function equals the spectral function multiplied with the Fermi distribution. One may wonder, whether our self-consistent Born approximation of the inelastic scattering with phonons is consistent with a Fermi distributed electron system. We could proof this, by inserting $\Sigma^<$ of Eq. (2.4.8) into the Keldysh equation Eq. (2.3.37) and verify that Eq. (2.2.15) is a solution. However, Datta has already shown in [7] that Eq. (2.2.15) holds already, when the lesser self-energy obeys

$$\Sigma^<\left(\vec{x}_1,\vec{x}_2,\omega\right)=-f\left(\hbar\omega,\mu\right)\left[\Sigma^R\left(\vec{x}_1,\vec{x}_2,\omega\right)-\Sigma^A\left(\vec{x}_1,\vec{x}_2,\omega\right)\right]. \qquad (2.4.10)$$

In order to proof that the electrons are distributed according to the Fermi distribution, we apply the Eqs. (2.2.15), (2.4.8), (2.4.9) and (2.4.10) and derive a condition for the phonon distribution. When this condition was not met, we had achieved a contradiction and the function f had to differ from the Fermi distribution. In this way, we derive a condition for the phonon self-energy.

We first insert Eq. (2.2.15) in the lesser self-energy Eq. (2.4.8)

$$\begin{aligned}
& i\Sigma^<\left(\vec{x}_3,\vec{x}_4,\omega\right) \\
= \; & \frac{1}{(2\pi)^3}\int \mathrm{d}\vec{q}|U_q|^2\,\mathrm{e}^{i\vec{q}\cdot(\vec{x}_3-\vec{x}_4)}\left[-n_q f\left(\hbar\omega-\hbar\omega_q,\mu\right)A\left(\vec{x}_3,\vec{x}_4,\omega-\omega_q\right)\right. \\
& \left.-\left(1+n_q\right)f\left(\hbar\omega+\hbar\omega_q,\mu\right)A\left(\vec{x}_3,\vec{x}_4,\omega+\omega_q\right)\right]. \qquad (2.4.11)
\end{aligned}$$

Next, we utilize Eq. (2.2.15) in the formulas for the retarded and advanced self-energies

$$\begin{aligned}
&\Sigma^{R,A}\left(\vec{x}_3,\vec{x}_4,\omega\right)\\
=\;&\frac{1}{(2\pi)^3}\int \mathrm{d}\vec{q}|U_q|^2\,\mathrm{e}^{i\vec{q}\cdot(\vec{x}_3-\vec{x}_4)}\left[n_q G^{R,A}\left(\vec{x}_3,\vec{x}_4,\omega+\omega_q\right)+\left(1+n_q\right)G^{R,A}\left(\vec{x}_3,\vec{x}_4,\omega-\omega_q\right)\right]\\
&\pm\frac{i}{(2\pi)^3}\int \mathrm{d}\vec{q}|U_q|^2\,\mathrm{e}^{i\vec{q}\cdot(\vec{x}_3-\vec{x}_4)}\left[\frac{1}{2}f\left(\hbar\omega-\hbar\omega_q,\mu\right)A\left(\vec{x}_3,\vec{x}_4,\omega-\omega_q\right)\right.\\
&\left.-\frac{1}{2}f\left(\hbar\omega+\hbar\omega_q,\mu\right)A\left(\vec{x}_3,\vec{x}_4,\omega+\omega_q\right)\right]+\int \mathrm{d}\omega'\int \mathrm{d}\vec{q}\left[\frac{|U_q|^2}{(2\pi)^4}\mathrm{e}^{i\vec{q}\cdot(\vec{x}_3-\vec{x}_4)}\right.\\
&\left.\times f\left(\hbar\omega-\hbar\omega',\mu\right)A\left(\vec{x}_3,\vec{x}_4,\omega-\omega'\right)\mathrm{Pr}\left(\frac{1}{\omega'+\omega_q}-\frac{1}{\omega'-\omega_q}\right)\right].
\end{aligned}\tag{2.4.12}$$

Here, the upper sign refers to the retarded, the lower to the advanced self-energy. When we take the difference of both self-energies, the principle value integrals cancel and we get

$$\begin{aligned}
&i\left(\Sigma^R\left(\vec{x}_3,\vec{x}_4,\omega\right)-\Sigma^A\left(\vec{x}_3,\vec{x}_4,\omega\right)\right)\\
=\;&\frac{1}{(2\pi)^3}\int \mathrm{d}\vec{q}|U_q|^2\,\mathrm{e}^{i\vec{q}\cdot(\vec{x}_3-\vec{x}_4)}\left[\left(n_q+f\left(\hbar\omega+\hbar\omega_q,\mu\right)\right)A\left(\vec{x}_3,\vec{x}_4,\omega+\omega_q\right)\right.\\
&\left.+\left(1+n_q-f\left(\hbar\omega-\hbar\omega_q,\mu\right)\right)A\left(\vec{x}_3,\vec{x}_4,\omega-\omega_q\right)\right].
\end{aligned}\tag{2.4.13}$$

When we compare the last equation with Eq. (2.4.11), it is easy to see that Eq. (2.4.10) is only fulfilled when the following relations of f and n_q hold

$$f\left(\hbar\omega,\mu\right)\left[n_q+f\left(\hbar\omega+\hbar\omega_q,\mu\right)\right]=\left(1+n_q\right)f\left(\hbar\omega+\hbar\omega_q,\mu\right),\tag{2.4.14}$$

$$f\left(\hbar\omega,\mu\right)\left[1+n_q-f\left(\hbar\omega-\hbar\omega_q,\mu\right)\right]=n_q f\left(\hbar\omega-\hbar\omega_q,\mu\right).\tag{2.4.15}$$

These equations are fulfilled, when f and n_q are the Fermi and Bose distributions, respectively. Therefore, the electron distribution in equilibrium equals the Fermi distribution (i.e. Eq. (2.4.10) holds), if n_q equals the Bose distribution. In contrast, when we approximate the phonon distribution function, the distribution of electrons in equilibrium will deviate the stronger from the Fermi distribution the more important phonon scattering is (see Sec. 3.5.3). It is worth to mention, that Eq. (2.4.10) does not require the self-consistent Born approximation to be converged. Instead, Eq. (2.2.15) holds for any term of the scattering perturbation expansion.

2.4.3 Scattering on charged impurities

We consider a large number N of randomly distributed ionized impurities. Since the actual positions of the impurities are unknown, we can only calculate expectation values with respect to the impurity distribution probability. Let $P\left(\vec{r}_1,\vec{r}_2,\ldots,\vec{r}_N\right)$ denote the probability to find the impurities at the positions $\left(\vec{r}_1,\vec{r}_2,\ldots,\vec{r}_N\right)$. We approximate the probability to find impurity i at $\vec{r}_i$ $\left(P\left(\vec{r}_i\right)\right)$ to be independent of the positions of the other impurities. Then the probability for a specific impurity distribution reads

$$P\left(\vec{r}_1,\vec{r}_2,\ldots,\vec{r}_N\right)=\prod_{i=1}^{N}P\left(\vec{r}_i\right).\tag{2.4.16}$$

We follow Kohn and Luttinger [24] and define the expectation value of any function F with respect to all impurity distributions by

$$\langle F(\vec{r}_1, \vec{r}_2, \ldots, \vec{r}_N)\rangle_{\text{imp}} = \int \prod_{i=1}^{N} \mathrm{d}\vec{r}_i P(\vec{r}_i)\, F(\vec{r}_1, \vec{r}_2, \ldots, \vec{r}_N)\,. \tag{2.4.17}$$

When we additionally assume the impurities to be homogeneously distributed over the device, the probability to find the impurity i in the normalization volume V reads

$$P(\vec{r}_i) = 1/V. \tag{2.4.18}$$

Since this interaction is a constant with respect to time, the equation of motion for the causal Green's function in linear order of V_{imp} can be derived straightforwardly (see Eq. (2.3.6) and e.g. [8])

$$\begin{aligned} & G^{--}(1;2) \\ = \; & G_0^{--}(1;2) + \left\langle \int \mathrm{d}3 G_0^{--}(1;3)\, G_0^{--}(3;2)\, V_{\text{imp}}(\vec{x}_3; \vec{r}_1, \vec{r}_2, \ldots, \vec{r}_N) \right\rangle_{\text{imp}} \\ = \; & G_0^{--}(1;2) + \left\langle \int \mathrm{d}3 G_0^{--}(1;3)\, G_0^{--}(3;2) \int \frac{\mathrm{d}\vec{q}}{(2\pi)^3} V_{\text{imp}}(\vec{q}) \sum_{i=1}^{N} \mathrm{e}^{i\vec{q}\cdot(\vec{x}_3 - \vec{r}_i)} \right\rangle_{\text{imp}} \end{aligned} \tag{2.4.19}$$

Except for the transforming factor of the scattering potential $\exp(i\vec{q}\cdot(\vec{x}_3 - \vec{r}_i))$, all functions in the last equation are independent of the impurity distribution. Therefore, we can average that sum independently from the rest

$$\begin{aligned} \left\langle \sum_{i=1}^{N} \mathrm{e}^{i\vec{q}\cdot(\vec{x}_3 - \vec{r}_i)} \right\rangle_{\text{imp}} &= \int \prod_{i=1}^{N} \mathrm{d}\vec{r}_i P(r_i) \sum_{j=1}^{N} \mathrm{e}^{i\vec{q}\cdot(\vec{x}_3 - \vec{r}_j)} \\ &= \frac{1}{V^N} \int \mathrm{d}\vec{r}_1 \mathrm{d}\vec{r}_2 \ldots \mathrm{d}\vec{r}_N \left(\mathrm{e}^{i\vec{q}\cdot(\vec{x}_3 - \vec{r}_1)} + \mathrm{e}^{i\vec{q}\cdot(\vec{x}_3 - \vec{r}_2)} + \ldots \mathrm{e}^{i\vec{q}\cdot(\vec{x}_3 - \vec{r}_N)} \right) \\ &= \frac{N}{V} \int \mathrm{d}\vec{r} \mathrm{e}^{i\vec{q}\cdot(\vec{x}_3 - \vec{r})} = N \frac{(2\pi)^3}{V} \delta(\vec{q})\,. \end{aligned} \tag{2.4.20}$$

Obviously, scattering at homogeneously distributed impurities adds in first order a constant to the free-particle's Green's function. The same is true for any propagation with an arbitrary number of scattering events at mutually different impurities. The pictorial versions of such constant terms read

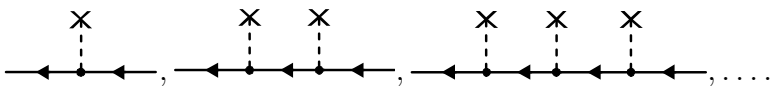

Constants can be merged with the system's energy and are therefore omitted from the calculations. This result is still approximately true, when the charged impurities are randomly distributed in a finite, but large volume (e.g. a finite doping area), as long as the exponents in Eq. (2.4.20) can grow large enough*. If the impurity density is too rapidly oscillating, the

*Large enough in the sense that $\sin(qx)/x$ may be approximated for large x with the delta distribution $\delta(q)$.

constant density of charged impurities has to be replaced with the position dependent impurity density $N(\vec{x})$ as will be done in Sec. 3.5.4.

The first nonvanishing expansion terms of the Green's function with respect to $V(\vec{q})$ describe the two-fold scattering at a single impurity

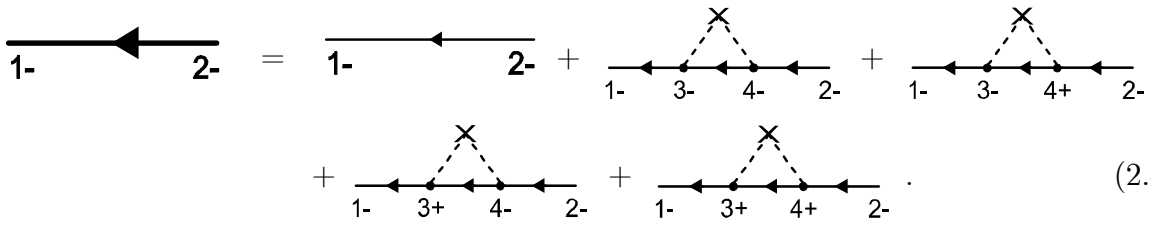

(2.4.21)

We define interaction lines for the averaged correlation of the scattering potential

$$\langle (-i)\, V_{\mathrm{imp}}(\vec{x}_1;\vec{r}_1,\vec{r}_2,\ldots,\vec{r}_N)\,(-i)\, V_{\mathrm{imp}}(\vec{x}_2;\vec{r}_1,\vec{r}_2,\ldots,\vec{r}_N)\rangle_{\mathrm{imp}} \quad = \quad$$

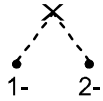

,

$$\langle (-i)\, V_{\mathrm{imp}}(\vec{x}_1;\vec{r}_1,\vec{r}_2,\ldots,\vec{r}_N)\, iV_{\mathrm{imp}}(\vec{x}_2;\vec{r}_1,\vec{r}_2,\ldots,\vec{r}_N)\rangle_{\mathrm{imp}} \quad = \quad$$

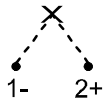

, ...

Utilizing the Feynman rules, the lesser self-energy obviously reads

$$-i\Sigma^{-+}(3;4) \quad = \quad$$

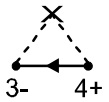

$$= \quad iG_0^{-+}(3;4)\,\langle V_{\mathrm{imp}}(\vec{x}_3;\vec{r}_1,\vec{r}_2,\ldots,\vec{r}_N)\, V_{\mathrm{imp}}(\vec{x}_4;\vec{r}_1,\vec{r}_2,\ldots,\vec{r}_N)\rangle_{\mathrm{imp}} \quad (2.4.22)$$

This is already the result, that we will need in later chapters. However, in order to complete this example, we further specify the formula for the self-energy. Therefore, we repeat the derivations of Eq. (2.4.20) in the case of these second order terms of the perturbation expansion and get

$$\begin{aligned}
&\langle V_{\mathrm{imp}}(\vec{x}_3;\vec{r}_1,\vec{r}_2,\ldots,\vec{r}_N)\, V_{\mathrm{imp}}(\vec{x}_4;\vec{r}_1,\vec{r}_2,\ldots,\vec{r}_N)\rangle_{\mathrm{imp}} \\
&= \frac{1}{V^N}\int\prod_{i=1}^{N}\mathrm{d}\vec{r}_i\frac{1}{(2\pi)^6}\int\mathrm{d}\vec{q}\mathrm{d}\vec{q}' V_{\mathrm{imp}}(\vec{q})\, V_{\mathrm{imp}}(\vec{q}')\sum_{j=1}^{N}\mathrm{e}^{i\vec{q}\cdot(\vec{x}_3-\vec{r}_j)}\mathrm{e}^{i\vec{q}'\cdot(\vec{x}_4-\vec{r}_j)} \\
&= \frac{N}{V}\frac{1}{(2\pi)^6}\int\mathrm{d}\vec{r}\mathrm{d}\vec{q}\mathrm{d}\vec{q}' V_{\mathrm{imp}}(\vec{q})\, V_{\mathrm{imp}}(\vec{q}')\,\mathrm{e}^{-i(\vec{q}+\vec{q}')\cdot\vec{r}}\mathrm{e}^{i\vec{q}\cdot\vec{x}_3}\mathrm{e}^{i\vec{q}'\cdot\vec{x}_4} \\
&= \frac{N}{V}\frac{1}{(2\pi)^3}\int\mathrm{d}\vec{q} V_{\mathrm{imp}}(\vec{q})\, V_{\mathrm{imp}}(-\vec{q})\,\mathrm{e}^{i\vec{q}\cdot(\vec{x}_3-\vec{x}_4)}. \qquad (2.4.23)
\end{aligned}$$

Here, we get a position dependent result which affects the propagation. Since impurity potentials such as the Debye-Hückel potential depend on the *absolute* value of the transferred momentum (rather than its direction), we get for $\Sigma^{<}$

$$-\Sigma^{-+}(3;4) = \Sigma^{<}(3;4) = G_0^{<}(3;4)\,\frac{N}{V}\frac{1}{(2\pi)^3}\int\mathrm{d}\vec{q}\,|V_{\mathrm{imp}}(q)|^2\,\mathrm{e}^{i\vec{q}\cdot(\vec{x}_3-\vec{x}_4)}. \qquad (2.4.24)$$

We get analogously for the causal self-energy*

$$\Sigma^{--}(3;4) = G_0^{--}(3;4)\,\frac{N}{V}\frac{1}{(2\pi)^3}\int\mathrm{d}\vec{q}\,|V_{\mathrm{imp}}(q)|^2\,\mathrm{e}^{i\vec{q}\cdot(\vec{x}_3-\vec{x}_4)}. \qquad (2.4.25)$$

*Please note the change of the sign is due to the fact that both vertices of Σ^{--} lie on the chronological branch.

This gives us for the retarded self-energy

$$\begin{aligned}\Sigma^R(3;4) &= \Sigma^{--}(3;4) + \Sigma^{-+}(3;4) \\ &= \left[G_0^{--}(3;4) - G_0^{-+}(3;4)\right] \frac{N}{V} \frac{1}{(2\pi)^3} \int \mathrm{d}\vec{q} |V_{\mathrm{imp}}(q)|^2 \, \mathrm{e}^{i\vec{q}\cdot(\vec{x}_3 - \vec{x}_4)} \\ &= G_0^R(3;4) \frac{N}{V} \frac{1}{(2\pi)^3} \int \mathrm{d}\vec{q} |V_{\mathrm{imp}}(q)|^2 \, \mathrm{e}^{i\vec{q}\cdot(\vec{x}_3 - \vec{x}_4)}. \end{aligned} \tag{2.4.26}$$

The discussion at the end of the preceding section applies also to these self-energies. This means, we get the self-energy in the self-consistent Born approximation by replacing the free-particle Green's functions in Eqs. (2.4.24) and (2.4.26) with exact ones.

Part II

Vertical stationary transport in semiconductor heterostructures

In the first part of this thesis, we have given a general overview of the nonequilibrium Green's functions formalism (NEGF). Thereby, we have followed the seminal work of many physicists in the 1960s. Many groups have applied the NEGF formalism on various transport problems since then, ranging from phononic [25] to electronic transport [26, 27], covering metals [28, 29], semiconductors [30] as well nanotubes [31, 32] and fullerenes [33] or even (organic) molecules [34, 35].

The complexity of these systems typically requires for a large number of approximate assumptions. In the area of electronic transport in semiconductor devices, some of the most prominent assumptions are:

- Ignoring energy dissipation or even incoherent scattering at all
- Limiting incoherent scattering to a finite area of the system
- Neglecting the position, energy and/or momentum dependence of scattering
- Solving wave functions and state occupancy independently
- Assuming the electron-supplying reservoirs to remain in equilibrium

The physical impact of these and other assumptions is often tedious to discuss, because first, the approximations are often done "in the middle" of the NEGF formalism which makes a physical interpretation difficult. Second, the complexity of the systems the NEGF formalism is applied to typically prohibits a discrimination between artifacts of the approximate assumptions and characteristic physics of the considered system. The complexity of many systems does not allow for an exact implementation of the NEGF formalism which makes it particularly difficult to judge the quality of such approximations. Maybe that is the most important reason, why a systematic study of most of the common approximations is still missing in literature.

In this part of the thesis, we assess most of the approximations that are typically applied in the area of NEGF. We compare the approximate results with results of exact calculations and analyze their physical impact in detail. Since our work is also limited by numerical demands, we limit our system to stationary electronic transport perpendicular to homogeneously grown semiconductor layers. We thereby consider one of the simplest transport problems of envelope function theory, i.e. transport of electrons in a single conduction band in the effective mass approximation. We thereby further assume the effective mass to be isotropic which limits our considerations to zink-blende type materials. However, this simple system offers a large variety of devices, ranging from homogeneous bulk semiconductors to quantum confined stark ladders. This simple system also allows for comparably exact solutions of the nonequilibrium Green's functions, which is an important prerequisite to unambiguously analyze the applicability and the physical impact of the approximations given above.

Nevertheless, there do exist devices in reality which can be described by this simple model. We focus in the end of this part on one of these systems - terahertz quantum cascade lasers (THz-QCLs). This relatively new class of lasers represents a promising candidate for the high performance requirements of heterodyne detection [36], gas phase spectroscopy [37], real time imaging [38] as well as for detectors in security applications. It is common to apply the NEGF formalism on cascade structures with periodic boundary conditions. Since this approach limits the Hilbert space on periodic solutions, it misses non-periodic phenomena such as hot electrons and device states that extend beyond a single period. In addition, periodic boundary conditions require for sufficient energy dissipation and are inadequate for the description of ballistic

transport. For these reasons, we develop a new type of boundary conditions that treat the QCL as an open quantum device, but simultaneously mimic the periodic nature of the device. We compare our theoretically predicted results with experimental data of a recently realized THz-QCL. The very good agreement with experiment is a nice example for the large capacity of the NEGF formalism to describe quantum transport in realistic environments. Results of our new type of boundary conditions allow us to clarify some highly debated questions in the area of THz-QCLs:

- Is the transport in THz-QCLs mainly coherent or incoherent?
- Which incoherent scattering mechanisms are most important?
- What is the impact of hot carriers on periodic systems?
- To which extend is electronic transport in QCLs periodic and how many periods have to be considered?
- Is the dependence of the threshold current on doping density determined by transport physics or wave guide optics?
- What dominates the temperature degradation of THz-QCL output performance?

Apart from answering these and related questions, we unveil disadvantages of state of the art QCL designs. We also propose several improved THz-QCLs that yield higher optical gain, smaller threshold currents, an improved electron periodicity and a higher resistivity to imperfection of the semiconductor growth.

Chapter 3

Method - Green's functions in vertical transport

3.1 Introduction

In the previous chapters, we have derived the nonequilibrium Green's function (NEGF) formalism in a very general manner. Therefore, we have to specify in this chapter our method on vertical electronic transport in semiconductor heterostructures. Thereby, we introduce several new developments concerning the scattering self-energies, the boundary conditions and an efficient numerical discretization of the Green's functions and self-energies.

We first represent all relevant formulas such as the Dyson and Keldysh equations as well as observables such as the local density and the current density in a spatial eigenfunction basis. In addition, we introduce several expectation values that are experimentally inaccessible, but contain valuable information about the device physics.

We derive and discuss the screening length in the Lindhard and Debye model and extend these formulas into the regime of incoherently scattered Green's functions. Since this cannot be found in literature, we show that incoherent scattering at finite temperatures increases the electronic screening length. Unfortunately, the self-consistent screening formula is numerically too demanding to be implemented on the transport calculations by default and we limit the screening in all transport calculations of this thesis to the Debye screening model. However, we first show that the numerically efficient Debye screening model is appropriate for all quantitative comparisons with experimental data that we present in this thesis.

We specify the rather general formulas for the scattering self-energies of the preceding chapter on all relevant scattering mechanisms. The scattering self-energies have to be approximated carefully in order to guarantee realistic scattering, but also to achieve a numerically feasible model. Since only few of our results (namely scattering with LO-phonons and rough interfaces) can be found in literature, we present the derivation of all implemented scattering self-energies in great detail to shed light on all the performed approximations. The perfect agreement of numerical results of our self-energies with analytical formulas of Fermi's golden rule demonstrate the validity of our approximations. Only the implementation of the GW_0-approximation for incoherent electron-electron interaction is meant as a rough estimate. We use this estimate in chapter 5 to find an upper limit for the influence of electron-electron scattering on transport characteristics of THz-QCLs. We derive a numerically efficient self-energy for the elastic scattering at ionized impurities and present a novel approach for the unscreened, inelastic scattering with longitudinal acoustic phonons. This later self-energy is in particular interesting, since its

symmetry allows for a numerically efficient separate solution of the retarded and the lesser Green's functions, while Pauli's principle is preserved. This is important to mention, since such a separate treatment of G^R and $G^<$ usually violates Pauli's principle, as will be discussed in greater detail in Sec. 4.3.3. This symmetry will be most valuable in the area of scattered quantum transport in higher dimensional devices (see Sec. 7.3). Furthermore, we exemplify in great detail that the scattering self-energies have to be determined in the self-consistent Born approximation. In particular, we show that first order and single Born approximations of the Dyson and Keldysh equations violate current conservation.

We also present in detail the implemented boundary conditions. We expand the well-known concept of contact self-energies by self-consistently including incoherent scattering within the semi-infinite lead regions. We will see in Sec. 4.2.2 that this self-consistency of the leads with the device is essential for reflectionless device/lead interfaces. Such reflections have been frequently neglected in literature. Since we will consider stationary transport in quantum cascade structures in later chapters, we expand the well-known concept of contact self-energies to leads with inhomogeneous conduction band profiles. This will allow us to consider the cascade structures as *open* quantum devices, in spite of applying the commonly used periodic boundary conditions. This new method will unveil unknown phenomena of transport in periodic geometries in the subsequent chapter 5.

The commonly used flatband conditions for the Poisson equation yield the problem of an incomplete bias drop within the device. Therefore, we introduce a new approach and solve the Poisson equation with Neumann boundary conditions with finite slopes of the conduction band profile at the device boundaries. These slopes are self-consistently determined in order to guarantee globally charge neutral devices as well as unambiguously defined applied bias voltages. Typically, the semi-infinite leads are considered to remain in equilibrium, regardless of the amount of current in biased devices. This assumption is only justified in the case of very small current densities (e.g. in the case of tunneling transport in quantum cascade lasers). Comparably low resistive devices such as $n-i-n$ resistors usually face rather high current densities which require for a self-consistent response of the leads. For this reason, we present a novel scheme to determine a change of the electron distribution in the leads self-consistently with the finite current density in the device.

A numerical implementation of NEGF faces several critical issues that we address in detail. For instance, a current conserving numerical implementation of incoherent scattering in the self-consistent Born approximation requires for the self-energies to precisely fulfill certain symmetry relations. While the analytical formulas follow this symmetry, their numerical implementation is very sensitive to small errors that arise from any finite numerical discretization. This is particularly important when energy and momentum are resolved on an inhomogeneous grid. We derive in detail several numerical conditions that are essential for a current conserving solution of the transport problem. We also present a numerically efficient solution of the lead surface Green's functions and present a flow chart of our NEGF algorithm that gives an overview of the self-consistently implemented transport equations and discretization schemes.

3.2 Fundamentals

3.2.1 Introduction

We begin our adaptation of the NEGF formalism on vertical transport through layered semiconductor heterostructures with the choice of the basis functions. Many different representations for the Green's functions can be found in literature. Most of them have been chosen to suit very specific devices. This is numerically efficient, however, it limits the transport model on specific problems. Thus, in order to guarantee highest flexibility, we choose similar to Datta [7] a real-space representation in growth direction. We present the Dyson and Keldysh equations in this representation and give the formulas for all noninteracting particle Green's functions. We discuss the physical origin of the divergence of these free-particle Green's functions with vanishing momentum and point out, how this divergence can be handled numerically.

3.2.2 Spatial eigenfunction representation

Alternative representations

We adapt the nonequilibrium Green's function formalism introduced in the first part of this thesis on electrons in semiconductor heterostructures. We consider the electrons in a single conduction band in the envelope function approximation, i.e. we calculate the envelope of the electronic wave function as a function of the lattice vector $\vec{R} = (x, y, z)$. We also consider the lattice vector to be continuous which requires the device structure to vary at least on nanometer length scale (large compared to the interatomic distance of the order of one Ångström). The complete electronic wave function is an integral of this envelope function multiplied with the Wannier function that reflects the periodicity of the crystal (see for further details e.g. [39]). For the transport problems in this part of the thesis, the periodicity of the crystal can be assumed to be unaffected by external fields and the determination of the electronic envelope function is completely sufficient.

We focus on the vertical transport through layered semiconductor heterostructures that are grown in the z-direction and homogeneous in the x- and y-directions. We consider the electron in a single conduction band in the effective mass approximation. We thereby assume the effective mass m^* to be a scalar. However, the effective mass is a function of position and energy due to different layer materials and nonparabolic dispersion relations, respectively.

The homogeneity of the device layers motivates the following product ansatz for the envelope of the electronic wave functions

$$\psi_{\hat{H}_0}(\vec{x}) = \frac{1}{\sqrt{A}} \mathrm{e}^{i\vec{k}_\parallel \cdot \vec{x}_\parallel} \psi_{\hat{H}_0}(z,t)\,. \tag{3.2.1}$$

Due to the homogeneity in (x, y) the lateral momentum $\hbar k_\parallel$ is a good quantum number. This justifies our ansatz of plain waves normalized in the area A for the lateral component of $\psi_{\hat{H}_0}$. Several different choices for $\psi_{\hat{H}_0}(z)$ can be found in literature. For example, Wannier [40] and Wannier-Stark functions [41] are most suited for quantum cascade structures. Functions composed of Airy functions [42, 43] are convenient for $n - i - n$ resistors and homogeneous systems. These choices are numerically advantageous when they limit the number of basis states in growth direction that are needed for converged results (e.g. less than 10 states per period in quantum cascade structures [41]). However, the choice of such specialized basis functions limits

the applicability of the respective transport model on a specific problem. For example, it will take many Airy functions to describe transport in a quantum cascade structure and vice versa.

Spatial eigenfunctions

Since the purpose of this part of the thesis is to enlighten the physical impact of common approximations applied on *various* systems, we have to preserve a high degree of flexibility. For this reason, we follow S. Datta [7] and represent the Green's functions on a spatial grid. Thus, we identify $\psi_{\hat{H}_0}(z)$ with eigenfunctions of the position operator $\hat{z}$

$$\hat{z}\psi_{\hat{H}_0}(z') = z'\psi_{\hat{H}_0}(z'). \tag{3.2.2}$$

When we discretize the spatial coordinate z on a homogeneous* mesh with grid spacing Δ, $\psi_{\hat{H}_0}$ is a rectangular function

$$\psi_{\hat{H}_0}(z) = \begin{cases} \sqrt{\Delta^{-1}}, \forall z \in [z - \Delta/2; z + \Delta/2] \\ 0, \text{ elsewhere} \end{cases}. \tag{3.2.3}$$

This function reaches in the limit of an infinitely small grid spacing the Dirac delta function

$$\lim_{\Delta \to 0} \psi_{\hat{H}_0}(z') = \delta(z - z'), \tag{3.2.4}$$

i.e. the position eigenfunction in the spatial representation (see [16]). The choice of this basis has the advantage that it allows to describe any kind of devices, ranging from highly confined systems such as quantum cascade structures to completely open devices such as $n - i - n$ resistors and even homogeneous systems. However, the number of basis states (i.e. the number of spatial grid points) that are required for a faithful description of structures consisting of many different layers can be large. Since the Green's functions and self-energies contain two spatial coordinates, a larger number of basis states increases the numerical demand tremendously. This effectively limits the maximum length as well as the maximum number of layers in the device. A possible solution is to implement an inhomogeneous spatial grid†. However, this is an issue of a device simulator and beyond the scope of this work.

Keldysh and Dyson equation in the stationary limit

Due to the chosen basis, the Green's functions and self-energies depend on two propagation coordinates (z_1, z_2), the lateral momentum $k_\parallel$ and (originally) on two propagation times (t_1, t_2). Since we consider the stationary limit, all entities are independent of the sum of the propagation times $((t_1 + t_2)/2)$. Thus, we Fourier transform with respect to the difference of the two propagation times $(t_1 - t_2)$ into the electronic energy E domain. When we set $t_2 = 0$, it is obvious that the differential operator Eq. (2.3.21) reads in the energy domain

$$\hat{G}_0^{-1}\left(z, k_\parallel, E\right) = E\hat{1} - \hat{H}_0\left(z, k_\parallel, E\right) - V(z)\,\hat{1} - e\Phi(z)\,\hat{1}. \tag{3.2.5}$$

Here, e is the negative elementary charge, Φ and V are the electrostatic Hartree potential and the single particle potential that accounts for material dependent conduction band offsets. The

*In an inhomogeneous grid, one has to replace the global grid spacing Δ in Eq. (3.2.3) with an individual spacing Δ_i for each grid point i.

†Utilizing (e.g.) the block integration method (see [44]).

later two are multiplied with the unitary operator $\hat{1}$. The Hamilton operator $\hat{H}_0\left(z, k_\parallel, E\right)$ reads

$$\hat{H}_0\left(z, k_\parallel, E\right) = \frac{-\hbar^2}{2}\frac{\mathrm{d}}{\mathrm{d}z}\frac{1}{m^*\left(z, E\right)}\frac{\mathrm{d}}{\mathrm{d}z} + \frac{\hbar^2 k_\parallel^2}{2m^*\left(z, E\right)}\hat{1}. \tag{3.2.6}$$

It is straightforward to derive the Fourier transformed Dyson and Keldysh equations from Eqs. (2.3.33) and (2.3.37)

$$\begin{aligned}
\hat{G}_0^{-1}\left(z_1, k_\parallel, E\right) G^R\left(z_1, z_2, k_\parallel, E\right) &= \delta\left(z_1 - z_2\right) + \int \mathrm{d}z_3 \Sigma^R\left(z_1, z_3, k_\parallel, E\right) G^R\left(z_3, z_2, k_\parallel, E\right), \\
\hat{G}_0^{-1}\left(z_1, k_\parallel, E\right) G^<\left(z_1, z_2, k_\parallel, E\right) &= \int \mathrm{d}3 \left[\Sigma^R\left(z_1, z_3, k_\parallel, E\right) G^<\left(z_3, z_2, k_\parallel, E\right)\right. \\
&\quad \left. + \Sigma^<\left(z_1, z_3, k_\parallel, E\right) G^{R\dagger}\left(z_3, z_2, k_\parallel, E\right)\right].
\end{aligned} \tag{3.2.7}$$

Wherever possible, we abbreviate the matrix shape with respect to (z_1, z_2) with bold type. In this way, integrals over the vertex coordinate are abbreviated with simple matrix products. For a given energy E and lateral momentum $k_\parallel$, the Dyson equation for the retarded (Eq. (2.3.33)) and the Keldysh equation for the lesser (Eq. (2.3.37)) Green's functions read in operator form

$$\left(E\mathbf{1} - \mathbf{H}_0 - \mathbf{V} - e\mathbf{\Phi} - \mathbf{\Sigma}^R\right)\mathbf{G}^R = \mathbf{1}, \tag{3.2.8}$$

$$\mathbf{G}^< = \mathbf{G}^R\mathbf{\Sigma}^<\mathbf{G}^{R\dagger}. \tag{3.2.9}$$

Here, the matrices $\mathbf{V}$ and $\mathbf{\Phi}$, are diagonal with $V\left(z\right)$ and $\Phi\left(z\right)$ on the diagonal, respectively.

3.2.3 Green's functions of noninteracting electrons and the role of $\sum^R$

We have to be careful when we call the following analytical formulas the "Green's functions of the noninteracting electrons". First, even a single electron in an idealized, homogeneous, and unbiased semiconductor at zero temperature does interact. It does not scatter with phonons, impurities etc., but it is still affected by the periodic potential of the semiconductor crystal. Second, the Green's functions that we present here, are not the total electronic Green's functions, but only Green's functions of the envelopes of the electronic wave functions. Still, the effect of the periodic potential can be summed in a constant effective electron mass, so that the envelope Green's functions are similar to free electron Green's functions. Therefore, it is straightforward to derive the envelope Green's functions of electrons in the conduction band of

a homogeneous, field-free, and ballistic semiconductor from Eqs. (2.3.43)

$$\begin{aligned}
G_0^{<}\left(z_1,z_2,\vec{k}_\parallel,E\right) &= 2im^*(E)\,f(E,\mu)\,\frac{\cos\left[k_z\left(k_\parallel,E\right)(z_1-z_2)\right]}{\hbar^2 k_z\left(k_\parallel,E\right)},\\
G_0^{>}\left(z_1,z_2,\vec{k}_\parallel,E\right) &= -2im^*(E)\left[1-f(E,\mu)\right]\frac{\cos\left[k_z\left(k_\parallel,E\right)(z_1-z_2)\right]}{\hbar^2 k_z\left(k_\parallel,E\right)},\\
G_0^{R}\left(z_1,z_2,\vec{k}_\parallel,E\right) &= G_0^{A}\left(z_2,z_1,\vec{k}_\parallel,E\right)^*\\
&= -\frac{im^*(E)\exp\left[ik_z\left(k_\parallel,E\right)|z_1-z_2|\right]}{\hbar^2 k_z\left(k_\parallel,E\right)},\\
G_0^{C}\left(z_1,z_2,\vec{k}_\parallel,E\right) &= -G_0^{AC}\left(z_2,z_1,\vec{k}_\parallel,E\right)^*\\
&= \frac{im^*(E)}{\hbar^2 k_z\left(k_\parallel,E\right)}\left\{-\exp\left[ik_z\left(k_\parallel,E\right)|z_1-z_2|\right]\right.\\
&\quad \left.+2f(E,\mu)\cos\left[k_z\left(k_\parallel,E\right)(z_1-z_2)\right]\right\}.
\end{aligned}\tag{3.2.10}$$

Here, we have used the Fermi function $f(E,\mu)$ and abbreviated with k_z the wave number in z-direction

$$k_z\left(k_\parallel,E\right)=\sqrt{2m^*(E)\,E/\hbar^2-k_\parallel^2}.\tag{3.2.11}$$

Obviously, all of these Green's functions diverge with vanishing k_z. The origin of this divergency is easiest understood with the spectral function

$$\begin{aligned}
A\left(z_1,z_2,k_\parallel,E\right) &= i\left[G^R\left(z_1,z_2,k_\parallel,E\right)-G^A\left(z_1,z_2,k_\parallel,E\right)\right]\\
&= \frac{2m^*(E)\cos\left(\sqrt{2m^*(E)\,E/\hbar^2-k_\parallel^2}\,|z_1-z_2|\right)}{\hbar^2\sqrt{2m^*(E)\,E/\hbar^2-k_\parallel^2}}.
\end{aligned}\tag{3.2.12}$$

We know already from Eq. (2.2.15) that the spectral function at equal propagation coordinates ($z_1=z_2$) matches the local density of states. Evaluated at vanishing lateral momentum $k_\parallel=0$, this function represents the density of states of a homogeneous one-dimensional semiconductor*

$$A\left(z,z,k_\parallel=0,E\right)=\sqrt{\frac{2m^*(E)}{\hbar^2 E}}.\tag{3.2.13}$$

Any observable, such as the density and the current depends on Green's functions *integrated* over the momentum $k_\parallel$ and energy E. After these integrals are preformed this $1/k_z$-divergence disappears. Therefore, this divergence is noncritical for the convergency of the numerical results.

Other divergencies can be observed, when the entry of the first operator in Eq. (3.2.8) vanishes: The retarded Green's function reaches a pole, whenever the electronic energy E matches an eigenvalue of the operator $\mathbf{H}_0+\mathbf{V}+e\mathbf{\Phi}+\mathbf{\Sigma}^R$. Such poles are called quasi-particle resonances. If Σ^R describes the electron-phonon interaction, these poles lie at the excitation energies of electrons that are surrounded by a cloud of phonons. It is obvious that the real part of the retarded self-energy changes the position of those poles on the real energy axis, whereas the imaginary part shifts the poles into the complex plane. The closer a pole lies to

*Note that the factor of 2 accounts for the spin degree of freedom.

the energy axis, the longer is the lifetime of the respective quasi particle resonance (see also the formula for the scattering rate in Eq. (3.5.12)) and the sharper is the resonance peak of the Green's functions with respect to real energies E. Consequently, the smaller the imaginary part of the self-energy is, the harder are the Green's functions to be resolved on a real energy axis E. In open nanodevices however, the electrons face a finite Σ^R and a finite lifetime even when no incoherent scattering is included: The electrons can interact with the leads. The fact that device electrons can leave the device limits their lifetime in the device and prevents G^R from divergence. This eases the numerical implementation of the NEGF formalism significantly. It is important to note that this lifetime is no numerical artifact. It is just a consequence of our decision to calculate the Green's functions in a finite area of an infinitely extended system. For instance, we can reproduce the analytical formulas of the completely coherent Green's function of Eqs. (3.2.10) in a finite area of a homogeneous infinite system exactly - as will be shown Sec. 3.6.2.

Still, great care has to be taken on the energy resolution of the Green's functions in order to ensure well converged results, as will be discussed in more detail in Sec. 3.7. In particular, any resonances of the Green's functions have to be well resolved and require energy and momentum to be discretized on an inhomogeneous self-adjusting grid. Although, such a discretization leads to numerical difficulties, it is a major prerequisite for a numerically efficient solution of the nonequilibrium Green's functions (see Sec. 3.7).

3.3 New and common observables

3.3.1 Introduction

We complement the equations of motion of the preceding section with the formulas for the local density and the current density. We take this as an opportunity to introduce the energy and spatially resolved density and current density that are of great use in the physical discussion of the next chapters. Finally, we follow Lee and Wacker [45] in the derivation of the optical absorption coefficient α in linear optical response. Since we derive α in the spatial representation of the Green's functions, we are able to define the spatial and frequency resolved absorption coefficient $\alpha(z,\omega)$. Although the spatially resolved α is valuable for the discussion of the physics in quantum cascade lasers, it cannot be found in literature.

3.3.2 Charge and current density

In order to apply the formula for the current density Eq. (2.2.9), we have to Fourier transform* the Green's functions with respect to the in-plane distance $(\vec{x}_{\parallel,1}-\vec{x}_{\parallel,2})$ and the duration of the propagation (t_1-t_2)

$$\begin{aligned} j(z_1) &\equiv \langle \hat{j}(z_1)\rangle \\ &= -\lim_{\substack{\vec{x}_2\to\vec{x}_1\\ t_2\to t_1}} \int \frac{\mathrm{d}^2k_\parallel}{(2\pi)^2}\frac{\mathrm{d}E}{2\pi\hbar}\frac{\mathrm{e}^{i\vec{k}_\parallel\cdot\left(\vec{x}_{\parallel,1}-\vec{x}_{\parallel,2}\right)}\mathrm{e}^{-iE(t_1-t_2)/\hbar}\hbar e}{m^*(z_1,E)}\left(\frac{\mathrm{d}}{\mathrm{d}z_1}-\frac{\mathrm{d}}{\mathrm{d}z_2}\right)G^<\left(z_1,z_2,k_\parallel,E\right) \\ &= -\lim_{z_2\to z_1}\int \mathrm{d}E\int \mathrm{d}^2k_\parallel \frac{\hbar e}{(2\pi)^3 m^*(z_1,E)}\left(\frac{\mathrm{d}}{\mathrm{d}z_1}-\frac{\mathrm{d}}{\mathrm{d}z_2}\right)G^<\left(z_1,z_2,k_\parallel,E\right). \end{aligned} \tag{3.3.1}$$

*Please note that the three-dimensional position vector is decomposed into the in-plane $(\vec{x}_\parallel)$ and growth (z) coordinate.

The limit of equal propagation coordinates simplifies the Fourier transformation into an integral over the in-plane momentum $k_\parallel$ and the energy E. Similar to A. Wacker [46], we define the energy and spatially resolved current density by ignoring the integral over the total energy E

$$j\left(z_1, E\right) \equiv -\lim_{z_2 \to z_1} \int \mathrm{d}^2 k_\parallel \frac{\hbar e}{\left(2\pi\right)^3 m^*\left(z_1, E\right)} \left(\frac{\mathrm{d}}{\mathrm{d}z_1} - \frac{\mathrm{d}}{\mathrm{d}z_2}\right) G^<\left(z_1, z_2, k_\parallel, E\right). \tag{3.3.2}$$

The conserved current in a stationary calculation has to be constant in space. Therefore, the integral of $j\left(z_1, E\right)$ over the energy has to be constant for all z_1. The function $j\left(z_1, E\right)$ contains information about the questions:

- At which energies relative to the conduction band propagates which amount of electrons?
- At which positions in the device do propagating electrons emit/absorb energy?
- What is the efficiency of energy filtering in tunneling devices?

We get in a very similar fashion the formula for the local density from Eq. (2.2.6)

$$n\left(z_1\right) \equiv \left\langle \hat{n}\left(z_1\right)\right\rangle = -\frac{2i}{\left(2\pi\right)^3} \int \mathrm{d}E \int \mathrm{d}^2 k_\parallel G^<\left(z_1, z_1, k_\parallel, E\right). \tag{3.3.3}$$

We can trivially extend A. Wacker's definition of $j\left(z, E\right)$ to the density by neglecting the energy integral. This gives us the definition of the energy and spatially resolved density [47]

$$n\left(z_1, E\right) \equiv -\frac{2i}{\left(2\pi\right)^3} \int \mathrm{d}^2 k_\parallel G^<\left(z_1, z_1, k_\parallel, E\right). \tag{3.3.4}$$

While this function is greater than or equal to zero, it gives similar information as the energy resolved current. However, it answers questions about the confined (or non-propagating) electrons:

- Where do the resonant states in the device lie and how much are they occupied?
- What is the in-plane distribution of the electrons in a specific resonant state?
- How well are electrons confined in resonant states?

3.3.3 Optical absorption in linear response

Introduction

We derive the formula for the optical absorption coefficient in the nonequilibrium Green's function formalism. Although, this derivation can be found in [48], we present details of this derivation for later reference. We also introduce the spatial and frequency resolved absorption coefficient $\alpha\left(z, \omega\right)$. This function nicely shows in which device regions light is emitted and absorbed which is most valuable for the optimization of quantum cascade lasers (see Sec. 5). Yet, results of such a function cannot be found in literature.

Perturbation of Green's functions in linear response

We start with the derivation of the change of the electronic Green's function due to the perturbing photonic field. Let us consider the small oscillating electric field $\vec{E}$ of a single photon of frequency ω that is polarized in z-direction

$$\vec{E}\left(\vec{r},t\right)=\vec{e}_z\int\frac{\mathrm{d}\omega}{2\pi}\exp\left(i\vec{l}_\parallel\left(\omega\right)\cdot\vec{x}_\parallel-i\omega t\right)\mathcal{E}\left(\omega\right). \tag{3.3.5}$$

Here, $\vec{l}_\parallel\left(\omega\right)$ is the photonic wave vector in the lateral direction and $\mathcal{E}$ is the field amplitude. In the Coulomb gauge, we get for the vector potential $\vec{A}$ ($\vec{E}\left(\vec{r},t\right)=-\partial_t\vec{A}\left(\vec{r},t\right)$)

$$\vec{A}\left(\vec{r},t\right)=\vec{e}_z\int\frac{\mathrm{d}\omega}{2\pi i\omega}\exp\left(i\vec{l}_\parallel\left(\omega\right)\cdot\vec{x}_\parallel-i\omega t\right)\mathcal{E}\left(\omega\right). \tag{3.3.6}$$

This perturbation enters the Hamiltonian of the system via the canonical momentum. We assume $\mathcal{E}$ to be small and neglect any terms squared in $\mathcal{E}\left(\omega\right)$. Therefore, the perturbing potential reads*

$$\delta\hat{V}\left(\vec{r},t\right)=-\frac{e}{2m^*\left(z\right)}\left(\hat{p}_zA_z\left(\vec{r},t\right)+A_z\left(\vec{r},t\right)\hat{p}_z\right). \tag{3.3.7}$$

All optically active devices in this thesis emit and absorb photons with wavelengths much larger ($\sim 100\ \mu$m) than the typical size of the device (~ 70 nm). Therefore, we neglect the spatial variation of the vector potential $A\left(\vec{r},t\right)\approx A\left(t\right)$. In this way, we ignore the photon momentum and any change of the electron momentum caused by the photon emission and absorption. In this way, we get a homogeneous perturbation in the frequency domain

$$\delta\hat{V}\left(\omega\right)=-\frac{e}{m^*\left(z\right)}A\left(\omega\right)\hat{p}_z=\frac{\hbar e}{m^*\left(z\right)\omega}\mathcal{E}\left(\omega\right)\frac{\mathrm{d}}{\mathrm{d}z}. \tag{3.3.8}$$

Due to the smallness of the optical field, perturbations in the Green's functions and self-energies can be linearized

$$G\left(z_1,z_2,k_\parallel,t_1,t_2\right)\approx G\left(z_1,z_2,k_\parallel,t_1-t_2\right)+\delta G\left(z_1,z_2,k_\parallel,t_1,t_2\right), \tag{3.3.9}$$

$$\Sigma\left(z_1,z_2,k_\parallel,t_1,t_2\right)\approx\Sigma\left(z_1,z_2,k_\parallel,t_1-t_2\right)+\delta\Sigma\left(z_1,z_2,k_\parallel,t_1,t_2\right). \tag{3.3.10}$$

We have Fourier transformed the difference of the temporal propagation coordinates into the energy domain before. However, since the perturbing field is time dependent, we have to perform Fourier transformations for two time coordinates, i.e. the difference of the propagation times (t_1-t_2) and the time coordinate of the photonic field. Since we use the left sided Dyson equations, i.e. the differential operator in Eq. (2.3.33) acts from the left on the retarded Green's function, the time variable of δV is t_1. Thus, the Fourier transformation of δG reads

$$\delta G\left(z_1,z_2,k_\parallel,t_1,t_2\right)=\int\frac{\mathrm{d}\omega}{2\pi}\exp\left(-i\omega t_1\right)\int\frac{\mathrm{d}E}{2\pi\hbar}\exp\left(-iE\left(t_1-t_2\right)/\hbar\right)\delta G\left(z_1,z_2,k_\parallel,E,\omega\right). \tag{3.3.11}$$

*For simplicity, we assume a parabolic effective mass. We will see in Sec. 5 that the effect of nonparabolic conduction bands in the laser devices of this thesis is negligible, anyway.

With this result, we derive in the appendix E.1 the equation of motion for the correction of the retarded and the advanced Green's functions. When we omit the in-plane momentum $k_\parallel$ for better readability, these equations read *

$$\delta\mathbf{G}^{R,A}(\omega,E)=\mathbf{G}^{R,A}(E+\hbar\omega)\,\delta V(\omega)\,\mathbf{G}^{R,A}(E)+\mathbf{G}^{R,A}(E+\hbar\omega)\,\delta\mathbf{\Sigma}^{R,A}(E+\hbar\omega,-E)\,\mathbf{G}^{R,A}(E)\,. \tag{3.3.12}$$

In a very similar fashion, we insert the results of the retarded and advanced Green's functions in the Keldysh equation and get for the Fourier transformed lesser Green's function (see appendix E.2)

$$\begin{aligned}&\delta\mathbf{G}^{<}(\omega,E)\\ =\;&\mathbf{G}^{R}(E+\hbar\omega)\,\delta V(\omega)\,\mathbf{G}^{<}(E)+\mathbf{G}^{<}(E+\hbar\omega)\,\delta V(\omega)\,\mathbf{G}^{A}(E)\\ &+\mathbf{G}^{R}(E+\hbar\omega)\,\delta\mathbf{\Sigma}^{R}(E+\hbar\omega,-E)\,\mathbf{G}^{<}(E)+\mathbf{G}^{<}(E+\hbar\omega)\,\delta\mathbf{\Sigma}^{A}(E+\hbar\omega,-E)\,\mathbf{G}^{A}(E)\\ &+\mathbf{G}^{R}(E+\hbar\omega)\,\delta\mathbf{\Sigma}^{<}(E+\hbar\omega,-E)\,\mathbf{G}^{A}(E)\,.\end{aligned} \tag{3.3.13}$$

Derivation of the absorption coefficient

With the knowledge of the δG, we can now calculate the changes of the current density due to the photonic field. The change of the current density is given by the current operator of Eq. (2.2.7) applied on $\delta G^<$

$$\begin{aligned}\delta j(z_1,\omega)\;=\;&-\lim_{z_2\to z_1}\frac{\hbar^2 e}{m^*(z)}\left(\nabla_{z_1}-\nabla_{z_2}\right)\int\frac{\mathrm{d}E}{2\pi\hbar}\int\frac{\mathrm{d}^2k_\parallel}{(2\pi)^2}\delta G^<\left(z_1,z_2,k_\parallel,\omega,E\right)\\ &-\frac{2\hbar e^2\mathcal{E}(\omega)}{m^*(z)\,\omega}\int\frac{\mathrm{d}E}{2\pi\hbar}\int\frac{\mathrm{d}^2k_\parallel}{(2\pi)^2}G^<\left(z_1,z_1,k_\parallel,E\right).\end{aligned} \tag{3.3.14}$$

The quotient of this current density with the electric field of the photon gives us the optical conductance

$$\sigma(z_1,\omega)=\frac{\delta j(z_1,\omega)}{\mathcal{E}(\omega)}. \tag{3.3.15}$$

When we ignore any vertex corrections $\delta\Sigma$, we can specify with the Eqs. (3.3.8), (3.3.13) and (3.3.14) a relatively short equation for the optical conductance

$$\begin{aligned}&\sigma(z_1,\omega)\\ =\;&\lim_{z_2\to z_1}\frac{\hbar^2e^2\left(\nabla_{z_2}-\nabla_{z_1}\right)}{m^*(z)^2(2\pi)^3\,\omega}\int\mathrm{d}E\mathrm{d}^2k_\parallel\mathrm{d}z_3\left[G^R\left(z_1,z_3,k_\parallel,E+\hbar\omega\right)\left.\frac{\mathrm{d}G^<\left(z',z_2,k_\parallel,E\right)}{\mathrm{d}z'}\right|_{z'=z_3}\right.\\ &\left.+G^<\left(z_1,z_3,k_\parallel,E+\hbar\omega\right)\left.\frac{\mathrm{d}G^A\left(z',z_2,k_\parallel,E\right)}{\mathrm{d}z'}\right|_{z'=z_3}\right]\\ &-2e^2\int\frac{\mathrm{d}E\mathrm{d}^2k_\parallel}{(2\pi)^3\,m^*(z_1)\,\omega}G^<\left(z_1,z_1,k_\parallel,E\right).\end{aligned} \tag{3.3.16}$$

In the beginning, we have assumed the photon to be polarized in growth direction (parallel to $\vec{e}_z$). Thus, the propagation of the photon is parallel to the homogeneous layers and is isotropic with respect to the in-plane direction. Therefore, the photon can be described with a

*Please note the matrix shape of the Green's functions and self energies with respect to (z_1,z_2).

one dimensional wave vector l. In order to derive the final formula for the optical absorption coefficient, we follow Jackson [49] and split the complex photon wave number l into a real and an imaginary part

$$l(z,\omega) = \tilde{\alpha}(z,\omega) + i\frac{\alpha(z,\omega)}{2}. \tag{3.3.17}$$

The real part $\tilde{\alpha}$ is the refraction index of the material whereas the imaginary part α describes the damping of the photonic wave function and equals the absorption coefficient. According to Jackson [49] the relations between α and $\tilde{\alpha}$ are

$$\tilde{\alpha}(z,\omega)^2 - \frac{\alpha(z,\omega)^2}{4} = \frac{\omega^2}{c^2}\,\mathrm{Re}\left(\frac{\varepsilon(z,\omega)}{\varepsilon_0\varepsilon_r(z)}\right), \tag{3.3.18}$$

$$\alpha(z,\omega)\,\tilde{\alpha}(z,\omega) = \frac{\omega^2}{c^2}\,\mathrm{Im}\left(\frac{\varepsilon(z,\omega)}{\varepsilon_0\varepsilon_r(z)}\right), \tag{3.3.19}$$

where c denotes the vacuum speed of light. The dielectric function $\varepsilon(z,\omega)$ is given by the conductance $\sigma(z,\omega)$

$$\varepsilon(z,\omega) = \varepsilon_0\varepsilon_r(z) + i\sigma(z,\omega)/\omega. \tag{3.3.20}$$

Here, ε_r and ε_0 denote the relative static dielectric constant and the dielectric constant of vacuum, respectively. Solving the second equation for α and inserting the result into the equation for $\tilde{\alpha}$, we get

$$\tilde{\alpha}(z,\omega)^4 - \frac{\omega^2}{c^2}\,\mathrm{Re}\left(\frac{\varepsilon(z,\omega)}{\varepsilon_0\varepsilon_r(z)}\right)\tilde{\alpha}(z,\omega)^2 - \frac{\omega^4}{4c^4}\left[\mathrm{Im}\left(\frac{\varepsilon(z,\omega)}{\varepsilon_0\varepsilon_r(z)}\right)\right]^2 = 0. \tag{3.3.21}$$

We consider only photons with a positive real part of the wave vector and therefore get

$$\tilde{\alpha}(z,\omega) = \frac{\omega}{\sqrt{2}c}\sqrt{\mathrm{Re}\left(\frac{\varepsilon(z,\omega)}{\varepsilon_0\varepsilon_r(z)}\right) + \left|\frac{\varepsilon(z,\omega)}{\varepsilon_0\varepsilon_r(z)}\right|}. \tag{3.3.22}$$

Finally we get an absorption coefficient that depends on the photon frequency as well as on the growth coordinate

$$\alpha(z,\omega) = \mathrm{Im}\left(\frac{\varepsilon(z,\omega)}{\varepsilon_0\varepsilon_r(z)}\right)\frac{\sqrt{2}\omega}{c}\left[\mathrm{Re}\left(\frac{\varepsilon(z,\omega)}{\varepsilon_0\varepsilon_r(z)}\right) + \left|\frac{\varepsilon(z,\omega)}{\varepsilon_0\varepsilon_r(z)}\right|\right]^{-1/2}. \tag{3.3.23}$$

We have already discussed above that the photon wave vector in all devices considered in this thesis exceeds the device dimensions by several orders of magnitude. Consequently, the photon does not propagate in a single semiconductor layer with a layer specific absorption coefficient, but its wave function extends over many layers and its propagation is due to an effective absorption coefficient averaged over the total device. Consequently, only the absorption coefficient averaged over the device length L is experimentally observable

$$\alpha(\omega) = \frac{1}{L}\int_0^L \mathrm{d}z\,\alpha(z,\omega). \tag{3.3.24}$$

Still, it is instructive to analyze results for the spatial dependent absorption coefficient. The sign of $\alpha(z,\omega)$ depends on whether the electronic occupation of energies E and $E+\hbar\omega$ at the position z is inverted and an optical transition between those energies is allowed. Since the complex susceptibility contains the full integral over $\mathrm{d}z_3$, local as well as nonlocal (diagonal) optical transitions are automatically included in $\alpha(z,\omega)$. Therefore, this function nicely shows where in the device photons are absorbed or emitted and what the energies of these photons are (see Sec. 5). Results of such a spatially dependent function cannot be found in literature.

Applicability of vertex corrections

We will discuss the numerical problems of an implementation of vertex correction in the case of electrostatic screening in Sec. (3.4.4). In general, we face the same situation in the case of the linear response to an electrodynamical perturbation. Even in the approximation of a spatially constant perturbation, these vertex corrections depend on the same variables as the scattering self-energies they originate from, in addition to the dependence of the photonic frequency. Furthermore, the vertex corrections $\delta\Sigma$ depend on the response of the Green's functions δG and vice versa - similar to the mutual dependence of the unperturbed Green's functions and self-energies. Consequently, proper vertex corrections require for a self-consistent solution of δG and $\delta\Sigma$. Therefore, the inclusion of vertex corrections of the scattering self-energies in the present elaborateness of the full momentum and energy dependence is numerically unfeasible. Banit *et al.* have approximated the scattering self-energies which allowed them to include the electron-photon vertex corrections self-consistently. They have shown for THz-QCLs that vertex corrections narrow the optical linewidths and increase the peak height of the absorption coefficient significantly. Thereby, optical absorption and emission are both equally affected. However, the peak gain energy remains unchanged [50]. Consequently, our model does not yield realistic *absolute* values of the absorption and emission lines in the device, so that external losses such as waveguide or mirror losses cannot be included consistently. However, qualitative changes of the light emission as well as the transparency of the active region of the device, i.e. the *zero point* of the absorption coefficient is successfully described without the vertex corrections.

3.4 Screening in random phase approximation

3.4.1 Introduction

This subsection is in so far an excursus from the vertical transport in heterostructures that we consider electrons in *homogeneous* systems and derive screening lengths resulting from the *homogeneous* electron density. However, the screening length enters the formulas of several scattering self-energies of later sections and we have to discuss the validity of a scalar and constant screening length in our model.

Typically, the dielectric function in the random phase approximation is either derived by the method of self-consistent field in the density matrix formalism [51], or by a diagrammatic analysis of the electron-electron interaction using Green's functions [10, 52]. Although these derivations can be found in many textbooks, we derive the static dielectric function for later reference. For instructive reasons, we thereby follow a mixture of both typical derivations and apply the self-consistent field approach on the Green's function method. This derivation is easier than the typical diagram technique, because we can apply the static limit at the beginning of the derivations and transform the Green's functions into the energy domain.

Typically, screening is considered for ballistic electrons in homogeneous system. We apply this approximation and derive the Lindhard formula for the dielectric function in the static limit. When we additionally take the limit of small electronic momenta, we end up with the screening length. Since it is rarely given in literature, we show a comparison of the screening length resulting from the Lindhard formula with the Debye screening length for various temperatures and electron densities.

Our detailed derivation of the Lindhard formula allows us to straightforwardly extend the

common formulas to the inclusion of incoherent scattering. We compare the two commonly applied screening lengths that are based on coherent transport with novel results of a self-consistent nonequilibrium Green's function calculation that takes into account incoherent scattering. We find and explain that the reduction of the quasi-particle life time effectively increases the screening length in homogeneous systems. However, we also show that our inclusion of incoherent scattering in the screening model is not complete and can only be considered as a first step towards a consistent treatment of realistic screening. Since the inclusion of incoherent scattering in the formulas derived in this section is numerically very demanding, we have to limit the screening in subsequent calculations of this thesis on the numerically efficient Debye screening model.

3.4.2 Perturbation of Green's functions in linear response

We consider the linear response of the Green's functions and self-energies in a homogeneous system. In such a system, the Green's functions and self-energies depend only on the difference of the propagation coordinates. In general, however, the corrections δG and $\delta\Sigma$ explicitly depend on both coordinates (as we will see below)

$$G\left(\vec{x}_1,\vec{x}_2,E\right) \approx G\left(\vec{x}_1-\vec{x}_2,E\right)+\delta G\left(\vec{x}_1,\vec{x}_2,E\right), \tag{3.4.1}$$

$$\Sigma\left(\vec{x}_1,\vec{x}_2,E\right) \approx \Sigma\left(\vec{x}_1-\vec{x}_2,E\right)+\delta\Sigma\left(\vec{x}_1,\vec{x}_2,E\right). \tag{3.4.2}$$

We derive in the appendix D.1 the change of the retarded and advanced Green's functions in a homogeneous three-dimensional system due to a small electrostatic potential $\delta V\left(\vec{x}\right)$

$$\begin{aligned}\delta G^{R,A}\left(\vec{x}_1,\vec{x}_2,E\right) = &\int \mathrm{d}\vec{x}_3 G^{R,A}\left(\vec{x}_1,\vec{x}_3,E\right)\delta V\left(\vec{x}_3\right)G^{R,A}\left(\vec{x}_3,\vec{x}_2,E\right)+\\ &\int \mathrm{d}\vec{x}_3\mathrm{d}\vec{x}_4 G^{R,A}\left(\vec{x}_1,\vec{x}_3,E\right)\delta\Sigma^{R,A}\left(\vec{x}_3,\vec{x}_4\right)G^{R,A}\left(\vec{x}_4,\vec{x}_2,E\right).\end{aligned} \tag{3.4.3}$$

Since we are only interested in the lowest order perturbation terms, we neglect all terms proportional to $\delta\Sigma$, i.e. we exclude any vertex corrections. Then we get for the change of the lesser Green's function (see appendix D.2)

$$\begin{aligned}\delta G^{<}\left(\vec{x}_1,\vec{x}_2,E\right) = &\int \mathrm{d}\vec{x}_3\mathrm{d}\vec{x}_4 G^{R}\left(\vec{x}_1,\vec{x}_3,E\right)\delta V\left(\vec{x}_3\right)G^{<}\left(\vec{x}_3,\vec{x}_2,E\right)+\\ &\int \mathrm{d}\vec{x}_3\mathrm{d}\vec{x}_4 G^{<}\left(\vec{x}_1,\vec{x}_3,E\right)\delta V\left(\vec{x}_3\right)G^{A}\left(\vec{x}_3,\vec{x}_2,E\right).\end{aligned} \tag{3.4.4}$$

In contrast to the unperturbed Green's functions, these equations show that the change of the Green's functions depend on both propagation coordinates. This is obvious, since the perturbing potential $\delta V\left(\vec{x}\right)$ is explicitly depending on a single spatial coordinate $\vec{x}$ which results in an inhomogeneous system. For later reference, we Fourier transform $\delta G^{<}$ with respect to both propagation coordinates (see Eq. (D.2.6))

$$\delta G^{<}\left(\vec{Q},\vec{q},E\right) = G^{R}\left(\vec{Q}+\vec{q},E\right)\delta V\left(\vec{Q}\right)G^{<}\left(\vec{q},E\right)+G^{<}\left(\vec{Q}+\vec{q},E\right)\delta V\left(\vec{Q}\right)G^{A}\left(\vec{q},E\right). \tag{3.4.5}$$

3.4.3 Static dielectric constant

Any change of the lesser Green's function causes a change of the electron density δn (see Eqs. (2.2.6) and (3.3.3))

$$\delta n\left(\vec{Q}\right)=-\frac{2i}{(2\pi)^4}\int \mathrm{d}E\mathrm{d}\vec{q}\delta G^{<}\left(\vec{Q},\vec{q},E\right). \tag{3.4.6}$$

With the formula of δn, our remaining derivation of the dielectric constant follows the standard method of self-consistent field: This change of the electronic density δn causes a change of the perturbing potential, i.e. the perturbed electrons screen the external potential δV_e with an induced potential $\delta V_i\left(\vec{x}\right)=\delta V\left(\vec{x}\right)-\delta V_e\left(\vec{x}\right)$. The induced potential obeys the Poisson equation

$$\nabla^2\left[\delta V\left(\vec{x}\right)-\delta V_e\left(\vec{x}\right)\right]=-\frac{e^2}{\varepsilon_0\varepsilon_r}\delta n\left(\vec{x}\right). \tag{3.4.7}$$

Of course, the effective change of the Green's function is due to the total potential $\delta V\left(\vec{x}\right)$, as has been derived in the preceding paragraph. In the momentum space, the Poisson equation reads

$$\begin{aligned}&-Q^2\delta V\left(\vec{Q}\right)+Q^2\delta V_e\left(\vec{Q}\right)\\ =\;&\frac{e^2}{\varepsilon_0\varepsilon_r}\frac{2i\delta V\left(\vec{Q}\right)}{(2\pi)^4}\\ &\times\int \mathrm{d}E\mathrm{d}\vec{q}\left[G^R\left(\vec{Q}+\vec{q},E\right)G^{<}\left(\vec{q},E\right)+G^{<}\left(\vec{Q}+\vec{q},E\right)G^A\left(\vec{q},E\right)\right].\end{aligned} \tag{3.4.8}$$

This gives us for the total potential

$$\begin{aligned}\delta V\left(\vec{Q}\right)\;=\;&\delta V_e\left(\vec{Q}\right)\left\{1+\frac{e^2}{\varepsilon_0\varepsilon_r Q^2}\frac{2i}{(2\pi)^4}\int \mathrm{d}E\mathrm{d}\vec{q}\left[G^R\left(\vec{Q}+\vec{q},E\right)G^{<}\left(\vec{q},E\right)\right.\right.\\ &\left.\left.+G^{<}\left(\vec{Q}+\vec{q},E\right)G^A\left(\vec{q},E\right)\right]\right\}^{-1}.\end{aligned} \tag{3.4.9}$$

It is common to define the dielectric function ε_d as the quotient of the external (unscreened) potential $\delta V_e\left(\vec{Q}\right)$ and the effective (total) potential $\delta V\left(\vec{Q}\right)$

$$\varepsilon_d\left(\vec{Q}\right)=\frac{\delta V_e\left(\vec{Q}\right)}{\delta V\left(\vec{Q}\right)}. \tag{3.4.10}$$

Consequently, the dielectric function in the static limit reads

$$\varepsilon_d\left(\vec{Q}\right)=1+\frac{e^2}{\varepsilon_0\varepsilon_r Q^2}\frac{2i}{(2\pi)^4}\int \mathrm{d}E\mathrm{d}\vec{q}\left[G^R\left(\vec{Q}+\vec{q},E\right)G^{<}\left(\vec{q},E\right)+G^{<}\left(\vec{Q}+\vec{q},E\right)G^A\left(\vec{q},E\right)\right]. \tag{3.4.11}$$

This formula is know as the Lindhard dielectric function. We introduce for later reference the retarded polarization P^R

$$P^R\left(\vec{Q}\right)=-i\frac{2}{(2\pi)^4\hbar}\int \mathrm{d}E\mathrm{d}\vec{q}\left[G^R\left(\vec{Q}+\vec{q},E\right)G^{<}\left(\vec{q},E\right)+G^{<}\left(\vec{Q}+\vec{q},E\right)G^A\left(\vec{q},E\right)\right] \tag{3.4.12}$$

which is typically used for ε_d in literature (see e.g. chapter 5 in [10])

$$\varepsilon_d\left(\vec{Q}\right) = 1 - \frac{\hbar e^2}{\varepsilon_0 \varepsilon_r Q^2} P^R\left(\vec{Q}\right). \tag{3.4.13}$$

3.4.4 Extension of known screening models for scattered electrons

Introduction

The next step in the derivation of a screening length is to approximate the Lindhard dielectric function Eq. (3.4.11) for small $\vec{Q}$. The best way how to apply the limit $\vec{Q} \to 0$ depends on whether incoherent scattering is included or not, i.e. whether analytical formulas for the Green's functions are known. In any case, as soon as the limit for small $\vec{Q}$ in the dielectric function is taken, the screening length ξ is already derived. In the case of a point like perturbing potential, the total (screened) potential reads in the momentum and spatial representation, respectively

$$\begin{aligned} \delta V\left(\vec{Q}\right) &= \frac{-e^2}{\varepsilon_0 \varepsilon_r \left(Q^2 + \xi^{-2}\right)}, \\ \delta V\left(\vec{x}\right) &= \frac{-e^2 \mathrm{e}^{-|\vec{x}|/\xi}}{4\pi \varepsilon_0 \varepsilon_r |\vec{x}|}. \end{aligned} \tag{3.4.14}$$

Screening length of free electrons

We first derive the analytical formula of the screening length in the case of vanishing incoherent scattering in equilibrium systems. For this purpose, we insert our analytical results for the free-particle Green's functions Eqs. (2.3.43) in the retarded polarization* Eq. (3.4.12)

$$\begin{aligned} i\frac{(2\pi)^4 \hbar}{2} P_0^R\left(\vec{Q}\right) &= \int \mathrm{d}E \mathrm{d}\vec{q} \left[G_0^R\left(\vec{Q}+\vec{q}, E\right) G_0^<\left(\vec{q}, E\right) + G_0^<\left(\vec{Q}+\vec{q}, E\right) G_0^A\left(\vec{q}, E\right) \right] \\ &= 2\pi i \,\mathrm{Pr} \int \mathrm{d}E \mathrm{d}\vec{q} \frac{\delta\left(E - \varepsilon\left(\vec{q}\right)\right)}{E - \varepsilon\left(\vec{Q}+\vec{q}\right)} f\left(\varepsilon\left(\vec{q}\right), \mu\right) \\ &\quad + 2\pi i \,\mathrm{Pr} \int \mathrm{d}E \mathrm{d}\vec{q} \frac{\delta\left(E - \varepsilon\left(\vec{Q}+\vec{q}\right)\right)}{E - \varepsilon\left(\vec{q}\right)} f\left(\varepsilon\left(\vec{Q}+\vec{q}\right), \mu\right) \\ &= 2\pi i \int \mathrm{d}\vec{q} \frac{f\left(\varepsilon\left(\vec{Q}+\vec{q}\right), \mu\right) - f\left(\varepsilon\left(\vec{q}\right), \mu\right)}{\varepsilon\left(\vec{Q}+\vec{q}\right) - \varepsilon\left(\vec{q}\right)}. \end{aligned} \tag{3.4.15}$$

Since we consider a homogeneous system in equilibrium, we have replaced $n_{\vec{k}}$ (the number of particles with momentum $\vec{k}$) in the Eqs. (2.3.43) with the Fermi distribution $f(E, \mu)$. We insert the last equation in Eq. (3.4.11) and get the static limit of the dielectric function at finite temperatures [53]

$$\varepsilon_d\left(\vec{Q}\right) = 1 + Q^{-2} \frac{e^2}{\varepsilon_0 \varepsilon_r} \frac{-2}{(2\pi)^3} \int \mathrm{d}\vec{q} \frac{f\left(\varepsilon\left(\vec{Q}+\vec{q}\right), \mu\right) - f\left(\varepsilon\left(\vec{q}\right), \mu\right)}{\varepsilon\left(\vec{Q}+\vec{q}\right) - \varepsilon\left(\vec{q}\right)}. \tag{3.4.16}$$

*This integral equals the retarded polarization of free-particle Green's functions P_0^R (see Sec. (3.5.6)).

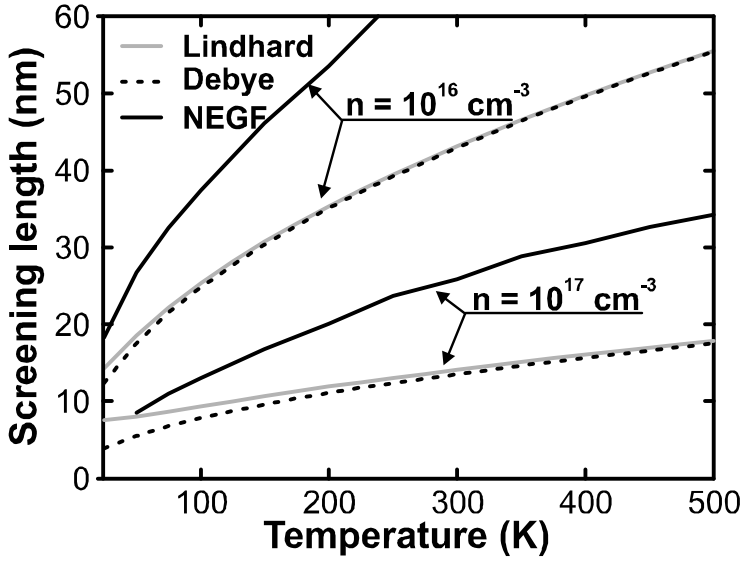

Figure 3.4.1: Screening length as a function of temperature in homogeneous n-doped GaAs at the doping densities $n = 10^{16}$ cm^{-3} and $n = 10^{17}$ cm^{-3}. The Debye screening length (dotted) approaches the ballistic Lindhard screening length (grey solid) from below. In contrast, the NEGF results of Eq. (3.4.24) including incoherent scattering with phonons and impurities exceed the ballistic results. Results at low temperatures, where a numerical solution of Eq. (3.4.24) is too demanding are not given.

In order to derive the screening length, we have to take the limit $\vec{Q} \to 0$. Thus, we expand the numerator and denominator in Eq. (3.4.16) in a Taylor series up to terms linear in $\vec{Q}$

$$f\left(\varepsilon\left(\vec{Q}+\vec{q}\right),\mu\right) - f\left(\varepsilon\left(\vec{q}\right),\mu\right) = \left.\frac{\partial f\left(\varepsilon,\mu\right)}{\partial\varepsilon}\right|_{\varepsilon(\vec{q})} \vec{Q}\cdot\left.\vec{\nabla}_{\vec{q}'}\varepsilon\left(\vec{q}'\right)\right|_{\vec{q}} \tag{3.4.17}$$

$$\varepsilon\left(\vec{Q}+\vec{q}\right) - \varepsilon\left(\vec{q}\right) = \vec{Q}\cdot\left.\vec{\nabla}_{\vec{q}'}\varepsilon\left(\vec{q}'\right)\right|_{\vec{q}}. \tag{3.4.18}$$

When we set this in Eq. (3.4.16), we get the lowest order of the dielectric function in the shape typically given in textbooks (see e.g. [52], note the factor of 2 is due to the spin degeneracy)

$$\begin{aligned}\varepsilon_d\left(\vec{Q}\right) &= 1+\frac{1}{\xi^2 Q^2} \\ &= 1+Q^{-2}\frac{e^2}{\varepsilon_0\varepsilon_r}\frac{-2}{\left(2\pi\right)^3}\int \mathrm{d}\vec{q}\left.\frac{\partial f\left(\varepsilon,\mu\right)}{\partial\varepsilon}\right|_{\varepsilon(\vec{q})}.\end{aligned} \tag{3.4.19}$$

Figure 3.4.1 shows a comparison of the ballistic Lindhard screening length ξ_{Lindhard} (grey solid)

$$\xi_{\mathrm{Lindhard}} = \left(\frac{e^2}{\varepsilon_0\varepsilon_r}\frac{-2}{\left(2\pi\right)^3}\int \mathrm{d}\vec{q}\left.\frac{\partial f\left(\varepsilon,\mu\right)}{\partial\varepsilon}\right|_{\varepsilon(\vec{q})}\right)^{-1/2} \tag{3.4.20}$$

and the Debye screening length ξ_{Debye} (dotted)

$$\xi_{\mathrm{Debye}} = \sqrt{\frac{\varepsilon_0\varepsilon_r}{e^2\beta n}} \tag{3.4.21}$$

for the case of homogeneous n-doped GaAs at various temperatures and ionized doping densities. The Debye screening length approaches the Lindhard formula only for high temperatures and low doping densities. This is easy to understand, since the Fermi distribution in the Debye formula is approximated with a Boltzmann distribution. In this thesis, screening at rather low temperatures can only be found in chapter 5. Although the device temperature in this chapter is typically set to 40 K, the averaged electron densities in the devices of that chapter are less than 6×10^{15} cm^{-3}. This density is small enough so that the Debye and Lindhard screening length are comparable. All other devices in this thesis where screening is taken into account are calculated at much higher device temperatures. For this reason, we apply the Debye screening length throughout this thesis.

Screening length in incoherent transport

In the last paragraph, we have derived the screening length in the coherent transport limit. There, we have seen, that the limit $\vec{Q} \to 0$ has to be taken carefully. The situation changes, when incoherent scattering is taken into account. Here, neither the peaks in the density of states are sharp δ-functions, nor do the poles of the retarded and advanced Green's functions lie exactly on the real energy axis (compare with Eq. (2.3.43)). A numerical implementation of the Lindhard screening length with scattered Green's functions requires us to calculate the fully scattered retarded polarization P^R. This becomes particularly difficult, when the scattering in the system is weak and the transport approaches the ballistic regime. In order to illustrate this, let us represent Eq. (3.4.12) in a homogeneous system with the (spatially resolved) Green's functions in our representation

$$\begin{aligned} & i\frac{(2\pi)^4\hbar}{2}P^R\left(\vec{Q}\right) \\ = \; & 2\pi\int \mathrm{d}E\mathrm{d}\vec{q}_\parallel\mathrm{d}\rho_z\left[\mathrm{e}^{iQ_z\rho_z}G^R\left(-\rho_z,\vec{Q}_\parallel+\vec{q}_\parallel,E\right)+\mathrm{e}^{-iQ_z\rho_z}G^A\left(-\rho_z,\vec{Q}_\parallel+\vec{q}_\parallel,E\right)\right] \\ & \times G^<\left(\rho_z,\vec{Q}_\parallel+\vec{q}_\parallel,E\right). \end{aligned} \tag{3.4.22}$$

Here, we utilize the fact that the Green's functions of homogeneous systems depend only on one spatial coordinate ρ_z, i.e. the difference of the two propagation coordinates in growth direction ($\rho_z = z_1 - z_2$). With finite incoherent scattering, the imaginary part of the denominator in the formula of G^R in Eq. (2.3.43) does not vanish. Therefore, we may set $\vec{Q}$ in the last formula to zero, because we do not divide by zero in doing so (in contrast to the ballistic situation of Eq. (3.4.19))

$$\begin{aligned} & i\frac{(2\pi)^4\hbar}{2}P^R(0) \\ = \; & 2\pi\int \mathrm{d}\rho_z\mathrm{d}E\mathrm{d}\vec{q}_\parallel\left[G^R\left(-\rho_z,\vec{q}_\parallel,E\right)+G^A\left(-\rho_z,\vec{q}_\parallel,E\right)\right]G^<\left(\rho_z,\vec{q}_\parallel,E\right). \\ \equiv \; & \int \mathrm{d}\rho_z\upsilon\left(\rho_z\right). \end{aligned} \tag{3.4.23}$$

This polarization gives us, with the definition of the screening length ξ Eq. (3.4.14) and the dielectric constant Eq. (3.4.13), the scattered static screening length

$$\xi^{-1} = \sqrt{-\frac{\hbar e^2}{\varepsilon_0\varepsilon_r}P^R(0)}. \tag{3.4.24}$$

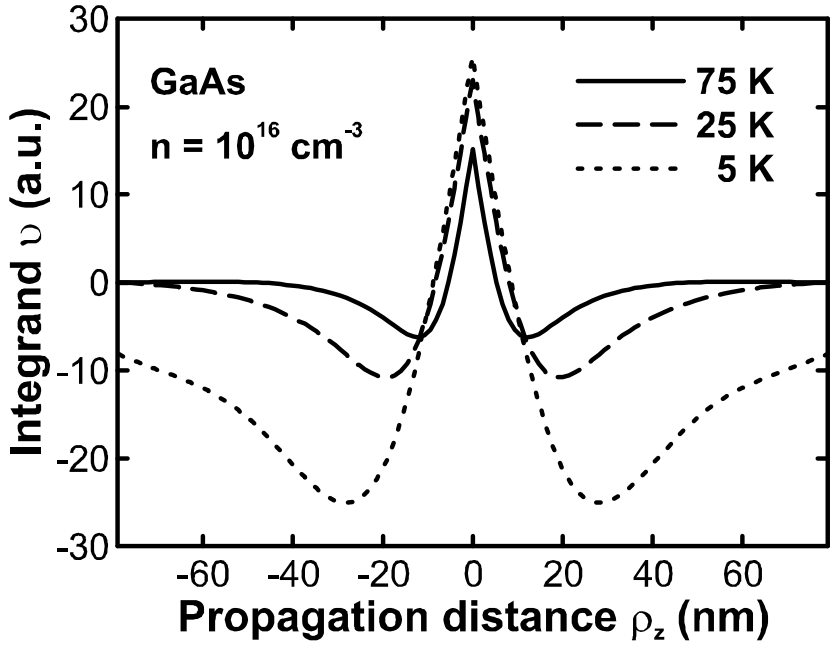

Figure 3.4.2: Integrand $\upsilon(q_z)$ of Eq. (3.4.23) as a function of the propagation distance ρ_z in homogeneous n-doped GaAs with $n = 10^{16}$ cm^{-3} at various temperatures. A minimum efficiency of incoherent scattering is necessary, so that $\upsilon(\rho_z)$ decays within the numerically implemented range.

The influence of incoherent scattering on the screening length can also be seen in Fig. 3.4.1. The black solid line shows numerical results of Eq. (3.4.24) with fully scattered Green's functions. Obviously, the screening length is enhanced when incoherent scattering is included. This can be understood from Eq. (3.4.16): We have already shown in Sec. 2.4.2 that the distribution of electrons in equilibrium does not deviate from the Fermi distribution, regardless whether incoherent scattering is implemented or not. Consequently, incoherent scattering does not change the numerator in Eq. (3.4.16). However, incoherent scattering shortens the lifetime of the electronic states which broadens and shifts resonances of all Green's functions. In particular, incoherent scattering shifts the poles of the retarded and advanced Green's functions away from the real energy axis into the complex plane. In the simplest consideration, the state broadening is described by a constant $i\gamma \in i\mathbb{R}$ in the denominator of G^R and G^A in Eqs. (2.3.43). Setting these modified functions in the integrand $P_0^R\left(\vec{Q}\right)$ of Eq. (3.4.16) we end up with a modified dielectric constant in the presence of scattering

$$\varepsilon_d\left(\vec{Q}\right) = 1 + Q^{-2}\frac{e^2}{\varepsilon_0\varepsilon_r}\frac{-2}{(2\pi)^3}\int \mathrm{d}\vec{q}\frac{f\left(\varepsilon\left(\vec{Q}+\vec{q}\right),\mu\right) - f\left(\varepsilon\left(\vec{q}\right),\mu\right)}{\varepsilon\left(\vec{Q}+\vec{q}\right) - \varepsilon\left(\vec{q}\right) - i\gamma}. \tag{3.4.25}$$

Since we take the limit $\vec{Q} \to 0$, it is obvious that the screening is the less efficient, the larger the denominator and accordingly the more efficient the incoherent scattering is.

Unfortunately, the integral in Eq. (3.4.23) with respect to the propagation distance ρ_z is numerically problematic, because the fully self-consistent Green's functions are only within the device exactly known. Consequently, we cannot determine this integral, when the integrand

$\upsilon(\rho_z)$ does not vanish within the device limits. Indeed, sufficient incoherent scattering lets this integrand υ in Eq. (3.4.23) decay fast enough and vanish within the device. This is illustrated in Fig. 3.4.2. It shows $\upsilon(\rho_z)$ of Eq. (3.4.23) in the case of homogeneous n-doped GaAs with a doping density of $n = 10^{16}$ cm^{-3} at different temperatures. If the device temperature is too low, incoherent scattering is too weak* and $\upsilon(\rho_z)$ exceeds the device limits which leads to an underestimation of $P^R(0)$ and wrong screening lengths. Since $G^<$ is proportional to the electron density, the peak of $\upsilon(\rho_z)$ at $\rho_z = 0$ depends on the electron density. Therefore, the minimum amount of scattering that is needed to let $\upsilon(\rho_z)$ decay within the device depends on the electron density, too (not given in Fig. 3.4.2). In the example of Fig. 3.4.2, a device temperature of 25 K is sufficient to model $\upsilon(\rho_z)$ within ± 80 nm. In stronger doped devices, this temperature is insufficient to let $\upsilon(\rho_z)$ decay within that range. Then, numerical result underestimate the Lindhard screening length. Such artificial values are omitted in Fig. 3.4.1.

3.4.5 Applicability of developed screening model

Nevertheless, Eq. (3.4.24) is a simplified result, because we have completely neglected the vertex corrections. In particular, when incoherent scattering is efficient, the correction terms δG in Eqs. (3.4.3) and (3.4.4) may be increasingly depend on corrections of the self-energies $\delta\Sigma$. This might compensate the enhancement of the screening length†. Unfortunately, $\delta\Sigma$ depends simultaneously on the variables of the perturbative potential δV as well as of the unperturbed self-energies Σ. For this reason, an exact implementation of $\delta\Sigma$ is futile. In addition, even screening without these vertex corrections is a numerically difficult task as we have seen in Fig. 3.4.2.

We have seen that the nonlocal range of the fully scattered retarded polarization P^R extends over large distances if the total incoherent scattering is inefficient. In calculations at temperatures below 50 K or at doping concentrations higher than 10^{17} cm^{-3} the exact‡ determination of P^R lies beyond the numerical feasibility. Since the slow decay of $\upsilon(\rho_z)$ in Eq. (3.4.23) is similar for different temperatures and electron densities, a possible solution is to extrapolate $\upsilon(\rho_z)$ for ρ_z exceeding the device boundaries. However, we have neither considered the screening in inhomogeneous devices, nor analyzed the effects of dynamic screening. For instance, the dynamic screening in the case of polar optical phonon scattering is known to partly compensate the static screening - at least for the mobility of homogeneous two dimensional electron gases [54].

There are various screening models that take into account the effect of inhomogeneous electron densities (see e.g. [55–57]). These models yield significantly varying electronic lifetimes in quantum cascade structures under the influence of electron-electron and electron-ionized impurity scattering (see [58]). Still, every screening model (be it frequency dependent or not) can be traced back to an approximate evaluation of the retarded polarization P^R. This means, we always face the problem of solving the integral in Eq. (3.4.23) with an integrand $\upsilon(\rho_z)$ that might leak out of the device. When inhomogeneous screening is important, the polarization depends on *two* propagation coordinates which a scalar screening length cannot handle. In this

*The same can be observed when the temperature is left constant, but important scattering mechanisms such as the scattering with phonons and impurities are ignored.

†Similar results have been seen in the case of vertex corrections of the optical absorption. Here, depending on the device, $\delta\Sigma$ may decrease or increase the emission and absorption linewidths (see Sec. 3.3.3).

‡Exact in the sense of a polarization with fully scattered Green's functions. Higher order terms such as vertex corrections are out of sight.

case, the scattering models describing the interaction of electrons with phonons and impurities have to be completely redefined. This is clearly beyond the scope of this thesis and we leave this interesting topic to future work. In the case of inhomogeneous electron densities, we average the electronic density over the entire device and approximate the screening with a constant Debye screening length. In this way, we might miss some physical phenomena, but get a numerically feasible theory.

3.5 Novel and revised scattering self-energies

3.5.1 Introduction

In this section, we derive and discuss in detail all scattering self-energies implemented in the vertical transport part of this thesis. The self-energies describing the scattering with polar optical phonons and scattering at rough interfaces have already been published in [22], but require for the adaptation into our representation. In addition, we derive novel numerically efficient self-energies for the inelastic scattering with acoustic phonons and elastic scattering at ionized impurities. We detail all derivations of the scattering self-energies in order to enlighten and discuss all applied approximations. Results of the numerically implemented self-energies show an excellent agreement with the analytical scattering rates of Fermi's golden rule in homogeneous systems. We also derive a novel self-energy for the inelastic electron-electron scattering based on the GW_0-approximation. This latter self-energy, however, is only meant to estimate the impact of inelastic electron-electron scattering on the transport characteristics of THz-QCLs (see chapter 5). We proof in the end of this section that a conserved current density requires for a self-consistent calculation of Green's functions and self-energies. We demonstrate that the self-consistent Born approximation is the minimum requirement for current conservation, when vertex corrections of the self-energies are neglected. We finally show that the condition of current conservation can be traced back to a fundamental symmetry relation of the two-particle Green's function.

3.5.2 Revision of scattering on screened polar optical phonons

Introduction

We derive the self-energy for the inelastic scattering of electrons with polar optical phonons in the self-consistent Born approximation. We start from the rather general formula given in Sec. 2.4.2 and thereby assume bulk phonons in thermal equilibrium. We apply the Fröhlich interaction potential and consider it to be screened according to the Debye screening length (as discussed in Sec. 3.4.5). We present in detail the necessary approximations we have to apply in order to limit the complexity of the numerical implementation. These approximations are reasonable which is illustrated by the nice agreement of our numerical results for the on-shell scattering rate with analytical results of Fermi's golden rule in homogeneous systems.

Isotropic phonons in equilibrium distribution

We have already derived the fundamental structure of the lesser self-energy for scattering with any kind of phonons* in Eq. (2.4.8)

$$\Sigma^{<}(\vec{x}_3,\vec{x}_4,\omega)=\frac{1}{(2\pi)^3}\int \mathrm{d}\vec{q}\,|U_q|^2\,\mathrm{e}^{i\vec{q}\cdot(\vec{x}_3-\vec{x}_4)}\left[n_q G^{<}(\vec{x}_3,\vec{x}_4,\omega-\omega_q)+(1+n_q)\,G^{<}(\vec{x}_3,\vec{x}_4,\omega+\omega_q)\right].$$

We can utilize the homogeneity of our devices in lateral direction and Fourier transform the self-energies with respect to $\left(\vec{x}_{\parallel,3}-\vec{x}_{\parallel,4}\right)$

$$\begin{aligned}\Sigma^{<}\left(z_3,z_4,k_\parallel,E\right) &= \frac{1}{(2\pi)^3}\int \mathrm{d}\vec{q}_\parallel\mathrm{d}q_z\left|U_{q_z,q_\parallel}\right|^2\mathrm{e}^{iq_z(z_3-z_4)}\left[n_q G^{<}\left(z_3,z_4,\left|\vec{k}_\parallel-\vec{q}_\parallel\right|,E-\hbar\omega_q\right)\right.\\ &\left.+(1+n_q)\,G^{<}\left(z_3,z_4,\left|\vec{k}_\parallel-\vec{q}_\parallel\right|,E+\hbar\omega_q\right)\right]. \qquad (3.5.1)\end{aligned}$$

In this self-energy, we have approximated the phonons with a bulk dispersion relation and a thermal distribution. It has been shown for the material compositions that we study in this thesis that the neglect of phonon confinement is acceptable [59, 60]. However, the distribution of the phonons may differ from an equilibrium one when the electrons are driven far from equilibrium and strongly interact with the phonon bath (see e.g. [61, 62]). Therefore, a thermal phonon distribution might cause deviations between our theoretical predictions and experiments. The quantitative comparisons of our results in this thesis with experimental data are limited to quantum cascade lasers. In this area, the electrons indeed heat up the phonon bath. However, this heating can be successfully modelled with a lattice temperature that exceeds the temperature of the device surroundings (heat sink) [63, 64]. Of course, in very small systems such as carbon nanotubes or molecules, a nonequilibrium phonon distribution as well as an explicit calculation of the phonon modes is known to be crucial [32, 65]. Such systems are not subject to this thesis.

Fröhlich interaction Hamiltonian

H. Fröhlich has considered in [66] the electronic scattering at lattice vibrations of polar materials. Displacements of oppositely charged atoms generate electric fields electrons scatter at. The interaction energy $\langle W\rangle$ of an electron in the field of such a displacement is given by

$$\langle W\rangle=-\int \mathrm{d}\vec{r}D\left(\vec{r},\vec{r}_{el}\right)\vec{\nabla}\cdot\vec{P}\left(\vec{r}\right), \qquad (3.5.2)$$

with $D\left(\vec{r},\vec{r}_{el}\right)$, the dielectric displacement at $\vec{r}$ caused by the electron at $\vec{r}_{el}$. The polarization of the lattice vibration $\vec{P}\left(\vec{r}\right)$ is proportional to the displacement. Therefore, only longitudinal phonons contribute to this scattering mechanism. Many textbooks about many-particle physics (see e.g. [10, 67]) as well as the seminal work of H. Fröhlich [66] give detailed derivations of the squared coupling constant $\left|U_{q_z,q_\parallel}\right|^2$ in Eq. (3.5.1) for the case of longitudinal polar optical phonons. Therefore, we give here only the result

$$\left|U_{q_z,q_\parallel}\right|^2=\frac{\gamma\left(q_\parallel^2+q_z^2\right)}{\left(q_\parallel^2+q_z^2+\xi^{-2}\right)^2}, \qquad (3.5.3)$$

*We have replaced the free Green's functions by the exact (scattered) ones and thereby applied the self-consistent Born approximation.

with

$$\gamma = e^2 \frac{\hbar\omega_q}{2\varepsilon_0}\left(\frac{1}{\varepsilon_\infty} - \frac{1}{\varepsilon_s}\right). \tag{3.5.4}$$

The static and dielectric constant at infinite frequency are given by ε_s and ε_∞, respectively. The Debye screening length is ξ and ω_q is the phonon dispersion. We have to emphasize that Eq. (3.5.3) has been derived with approximations. First, the total screening is assumed to be a sum of the screening due to valence band electrons (ε_0) and electronic (ξ) as well as phononic ($1/\varepsilon_\infty - 1/\varepsilon_s$) contributions. Actually, a rigorous derivation of the electronic screening given by the retarded polarization P^R (see Sec. 3.4) would require for the inclusion of phonon vertex corrections, i.e. phonon interaction lines in the electron bubble graphs (see Sec. 3.5.6). Instead, the electronic polarization is calculated in the random phase approximation which separates the upper three respective terms. Second, we approximate the electronic contribution of the dielectric function $\varepsilon(\vec{q},\omega)$ further and insert in Eq. (3.5.3) the Debye screening given by Eq. (3.4.19). While we have already discussed in Sec. 3.4 the numerical challenges that hinders us to implement screening realistically, we emphasize that we miss collective electronic excitations such as plasmons and consequently their interaction with phonons, too.

Numerical approximations

We approximate the dispersion relation of polar optical phonons to be constant $\hbar\omega_q = E_0$. Then, the phonon number n_q at the temperature T is given by a constant

$$n_q = n_0 = \left[\exp\left(E_0/k_B T\right) - 1\right]^{-1}. \tag{3.5.5}$$

Our next step is to carry out the integral over the phonon momentum in growth direction q_z analytically. In order to prepare this, we change the integration variable in Eq. (3.5.1) from the in-plane *phonon* momentum $\vec{q}_\parallel$ to the final in-plane *electron* momentum $\vec{l}_\parallel$

$$\begin{aligned}
&\Sigma^<\left(z_3, z_4, k_\parallel, E\right)\\
= &\frac{\gamma}{(2\pi)^3}\int_{-\infty}^{\infty}\mathrm{d}q_z \int \mathrm{d}\vec{l}_\parallel \frac{q_\parallel^2 + q_z^2}{\left(q_\parallel^2 + q_z^2 + \xi^{-2}\right)^2}\mathrm{e}^{iq_z(z_3-z_4)}\left[n_0 G^<\left(z_3, z_4, l_\parallel, E - E_0\right)\right.\\
&\left.+ (1+n_0)\, G^<\left(z_3, z_4, l_\parallel, E + E_0\right)\right].
\end{aligned} \tag{3.5.6}$$

Here, the transferred in-plane momentum is given by*

$$q_\parallel\left(\vec{k}_\parallel, \vec{l}_\parallel\right) = \sqrt{k_\parallel^2 + l_\parallel^2 - 2k_\parallel l_\parallel \cos\theta}, \tag{3.5.7}$$

with

$$\theta = \angle\left(\vec{k}_\parallel, \vec{l}_\parallel\right), \tag{3.5.8}$$

the angle between the initial and final electronic in-plane momentum. We follow the approach of Goodnick and Lugli [68] and approximate the maximum phonon wave vector to be much larger than the typical electron wave vector†. This allows us to take the integral $\mathrm{d}q_z$ over the total real axis instead of the first Brillouin zone ($[-\pi/a, \pi/a]$, with a being the lattice constant).

*We omit the coordinates of $q_\parallel$ in the following.

†The lattice constant in GaAs is 0.565 nm, which gives a 5.56 nm^{-1} phonon wave vector at the Brillouin zone edge. The momentum of an electron with the kinetic energy of 0.25 eV in GaAs is approximately 0.66 nm^{-1}.

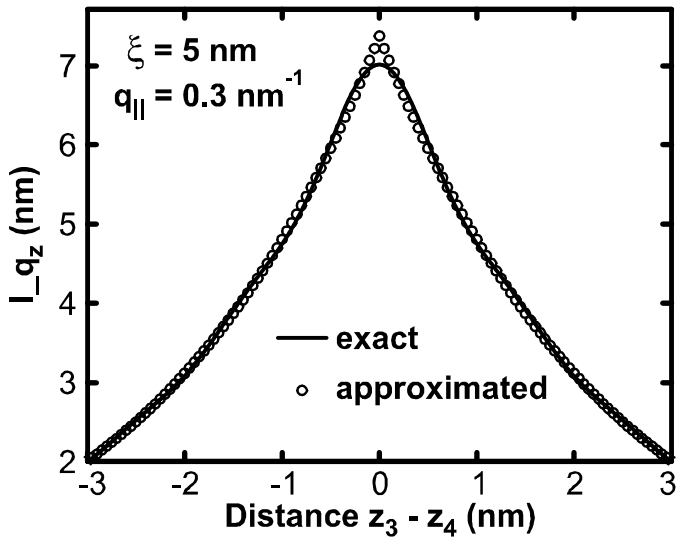

Figure 3.5.1: Exact (solid) and approximated (circles) solution of the integral I_q_z of Eq. (3.5.9). The screening length ξ of 5 nm and the transfered in-plane momentum $q_\parallel$ of 0.3 nm^{-1} are typical for electrons of approximately 100 meV kinetic energy in n-doped bulk GaAs with $n = 7.4 \times 10^{17}$ cm^{-3}.

This approximation simplifies the integral over the phonon momentum q_z significantly (see Eq. (F.0.5))

$$\begin{aligned} I\_q_z &\equiv \int_{-\pi/a}^{\pi/a} \mathrm{d}q_z \frac{q_\parallel^2 + q_z^2}{\left(q_\parallel^2 + q_z^2 + \xi^{-2}\right)^2} \mathrm{e}^{iq_z(z_3 - z_4)} \\ &\approx \int_{-\infty}^{\infty} \mathrm{d}q_z \frac{q_\parallel^2 + q_z^2}{\left(q_\parallel^2 + q_z^2 + \xi^{-2}\right)^2} \mathrm{e}^{iq_z(z_3 - z_4)} \\ &= \frac{\pi \exp\left(-\sqrt{q_\parallel^2 + \xi^{-2}}\,|z_3 - z_4|\right)}{\sqrt{q_\parallel^2 + \xi^{-2}}} \left(1 - \frac{\xi^{-2}\,|z_3 - z_4|}{2\sqrt{q_\parallel^2 + \xi^{-2}}} - \frac{\xi^{-2}}{2\left(q_\parallel^2 + \xi^{-2}\right)}\right). \end{aligned} \quad (3.5.9)$$

This approximation is well justified as can be seen in Fig. 3.5.1. It shows the approximated analytical solution as well as the numerically determined exact solution of the q_z-integral in Eq. (3.5.9) in a typical scattering situation of electrons in bulk n-doped GaAs. For the case of $z_3 = z_4$, we solve I_q_z analytically and implement the exact formula. In this way, we get numerical results that are even closer to the exact formula than those given by the symbols in Fig. 3.5.1. When we combine Eqs. (3.5.6) and (3.5.9), we get for the lesser self-energy

$$\begin{aligned} &\Sigma^< \left(z_3, z_4, k_\parallel, E\right) \\ &= \frac{\gamma\pi}{(2\pi)^3} \int \mathrm{d}\vec{l}_\parallel \frac{\mathrm{e}^{-\sqrt{q_\parallel^2 + \xi^{-2}}|z_3 - z_4|}}{\sqrt{q_\parallel^2 + \xi^{-2}}} \left(1 - \frac{\xi^{-2}\,|z_3 - z_4|}{2\sqrt{q_\parallel^2 + \xi^{-2}}} - \frac{\xi^{-2}}{2\left(q_\parallel^2 + \xi^{-2}\right)}\right) \\ &\left[n_0 G^< \left(z_3, z_4, l_\parallel, E - E_0\right) + (1 + n_0)\, G^< \left(z_3, z_4, l_\parallel, E + E_0\right)\right]. \end{aligned} \quad (3.5.10)$$

Analogously, we derive from Eqs. (2.4.9) and (3.5.9) the formula for the retarded self-energy

$$\begin{aligned}
&\Sigma^R\left(z_3, z_4, k_\parallel, E\right) \\
&= \frac{\gamma\pi}{(2\pi)^3}\int \mathrm{d}\vec{l}_\parallel \frac{\mathrm{e}^{-\sqrt{q_\parallel^2+\xi^{-2}}|z_3-z_4|}}{\sqrt{q_\parallel^2+\xi^{-2}}}\left(1-\frac{\xi^{-2}\,|z_3-z_4|}{2\sqrt{q_\parallel^2+\xi^{-2}}}-\frac{\xi^{-2}}{2\left(q_\parallel^2+\xi^{-2}\right)}\right) \\
&\times\left[(1+n_0)\,G^R\left(z_3, z_4, l_\parallel, E-E_0\right)+n_0 G^R\left(z_3, z_4, l_\parallel, E+E_0\right)+\frac{1}{2}G^<\left(z_3, z_4, l_\parallel, E-E_0\right)\right. \\
&\left.-\frac{1}{2}G^<\left(z_3, z_4, l_\parallel, E+E_0\right)+i\int\frac{\mathrm{d}\tilde{E}}{2\pi}G^<\left(z_3, z_4, l_\parallel, \tilde{E}\right)\left(\mathrm{Pr}\frac{1}{E-\tilde{E}-E_0}-\mathrm{Pr}\frac{1}{E-\tilde{E}+E_0}\right)\right].
\end{aligned} \tag{3.5.11}$$

Svizhenko et al. [69] have shown in one-dimensional systems that the principal value integrals of the last line in Eq. (3.5.11) shift the energies of resonant states. In contrast to this, we find that the larger degree of freedom of electrons in *three*-dimensional heterostructures reduces the influence of these principal value integrals strongly. Therefore, similar to many publications in literature [22, 40, 45] we neglect these principal value integrals and thereby reduce the numerical effort significantly. Due to the complex prefactor of these terms, the scattering rate is unaffected by this neglect and the analytical result of Fermi's Golden rule can nicely be reproduced. This is illustrated in Fig. 3.5.2. It shows results for a homogeneously n-doped GaAs device with $n = 2\times10^{18}$ cm^{-3}. This devices is calculated in equilibrium at room temperature while only scattering with polar optical phonons is included. In this homogeneous situation, the Green's functions and self-energies depend only on the difference of the propagation coordinates ($r = z - z'$). We Fourier transform the imaginary part of the retarded self-energy with respect to r in order to get the scattering rate Γ [70]

$$\Gamma\left(k_\parallel, k_z, E\right) = -\frac{2}{\hbar}\,\mathrm{Im}\int \mathrm{d}r\,\exp\left(ik_z r\right)\Sigma^R\left(r, k_\parallel, E\right). \tag{3.5.12}$$

We evaluate Γ at

$$k_z = \sqrt{2m^*\left(E\right)E/\hbar^2 - k_\parallel^2}, \tag{3.5.13}$$

which gives us the on-shell scattering rate of bulk electrons with energy E

$$E = \frac{\hbar^2\left(k_\parallel^2+k_z^2\right)}{2m^*\left(E\right)}. \tag{3.5.14}$$

The black line in Fig. 3.5.2 shows the scattering rate Γ resulting from Eq. (3.5.12) while the gray line shows results of Fermi's Golden rule (see e.g. [67]). Due to the high electron density, the chemical potential lies at approximately 90 meV above the conduction band edge (at 0 meV). In this case, holes in the conduction band at energies lower than the chemical potential contribute to the total scattering rate (see Sec. 6.3 C in [10]). Therefore, the Fermi Golden rule result is a sum of scattering probabilities of four kinds of scattering events: emission and absorption of LO-phonons by electrons and holes in the conduction band. All these scattering mechanisms are included in the self-energy of Eq. (3.5.11).

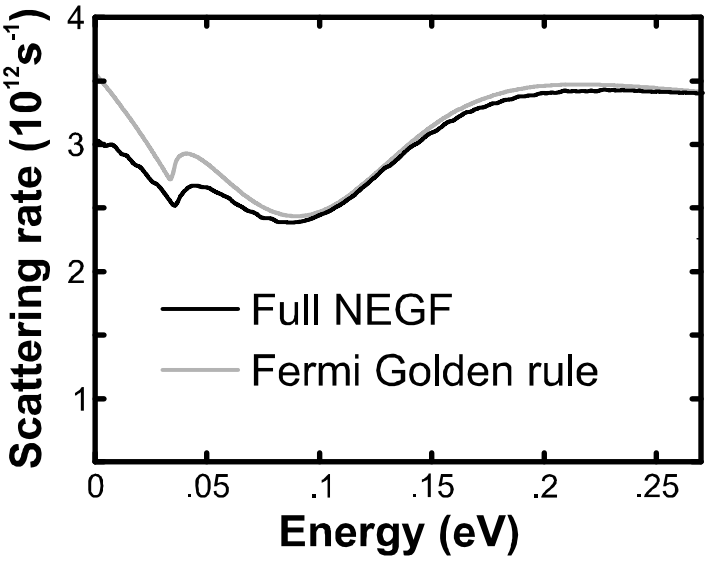

Figure 3.5.2: On-shell scattering rate of electrons with screened polar optical phonons in homogeneous n-doped GaAs at 300 K. The doping concentration is $2 \times 10^{18}\text{cm}^{-3}$ and the screening length is set to 5nm for comparison. Results of NEGF calculations (black) agree nicely with Fermi's Golden rule (grey). The scattering rate below the chemical potential at approximately 90 meV originates mainly from the scattering of conduction band holes.

3.5.3 Novel self-energy for scattering on acoustic phonons

Introduction

We derive the scattering self-energies for the interaction of electrons with longitudinal acoustic phonons. Since we start with the general formula of Eq. (2.4.8), we assume bulk phonons in equilibrium. It is common in literature, to consider elastic scattering with acoustic phonons and to approximate the phonon distribution in the high temperature limit. Thus, we first derive the elastic scattering self-energy in this approximation. However, a neglect of the acoustic phonon energy underestimates the electron thermalization.

For this reason, we introduce a new inelastic self-energy for the *unscreened* interaction of electrons with acoustic phonons. We show that this inelastic self-energy obeys a numerically important symmetry relation that decouples the retarded self-energy from the lesser Green's function. However, this self-energy still requires for the high temperature approximation of the phonon distribution. We show in detail that this approximation causes the equilibrium electron distribution to deviate from the Fermi distribution.

For completeness, we also derive a new inelastic scattering self-energy for the *screened* interaction with acoustic phonons. However, this kind of screening should not play a significant role in vertical transport, but increases the numerical load significantly. Thus, we consider the inelastic scattering with acoustic phonons to be unscreened throughout this thesis.

Isotropic phonons in equilibrium distribution

Similar to Sec. 3.5.2, we start our derivations of the acoustic phonon self-energies with Eq. (2.4.8)

$$\Sigma^{<}\left(\vec{x}_3,\vec{x}_4,\omega\right)=\frac{1}{\left(2\pi\right)^3}\int \mathrm{d}\vec{q}\left|U_q\right|^2\mathrm{e}^{i\vec{q}\cdot\left(\vec{x}_3-\vec{x}_4\right)}\left[n_q G^{<}\left(\vec{x}_3,\vec{x}_4,\omega-\omega_q\right)+\left(1+n_q\right)G^{<}\left(\vec{x}_3,\vec{x}_4,\omega+\omega_q\right)\right].$$

Thereby, we consider the acoustic phonons to be neither affected by the inhomogeneity of the device structure, nor by any nonequilibrium phenomena (see the discussion in Sec. 3.5.2). Consequently, we consider Bose distributed bulk phonons in the following.

Deformation-potential interaction

Lawaetz has shown in [71], that the deformation potential method of Bardeen and Shockley [72] may be applied on the scattering of electrons on acoustic phonons. This method is basically a Taylor expansion of the scattering potential in the phonon momentum $\vec{q}$ as we will see in the following. In the case of vanishing screening, Kittel and Fong derive in [73] the change of the electronic energy δE in lowest order of the lattice deformation $\Delta\left(\vec{x}\right)$ of an acoustic phonon

$$\delta E\left(\vec{x}\right)=D\Delta\left(\vec{x}\right). \tag{3.5.15}$$

We assume an isotropic change of the electronic energy, which results in a constant and scalar deformation potential D. The lattice is only distorted when adjacent crystal atoms are not displaced simultaneously. Therefore, the deformation is proportional to the spatial derivative of the atomic displacement $\vec{R}\left(\vec{x}\right)$

$$\Delta_\mu\left(\vec{x}\right) = \vec{\nabla}\cdot\vec{R}_\mu\left(\vec{x}\right), \tag{3.5.16}$$

$$\vec{R}_\mu\left(\vec{x}\right) = \sum_{\vec{q}}\vec{e}_{\vec{q},\mu}\sqrt{\frac{\hbar}{2V\rho\omega_{\vec{q},\mu}}}\left(\hat{a}_{\vec{q},\mu}\left(t\right)+\hat{a}^{\dagger}_{-\vec{q},\mu}\left(t\right)\right)\mathrm{e}^{i\vec{q}\cdot\vec{x}}. \tag{3.5.17}$$

The acoustic phonon of frequency is $\omega_{\vec{q},\mu}$ and the phonon polarization is given by the unit vector $\vec{e}_{\vec{q},\mu}$. Therefore, the perturbing potential of the phonon reads

$$\begin{aligned}\hat{U}\left(\vec{x},t\right) &= \hat{\psi}^{\dagger}_{\hat{H}_0}\left(\vec{x},t\right)\sum_{\vec{q},\mu}D\sqrt{\frac{\hbar}{2V\rho\omega_{\vec{q},\mu}}}\left(\vec{e}_{\vec{q},\mu}\cdot\vec{\nabla}\mathrm{e}^{i\vec{q}_\mu\cdot\vec{x}}\right)\left(\hat{a}_{\vec{q},\mu}\left(t\right)+\hat{a}^{\dagger}_{-\vec{q},\mu}\left(t\right)\right)\hat{\psi}_{\hat{H}_0}\left(\vec{x},t\right)\\ &= \hat{\psi}^{\dagger}_{\hat{H}_0}\left(\vec{x},t\right)\sum_{\vec{q}}iD\sqrt{\frac{\hbar}{2V\rho\omega_{\vec{q}}}}q\mathrm{e}^{i\vec{q}\cdot\vec{x}}\left(\hat{a}_{\vec{q}}\left(t\right)-\hat{a}^{\dagger}_{-\vec{q}}\left(t\right)\right)\hat{\psi}_{\hat{H}_0}\left(\vec{x},t\right).\end{aligned} \tag{3.5.18}$$

According to the scalar deformation potential D, this scattering self-energy is finite only for longitudinal phonons* which cancels the sum over different phonon modes μ in the last equation. Therefore, no sum over phonon modes gets involved into the self-energy and we can apply Eq. (3.5.1). For the unscreened scattering with acoustic phonons, the scattering potential reads

$$\left|U_{q_z,\vec{q}_\parallel}\right|^2=\frac{\hbar D^2}{2\rho\omega_q}q^2. \tag{3.5.19}$$

*This changes in the case of elastic anisotropy (see e.g. table IV in [74]).

In contrast to polar optical phonons, the energy of acoustic phonons depends on the phonon wave vector. Even if we linearize the acoustic phonon dispersion (similar to e.g. Jacoboni and Lugli [75]) with the sound velocity v_s

$$\omega_q \approx v_s \sqrt{q_\parallel^2 + q_z^2} = v_s q, \tag{3.5.20}$$

we face the problem, that the Green's functions explicitly depend on all three components ($\vec{q}_\parallel$ and q_z) of the phonon wave vector. Consequently, the self-energy requires for *three*-dimensional integrals for every in-plane momentum $\vec{k}_\parallel$, every energy E and every spatial grid point tuple (z_3, z_4). It turns out, that *two*-dimensional integrals at every coordinate $\left(z_3, z_4, \vec{k}_\parallel, E\right)$ are numerically feasible, though already quite demanding. *Three*-dimensional integrals, however, are beyond state of the art hardware and further approximations are necessary.

Unscreened elastic scattering at high temperatures

A rather common approach [22, 76] is to ignore the phonon contributions in the energy arguments of the Green's functions in Eq. (3.5.1)

$$E \pm \hbar\omega_q \approx E \tag{3.5.21}$$

and to additionally assume high temperatures (equipartition approximation, see e.g. [67])

$$k_B T \gg \hbar\omega_q. \tag{3.5.22}$$

With these approximations, the Bose distribution can be simplified to

$$n_q + 1 \approx n_q \approx \frac{k_B T}{\hbar\omega_q} = \frac{k_B T}{\hbar v_s q}. \tag{3.5.23}$$

This approximation is the worse, the larger the phonon energy is. The most frequent material in this thesis is GaAs which contains acoustic phonons up to approximately 19 meV. At this phonon energy*, the equipartition approximation is well justified for phonon bath temperatures above approximately 30 K as illustrated in Fig. 3.5.3. This figure shows the exact (solid) as well as the approximated (Eq. (3.5.23), dashed) result of $(1 + 2n_q)$ at 19 meV. This latter term appears in the phonon self-energy in Eq. (3.5.1).

When we apply the Eq. (3.5.23) on Eq. (3.5.1), the formula for the lesser self-energy reads

$$\Sigma^< \left(z_3, z_4, k_\parallel, E\right) = \frac{1}{(2\pi)^3} \frac{k_B T D^2}{\rho v_s^2} \int \mathrm{d}\vec{q}_\parallel \mathrm{d}q_z \mathrm{e}^{iq_z(z_3 - z_4)} G^< \left(z_3, z_4, \left|\vec{k}_\parallel - \vec{q}_\parallel\right|, E\right). \tag{3.5.24}$$

When we assume the maximum phonon momentum to be larger than the maximum in-plane momentum of the electrons (see also the discussion in Sec. 3.5.2), we get very similar to Lake *et al.* [22] for the lesser scattering self-energy

$$\Sigma^< \left(z_3, z_4, k_\parallel, E\right) = \frac{1}{(2\pi)^2} \frac{k_B T D^2}{\rho v_s^2} \delta\left(z_3 - z_4\right) \int \mathrm{d}\vec{l}_\parallel G^< \left(z_3, z_4, l_\parallel, E\right). \tag{3.5.25}$$

This scattering self-energy describes elastic scattering processes. Therefore, terms involving the lesser Green's function in the formula of the retarded self-energy Eq. (2.4.9) vanish exactly and the retarded self-energy can be derived from Eq. (3.5.25) by replacing the "<"with "R".

*Smaller phonon energies improve the equipartition approximation.

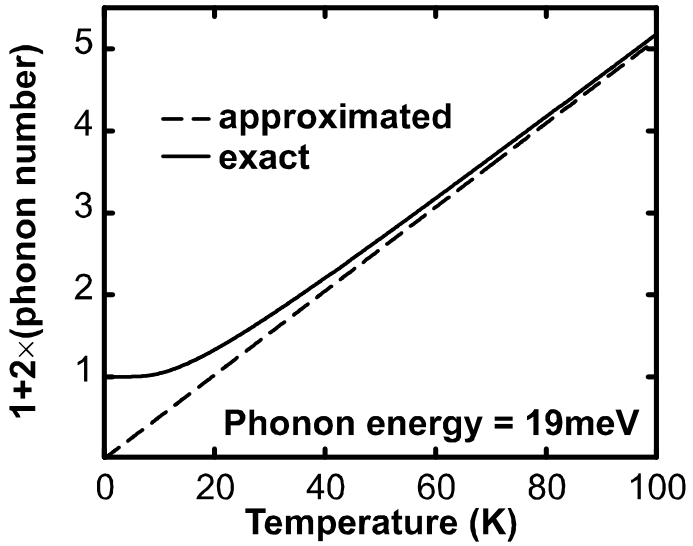

Figure 3.5.3: Phonon number dependent prefactor in the integral of Eq. (3.5.1) at 19 meV phonon energy as a function of the bath temperature. The high temperature approximation described in the text (dashed) converges with the exact solution (solid) at approximately 40 K. Both curves converge the faster, the smaller the phonon energy is.

Unscreened inelastic scattering at high temperatures

An elastic approximation of the scattering with acoustic phonons misses an important physical effect: This scattering offers the opportunity to dissipate arbitrary small amounts of energy. In particular, when the electronic energy is insufficient to emit polar optical phonons, such an elastic treatment of acoustic phonons may underestimate electron thermalization. Setting the energy of acoustic phonons to a constant, but finite value (as done by Lee and Wacker [45]) still limits the minimum amount of dissipated energy.

Instead, we approximate the inelasticity of this scattering mechanism by replacing the Green's function in Eq. (3.5.25) with an energetical average $\tilde{G}$ over the range of the LA-phonon spectrum around the initial energy E. Thereby we introduce a normalizing function h_E with an appropriate compact support that represents this energy range

$$\begin{aligned}\tilde{G}^{</R}\left(z_3, z_4, l_\parallel, \tilde{E}\right) &= \int_0^\infty h_E\left(\left|E' - \tilde{E}\right|\right) G^{</R}\left(z_3, z_4, l_\parallel, E'\right) \mathrm{d}E' \\ &= \frac{1}{2\hbar\omega_D} \int_{E-\hbar\omega_D}^{E+\hbar\omega_D} G^{</R}\left(z_3, z_4, l_\parallel, E'\right) \mathrm{d}E', \\ &\forall \tilde{E} \in [E - \omega_D, E + \omega_D]\,. \end{aligned} \tag{3.5.26}$$

Hereby, the Debye frequency ω_D limits the width of that average. In connection with the equipartition approximation of the preceding subsection, we numerically benefit from this approximation in three ways. First, we can still perform the q_z integral in Eq. (3.5.1) analytically and get a δ-function similarly to Eq. (3.5.25)

$$\Sigma^{<}\left(z_3, z_4, k_\parallel, E\right) = \frac{1}{(2\pi)^2} \frac{D^2 k_B T}{\rho v_s^2 2\hbar\omega_D} \delta\left(z_3 - z_4\right) \int_{E-\hbar\omega_D}^{E+\hbar\omega_D} \mathrm{d}E' \int \mathrm{d}\vec{l}_\parallel G^{<}\left(z_3, z_4, l_\parallel, E'\right). \tag{3.5.27}$$

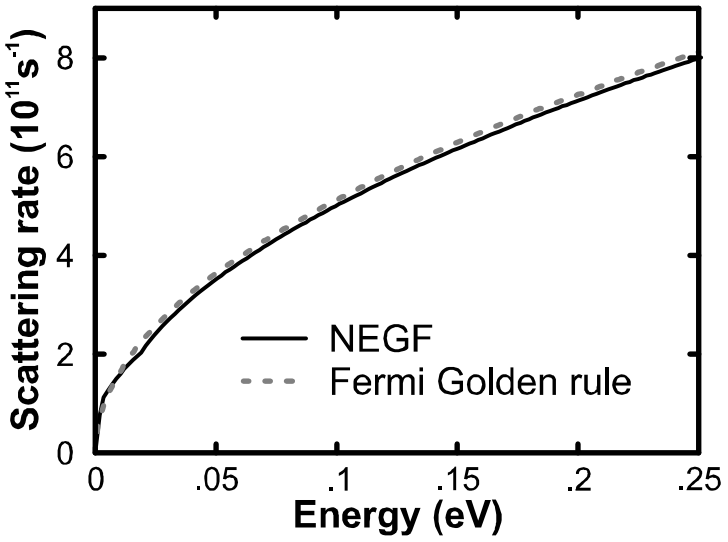

Figure 3.5.4: On-shell scattering rate of electrons by longitudinal acoustic phonons in bulk n-doped GaAs at 300K and $n = 2 \times 10^{18}\text{cm}^{-3}$. The Fermi Golden rule (dotted) and the NEGF calculation (full line) match perfectly.

Second, we have implemented the scattering with acoustic phonons inelastically including the possibility to dissipate arbitrary small energies. Third, when we apply these approximations on Eq. (2.4.9), all terms containing $G^<$ vanish exactly and the retarded self-energy is independent of the lesser Green's functions

$$\Sigma^R\left(z_3, z_4, k_\parallel, E\right) = \frac{1}{(2\pi)^2}\frac{D^2 k_B T}{\rho v_s^2 2\hbar\omega_D}\delta\left(z_3 - z_4\right)\int_{E-\varepsilon}^{E+\varepsilon} \mathrm{d}E' \int \mathrm{d}\vec{l}_\parallel G^R\left(z_3, z_4, l_\parallel, E'\right). \qquad (3.5.28)$$

As long as Σ^R does not depend on $G^<$, the Dyson equation decouples from the Keldysh equation* and may be solved independently. We will show in Sec. 4.3.3 that a *neglect* of the $G^<$-terms that typically enter the formulas of inelastic retarded self-energies violates the Pauli blocking. In the case of Eq. (3.5.28) these terms just vanish exactly, because of the symmetry of the approximation. Therefore, if all implemented inelastic self-energies are of the type of Eqs. (3.5.27) and (3.5.28), the Dyson equation decouples from the Keldysh equation naturally while the Pauli principle is still conserved. We will apply a very similar approximation on the acoustic phonon self-energy in Sec. 6.3. The numerical complexity of the multi-dimensional transport calculations in chapter III prohibits a self-consistent coupling of $G^<$ and G^R. Therefore, the symmetry of the inelastic scattering self-energies seen above becomes exceptionally important in that chapter.

Figure 3.5.4 shows that our self-energy Eq. (3.5.28) perfectly reproduces the on-shell scattering rate of Fermi's Golden rule (see Eq. (3.5.12) for the definition of the scattering rate). However, we have to admit a drawback of this approximation. Any system in equilibrium with an inelastic scattering self-energy taken into account, has to reproduce the Fermi distribution. This is only the case, if the phonon distribution n_q fulfills Eqs. (2.4.14) and (2.4.15) which require n_q to equal the Bose distribution (see the discussion in Sec. 2.4.2). Since we approximate the Bose distribution with Eq. (3.5.23), the Eq. (2.4.10) is no longer fulfilled and the occupancies of the electronic states in equilibrium deviate from Fermi distributions. This is illustrated

*The only influence of $G^<$ in this case is via the electrostatic potential Φ.

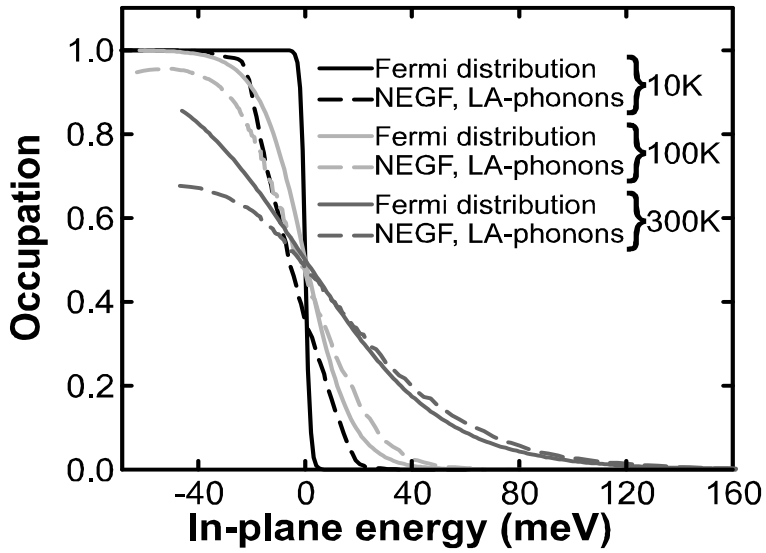

Figure 3.5.5: In-plane electron distribution in the first state of a 10 nm wide $In_{.0165}Ga_{.9835}As$ quantum well at equilibrium and various temperatures. The dashed lines show occupations resulting from NEGF calculations when inelastic scattering with LA-phonons is the only included incoherent scattering mechanism. The Fermi distributions are depicted with solid lines. The zero in energy marks the chemical potential.

in Fig. 3.5.5 as it shows the electronic occupation of the first state of an unbiased 10 nm wide $In_{.0165}Ga_{.9835}As$ quantum well that is surrounded by 10 nm thick GaAs layers at various temperatures. The only implemented scattering self-energies are given by Eqs. (3.5.27) and (3.5.28). The zero of energy is set to the chemical potential of the device and energies below the conduction band edge are neglected. The high energy tail of the calculated distributions agree the better with Fermi distributions, the higher the device temperature is. However, the occupations at energies below the chemical potential are underestimated at any temperature.Apart from these deviations from the Fermi distribution, Eqs. (3.5.27) and (3.5.28) are numerically efficient and describe the probability for inelastic scattering with acoustic phonons well enough. Since the deviations from the Fermi distribution become negligible when a more efficient inelastic scattering self-energy such as scattering with polar optical phonons is included, we implement the approximated self-energies Eqs. (3.5.27) and (3.5.28) in all NEGF calculations of vertical transport in heterostructures.

Screened inelastic scattering

Boguslawski and Mycielski have shown in [77, 78] that the scattering potentials of phonons are screened. Therefore, we - at least - derive a self-energy for the screened inelastic interaction with acoustic phonons. Though, the result is numerically too demanding for state of the art hardware and we implement the unscreened self-energies Eqs. (3.5.27) and (3.5.28) throughout this part of the thesis.

When we assume a Debye screening for the conduction band electrons the squared scattering potential reads

$$\left|U_{q_z,\vec{q}_\parallel}\right|^2 = \frac{\hbar D^2}{2\rho\omega_q} q^2 \left(\frac{q^2}{q^2+\xi^{-2}}\right)^2 . \tag{3.5.29}$$

Once again, we linearize the phonon dispersion with the sound velocity v_s and take the energetical average of the Green's function in the formula for the self-energies as given in Eq. (3.5.26)

$$\begin{aligned}
&\Sigma^{<,R}\left(z_3, z_4, k_{\|}, E\right) \\
= \;& \frac{D^2}{4\left(2\pi\right)^3 \omega_D \rho v_s} \int \mathrm{d}\vec{q}_{\|} \int_{-\pi/a}^{\pi/a} \mathrm{d}q_z \frac{q^5}{\left(q^2+\xi^{-2}\right)^2} \mathrm{e}^{iq_z(z_3-z_4)} \\
& \times \left(1+2n_q\right) \int_{E-\hbar\omega_D}^{E+\hbar\omega_D} G^{<,R}\left(z_3, z_4, \left|\vec{k}_{\|}-\vec{q}_{\|}\right|, E'\right) \mathrm{d}E'. \qquad (3.5.30)
\end{aligned}$$

In contrast to both preceding derivations of the acoustic phonon self-energies, n_q is still the exact Bose distribution

$$n_q = \left[\exp\left(\hbar v_s q / k_B T\right) - 1\right]^{-1}. \qquad (3.5.31)$$

The q_z-integral in Eq. (3.5.30) does not depend on the Green's function and can be solved prior to the actual device calculations. Still, this integral depends on at least four variables and is very demanding to be solved*

$$I\_ac \equiv \int_{-\pi/a}^{\pi/a} \mathrm{d}q_z \frac{q^5\left(1+2n_q\right)}{\left(q^2+\xi^{-2}\right)^2} \exp\left(iq_z\left|z_3-z_4\right|\right). \qquad (3.5.32)$$

However, when we apply the high temperature approximation of Eq. (3.5.23), this expression can be solved analytically†,

$$\begin{aligned}
&I_ac \approx \frac{2k_BT}{\hbar v_s} \int_{-\pi/a}^{\pi/a} \mathrm{d}q_z \frac{q^4}{\left(q^2+\xi^{-2}\right)^2} \exp\left(iq_z\left|z_3-z_4\right|\right) \\
= \;& \frac{4k_BT \sin\left(\pi\left|z_3-z_4\right|/a\right)}{\hbar v_s\left|z_3-z_4\right|} + \frac{2k_BT\xi^{-4}\pi\cos\left(\pi\left|z_3-z_4\right|/a\right)}{\hbar v_s a\left(q_{\|}^2+\xi^{-2}\right)\left(q_{\|}^2+\xi^{-2}+\pi^2/a^2\right)} \\
& + \frac{k_BT\xi^{-2}}{2\hbar v_s\sqrt{q_{\|}^2+\xi^{-2}}^3} \left[\mathrm{e}^{-\left|z_3-z_4\right|\sqrt{q_{\|}^2+\xi^{-2}}} \left[i\,\mathrm{Ei}\left(1,-\kappa^*\right) - i\,\mathrm{Ei}\left(1,-\kappa\right) - 2\pi\right]\right. \\
& \times \left(3\xi^{-2}+4q_{\|}^2-\sqrt{q_{\|}^2+\xi^{-2}}\xi^{-2}\left|z_3-z_4\right|\right) + \mathrm{e}^{\left|z_3-z_4\right|\sqrt{q_{\|}^2+\xi^{-2}}} \\
& \left.\times \left[i\,\mathrm{Ei}\left(1,\kappa^*\right) - i\,\mathrm{Ei}\left(1,\kappa\right)\right]\left(3\xi^{-2}+4q_{\|}^2+\sqrt{q_{\|}^2+\xi^{-2}}\xi^{-2}\left|z_3-z_4\right|\right)\right]. \qquad (3.5.33)
\end{aligned}$$

Here, we have abbreviated

$$\kappa \equiv \frac{i\pi}{a}\left|z_3-z_4\right| + \sqrt{q_{\|}^2+\xi^{-2}}\left|z_3-z_4\right|, \qquad (3.5.34)$$

which appears in the argument of the exponential integral

$$\mathrm{Ei}\left(v,x\right) \equiv \int_1^{\infty} \exp\left(-\zeta x\right)\zeta^{-v}\mathrm{d}\zeta. \qquad (3.5.35)$$

*This integral depends on the device temperature, the lattice constant, the distance of the propagation coordinates, the screening length and the transfered in-plane momentum.

†We have used commercial software for this integral. Therefore, the derivation is not given here.

We have not implemented this "version"of the inelastic scattering with acoustic phonons, because of its numerical requirements. Screening becomes important when the screening length is comparable to or smaller than the phonon wave length (see e.g. [79]). However, the phonon wave vector in n-doped GaAs reaches quite large values

$$q \leq 5.6 \text{ nm}^{-1}, \tag{3.5.36}$$

whereas the inverse Debye screening length for $n = 10^{17}$ cm^{-3} at 40 K is approximately 0.2 nm^{-1}. Furthermore, scattering with acoustic phonons is in most of the devices considered in this work (except those in chapter III) one of the weakest scattering mechanisms. Thus, the numerical effort needed to implement Eqs. (3.5.33) and (3.5.30) is not justifiable. Instead we use the unscreened formulas of Eqs. (3.5.27) and (3.5.28) throughout this thesis.

3.5.4 New self-energy for scattering on ionized impurities

Introduction

Several models for the electronic scattering at ionized impurities can be found in literature. We first discuss and justify our choice of the Brooks-Herring model for the impurity scattering potential. Then we extend the formula derived in Sec. 2.4.3 to inhomogeneously distributed ionized impurities. Thereby, we derive a self-energy that is already given in literature.

However, the complexity of this known formula is too high for a numerical implementation. For this reason, we introduce a novel approximation for the remote scattering of electrons at charged impurities. This approximation reduces the complexity of the charged impurity self-energies and allows for an efficient numerical implementation of this kind of scattering. We discuss in detail the validity limit of this approximation and show that our formula nicely reproduces Fermi's golden rule.

Brooks-Herring scattering model

We have already derived the self-energies Eqs. (2.4.24) and (2.4.26) for scattering at homogeneously distributed ionized impurities before

$$\Sigma^{<,R}(3;4) = G^{<,R}(3;4)\, N_D \frac{1}{(2\pi)^3} \int \mathrm{d}\vec{q} |V_{\text{imp}}(q)|^2 \, \mathrm{e}^{i\vec{q}\cdot(\vec{x}_3 - \vec{x}_4)}.$$

Here, N_D is the homogeneous density of ionized impurities. However, in the case of inhomgeneously distributed impurities, we have to reconsider the scattering self-energy. We have shown in Sec. 2.4.3 that the first order contribution of homogeneously distributed impurities is a constant shift of the electronic energy. In the case of inhomogeneously distributed impurities, the first order contribution of the impurities can be considered in the Poisson equation (see Eq. (3.6.11)) in terms of a spatially dependent (background) charge. We have also seen in Sec. 2.4.3 that the second order generates the self-energy and has to be reconsidered explicitly. In order to extend the consideration of Sec. 2.4.3 to inhomogeneous scattering, we first have to replace the probability to find the impurity i at $\vec{r}_i$ in Eq. (2.4.18) with the probability of the inhomogeneously distributed impurities

$$P(\vec{r}_i) = \frac{N_D(\vec{r}_i)}{N}. \tag{3.5.37}$$

Here, the total number of impurities N is given by the integral of the impurity density over the total volume V

$$\int_V N_D\left(\vec{r}\right) \mathrm{d}\vec{r} = N. \tag{3.5.38}$$

Second, we have to average the product of the impurity potentials at $\vec{x}_3$ and $\vec{x}_4$ over all possible distributions of the N impurities (compare Sec. 2.4.3) weighted with the probability of Eq. (3.5.37)

$$\begin{aligned}
&\left\langle V_{\mathrm{imp}}\left(\vec{x}_3;\vec{r}_1,\vec{r}_2,\ldots,\vec{r}_N\right) V_{\mathrm{imp}}\left(\vec{x}_4;\vec{r}_1,\vec{r}_2,\ldots,\vec{r}_N\right)\right\rangle_{\mathrm{imp}} \\
= &\frac{1}{N^N}\int \prod_{i=1}^{N} \mathrm{d}\vec{r}_i N_D\left(\vec{r}_i\right) \frac{1}{\left(2\pi\right)^6} \int \mathrm{d}\vec{q}\mathrm{d}\vec{q}' V_{\mathrm{imp}}\left(\vec{q}\right) V_{\mathrm{imp}}\left(\vec{q}'\right) \sum_{j=1}^{N} \mathrm{e}^{i\vec{q}\cdot\left(\vec{x}_3-\vec{r}_j\right)} \mathrm{e}^{i\vec{q}'\cdot\left(\vec{x}_4-\vec{r}_j\right)} \\
= &\frac{N\left(\int N_D\left(\vec{r}\right)\mathrm{d}\vec{r}\right)^{N-1}}{N^N} \int \mathrm{d}\vec{r} N_D\left(\vec{r}\right) \frac{1}{\left(2\pi\right)^6} \int \mathrm{d}\vec{q}\mathrm{d}\vec{q}' V_{\mathrm{imp}}\left(\vec{q}\right) V_{\mathrm{imp}}\left(\vec{q}'\right) \mathrm{e}^{i\vec{q}\cdot\left(\vec{x}_3-\vec{r}\right)} \mathrm{e}^{i\vec{q}'\cdot\left(\vec{x}_4-\vec{r}\right)} \\
= &\frac{1}{\left(2\pi\right)^6} \int \mathrm{d}\vec{r}\mathrm{d}\vec{q}\mathrm{d}\vec{q}' N_D\left(\vec{r}\right) V_{\mathrm{imp}}\left(\vec{q}\right) V_{\mathrm{imp}}\left(\vec{q}'\right) \mathrm{e}^{-i\left(\vec{q}+\vec{q}'\right)\cdot\vec{r}} \mathrm{e}^{i\vec{q}\cdot\vec{x}_3} \mathrm{e}^{i\vec{q}'\cdot\vec{x}_4}.
\end{aligned} \tag{3.5.39}$$

We can utilize the homogeneity of the system in the in-plane direction ($N_D\left(\vec{r}\right) = N_D\left(z\right)$) and perform some of the in-plane integrals ($\vec{q} = \left(\vec{q}_\parallel, q_z\right)$)

$$\begin{aligned}
&\left\langle V_{\mathrm{imp}}\left(\vec{x}_3;\vec{r}_1,\vec{r}_2,\ldots,\vec{r}_N\right) V_{\mathrm{imp}}\left(\vec{x}_4;\vec{r}_1,\vec{r}_2,\ldots,\vec{r}_N\right)\right\rangle_{\mathrm{imp}} \\
= &\frac{1}{\left(2\pi\right)^4} \int \mathrm{d}z\mathrm{d}q_z\mathrm{d}q_z'\mathrm{d}\vec{q}_\parallel N_D\left(z\right) \mathrm{e}^{-i\left(q_z+q_z'\right)z} \mathrm{e}^{iq_z z_3} \mathrm{e}^{iq_z' z_4} \mathrm{e}^{i\vec{q}_\parallel\cdot\left(\vec{x}_{\parallel 3}-\vec{x}_{\parallel 4}\right)} V_{\mathrm{imp}}\left(\vec{q}_\parallel, q_z\right) V_{\mathrm{imp}}\left(-\vec{q}_\parallel, q_z'\right) \\
= &\frac{1}{\left(2\pi\right)^2} \int \mathrm{d}z\mathrm{d}\vec{q}_\parallel N_D\left(z\right) \mathrm{e}^{i\vec{q}_\parallel\cdot\left(\vec{x}_{\parallel 3}-\vec{x}_{\parallel 4}\right)} V_{\mathrm{imp}}\left(\vec{q}_\parallel, z_3-z\right) V_{\mathrm{imp}}\left(-\vec{q}_\parallel, z_4-z\right).
\end{aligned} \tag{3.5.40}$$

The most common models for the scattering potential of ionized impurities V_{imp} are the model of Brooks and Herring [80] and the model of Conwell and Weisskopf [81]. While the model of Conwell and Weisskopf is based on a Rutherford like scattering of electrons on bare Coulomb potentials, Brooks and Herring describe the impurity potential as being screened by free carriers*

$$V_{\mathrm{imp}}\left(\vec{r}\right) = \frac{\mathrm{e}^2}{4\pi\varepsilon_0\varepsilon_r} \frac{\mathrm{e}^{-r/\xi}}{r}, \tag{3.5.41}$$

$$V_{\mathrm{imp}}\left(\vec{q}\right) = \frac{\mathrm{e}^2}{\varepsilon_0\varepsilon_r} \frac{1}{q^2+\xi^{-2}}. \tag{3.5.42}$$

This latter approach is valid, if the constant screening length ξ is much larger than the electronic wave length, which requires high temperatures and low carrier densities. For higher densities and low temperatures, the incorporation of more realistic screening has been shown to be essential [82], whereas the limit of negligible free carrier screening is better described by the approach of Conwell and Weisskopf [75]. A detailed overview of the various refinements to the approach of Brooks and Herring has been given by Chattopadhyay [83]. In this thesis, all experiments which we compare our theoretical results with (i.e. THz quantum cascade lasers) are set in the regime of the approach of Brooks and Herring. Therefore, we derive the impurity self-energies with the scattering potential of Eq. (3.5.41) and use the Debye screening length.

*The relative sign of this potential, i.e. whether the impurity is repulsive or attractive, does not influence the scattering self energy.

The two-dimensional Fourier transform of the Debye-Hückel potential, which we require in Eq. (3.5.40), reads (see [22, 84])

$$V\left(\vec{q}_{\parallel}, r_z\right) = \frac{e^2}{2\varepsilon_0\varepsilon_r}\frac{\exp\left(-Q_{\parallel}\left(q_{\parallel}\right)|r_z|\right)}{Q_{\parallel}\left(q_{\parallel}\right)}, \tag{3.5.43}$$

with

$$Q_{\parallel}\left(q_{\parallel}\right) = \sqrt{\xi^{-2} + q_{\parallel}^2}. \tag{3.5.44}$$

When we insert Eqs. (3.5.43) and (3.5.40) in the general formula for the impurity self-energy Eq. (2.4.22), we get

$$\begin{aligned}\Sigma^{<,R}(3;4) &= G^{<,R}(3;4)\left(\frac{e^2}{4\pi\varepsilon_0\varepsilon_r}\right)^2 \int \mathrm{d}z\mathrm{d}\vec{q}_{\parallel} N_D(z)\,\mathrm{e}^{i\vec{q}_{\parallel}\cdot\left(\vec{x}_{\parallel 3}-\vec{x}_{\parallel 4}\right)} \\ &\quad\times\frac{\exp\left(-Q_{\parallel}\left(q_{\parallel}\right)\left(|z_3-z|+|z_4-z|\right)\right)}{Q_{\parallel}\left(q_{\parallel}\right)^2}.\end{aligned} \tag{3.5.45}$$

Finally, we have to Fourier transform with respect to the in-plane momentum in order to get the self-energy in the representation of Eq. (3.2.1). Similar to the result of Lake *et al.* [22], we get

$$\begin{aligned}\Sigma^{<,R}\left(z_3, z_4, \vec{k}_{\parallel}, E\right) &= \left(\frac{e^2}{4\pi\varepsilon_0\varepsilon_r}\right)^2 \int \mathrm{d}\vec{q}_{\parallel}\mathrm{d}z N_D(z)\, G^{<,R}\left(z_3, z_4, q_{\parallel}, E\right) \\ &\quad\times\frac{\exp\left(-Q_{\parallel}\left(\left|\vec{k}_{\parallel}-\vec{q}_{\parallel}\right|\right)\left(|z_3-z|+|z_4-z|\right)\right)}{Q_{\parallel}\left(\left|\vec{k}_{\parallel}-\vec{q}_{\parallel}\right|\right)^2}.\end{aligned} \tag{3.5.46}$$

Unfortunately, this result requires for a three-dimensional integral for each value of $\left(z_3, z_4, k_{\parallel}, E\right)$. It turned out that a numerical implementation of such a self-energy is far too time consuming and an approximation of the self-energy is necessary.

Averaged remote scattering

The scattering self-energy of the last paragraph is only in so far "exact", that the correlation function of impurities is not further approximated. However, the assumption of a constant screening length ξ is already a significant approximation and in reality, screening in inhomogeneous devices is neither homogeneous, nor constant with respect to momentum and frequency (see Sec. 3.4). In inhomogeneous systems, it would be a better ansatz to describe the screening of charges with a polarization that depends on both propagation coordinates and is capable to describe the many particle effects correctly (see e.g. [10] and Sec. 3.5.6). However, such a dielectric function is far beyond the capabilities of state of the art hardware and we have to stick to a simplified screening model.

Against this background, it appears useless to put great efforts in an "exact"numerical implementation of Eq. (3.5.46) including the full spatial dependence of the doping density $N_D(z)$. Instead, we introduce a new approach and approximate the position dependent number of charged impurities $N(\vec{r})$ in Eq. (3.5.39) with its average $\langle N_D\rangle_{\vec{x}_3,\vec{x}_4}$ along the shortest propagation path between both propagation coordinates $\vec{x}_3$ and $\vec{x}_4$. In this way, we approximate

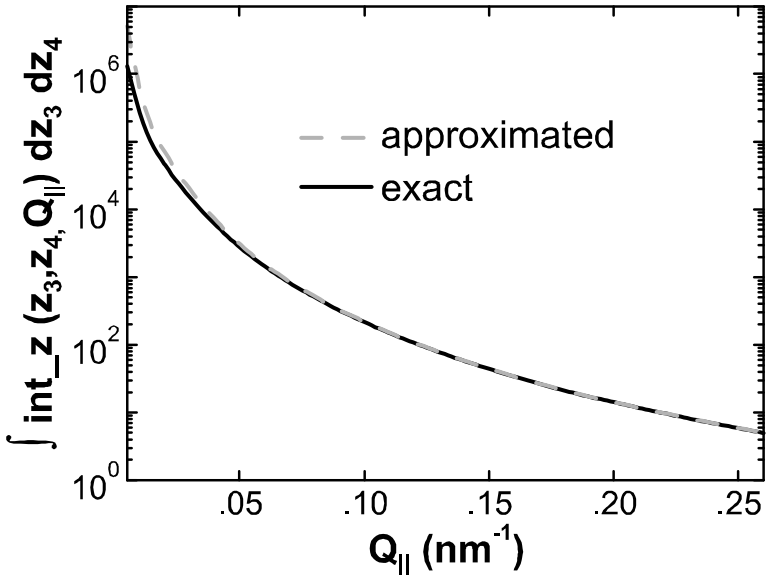

Figure 3.5.6: The function int_z of Eq. (3.5.49) integrated over both propagation coordinates. The approximation (grey dashed) of int_z deviates from the exact one (solid) only for small $Q_{\parallel}$.

the influence of scattering at inhomogeneously distributed charged impurities with an effective scattering at homogeneously distributed impurities. The remaining derivations are analogous to those of Sec. 2.4.3 and we end up with the self-energies

$$\Sigma^{<,R}(3;4) = G^{<,R}(3;4)\,\langle N_D\rangle_{\vec{x}_3,\vec{x}_4}\,\frac{1}{(2\pi)^3}\int \mathrm{d}\vec{q}\,|V_{\mathrm{imp}}(q)|^2\,\mathrm{e}^{i\vec{q}\cdot(\vec{x}_3-\vec{x}_4)}. \tag{3.5.47}$$

In the case of quasi one dimensional heterostructures, this average reads

$$\langle N_D\rangle_{z_3,z_4} = \begin{cases} N_D(z_3)\,, \text{ for } z_3 = z_4 \\ \frac{1}{z_4-z_3}\int_{z_3}^{z_4}\mathrm{d}\zeta N_D(\zeta)\,, \text{ elsewhere} \end{cases}. \tag{3.5.48}$$

In order to assess the validity of this approximation, we consider the $\mathrm{d}z$ integral that appears in the "exact"self-energy of Eq. (3.5.46)

$$\begin{aligned} int\_z\left(z_3,z_4,Q_{\parallel}\right) &= \int \mathrm{d}z N_D(z)\exp\left(-Q_{\parallel}\left(|z_3-z|+|z_4-z|\right)\right)/Q_{\parallel}^2 \\ &\approx \langle N_D\rangle_{z_3,z_4}\int \mathrm{d}z\exp\left(-Q_{\parallel}\left(|z_3-z|+|z_4-z|\right)\right)/Q_{\parallel}^2. \end{aligned} \tag{3.5.49}$$

The smaller the value of $Q_{\parallel}$, the slower the integrand in Eq. (3.5.49) decays with the distances between z, z_3 and z_4. This means (see Eq. (3.5.44)), the smaller the transferred momentum in devices with large screening lengths is, the more important is the actual shape of the impurity density $N_D(z)$ and the more is the function int_z affected by our approximation. This is illustrated in Fig. 3.5.6 as it shows the approximated as well as the exact integral of Eq. (3.5.49), integrated over z_3 and z_4 for various values of $Q_{\parallel}$ in the case of an impurity density with a compact support*

$$N_D(z) \propto \begin{cases} 1, \forall\,|z| \le 7 \text{ nm} \\ 0, \text{ else} \end{cases}. \tag{3.5.50}$$

*Such a impurity density is typical for the THz-quantum cascade lasers of chapter 5.

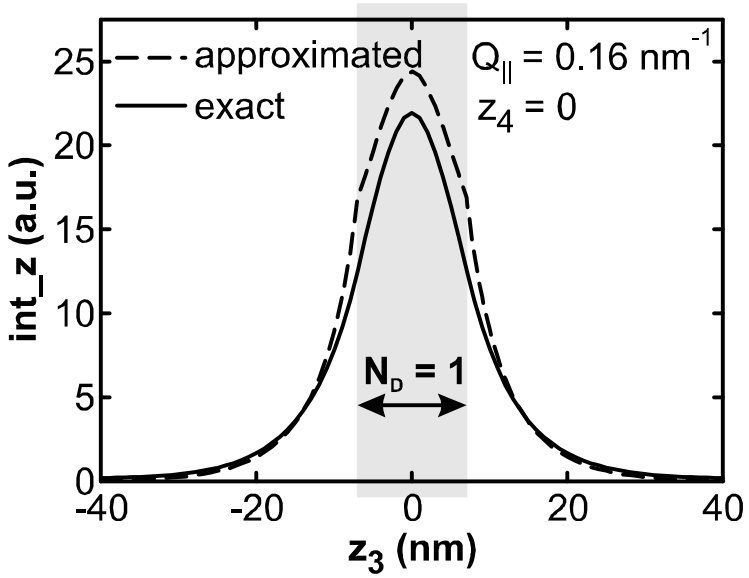

Figure 3.5.7: The function $int\_z\left(z_3, z_4 = 0, Q_\parallel\right)$ of Eq. (3.5.49) at $Q_\parallel = 0.16$ nm^{-1}. The impurity density $N_D\left(z\right)$ given in Eq. (3.5.50) and is finite only in the gray shaded region. Note that the propagation coordinate z_4 is centered in the compact support of $N_D\left(z\right)$.

Figure 3.5.6 shows that the approximation of Eq. (3.5.49) effectively overestimates scattering only for rather small transferred in-plane momenta. If the screening length is shorter than 20 nm (which corresponds to $Q_\parallel > 0.05$ nm^{-1}), the discrepancy of the effective scattering strength is negligible.

The direct path between z_3 and z_4 may cross an area with finite $N_D\left(z\right)$. Then, the approximation of int_z (dashed) overestimates the exact solution (solid) for values of z_3 close to and within the compact support of $N_D\left(z\right)$, as can be seen in Fig. 3.5.7. It shows int_z in the case of the impurity density in Eq. (3.5.50) with z_4 centered in the compact support of $N_D\left(z\right)$. However, when the direct path between z_3 and z_4 does not touch the compact support of N_D, i.e.

$$|z_3| > 7 \text{ nm} \ \wedge \ |z_4| > 7 \text{ nm} \tag{3.5.51}$$

the approximation of Eq. (3.5.49) underestimates the scattering (see Fig. 3.5.8). Consequently, we partly neglect remote scattering at charged impurities. Nevertheless, nonlocality of quantum mechanics as well as the self-consistent Born approximation ensure that a propagation between points z_3 and z_4 that fulfill Eq. (3.5.51) is still affected by scattering at the charged impurities.

Finally, we have to Fourier transform Eq. (3.5.47) with respect to the in-plane propagation coordinates and end up with

$$\begin{aligned}\Sigma^{<,R}\left(z_3, z_3, k_\parallel, E\right) &= \frac{\langle N_D\rangle_{z_3,z_4}\, e^4}{4\varepsilon_0^2\varepsilon_r^2\left(2\pi\right)^2}\int \mathrm{d}\vec{q}_\parallel \left[\frac{|z_3 - z_4| + 1/\sqrt{\xi^{-2}+q_\parallel^2}}{\xi^{-2}+q_\parallel^2}\mathrm{e}^{-\sqrt{\xi^{-2}+q_\parallel^2}|z_3-z_4|}\right. \\ &\left.\times G^{<,R}\left(z_3, z_4, \left|\vec{k}_\parallel - \vec{q}_\parallel\right|, E\right)\right].\end{aligned} \tag{3.5.52}$$

Here, we have used the autocorrelation function of the two-dimensional Fourier transform of

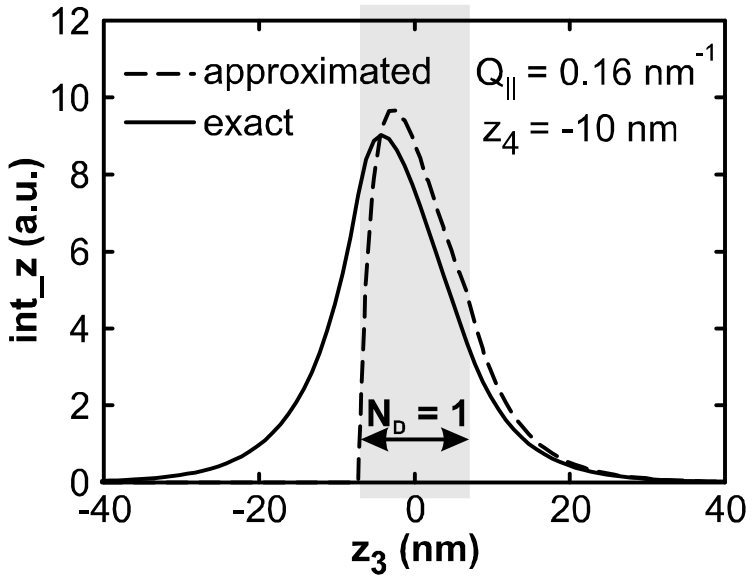

Figure 3.5.8: Same as in Fig. 3.5.7, but with $z_4 = -10$ nm, i.e. outside of the compact support of $N_D(z)$ (grey shaded region).

the Debye-Hückel potential (see Eq. (3.5.43) and [84])

$$\begin{aligned} & \frac{e^4}{4\varepsilon_0^2\varepsilon_r^2}\int_{-\infty}^{\infty}\frac{\exp\left(-\sqrt{\xi^{-2}+q_\parallel^2}\,|r_z-\rho|\right)\exp\left(-\sqrt{\xi^{-2}+q_\parallel^2}\,|\rho|\right)}{\xi^{-2}+q_\parallel^2}\mathrm{d}\rho \\ = & \frac{e^4}{4\varepsilon_0^2\varepsilon_r^2\left(\xi^{-2}+q_\parallel^2\right)}\left(|r_z|+1/\sqrt{\xi^{-2}+q_\parallel^2}\right)\exp\left(-\sqrt{\xi^{-2}+q_\parallel^2}\,|r_z|\right). \end{aligned} \tag{3.5.53}$$

Fig. 3.5.9 illustrates that Eq. (3.5.52) nicely reproduces the on-shell scattering rate of Fermi's Golden rule in a homogeneous GaAs system (see Eq. (3.5.12) for the definition of the scattering rate).

3.5.5 Revised description of scattering on rough interfaces

Introduction

Parts of the derivation of the interface roughness self-energy as well its formula can be found in literature (e.g. [22, 45, 85]). However, we have to adapt the self-energy in the representation of Eq. (3.2.1) and clarify the involved approximations. Therefore, and for the sake of completeness, we derive the self-energies for scattering at rough interfaces in detail. There are two different models for the in-plane roughness correlation function, i.e. one model applying Gaussian, and one model applying exponential correlation functions. Although we do not find significant differences of these models in the results of later chapters, we derive and implement the roughness self-energy for both models.

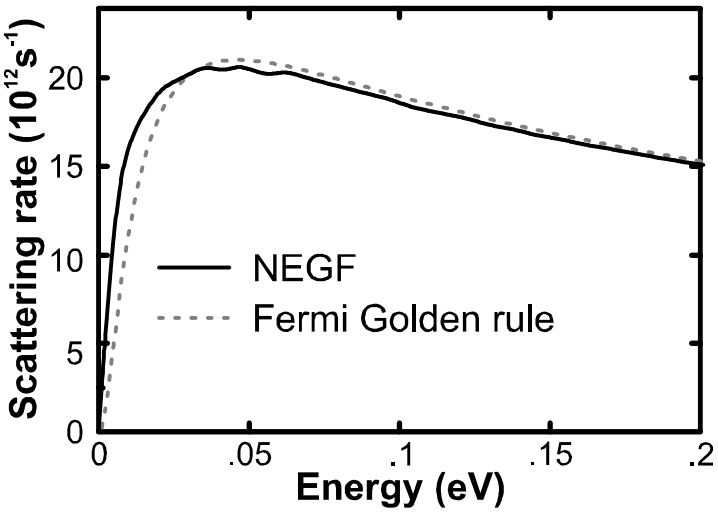

Figure 3.5.9: On-shell scattering rate of electrons by charged impurities at 300 K in homogeneous n-doped GaAs. The doping concentration is $2 \times 10^{18}\mathrm{cm}^{-3}$. The screening length was set constant to 5 nm for comparison (instead of the realistic 3 nm). The dotted line (Fermi Golden rule) and the full line (NEGF calculation) agree nicely.

General formula

There are two fundamentally different models for the interface roughness scattering in literature*. In the first model, rough interfaces of quantum wells cause fluctuating well widths and fluctuating confinement energies of resonant states. In this model, the scattering potential is identified with the change of the well eigenenergies [86, 87]. In the second model, fluctuations of the band potential offset yields the scattering potential [22, 88]. We favor the latter model, because it does not require the existence of confined states, nor the distinguishability of level broadening by rough interfaces from other mechanisms. Anyway, B. R. Nag has shown in [85] that both models agree well for quantum wells of various dimensions and materials.

We first have to find the perturbing potential. Let us consider two homogeneously grown layers of different potential offset as depicted in Fig. 3.5.10. The perturbing potential is defined as the difference of the realistic potential $V(\vec{x})$ and the idealized one $V_{\mathrm{ideal}}(z)$ (dashed in the Fig. (3.5.10))

$$V_{IR}(\vec{x}) \equiv V(\vec{x}) - V_{\mathrm{ideal}}(z). \tag{3.5.54}$$

The potential difference of the two materials is denoted with δV

$$\delta V \equiv V(A) - V(B), \tag{3.5.55}$$

where the points A and B lie within the different materials. The realistic potential does not depend on the in-plane coordinates $\vec{r}_{\parallel} = (x, y)$ for all growth coordinates z outside the roughness area $\Omega \equiv [C - \Lambda/2, C + \Lambda/2]$, where C is the midpoint of the ideal interface and Λ is the roughness step height. The ideal potential differs from the realistic one only within the roughness area Ω

$$V_{\mathrm{ideal}}(z) = \begin{cases} V(B) + \delta V/2, \forall z \in \Omega \\ V(\vec{x}), \text{ else} \end{cases}. \tag{3.5.56}$$

*Not to be confused with the two models for the in-plane interface correlation.

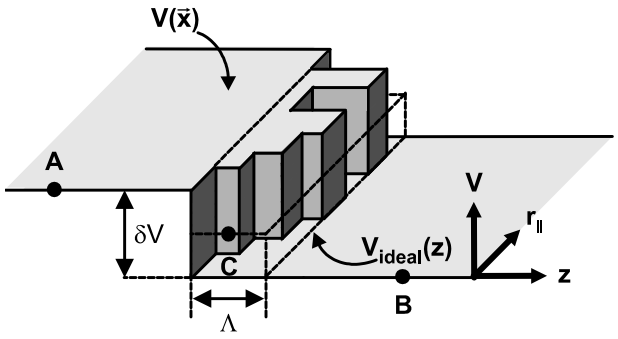

Figure 3.5.10: Schematic of the conduction band profile at the interface of two different homogeneous layers with potential difference δV. The realistic profile $V(\vec{x})$ deviates from the ideal potential $V_{\text{ideal}}(z)$ (dashed), which is averaged along the in-plane coordinate $\vec{r}_{\parallel}$, within an area of stepheight Λ around the interface point C. A and B are two neighboring points of the spatial discretization.

Hereby, we have approximated the two different materials to be equally likely in Ω. We approximate the realistic potential drop between both layers to be steep and denote the dependent midpoint of the realistic interface at (x,y) with $C^*(x,y)$. Therefore, we get for the interface potential

$$V_{IR}(x,y,z) = \left[\theta(z-C-\Lambda/2) + \theta(z-C+\Lambda/2) - 2\theta(z-C^*(x,y))\right]\delta V/2. \tag{3.5.57}$$

Since a detailed knowledge of the (x,y)-dependence of the realistic interface is futile, we have to take the average of the interface roughness potential $V_{IR}(\vec{x})$ in the (x,y)-direction. For this purpose, we assume the probability to find the realistic midpoint $C^*(x,y)$ at a specific $z \in \Omega$ to be constant. In this way, we assume a random distribution of the interface midpoint in Ω. Then, the two possible values of $V_{IR}(x,y,z)$, i.e. $\pm\delta V/2$ are equally likely and the (x,y)-average of the roughness potential $\langle V_{IR}(z)\rangle_{(x,y)}$ vanishes exactly. Consequently, scattering at rough interfaces in first non-vanishing order is a second order process and its derivation is completely analogue to the scattering at charged impurities (compare Eq. (2.4.22)). The only differences lie in the shape of the scattering potential - the position of the interface point has to be averaged in a similar manner as the impurity position.

$$-i\Sigma_{34}^{-+} = i\Sigma_{34}^{<} = \tag{3.5.58}$$

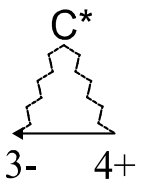

The later Feynman graph can be translated* according to the rules given in Sec. 2.3.3

$$i\Sigma^{<,R}\left(z_3,z_4,\vec{r}_{\parallel,3},\vec{r}_{\parallel,4},E\right) = iG^{<,R}\left(z_3,z_4,\vec{r}_{\parallel,3},\vec{r}_{\parallel,4},E\right)\left(-iU^{\dagger}\left(z_3,\vec{r}_{\parallel,3}\right)\right)\left(iU\left(z_4,\vec{r}_{\parallel,4}\right)\right). \tag{3.5.59}$$

Of course, the perturbing potential U equals the interface roughness potential. Since the position of C^* is unknown, we have to average (as done above for the linear order) the product

*We utilize the fact that scattering at rough interfaces is elastic.

of the perturbing potentials with respect to the actual interface configuration

$$\Sigma^{<,R}\left(z_3, z_4, \vec{r}_{\parallel,3}, \vec{r}_{\parallel,4}, E\right) = G^{<,R}\left(z_3, z_4, \vec{r}_{\parallel,3}, \vec{r}_{\parallel,4}, E\right) \left\langle V_{IR}\left(z_3, \vec{r}_{\parallel,3}\right) V_{IR}\left(z_4, \vec{r}_{\parallel,4}\right)\right\rangle_{(x,y)}, \ \forall z_3, z_4 \in \Omega. \tag{3.5.60}$$

In general, this average depends on the growth coordinates z_3 and z_4. However, since modern molecular beam epitaxy techniques allow for (depending on the growth direction) almost mono atomic or mono molecular resolved growth of layers, a typical roughness area Ω extends only over a few Angstrom which is much smaller than the typical numerical resolution. Therefore, we approximate the correlation of the interface roughness potential to be constant in Ω

$$\left\langle V_{IR}\left(x_3, y_3, z_3\right) V_{IR}\left(x_4, y_4, z_4\right)\right\rangle_{(x,y)} = \left\langle V_{IR}\left(x_3, y_3, C\right) V_{IR}\left(x_4, y_4, C\right)\right\rangle_{(x,y)}, \ \forall z_3, z_4 \in \Omega. \tag{3.5.61}$$

This results in the self-energies

$$\Sigma^{<,R}\left(z_3, z_4, \vec{r}_{\parallel,3}, \vec{r}_{\parallel,4}, E\right) = G^{<,R}\left(z_3, z_4, \vec{r}_{\parallel,3}, \vec{r}_{\parallel,4}, E\right) \left\langle V_{IR}\left(\vec{r}_{\parallel,3}, C\right) V_{IR}\left(\vec{r}_{\parallel,4}, C\right)\right\rangle_{(x,y)}, \ \forall z_3, z_4 \in \Omega. \tag{3.5.62}$$

Since Ω is typically smaller than the numerical grid spacing Δ, we assume the self-energies to be finite only when its both propagation coordinates lie on the ideal midpoint C and interpolate the self-energy linearly due to the roughness step height (Λ, see Fig. 3.5.10)

$$\begin{aligned} &\Sigma^{<,R}\left(z_3, z_4, \vec{r}_{\parallel,3}, \vec{r}_{\parallel,4}, E\right) \\ = &\begin{cases} \frac{\Lambda}{\Delta} G^{<,R}\left(C, C, \vec{r}_{\parallel,3}, \vec{r}_{\parallel,4}, E\right) \left\langle V_{IR}\left(\vec{r}_{\parallel,3}, C\right) V_{IR}\left(\vec{r}_{\parallel,4}, C\right)\right\rangle_{(x,y)}, & \text{if } z_3, z_4 = C \\ 0, \text{ else} \end{cases}. \end{aligned} \tag{3.5.63}$$

However, in a spatial discretized grid, no point lies directly on a steep interface, since the interface is always at the center between two adjacent points. Therefore, we distribute one half of this self-energy on each point that is adjacent to the interface and approximate the Green's function on the interface with the Green's function of the respective adjacent grid point. It is worth to note that the prefactor of Λ^2 in formulas often found in literature originates from the transformation of z_1 and z_2 in the commonly used delocalized basis states (see e.g. [45]).

Gaussian roughness correlation

It is a common approximation to assume a Gaussian shaped in-plane interface roughness autocorrelation $\left\langle V_{IR}\left(\vec{r}_{\parallel,3}, C\right) V_{IR}\left(\vec{r}_{\parallel,4}, C\right)\right\rangle_{(x,y)}$ (see e.g. [85, 89, 90])

$$\left\langle V_{IR}\left(\vec{r}_{\parallel,3}, C\right) V_{IR}\left(\vec{r}_{\parallel,4}, C\right)\right\rangle_{(x,y)} = \left\langle V_{IR}\left(C\right) V_{IR}\left(C\right)\right\rangle \left(\vec{r}_{\parallel,3} - \vec{r}_{\parallel,4}\right) = \frac{\delta V^2}{4} \exp\left(-\frac{\left|\vec{r}_{\parallel,3} - \vec{r}_{\parallel,4}\right|^2}{\lambda^2}\right), \tag{3.5.64}$$

with λ, the correlation length of the roughness in (x, y)-direction. We set this autocorrelation in Eq. (3.5.63) and Fourier transform with respect to the difference of the in-plane propagation coordinates $\vec{r}_{\parallel,3} - \vec{r}_{\parallel,4}$

$$\Sigma^{<,R}\left(C, C, \vec{k}_{\parallel}, E\right) = \frac{\lambda^2}{4\pi} \frac{\delta V^2}{4} \int \mathrm{d}\vec{q}_{\parallel} \exp\left(-\left(\vec{k}_{\parallel} - \vec{q}_{\parallel}\right)^2 \lambda^2/4\right) G^{<}\left(C, C, \vec{q}_{\parallel}, E\right). \tag{3.5.65}$$

Since both, the self-energies and the Green's functions do only depend on the absolute value of the in-plane momentum, we can perform the integral over the in-plane scattering angle

analytically and get the result of Lake *et al.* [22]

$$\begin{aligned}
&\Sigma^{<}\left(C,C,k_{\parallel},E\right)\\
=\;&\frac{\lambda^2}{4\pi}\frac{\delta V^2}{4}\int_0^{\infty}\mathrm{d}q_{\parallel}q_{\parallel}\int_0^{2\pi}\mathrm{d}\phi\exp\left(-\left(k_{\parallel}^2+q_{\parallel}^2-2k_{\parallel}q_{\parallel}\cos\phi\right)\lambda^2/4\right)G^{<}\left(C,C,q_{\parallel},E\right)\\
=\;&\frac{\lambda^2}{4\pi}\frac{\delta V^2}{4}\exp\left(-k_{\parallel}^2\lambda^2/4\right)\int\mathrm{d}q_{\parallel}^2\mathrm{I}_0\left(\frac{k_{\parallel}q_{\parallel}\lambda^2}{2}\right)\exp\left(-q_{\parallel}^2\lambda^2/4\right)G^{<}\left(C,C,q_{\parallel},E\right), \quad (3.5.66)
\end{aligned}$$

with the modified Bessel function

$$\mathrm{I}_0\left(x\right)=\frac{1}{\pi}\int_0^{\pi}\mathrm{d}\phi\exp\left(x\cos\phi\right). \quad (3.5.67)$$

Exponential shaped roughness correlation

Studies of different material systems [90, 91] have shown, that an exponential shape of the roughness autocorrelation may better reproduce experimental data. Therefore, we also derive the interface roughness self-energy for this model. Here, the autocorrelation of the scattering potential reads

$$\left\langle V_{IR}\left(C\right)V_{IR}\left(C\right)\right\rangle_{(x,y)}\left(\vec{r}_{\parallel,3}-\vec{r}_{\parallel,4}\right)=\frac{\delta V^2}{4}\exp\left(-\frac{\left|\vec{r}_{\parallel,3}-\vec{r}_{\parallel,4}\right|}{\lambda}\right). \quad (3.5.68)$$

Analogue to the preceding paragraph, we set this function in Eq. (3.5.63) and Fourier transform with respect to $\vec{r}_{\parallel,3}-\vec{r}_{\parallel,4}$. Thereby, we require the Fourier transform of the autocorrelation function

$$\left\langle V_{IR}\left(C\right)V_{IR}\left(C\right)\right\rangle_{(x,y)}\left(\vec{k}_{\parallel}\right)=\frac{\delta V^2}{2}\frac{\pi\lambda^2}{\left(1+k_{\parallel}^2\lambda^2\right)^{3/2}}. \quad (3.5.69)$$

We utilize the homogeneity of the system in (x,y) and perform the angle integral of the convolution

$$\begin{aligned}
&\Sigma^{<}\left(C,C,k_{\parallel},E\right)\\
=\;&\frac{\lambda^2}{4\pi}\frac{\delta V^2}{2}\int_0^{\infty}\mathrm{d}q_{\parallel}\int_0^{2\pi}\mathrm{d}\phi\frac{q_{\parallel}G^{<}\left(C,C,q_{\parallel},E\right)}{\left[1+\left(k_{\parallel}^2+q_{\parallel}^2-2k_{\parallel}q_{\parallel}\cos\phi\right)\lambda^2\right]^{3/2}}\\
=\;&\frac{\lambda^2}{\pi}\frac{\delta V^2}{2}\int_0^{\infty}\mathrm{d}q_{\parallel}\mathrm{E}\left(2\sqrt{\frac{\lambda^2k_{\parallel}q_{\parallel}}{1+\lambda^2\left(k_{\parallel}+q_{\parallel}\right)^2}}\right)\\
&\times\frac{q_{\parallel}G^{<}\left(C,C,q_{\parallel},E\right)}{\sqrt{1+\lambda^2\left(k_{\parallel}+q_{\parallel}\right)^2}\left(1+\lambda^2\left(k_{\parallel}-q_{\parallel}\right)^2\right)}. \quad (3.5.70)
\end{aligned}$$

Here, $\mathrm{E}\left(x\right)$ denotes the complete elliptical integral of the second kind

$$\mathrm{E}\left(x\right)=\int_0^{z}\frac{\sqrt{1-k^2t^2}}{1-t^2}\mathrm{d}t. \quad (3.5.71)$$

3.5.6 New approximate self-energy for electron-electron scattering

Introduction

The electron-electron scattering is subject to many-particle physics textbooks. Therefore, we do not derive the fundamental formula in detail, but summarize them only. We discuss that the full GW-approximation is beyond the scope of this thesis and implement the GW_0-approximation in the static limit for small transferred momenta. In this way, we consider the electron-electron interaction as a screened inelastic scattering of the explicitly calculated electrons with electrons of an artificial homogeneous electron gas that remains in equilibrium. The self-energies of this approximation are novel to the NEGF literature and are only meant to estimate the relevance of the electron-electron scattering in quantum cascade lasers in chapter 5.

Fundamentals

The general shape of the electron-electron self-energies in the GW-approximation is extensively discussed in every textbook about many-particle physics. Therefore, we only summarize the most important formulas for this self-energy.

In the GW-approximation, the self-energies read (see Sec. 2.3.3 for the pictogram)

$$i\Sigma(1;2) = \quad = -i\hbar W(1;2)\, iG(1;2)\,. \tag{3.5.72}$$

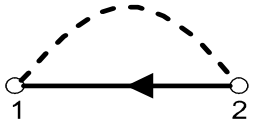

The interaction line W has its own time ordering. Following the Langreth theorem or considering G and W as matrices in the sense of Eqs. (2.3.17) and (2.3.18), the explicit formulas of the retarded and lesser self-energy are given by

$$\Sigma^{<}(1;2) = -\Sigma^{-+}(1;2) = i\hbar W^{<}(1;2)\, G^{<}(1;2)\,, \tag{3.5.73}$$

$$\Sigma^{R}(1;2) = i\hbar G^{R}(1;2)\, W^{R}(1;2) + i\hbar G^{<}(1;2)\, W^{R}(1;2) + i\hbar G^{R}(1;2)\, W^{<}(1;2)\,. \tag{3.5.74}$$

We calculate the retarded interaction line $W^{R}(1;2)$ including an infinite number of sequential Fermion "bubbles"described by the polarization P

$$\begin{aligned} & -i\hbar W^{R}(1;2) \\ = \quad & \quad + \quad + \quad + \ldots \\ = \quad & \frac{\quad}{\delta(4-2) - \quad} \\ = \quad & -i\hbar W(1-4)\left[\delta(4-2) - iP^{R}(4;3)\,(-i\hbar)\,W(3-2)\right]^{-1}, \end{aligned} \tag{3.5.75}$$

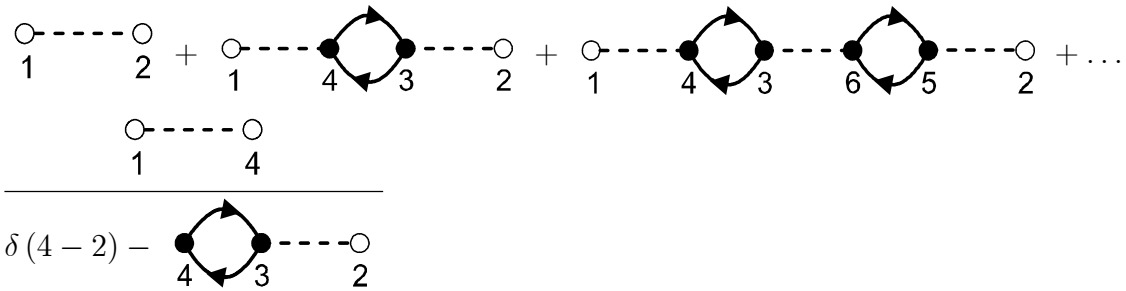

and analogously to Eq. (2.3.37) the lesser interaction line reads (see also [92])

$$-i\hbar W^{<}(1;2) = \ldots = (-i\hbar)\, W^{R}(1;3)\, iP^{<}(3;4)\, i\hbar W^{A}(4;2)\,. \tag{3.5.76}$$

Here, $W(1-2)$ is the bare Coulomb potential ($\vec{r} = \vec{x}_1 - \vec{x}_2$, $\tau = t_1 - t_2$)

$$W(\vec{r}, \tau) = \frac{e^2}{4\pi\varepsilon_0\varepsilon_r}\frac{1}{r}\delta(\tau) \tag{3.5.77}$$

and the advanced interaction line is given by

$$W^A(4;2) = W^{R\dagger}(4;2). \tag{3.5.78}$$

The polarization functions are contour ordered products of Green's functions - including a factor of (-1) that accounts for the closed Fermi loop (see Sec. 2.3.3)

$$\begin{aligned} iP^R(1;2) &= \quad \text{ 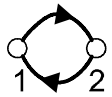 } \\ &= 2(-1)\,iG^<(1;2)\,iG^A(2;1) + 2(-1)\,iG^R(1;2)\,iG^<(2;1), \qquad (3.5.79) \\ iP^<(1;2) &= 2G^<(1;2)\,G^>(2;1) \\ &= 2G^<(1;2)\left[G^R(1;2) - G^A(1;2) + G^<(1;2)\right] \qquad (3.5.80) \end{aligned}$$

The factor of 2 in the last equations accounts for the two different spin configurations of the polarization.

Retarded interaction line

We have already explicitly derived the retarded polarization in Sec. 3.4. There, we have seen that the retarded interaction line W^R in the momentum representation may be written as

$$W^R(\vec{q}, \omega) = W(\vec{q})/\varepsilon_d(\vec{q}, \omega), \tag{3.5.81}$$

with the bare Coulomb potential

$$W(\vec{q}) = \frac{e^2}{\varepsilon_0\varepsilon_r}\frac{1}{q^2} \tag{3.5.82}$$

and the dielectric function*

$$\varepsilon_d(\vec{q}, \omega) = 1 - \hbar W(\vec{q}, \omega)\, P^R(\vec{q}, \omega)$$

with the retarded polarization (see Eq. (3.4.12))

$$\begin{aligned} iP^R(\vec{q}, \omega) &= \frac{2}{(2\pi)^4\hbar}\int \mathrm{d}E\mathrm{d}\vec{Q}\left[G^R\left(\vec{Q}+\vec{q}, E+\hbar\omega\right)G^<\left(\vec{Q}, E\right)\right. \\ &\quad \left. + G^<\left(\vec{Q}+\vec{q}, E+\hbar\omega\right)G^A\left(\vec{Q}, E\right)\right]. \qquad (3.5.83) \end{aligned}$$

In a full GW-approximation of the electron-electron interaction, the retarded polarization has to be calculated with fully scattered Green's functions G (as given in the last equation). We have already discussed in Sec. 3.4.4 several numerical challenges that complicate already an implementation of a *static* P^R when it depends on the full G. Furthermore, Holm and von

*Actually, we have only calculated the static dielectric constant and the static retarded polarization. However, the derivation of the dynamical response is completely analogue to the derivations in Sec. 3.4.2 with a time dependent perturbative potential $\delta V(\vec{x}_3, t_3)$.

Barth have shown in [93, 94] that a full GW-approximation yields wrong quasi particle spectra. They find that, unless vertex corrections are included, a GW_0-approximation gives more accurate results. Similar to the calculation of the optical absorption coefficient (see Sec. 3.3.3), the inclusion of vertex corrections is numerically futile when the full momentum and energy dependence of the self-energies is accounted for. Therefore, we apply the GW_0-approximation and calculate the retarded polarization with the free particle Green's functions of Eq. (2.3.43)

$$\begin{aligned} iP_0^R\left(\vec{q},\omega\right) &= \frac{2}{\left(2\pi\right)^4\hbar}\int \mathrm{d}E\mathrm{d}\vec{Q}\left[G_0^R\left(\vec{Q}+\vec{q},E+\hbar\omega\right)G_0^<\left(\vec{Q},E\right)\right. \\ &\quad \left.+G_0^<\left(\vec{Q},E\right)G_0^A\left(\vec{Q}-\vec{q},E-\hbar\omega\right)\right]. \end{aligned} \tag{3.5.84}$$

In this way, we assume the explicitly calculated electrons (represented in Eq. (3.5.72) by G) to scatter with a homogeneous electron gas that remains in equilibrium (represented by G_0), regardless of the actual device structure or applied bias voltages. Consequently, material dependent properties such as the effective mass enter the polarization as device averaged scalars*

$$\begin{aligned} & iP_0^R\left(\vec{q},\omega\right) \\ = & \frac{2i}{\left(2\pi\right)^2\hbar}\,\mathrm{Pr}\int \mathrm{d}E\mathrm{d}Q\mathrm{d}\cos\phi Q^2 f\left(\frac{\hbar^2Q^2}{2m^*},\mu\right)\delta\left(E/\hbar-\frac{\hbar Q^2}{2m^*}\right) \\ & \times\left[\frac{1}{E+\hbar\omega-\frac{\hbar^2}{2m^*}\left(Q^2+q^2+2Qq\cos\phi\right)}+\frac{1}{E-\hbar\omega-\frac{\hbar^2}{2m^*}\left(Q^2+q^2-2Qq\cos\phi\right)}\right] \\ = & -\frac{2i}{\left(2\pi\right)^2\hbar}\,\mathrm{Pr}\int \mathrm{d}Q\mathrm{d}\cos\phi Q^2 f\left(\frac{\hbar^2Q^2}{2m^*},\mu\right) \\ & \times\left[\frac{1}{\frac{\hbar^2}{2m^*}q^2+\frac{\hbar^2}{m^*}Qq\cos\phi-\hbar\omega}+\frac{1}{\frac{\hbar^2}{2m^*}q^2+\frac{\hbar^2}{m^*}Qq\cos\phi+\hbar\omega}\right] \\ = & -\frac{im^*}{2\pi^2\hbar^3q}\,\mathrm{Pr}\int Q\mathrm{d}Q f\left(\frac{\hbar^2Q^2}{2m^*},\mu\right) \\ & \times\left[\ln\left(\frac{\frac{\hbar^2}{2m^*}q^2+\frac{\hbar^2}{m^*}Qq-\hbar\omega}{\frac{\hbar^2}{2m^*}q^2-\frac{\hbar^2}{m^*}Qq-\hbar\omega}\right)+\ln\left(\frac{\frac{\hbar^2}{2m^*}q^2+\frac{\hbar^2}{m^*}Qq+\hbar\omega}{\frac{\hbar^2}{2m^*}q^2-\frac{\hbar^2}{m^*}Qq+\hbar\omega}\right)\right]. \end{aligned} \tag{3.5.85}$$

It is worth to note that the last equation equals Eq. 5.1.22 in [10], modified with a Fermi distribution f at finite temperatures instead of $T=0$.

Finally, we substitute the integration variable ($E=\hbar^2Q^2/2m^*$) and get

$$\begin{aligned} & iP_0^R\left(\vec{q},\omega\right) \\ = & -\frac{im^{*2}}{2\pi^2\hbar^5q}\,\mathrm{Pr}\int \mathrm{d}E f\left(E,\mu\right)\ln\frac{\left(\frac{\hbar^2}{2m^*}q^2+\frac{\hbar^2}{m^*}\sqrt{2m^*E/\hbar^2}q\right)^2-\hbar^2\omega^2}{\left(\frac{\hbar^2}{2m^*}q^2-\frac{\hbar^2}{m^*}\sqrt{2m^*E/\hbar^2}q\right)^2-\hbar^2\omega^2}. \end{aligned} \tag{3.5.86}$$

*This result is equal to Eq. 5.1.22 in [10], modified with a Fermi distribution f at finite temperatures instead of $T=0$.

When we set this in Eq. (3.5.81), we get for the retarded interaction line

$$W_0^R\left(\vec{q},\omega\right)=\frac{e^2}{\varepsilon_0\varepsilon_r}$$
$$\times\left[q^2+\frac{e^2m^{*2}}{2\pi^2\hbar^4\varepsilon_0\varepsilon_r q}\,\mathrm{Pr}\int\mathrm{d}E f\left(E,\mu\right)\ln\frac{\left(\frac{\hbar^2}{2m^*}q^2+\frac{\hbar^2}{m^*}\sqrt{2m^*E/\hbar^2}q\right)^2-\hbar^2\omega^2}{\left(\frac{\hbar^2}{2m^*}q^2-\frac{\hbar^2}{m^*}\sqrt{2m^*E/\hbar^2}q\right)^2-\hbar^2\omega^2}\right]^{-1}\quad(3.5.87)$$

Unfortunately, the last equation is numerically still to tedious to implement, because in the representation of Eq. (3.2.1) this interaction line has to be (numerically) convoluted with Green's functions with respect to the in-plane momentum and (numerically) Fourier transformed with respect to the momentum in growth direction. In addition, we implement the discretization of the in-plane momentum on a device dependent grid (see Sec. 3.7), so that this convolution has to evaluated frequently. However, we only want to estimate the thermalization of electrons in THz-QCLs due to the higher order electron-electron scattering (see Sec. 5). Therefore, we approximate Eq. (3.5.87) in the static limit with small values of $\vec{q}$. Electronic states in THz-QCLs are usually only weakly occupied, so that we additionally approximate the Fermi distribution $f\left(E,\mu\right)$ of the (artificial) homogeneous electron gas with the Boltzmann distribution. As we have seen in Sec. 3.4.4, these approximations yield the constant Debye screening length and a very simple dielectric function (see Eq. (3.4.21))

$$\varepsilon_d\left(\vec{q}\right)=1+q^{-2}\xi_{\mathrm{Debye}}^{-2}.\quad(3.5.88)$$

Of course, this eases the retarded interaction line tremendously (see Eq. (3.5.81))

$$W_0^R\left(\vec{q}\right)=\frac{e^2}{\varepsilon_0\varepsilon_r\left(q^2+\xi_{\mathrm{Debye}}^{-2}\right)},\quad(3.5.89)$$

which allows us to perform the Fourier transformation into the spatial representation analytically (see [84])

$$W_0^R\left(z_1-z_2,q_\parallel\right)=\frac{e^2}{2\varepsilon_0\varepsilon_r}\frac{\exp\left(-\sqrt{\xi_{\mathrm{Debye}}^{-2}+q_\parallel^2}\left|z_1-z_2\right|\right)}{\sqrt{\xi_{\mathrm{Debye}}^{-2}+q_\parallel^2}}.\quad(3.5.90)$$

Lesser interaction line

The lesser interaction line $W^<$ and the lesser polarization $P^<$ in the momentum and frequency representation are given by (see Eq. (3.5.76))

$$W^<\left(\vec{q},\omega\right)=-\hbar W^R\left(\vec{q},\omega\right)P^<\left(\vec{q},\omega\right)W^{R\dagger}\left(\vec{q},\omega\right),\quad(3.5.91)$$

$$iP^<\left(\vec{q},\omega\right)=\frac{2}{\left(2\pi\right)^4\hbar}\int\mathrm{d}E\mathrm{d}\vec{Q}G^<\left(\vec{Q}+\vec{q},E+\hbar\omega\right)\left[G^R\left(\vec{Q},E\right)-G^A\left(\vec{Q},E\right)+G^<\left(\vec{Q},E\right)\right].\quad(3.5.92)$$

As discussed in the preceding paragraph, we apply the GW_0-approximation and approximate the Green's functions in the formula for the lesser polarization with the free Green's functions of homogeneous bulk systems. Since, these functions are known analytically (see Eq. (2.3.43)),

we can solve the energy $\mathrm{d}E$ and momentum $\mathrm{d}\vec{Q}$ integrals analytically, as done in the following. In the appendix G, we insert the free Green's functions in Eq. (3.5.92) and assume the bulk dispersion relation $\varepsilon\left(\vec{k}\right) = \hbar^2 k^2/2m^*$ (see Eq (G.0.4))

$$iP_0^{<}\left(\vec{q},\omega\right) = \frac{2}{\pi}\frac{m^{*2}}{q\hbar^5}\int \mathrm{d}E\left(1-f\left(E,\mu\right)\right)f\left(E+\hbar\omega,\mu\right). \tag{3.5.93}$$

We can solve the remaining integral over the electronic energy E analytically and get for the lesser polarization

$$iP_0^{<}\left(\vec{q},\omega\right) = -\frac{2}{\pi}\frac{m^{*2}}{q\hbar^5}\frac{k_BT}{\mathrm{e}^{\hbar\omega/k_BT}-1}\ln\left(\frac{\mathrm{e}^{(\hbar\omega-\mu)/k_BT}+1}{\mathrm{e}^{-\mu/k_BT}+1}\right). \tag{3.5.94}$$

However, we have approximated the Fermi distribution of the artificial homogeneous electron gas with the Boltzmann distribution when we have derived the retarded interaction line W_0^R in the preceding paragraph

$$f\left(E,\mu\right) \approx \mathrm{e}^{-(E-\mu)/k_BT}. \tag{3.5.95}$$

Thus, we repeat this approximation for consistency. The total density n_e of the (artificial) homogeneous electron gas that is represented by G_0 in the interaction line (see above) is given by

$$\begin{aligned} n_e &= \frac{2}{\left(2\pi\right)^3}\int \mathrm{d}\vec{k} f\left(\vec{k},\mu\right) \approx \frac{4m^*}{\hbar^2\left(2\pi\right)^2}\int \mathrm{d}E\mathrm{e}^{-(E-\mu)/k_BT}\sqrt{2m^*E/\hbar^2} \\ &= 2\left(\frac{m^*k_BT}{2\pi\hbar^2}\right)^{3/2}\mathrm{e}^{\mu/k_BT}. \end{aligned} \tag{3.5.96}$$

Then, the lesser polarization reads

$$\begin{aligned} iP_0^{<}\left(\vec{q},\omega\right) &= \frac{2}{\pi}\frac{m^{*2}}{q\hbar^5}\int_0^\infty \mathrm{d}E\left(1-\mathrm{e}^{-(E-\mu)/k_BT}\right)\mathrm{e}^{-(E+\hbar\omega-\mu)/k_BT} \\ &= \frac{1}{\pi}\frac{m^{*2}}{q\hbar^5}k_BT\mathrm{e}^{-\hbar\omega/k_BT}\left[n_e\left(\frac{2\pi\hbar^2}{m^*k_BT}\right)^{3/2} - \frac{n_e^2}{4}\left(\frac{2\pi\hbar^2}{m^*k_BT}\right)^3\right]. \end{aligned} \tag{3.5.97}$$

We have derived the retarded interaction lines W_0^R in the static limit ($\omega \to 0$). Therefore, we apply the same limit on the lesser interaction line $W_0^<$

$$\begin{aligned} W_0^{<}\left(z_1-z_2,q_\parallel\right) &= \frac{\hbar}{2\pi}\int \mathrm{d}q_z\mathrm{e}^{iq_z(z_1-z_2)}W^R\left(\vec{q}\right)P_0^{<}\left(\vec{q}\right)W^{R\dagger}\left(\vec{q}\right) \\ &= -\frac{i}{2\pi^2}\frac{e^4m^{*2}k_BT}{\varepsilon_0^2\varepsilon_r^2\hbar^4}\left[n_e\left(\frac{2\pi\hbar^2}{m^*k_BT}\right)^{3/2} - \frac{n_e^2}{4}\left(\frac{2\pi\hbar^2}{m^*k_BT}\right)^3\right] \\ &\quad \times \int_{-\infty}^{\infty}\mathrm{d}q_z\frac{\exp\left[iq_z\left(z_1-z_2\right)\right]}{q\left(q^2+\xi_{\mathrm{Debye}}^{-2}\right)^2}. \end{aligned} \tag{3.5.98}$$

Self-energies

We have seen in the representation of position and time of Eq. (3.5.72) that the scattering self-energies are products of the interaction lines W and Green's functions G. When we Fourier transform this product into the frequency (or energy) representation, we get convolutions of W and G. Thereby, we may consider the energy argument of the Green's function as the "final" energy, i.e. the electronic energy after the scattering event. Whereas, the energy or frequency argument of W equals the transferred energy. Consequently, the frequency dependence of W limits the maximum amount of transferred energy in an electron-electron scattering event. An example of this frequency behavior of the interaction line is given in Eq. (3.5.97). Here, the factor $\mathrm{e}^{-\hbar\omega/k_BT}$ efficiently limits the transferred energy to approximately k_BT. However, for the numerical feasibility, we have derived the retarded interaction line in the static limit and have thereby lost the limitation of the energy transfer. In order to avoid wrong self-energies, we introduce a temperature dependent frequency cut-off of the kind of $\mathrm{e}^{-\hbar\omega/k_BT}$ and get for the self-energies

$$\Sigma^{<}\left(z_1,z_2,k_\parallel,E\right)=\frac{i}{(2\pi)^3}\int \mathrm{d}E'\mathrm{d}\vec{l}_\parallel \mathrm{e}^{-\frac{|E-E'|}{k_BT}} G^{<}\left(z_1,z_2,\left|\vec{k}_\parallel-\vec{l}_\parallel\right|,E'\right) W_0^{<}\left(z_1-z_2,l_\parallel\right), \tag{3.5.99}$$

$$\begin{aligned}&\Sigma^{R}\left(z_1,z_2,k_\parallel,E\right)\\ =\;&\frac{i}{(2\pi)^3}\int \mathrm{d}E'\mathrm{d}\vec{l}_\parallel \mathrm{e}^{-\frac{|E-E'|}{k_BT}}\Big[W_0^{R}\left(z_1-z_2,l_\parallel\right) G^{R}\left(z_1,z_2,\left|\vec{k}_\parallel-\vec{l}_\parallel\right|,E'\right)+W_0^{R}\left(z_1-z_2,l_\parallel\right)\\ &\times G^{<}\left(z_1,z_2,\left|\vec{k}_\parallel-\vec{l}_\parallel\right|,E'\right)+W_0^{<}\left(z_1-z_2,l_\parallel\right) G^{R}\left(z_1,z_2,\left|\vec{k}_\parallel-\vec{l}_\parallel\right|,E'\right)\Big].\end{aligned} \tag{3.5.100}$$

Figure 3.5.11 shows the scattering rates versus the electronic energy for these approximate scattering self-energies in the case of homogeneous GaAs in equilibrium at a lattice temperature of 40 K and a electron density of 1.2×10^{16} cm^{-3} which is typical for THz-QCLs (see Sec. 5). The results are comparable with the rates of the LO-phonon scattering which is in agreement with findings of Monte-Carlo calculations in [95].

3.5.7 Current conservation

Introduction

Any stationary transport model has to yield a spatially constant (i.e. conserved) current density and the nonequilibrium Green's function theory is no exception from this rule. We emphasize, however, that the self-energies of the preceding sections project the Green's functions on a nonunitary subsystem. We show that the minimum requirement for current conservation in such a subsystem is a self-consistent implementation of scattering. In particular, the first order Born and the single Born approximation violate the current conservation. We calculate the current violation in the example of simple model self-energies and proof that the self-consistent Born approximation is sufficient for a current conserving scattering model. For instructive reasons, we translate the condition for current conservation into the comprehensible shape of the detailed balance. Nevertheless, the condition for current conservation has already implicitly been introduced by Kadanoff and Baym in [5] which we explain in the end of this subsection.

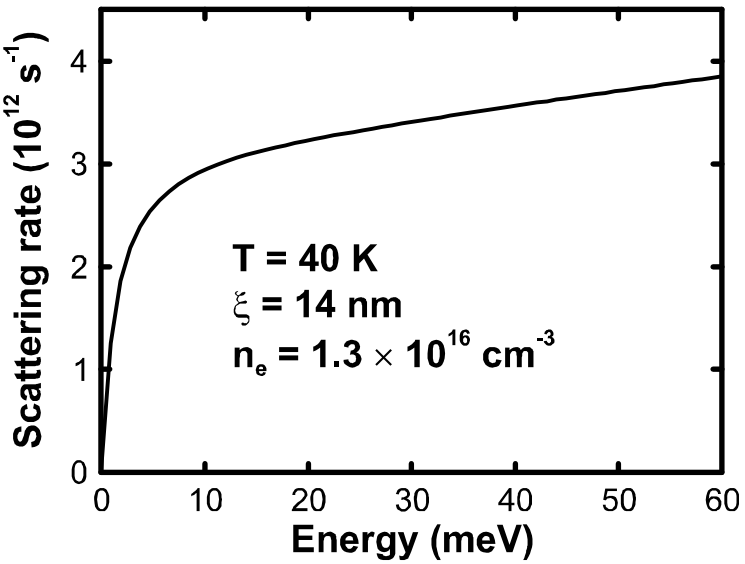

Figure 3.5.11: Scattering rate resulting from the approximative electron-electron scattering self energies of Eqs. (3.5.99) and (3.5.100) in homogeneous GaAs at 40 K in equilibrium. The non-local scattering range is limited to 8 nm, the screening length ξ is set to 14 nm and the electron density is $n_e = 1.3 \times 10^{16}$ cm^{-3}.

Fundamentals

Most of the approximations in the scattering self-energies of the preceding subsections correspond to traces over parts of the system's Hilbert space. In particular, we explicitly calculate neither phonon nor impurity Green's functions and neglect changes of the phonons and impurities due to the scattering with electrons. In this way, phonons and impurities are considered to be part of an environment that is independent of the physics in the device. Therefore, all device Green's functions are Green's functions of the total system traced over all possible configurations of the environmental variables (including phonons and impurities)*. In general, such traced subsystems obey a nonunitary time evolution [97]. This nonunitary evolution of the subsystem is responsible for the fact that the current density in NEGF calculations including self-energies of the previous subsections is not automatically conserved. However, all Green's functions in this thesis are determined in the stationary limit and the continuity equation

$$e\frac{\mathrm{d}}{\mathrm{d}t}n\left(\vec{x},t\right) = -\nabla_{\vec{x}} \cdot \vec{j}\left(\vec{x},t\right) \tag{3.5.101}$$

requires for any current density to be constant in space. Therefore, one either has to avoid the decomposition of the system into an environment and a device and treat the interactions nonperturbatively (e.g. using polaron Green's functions in the case of electron-phonon interaction [98]), or one guarantees the particle and current conservation in the nonunitary subsystem by implementing the self-consistent Born approximation or proper vertex corrections. In this thesis, we implement "only"the self-consistent Born approximation and leave a thorough analyzation of the vertex corrections to future work.

*For example, the distribution of the impurities or the precise number of system phonons. It is worth to note that the introduction of leads does not disturb the orthonormality of the scattering states (see [96]).

First order Born approximation

In order to show that the first order Born approximation violates current conservation, we consider in the following electrons in a single parabolic conduction band of a homogeneous device in equilibrium. The lesser Green's function given in this approximation ($G_1^<$) is a sum of the ballistic Green's function $G_0^<$ and the first perturbation term

$$\begin{aligned} G_1^< \left(z_1, z_2, k_\parallel, E\right) &= G_0^< \left(z_1, z_2, k_\parallel, E\right) + \int \mathrm{d}z_3 \mathrm{d}z_4 \left[G_0^R \left(z_1, z_3, k_\parallel, E\right)\right. \\ &\quad \left. \times \Sigma_0^< \left(z_3, z_4, k_\parallel, E\right) G_0^A \left(z_4, z_2, k_\parallel, E\right)\right]. \end{aligned} \tag{3.5.102}$$

Let us assume a very simple point-like scattering (see Eq. (3.2.10) for $G_0^<$)

$$\begin{aligned} \Sigma_0^< \left(z_3, z_4, k_\parallel, E\right) &= \alpha G_0^< \left(z_3, z_4, k_\parallel, E\right) \delta\left(z_3 - z_4\right) \delta\left(z_3\right) \\ &= \alpha 2 i m^* f\left(E, \mu\right) \frac{\delta\left(z_3 - z_4\right) \delta\left(z_3\right)}{\hbar^2 k_z \left(k_\parallel, E\right)}. \end{aligned} \tag{3.5.103}$$

Although this self-energy appears to be very artificial, almost all realistic scattering self-energies of the preceding subsections include terms of this shape. We just insert this self-energy in Eq. (3.5.102) and get for the first order correction term

$$\begin{aligned} \delta G^< \left(z_1, z_2, k_\parallel, E\right) &= G_1^< \left(z_1, z_2, k_\parallel, E\right) - G_0^< \left(z_1, z_2, k_\parallel, E\right) \\ &= \frac{2 i \alpha f\left(E, \mu\right) m^{*3}}{\hbar^6 k_z^3 \left(k_\parallel, E\right)} \mathrm{e}^{i k_z \left(k_\parallel, E\right) |z_1|} \mathrm{e}^{-i k_z \left(k_\parallel, E\right) |z_2|}. \end{aligned} \tag{3.5.104}$$

The contribution of the correction term to the current density is proportional to (compare Eq. (3.3.1))

$$\lim_{z_2 \to z_1} \left(\frac{\mathrm{d}}{\mathrm{d}z_1} - \frac{\mathrm{d}}{\mathrm{d}z_2}\right) \delta G^< \left(z_1, z_2, k_\parallel, E\right) = -\frac{4 \alpha f\left(E, \mu\right) m^{*3}}{\hbar^6 k_z^2 \left(k_\parallel, E\right)} \mathrm{sign}\left(z_1\right). \tag{3.5.105}$$

Obviously, the equilibrium current density in the first order Born approximation is neither spatially constant nor does it vanish.

Single and self-consistent Born approximation

In this thesis, we apply the self-consistent Born approximation on all incoherent scattering mechanisms, because this trivially conserves the current as will be shown in the following. It is straightforward (see e.g. [7]) to derive the equation for the spatial derivative of the current density

$$\frac{\mathrm{d}}{\mathrm{d}z} j\left(z\right) = -\frac{e}{h \left(2\pi\right)^2} \int \mathrm{d}E \int \mathrm{d}^2 k_\parallel I\left(z, z, k_\parallel, E\right). \tag{3.5.106}$$

When we abbreviate the matrix shape of the Green's functions and self-energies with respect to (z_1, z_2) with bold type*, the integrand I reads for a given tuple of $\left(k_\parallel, E\right)$

$$\mathbf{I} = \mathbf{\Sigma}^< \mathbf{G}^A - \mathbf{G}^< \mathbf{\Sigma}^A + \mathbf{\Sigma}^R \mathbf{G}^< - \mathbf{G}^R \mathbf{\Sigma}^<. \tag{3.5.107}$$

*The matrix product includes an integral over these coordinates which both matrices of the product depend on.

In order to illustrate that the self-consistent Born approximation is required for the current conservation, let us consider an artificial elastic scattering self-energy of the kind

$$\mathbf{\Sigma}^{</R/A}\left(\vec{k}_{\parallel},E\right)=\alpha\mathbf{G}^{</R/A}\left(\vec{k}_{\parallel},E\right), \tag{3.5.108}$$

with α, an arbitrary non-vanishing complex constant. Neither the energy, nor the momentum is changed by this artificial scattering self-energy, but it is sufficient for illustration. Since the self-energy is depending on the Green's function, the Green's functions in Eq. (3.5.107) are one order higher in the expansion of scattering. Therefore, the integrand $\mathbf{I}_n$ of the n-th order reads for a given pair $\left(k_{\parallel},E\right)$

$$\mathbf{I}_n=\alpha\mathbf{G}^{<}_{n-1}\mathbf{G}^{A}_{n}-\mathbf{G}^{<}_{n}\alpha\mathbf{G}^{A}_{n-1}+\alpha\mathbf{G}^{R}_{n-1}\mathbf{G}^{<}_{n}-\mathbf{G}^{R}_{n}\alpha\mathbf{G}^{<}_{n-1}. \tag{3.5.109}$$

The index n equals 1 in a single Born approximation*. If α is finite and the scattering self energies are non-local†, the integrand I_1 does not vanish (note that $G_0\neq G_1$) and current is not conserved. In the self-consistent Born approximation ($n\rightarrow\infty$), however, the Green's function of consecutive scattering orders do not differ

$$\mathbf{G}_{n}^{</R/A}\left(\vec{k}_{\parallel},E\right)=\mathbf{G}_{n-1}^{</R/A}\left(\vec{k}_{\parallel},E\right),\text{ for }n\rightarrow\infty. \tag{3.5.110}$$

Then, every two adjacent terms in the integrand $\mathbf{I}_n$ of Eq. (3.5.109) cancel each other and the current is trivially conserved. For finite n, the violation of the current conservation is proportional to the respective highest order of implemented scattering

$$\mathbf{I}_n=\alpha\mathbf{G}^{<}_{n}\left(\mathbf{G}^{A}_{n}-\mathbf{G}^{A}_{n-1}\right)-\alpha\left(\mathbf{G}^{<}_{n}-\mathbf{G}^{<}_{n-1}\right)\mathbf{G}^{A}_{n}-\alpha\left(\mathbf{G}^{R}_{n}-\mathbf{G}^{R}_{n-1}\right)\mathbf{G}^{<}_{n}+\alpha\mathbf{G}^{R}_{n}\left(\mathbf{G}^{<}_{n}-\mathbf{G}^{<}_{n-1}\right). \tag{3.5.111}$$

Consequently, if the series expansion of the scattering mechanisms converges, i.e. higher order Feynman graphs are smaller than lower order graphs, the current density is from one iteration to the next better conserved.

Detailed balance

Since it is instructive and simplifies later considerations, we integrate the divergence of the current density along the device of length L

$$\begin{aligned}\int_0^L \mathrm{d}z\frac{\mathrm{d}}{\mathrm{d}z}j\left(z\right) &= j\left(L\right)-j\left(0\right)\\ &= -\frac{e}{h\left(2\pi\right)^2}\int\mathrm{d}E\int\mathrm{d}^2k_{\parallel}\,\mathrm{Tr}\,\mathbf{I}\left(k_{\parallel},E\right).\end{aligned} \tag{3.5.112}$$

This trace allows us to interchange the matrices in I and to simplify the integrand for a given tuple $\left(k_{\parallel},E\right)$

$$\mathrm{Tr}\,\mathbf{I}=\mathrm{Tr}\,\mathbf{\Sigma}^{<}\left(\mathbf{G}^{A}-\mathbf{G}^{R}\right)-\mathrm{Tr}\,\mathbf{G}^{<}\left(\mathbf{\Sigma}^{A}-\mathbf{\Sigma}^{R}\right). \tag{3.5.113}$$

*Please note that it does not equal the first order Born approximation, since the single Born approximation contains an infinite series of Feynman graphs, whereas the single Born approximation consists of two graphs.

†Otherwise, the multiplied Green's function in Eq. (3.5.109) may be interchanged and the integrand vanishes with Eq. (2.2.15). In nonequilibrium and with scattering mechanisms that change energy and/or momentum, Eq. (2.2.15) does not hold and I_1 does not vanish irrespective of a spatially diagonal Σ.

Utilizing the definitions of the retarded and advanced functions we get

$$\begin{aligned} \operatorname{Tr} \mathbf{I} &= \operatorname{Tr} \boldsymbol{\Sigma}^{<} \left(\mathbf{G}^{<} - \mathbf{G}^{>}\right) - \operatorname{Tr} \mathbf{G}^{<} \left(\boldsymbol{\Sigma}^{<} - \boldsymbol{\Sigma}^{>}\right) \\ &= \operatorname{Tr} \left(\mathbf{G}^{<} \boldsymbol{\Sigma}^{>} - \mathbf{G}^{>} \boldsymbol{\Sigma}^{<}\right). \end{aligned} \tag{3.5.114}$$

This expression resembles the principle of detailed balance. Every ">"function is closely related to the "empty states", whereas every "<"function contains information about the occupation of the states. The Green's functions of the tuple $\left(k_{\parallel}, E\right)$ contain the information about how many electrons (or holes) are given in $\left(k_{\parallel}, E\right)$, whereas the self-energies of this tuple show how many electrons (or holes) of $\left(k_{\parallel}, E\right)$ scatter with those of other tuples $\left(k'_{\parallel}, E'\right)$. Therefore, the loss of particles of kind $\left(k_{\parallel}, E\right)$ is given by $\mathbf{G}^{<}\left(k_{\parallel}, E\right) \boldsymbol{\Sigma}^{>}\left(k_{\parallel}, E\right)$, while the gain of particles of kind $\left(k'_{\parallel}, E'\right)$ given by $\mathbf{G}^{>}\left(k'_{\parallel}, E'\right) \boldsymbol{\Sigma}^{<}\left(k'_{\parallel}, E'\right)$. In order to conserve the particle flux, the later two expressions have to be equal which gives us Eq. (3.5.114).

In the simple scattering example given above, neither energy nor momentum was changed. Therefore, $\left(k_{\parallel}, E\right)$ equals $\left(k'_{\parallel}, E'\right)$. We discuss in Sec. 3.7.3 examples of more realistic scattering mechanisms that change energy E and momentum $k_{\parallel}$. Then, only the integral of $\operatorname{Tr} \mathbf{I}\left(k_{\parallel}, E\right)$ over energy E and in-plane momentum $k_{\parallel}$ vanishes.

Symmetry of the two-particle Green's function

We have exemplified above in great detail that current conservation requires for the Green's function and the self-energies to be of the same scattering order. In fact, we could have skipped those considerations when we remembered that the self-energies have been introduced in Sec. 1.4 in order to approximate the two-particle Green's functions by terms of the kind (neglecting the specific time ordering)

$$-i\hbar W\left(\vec{x}_1, t_1; \vec{x}_3, t_3\right) G_2\left(\vec{x}_1, t_1; \vec{x}_4, t_4; \vec{x}_2, t_2; \vec{x}_3, t_3\right) = \Sigma\left(\vec{x}_1, t_1; \vec{x}_3, t_3\right) G\left(\vec{x}_4, t_4; \vec{x}_2, t_2\right). \tag{3.5.115}$$

Therefore, we could have justified the necessity of the self-consistent Born approximation with the prerequisite for any particle-conserving approximation of the two-particle Green's function G_2 given in Eq. (1.4.14)

$$G_2\left(\vec{x}_1, t_1; \vec{x}_4, t_4; \vec{x}_2, t_2; \vec{x}_3, t_3\right) \stackrel{!}{=} G_2\left(\vec{x}_4, t_4; \vec{x}_1, t_1; \vec{x}_3, t_3; \vec{x}_2, t_2\right).$$

When we apply this symmetry relation on the product of the one-particle Green's function and self-energy, we get

$$\Sigma\left(\vec{x}_1, t_1; \vec{x}_3, t_3\right) G\left(\vec{x}_4, t_4; \vec{x}_2, t_2\right) \stackrel{!}{=} \Sigma\left(\vec{x}_4, t_4; \vec{x}_2, t_2\right) G\left(\vec{x}_1, t_1; \vec{x}_3, t_3\right). \tag{3.5.116}$$

If the self-energy Σ is proportional to a Green's function $\tilde{G}$ (as in our example of Eq. (3.5.108)), then the last equation obviously requires the Green's function G and the Green's function $\tilde{G}$ to be of the same scattering order. This is trivially the case in the self-consistent Born approximation.

3.6 Revision of open boundary conditions

3.6.1 Introduction

In this thesis, we consider the transport as a scattering problem of electrons propagating between reservoirs. Consequently, all devices in this thesis are considered to be open quantum

devices. We begin this section with a brief introduction of the common concept of contact self-energies that account for the coupling of the device to homogeneous leads. However, we extend this method by the inclusion of non-local incoherent scattering within the leads as well as by the novel multiquantum well lead model that mimics the periodicity of cascade structures.

Typically, the Poisson equation is either solved with Dirichlet or flat band boundary conditions. While Dirichlet boundary conditions do not automatically preserve global charge neutrality, flat band conditions may lead to ambiguously defined bias voltages. Therefore, we introduce a new type of Neumann boundary conditions that have to be determined self-consistently with the conduction band profile in the device. In this way, we guarantee that the applied bias voltage drops completely within the device, while the device itself remains in total charge neutral.

Furthermore, we discuss the common assumption that leads remain in equilibrium even in the presence of finite current densities in the device. It is known that a significant current in the device requires for a response of the electron distribution in the leads. We recall several common approaches for such lead responses and discuss their applicability. Finally, we extend the model of shifted Fermi distributions to the case of arbitrary transport that may vary from coherent propagation to strongly scattered propagation.

3.6.2 Model extension to arbitrary lead density of states

Introduction

We present the fundamental concept of contact self-energies for homogeneous semi-infinite leads introduced by Datta [7]. We show that this concept exactly reproduces the analytical results for ballistic Green's functions in homogeneous devices. We extend this concept to the case of non-local incoherent scattering included within the semi-infinite leads. Furthermore, we expand Datta's method of contact self-energies to the case of periodic semi-infinite leads. This expansion is in particular important when we consider transport in superlattices and cascade structures in chapter 5. We briefly discuss the implementation of metallic ohmic leads in semiconductor nanodevices at the end of this subsection.

Fundamentals

A straightforward spatial discretization of Eq. (3.2.8) for transport in open devices requires for the inversion of an infinite matrix. Fortunately, it has been shown [7] and frequently used [99–102] that the limitation of the calculations on a finite area of interest (i.e. the device) reduces the solution of the Green's function to the inversion of a finite matrix. Thereby, the semi-infinite leads that surround the device are commonly implemented in terms of contact self-energies. For later reference, we give a brief derivation of the contact self-energies.

We start with Eq. (3.2.8) and divide the infinite matrix $\mathbf{G}^R$ for a given lateral momentum $k_\parallel$ and energy E into device (subscript d) and lead (subscript l) submatrices

$$\mathbf{G}^R = \begin{pmatrix} \mathbf{G}_l^{R-1} & \tilde{\boldsymbol{\tau}} \\ \boldsymbol{\tau} & \mathbf{G}_d^{R-1} \end{pmatrix}^{-1}, \tag{3.6.1}$$

with

$$\mathbf{G}_l^{R-1} = E\mathbf{1} - \mathbf{H}_{0,l} - \mathbf{V}_l - e\boldsymbol{\Phi}_l - \boldsymbol{\Sigma}_l^R \tag{3.6.2}$$

and

$$\mathbf{G}_d^{R-1} = E\mathbf{1} - \mathbf{H}_{0,d} - \mathbf{V}_d - e\boldsymbol{\Phi}_d - \boldsymbol{\Sigma}_d^R. \tag{3.6.3}$$

Here $\boldsymbol{\tau}$ and $\tilde{\boldsymbol{\tau}}$ contain the non-diagonal elements of the inverse retarded Green's function in Eq. (3.2.8) close to the boundaries between the device and the respective lead. In this way, Eqs. (3.6.2) and (3.6.3) represent the semi-infinite lead and the isolated device, respectively. We follow Datta [7] and implement the connection of the device to the semi-infinite lead in the equations of the device Green's functions in terms of contact self-energies $\Sigma_{con}\left(z, z', k_{\parallel}, E\right)$. Hence, we calculate the exact retarded Green's function of the open device by inverting the finite matrix of the isolated device added by $\mathbf{\Sigma}_{con}^{R}$ (for a given $\left(k_{\parallel}, E\right)$)

$$\mathbf{G}_{d}^{R} = \left(E\mathbf{1} - \mathbf{H}_{0,d} - \mathbf{V}_{d} - e\mathbf{\Phi}_{d} - \mathbf{\Sigma}_{d}^{R} - \mathbf{\Sigma}_{con}^{R}\right)^{-1}, \tag{3.6.4}$$

with

$$\mathbf{\Sigma}_{con}^{R} = \boldsymbol{\tau}\mathbf{G}_{l}^{R}\tilde{\boldsymbol{\tau}}. \tag{3.6.5}$$

Since $G_{l}^{R}\left(z, z', k_{\parallel}, E\right)$ is the solution of Eq. (3.6.2) that lacks the modification by a contact self-energy, it is the surface Green's function of the respective semi-infinite lead. The remaining paragraphs of this section focus on the determination of $G_{l}^{R}\left(z, z', k_{\parallel}, E\right)$.

Before we do this, it is important to note that the above scheme defines the charge transport as a scattering problem of source and drain leads with the active device in between. The electrons enter the device in "propagating eigenstates"of the lead Hamiltonian, represented by the respective surface Green's function [103]. We put "propagating eigenstates"in apostrophes, because non-Hermitian Hamilton operators actually do not possess real eigenvalues, i.e. every electronic state has a finite lifetime. Furthermore, electrons that do not propagate, but are strongly damped by incoherent scattering may still enter the device and thereby contribute up to some extend to the surface Green's function of the lead. Nevertheless, most of the surface Green's function is carried by freely developing electrons and in that sense we want to understand the above statement. We also want to emphasize that the implementation of contact self-energies is per se no approximation. It is only a method to limit the NEGF calculation on a finite area. Approximations come only into play, if the surface Green's functions of the leads $\mathbf{G}_{l}^{R}$ are for some reasons unknown and hard to determine.

Homogeneous leads

The most commonly assumed lead type for open devices is the homogeneous lead. The original idea behind this lead model is that all the relevant physics "happen" within the device. Interferences, confined states, local electrostatic charges among other physical phenomena that might lead to inhomogeneous physical properties and observables are assumed to be solely located within the device. In this lead model, the envelope functions of the electrons that enter the device equal plain waves.

In this thesis, we implement this model by continuing the physical properties at every marginal device point $z = \mathrm{P}$ into the adjacent lead, i.e.

$$\begin{aligned} H_{0,l}\left(z, k_{\parallel}, E\right) &= H_{0,d}\left(\mathrm{P}, k_{\parallel}, E\right), \\ V_{l}\left(z\right) &= V_{d}\left(\mathrm{P}\right), \\ \Phi_{l}\left(z\right) &= \Phi_{d}\left(\mathrm{P}\right), \\ m_{l}^{*}\left(z, E\right) &= m_{d}^{*}\left(\mathrm{P}, E\right), \end{aligned} \tag{3.6.6}$$

and

$$\Sigma_{l}^{R}\left(z, z+\zeta, k_{\parallel}, E\right) = \Sigma_{d}^{R}\left(\mathrm{P}, \mathrm{P}+\zeta, k_{\parallel}, E\right). \tag{3.6.7}$$

The last equation, i.e. the continuation of the scattering self-energies into the leads is analogous to the scheme proposed by Svizhenko *et. al.* [104]. However, we additionally maintain the full non-local character of the self-energies within the leads as well as in the transitions of electron between the leads and the device. Consequently, the off-diagonal matrices $\boldsymbol{\tau}$ and $\tilde{\boldsymbol{\tau}}$ of Eq. (3.6.5) contain non-local elements of the scattering self-energies close to the boundaries in addition to the non-local elements that result from the free-particle part of the Hamiltonian $\mathbf{H}_0$. We consider the leads to be field-free and set the Hartree potential in each lead Φ_l to a constant.

In the case of vanishing incoherent scattering in the leads, the analytical formula for the respective contact self-energy is well known (see [7] for the derivation*)

$$\Sigma^R_{con}\left(z, z', k_\parallel, E\right) = -\frac{\hbar^2}{2m^*_d\left(\mathrm{P}, E\right)} \exp\left(ik_z\left(k_\parallel, E\right)\Delta\right) \delta\left(z - \mathrm{P}\right) \delta\left(z' - \mathrm{P}\right), \tag{3.6.8}$$

with

$$\begin{aligned} k_z\left(k_\parallel, E\right) = &\sqrt{2m^*_d\left(\mathrm{P}, E\right)/\hbar^2} \\ &\times \sqrt{E - V_d\left(\mathrm{P}\right) - e\Phi_d\left(\mathrm{P}\right) - \frac{\hbar^2 k_\parallel^2}{2m^*_d\left(\mathrm{P}, E\right)}}. \end{aligned} \tag{3.6.9}$$

Here, the homogeneous grid spacing is given by Δ. When we attach these leads to a homogeneous device and ignore any incoherent scattering, the numerically determined Green's functions in the device has to equal Eq. (3.2.10). This is illustrated in Fig. 3.6.1 as it shows the $k_\parallel$-integrated retarded Green's function $\mathbf{G}^R$ for electrons in the parabolic† conduction band of homogeneous GaAs in equilibrium (see Eq. (3.2.10))

$$\int \mathrm{d}^2 k_\parallel G^R_0\left(z, z', k_\parallel, E\right) = -\frac{2\pi m^*}{\hbar^2} \frac{\mathrm{e}^{i\sqrt{2m^*E/\hbar^2}|z-z'|} - 1}{|z - z'|}. \tag{3.6.10}$$

The perfect agreement of the numerical solution (dots) with the analytical expression (lines) of Eq. (3.6.10) nicely demonstrates the accurateness of the contact self-energy method.

In the general case, when incoherent non-local scattering is present or barriers in the leads confine the electronic wave functions, the analytical formula for the lead surface Green's function is unknown. Then, we have to determine $\mathbf{G}^R_l$ numerically and apply some approximations as will be discussed in the next paragraph and in Sec. 3.7.4.

Multiquantum well and single period lead model

The homogeneous lead model of the preceding paragraph might be inadequate in periodic heterostructures such as superlattices or quantum cascade lasers. Since such devices typically consist of several hundreds of periodically repeated layers, the explicit calculation of the Green's functions of the entire device is numerically prohibitive. Instead, we extend the method of contact self-energies beyond the well-known homogeneous leads and model the periods surrounding the explicitly calculated periods of the active device by the multiquantum well lead model.

This model considers field-free multiquantum well structures within the leads that repeat the multiquantum well geometry of the device [105] (see Sec. 3.7.4 for numerical details). In this

*Please note that the discretization of $\delta(z)$ introduces the factor $1/\Delta$.

†We have neglected the nonparabolicity in this comparison.

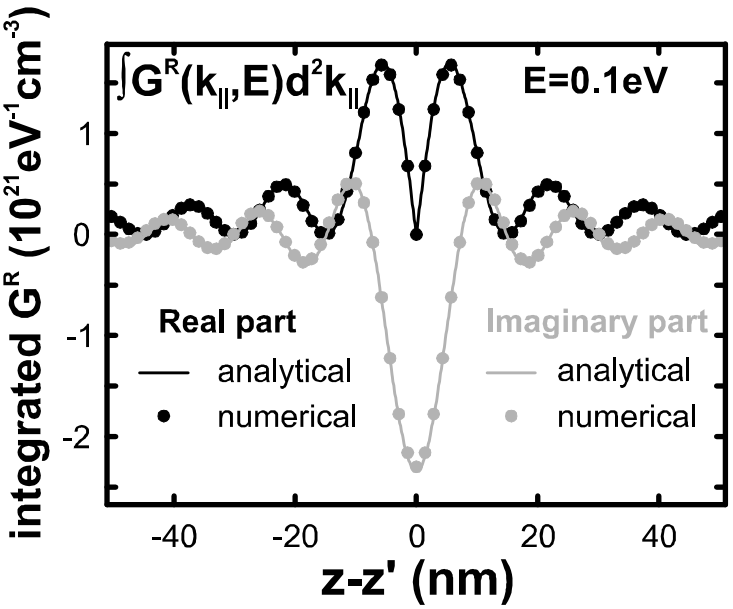

Figure 3.6.1: Real (black) and imaginary (grey) part of the retarded Green's function in homogeneous GaAs at equilibrium in the absence of incoherent scattering, integrated over the in-plane momentum $k_{\|}$ and at the electronic energy $E = 0.1$ eV. The numerical solution (dots) of the isolated device connected to leads via contact self-energies perfectly matches the analytical expression of Eq. (3.6.10) (lines).

model, the electrons in the leads effectively propagate in eigenstates of the periodic heterostructure and enter the device with a density of states that mimics the situation in a multi-period system more realistically than homogeneous leads. In the multiquantum well lead model, we do not calculate the scattering self-energies within the leads, but use a constant retarded self-energy $\Sigma_l^R\left(z, z', k_{\|}, E\right) = -i\hbar\delta\left(z - z'\right)/2\tau_{sc}$ therein. The nonlocal part of the device self-energies that leaks into the leads is cut off accordingly. We introduce a transition zone of 6 nm between the device and the leads. In this area, the Poisson equation, the Green's functions and self-energies are solved self-consistently in order to smoothen the electronic transitions between the device and the leads. The results in the quantum cascade lasers (QCLs) of this thesis do not depend on the details of the scattering self-energies within the leads due to the efficient limitation of the transport by the QCL barriers (see also Sec. 5.2.2). A typical value for τ_{sc} is of the order of 0.1 ps. We would like to emphasize that scattering within the leads does play an important role in devices with low barriers close to the leads (see Sec. 4.2.2).

The THz-QCL structures that we analyze in chapter 5 contain injector wells at the source sided boundary. These injector wells filter incoming electrons from the source which effectively damps the electronic wave function of lead electrons. In this case, details of the density of states in the leads turn out to have only minor influence on the transport characteristics of the active THz-QCL period in the device. In order to analyze this behavior in Sec. 5.2.2 we introduce a simplification of the multiquantum well lead model which we term the single period lead model. This model equals the multiquantum well lead model except that the conduction band in the lead is constant and lacks any confining barriers.

Ohmic contacts

According to [106], an ohmic contact is a metal-semiconductor contact that has a negligible junction resistance relative to the total resistance of the semiconductor device. Such a contact does not perturb the device performance and supplies the required current with a voltage drop that is much smaller than the drop across the active device. In the following, we add a discussion that an ohmic contact may be modelled with the homogeneous lead model.

Typical metals attached to semiconductor devices face (apart from different effective masses) a several eV deep conduction band difference to the active device. If we implemented that difference as an abrupt rise in the conduction band, the electron momenta in the semiconductor device and the lead would differ significantly. Such a difference yields large interferences in the vicinity of the leads. This situation clearly violates the definition of an ohmic contact.

Instead of an abrupt crossing from metal to semiconductor, an ohmic contact must have a transition area between the semiconductor device and the metallic lead which ensures smooth electronic transitions in between. The average material properties in this transition area gradually transform from the pure metallic to the pure semiconductor values. Close to the device, however, the electrons maintain the pure semiconductor density of states. The large difference in the conduction band offsets of metal and semiconductor effectively reflect all electrons with a metallic density of states. These reflections do not generate interferences, because any electron in the transition area faces a comparably short lifetime which damps any spatial correlation. This lifetime is limited by incoherent scattering at randomly distributed islands of metal or semiconductor material properties as well as by efficient electron-electron scattering according to the large number of electrons in the metallic leads. Consequently, the surface Green's functions of ohmic leads are indistinguishable from surface Green's functions of homogeneous semiconductor leads.

3.6.3 Novel electrostatic boundary conditions

Introduction

The Poisson equation is a second order differential equation and consequently requires for two boundary conditions. We present our boundary conditions for equilibrium and nonequilibrium calculations. We apply Neumann boundary conditions with a finite electric field at the boundaries that guarantees unambiguously defined applied bias voltages. These boundary conditions only partly agree with common approaches in literature as we discuss and justify in detail.

Boundary conditions in equilibrium

Any electrostatically charged device attracts or repulses electrons from or into the leads. Consequently, if no other driving forces (e.g. exciting laser beams) exist, any device has to reach global charge neutrality in the stationary limit. Therefore, we solve the Poisson equation*

$$\frac{\mathrm{d}}{\mathrm{d}z}\varepsilon_0\varepsilon_r(z)\frac{\mathrm{d}}{\mathrm{d}z}\Phi(z) = -en(z) + eN_D(z) \tag{3.6.11}$$

under the condition of global charge neutrality. This means, the first boundary condition of the Poisson equation requires the electric displacement x to be *equal* at both device boundaries

*Note that the local electron density $n(z)$ is a functional of the Green's functions which depend on Φ again. Therefore, the Poisson equation and the Green's functions have to be solved self-consistently.

(at $z = 0$ and $z = L$)

$$\varepsilon_0 \varepsilon_r (0) \left.\frac{\mathrm{d}}{\mathrm{d}z}\Phi(z)\right|_{z=0} = x,$$
$$\varepsilon_0 \varepsilon_r (L) \left.\frac{\mathrm{d}}{\mathrm{d}z}\Phi(z)\right|_{z=L} = x. \tag{3.6.12}$$

Please note the previously introduced material dependent relative static dielectric constant $\varepsilon_r(z)$ and the position dependent number of ionized dopant atoms $N_D(z)$. In equilibrium (subindex eq), we assume vanishing electric fields at the device boundaries. Thus, the second boundary condition for the Poisson equation reads

$$x_{\mathrm{eq}} = 0. \tag{3.6.13}$$

Depending on the actual device structures, these conditions may lead to finite built-in potentials

$$V_{\mathrm{built-in}} \equiv -e\left[\Phi_{\mathrm{eq}}(L) - \Phi_{\mathrm{eq}}(0)\right]. \tag{3.6.14}$$

While the Poisson potential and the Green's functions are calculated self-consistently, these two boundary conditions allow the average conduction band edge to float up and down relative to the chemical potentials of the leads (see Sec. 3.6.4). The higher the average conduction band edge lies, the less electrons are given in the device (and vice versa). In this way, global charge neutrality is self-consistently achieved.

Boundary conditions in nonequilibrium

In the area of device simulations, it is common to solve the Poisson equation with either Dirichlet or Neumann boundary conditions. The Dirichlet boundary conditions are typically chosen such that the difference of the conduction band edges at the device boundaries equals the applied bias voltage [107, 108]. In contrast, the Neumann boundary conditions are typically applied with vanishing slope of the electrostatic potential (flat band) [109, 110]. While Dirichlet boundary conditions are inappropriate with Eq. (3.6.12), it is known that when flat band conditions are applied, the difference of the conduction band at the left and right device boundary differs from the applied bias voltage (see also Sec. 4.2.3). Usually, the remaining bias drop is then addressed to contact resistances [111].

In contrast, we define the boundary conditions for the Poisson equation such that the Hartree potential Φ always drops within the device by exactly the amount of the predefined applied bias (added by the built-in potential $V_{\mathrm{built-in}}$). Then, the applied bias is always unambiguously defined, irrespective of the implemented lead model. For this purpose, we apply the Neumann boundary conditions Eqs. (3.6.12) also in nonequilibrium. But we adjust the electric displacement x in such a way that the predefined bias drops within the device

$$x:$$
$$e\left[\Phi(L) - \Phi(0)\right] = \mu_L - \mu_R - V_{\mathrm{built-in}}. \tag{3.6.15}$$

Here, this bias voltage is defined by the difference between the chemical potentials of the left (μ_L) and right (μ_R) lead as will be discussed in more detail in Sec. 3.6.4.

It is worth to mention that the inclusion of the self-consistent Poisson potential represents the electron-electron interaction in the Hartree approximation. This approximation averages

the summed Coulomb potential of every electron into a mean field and equals the lowest order of a perturbation expansion in the electron-electron interaction potential. In Sec. 2.3.4, we have shown that terms with different signs in the temporal ordering vanish in the lowest order perturbation expansion of instantaneous two-particle interactions. Thus, the Poisson potential Φ enters the Dyson equation (see Eq. (3.2.8)), whereas the Keldysh equation does not explicitly depend on Φ.

3.6.4 New self-consistent model for lead electron distribution

Introduction

The electron distribution in leads of biased devices is subject to a long and still open debate. A finite device current in the device transfers electrons from the source to the drain and causes, if not compensated properly, charge accumulations near and in the leads. We present and discuss the different approaches that have been implemented in literature to account for this effect. Typically, a lead electron distributions is implemented that responses to a finite current in the device.

The current density in quantum cascade lasers is efficiently suppressed by the quantum barriers. In these devices we apply a numerically efficient approach and assume equilibrium Fermi distributions in the leads. Albeit, we include a finite electric fields at the device boundaries. In low resistive devices, however, we show that the electron distribution has to be determined self-consistently with the electron density in the device. In such devices, we shift the Fermi distribution so that all electric fields at the device surfaces are screened. Although this is a novel approach (in particular in the area of nonequilibrium Green's function calculations), we note that it agrees in specific devices with a suggestion of W. Pötz.

Fundamentals

Analogous to the scheme for the retarded Green's function, it is common to modify Eq. (3.2.9) with a lesser contact self-energy $\mathbf{\Sigma}^{<}_{con}$ to determine the lesser Green's function of a finite section of an open device

$$\mathbf{G}^{<}_{d} = \mathbf{G}^{R}_{d} \left(\mathbf{\Sigma}^{<}_{d} + \mathbf{\Sigma}^{<}_{con} \right) \mathbf{G}^{R\dagger}_{d}. \tag{3.6.16}$$

In equilibrium, Eq. (2.2.15) holds for the surface Green's functions and it is straightforward to derive the lesser contact self-energy [22, 70]

$$\mathbf{\Sigma}^{<}_{con,\mathrm{eq}} \left(k_{\parallel}, E \right) = -f \left(E, \mu \right) \left[\mathbf{\Sigma}^{R}_{con} \left(k_{\parallel}, E \right) - \mathbf{\Sigma}^{R\dagger}_{con} \left(k_{\parallel}, E \right) \right]. \tag{3.6.17}$$

There is a lengthy and still open debate about the appropriate boundary conditions for open devices in nonequilibrium situations. The underlying physical problem is that a finite current in the device transfers electrons from the source to the drain. Therefore, the leads have to respond self-consistently to the device current in order to avoid artificial charge accumulations at the device boundaries and within the leads [112, 113].

It is common in literature to assume $\mathbf{\Sigma}^{<}_{con}$ to be given by Eq. (3.6.17). However, we have to emphasize that this equation requires the validity of the fluctuation-dissipation theorem Eq. (2.2.15) for the surface Green's function of the leads. Since this theorem only holds in equilibrium, this assumption is only (approximately) valid if the electrons in the leads are only "slightly"affected by a finite current in the device. To our knowledge, the only approach

in literature* that avoids Eq. (2.2.15) has been suggested by Pötz in [115]. Therein, Pötz determines the electron distribution in the leads self-consistently with the density matrices in the device under the constraints of charge neutrality and maximized entropy in the leads [115]. However, this approach requires for a maximization of the entropy with respect to at least three Lagrangian parameters. The complexity and numerical demands of such a scheme in the area of NEGF including incoherent scattering is not feasible. Therefore, we follow the widespread approach and apply Eq. (2.2.15) on the lead Green's functions. Then, charge accumulations in and close to the leads can only be avoided via self-consistent changes of the electron distribution in the leads, i.e. changes of $f\left(E,\mu\right)$ in Eq. (3.6.17).

Assumption of leads in equilibrium

Probably, the most efficient ansatz for such a response of the leads is to apply flat band conditions on the Poisson equation and to assume equilibrium Fermi distributions f with constant chemical potentials for the electron distributions in the leads [116–118]. Then, the conduction band edges in the leads are permitted to freely float "up and down"in energy, irrespective of the applied bias voltage. Depending on the current density amplitude, the conduction band edge is lowered in the source and raised in the drain. This usually results in a difference of the lead conduction band edges that deviates from the difference of the chemical potentials in the leads [109, 119]. Since the difference of the chemical potentials is identified as the applied voltage (see Sec. 3.6.3), the remaining bias voltage is assumed to drop within the leads according to unknown contact resistances [111, 120]. The fraction of the applied bias that drops inside the leads is only small if the current density in the device is negligible compared to the number of electrons the leads supply [119].

Instead of the "free floating"conduction band edge in the leads, Pötz has suggested in [113] to explicitly calculate the number of transferred electrons and to adjust the energy difference of the conduction band edge and the chemical potential in the leads accordingly. However, both models assume equilibrium Fermi distributions in the leads which restricts them to highly resistive devices [113].

We follow this scheme in the multiquantum well and the single period lead model in so far that we apply Fermi distributions in the leads. These models are only applied on quantum cascade structures in which the transport is dominated by tunneling and energy relaxation between confined states and the resulting current density is comparably small. However, we do not assume flat band boundary conditions for the Poisson equation in these devices, but use self-consistently determined electric fields for the electrostatic boundary conditions as described in the preceding subsection. This ensures that the total applied bias drops within the device and justifies the assumption of vanishing potential drop in the field free leads (see Sec. 3.6.2).

Model for finite current in the leads

In the case of low resistive devices such as $n-i-n$ resistors, we follow another common approach [42, 109, 112] and assume the distribution of electrons in the leads to equal a Fermi distribution shifted by the amount of k_D

$$f\left(k_{\parallel},k_D,E,\mu\right)=\left[\exp\left(\beta\left(\tilde{E}-\mu\right)\right)+1\right]^{-1}, \tag{3.6.18}$$

*There are approaches on nonequilibrium leads in the area of Monte-Carlo simulations, but they do not include quantum mechanical effects (see e.g. [114]).

with

$$\tilde{E} = \frac{\hbar^2}{2m_l^*(E)} \left[k_\parallel^2 + (k_z(E) \mp k_D)^2\right]. \tag{3.6.19}$$

The upper sign in the formula for $\tilde{E}$ refers to the source, the lower to the drain lead. The variable k_D shifts the center of the Fermi sphere parallel to the momentum in growth direction

$$\begin{aligned} k_z(E) = &\sqrt{2m_l^*(E)/\hbar^2} \\ &\times \sqrt{E - V_l - e\Phi_l - \frac{\hbar^2 k_\parallel^2}{2m_l^*(E)}}. \end{aligned} \tag{3.6.20}$$

In this way, the electron distribution in the leads deviates from the equilibrium distribution and a finite current density in the leads is accounted for. The chemical potentials in the leads are set constant and define the applied bias voltage. Similar to the leads in equilibrium, we apply the self-consistent boundary conditions of the Poisson equation in Sec. 3.6.3 so that the applied bias voltage is unambiguously defined.

Several different models for the determination of k_D exist. One approach utilizes the constraint of flux conservation [121]. For example, Laux *et al.* [109] determine k_D by

$$k_{D,\text{Laux}} = \frac{m_{\text{cond}} j}{n_l e \hbar}, \tag{3.6.21}$$

with the conductivity mass m_{cond} and the number of current carrying electrons in the leads n_l. In contrast, Frensley [112] calculates the drift vector k_D with a given drift mobility μ_e

$$k_{D,\text{Frensley}} = -\mu_e m_l^* \left.\frac{\mathrm{d}}{\mathrm{d}z}\Phi(z)\right|_{z=l} \tag{3.6.22}$$

and applies Dirchlet boundary conditions for the Hartree potential $\Phi(z)$ in order to ensure local charge neutrality sufficiently far away from the device boundaries. Those models have in common that they assume a certain relationship between k_D and the current density j. The nature of charge transport, however, depends on many aspects such as the device structure, resonances in the scattering mechanisms, the applied voltage etc. and may vary from the ballistic to the diffusive regime. A shift of the Fermi spheres of coherently propagating electrons results in a much higher current density as if the electrons scatter strongly and effectively experience a drift diffusion. In addition, a shifted Fermi distribution in the leads* surely differs from the distribution in the device in the case of transport through devices with momentum and energy dependent transmission coefficients (see also Fig. 4.3.12). If k_D is not adjusted properly, interferences between the electron distribution in the leads and the distribution in the device close to the leads are inevitable. In fact, we show in Sec. 4.2.3 that values for k_D determined in the ways described above still lead to charge accumulations near the leads. Therefore, the introduction of k_D in the leads is only a first step towards a consistent treatment of the current in the leads. For these reasons, a relationship between k_D and the current density cannot be predicted for arbitrary devices. Instead, we determine k_D self-consistently with the Green's functions in the device under the condition of vanishing charge accumulations and - accordingly - vanishing electric fields close to the leads. Non-vanishing electric fields near the boundaries would accelerate or decelerate electrons in the adjacent leads which results in changes of k_D.

*If the assumption of Eq. (2.2.15) for the Green's functions of current carrying leads does not fail additionally.

Thus, such electric fields cannot exist in the stationary limit. If we denote the shift of the Fermi sphere in the left and right lead with $k_{D,L}$ and $k_{D,R}$, respectively, these shifts have to be chosen such that

$$k_{D,L}, k_{D,R} : x = 0, \tag{3.6.23}$$

where x is the dielectric displacement at the device boundaries in Eq. (3.6.12). If the homogeneous device region close to the boundaries is large enough, the condition of vanishing electric fields entails a local charge neutrality at the boundaries. In this way, our model for k_D agrees with the suggestion of Pötz in [113] to set k_D such that the device/contact boundary is charge neutral.

A single condition for two unknown variables ($k_{D,L}$ and $k_{D,R}$) is insufficient. Therefore, we have to additionally introduce another relation for the shifts of the Fermi spheres of the leads in order to achieve a well-posed problem. For this purpose, we assume - similar to Laux *et al.* - that k_D is proportional to the effective mass and inverse proportional to the electron density in the leads*

$$\frac{k_{D,L}}{k_{D,R}} = \frac{m_L^* n_R}{m_R^* n_L}. \tag{3.6.24}$$

This lead model collapses in the case of large bias voltages in faintly doped low resistive devices. Then, the drift vectors may eventually grow to such high values that the complete Fermi sphere of either lead is shifted beyond the device boundary, i.e. k_z in Eq. (3.6.20) is smaller than k_D for all occupied energies E. Then a further increase of k_D does not influence the charge accumulation near the respective device boundary and unscreened electric fields emerge there. This is approximately the case, when one of the k_D's equals the respective Fermi vector. Thus, we have to limit the shift of the Fermi spheres $k_{D,L}, k_{D,R} \in \left[0; \sqrt[3]{3\pi^2 n_l}\right]$. Even higher applied bias voltages can be accounted for by setting the k_D's to their highest value and allowing x in Eq. (3.6.12) to reach finite values. However, we have to emphasize that the approximation of a shifted Fermi distribution in the leads becomes doubtful in this regime. Alternative approaches that determine the electron distribution in the leads under the constraint of maximum entropy as suggested by Pötz [115] are surely more reasonable in these situations.

3.7 Numerical details

3.7.1 Introduction

In the last section of this chapter, we present all details that are necessary to reproduce the numerical results of vertical transport presented in this thesis. A very important aspect is the proper discretization of the electronic energy E and in-plane momentum $k_\parallel$, because a converged solution of the Keldysh and Dyson equation critically depends on a sufficiently fine resolution of all relevant electronic states. A "straightforward"solution to this issue would be a homogeneous but very fine grid in E and $k_\parallel$. However, the numerical load efficiently limits the maximum number of discretization points in E and $k_\parallel$. Therefore, we have developed a novel self-adaptive grid for the electronic energy and the in-plane momentum that redistributes a given number of discretization points according to the energy resolved density and the spectral function. In this way, we guarantee that all electronic resonances are well resolved, but we also efficiently limit and control the numerical load.

*We use an energy averaged mass in the case of non-parabolic conduction bands.

We have shown in Sec. 3.5.7 that scattering self-energies have to be calculated in the self-consistent Born approximation as a minimum prerequisite for the current conservation. In this section, we derive several additional conditions that numerically discretized self-energies have to fulfill for a conserved current density. Although novel to literature, these conditions become particularly critical, when energy E and/or momentum $k_{\|}$ are discretized on an inhomogeneous grid.

Several methods can be found in literature for the solution of the surface Green's functions of arbitrary semi-infinite leads. We extend the well-known iterative methods in order to include non-local scattering self-energies as well as periodic conduction band profiles within the leads. In addition, we detail a numerically efficient solution scheme that determines the surface Green's functions of the leads in parallel with the iterative calculations of device Green's functions and self-energies. We complete this section with an overview of our algorithm and illustrate it with a flowchart.

3.7.2 Novel self-adaptive discretization

Introduction

All Green's functions and self-energies are represented in a real space basis with a homogeneous grid spacing Δ. We consider in Sec. 5 devices with barrier widths that are incommensurable with Δ. In these cases, we compensate the coarseness of this real space grid by slightly modifying the material's barrier heights in such a way that the product of their width and height is preserved. Calculations of the same devices but with different grid spacing yield very similar results which justifies this approximation.

In contrast, Green's functions and self-energies are quite sensitive to a proper resolution in the in-plane momentum $k_{\|}$ and energy E. Unfortunately, the self-consistent Born approximation of the scattering mechanisms requires for frequent updates of Green's functions and self-energies. Therefore, these functions have to be stored in RAM during the iterations of the self-energies, Keldysh and Dyson equations which limits the maximum number of grid points in $k_{\|}$ and E (typically around 130 points) and requires for an inhomogeneous grid* in both, E and $k_{\|}$. All integrals with respect to E or $k_{\|}$ involving numerically determined Green's functions are solved with the trapezoidal quadrature method. We introduce two novel independent self-adaptive grids for the energy E and momentum $k_{\|}$ space.

Numerical grid in energy E

We denote the number of grid points in E with N_E. The first step in setting the strictly increasing grid $E(i)$ is the determination of the minimum $E(1)$ and maximum $E(N_E)$ value of the considered electronic energy interval. The value $E(1)$ equals the minimum value of the conduction band edge in the total device and may change during the iterations of the Poisson equation. The maximum value $E(N_E)$ is determined such that it lies well above the highest occupied state

$$E(N_E) = \max\left(-k_B T \ln f_{\min}, 2E_0\right) + \max\left(\mu_L, \mu_R\right). \tag{3.7.1}$$

Here, E_0 is the energy of a longitudinal polar optical phonon and $f_{\min}$ is the state occupancy that we consider to be "empty"(typically, $f_{\min} \approx 5 \times 10^{-5}$). At low temperatures, this value

*A homogeneous discretization with a constant grid spacing fine enough to achieve convergency requires too much storage.

is reached at energies close to the chemical potential of the source ($\max(\mu_L, \mu_R)$). Then, the maximum of the first term in Eq. (3.7.1) equals two LO-phonon energies and ensures that electrons in the highest significantly occupied state may still absorb LO-phonons. It is worth to mention that the chemical potentials are set constant during the calculations and therefore define the zero point of the energy grid. The initial energy grid is defined as a power law in the grid point number i. When an energy resolved density $n(z, E)$ (see Eq. (3.3.4)) is obtained in a previous iteration*, the energy E is discretized according to the average of $n(z, E)$ in the total device

$$n(E) \equiv \frac{1}{L} \int_0^L \mathrm{d}z n(z, E). \tag{3.7.2}$$

The maxima of this function correspond to those energies that many electrons possess. These energies should be best resolved. Therefore, we translate this function into a step size function $w_E(i)$

$$w_E(i) = \gamma_E \max_E [n(E)] - n\left(\tilde{E}(i)\right), \tag{3.7.3}$$

with a typical value† of $\gamma_E = 1.1$. Here, the energy grid $\tilde{E}(i)$ represents the previous energy discretization. The more electrons are given at a specific energy, the more points of the new energy grid are set close to this energy

$$E(i) = \delta_{i,1} E(1) + (1 - \delta_{i,1}) \left[E(i-1) + \frac{w_E(i)}{\sum_{i=2}^{N_E} w_E(i)} \left[E(N_E) - E(1) \right] \right]. \tag{3.7.4}$$

In this way, the constant number of grid points in energy are self-adaptively redistributed whenever a new solution of the Poisson equation is achieved. Figure 3.7.1 exemplifies a typical computational situation of a device with several resonances that have to be resolved with 130 energy grid points i using Eq. (3.7.4). The energy resolved density (black dots) shows several maxima in energy. The energy grid points (grey) are closely lying to each other in the areas around these maxima. This energy grid is effectively a composition of several homogeneous grids with varying grid resolution. We have also tried discretizations with clearer inhomogeneous behavior (e.g. involving powers of $w_E(i)$), however, this scheme turned out to be best for a stable convergency.

Numerical grid in in-plane momentum $k_\parallel$

We have discussed in Sec. 3.2.3 that the free particle Green's functions in spatial representation diverge when the total electron energy is carried by the in-plane motion. In the presence of complex self-energies, these divergencies become resonant peaks in the k_z-dependence of the Green's functions. In order to ease the resolution of these resonances, we represent the in-plane momentum $k_\parallel$ as an energy

$$E_z = E - \hbar^2 k_\parallel^2 / (2m^*(z = 0, E)). \tag{3.7.5}$$

Then, the resonance appears whenever E_z vanishes, irrespective of the value of E. The energy E_z has to be discretized in the interval of all available energies, i.e. $E_z \in [E(1); E(N_E)]$. We denote the number of grid points in E_z with N_{E_z}. Similar to the discretization in E, we

*That is a previous iteration of the Green's functions, the self energies and the Poisson equation.

†The closer γ_E is to 1 ($\gamma_E > 1$), the more the grid points are concentrated around the maximum of $n(E)$.

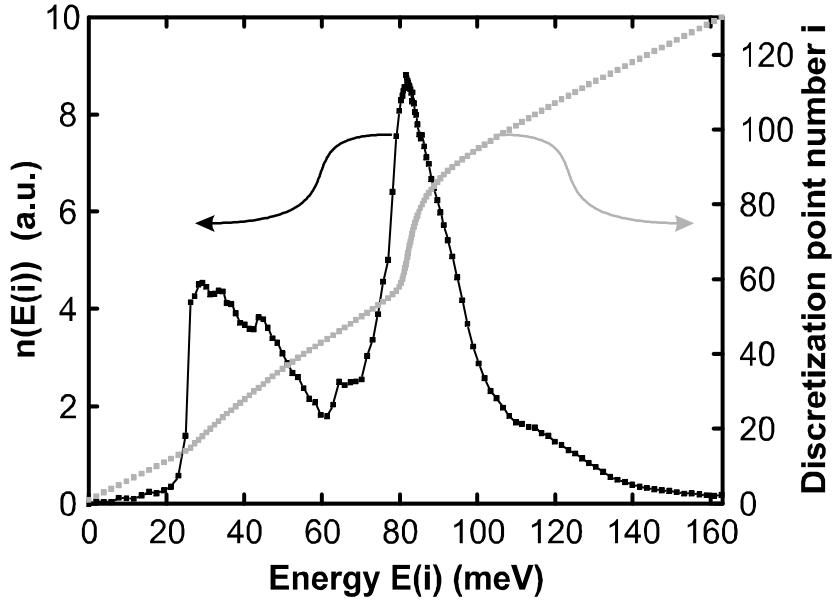

Figure 3.7.1: Discretized energy resolved electron density $n\left(E\left(i\right)\right)$ (black dots) and the resulting energy grid $E\left(i\right)$ (grey dots) for the GaAs/$Al_{.15}Ga_{.85}$As QCL of Ref. [122] at 50 mV/period, 200 K lattice temperature and a sheet doping concentration of 1.9×10^{10} cm^{-2}. The black line is meant to guide the eye.

initiate the grid in E_z with a power law in the grid point number j. Whenever a new solution of the Poisson equation is achieved and the grid in E has changed, the discretization of E_z gets updated. For this purpose, we utilize the diagonal of the spectral function at the maximum energy $E\left(N_E\right)$, integrated over the total device

$$A\left(E_z\right) \equiv \int A\left(z, z, E_z, E\left(N_E\right)\right) \mathrm{d}z \tag{3.7.6}$$

and identify the electronic resonances by the maxima of $A\left(E_z\right)$. Let us assume $N_r < N_{E_z}$ maxima of $A\left(E_z\left(j\right)\right)$ in the previous discretization of E_z, i.e. in the $\tilde{E}_z$ grid, and denote the abscissae of these maxima with $\tilde{E}_z\left(j_\upsilon\right)$ with $\upsilon \in \{1, \ldots, N_r\}$. Then, we divide the total range of E_z into N_r intervals Ω_υ around these resonance energies

$$\Omega_\upsilon \equiv \begin{cases} \left[E\left(1\right); \tilde{E}_z\left(j_1\right)/2 + \tilde{E}_z\left(j_2\right)/2\right), \text{ for } \upsilon = 1 \\ \left[\tilde{E}_z\left(j_{\upsilon-1}\right)/2 + \tilde{E}_z\left(j_\upsilon\right)/2; \tilde{E}_z\left(j_\upsilon\right)/2 + \tilde{E}_z\left(j_{\upsilon+1}\right)/2\right), \text{ for } 1 < \upsilon < N_r \\ \left[\tilde{E}_z\left(j_{N_r-1}\right)/2 + \tilde{E}_z\left(j_{N_r}\right)/2; E\left(N_E\right)\right], \text{ for } \upsilon = N_r \end{cases} . \tag{3.7.7}$$

The grid points of the new E_z grid are distributed in the intervals Ω_υ according to a weighting function $w_{E_z}\left(\upsilon\right)$

$$w_{E_z}\left(\upsilon\right) = \frac{\int_0^{E(N_E)} \mathrm{d}E \int_{\Omega_\upsilon} \mathrm{d}E_z \int \mathrm{d}z \, \mathrm{Im}\left(G^<\left(z, z, E_z, E\right)\right)}{\int_0^{E(N_E)} \mathrm{d}E \int_0^{E} \mathrm{d}E_z \int \mathrm{d}z \, \mathrm{Im}\left(G^<\left(z, z, E_z, E\right)\right)}. \tag{3.7.8}$$

This weighting function w_{E_z} is the larger, the more electrons are given in the respective energy interval Ω_υ (see the formula for the electron density, Eq. (3.3.3)). The number of grid points

N_υ for the interval Ω_υ reads

$$N_\upsilon = w_{E_z}(\upsilon)\, N_{E_z}. \tag{3.7.9}$$

Finally, we define the new E_z grid for the N_υ grid points of each interval Ω_υ by a piecewise defined exponential function

$$\begin{aligned} & E_z(j) \\ = & \begin{cases} A_\upsilon^- \mathrm{e}^{\gamma_{E_z}\left(j-\sum_{l=1}^{\upsilon-1} N_l - 1\right)} + C_\upsilon^-, \forall j \in \left\{\sum_{l=1}^{\upsilon-1} N_l + 1, \ldots, \sum_{l=1}^{\upsilon-1} N_l + \frac{N_\upsilon}{2}\right\} \\ A_\upsilon^+ \mathrm{e}^{-\gamma_{E_z}\left(j-\sum_{l=1}^{\upsilon-1} N_l - N_\upsilon/2 - 1\right)} + C_\upsilon^+, \forall j \in \left\{\sum_{l=1}^{\upsilon-1} N_l + \frac{N_\upsilon}{2} + 1, \ldots, \sum_{l=1}^{\upsilon} N_l\right\} \end{cases} \end{aligned} \tag{3.7.10}$$

with

$$\begin{aligned} A_\upsilon^- &= \left[\tilde{E}_z(j_{\upsilon-1}) - \tilde{E}_z(j_\upsilon)\right] / \left[2 - 2\exp\left(\gamma_{E_z}(N_\upsilon/2-1)\right)\right], \forall \upsilon > 1 \\ C_\upsilon^- &= \tilde{E}_z(j_\upsilon)/2 + \tilde{E}_z(j_{\upsilon-1})/2 - A_\upsilon^-, \forall \upsilon > 1 \\ A_\upsilon^+ &= \left[\tilde{E}_z(j_\upsilon) - \tilde{E}_z(j_{\upsilon+1})\right] / \left[2 - 2\exp\left(-\gamma_{E_z}(N_\upsilon/2-1)\right)\right], \forall \upsilon < N_r \\ C_\upsilon^+ &= \tilde{E}_z(j_\upsilon) - A_\upsilon^+, \forall \upsilon < N_r. \end{aligned} \tag{3.7.11}$$

The boundary values of $A^\pm$ and $C^\pm$ are given by

$$\begin{aligned} A_1^- &= \left[E(1) - \tilde{E}_z(j_1)\right] / \left[1 - \exp\left(\gamma_{E_z}(N_1/2-1)\right)\right] \\ C_1^- &= E(1) - A_1^-, \\ A_{N_r}^+ &= \left[\tilde{E}_z(j_{N_r}) - E(N_E)\right] / \left[1 - \exp\left(-\gamma_{E_z}(N_{N_r}/2-1)\right)\right] \qquad (3.7.12) \\ C_{N_r}^+ &= \tilde{E}_z(j_{N_r}) - A_{N_r}^+. \qquad (3.7.13) \end{aligned}$$

The smaller the absolute value of $\gamma_{E_z} < 0$ is, the more homogeneous is $E_z(j)$. A typical value for γ_{E_z} is -0.3. The shape of this piecewise defined exponential function for $\gamma_{E_z} = -0.3$ is illustrated in Fig. 3.7.2. It shows $A(E_z)$ of a resonant tunneling diode (RTD) with a single confined state resolved by 50 grid points. The two exponential functions describe energies below and above the resonance energy at 41.66 meV, respectively. Close to the resonance, the grid spacing is refined down to 0.01 meV, whereas the largest grid spacing far from resonance reaches up to 12 meV. The weighting of the respective maxima in $A(E_z)$ becomes important in devices with several resonant states, as can be seen in Fig. 3.7.3. Here, the spectral function $A(E_z)$ of a GaAs/AlGaAs QCL with several resonant states is resolved with 130 grid points. In this example, electrons predominantly occupy energies up to 90 meV, whereas states at higher energies are almost empty. This requires most of the 130 grid points to be spent on lower energies, as is accounted for by the weighting $w_{E_z}(j)$ in Eq. (3.7.8). Therefore, the resonant state at approximately 115 meV is poorly resolved.

Spectral function at vanishing in-plane momentum

In later sections, we will present graphs of the spectral functions at vanishing in-plane momentum in order to illustrate the shape and position of electronic states in various devices. Actually, this requires us to extract those values of $A(z, z, E_z, E)$ where E_z is as close to E as possible, i.e. $A\left(z, z, k_\parallel = 0, E\right) = A(z, z, E_z = E, E)$. This results in a discretization of the device states according to E. Since the grid in E is chosen such that the electron density in spite

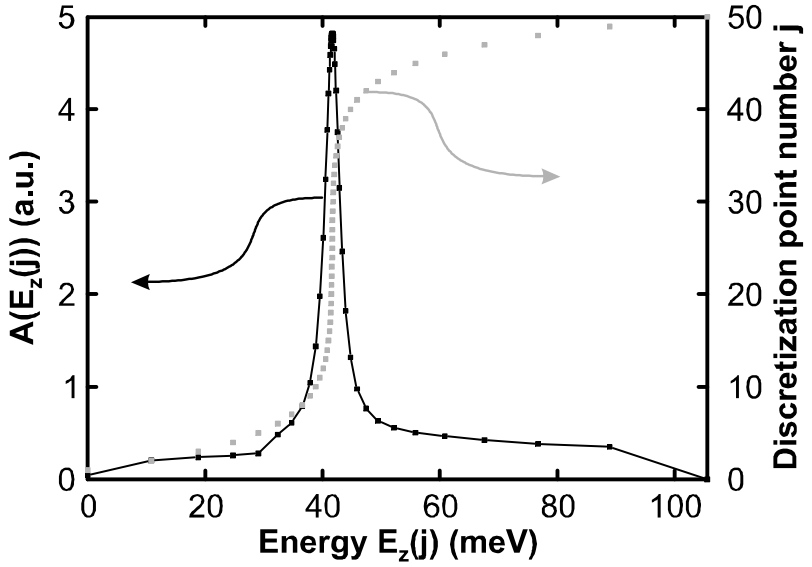

Figure 3.7.2: Spatially integrated spectral function $A(E_z)$ (black dots) discretized on the inhomogeneous energy grid $E(z)$ (grey dots) for a calculation of a resonant tunneling diode at 100 K and an applied electric field of 10 kV/cm. The RTD consists of two 4 nm wide $Al_{.15}Ga_{.85}As$ barriers enclosing a 10 nm wide GaAs quantum well and is homogeneously n-doped with $n = 1.2 \times 10^{16}$ cm^{-3}. The black line is only meant to guide the eye.

of electron resonances is best resolved, peaks in the spectral function may be poorly resolved by $A(z, z, E_z = E, E)$. However, the electronic states for a given value of E_z do not significantly vary with $k_\parallel$, as is shown in Fig. 3.7.4. It shows the spectral function $A\left(z, z, k_\parallel, E\right)$ at two different values of $k_\parallel$ as well as $A(z, z, E_z, E(N_E))$ in the center of a RTD. Neither the shape nor the resonant energy of the confined state of the RTD depends on the in-plane momentum $k_\parallel$ which is the reason for the agreement of $A(z, z, E_z, E(N_E))$ with the other two curves. The small differences between the curves in Fig. 3.7.4 are due to the finite grid resolution in E and E_z, which both have been set homogeneous for a better comparison. Therefore, we may assume the spectral function to explicitly depend only on the energy E_z. This allows us to depict the electronic states by a well resolved spectral function in the E_z representation

$$A\left(z, z, k_\parallel = 0, E\right) = A(z, z, E_z = E, E) \approx A(z, z, E_z, E(N_E)). \tag{3.7.14}$$

3.7.3 Numerical conditions for current conservation

Introduction

We illustrate in the following that a numerical implementation of realistic self-energies in the self-consistent Born approximation (such as derived in Sec. 3.5) has to be done very carefully whenever energy and/or in-plane momentum are discretized on an inhomogeneous grid. We derive several conditions that a discretization of self-energies on inhomogeneous grids have to fulfill in order to avoid artificial violation of current conservation. To the best of our knowledge, these conditions - although they are a critical prerequisite for reasonable results - can not be found in literature.

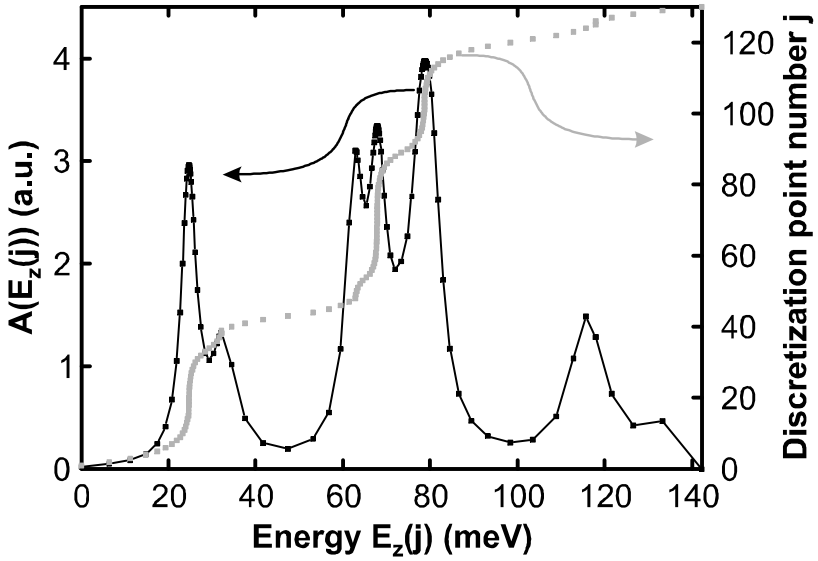

Figure 3.7.3: Discretized spectral function $A\left(E_z\right)$ (black dots) and its inhomogeneous energy grid $E\left(z\right)$ (grey dots) for the GaAs/$Al_{.15}Ga_{.85}$As QCL of Ref. [122] at 50 mV/period, 40 K lattice temperature and a sheet doping concentration of 1.9×10^{10} cm^{-2}. The black line is meant to guide the eye.

Continuous spectrum of dissipated energy

Let us assume an inelastic scattering process with a continuous spectrum of dissipated energy (such as the inelastic scattering with longitudinal acoustic phonons in Sec. 3.5.3)

$$\mathbf{\Sigma}^{<}\left(k_{\parallel}, E\right) = c \int_{E-E^{-}}^{E+E^{+}} \mathrm{d}E' \int_{0}^{\sqrt{2mE'}/\hbar} \mathrm{d}l_{\parallel} l_{\parallel} \mathbf{h}\left(k_{\parallel}, l_{\parallel}, E, E'\right) \mathbf{G}^{<}\left(l_{\parallel}, E'\right). \tag{3.7.15}$$

Hereby, all prefactors and functions that enter the self-energy except the Green's functions are abbreviated with $\mathbf{h}$. This function equals mainly the interaction potential and describes the scattering of electrons with in-plane momentum $l_{\parallel}$ and energy E' into a state with in-plane momentum $k_{\parallel}$ and energy E. The maximum amounts of dissipated and absorbed energies are given by E^{-} and E^{+}, respectively*. In the case of phonons, these two values are the same. However, for reasons discussed later, we introduce two different values. It is clear that after this formula is discretized, the momenta $k_{\parallel} = k_{\parallel}\left(k\right)$ with $k \in \{1, \ldots, L_i\}$ and energies $E = E\left(i\right)$ with $i \in \{1, \ldots, N\}$ become discrete and every integral is given as a sum

$$\begin{aligned} \int_{0}^{\infty} \mathrm{d}E \mathbf{f}\left(E\right) &\approx \int_{0}^{E_{\max}} \mathrm{d}E \mathbf{f}\left(E\right) = \sum_{i=1}^{N} a_i \mathbf{f}_i \\ \int_{0}^{\sqrt{2mE'}/\hbar} \mathrm{d}k_{\parallel} k_{\parallel} \mathbf{f}\left(k_{\parallel}, E\right) &= \sum_{k=1}^{L_i} b_{k,i} \mathbf{f}_{k,i}. \end{aligned} \tag{3.7.16}$$

Hereby and in the following, any discretized abscissae of the functions (except the spatial coordinates that are considered in the matrix shape) are denoted with indices, i.e.

$$\mathbf{f}_{k,i} = f\left(z, z', k_{\parallel}\left(k\right), E\left(i\right)\right). \tag{3.7.17}$$

*We denote these energies with x^{-} and x^{+} on the discretized energy mesh.

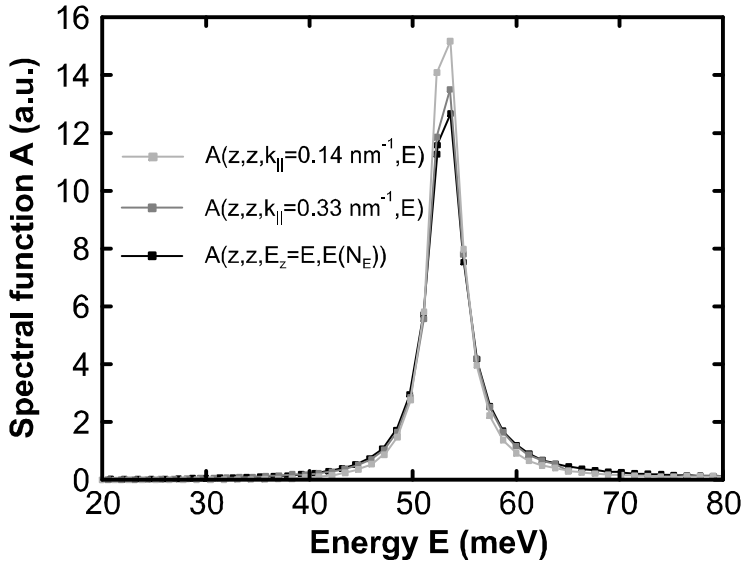

Figure 3.7.4: Spectral function $A\left(z,z,k_{\parallel},E\right)$ for various in-plane momenta $k_{\parallel}$ (light and dark grey dots) in the center of a RTD at 100 K and an applied electric field of 17 kV/cm. The RTD consists of two 4 nm wide $Al_{.15}Ga_{.85}As$ barriers enclosing a 10 nm wide GaAs quantum well and is homogeneously n-doped with $n = 1.2 \times 10^{16}$ cm^{-3}. The spectral functions $A\left(z,z,k_{\parallel},E\right)$ agree with the spectral function $A\left(z,z,E_z = E,E_{\max}\right)$ (black dots). The in-plane momentum $k_{\parallel}$ of the later function equals $\sqrt{2m^*\left(E_{\max}\right)\left(E_{\max}-E\right)}/\hbar$. The lines are meant to guide the eye.

The parameters a_i and $b_{k,i}$ depend on the quadrature scheme as well as on the grid the functions are discretized on. Since the maximum value of the momentum $k_{\parallel} \leq \sqrt{2mE\left(i\right)}/\hbar = k_{\parallel}\left(L_i\right)$ depends on the energy E, the discretization of the integral with respect to $k_{\parallel}$ depends on i and k (this gives a $b_{k,i}$). The maximum considered energy $E_{\max}$ is chosen such that $G^{<}$ as well as $\Sigma^{<}$ vanish for $E > E_{\max} = E\left(N\right)$. Discretized in this manner, the lesser self-energy of Eq. (3.7.15) reads*

$$\mathbf{\Sigma}^{<}_{k,i} = \sum_{j=i-x_i^-}^{i+x_i^+} \sum_{l=1}^{L_j} a_j b_{l,j} \mathbf{h}_{k,l,i,j} \mathbf{G}^{<}_{l,j}. \tag{3.7.18}$$

Whenever the energy E is discretized on an inhomogeneous grid, the discretized interaction range of Eq. (3.7.15) depends on the energy E and its index i ($E^+ + E^- \rightarrow x_i^+ + x_i^-$). The condition for current conservation, i.e. the condition that Eq. (3.5.114) vanishes, reads in the discretized form

$$\mathrm{Tr} \sum_{i=1}^{N} \sum_{k=1}^{L_i} a_i b_{k,i} \mathbf{\Sigma}^{<}_{k,i} \mathbf{G}^{>}_{k,i} \stackrel{!}{=} \mathrm{Tr} \sum_{i=1}^{N} \sum_{k=1}^{L_i} a_i b_{k,i} \mathbf{\Sigma}^{>}_{k,i} \mathbf{G}^{<}_{k,i}. \tag{3.7.19}$$

*The "greater than"self energy ($\Sigma^{>}$) can be deduced from the last equation by replacing the superscripts "<"with ">".

When we set in the self-energies in the last equation, we get for the condition of current conservation

$$\mathrm{Tr}\sum_{i=1}^{N}\sum_{k=1}^{L_i}\sum_{j=i-x_i^-}^{i+x_i^+}\sum_{l=1}^{L_j} a_i b_{k,i} a_j b_{l,j} \mathbf{h}_{k,l,i,j} \mathbf{G}^{>}_{k,i} \mathbf{G}^{<}_{l,j} \stackrel{!}{=} \mathrm{Tr}\sum_{i=1}^{N}\sum_{k=1}^{L_i}\sum_{j=i-x_i^-}^{i+x_i^+}\sum_{l=1}^{L_j} a_i b_{k,i} a_j b_{l,j} \mathbf{h}_{k,l,i,j} \mathbf{G}^{<}_{k,i} \mathbf{G}^{>}_{l,j}. \tag{3.7.20}$$

In order to ease the comparison of both side of this equation, we limit ourselves on terms of a given final energy $E\,(j)$. In order to keep the formulas readable, we pick out some terms of the right side ($r.s.$) of Eq. (3.7.20). In particular, we concentrate on the terms with $j = i + x$, with a value of x within the absorption range ($0 < x \leq x_i^+$). The maximum of the energy indices i and j is N, so that terms for $i > N - x + 1$ (i.e. for $j > N$) vanish. Therefore, the terms with $j = i + x$ of the right side of Eq. (3.7.20) read

$$\begin{aligned} r.s.\,(j = i + x) &= \mathrm{Tr}\sum_{i=1}^{N-x}\sum_{k=1}^{L_i}\sum_{l=1}^{L_{i+x}} a_i b_{k,i} a_{i+x} b_{l,i+x} \mathbf{h}_{k,l,i,i+x} \mathbf{G}^{<}_{k,i} \mathbf{G}^{>}_{l,i+x} \\ &= \mathrm{Tr}\sum_{i=1+x}^{N}\sum_{k=1}^{L_{i-x}}\sum_{l=1}^{L_i} a_{i-x} b_{k,i-x} a_i b_{l,i} \mathbf{h}_{k,l,i-x,i} \mathbf{G}^{<}_{k,i-x} \mathbf{G}^{>}_{l,i}. \end{aligned} \tag{3.7.21}$$

We have shifted the summation variable i in the last line for convenience. Similar terms can be found on the left side ($l.s.$) of Eq. (3.7.20). These terms correspond to the emission of a photon of energy index x, i.e. we pick out the terms (assuming they exist, see below) with $j = i - x$. Then, the energy index i has to be greater than $1 + x$

$$\begin{aligned} l.s.\,(j = i - x) &= \mathrm{Tr}\sum_{i=1+x}^{N}\sum_{k=1}^{L_i}\sum_{l=1}^{L_{i-x}} a_i b_{k,i} a_{i-x} b_{l,i-x} \mathbf{h}_{k,l,i,i-x} \mathbf{G}^{>}_{k,i} \mathbf{G}^{<}_{l,i-x} \\ &= \mathrm{Tr}\sum_{i=1+x}^{N}\sum_{l=1}^{L_i}\sum_{k=1}^{L_{i-x}} a_i b_{l,i} a_{i-x} b_{k,i-x} \mathbf{h}_{l,k,i,i-x} \mathbf{G}^{>}_{l,i} \mathbf{G}^{<}_{k,i-x}. \end{aligned} \tag{3.7.22}$$

We have exchanged the summation variables k and l in the second line of this equation for convenience. The comparison of this left side with the ride side in Eq. (3.7.21) shows that both sums are equal when three conditions are fulfilled.

The first condition affects the coupling potential. A comparison of Eqs. (3.7.21) and (3.7.22) shows that

$$\mathbf{h}_{k,l,i-x,i} \stackrel{!}{=} \mathbf{h}_{l,k,i,i-x}. \tag{3.7.23}$$

Of course, the interaction potential for a transition from $\left(k_\parallel, E\right)$ to $\left(l_\parallel, E'\right)$ is the same as for the inverse transition and depends only on the transferred in-plane momentum and the transferred energy. Therefore, the equation holds

$$\mathbf{h}\left(\vec{k}_\parallel, \vec{l}_\parallel, E, E'\right) = \mathbf{h}\left(\vec{l}_\parallel, \vec{k}_\parallel, E', E\right) = \mathbf{h}\left(\left|\vec{k}_\parallel - \vec{l}_\parallel\right|, |E - E'|\right). \tag{3.7.24}$$

This condition is in agreement with similar findings in the position space [123].

The second condition that we can extract from Eqs. (3.7.21) and (3.7.22) affects the numerical integration schemes. It is important, that the same quadrature schemes that are used for calculating the self-energies are also used for the determination of any observables - in particular for the current density. Otherwise, the integration factors a and b in Eq. (3.7.20) that

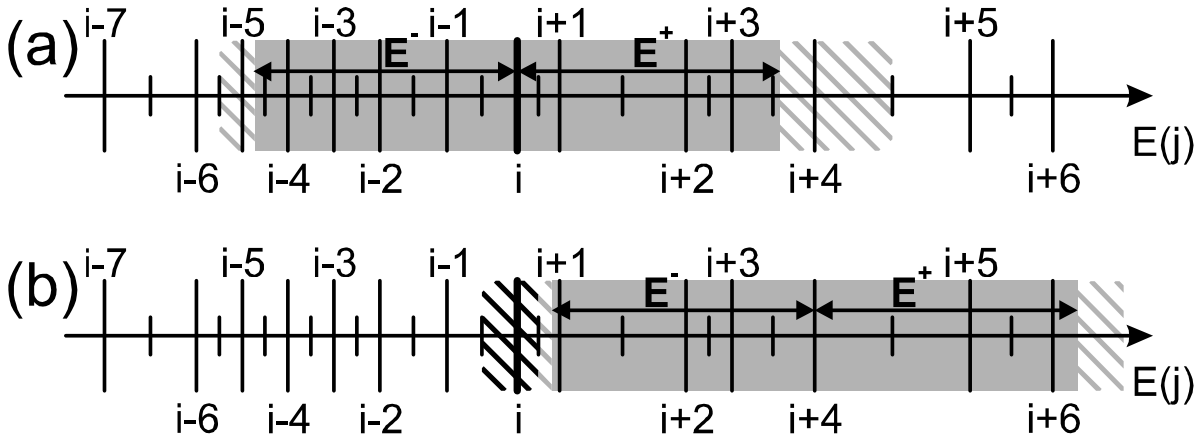

Figure 3.7.5: Schematics of inhomogeneously discretized energies $E(j)$. The short vertical lines delimit energy intervals that are labeled with the respective interval numbers j. The emission and absorption spectra are continuous (grey shaded intervals). (a) The finite resolution requires to increase the maximum amount of dissipated (E^-) and absorbed energies (E^+) for electrons in the interval around $E(i)$ as depicted with the hatched intervals. (b) same as a) for electrons with energy $E(i+4)$. However, the interaction range of electrons at $E(i)$ requires for an additional increase of the emission limits which is marked with the black hatched interval.

originate from the integrals in the self-energies would differ from those that originate from the integrals of the current density.

Finally, every transition process taken into account has to be described twice: once as the loss of particles from $(k_\parallel, E)$ to $(l_\parallel, E')$ and once as the gain of particles in $(l_\parallel, E')$ from $(k_\parallel, E)$. This gives us further conditions* for the numerical interaction limits

$$\begin{aligned} x_i^+ &\stackrel{!}{=} x^-_{i+x_i^+},\ \forall i \in \{1,\ldots,N\}, \\ x_i^- &\stackrel{!}{=} x^+_{i-x_i^-},\ \forall i \in \{1,\ldots,N\}. \end{aligned} \tag{3.7.25}$$

These conditions are trivially given in the case of a homogeneous grid in the energy E, because then, the interaction limits are constant ($x_i^+ = x_j^-,\ \forall i,j$). In systems with inhomogeneously discretized energy, however, these conditions have to be treated with care and it might become necessary to change the phonon energy according to the energy grid in order to guarantee Eqs. (3.7.25). This is illustrated in Figs. 3.7.5 (a) and (b). They show an example of the discretized energies $E(j)$ around the point $E(i)$ (long vertical lines). Every value of $E(j)$ labels the area $[E(j-1)/2 + E(j)/2;\ E(j+1)/2 + E(j)/2]$. Its limits are marked with the short vertical lines. The homogeneously grey shaded areas in Fig. 3.7.5 (a) depict the interval of $[E(i) - E^-;\ E(i) + E^+]$, with the analytical values $E^+ = E^-$ of Eq. (3.7.15). All final energies that electrons with the initial energy of $E(i)$ can reach after a single emission or absorption process according to Eq. (3.7.15) lie within this interval. However, the discretized version of this interval, i.e. the discretized E'-integral of Eq. (3.7.15) contains Green's functions of the energies $\{E(i-5), E(i-4), \ldots, E(i+3), E(i+4)\}$. Therefore, the numerically discretized version of this interval is extended by the hatched areas. In addition, Eqs. (3.7.25) also cause extensions of such intervals, as illustrated in Fig. 3.7.5 (b). Originally, the emission range of

*We have already assumed that these conditions are met in Eq. (3.7.22).

the energy $E(i+4)$ reaches down to $E(i+1)$, i.e. $x^-_{i+4} = 3$. Since electrons in the interval of $E(i)$ scatter up to $E(i+4)$, i.e. $x^+_i = 4$, the emission range of $E(i+4)$ has to be extended even further (see black hatched area in Fig. 3.7.5 (b)).

Discrete spectrum of dissipated energy

The situation becomes more complicated, if the amount of dissipated or absorbed energy equals a constant E_0. In addition, the functions $\mathbf{h}$ may depend on the question whether energy is dissipated or absorbed. Both cases are given for the example of scattering with LO-phonons in Eq. (3.5.10). Here, we have to introduce the functions $\mathbf{h}^+$ for absorption and $\mathbf{h}^-$ for emission*

$$\begin{aligned}\mathbf{\Sigma}^<\left(k_\parallel, E\right) &= \int \mathrm{d}l_\parallel^2 \Big[\mathbf{h}^+\left(\left|\vec{k}_\parallel - \vec{l}_\parallel\right|, E_0\right)\mathbf{G}^<\left(l_\parallel, E+E_0\right) \\ &\quad +\mathbf{h}^-\left(\left|\vec{k}_\parallel - \vec{l}_\parallel\right|, E_0\right)\mathbf{G}^<\left(l_\parallel, E-E_0\right)\Big], \qquad (3.7.26)\\ \mathbf{\Sigma}^>\left(k_\parallel, E\right) &= \int \mathrm{d}l_\parallel^2 \Big[\mathbf{h}^-\left(\left|\vec{k}_\parallel - \vec{l}_\parallel\right|, E_0\right)\mathbf{G}^>\left(l_\parallel, E+E_0\right) \\ &\quad +\mathbf{h}^+\left(\left|\vec{k}_\parallel - \vec{l}_\parallel\right|, E_0\right)\mathbf{G}^>\left(l_\parallel, E-E_0\right)\Big]. \qquad (3.7.27)\end{aligned}$$

Unfortunately, a straightforward discretization of these self-energies violates current conservation, as we will show in the following. Such a straightforward discretization reads

$$\begin{aligned}\mathbf{\Sigma}^<_{k,i} &= \sum_{l=1}^{L_{i+x_i^+}} b_{l,i+x_i^+}\mathbf{h}^+_{|k-l|,x_i^+}\mathbf{G}^<_{l,i+x_i^+} + \sum_{l=1}^{L_{i-x_i^-}} b_{l,i-x_i^-}\mathbf{h}^-_{|k-l|,x_i^-}\mathbf{G}^<_{l,i-x_i^-}, \qquad \text{(wrong)}\\ \mathbf{\Sigma}^>_{k,i} &= \sum_{l=1}^{L_{i+x_i^+}} b_{l,i+x_i^+}\mathbf{h}^-_{|k-l|,x_i^+}\mathbf{G}^>_{l,i+x_i^+} + \sum_{l=1}^{L_{i-x_i^-}} b_{l,i-x_i^-}\mathbf{h}^+_{|k-l|,x_i^-}\mathbf{G}^>_{l,i-x_i^-}. \qquad \text{(wrong)}\end{aligned}$$

Here, the discretized energy that is the closest one to the final energy $E(i)\pm E_0$ is chosen for final energy E'. In this way, the transferred energy E_0 depends on the initial energy $E = E(i)$ and varies accordingly to the inhomogeneity of the energy grid (an example is given in Fig. 3.7.6). With the self-energies of the last equations, the discretized equation for the current conservation (see Eq. (3.7.19)) reads

$$\begin{aligned}&\mathrm{Tr}\sum_{i=1}^{N}\sum_{k=1}^{L_i}\sum_{l=1}^{L_{i+x_i^+}} a_i b_{k,i} b_{l,i+x_i^+}\mathbf{h}^+_{|k-l|,x_i^+}\mathbf{G}^<_{l,i+x_i^+}\mathbf{G}^>_{k,i}\\ &+\mathrm{Tr}\sum_{i=1}^{N}\sum_{k=1}^{L_i}\sum_{l=1}^{L_{i-x_i^-}} a_i b_{k,i} b_{l,i-x_i^-}\mathbf{h}^-_{|k-l|,x_i^-}\mathbf{G}^<_{l,i-x_i^-}\mathbf{G}^>_{k,i}\\ &\overset{!}{=}\mathrm{Tr}\sum_{i=1}^{N}\sum_{k=1}^{L_i}\sum_{l=1}^{L_{i-x_i^-}} a_i b_{k,i} b_{l,i-x_i^-}\mathbf{h}^+_{|k-l|,x_i^-}\mathbf{G}^>_{l,i-x_i^-}\mathbf{G}^<_{k,i}\\ &+\mathrm{Tr}\sum_{i=1}^{N}\sum_{k=1}^{L_i}\sum_{l=1}^{L_{i+x_i^+}} a_i b_{k,i} b_{l,i+x_i^+}\mathbf{h}^-_{|k-l|,x_i^+}\mathbf{G}^>_{l,i+x_i^+}\mathbf{G}^<_{k,i}. \qquad (3.7.28)\end{aligned}$$

*Apart from the coupling constants and prefactors, $\mathbf{h}^-$ contains the phonon occupation factor n_0 and $\mathbf{h}^+$ the factor n_0+1.

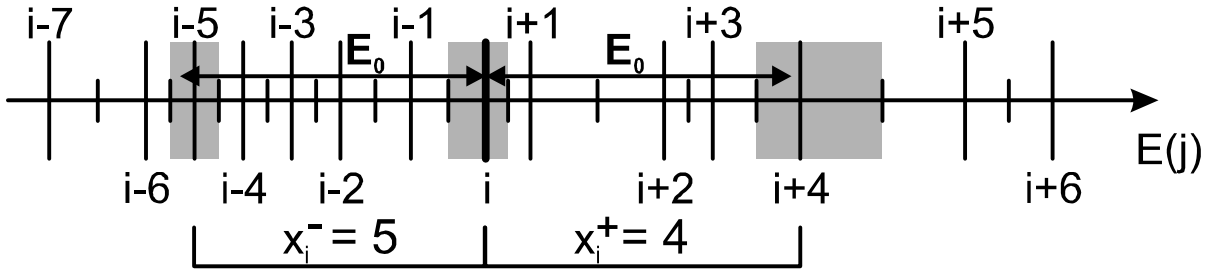

Figure 3.7.6: Same as in Fig. 3.7.5, but with a discrete emission and absorption energy E_0. Here, electrons in the interval around $E(i)$ are assumed to transfer only into the intervals around $E(i-5)$ and $E(i+4)$. These energies are the closest to $E(i) \pm E_0$, respectively.

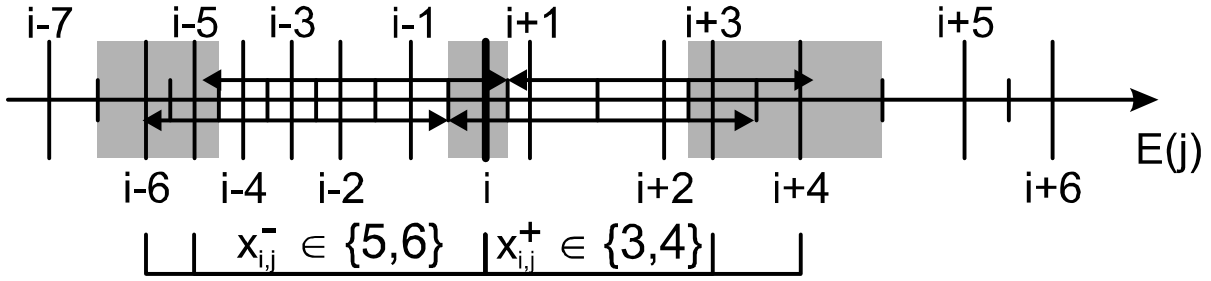

Figure 3.7.7: Same as in Fig. 3.7.5, but with a discrete emission and absorption energy E_0. In contrast to Fig. 3.7.6, the discretized energy E_0 is kept constant. This causes the electrons around $E(i)$ to scatter into several other energy intervals, but ensures current conservation.

In order to simplify the comparison of both sides of this equation, we shift the summation variable of the sums on the right side ($r.s.$) of the last equation similar to the preceding paragraph

$$\begin{aligned} r.s. \;=\; & \mathrm{Tr} \sum_{j=1}^{N} \sum_{k=1}^{L_{j+x_j^+}} \sum_{l=1}^{L_j} a_{j+x_j^+} b_{k,j+x_j^+} b_{l,j} \mathbf{h}^{+}_{|k-l|,x_j^+} \mathbf{G}^{<}_{k,j+x_j^+} \mathbf{G}^{>}_{l,j} \\ & + \mathrm{Tr} \sum_{j=1}^{N} \sum_{k=1}^{L_{j-x_j^-}} \sum_{l=1}^{L_j} a_{j-x_j^-} b_{k,j-x_j^-} b_{l,j} \mathbf{h}^{-}_{|k-l|,x_j^-} \mathbf{G}^{<}_{k,j-x_j^-} \mathbf{G}^{>}_{l,j}. \end{aligned} \tag{3.7.29}$$

Here, we have already utilized the conditions of current conservation that has been given in Eq. (3.7.25). Nevertheless, the current is obviously not conserved, when $a_i \neq a_{i \pm x_i^{\pm}}$ as is the case in an inhomogeneous energy grid.

In order to understand the origin of this violation and to find a solution for it, we have to analyze the implications of a discretization of Eqs. (3.7.26) and (3.7.27) in more detail. The analytical scattering self-energies Eqs. (3.7.26) and (3.7.27) only allow for the electrons with the energy E to scatter via emission of E_0 into states with exactly the energy $E - E_0$. This is in contrast to the "simple"discretization seen above, where E_0 varied with the grid. However, when the transferred energy E_0 is kept constant while the energy is discretized, situations arise in which electrons of an energy interval labeled with $E(i)$ scatter via emission of E_0 into several other energy intervals. This is the case, e.g., if the interval Ω_i around the initial energy $E(i)$ is

large enough such that electrons in Ω_i scatter via emission of the energy E_0 into states of N_i^- smaller energy intervals ($N_i^- = 2$ in the example of Fig. 3.7.7)

$$E - E_0 \in \Omega' = \sum_{j=1}^{N_i^-} \Omega_{i-x_{i,j}^-},\ \forall E \in \Omega_i. \tag{3.7.30}$$

In this way, the discretization of the emitted* energy E_0 depends on both, the initial and the final interval label

$$E_0 \to x_{i,j}^- \in \left\{ x_{i,1}^-, \ldots x_{i,N_i^-}^- \right\}. \tag{3.7.31}$$

Therefore, an analytical transition between two energies E and E' is distributed on several numerical transitions of discretized energies $E(i)$ and $E(j)$ that lie close the E and E'. The larger the energy interval around one of these discretized energies is, the larger is the contribution of electrons with energies in that interval. Thus, we weight the respective terms in the self-energies with the integral over the involved discretized energy intervals

$$\begin{aligned}
\mathbf{\Sigma}_{k,i}^{<} &= \sum_{j=1}^{N_i^+} \sum_{l=1}^{L_{i+x_{i,j}^+}} \frac{a_{i+x_{i,j}^+}}{\tilde{\Omega}_{i,j}^+} b_{l,i+x_{i,j}^+} \mathbf{h}_{|k-l|,x_{i,j}^+}^+ \mathbf{G}_{l,i+x_{i,j}^+}^{<} \\
&\quad + \sum_{j=1}^{N_i^-} \sum_{l=1}^{L_{i-x_{i,j}^-}} \frac{a_{i-x_{i,j}^-}}{\tilde{\Omega}_{i,j}^-} b_{l,i-x_{i,j}^-} \mathbf{h}_{|k-l|,x_{i,j}^-}^- \mathbf{G}_{l,i-x_{i,j}^-}^{<},
\end{aligned} \tag{3.7.32}$$

$$\begin{aligned}
\mathbf{\Sigma}_{k,i}^{>} &= \sum_{j=1}^{N_i^+} \sum_{l=1}^{L_{i+x_{i,j}^+}} \frac{a_{i+x_{i,j}^+}}{\tilde{\Omega}_{i,j}^+} b_{l,i+x_{i,j}^+} \mathbf{h}_{|k-l|,x_{i,j}^+}^- \mathbf{G}_{l,i+x_{i,j}^+}^{>} \\
&\quad + \sum_{j=1}^{N_i^-} \sum_{l=1}^{L_{i-x_{i,j}^-}} \frac{a_{i-x_{i,j}^-}}{\tilde{\Omega}_{i,j}^-} b_{l,i-x_{i,j}^-} \mathbf{h}_{|k-l|,x_{i,j}^-}^+ \mathbf{G}_{l,i-x_{i,j}^-}^{>}.
\end{aligned} \tag{3.7.33}$$

We normalize the transition between $E(i)$ and $E\left(j = i \pm x_{i,j}^{\pm}\right)$ with the inverse of $\tilde{\Omega}_{i,j}^{\pm}$. Actually, the normalization factors $\tilde{\Omega}_{i,j}^{\pm}$ have to match the integrals over all energies that electrons taking part at the respective transitions can possess. In the limit of an infinite number of energy grid points, the integral over the final energies of electrons taking part at a specific transition equals the integral over the initial energies of the inverse transition. However, a finite resolution may cause ambiguities concerning which final energies a specific emission and its corresponding absorption involve. Therefore, we define the normalization quotients as the arithmetic mean of both energy integrals

$$\tilde{\Omega}_{i,j}^+ \equiv \frac{1}{2} \sum_{l=1}^{N_i^+} a_{i+x_{i,l}^+} + \frac{1}{2} \sum_{l=1}^{N_{i+x_{i,j}^+}^-} a_{i+x_{i,j}^+ - x_{i+x_{i,j}^+,l}^-}, \tag{3.7.34}$$

$$\tilde{\Omega}_{i,j}^- \equiv \frac{1}{2} \sum_{l=1}^{N_i^-} a_{i-x_{i,l}^-} + \frac{1}{2} \sum_{l=1}^{N_{i-x_{i,j}^-}^+} a_{i-x_{i,j}^- + x_{i-x_{i,j}^-,l}^+}. \tag{3.7.35}$$

*We get the analogue behavior for the absorption of E_0.

In order to show, that the later self-energies conserve the current, we require the following symmetry relation of the normalization factors*

$$\begin{aligned}\tilde{\Omega}^{+}_{v-x^{-}_{v,w},w} &= \frac{1}{2}\sum_{l=1}^{N^{+}_{v-x^{-}_{v,w}}} a_{v-x^{-}_{v,w}+x^{+}_{v-x^{-}_{v,w},l}} + \frac{1}{2}\sum_{l=1}^{N^{-}_{v-x^{-}_{v,w}+x^{+}_{v-x^{-}_{v,w},w}}} a_{v-x^{-}_{v,w}+x^{+}_{v-x^{-}_{v,w},w}-x^{-}_{v-x^{-}_{v,w}+x^{+}_{v-x^{-}_{v,w},w},l}} \\ &= \frac{1}{2}\sum_{l=1}^{N^{+}_{v-x^{-}_{v,w}}} a_{v-x^{-}_{v,w}+x^{+}_{v-x^{-}_{v,w},l}} + \frac{1}{2}\sum_{l=1}^{N^{-}_{v}} a_{v-x^{-}_{v,l}} = \tilde{\Omega}^{-}_{v,w}, \qquad (3.7.36)\end{aligned}$$

$$\begin{aligned}\tilde{\Omega}^{-}_{v+x^{+}_{v,w},w} &= \frac{1}{2}\sum_{l=1}^{N^{-}_{v+x^{+}_{v,w}}} a_{v+x^{+}_{v,w}-x^{-}_{v+x^{+}_{v,w},l}} + \frac{1}{2}\sum_{l=1}^{N^{+}_{v+x^{+}_{v,w}-x^{-}_{v+x^{+}_{v,w},w}}} a_{v+x^{+}_{v,w}-x^{-}_{v+x^{+}_{v,w},w}+x^{+}_{v+x^{+}_{v,w}-x^{-}_{v+x^{+}_{v,w},w},l}} \\ &= \frac{1}{2}\sum_{l=1}^{N^{-}_{v+x^{+}_{v,w}}} a_{v+x^{+}_{v,w}-x^{-}_{v+x^{+}_{v,w},l}} + \frac{1}{2}\sum_{l=1}^{N^{+}_{v}} a_{v+x^{+}_{v,l}} = \tilde{\Omega}^{+}_{v,w}. \qquad (3.7.37)\end{aligned}$$

We insert the self-energies in Eqs. (3.7.32) and (3.7.33) in the discretized condition for current conservation Eq. (3.7.19)

$$\begin{aligned}&\mathrm{Tr}\sum_{i=1}^{N}\sum_{k=1}^{L_i}\sum_{j=1}^{N^{+}_{i}}\sum_{l=1}^{L_{i+x^{+}_{i,j}}} a_i b_{k,i}\frac{a_{i+x^{+}_{i,j}}}{\tilde{\Omega}^{+}_{i,j}} b_{l,i+x^{+}_{i,j}}\mathbf{h}^{+}_{|k-l|,x^{+}_{i,j}}\mathbf{G}^{<}_{l,i+x^{+}_{i,j}}\mathbf{G}^{>}_{k,i} \\ &+\mathrm{Tr}\sum_{i=1}^{N}\sum_{k=1}^{L_i}\sum_{j=1}^{N^{-}_{i}}\sum_{l=1}^{L_{i-x^{-}_{i,j}}} a_i b_{k,i}\frac{a_{i-x^{-}_{i,j}}}{\tilde{\Omega}^{-}_{i,j}} b_{l,i-x^{-}_{i,j}}\mathbf{h}^{-}_{|k-l|,x^{-}_{i,j}}\mathbf{G}^{<}_{l,i-x^{-}_{i,j}}\mathbf{G}^{>}_{k,i} \\ &\stackrel{!}{=}\mathrm{Tr}\sum_{i=1}^{N}\sum_{k=1}^{L_i}\sum_{j=1}^{N^{-}_{i}}\sum_{l=1}^{L_{i-x^{-}_{i,j}}} a_i b_{k,i}\frac{a_{i-x^{-}_{i,j}}}{\tilde{\Omega}^{-}_{i,j}} b_{l,i-x^{-}_{i,j}}\mathbf{h}^{+}_{|k-l|,x^{-}_{i,j}}\mathbf{G}^{<}_{k,i}\mathbf{G}^{>}_{l,i-x^{-}_{i,j}} \\ &+\mathrm{Tr}\sum_{i=1}^{N}\sum_{k=1}^{L_i}\sum_{j=1}^{N^{+}_{i}}\sum_{l=1}^{L_{i+x^{+}_{i,j}}} a_i b_{k,i}\frac{a_{i+x^{+}_{i,j}}}{\tilde{\Omega}^{+}_{i,j}} b_{l,i+x^{+}_{i,j}}\mathbf{h}^{-}_{|k-l|,x^{+}_{i,j}}\mathbf{G}^{<}_{k,i}\mathbf{G}^{>}_{l,i+x^{+}_{i,j}}. \qquad (3.7.38)\end{aligned}$$

We shift the summation variables of the left side of this equation (with the help of Eqs. (3.7.36) and (3.7.37))

$$\begin{aligned}l.s. \;=\; &\mathrm{Tr}\sum_{v=1}^{N}\sum_{w=1}^{N^{+}_{v-x^{-}_{v,w}}}\sum_{k=1}^{L_{v-x^{-}_{v,w}}}\sum_{l=1}^{L_v}\frac{a_{v-x^{-}_{v,w}}a_v}{\tilde{\Omega}^{+}_{v-x^{-}_{v,w},w}} b_{k,v-x^{-}_{v,w}} b_{l,v}\mathbf{h}^{+}_{|k-l|,x^{-}_{v,w}}\mathbf{G}^{<}_{l,v}\mathbf{G}^{>}_{k,v-x^{-}_{v,w}} \\ &+\mathrm{Tr}\sum_{v=1}^{N}\sum_{k=1}^{L_{v+x^{+}_{v,w}}}\sum_{w=1}^{N^{-}_{v+x^{+}_{v,w}}}\sum_{l=1}^{L_v} b_{k,v+x^{+}_{v,w}}\frac{a_{v+x^{+}_{v,w}}a_v}{\tilde{\Omega}^{-}_{v+x^{+}_{v,w},w}} b_{l,v}\mathbf{h}^{-}_{|k-l|,x^{+}_{v,w}}\mathbf{G}^{<}_{l,v}\mathbf{G}^{>}_{k,v+x^{+}_{v,w}}. \qquad (3.7.39)\end{aligned}$$

Now, we can see by a direct comparison that both sides of the Eq. (3.7.38) agree and the current is indeed conserved.

*Please note that $x^{\pm}_{v,w} = x^{\mp}_{v\pm x^{\pm}_{v,w},w}$.

3.7.4 Efficient solution of lead Green's functions

Introduction

The interaction of device electrons with the attached leads is described by contact self-energies. The implementation of these contact self-energies requires for the knowledge of the lead surface Green's functions. When incoherent scattering or confining barriers are included within the leads, the lead surface Green's functions have to be determined numerically. We present a new efficient iterative solution scheme for a parallel solution of the lead and device Green's functions. We specify this scheme on the homogeneous and multiquantum well lead model.

Homogeneous leads

We have seen in Sec. 3.6.2 that the inclusion of incoherent scattering in homogeneous leads requires for the lead surface Green's function $\mathbf{G}_l^R\left(k_\parallel, E\right)$, i.e. the solution of Eq. (3.6.2). In general situations, no analytical expression is available for such a non-ballistic surface Green's function. Accordingly, we have to numerically invert a semi-infinite matrix for the exact solution of $\mathbf{G}_l^R\left(k_\parallel, E\right)$. This can be done iteratively as e.g. described in [124, 125] for sophisticated ballistic leads. Since we have to determine the device Green's functions and self-energies already iteratively, the iterative solution of $\mathbf{G}_l^R\left(k_\parallel, E\right)$ is best done in parallel to the device calculations, as we describe in the following.

For convenience, we add the iteration number as a subscript to all iterated Green's functions, scattering and contact self-energies as well as inverse Green's functions. We begin our iterations with the calculation of the ballistic Green's functions of the device $\mathbf{G}_{d,0}^R\left(k_\parallel, E\right)$ connected to ballistic leads via the ballistic lead self-energy $\mathbf{\Sigma}_{con,0}^R\left(k_\parallel, E\right)$ of Eq. (3.6.8). Then, we calculate the scattering self-energies of the device in lowest order (i.e. single Born approximation, $\mathbf{\Sigma}_{d,1}^R\left(k_\parallel, E\right) \neq 0$). The next step is the determination of the surface Green's functions of a semi-infinite lead that contains incoherent scattering. For this purpose, we explicitly calculate the retarded Green's function in a layer of width L close to the surface of a new semi-infinite lead. The retarded Green's function of this lead reads close to the surface for a given tuple $\left(k_\parallel, E\right)$

$$\mathbf{G}_{l,1}^R = \left(E\mathbf{1} - \mathbf{H}_{0,l} - \mathbf{V}_l - e\mathbf{\Phi}_l - \mathbf{\Sigma}_{l,1}^R - \mathbf{\Sigma}_{con,0}^R\right)^{-1}. \tag{3.7.40}$$

Hereby, the scattering self-energy in the lead $\mathbf{\Sigma}_{l,1}^R$ equals the self-energy of the device at its boundary grid point 1 and the scattering correlations to points deeper within the device $(2, 3, \ldots)$

$$\mathbf{\Sigma}_{l,1}^R = \begin{pmatrix} \ddots & \ddots & \vdots & \vdots & \iddots & \iddots \\ \ddots & \left(\mathbf{\Sigma}_{d,1}^R\right)_{1,1} & \left(\mathbf{\Sigma}_{d,1}^R\right)_{1,2} & \left(\mathbf{\Sigma}_{d,1}^R\right)_{1,3} & \left(\mathbf{\Sigma}_{d,1}^R\right)_{1,4} & \iddots \\ \cdots & \left(\mathbf{\Sigma}_{d,1}^R\right)_{2,1} & \left(\mathbf{\Sigma}_{d,1}^R\right)_{1,1} & \left(\mathbf{\Sigma}_{d,1}^R\right)_{1,2} & \left(\mathbf{\Sigma}_{d,1}^R\right)_{1,3} & \cdots \\ \cdots & \left(\mathbf{\Sigma}_{d,1}^R\right)_{3,1} & \left(\mathbf{\Sigma}_{d,1}^R\right)_{2,1} & \left(\mathbf{\Sigma}_{d,1}^R\right)_{1,1} & \left(\mathbf{\Sigma}_{d,1}^R\right)_{1,2} & \cdots \\ \iddots & \left(\mathbf{\Sigma}_{d,1}^R\right)_{4,1} & \left(\mathbf{\Sigma}_{d,1}^R\right)_{3,1} & \left(\mathbf{\Sigma}_{d,1}^R\right)_{2,1} & \left(\mathbf{\Sigma}_{d,1}^R\right)_{1,1} & \ddots \\ \iddots & \iddots & \vdots & \vdots & \ddots & \ddots \end{pmatrix}. \tag{3.7.41}$$

Typically, the length L of this layer equals 10 nm, but at least it has to equal the maximum range in $|z - z'|$ of the non-local interactions given in $\mathbf{\Sigma}_{d,1}^R\left(k_\parallel, E\right)$. This layer is connected via $\mathbf{\Sigma}_{con,0}^R$ to the ballistic lead of the previous iteration. In this way, the new semi-infinite lead

matches the homogeneous ballistic lead of the first iteration added by a layer of width L close to the surface. This additional layer contains the same material properties as the ballistic lead but includes incoherent scattering. We complete the first iteration by calculating the contact self-energy connecting our device to the new lead (compare Eq. (3.6.5))

$$\mathbf{\Sigma}^R_{con,1}\left(k_\parallel, E\right) = \boldsymbol{\tau}_1\left(k_\parallel, E\right)\mathbf{G}^R_{l,1}\left(k_\parallel, E\right)\tilde{\boldsymbol{\tau}}_1\left(k_\parallel, E\right). \tag{3.7.42}$$

The lesser contact self-energy of the first and all subsequent iterations is calculated according to Eq. (3.6.17) with an equilibrium or shifted Fermi distribution depending on the device current density (see Sec. 3.6.4).

In every iteration, we define a new semi-infinite lead that consists of a finite layer of length L in which the device scattering self-energy of the preceding iteration is included in the manner of Eq. (3.7.41) and that is connected to the semi-infinite lead of the preceding iteration. Consequently, the n-th iteration of the retarded lead surface Green's function reads for a given tuple $\left(k_\parallel, E\right)$

$$\mathbf{G}^R_{l,n} = \left(E\mathbf{1} - \mathbf{H}_{0,l} - \mathbf{V}_l - e\mathbf{\Phi}_l - \mathbf{\Sigma}^R_{l,n-1} - \mathbf{\Sigma}^R_{con,n-1}\right)^{-1} \tag{3.7.43}$$

with

$$\mathbf{\Sigma}^R_{con,n-1} = \boldsymbol{\tau}_{n-1}\mathbf{G}^R_{l,n-1}\tilde{\boldsymbol{\tau}}_{n-1}. \tag{3.7.44}$$

At convergence $\mathbf{G}^R_{l,n} = \mathbf{G}^R_{l,n-1}$ and the surface Green's function describes a homogeneous semi-infinite lead that includes exactly the same scattering that is present in the device close to the device boundary. We have to note that the Green's functions for spatial coordinates that are closer to the leads than the non-local range of the scattering self-energies are affected by the approximate determination of the lead Green's functions. In this region, the current is not exactly conserved and the device observables have to be determined outside of this region. This requires us to enlarge the device region by a transition zone (see Sec. 4.2.2).

An alternative approach for the numerical determination of surface Green's functions of semi-infinite leads is based on the transfer-matrix method [126–129]. This method is in particular efficient when the equations of motion (Schrödinger, Dyson or Keldysh equations) are almost diagonal in the respective representation. The non-local scattering self-energies in the spatial representation of this thesis yield entries in the Dyson equation that are far off-diagonal. This limits the minimum length L of the lead layers of our iterative solution scheme (see above) as well as the minimum size of the "building block" in the transfer matrix method. Thereby, the numerical load of both schemes is increased [130]. However, most of the computational time is invested in the determination of the scattering self-energies and their full energy and momentum dependence described in Sec. 3.5. Thus, the numerical effort in calculating $\mathbf{G}^R_l$ is comparably insignificant and our iterative method is sufficiently effective.

Multiquantum well leads

The second lead model that we have presented in Sec. 3.6.2, namely the multiquantum well lead model, does not treat the scattering in the leads self-consistently with the scattering in the device. However, we still have to determine the surface Green's function of a semi-infinite lead that consists of a periodic repetition of one or several quantum wells and barriers. Similar to the last paragraph, we solve this Green's function in an iterative manner. In particular, the lead Green's function of the first iteration $\mathbf{G}^R_{l,1}$ is explicitly calculated in a layer of width L that is connected via the contact self-energy $\mathbf{\Sigma}^R_{con,0}$ of Eq. (3.6.8) to a homogeneous semi-infinite lead

$$\mathbf{G}^R_{l,1} = \left(E\mathbf{1} - \mathbf{H}_{0,l} - \mathbf{V}_l - e\mathbf{\Phi}_l - \mathbf{\Sigma}^R_l - \mathbf{\Sigma}^R_{con,0}\right)^{-1}. \tag{3.7.45}$$

In contrast to the homogeneous lead model, however, the conduction band and the effective mass in the lead ($\mathbf{V}_l$ and $m_l^*(z,E)$) are not constant, but vary with the growth coordinate according to the lead period of length L. Since cascade structures typically yield relatively small current densities, the lesser contact self-energy of all iterations is calculated according to Eq. (3.6.17) with an equilibrium Fermi distribution. Due to our electrostatic boundary conditions in cascade structures, a finite electric field persists at the device boundaries. Nevertheless, we use field-free leads and do not continue the electric field at the device boundary into the leads. Otherwise, the chemical potential in the leads and accordingly the applied bias voltage would become ambiguous (varying with the growth coordinate in the leads). The rest of the iterative solution scheme of the lead surface Green's function follows the same tenor as our algorithm for the homogeneous leads in the preceding paragraph. The Green's functions and self-energies in the device are calculated in parallel with the lead surface Green's functions. Thereby, the n-th iteration of the retarded lead surface Green's function reads for a given $\left(k_\parallel, E\right)$

$$\mathbf{G}_{l,n}^R = \left(E\mathbf{1} - \mathbf{H}_{0,l} - \mathbf{V}_l - e\mathbf{\Phi}_l - \mathbf{\Sigma}_l^R - \mathbf{\Sigma}_{con,n-1}^R\right)^{-1} \tag{3.7.46}$$

and the n-th contact self energy reads

$$\mathbf{\Sigma}_{con,n-1}^R\left(k_\parallel, E\right) = \boldsymbol{\tau}_{n-1}\left(k_\parallel, E\right)\mathbf{G}_{l,n-1}^R\left(k_\parallel, E\right)\tilde{\boldsymbol{\tau}}_{n-1}\left(k_\parallel, E\right). \tag{3.7.47}$$

Due to the inhomogeneity of the electronic density close to the device boundaries, we cannot copy the scattering self-energy of the device into the leads - as is done in the homogeneous lead model. Instead, we assume a constant scattering rate in the leads

$$\Sigma_l^R\left(z, z', k_\parallel, E\right) = -i\hbar\delta\left(z - z'\right)/2\tau_{sc}. \tag{3.7.48}$$

The current density and the optical gain in the device do not depend on the choice of the lifetime τ_{sc}, if τ_{sc} is set to values smaller or equal to typical lifetimes of the confined states in the device. If the assumed value of τ_{sc} is too large, the electrons in the leads are better confined than in the device and the leads become highly reflective. Then, the device observables significantly depend on τ_{sc}. If the lifetime τ_{sc} is small enough, the device observables converge which indicates that the device physics do not depend on the details of our lead model (see Sec. 4.2.2).

In addition, we avoid artificial dependencies on numerical details in the lead by inserting transition zones of typically 6 nm between the leads and the device. In these areas, all Green's functions, self-energies and the Poisson equation are solved self-consistently (as a part of the device) in order to smoothen electronic transitions between the field-free leads and the biased device. Otherwise, the kink in the conduction band might cause artificial interferences within the device. In addition, the inclusion of small sections of the leads in the device region allows us to automatically include the lead resonances in the self-adaptive grid (see Sec. 3.7.2).

Therefore, the lengths of the explicitly calculated devices with multiquantum well leads attached exceed integer multiples of the cascade periodicity length by the two transition zones at the boundaries. Furthermore, it appeared to improve the numerical stability, if the boundary between a transition zone and the respective lead lies within a quantum well.

For the cascade devices in this thesis, it turned out that the device physics converge very rapidly with the density of states in the leads. Actually, a contact self-energy $\mathbf{\Sigma}_{con,1}^R$ that corresponds to a semi-infinite lead that is homogeneous except of one quantum well at the boundary is sufficient to mimic the density of states of electrons in cascade periods adjacent to the device. Correlations between device electrons and lead electrons in quantum wells beyond the second lead barrier appear to be highly suppressed. Therefore, we find the potential profile deeper within the contacts to have negligible influence on the device characteristics.

3.7.5 Flow chart

We initialize our algorithm with a ballistic calculation of the device with a linear Hartree potential that drops in the device by the amount of the applied bias voltage. The electronic energy E and the kinetic energy in growth direction E_z (see Eq. (3.7.5)) are thereby discretized with a power law in the respective discretization point numbers. We use the spatially resolved density $n(z)$ for the two convergence parameters of the two iteration circles that we discuss in the following. We initiate both parameters ($n_{outer}(z)$ and $n_{inner}(z)$) with the spatially resolved density of the ballistic calculation (see Fig. 3.7.8).

In the main part of the algorithm, we have to determine the device Green's functions and scattering self-energies, the surface Green's functions of the leads and the resulting contact self-energies, the boundary conditions of the Poisson equation, and (optionally) the shift of the Fermi spheres in the leads. It turned out that these mutually dependent functions can be solved in a two level hierarchy, as is illustrated in Fig. 3.7.8. In an inner circle, the scattering self-energies, the contact self-energies, and the Green's functions are solved iteratively. During these iterations, neither the Poisson potential nor the discretization of the energies E and E_z are changed. All self-energies and Green's functions are iterated in the inner circle until the L1-norm of the relative change of the local density of two successive iterations (see Fig. 3.7.8) at every device point z is smaller than the inner convergence limit ε_{inner}

$$\max \left| \frac{n_{inner}(z) - n_{temp}(z)}{n_{inner}(z)} \right| < \varepsilon_{inner}, \tag{3.7.49}$$

with typical values for undamped iterations $\varepsilon_{inner} \approx 5 \times 10^{-5}$. This limit guarantees well converged Green's functions and self energies and typically results in a relative deviation of the current density $j(z)$ from its spatial device average better than 0.05% (see Sec. 3.7.3). We also determine during these iterations the device averages of the spectral function and the energy resolved density for later updates of the discretization in E and E_z.

When the inner iterations are converged, the Poisson equation is solved with the predictor-corrector approach described in reference [131]. After each solution of the Poisson equation, the boundary condition for the Poisson equation is updated so that the total bias drops within the device. If the current in the leads is additionally accounted for, the shift of the Fermi sphere k_D in the leads is updated according to the new boundary condition of the Poisson equation in order to screen electric fields at the device boundaries*. Since the Poisson equation is solved under the condition of global charge neutrality, the average value of the conduction band edge gets shifted up- or downwards between successive iterations relative to the constant chemical potentials in the leads. This simultaneously shifts any resonance of the device averaged spectral function $A(E_z)$ and energy resolved electron density $n(E)$. Therefore, we shift $A(E_z)$ and $n(E)$ parallel to the Poisson potential and adapt the new grid in E and E_z according to the peaks of the shifted $A(E_z)$ and $n(E)$.

Inner and outer circles are iterated until the converged densities of two successive inner circles differ negligibly

$$\max \left| \frac{n_{inner}(z) - n_{outer}(z)}{n_{outer}(z)} \right| < \varepsilon_{outer}. \tag{3.7.50}$$

The convergence limit of the outer iteration circle ε_{outer} is set close to but higher than ε_{inner}.

*It is often better to explicitly use flatband conditions for Φ and to adjust k_D such that a vanishing slope of Φ at the boundaries fulfills Eq. (3.6.15).

Typically, values of ε_{outer} smaller than or equal 10^{-4} guarantee well converged boundary conditions and device observables.

3.8 Conclusion

In this chapter, we have adapted the nonequilibrium Green's function formalism to the stationary vertical transport in layered semiconductor devices. In the first sections of this chapter, we have followed common approaches and represented the Green's functions, the equations of motion and important observables in the position eigenfunction representation. We have derived the Lindhard and Debye screening lengths and compared them with resulting screening lengths of a new screening model which self-consistently includes incoherent scattering. Unfortunately, we have found several numerical issues of this self-consistent screening model that prohibit its implementation on our transport calculations. Nevertheless, we have demonstrated that the Debye screening length is a good approximation for the THz quantum cascade lasers of this thesis.

In order to clarify our approximations, we have derived in great detail the electronic self-energies describing the inelastic scattering with polar optical and acoustic phonons, the elastic scattering at ionized impurities and rough interfaces and the inelastic electron-electron interaction in the static GW_0 approximation. In particular, the self-energies for the (numerically efficient) elastic scattering at charge impurities, the inelastic scattering with acoustic phonons and the present shape of the inelastic electron-electron interaction cannot be found in literature. While the latter one is only meant as a rough estimate, all other self-energies are implemented as faithfully as numerically feasible. The nice agreement of the on-shell scattering rates with Fermi's golden rule in homogeneous GaAs have illustrated the accurateness of our scattering model. We have also proven and explained in detail that the self-consistent Born approximation is the minimal requirement for a conserved current, when vertex corrections are neglected.

It is a well-known technique to implement contact self-energies to the equations of motion so that the Green's functions describe open devices. However, we have expanded this method in order to include leads with inhomogeneous conduction band profiles. This new development is essential for the successfully description of quantum cascade structures as open devices and allows us in subsequent chapters to unveil unexpected phenomena in quantum cascade lasers. Typically, the Poisson equation is solved with vanishing surface electric fields. However, this method yields ambiguous applied bias voltages. Therefore, we have introduced a new self-consistent boundary condition for the Poisson equation that ensures globally charge neutral devices and simultaneously guarantees unambiguously defined bias voltages. It is a long debated issue how to consider current conservation beyond the device boundaries. In order to avoid charge accumulations at and close to the leads, we have modified the method of shifted Fermi distributions in the leads by a self-consistently determined response of the lead electron distribution. This new method guarantees that electric fields in homogeneous leads are exactly screened.

In order to ensure that the iterative solution of the multiple nonlinear differential equations of our method converges reasonably fast, we have introduced a self-adaptive discretization of the Green's functions in energy and in-plane momentum. We have pointed out in great detail that such an inhomogeneous representation has to be implemented very accurately. In particular, we have derived several new conditions for the numerical implementation of the scattering self-energies that are essential for current conservation. Finally, we have presented

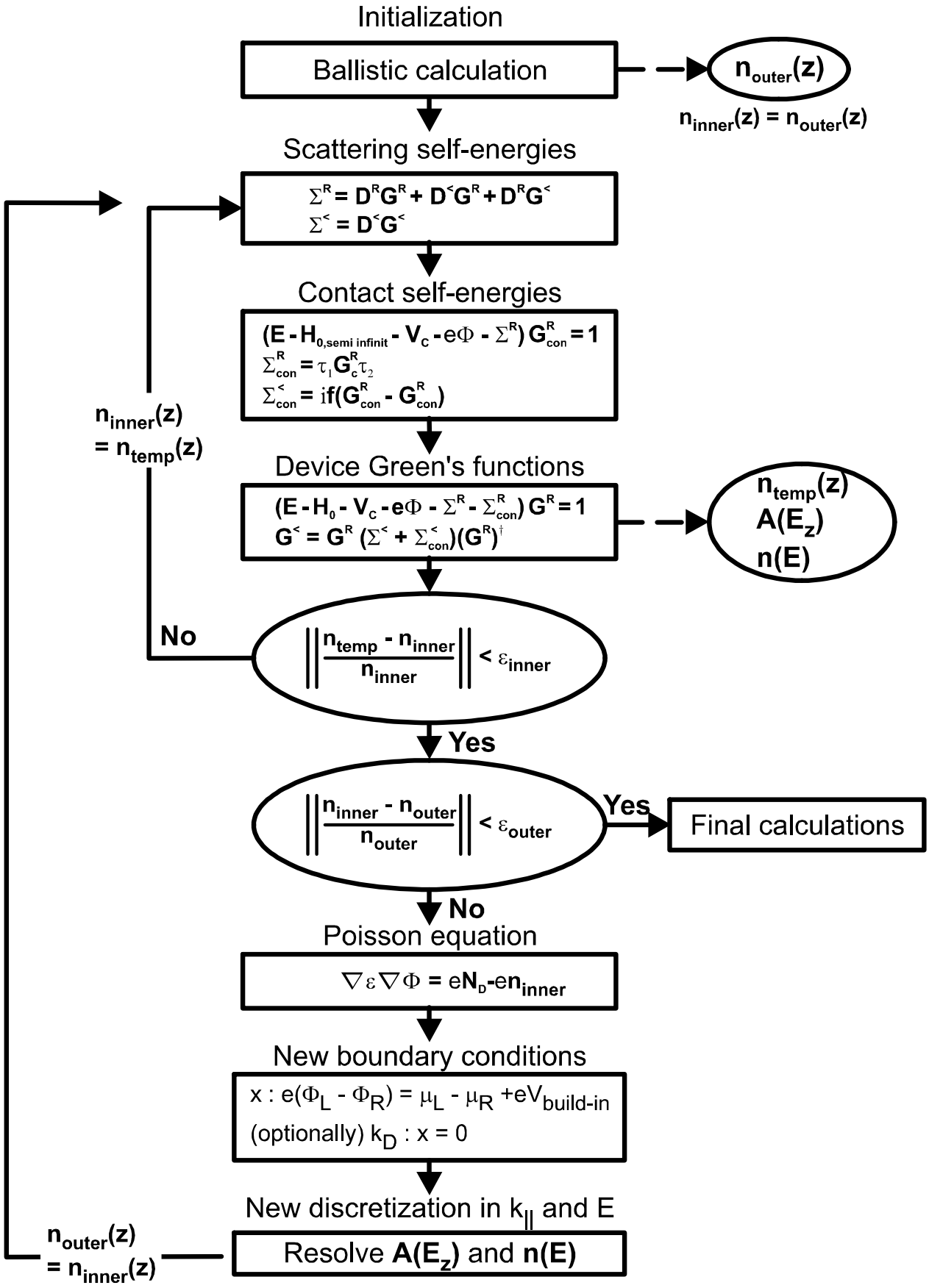

Figure 3.7.8: Flowchart of the numerical implementation of NEGF with scattering and ohmic contacts. Please refer to the text for a detailed description.

an efficient algorithm for the iterative solution of the Poisson equation, the Green's functions and self-energies of the device and the leads.

Chapter 4

New results and assessment of common approximations

4.1 Introduction

It is an important prerequisite for any transport calculation to prove that the implemented approximations cause no artifacts. Unfortunately, the NEGF formalism consists of a relative complex system of nonlinear partial differential equations. Thus, it is relatively hard to predict the impact of the many approximations given in literature and to judge under which circumstance which approximation may be applied. An almost fail-safe way to evaluate approximations in any formalism is to consider transport in simple, easily comprehensible devices and to compare results of the approximated calculations with results of calculations that avoid the respective approximation. If the device is simple enough, the physical impact of the approximations become obvious and a prediction of their limitations is straightforward.

This is indeed the purpose of this section. The limitation on vertical transport in semiconductor devices of this part of the thesis allows us to avoid most of the approximations that can be found in the NEGF literature. Nevertheless, we can apply these approximations and compare the resulting observables. In this way, we assess the applicability of many approximations. Thus, the results of this section are important for any NEGF transport calculation in arbitrary systems.

Our results for homogeneous devices as well as $n-i-n$ resistors demonstrate the importance of proper boundary conditions in quantum transport calculations. We show that reflectionless interfaces between the device and the leads are essential, if homogeneous electron densities at the device boundaries are expected. This requires for a self-consistent solution of the leads and the device which is often missed in literature. If no barriers efficiently suppress the current density in the device, the assumption of equilibrium electron distributions in the leads additionally fails. Then, the lead-device self-consistency has to further include a self-consistently determined nonequilibrium electron distribution in the leads. We have presented in the preceding chapter novel and efficient algorithms for the self-consistent solution of leads and device and show in this chapter that they indeed guarantee reliable results.

Typical approximations in literature apply to the scattering self-energies within the device. We analyze the impact of common approximations on the transport in resonant tunneling diodes and quantum wells. We illustrate artifacts of ballistic calculations and the necessity of a careful implementation of inelastic scattering. We show that common approximations in literature may lead to wrong results such as wrong alignment conditions, underestimated scat-

tering rates and the violation of Pauli's principle. The coupled system of differential equations is sometimes approximated such that parts of the system can be solved separately. We identify the maximum state occupancy up to which this approximation may be applied. Furthermore, we illustrate that the frequently ignored off-diagonal elements of the scattering self-energies contribute significantly to the scattering rates. We show that the widespread assumption of momentum independent scattering matrix elements has to be done for each device individually. Still, all presented scattering mechanisms are critically affected by this momentum dependence and the approximated scattering rates may differ considerably from Fermi's golden rule. The numerically most efficient scattering model, i.e. the Büttiker probe model, misses several physical effects. We point out these effects and discuss the advantages and disadvantages of the Büttiker probe model.

If not states otherwise, we include in all calculations of this chapter incoherent scattering with polar optical phonons, acoustic phonons, charged impurities and the electron-electron interaction in the Hartree approximation.

4.2 Approximations of lead electrons

4.2.1 Introduction

Transport within the leads is subject to many approximations, because the leads per se have been introduced in order to limit the exact calculations on the device area. However, we show that the approximations within the leads have to be done very carefully in order to avoid artificial results for device obserables. Unfortunately, this is often missed in literature. The common approximations of the leads can be categorized into two sections: approximations on the lead density of states and approximations of the lead electron distribution.

First, we illustrate that the density of states of lead electrons has to match the density of states of device electrons close to the leads, if the electrons are expected to enter and leave the device without reflections. For this reason, the calculations of the lead Green's functions have to include exactly the same scattering self-energies that are given in the device. This is the case in our expansion of the homogeneous lead model that includes incoherent scattering self-consistently with incoherent scattering in the device. Fortunately, reflections caused by a mismatch in the scattering within the leads and the device are comparably small in the case of the multiquantum well lead model. Therefore, we demonstrate that scattering in the multiquantum well lead model can be efficiently modelled with a constant lifetime. However, in both lead models, the scattering self-energies in the leads are not calculated in self-consistent Born approximation and the current density within the leads is not conserved (see Sec. 3.5.7). We show that nonlocal scattering close to the leads projects this violation of current conservation into device regions close to the leads. For this reason, we have to extend the area in which Green's functions and self-energies are exactly solved beyond the actual device region by the range of nonlocal scattering.

The second aspect of approximations in the leads is the lead electron distribution in the presence of a finite device current and has been controversially discussed in literature. We illustrate the well-known fact that the assumption of Fermi distributions for the lead electrons causes ambiguities in the applied bias voltage when the device current density is comparably large. We show that the electron distribution in source and drain leads of low resistive devices have to self-consistently react on the current density in the device. We agree with findings

in literature that *shifted* Fermi distributions are appropriate to model nonequilibrium electron distributions in the leads. However, we find that a self-consistent determination of this shift is mandatory. We show that a predefined relation between k_D and the device current density - as is typically assumed in literature - is only valid up to moderate* current densities.

4.2.2 Scattering in the leads

Introduction

The influence of approximations in the lead model is especially large in low resistive devices such as homogeneous systems and $n-i-n$ resistors. In these devices, we expect the electron density close to the leads to equal the homogeneous density of ionized dopant atoms and we use these systems as sensitive test cases for the homogeneous lead models. Since it is completely ignored in literature, we show that artificial electron oscillations at the device boundaries develop when incoherent scattering is only implemented within the device and neglected within the leads. These oscillations are particularly effective in low resistive devices when no damping quantum barriers exist.

In contrast, the multiquantum well lead model naturally yields quantum interferences in the device, because it mimics confined states in the leads. We show that the device observables do not critically depend on the lifetime of the lead states. Thus, the scattering in the multiquantum well leads can be modelled with a constant.

The major purpose of the contact self-energies is to limit the exact calculations on the finite device region and to approximate the surroundings. A common approximation is to assume the fluctuation-dissipation theorem within the leads and to avoid a self-consistent calculation of Green's functions and scattering self-energies within the leads. Due to numerical limitations, we follow this approach, but we illustrate that nonlocal scattering of device electrons close to the leads extends the violation of current conservation within the leads into the device. This has not been discussed in literature before, but it requires for a careful treatment of the device/lead boundary regions. For instance, we introduce transition zones in the multiquantum well lead model and use sufficiently long homogeneous regions at the device boundaries in the case of the homogeneous lead model.

Homogeneous lead model

It is a common approach in the area of NEGF calculations to attach ballistic leads to open devices even when incoherent scattering in the device is included [132–135]. Then, the surface Green's functions of the leads are either known analytically (see Eq. (3.6.8)) or have to be determined only once at the beginning of the calculations which reduces the numerical load significantly. Such an approximation, however, has to be done with great care. In particular, when the carriers should not face interferences at the boundaries but are expected to build up a constant density, the carrier density of states in the leads has to match the carrier density of states at the respective device boundary. In this case, the self-consistent inclusion of scattering in the leads as described in Sec. 3.6.2 is inevitable. This is illustrated in Fig. 4.2.1. It shows results of two NEGF calculations of a homogeneous 50 nm GaAs device in equilibrium. The lattice temperature in both calculations is 300 K. For better visibility we include scattering with phonons, but neglect the electron-electron interaction and use a constant conduction

*This limit is depending on the device details.

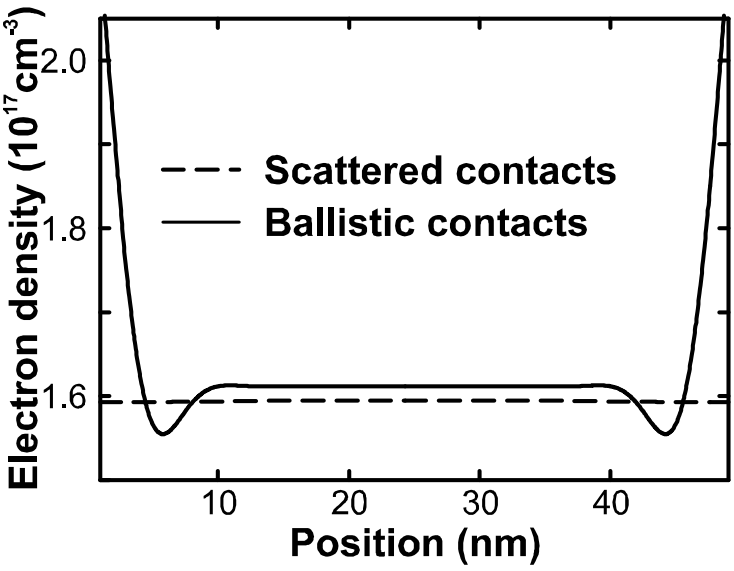

Figure 4.2.1: Electron density in an homogeneous GaAs device at 300K with a constant conduction band. The implementation of scattering in the contacts (dotted line) is needed to yield a constant electron density. Ballistic contacts (full line) cause strong interferences.

band Φ that equals the constant chemical potential μ. Therefore, we expect a constant electron density throughout the device. Indeed, Fig. 4.2.1 shows a constant electron density (dashed line) when scattering is self-consistently included in the leads. In contrast, when ballistic leads are attached to the device, the mismatch in the electronic density of states of leads and device cause significant interferences close to the device boundaries which results in an inhomogeneous electron density (solid line) (for similar findings in the area of Büttiker probes see [119, 136]).

Obviously, these artificial interferences build up charge accumulations close to the device boundaries. If the Poisson equation is solved self-consistently, the conduction band gets distorted accordingly. Then in such a self-consistent solution of the Poisson equation and the Green's functions, the deviations from a homogeneous density get damped depending on the amount of doping. Nevertheless, we have found for conduction band electrons in GaAs at 300 K and homogeneous doping concentrations below 5×10^{17} cm^{-3} significant deviations from homogeneity in the presence of these artificial interferences. We have to emphasize that the relative importance of the scattering in the leads depends on the device parameters (effective mass, lattice temperature, etc.). Therefore, the validity of the approximate ballistic lead model has to be explicitly checked for every device. In order to avoid the risk of artificial results in this thesis, we include scattering in the leads self-consistently with the scattering in the device whenever the transitions between device and leads are expected to be reflectionless, i.e. whenever homogeneous leads are applied.

In contrast, the neglect of scattering in the leads is an appropriate approximation when the transition zones between leads and device are highly reflective, as e.g. in molecular junctions [137, 138]. In such devices, large interferences at the device boundaries are due to the system's properties (e.g. large differences between lead and device material properties). Then, artificial interferences that originate from missing scattering in the leads are typically much smaller and can be neglected.

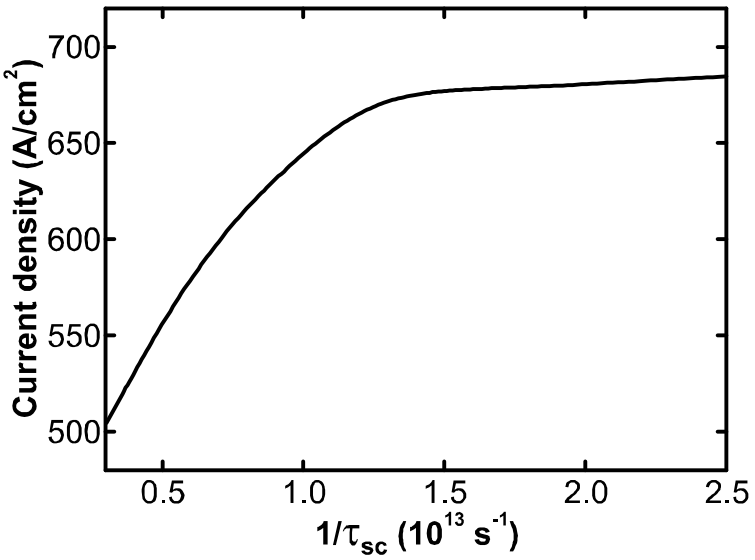

Figure 4.2.2: Current density of the GaAs/$Al_{.15}Ga_{.85}$As QCL of Ref. [122] at 54 mV/period, 40 K lattice temperature and a sheet doping concentration of 1.9×10^{10} cm^{-2} as a function of the inverse electron lifetime in the leads.

Multiquantum well lead model

We have found in the multiquantum well lead model that the current and the optical gain do not depend on details of the scattering in the leads - if enough scattering in the leads is included. The electrons in the multiquantum well leads are localized in confined states. Thus, an underestimated lead state lifetime yields artificially tight alignment conditions between the lead states and electronic resonances in the device. Then the device current is dominated by the approximated lifetime $1/\tau_{sc}$ of the lead states instead of the physics in the device. Therefore, the linewidth of lead states has to match or slightly exceed the typical linewidth of states in the device in order to avoid artifacts. It is important to note that the observables converge with $1/\tau_{sc}$, as is shown in Fig. 4.2.2 for the current density of the GaAs/$Al_{.15}Ga_{.85}$As QCL of Ref. [122]. In this device, we find that the current and all other observables stay essentially constant if $1/\tau_{sc}$ exceeds* 1.5×10^{13} s^{-1} which lies in the range of typical linewidths of the device states. In contrast, the transitions between lead and device get efficiently suppressed for larger lifetimes τ_{sc}.

Current conservation close to the leads

We have shown in Sec. 3.7.3 that the current is conserved, when the self-consistent Born approximation is applied on all Green's functions and self-energies. Actually, we apply the self-consistent Born approximation "only"within the device and approximate the scattering self-energies in the leads (see Eq. (3.6.17)). The self-energies of polar optical phonon in Sec. 3.5.2 and charged impurity scattering in Sec. 3.5.4 have a finite nonlocal scattering range. Thus, they contribute to the Green's functions for finite differences of the two propagation coordinates $(z - z')$. Consequently, electrons close to the device boundaries can leave the device by a nonlocal scattering event with a phonon or a charged impurity. In this way, the device

*As long as $1/\tau_{sc}$ does not lie at unphysically high values.

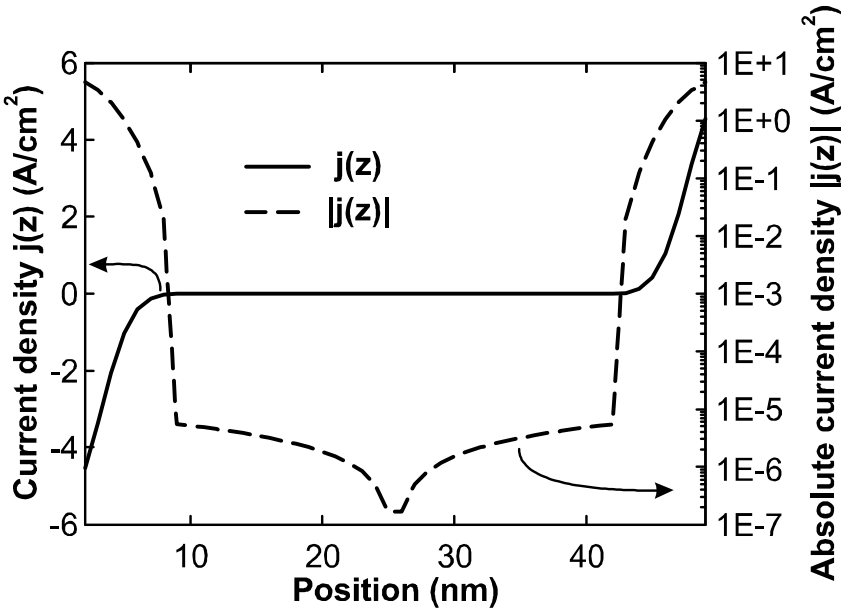

Figure 4.2.3: Current density (solid) and its absolute value (dashed) as a function of growth coordinate in the device of Fig. 4.2.1. In an area of 8 nm close to the leads, device electrons interact with lead electrons via the nonlocal scattering self-energies. In this area the device current is not conserved, because the lead Green's functions are not given in the self-consistent Born approximation.

Green's functions for spatial coordinates that lie in a distance to the leads smaller or equal the nonlocal range of the scattering self-energies are directly affected by the approximate treatment of scattering within the leads. This is illustrated in Fig. 4.2.3 as it shows the spatially resolved current density $j\,(z)$ in the device of Fig. 4.2.1. In this calculation, the non-local range of all scattering self-energies is limited to 8 nm for illustrative reasons*. Since this device is calculated in equilibrium, we expect the current to vanish at every device point. This is numerically quite well fulfilled in the interior of the device. The remaining small but finite absolute value of $j\,(z)$ for positions $z \in [8\text{ nm}; 42\text{ nm}]$ (see the dashed line in Fig. 4.2.3) originates from the fact that only 20 iterations of the Green's functions and self-energies are performed. This number of iterations is sufficient to guarantee well converged observables. However, the Green's functions of the last two iterations (i.e. G_{19} and G_{20}) still slightly differ which yields a small violation of current conservation (compare Eq. (3.5.110)). Close to the leads within the non-local range of the scattering self-energies (i.e. $z \notin [8\text{ nm}; 42\text{ nm}]$ in Fig. 4.2.3), however, $j\,(z)$ remains finite and the current is not conserved. Thus, we ensure that the device observables are not affected by the physics in the regions close to the leads either by increasing the homogeneous device regions close to homogeneous leads or by introducing transition zones† as in the case of multiquantum well leads (see Sec. 3.6.2).

*However, this is close to the actual range of the scattering self-energies in similar devices (see Sec. 4.3.4).

†These zones are introduced for two other reasons: First, to include the lead resonances in the self-adaptive grid and second, to smoothen the transitions between field-free leads and the biased device.

4.2.3 Current density in the leads

Introduction

In this subsection, we illustrate the charge accumulation in transport calculations when current in the leads is neglected. We compare different approaches for the solution of this issue. First, we show that finite electric fields at the device boundaries prohibit smooth electronic transitions between the device and the leads and cause charge accumulation at the device boundaries. We demonstrate in detail that the often used lead model [111, 119, 120] of flatband boundary conditions for the Hartree potential and equilibrium electron distributions in the leads increasingly faces ambiguities with larger current densities. This has motivated several studies in literature that introduce a shifted Fermi distribution for the lead electron distribution. In this previous work, the shift k_D is determined as a function of material parameters, the device current density or as function of an electric field at the device surface. Yet, we show that a constant relation between the shift k_D and the device current cannot hold for arbitrary devices and arbitrary applied bias voltages. Our model of a self-consistently determined shift of the Fermi distribution in the leads (see Sec. 3.6.4), however, ensures unambiguously defined applied bias voltages and allows for the determination of I-V characteristics up to rather high current densities.

Locally charge neutral device boundaries

It has been discussed in [112, 113] (see Sec. 3.6.4) that finite device current densities lead to artificial charge accumulations at the device boundaries, if the electron distribution in the leads is assumed to be unaffected by the finite current. We illustrate this charging of the device boundaries in a 80 nm wide $n^{++} - i - n^{+}$ resistor at a temperature of 50 K. The resistor consists of a 10.7 nm intrinsic GaAs layer that separates a 32 nm wide n-doped region with $n = 2 \times 10^{18}$ cm^{-3} on the source side and a 37.3 nm wide n-doped region with $n = 1 \times 10^{18}$ cm^{-3} on the drain side of the device (see the grey line in Fig. 4.2.4 (a) for the ionized dopant concentration). The asymmetry of the device yields a build-in potential of $V_{\mathrm{built-in}} = -34.2$ meV in equilibrium. We apply a bias voltage of 40 meV which results in 5.8 meV for the expected difference of the lead conduction band edges. The self-consistently determined electron densities and conduction band profiles of this resistor are given in Figs. 4.2.4 (a) and (b), respectively. Here, we have applied four different lead models:

The (blue) dashed lines in Figs. 4.2.4 (a) and (b) represent results of NEGF calculations with an equilibrium Fermi distribution in the leads and a self-consistently determined finite electric field at the boundaries. This field is set such that the potential drop within the device matches the expected 5.8 meV. Due to the finite current density in the device ($j = 1.4 \times 10^6$ A/cm^2), the vanishing average velocity of the lead electrons cannot guarantee current conservation beyond the device boundaries. This is also indicated by the self-consistent solution of the Poisson equation that maintains an attractive electric field near the source (see dashed line in Fig. 4.2.4 (b)). This field accelerates the incoming source electrons and is accompanied by a depletion of electrons near the source (see dashed line in Fig. 4.2.4 (a)). At the drain, the lead electrons also get accelerated into the direction of the current density which is opposite to the velocity they enter the device with. Therefore, electrons entering the device are slowed down and accumulated near the drain.

A very similar behavior can be seen in the dash-dotted lines that represent results of NEGF calculations with a constant shift of the Fermi sphere in the source ($k_{D,L} = 0.04$ nm^{-1}) and drain

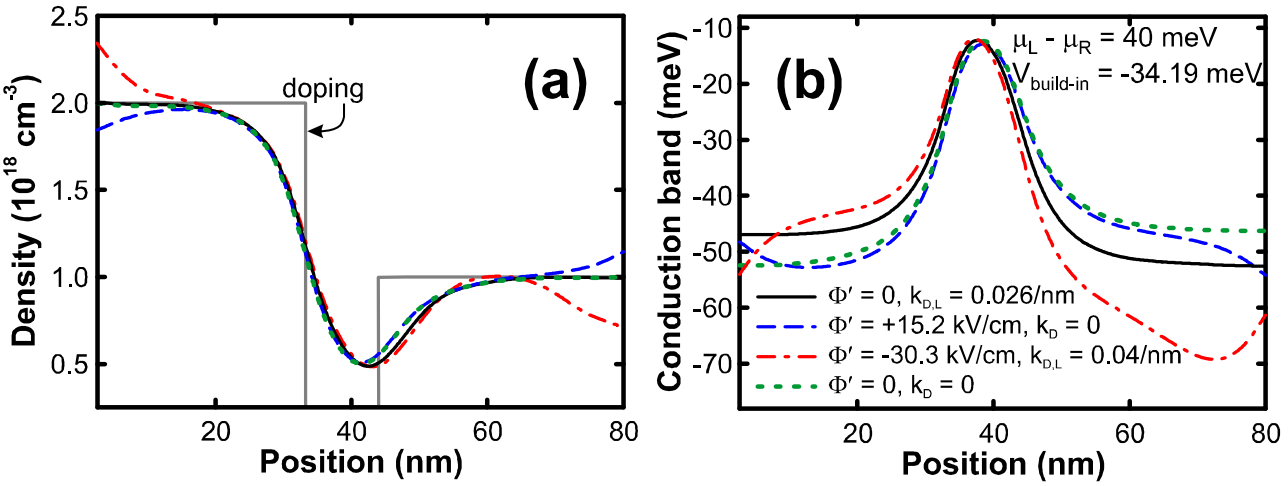

Figure 4.2.4: NEGF results of four different lead models for the electron density (a) and self-consistently determined conduction band profile (b) of a $n^{++} - i - n^{+}$ GaAs resistor at 50 K and 40 mV applied bias voltage. The green dotted lines depict results of equilibrium leads and flatband conditions for the Poisson equation. In contrast, the black solid line shows results of our lead model that includes a self-consistently determined shift of the Fermi sphere as discussed in Sec. 3.6.4. The red dash-dotted and blue dashed lines show results with constant but larger and smaller shifts of the lead Fermi spheres, respectively. The finite electric field at the boundary of the later two models is set such that the total applied bias drops within the device. Further details are given in the text.

lead ($k_{D,R} = 2k_{D,L}$, see Eq. (3.6.24)) which is slightly smaller* than the suggested value of Laux *et al.* (see [109] and Eq. (3.6.21)). The self-consistently determined Hartree potential is again solved with finite electric fields at the boundaries in order to guarantee the expected conduction band drop of 5.8 meV. In this model, the shift of the Fermi sphere in the source is too large and the lead electrons are faster than the nearby device electrons. This yields the exact opposite device behavior close to the leads compared to the previous lead model: Decelerating fields close to the leads, an accumulation of electrons near the source and a depletion of electrons near the drain. Actually, the lead model of Laux *et al.* requires for flatband boundary conditions of the Poisson equation. However, flatband boundary conditions and a $k_{D,L}$ of 0.04 nm^{-1} result in a conduction band drop exceeding the applied bias, as we explain below.

The black solid lines depict results of our lead model described in Sec. 3.6.4. In contrast, the green dotted lines show results of calculations with flatband boundary conditions for the Poisson equation and equilibrium Fermi distributions in the leads. Thus, the green dotted line represents results of the commonly used lead model (e.g. [111, 119, 120]). Both models almost coincide in the resulting density shown in Fig. 4.2.4 (a). In particular, both models yield electron densities at the device boundaries that equal the ionized dopant concentration which results in charge neutral leads. This is due to the vanishing electric fields at the boundaries. However, an equilibrium electron distribution in the lead yields a difference of the lead conduction band edges of -6.2 meV which contradicts the expected 5.8 meV (dotted line in Fig. 4.2.4 (b)). The larger the shifts of the Fermi spheres in the leads are, the more electrons enter the device from

*The resulting current density of this calculation is 2.6×10^6 A/cm^2 which actually yields an even larger shift of the Fermi sphere in the source by $k_{D,L} = 0.047$ nm^{-1}.

the source and the less electrons originate from the drain. Simultaneously, the self-consistent conduction band edge of the source gets shifted upwards and the conduction band edge of the drain gets shifted downwards in order to compensate the changes of the Fermi spheres and thereby to maintain the global charge neutrality [121]. Therefore, an equilibrium distribution in the leads underestimates the potential drop within the device. Whereas in this example, the shift of the source Fermi distribution $k_{D,L}$ according to Laux *et al.* (see [109] and Eq. (3.6.21)) exceeds the self-consistently determined $k_{D,L}$ and thus results in an overestimated potential drop.

Frensley uses in [112] an alternative approach and selects k_D to be proportional to the electric fields at the device boundaries. Since he applies Dirichlet boundary conditions on the Poisson equation, these electric fields are finite. However, we have shown above that such fields yield undesirable charge accumulations close to the leads. Furthermore, the approach of Frensley requires a known analytical relation between the device current and the shift of the Fermi spheres, e.g. a known electron mobility. In general devices, however, transport may vary from the ballistic to the diffusive regime which results for the same value of k_D in different current densities. In summary, we find that only a self-consistently determined k_D can guarantee that the potential drop within arbitrary devices matches the respective applied bias voltage while the device/lead boundaries remain field-free.

Effects of nonequilibrium leads

A finite shift of the lead Fermi distributions in the direction of the conduction band drop increases the current density in the device. Accordingly, the assumption of an equilibrium electron distribution in the leads significantly underestimates the current density. This is illustrated in Fig. 4.2.5 as it shows the current density of the $n^{++}-i-n^{+}$ structure in Fig. 4.2.4 as a function of the applied bias voltage. The black solid line shows the I-V characteristic of our lead model with self-consistently determined shifts of the lead Fermi distributions, whereas the black dotted line depicts results of the commonly used equilibrium leads. In both cases, the electric fields at the boundaries vanish and incoherent scattering with phonons and impurities is included. Obviously, our model including shifted Fermi distributions yields a larger low field mobility (˜2286 $\mathrm{cm^2V^{-1}s^{-1}}$) as well as a larger current density at higher electric fields. The low field mobility (˜1330 $\mathrm{cm^2V^{-1}s^{-1}}$) and the current density of the equilibrium lead model is smaller for two reasons. First, in the equilibrium lead model a significant bias voltage is assumed to drop within the leads. This "lead bias"is illustrated by the gray dotted line where we consider the difference of the conduction band edges of the two equilibrium leads as the bias voltage. Thus, the gray dotted line equals the black dotted line shifted to lower bias voltages by the amount of the "lead bias". For this $n^{++}-i-n^{+}$ structure, this lead bias drop exceeds 20 % of the total applied bias voltage. Such a large portion of the total applied bias is clearly too much to be accounted for within a homogeneous, field-free lead. A second reason for the discrepancy to our model lies in the vanishing current density in the equilibrium leads. This lack of lead current maintains an additional resistance between the device and the leads (see the arrows in Fig. 4.2.5). In summary, we cannot simultaneously assume the leads of such a highly conductive device to be homogeneous *and* to supply electrons with an equilibrium distribution.

However, the assumption of an additional bias drop within the leads is approximately valid in highly resistive devices. We find in tunneling devices such as resonant tunneling diodes that the self-consistently determined shifts of the Fermi spheres are small and the "lead bias"in the equilibrium lead model is much smaller than the total applied bias voltage (approximately 5 %

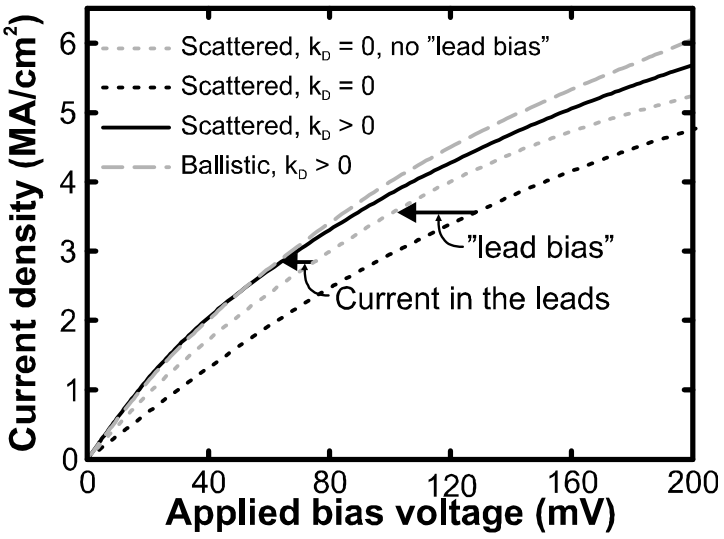

Figure 4.2.5: Current density as a function of applied bias voltage for the $n^{++}-i-n^{+}$ resistor in Fig. 4.2.4 for various lead models. Calculations with the commonly applied model of equilibrium leads (black dotted) yield smaller current densities than calculations with our lead model of self-consistently shifted lead Fermi distributions (black solid). A portion of this discrepancy can be addressed to the "lead voltage"in the equilibrium lead model. This is shown by the difference of the black and the gray dotted line. The latter represents results with equilibrium leads where the difference of the lead conduction band edges is considered as the applied bias voltage. The gray dashed line depicts results of our lead model when all incoherent scattering mechanisms are neglected and is given for later reference.

in the resonant tunneling diode of [113]). Therefore, in such devices, results of our lead model and of the equilibrium lead model are very similar.

Figure 4.2.6 shows the self-consistently determined shift of the Fermi distribution in the source ($k_{D,L}$) of the $n^{++}-i-n^{+}$ structure in Fig. 4.2.4 as a function of the current density. Calculations ignoring any incoherent scattering (dashed) yield smaller shifts compared to calculations that include scattering with phonons and impurities (solid). However, the fundamental shape of k_D is the same in both calculations. We find an almost linear relation between the current density and the shift of the Fermi spheres in the leads for current densities up to approximately 3 MAcm^{-2}. In this regime, the shift k_D could be predicted with the model of Laux *et al.* [109], albeit the conductivity mass is rather small (approximately 0.03 m_0) due to the inefficient incoherent scattering. With higher current densities, more of the electron density is shifted into the intrinsic device area and less electrons are located close the leads. Thus, the shifts of the Fermi spheres in the leads have to be increased superlinearly in order to maintain the required difference of the lead conduction band edges*.

*See the discussion of Fig. 4.2.4 for the relation between k_D and the lead conduction band edges.

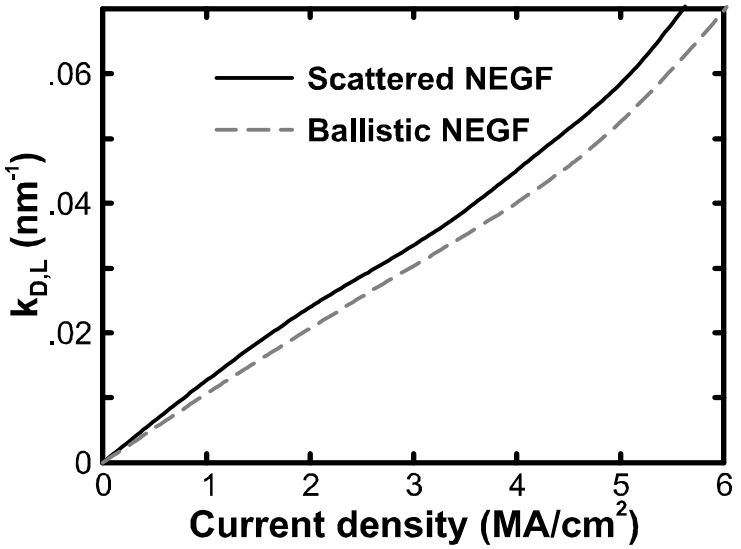

Figure 4.2.6: Self-consistently determined shift of the Fermi distribution in the source of the $n^{++} - i - n^{+}$ resistor of Fig. 4.2.4 as a function of current density. Coherently propagating electrons (dashed) require a smaller shift than electrons scattered by phonons and impurities (solid) in order to maintain the same current density.

4.3 Approximations of the device self-energies

4.3.1 Introduction

Most of the complexity of the NEGF formalism and accordingly most of the numerical load originates from the scattering self-energies. For this reason, most of the approximations in literature apply to the scattering self-energies in the device. The most efficient, but also crudest approximation is to ignore scattering at all and to consider only ballistic transport. We have seen in Sec. 4.2.3 that such an approximation may indeed give almost the same results in $n^{++} - i - n^{+}$ resistors as calculations including scattering. However, we show that a ballistic calculation fails as soon as confined states are involved in the transport. Then, inelastic scattering is essential for realistic I-V characteristics.

Inelastic scattering self-energies in the self-consistent Born approximation require for the solution of a set of coupled nonlinear differential equations. A prominent approximation in literature decouples several of the differential equations and solves them separately. In this way, the complexity of the system is greatly reduced. While it is only known that this approximation violates Pauli's principle, we identify the circumstances under which this approximation may be applied.

We have seen in the Sec. 4.2.2 that non-local incoherent scattering close to the leads requires for a spatial extension of the explicitly calculated device. In addition, the solution of the device Green's functions is numerically the more expensive, the more scattering correlation between different device points exist. Therefore, it is a popular approximation to assume only local scattering events. We illustrate the contribution of nonlocal scattering events to the total scattering rates of LO-phonons and charged impurities and give clues to which range the nonlocality of the self-energies in arbitrary devices may be limited.

Most of the computational time is spent on the solution of the momentum integrals in the

formulas of the scattering self-energies. The respective scattering potentials necessitate the solution of these integrals for every individual scattering mechanism. Thus, it is a widespread approximation to assume momentum independent scattering potentials and to solve these integrals for all scattering mechanisms only once. We show that this approximation yields results comparable to calculations including exact self-energies. However, we emphasize that the approximated results critically depend on the assumed scattering strength. This strength is hard to predict for every individual device.

Another popular approximation for incoherent scattering has been introduced by Büttiker in [139], i.e. the model of Büttiker probes. In this model, the total scattering self-energy is approximated with a given function. We discuss in detail advantages and disadvantages of this approximation. In particular, we show that Büttiker probes fail to yield qualitative descriptions if applied on devices that are driven too far from equilibrium.

4.3.2 Relevance of incoherent scattering

Introduction

It is often argued that transport in devices of short length scales and at low temperatures can be well described by ballistic transport models if the coherence length exceeds the device dimensions [100, 117, 140]. In agreement with this statement, we have seen in the I-V characteristics of the $n^{++}-i-n^{+}$ resistor in Sec. 4.2.3 that ballistic transport models can eventually reproduce realistic results in a short device lacking any confined states (see dashed lines in Figs. 4.2.5 and 4.2.6). However, it has been shown in [119] that electrons confined in bound or quasi bound states affect the transport in any open device via the self-consistently determined Poisson potential. In ballistic transport calculations, the occupancy of those states is typically underestimated if no additional model accounts for the inelastic scattering of electrons into these states [119, 141]. In addition to this finding, we show that even the I-V characteristics of faintly doped devices are significantly affected by incoherent scattering, although the electrostatic potential does not influence the conduction band profile. We limit our considerations to a simple device with very few confined states, i.e. a faintly doped resonant tunneling diode (RTD). With this device, we show that ballistic models fail to describe transport whenever bound or quasi bound states are involved in transport, irrespective whether the charge distribution is modelled realistically or what the actual length scale of the device is.

Assessment

We consider a 40 nm GaAs/$Al_{.3}Ga_{.7}As$ resonant tunneling diode (RTD) at 100 K and different scattering environments. The RTD consists of two 3 nm wide $Al_{.3}Ga_{.7}As$ barriers and a 5 nm quantum well in the center. The GaAs layers are n-doped with $n = 2 \times 10^{16}$ cm^{-3} whereas the $Al_{.3}Ga_{.7}As$ barriers are undoped. The average doping of this device and accordingly, the number of lead electrons that enter the device is so small that the Fermi distributions in the leads are (maximally) shifted by the Fermi wave vector (see Sec. 3.6.4) and a finite homogeneous electric field in the device persists for all applied voltages. Thus, a comparison with realistic devices requires for an extension of this device to wider (or heavier doped) GaAs layers surrounding the $Al_{.3}Ga_{.7}As$ barriers. For the statement of this section, however, the considered small electron density is advantageous.

Figure 4.3.1 shows a comparison of the calculated I-V characteristics including all incoherent scattering mechanisms (full line) with a ballistic calculation (dotted) and a simplified model

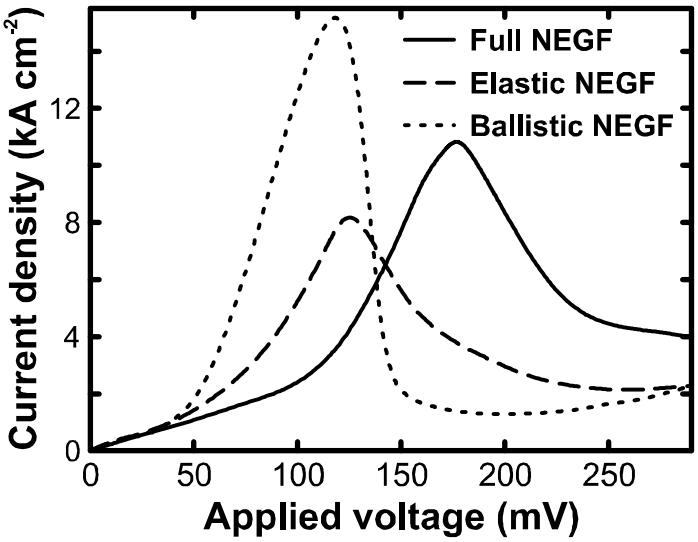

Figure 4.3.1: I-V characteristics of a 40 nm GaAs/Al_3Ga_7As resonant tunneling diode at 100 K in different transport models. The solid line depicts results of calculations including all relevant scattering mechanisms (solid line). Results of calculations including only elastic scattering mechanisms (dashed) and results of ballistic calculations, i.e. calculations neglecting any incoherent scattering mechanism (dotted) are given for comparison. As is explained in the main text, inelastic scattering shifts the peak to higher voltages, wheras elastic scattering reduces the peak current density and enhances the valley current.

(dashed) that includes only the elastic scattering with acoustic phonons of Eq. (3.5.25) and with charged impurities of Eq. (3.5.52). In particular the ballistic calculation is several orders of magnitudes faster than calculations including scattering.

However, inelastic scattering is required to occupy the triangular quasi-bound state that forms in front of the left barrier of any RTD under forward bias (see Fig. 4.3.2 (a)). This state acts as feeding reservoir for the RTD; in fact, the peak current occurs at a bias voltage where this quasi-bound state is aligned with the resonant quantum well state [42]. This is illustrated in Fig. 4.3.2 (a) that depicts the potential profile and the energy resolved electron density, defined by Eq. (3.3.4) at the bias voltage of 190 mV. Note that the electrons that enter the device from the source first loose energy before they traverse the resonant state in the well (arrow in Fig. 4.3.2 (a)).

If we neglect any kind of scattering [109] (i.e. assume ballistic transport), the RTD functions in an entirely different way. This is shown in Fig. 4.3.2 (b). It shows the energy resolved electron density of the same situation as in Fig. 4.3.2 (a), but without any incoherent scattering. Electrons propagate ballistically from the source to the barrier and maintain their (high) energy that lies above the resonance energy in the well. In that case, the I-V characteristic is entirely determined by the properties of the lead rather than by details of the conduction band in the device. In particular, the resonance of the ballistic I-V characteristic of Fig. 4.3.1 is reached, when the conduction band edge of the source is aligned with the resonant state of the RTD.

The same resonance condition holds for the dashed line in Fig. 4.3.1 which depicts results of a calculation ignoring any incoherent scattering except for the elastic scattering with acoustic phonons and charged impurities of Eqs. (3.5.25) and (3.5.52), respectively (dashed in Fig. 4.3.1). Since no energy dissipation is included, the resonance bias of the elastic I-V characteristic

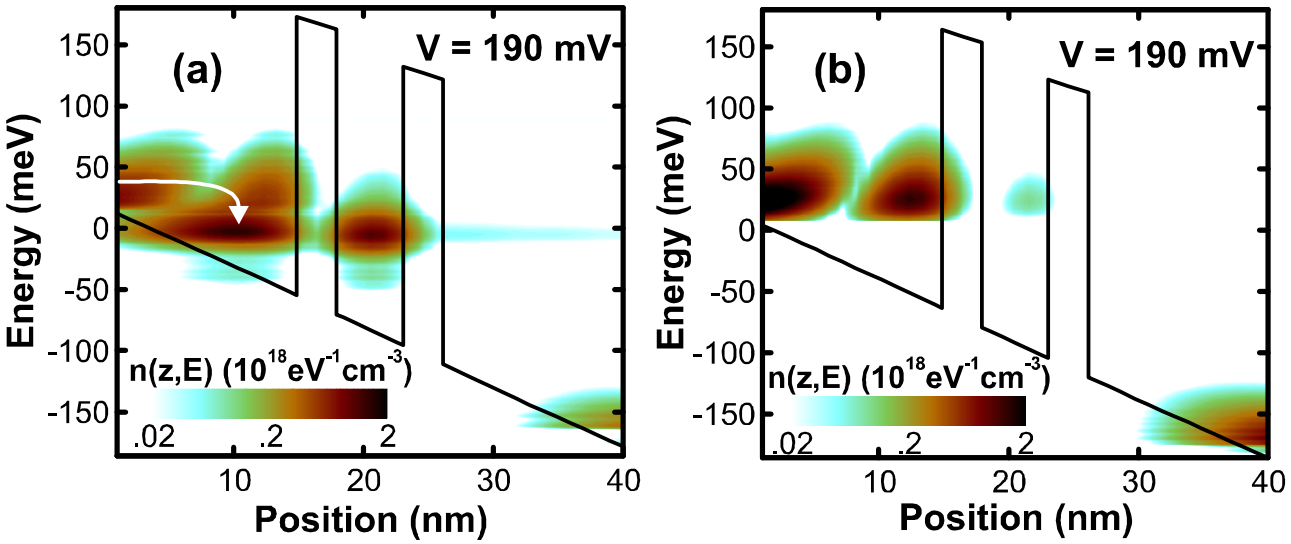

Figure 4.3.2: (a) Conduction band profile of the GaAs/$Al_{.3}Ga_{.7}As$ resonant tunneling structure of Fig. 4.3.1, plotted at the bias voltage of 190 mV. The energy resolved electron density is shown as a contour plot. The arrow is meant to guide the eye and shows the trapping of electrons into the triangular quasi-bound state in front of the barriers. (b) same as in (a), but any incoherent scattering is ignored and the triangular quasi-bound state in front of the barriers remains empty.

matches the one of the ballistic calculation. However, elastic scattering reduces the lifetime of the resonant state and thereby reduces the "sharpness"of the resonance condition. In this way, the peak of the *I-V* characteristic gets broadened and reduced compared to the ballistic result.

Above approximately 150 mV applied bias, the conduction band edge of the source lies clearly higher in energy than the resonance energy E_{RTD} of the RTD state. Then, the kinetic energy in the growth direction $E_z = E + \hbar^2 k_{\|}^2/2m^*$ of all electrons in the source exceeds the resonance energy E_{RTD}. Consequently, the ballistic current is strongly suppressed at this voltage. In contrast, when elastic scattering with phonons and impurities is included, the electronic momentum can be changed. In particular, the energy difference of the electron motion in growth direction E_z and the RTD state energy E_{RTD} ($E_z - E_{RTD} > 0$) can be shifted into the in-plane electronic momentum. Thereby, some electrons are accelerated with respect to their in-plane motion and, more importantly, their energy in growth direction is reduced accordingly. In this way, elastic scattering increases the number of electrons with a kinetic energy in growth direction that matches the resonant energy of the RTD ($E_z = E_{RTD}$). Thereby, initially off-resonant electrons can efficiently tunnel through the RTD state after they have elastically scattered with phonons and/or impurities. For this reason, the valley current of NEGF calculations including elastic scattering significantly exceeds the valley current of ballistic calculations (see Fig. 4.3.1).

Conclusion

In summary, the transport characteristics of simple resonant tunneling diodes (RTD's) require for the inclusion of energy dissipation and momentum randomization. Otherwise, neither the calculated resonant voltages and the peak current densities nor the valley current densities are

reliable. Since every quantum device can be regarded as a sequence of quantum wells and RTD's, we can generalize this result: Any confined state that either influences charge transport by electrostatic repulsion (as shown in [119]) or by introducing specific resonance conditions, requires for a transport model that carefully includes energy dissipation as well as (depending on the device dimensionality) momentum randomization. Only if the device lacks any confined state, as e.g. in the $n^{++} - i - n^{+}$ device of Sec. 4.2.3, ballistic calculations may indeed yield realistic results. Nevertheless, we will find in Sec. 5.3.2 an exception to this rule, i.e. low doped THz quantum cascade lasers biased at a specific voltage. In these particular situations, most of the current is carried by a single delocalized state. Then, results of a ballistic calculation indeed approach results of calculations including energy dissipation. However, such coincidences are hard to predict without full calculations. In general, a careful inclusion of all inelastic and elastic processes is essential to capture all physical mechanisms that determine the charge transport.

4.3.3 Pauli blocking

Introduction

Inelastic scattering mechanisms such as the scattering with polar optical phonons involve the lesser Green's function in the formula for the retarded self-energy (see Eq. (3.5.11)). In consequence, the Dyson and Keldysh equations are coupled via the scattering self-energies and we have to solve for the lesser Green's functions and self-energies self-consistently with the solution of the retarded functions. Lake *et al.* have suggested in [22] to neglect any term in the formula of $\mathbf{\Sigma}^R$ that contains $\mathbf{G}^<$ and thereby to decouple the solution for the retarded functions from the calculation of the lesser functions. This approximation reduces the amount of storage and time consumption tremendously. However, Lake *et al.* have mentioned that this approximation violates Pauli blocking and is therefore only applicable on devices with low electron densities. Since it has not been done in literature, we analyze the violation of the Pauli blocking *quantitatively* and present a concrete density limit up to which this approximation may indeed be applied.

Assessment

We have performed an exact as well as an in the way suggested in [22] decoupled NEGF calculation of a GaAs/$In_{.14}Ga_{.86}As$ quantum well. The total length of the device is 50 nm with 16 nm intrinsic region embedded in between two 17 nm n-doped regions with $n = 10^{18}$ cm^{-3} each. Within the intrinsic region, there is a 12 nm $In_{.14}Ga_{.86}As$ quantum well of 150 meV depth. In equilibrium, Eq. (2.2.15) holds and we can extract a function f that has to equal the electron distribution

$$f\left(z, k_{\parallel}, E\right) \equiv -iG^{<}\left(z, z, k_{\parallel}, E\right) / A\left(z, z, k_{\parallel}, E\right) \stackrel{!}{=} f\left(E, \mu\right). \tag{4.3.1}$$

In fact, it turns out that the imaginary part of $f\left(z, k_{\parallel}, E\right)$ vanishes and its real part is independent of $k_{\parallel}$. However, f is only independent of z in the exact calculation, i.e. when the coupling between lesser and retarded functions is fully accounted for. This can be understood from Fig. 4.3.3, which shows the Fermi distribution (grey dots) and the real part of the function $f\left(z, k_{\parallel}, E\right)$ in the exact (full line) and the approximated (dashed line) calculation in the middle of the $In_{.14}Ga_{.86}As$ quantum well. The zero in energy marks the chemical potential of the device. The calculation including the full coupling of $\mathbf{G}^R$ and $\mathbf{G}^<$ perfectly reproduces

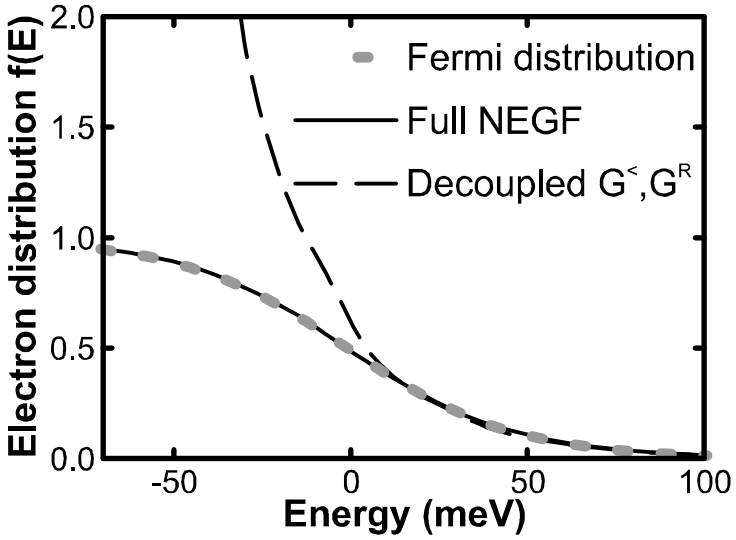

Figure 4.3.3: Equilibrium electron distribution of a 12 nm wide GaAs/$In_{.14}Ga_{.86}As$ quantum well at 300 K calculated with fully self-consistent NEGF (full line) and with decoupled retarded and lesser Green's functions (dashed). The zero of energy is the chemical potential. The full NEGF result faithfully yields the Fermi distribution (grey dots), in contrast to the decoupled model that violates the Pauli principle.

the Fermi distribution, whereas the result of the decoupled calculation differs from the Fermi distribution significantly. It even exceeds the limit of 1 at energies that correspond to highly occupied states. Since we assume a Fermi distribution in the leads, this difference decreases towards the boundaries and creates the spatial inhomogeneity of f in the approximated solution of $\Sigma^<$. The physics behind this approximation can be understood in Fig. 4.3.4. It shows results for a homogeneously n-doped GaAs device at room temperature in equilibrium, where, for an easier comparison, only scattering with polar optical phonons is included. We have already seen in Fig. 3.5.2 that the scattering rate of the fully coupled calculation agrees nicely with Fermi's Golden rule. For comparison, those scattering rates resulting from the exact NEGF calculation (black dotted) and resulting from the Fermi's Golden rule (gray dotted) are also given in Fig. 4.3.4. In addition, the black solid line in Fig. 4.3.4 depicts the scattering rate that results from an approximated NEGF calculation with $\mathbf{G}^R$ and $\mathbf{G}^<$ decoupled as described above. It agrees with the gray line that shows the scattering kernel for electrons scattering with polar optical phonons, i.e. the scattering rate without the occupancy factor of the final states. Obviously, only the contributions of $\mathbf{G}^<$ in the formula of $\mathbf{\Sigma}^R$ are responsible for the Pauli blocking. These contributions account for the hole-like scattering in heavily doped semiconductor conduction bands (described in [10]) and prohibit the filling of the electronic states beyond the Fermionic limit.

Conclusion

Figure 4.3.3 shows that the decoupling of inelastic retarded self-energies from $G^<$ is only applicable when the occupation of all relevant electronic states is smaller than approximately 0.3. Otherwise, many particle effects such as hole-like scattering in the conduction band and the Pauli blocking become relevant. Even when the state occupancy is beneath this limit, the re-

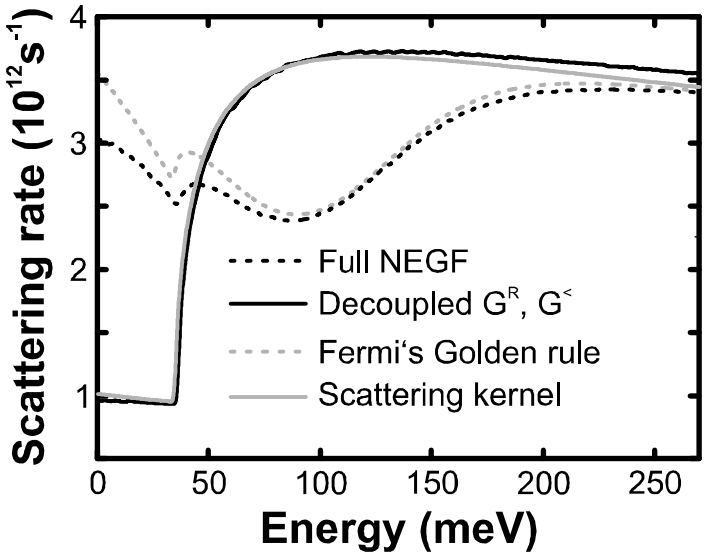

Figure 4.3.4: On-shell scattering rate of electrons scattered by screened polar optical phonons in homogeneous n-doped GaAs at 300 K. The doping concentration is 2×10^{18} cm^{-3} and the screening length is set to 5 nm for comparison. The result of a decoupled calculation of G^R and $G^<$ (black solid line) matches the scattering kernel of Fermi's Golden rule, i.e. the scattering rate without occupation factors (gray solid line). The result from a full NEGF calculation (black dotted line) agrees nicely with Fermi's Golden rule (grey dotted line).

tarded Green's functions and accordingly the retarded self-energies are influenced by the lesser Green's function via the Poisson potential. Only in faintly doped devices such as some THz-QCLs discussed in this thesis, the solution of the retarded self-energies completely separates from the solution of $\mathbf{G}^<$. Nevertheless, we do not apply this approximation in calculations of other sections than this one.

We have to mention an exception of the finding in this section, i.e. the approximated inelastic self-energy with longitudinal acoustic phonons in Eq. (3.5.28). Due to the symmetry of the energy averaged Green's functions in this self-energy, the contributions of $\mathbf{G}^<$ to the retarded self-energy cancel. In this case, the retarded self-energy is naturally independent of $\mathbf{G}^<$ while the Pauli blocking is obeyed.

4.3.4 Scattering correlations

Introduction

Weber *et al.* have shown in [142] for THz quantum cascade lasers that non-diagonal entries of the density matrix represented in a basis of Wannier-Stark states have significant influence on stationary observables such as current density and optical gain. The relevance of non-diagonal elements is important for any numerical implementation of scattering self-energies, since non-diagonal self-energies increase the numerical load in the calculation of Green's functions and self-energies significantly [143]. In particular, the numerically very efficient recursive algorithms for the determination of Green's functions (see e.g. [22, 104]) become inefficient if non-diagonal scattering has to be included. In this section, we add to the finding of Weber *et al.* that in the spatial representation non-diagonal entries of the scattering self-energies, i.e. nonlocal

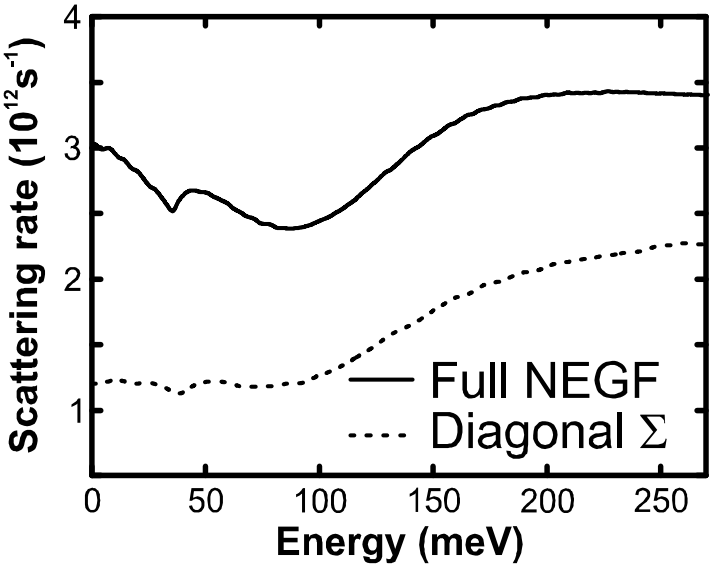

Figure 4.3.5: On-shell scattering rate of electrons scattered by screened polar optical phonons in the same situation as in figure Fig. 3.5.2. The scattering rate resulting from the calculation with a diagonal self-energy (dashed line) is much lower than in a full NEGF calculation (full line).

scattering also significantly contribute to the stationary physics and may not be neglected. We find rough estimates for the limits of the nonlocal range of scattering in weakly confined devices as well as in quantum cascade structures. In order to ensure realistic scattering, however, we implement the full nonlocal scattering range in all vertical transport calculations in this thesis.

Assessment - homogeneous systems

Most of the scattering potentials in the formulas for the scattering self-energies in Sec. 3.5 do not vanish for finite distances between the two spatial coordinates z and z'. In addition, the ballistic Green's functions in weakly confined systems decay relatively slowly with $z-z'$ (see Fig. 3.6.1). Consequently, the effective range of the scattering self-energies may expand over relatively large distances. Nevertheless, it is a common approximation in open systems to assume spatially diagonal self-energies [132, 133, 144]. We analyze the effect of this approximation in the case of electron scattering with polar optical phonons in the homogeneously n-doped GaAs device, that has already been analyzed in Figs. 3.5.2 and 4.3.4. Figure 4.3.5 shows results for the scattering rate in the case of a full nonlocal implementation of the scattering with polar optical phonons (full line) and results, where only on-site elements (at a lattice spacing of 1 nm) are accounted for (dotted line). Obviously, the nonlocal elements, i.e. entries of the scattering self-energy with $z \neq z'$, contribute significantly to the scattering rate. This result is consistent with similar findings of Klimeck *et al.* in [143] for resonant tunneling diodes. In order to quantify these contributions, Fig. 4.3.6 illustrates the $k_{\|}$-integrated retarded self-energy as a function of the distance between the two propagation coordinates z and z' in the case of electrons scattered with LO-phonons in homogeneous GaAs at the energy of $E = 0.15$ eV relative to the conduction band edge. Both, the imaginary (black) as well as the real part (gray) of the retarded self-energy extend over almost 10 nm in the difference of the propagation coordinates.

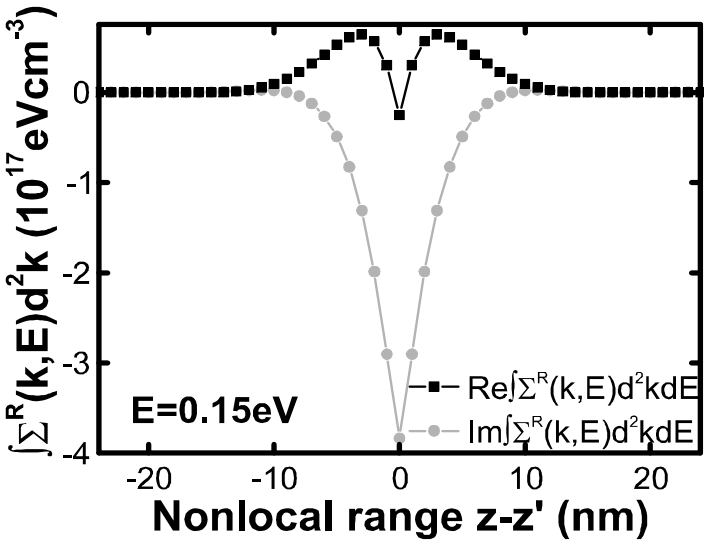

Figure 4.3.6: Real (gray) and imaginary (black) part of the retarded self-energy for electronic scattering with polar optical phonons in homogeneous GaAs at room temperature. The self-energy is integrated over the in-plane momentum $k_{\|}$ at an energy $E = 0.15$ eV and given as a function of the difference of the two propagation coordinates $z - z'$. The electrostatic screening length is set to 5 nm for comparison. The lines are meant to guide the eyes.

We find very similar results for the scattering at charge impurities. Thus, in order to cover all relevant scattering events, we extend the implemented nonlocal range of the self-energies in weakly confined systems to approximately twice the device screening length.

Assessment - multiquantum well devices

The screening length in faintly doped devices with many confined states such as THz-QCLs can reach values comparable with the length of the explicitly calculated device. Fortunately, the confining barriers in these devices efficiently limit correlations across one or several device barriers. This is illustrated in Fig. 4.3.7. It shows the calculated retarded self-energy for the scattering with polar optical phonons in the 6.6 nm wide quantum well of the GaAs/$Al_{.15}Ga_{.85}$As QCL of Ref. [122] at a lattice temperature of 40 K and a voltage of 50 mV per period. As can be seen in this figure, the nonlocal range of the self-energy is effectively limited within a single quantum well, in spite of a large Debye screening length of 26 nm that results from the low average electron density in this device. Lee *et al.* have shown in [41] that the current density of THz-QCLs in a position eigenfunction representation is well described with on-site scattering self-energies. Since the spatial discretization in [41] contains only one or two spatial eigenfunctions per quantum well, their statement coincides with our results.

Alternative representations

We have seen with their nonlocal range that the scattering self-energies represented in spatial eigenfunctions couple many different basis functions (i.e. grid points). This is undesirable, because it increases the numerical load. Thus, several approaches can be found in literature that avoid the spatial eigenfunction representation and attempt to (partly) diagonalize the Green's

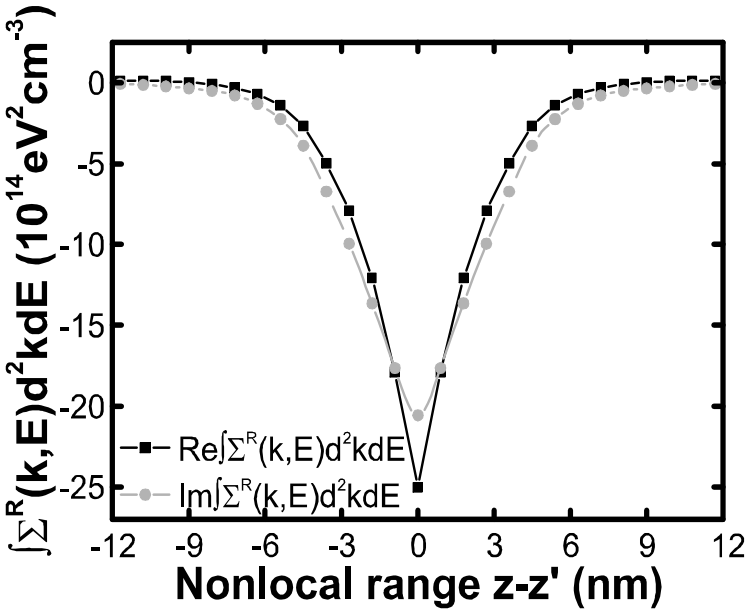

Figure 4.3.7: Real (gray) and imaginary (black) part of the retarded self-energy for electronic scattering with polar optical phonons in the central quantum well of the THz-QCL of Ref. [122] at 40 K and 50 mV bias per period. The self-energy is integrated over the in-plane momentum $k_{\|}$ and energy E and it is given as a function of the difference of the two propagation coordinates $z - z'$. The low electron density in the device results in a Debye screening length of 26 nm. The lines are meant to guide the eyes.

functions and self-energies. They either represent the Green's functions in eigenfunctions of the Hamiltonian of the ballistic isolated device [40, 45] or (in the case of multi dimensional problems) by applying a separation ansatz for systems with confining potentials perpendicular to a propagation direction, i.e. a mode-space approach [7, 145]. Both approaches offer a great reduction of the numerical load during the determination of the Green's functions. The separation ansatz reduces the system's dimensionality, while the eigenfunction representation allows for the reduction of the number of basis states. However, the mode-space approach fails if the electronic propagation is not collinear but is scattered (coherently or via scattering self-energies) into different spatial directions [146]. The Green's functions in the eigenfunction representation become increasingly non-diagonal, when the actual electronic states deviate significantly from the basis functions as is the case in open systems [147] or in the presence of scattering transitions between the basis states [41]. One also has to be aware of the fact that depending on how many basis states are neglected in this approach, spatially resolved information in the interior of the devices may become inaccurate (see [41, 147]). Since such spatial information usually ease the interpretation of I-V characteristics significantly (see e.g. Sec. 5.3), the loss of this information may be very undesirable.

Conclusion

Although the spatial representation may be numerically inefficient, it offers reliable spatial information in the total considered device and limits the non-diagonality of the scattering self-energies in a physically comprehensible manner. Nevertheless, the non-diagonal contributions

of the scattering self-energies are essential in this representation. A neglect of non-diagonal elements of the scattering self-energies has to be compensated e.g. with a scaling of the remaining diagonal elements, as has been done in [143]. However, such a scaling is problematic, when the non-local range of the scattering self-energies is unknown. We find only clues for this range in the cases of narrow quantum wells and nearly homogeneous devices. If the system under consideration is in between these limits, e.g. consists of broad quantum wells (comparable with the screening length), the effective range of the nonlocal scattering self-energies is hard to predict. In order to avoid numerical artifacts in this thesis, we implement the scattering self-energies with their full nonlocal behavior.

4.3.5 Momentum dependence of scattering self-energies

Introduction

Most of the computational time of our algorithm is spent on the calculation of the scattering self-energies. In particular, the self-energy integrals over the in-plane momentum that depend on one or several additional parameters such as the initial in-plane momentum, initial energy, or the two propagation coordinates (see e.g. Eq. (3.5.52)) are numerically demanding. We analyze in this section how strongly the scattering self-energies depend on details of the in-plane momentum. Basically two different approaches can be found in literature that simplify the momentum dependence of the scattering self-energies. The first approach just simplifies the momentum dependence of the self-energies, while the second approach goes beyond and approximates the total self-energy with a predefined function. We analyze the second approach in the next section and introduce here the frequently applied scheme of Wacker *et al.* to evaluate the scattering potentials at "typical"in-plane momenta. We show that such typical momenta critically depend on the device details. In order to choose these typical momenta correctly, we determine the scattering self-energies with averaged scattering potentials, instead. In this new scheme, we show that the approximated results quite well reproduce results of calculations including exact self-energies. Thus, we find in summary that the in-plane dependence of the scattering self-energies may indeed be approximated. However, the typical momenta have to chosen very carefully. Our approach of averaged scattering potentials guarantees the correct typical momenta, but does not give a numerical advantage against the exact calculation.

Assessment

Wacker *et al.* have introduced in [148] a numerically very efficient approximation for the scattering self-energies in superlattices. They ignore any dependence of the coupling matrix elements on the in-plane momentum and evaluate these elements at "typical"initial and final in-plane momenta k_{typ} and l_{typ}. In this approach, e.g. the retarded self-energy for the interaction with charged impurities (compare with Eq. (3.5.52)) simplifies to [45]

$$\Sigma^R\left(z,z',k_\parallel,E\right) = V\left(z,z',k_{\mathrm{typ}},l_{\mathrm{typ}}\right)\int \mathrm{d}l_\parallel l_\parallel G^R\left(z,z',l_\parallel,E\right). \tag{4.3.2}$$

The remaining integral over the in-plane momentum of the Green's function does neither depend explicitly on the spatial coordinates nor on an initial energy or momentum. Obviously, once this integral is performed it can be used for all in this way approximated self-energies which results in a tremendous saving of computational time. However, there are several drawbacks of this approximation.

First, in this approximation, distinct scattering mechanisms differ only in the coupling constant $V\left(z,z',k_{\mathrm{typ}},l_{\mathrm{typ}}\right)$. In particular, they exhibit similar scattering kernels with the same energy dependence. Second, the shape of the approximated scattering self-energies essentially agree with the on-site scattering self-energy of longitudinal acoustic phonons in Sec. 3.5.3. Thus, the scattering kernel of the self-energy in Eq. (4.3.2) can only deviate from the scattering kernel given in Fig. 3.5.4 due to nonlocal scattering events (proportional to $V\left(z,z',k_{\mathrm{typ}},l_{\mathrm{typ}}\right)$ for $z\neq z'$). Such nonlocal events are typically less likely than the on-site scattering (see Figs. 4.3.6 and 4.3.7). Therefore, this approximation may underestimate scattering for electrons with low and overestimate scattering for electrons with high kinetic energies, when e.g. applied on scattering with charge impurities (compare Figs. 3.5.9 and 3.5.4) or polar optical phonons (compare Fig. 3.5.2 and 3.5.4), whereas scattering with acoustic phonons is naturally well described within this approximation. Third, the quality of this approximation depends critically on the chosen values of typical in-plane momenta $(k_{\mathrm{typ}},l_{\mathrm{typ}})$. In order to illustrate this, we consider the scattering potentials for polar optical phonon (pop) and charged impurity (imp) scattering

$$V_{\mathrm{pop}}\left(z,z',k_{\parallel},l_{\parallel}\right) \equiv \int_0^{2\pi}\mathrm{d}\theta\frac{\mathrm{e}^{-\sqrt{q_{\parallel}^2+\xi^{-2}}|z_3-z_4|}}{\sqrt{q_{\parallel}^2+\xi^{-2}}}\left(1-\frac{\xi^{-2}\left|z_3-z_4\right|}{2\sqrt{q_{\parallel}^2+\xi^{-2}}}-\frac{\xi^{-2}}{2\left(q_{\parallel}^2+\xi^{-2}\right)}\right), \tag{4.3.3}$$

$$V_{\mathrm{imp}}\left(z,z',k_{\parallel},l_{\parallel}\right) \equiv \int_0^{2\pi}\mathrm{d}\theta\frac{\left|z_3-z_4\right|+1/\sqrt{q_{\parallel}^2+\xi^{-2}}}{q_{\parallel}^2+\xi^{-2}}\mathrm{e}^{-\sqrt{q_{\parallel}^2+\xi^{-2}}|z_3-z_4|}, \tag{4.3.4}$$

with

$$q_{\parallel}^2=k_{\parallel}^2+l_{\parallel}^2-2k_{\parallel}l_{\parallel}\cos\theta. \tag{4.3.5}$$

These functions are part of the integrand in the formulas for the self-energies in Eqs. (3.5.10) and (3.5.52). In our representation, these are the functions that have to be approximated in the approach of Wacker *et al.* They vary significantly with $k_{\parallel}$ and - due to the symmetry - with $l_{\parallel}$, as is illustrated in Fig. 4.3.8 for typical scattering events in GaAs. Obviously, a mistake in the choice of the tuple $(k_{\mathrm{typ}},l_{\mathrm{typ}})$ leads to significantly over- or underestimated scattering strengths. The current in different devices with different transport characteristics is carried by charge carriers of different (averaged) energy and momenta. According to the momentum dependence of the scattering potentials, the scattering probability of these carriers differs strongly. Thus, a proper choice of $(k_{\mathrm{typ}},l_{\mathrm{typ}})$ for the typical scattering strength has to be redone for every device and every applied voltage (see also [149]).

In order to simplify the assessment of momentum independent scattering potentials, we introduce a similar but device independent approximation. Instead of approximating the coupling potentials with their values at typical in-plane momenta, we take the average of the coupling potentials $V\left(z,z',k_{\parallel},l_{\parallel}\right)$ with respect to $k_{\parallel}$ and $l_{\parallel}$. Apart from the scattering with longitudinal acoustic phonons, all coupling potentials vanish in the limit of infinite transferred in-plane momenta $\lim_{|k_{\parallel}-l_{\parallel}|\to\infty}V\left(z,z',k_{\parallel},l_{\parallel}\right)=0$. Consequently, our approximation (as well as the one of Wacker *et al.* [148]) tends to underestimate scattering for electrons with low energies (and small values for $\left|\vec{k}_{\parallel}-\vec{l}_{\parallel}\right|$) while it overestimates scattering otherwise. This is illustrated in Fig. 4.3.9 which depicts the scattering rate for electrons interacting with polar optical phonons in bulk GaAs with the device parameters of Fig. 3.5.2. The solid line depicts the realistic scattering rate resulting of Eq. (3.5.11) which has been shown in Fig. 3.5.2 to nicely agree with Fermi's

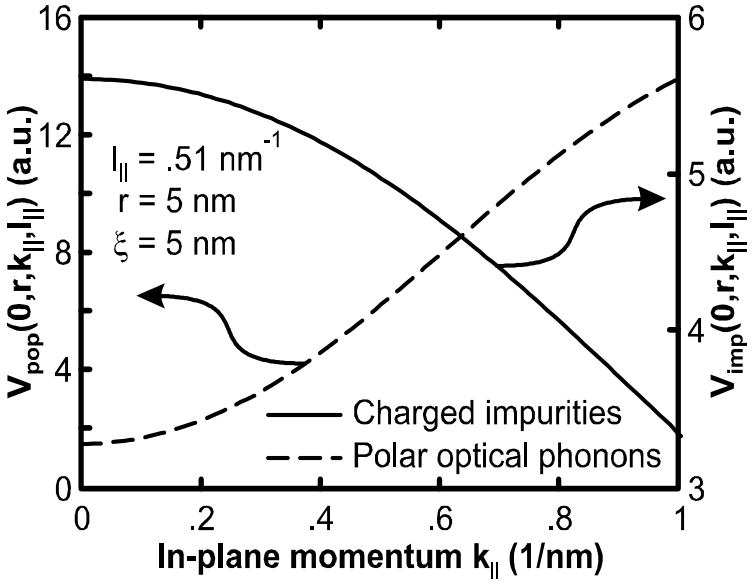

Figure 4.3.8: Scattering potentials for charged impurities (solid) and polar optical phonons (dashed) at an in-plane momentum $l_{\|} = 0.51$ nm^{-1} as functions of the in-plane momentum $k_{\|}$. The difference of the two propagation coordinates r and the screening length ξ are set to 5 nm.

Golden rule. The dashed line shows the result, when the scattering potential is averaged over $k_{\|}$ and $l_{\|}$.

The neglect of the momentum dependence of the scattering self-energies is mainly applied on charge transport in QCLs [45, 150]. Therefore, we analyze the approximation of momentum averaged coupling potentials on the electron transport in the GaAs/Al$_{.15}$Ga$_{.85}$As THz-QCL of Ref. [122]. The solid line in Fig. 4.3.10 shows the I-V characteristics of this THz-QCL at a temperature of 40 K and a sheet doping density of 1.9×10^{10} cm^{-2}. The dashed line shows results of the same device, but with the scattering self-energies approximated in the manner described above. The larger the applied bias voltage is, the higher is the average electron energy in the device and the more is the incoherent scattering overestimated by the momentum average of the scattering potentials. We will show in Sec. 5.3.2 that incoherent scattering mainly enhances the current density in THz-QCLs. For this reason, the current density at higher voltages in Fig. 4.3.10 that results from NEGF calculations with approximated self-energies exceeds the current density resulting from an exact implementation of momentum dependent scattering.

Conclusion

The numerical implementation of the scattering self-energies given in this thesis is numerically very demanding. An extension of the NEGF formalism including self-energies of the kind in Sec. 3.5 on higher dimensional systems, such as two-dimensional electron gases or multi-band transport is for the state of the art hardware numerically unfeasible. Further approximations are necessary to circumvent the limitation on quasi one-dimensional systems. However, as we have detailed in this subsection, any approximation on the momentum and energy dependence of the scattering potentials has to be done with great care in order to avoid artificial results that may even prohibit qualitative statements. In summary, we agree with findings of Schmilau and Pereira [149] that an approximation of typical in-plane momenta as suggested by Wacker

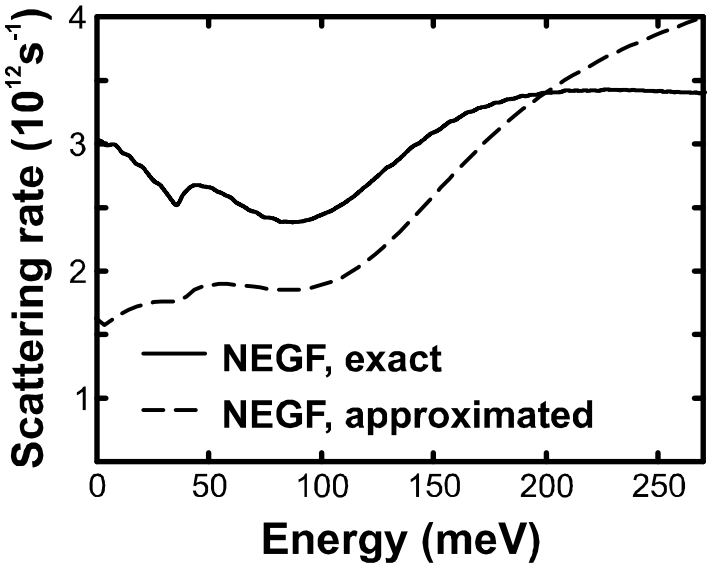

Figure 4.3.9: On-shell scattering rate of electrons by screened polar optical phonons in the same situation as in figure Fig. 3.5.2. The approximation of momentum independent scattering potentials (dashed) undestimates scattering for electrons with small and overestimates scattering for electrons with large energies. We have already shown in Fig. 3.5.2 that the exact calculation (solid) nicely reproduces Fermi's Golden rule.

et al. [148] has to be redone for every individual device. The average of the scattering potential introduced in this section is a first step towards an "automated"finding of the momentum independent scattering potential. However, it still requires for an integral over the initial and final momenta and does not provide numerical benefit. Nevertheless, this new approach yields similar *I-V* characteristics for THz-QCLs as exact implementations of the scattering self-energies.

4.3.6 Büttiker probes

Introduction

A numerically very efficient approximation has been introduced by Büttiker [139] and frequently implemented in literature [47, 119, 145, 151]. We give a brief introduction into the Büttiker probe scattering model and discuss its advantages and disadvantages. In particular, we compare results of NEGF calculations including exact scattering self-energies with calculations of the Büttiker probe model. We illustrate that the Büttiker probe model overestimates the thermalization of subband distributions and misses the correct energy dependence of scattering. Depending on the actual device structure, the Büttiker probe model yields state occupancies that qualitatively deviate from realistic results.

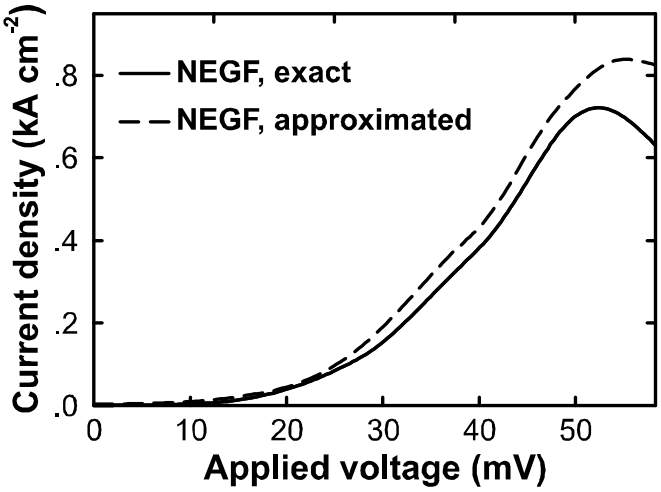

Figure 4.3.10: Current density versus applied bias voltage per period of the GaAs/$Al_{.15}Ga_{.85}As$ QCL of Ref. [122] at 40 K lattice temperature and a sheet doping concentration of 1.9×10^{10} cm^{-2}. The current density resulting from momentum averaged scattering potentials exceeds the current of an exact implementation of the scattering self-energies.

Scattering model

In the Büttiker probe model, any incoherent scattering of device electrons is modelled with artificial contacts within the device - so called Büttiker probes (compare with Eq. (3.6.8))

$$\Sigma^R\left(z, z', k_\parallel, E\right) = -c\frac{\hbar^2}{2m^*\Delta^2}\delta\left(z - z'\right)\exp\left[ik_z\left(z, k_\parallel, E\right)\Delta\right]. \tag{4.3.6}$$

Here, c is a nonvanishing dimensionless constant $c \in \mathbb{R}$, the homogeneous spatial grid resolution is given by Δ and the substitution k_z is similar to Eq. (3.6.9)

$$\begin{aligned} k_z\left(z, k_\parallel, E\right) = &\sqrt{2m^*\left(z, E\right)/\hbar^2} \\ &\times\sqrt{E - V\left(z\right) - e\phi\left(z\right) - \frac{\hbar^2 k_\parallel^2}{2m^*\left(z, E\right)}}. \end{aligned} \tag{4.3.7}$$

In addition to the approximation of energy and momentum independent scattering potentials in Sec. 4.3.5, this approach also approximates the Green's functions in the formulas for the self-energies. Alternative but similar approaches use energy dependent Büttiker probe parameters $c(E)$ [136, 152] or completely constant retarded self-energies [111, 147, 153]. The energy dependent probe parameters are particularly interesting, since they can be fitted in order to reproduce certain scattering rates. Nevertheless, all of these approaches have in common, that the lesser self-energy is assumed to be a product of the imaginary part of the retarded self-energy and a Fermi distribution - as is also assumed for the contact self-energies in this thesis (see Eq. (3.6.17)). The chemical potentials of the respective Fermi distributions in those artificial leads are determined such that the current is conserved (see Eq. (3.5.114)).

These approximated scattering self-energies offer several numerical advantages. First, the iterations between the Green's functions and self-energies which are required in the self-consistent Born approximation are avoided. Second, the Büttiker probe self-energies represent inelastic

scattering mechanisms and once they are implemented, efficient energy dissipation is accounted for. In contrast to our findings for realistic scattering self-energies in Sec. 4.3.3, the retarded Büttiker probe self-energy is independent of the lesser Green's function. Still, the highest state occupancy is limited by 1, because the electron distributions in the artificial leads are already (limited) Fermi distributions. Finally, the absolute value of the probe parameter c is a convenient "turning knob"with which the transport in any device can be tuned from ballistic to diffusive (as e.g. done in [139]).

Assessment

Scattering strength Unfortunately, these numerically very appealing advantages can also be regarded as disadvantages in many circumstances as we now point out. The first issue arises when we implement Eq. (4.3.6): What value (or function in E) is to be chosen for c? We have seen in Sec. 4.3.4 that the contributions of nonlocal scattering events to the total scattering rate depends on device parameters. That is the reason why Klimeck *et al.* used in [143] *device dependent* scaling factors to compensate discrepancies of their local scattering model to the realistic non-diagonal self-energies. Similar findings have been given in [149] concerning the approximation of Wacker *et al.* of momentum independent scattering potentials (see Sec. 4.3.5). The approximation in Eq. (4.3.6) goes clearly far beyond those two approximations. Thus we expect NEGF calculations with Büttiker probe self-energies to yield "only"qualitative results. Since the Büttiker probe self-energy is a local scattering self-energy, the parameter c directly determines the scattering rate. In homogeneous devices, such self-energies exhibit sinusoidal scattering rates

$$\Gamma(E) \propto c \sin\left(\sqrt{2m^*(E)\,E/\hbar^2}\Delta\right). \tag{4.3.8}$$

Thus, one may either estimate the probe parameter c from a mobility (see e.g. [132]) or from exact NEGF calculations of appropriate, numerically efficient test samples.

Resonances in the spectral function The missing self-consistency between the Green's functions and the self-energies prohibits a realistic inclusion of resonant scattering such as the scattering between different confined states or resonant phonon energies. In particular, when the retarded self-energy has the shape of Eq. (4.3.6) or equals a constant, the electrons scatter as if their target states are part of a continuum irrespective of the actual device structure. Depending on the scattering strength, this yields an overestimated density of states in the gap between successive confined states or subbands. Therefore, Eq. (4.3.6) should only be applied on devices with hardly any confined states - as is typically done in literature. In systems with many confining barriers such as quantum cascade structures, one should at least mimic confined states within the Büttiker leads, e.g. with Lorentzian functions.

State occupancy far from equilibrium Another issue becomes important when the system under consideration is driven far from equilibrium. Then, the occupancies of the electronic states deviate significantly from a simple Fermi distribution. In this case, the Fermi distributions in the artificial leads of the Büttiker probe model may even fail qualitative predictions. An example of such a situation is illustrated in Fig. 4.3.11. It shows a contour plot of the energy and spatial resolved electron density $n(z, E)$ of the quantum well of Fig. 4.3.3 at a bias voltage of 200 meV. For the purpose of an easier comparison, we have neglected shifts of the Fermi distributions in the leads that would complicate the estimate of Fermi distributions within the

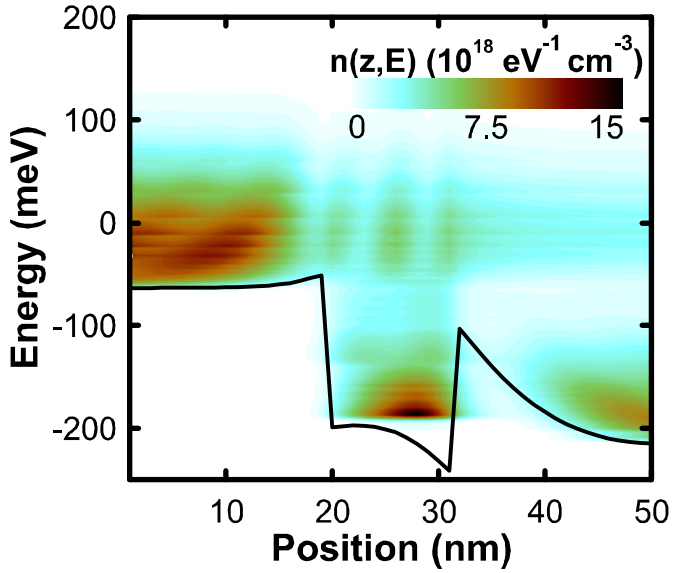

Figure 4.3.11: Contour plot of the energy and spatially resolved density $n(z, E)$ of the quantum well of Fig. 4.3.3 at a bias voltage of 200 mV. The solid line indicates the self-consistent potential profile which drops by 150 meV within the device due to the equilibrium electron distributions that are used in this calculation. The zero in energy marks the chemical potential of the source.

device. Instead, we have applied the commonly used lead model, i.e. flatband conditions for the Poisson equation and equilibrium electron distributions in the leads (see also Sec. 4.2.3). This results in a self-consistently determined conduction band difference of 150 meV (solid line in Fig. 4.3.11). The zero in energy marks the chemical potential of the source. The maxima of $n(z, E)$ within the quantum well clearly illustrate three resonant states. Obviously, the third state at the confinement energy of $E_3 = -57$ meV gets coherently filled with electrons originating from the source. These electrons emit a sequence of up to three LO-phonons and thereby occupy the second (at $E_2 = -131$ meV) and the first quantum well state (at $E_1 = -186$ meV). In addition, the first state leaks into the drain sided barrier and thereby gets occupied by electrons originating from the drain. Due to the different filling mechanisms, the occupation of the three well states differ significantly from each other.

We have introduced in Eq. (4.3.1) the formula for the distribution function in equilibrium. In order to illustrate the state occupancy of the quantum well in Fig. 4.3.11, we assume that the distribution function in nonequilibrium is also given by Eq. (4.3.1). Of course, the resulting function f may not be literally taken as the state occupancy, since it is depending on the spatial coordinate z. Nevertheless, it is an instructive function that is "strongly related"to the state occupation and it is useful for a comparison between results including self-energies given in Sec. 3.5 and results of the Büttiker probe model.

For the purpose of such a comparison, Figs. 4.3.12 (a) and (b) show the function f at $z = 28$ nm for the three quantum well states of Fig. 4.3.11 as a function of the electronic energy E. Thereby, the in-plane momentum is depending on the confinement energy E_i and the total energy E

$$k_{\parallel} = \sqrt{2m^* (E - E_i)/\hbar^2}, i = 1, 2, 3. \tag{4.3.9}$$

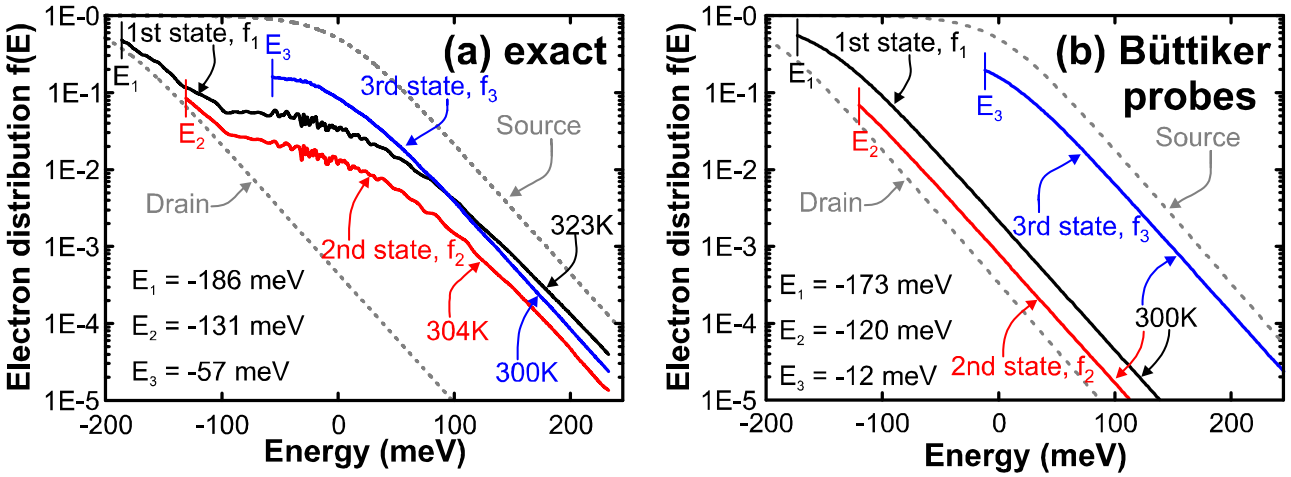

Figure 4.3.12: Approximative electron distribution in the first (black), second (red) and third (blue) state of the quantum well of Fig. (4.3.11) at the position $z = 28$ nm and 300 K lattice temperature. The gray dotted lines depict the Fermi distributions of the source and drain lead and are given for comparison. (a) Results of NEGF calculations including the self-energies of Sec. 3.5 in the self-consistent Born approximation. The temperatures for the confined states (first state: 323 K, second state: 304 K, third state: 300 K) have been extracted from fitted Fermi distributions. (b) Distribution functions resulting from NEGF calculations with Büttiker probes of the kind of Eq. (4.3.6). The Büttiker probe data are taken from [154] with kind approval of P. Greck.

Thus, the function f_i illustrates* the in-plane electron distribution of the quantum well state i. Figure 4.3.12 (a) shows the functions f_i resulting from a NEGF calculation including the rather exact self-energies given in Sec. 3.5. We have seen above that the third well state gets efficiently filled by the source. For this reason, the electron occupancy f_3 of the third state (blue) can be very well fitted with the Fermi distribution of the source (gray dotted) divided by a factor of 5. This factor comes about by two mechanisms. First, in a ballistic calculation, the electrons of the third state can leave the device via the drain while no electrons from the drain enter this state according to the low lying chemical potential of the drain. In this case, this state is only half as much filled as the electronic states of the source. Second, when energy dissipation is included, the electrons of the third state additionally scatter into the second and first well state. In the situation of Fig 4.3.12, these additional losses reduce f_3 by another factor of 2.5. The second and the first well states are accordingly higher occupied than the Fermi distribution of the drain (see Fig. 4.3.12 (a)). In particular, the functions f_1 and f_2 show a "bump"at the energy of -93 meV. Here, the occupancy of both states significantly deviate from the Fermi distribution of the drain. The energy of -93 meV equals the confinement energy E_3 of the third state minus the energy of one LO-phonon. Thus, this "bump"is generated by electrons from the third well state that emit one LO-phonon and enter the first and second well state. Since the lower two states are only weakly confined, the probability for electrons of these two states to leave the device is larger than to emit additional phonons and thermalize further.

The comparison of the high energy behavior† of the functions f_i with the Fermi distribution

*Or better: "is strongly related to".

†We have fitted Fermi distributions to the function f for energies larger than 100 meV in order to extract

functions in the source and drain lead shows that only the temperature of the third well state matches the device temperature of 300 K. In contrast, the high energy slope of the electron distribution in the second (red) and in the first (black) well state correspond to a temperature of 304 K and 323 K, respectively. The physical reason for this heating lies in the energy difference of the well states. The energy difference between the third and second well state (74 meV) approximately agrees with the energy of two LO-phonons (72 meV). Thus, after the emission of two LO-phonons, the electrons enter the second well state with almost the same in-plane momentum they have left the third state with. Consequently, the electron distribution in the second state has almost the same temperature as the third state. In contrast, the energy difference of the second and first well state (55 meV) is incommensurable with the LO-phonon energy. Thus, a significant fraction of the state energy difference is transferred into the in-plane motion during the electronic transition. Therefore, the temperature of the electron distribution in the lowest lying well state is significantly increased. Due to the large device temperature, the relative temperature increase of 23 K may seem to be rather small. However, this heating of the electron distribution becomes more important if the device temperature is smaller and the off-resonant emission of LO-phonons becomes more efficient. An example of electron distributions that deviate strongly from the Fermi distribution will be discussed in Sec. 5.3.5. There, we will find this effect to be critical for the device performance.

In contrast to these findings, NEGF calculations with the Büttiker probe scattering model yield completely thermalized state occupancies. This is illustrated in Fig. 4.3.12 (b) which shows the results of the same device as in Fig. 4.3.12 (a), but all scattering self-energies are replaced with Büttiker probes of the kind of Eq. 4.3.6 with a parameter $c = 0.003$. This probe parameter is chosen such that the resulting energy resolved density $n(z, E)$ is comparable to the one given in Fig. 4.3.11. In particular, the scattering strength is tuned such that the second well state is the least occupied one. However, the Büttiker probes underestimate the scattering of the third well state which results in a higher occupation of this state: The occupancy of the third state can be fitted with the Fermi distribution of the source divided by a factor of 3 (instead of a factor of 5 as in Fig. 4.3.12 (a)).

According to the constant temperature of the Büttiker probes, all three well distribution functions decay in energy parallel to the Fermi distribution functions of the source and drain. Neither a "bump", nor a heated high energy slope can be found in the distribution functions of the lower lying well states. It is also worth to note that the energies of the two lower lying well states (E_1 and E_2) are comparable in both scattering models. In contrast, the predicted confinement energy of the third well state differs significantly in both scattering models (see Figs. 4.3.12 (a) and (b)). This can be addressed to the fact that scattering of electrons in the third state is underestimated by the Büttiker probe model. We have seen in Fig. 4.3.7 that the real part and the imaginary part of the retarded LO-phonon self-energy of electrons in quantum wells are similar. Thus, in addition to the reduction of the state occupancy, the scattering with polar optical phonons also shifts the confinement energy E_3. This shift is also underestimated in the Büttiker probe model.

It could be a possible "work-around"for the missing "bump"in the state occupancies of the lower lying well states to avoid Fermi distribution functions in the Büttiker probes. Instead, one could assume the electron distribution in the artificial Büttiker leads to equal a linear interpolation of the distribution functions of source and drain. Then, a spatial dependent interpolation factor rather than a spatial dependent chemical potential has to be determined

---

the temperature.

in order to guarantee current conservation.

Conclusion

In summary, we have exemplified that the applicability of the Büttiker probe model is limited to qualitative results of devices close to or at equilibrium, with a small or (preferably) vanishing number of confined states. We have also shown that the heating of the in-plane electron distribution in the confined states of a biased quantum well cannot be reproduced by Büttiker probes, because the Büttiker probe model overestimates the thermalization of the state occupancies. We will show in Sec. 5.3.5 results of THz-QCLs that critically depend on a realistic implementation of this heating. In particular, when the electronic state occupancy is inverted, observables of NEGF calculations with the Büttiker probe model will deviate significantly from results of our implementation. Nevertheless, Büttiker probes represent the numerically most efficient approach to extend ballistic calculations into the regime of incoherent scattering. They are definitely most useful to check whether phenomena found in ballistic calculations persist in the presence of energy dissipation. Our suggested modifications of the Büttiker probe model according to the presence of confined states and nonequilibrium state occupancies do not increase the numerical load, but might significantly improve the applicability of this scattering model.

4.4 Conclusion

In this section, we have pointed out that approximations of the lead self-energies often cause artifacts near the device boundaries. When no quantum barriers are located near the device boundaries and incoherent scattering in the device is included, the inclusion of incoherent scattering in the lead is essential. We have found a similar importance for the inclusion of a finite current in leads of low resistive devices. For this reason, it is common to introduce a shift k_D of the Fermi spheres in the leads and to assume k_D to depend linearly on the device current density. However, we have shown that k_D starts to deviate from linearity for moderate current densities. For this reason, we determine k_D self-consistently in low resistive devices.

We have shown that inelastic scattering must be included if any (partly) confined device state is involved in the transport. When inelastic scattering is included, however, the retarded Green's function explicitly depend on the lesser Green's function which increases the complexity of the NEGF calculations significantly. Therefore, approximations exist in literature that ignore this dependence. It is known that this approximation violates Pauli's principle. However, we have found that this approximation is valid if all device states are less occupied than approximately 30 %. Thus, if the doping in the device is small enough, this approximation is a numerically very valuable.

Other approaches can be found in literature that neglect the scattering correlations between different spatial points and approximate the dependence of the scattering self-energy on the transferred momentum and energy. At least the scattering correlations can be limited to approximately twice the screening length in low resistive devices or to the typical extension of confined device states in devices with many confining barriers. In contrast, we show that the energy and momentum dependence of scattering may no be approximated device independently. Thus, simplifications on the momentum and energy characteristics of scattering have to be done with great care and adapted for each individual device. The approach of Büttiker

probe self-energies represents a highly simplified example of such a momentum and energy independent scattering model. We show that this model is effectively limited to qualitative results of devices close to equilibrium. The electron distribution of confined states equals only in and close to equilibrium a Fermi distribution with the temperature of the environment. Larger applied voltages can heat up the electronic distributions significantly, which a Büttiker probe model notoriously underestimates.

Chapter 5

New results on THz quantum cascade lasers

5.1 Introduction

The original purpose of our NEGF calculations of vertical transport in semiconductor heterostructures is to assess typical approximations. Nevertheless, there is a class of devices that have recently attracted great interest and can be modelled with single conduction band systems, i.e. the terahertz quantum cascade lasers.

A realistic quantum cascade device consists of a large number of periodically repeated multiquantum well structures that are coupled to leads. A fully quantum mechanical transport calculation through such an extended device is numerically unfeasible. Therefore, one needs to develop contact models that faithfully reproduce the intrinsic transport properties of the active region of quantum cascade lasers (QCLs) while simultaneously limiting the simulation region to effectively one or a few periods. Several quantum transport models based on density matrix approaches [155–157], the semiclassical Boltzmann equation [158–160] and nonequilibrium Green's functions have been developed [40, 45, 161]. All of these approaches share a common *a priori* assumption, namely the strict periodicity of the electronic states and their occupancy. To be precise, the electronic resonance states are assumed to be offset by an amount equal to eFa in each QCL period, where F is the electric field and a is the QCL period, but equally occupied in each period. While the use of such periodic boundary conditions greatly simplifies the analysis, it limits the solutions to a small subset of the Hilbert space. Non-periodic effects, such as coherent tunneling through extended states across one or several QCL periods (see Sec. 5.3.2), hot electron effects, or differences near source and drain contacts (see Sec. 5.3.5) are left out by such an approach. The transport equations are solved in a field- and/or device-dependent basis and take only into account electronic states that are well confined within a single or a few QCL periods [45]. As a consequence, it is not possible to selectively turn off inelastic scattering channels, or consider open quantum devices with leads.

We have already introduced in chapter 3 our implementation of NEGF calculations for stationary charge transport in *open* quantum systems that are connected to dissipative leads. Therefore, we only briefly summarize the differences of our method from previous NEGF implementations for QCLs [40, 162–164].

First, we use a real space basis that is not field dependent and provides a uniform and device-independent resolution of the Green's functions in space and energy. This guarantees current conservation regardless of the implemented complexity of the scattering self-energies

[41] and allows us to consider limiting cases including spatially homogeneous systems. Second, we do not impose field-periodic boundary conditions. Instead, the electrons enter and leave the device via travelling eigenstates of the semi-infinite leads. This allows us to capture non-periodic phenomena as well as investigate spatially extended, energetically higher lying states. In the leads, the electrons are assumed to remain in equilibrium which unambiguously defines the applied bias, regardless of the dissipation within the device [103]. This allows us to selectively turn on and off some or all scattering mechanisms and analyze their relative importance. Third, we implement the scattering mechanisms in their full momentum and energy dependence and do not rely on the commonly used approximation of momentum independent scattering matrix elements [45]. The only significant simplification that we are forced to use is related to the fact that we can explicitly calculate only a few active QCL periods. To this end, we have developed a model for the contacts that mimics the effect of many QCL periods by modifying the density of states within the lead regions.

We proof in Sec. 5.2 that our model faithfully reproduces the electronic transport in various THz-QCLs. We exemplify this with a quantitative comparison of experimental data of a THz-QCL [165] with our calculated current-voltage (I-V) characteristics and optical gain spectra. This device belongs to a popular class of QCLs that have been frequently fabricated in the last years, i.e. the resonant phonon THz-QCLs consisting of periodic repetitions of four quantum wells [122, 166, 167]. In this type of QCL, electrons are coherently injected into the upper laser level from an injector well. Electrons of the lower laser level are supposed to resonantly emit a LO-phonon when they enter the collector well. Thus, coherent and incoherent transport is expected to be equally important in this type of QCL which is a nice opportunity to test the quality of transport predictions in the NEGF formalism. Indeed, we find an excellent agreement with experiment for bias voltages up to the threshold voltage. We theoretically reproduce the linear and superlinear increase of the threshold current with doping density and correctly reproduce the maximum operating laser temperature. These agreements allow us to analyze the stationary transport in this THz-QCL in Sec. 5.3.

Since we treat the QCL as an open quantum device, we can selectively turn off individual scattering mechanisms and uncover the balance between coherent and incoherent transport as well as the dominant energy relaxation mechanisms. We identify the physical mechanisms that lead to occupation inversion and that determine the thermal load during laser operation. We furthermore unveil non-periodic effects that reduce the output performance of this resonant phonon THz-QCL.

These findings allow us in Sec. 5.4 to propose several improvements of the THz-QCL design. We show how to successfully suppress coherent leakage currents that increase the number of hot electrons and reduce the occupation inversion. Rough interfaces efficiently mediate non-radiative transitions between the laser states. We propose a THz-QCL with a diagonal laser transition that yields a larger optical gain than the typical resonant phonon QCL and is almost insensitive to rough interfaces. Furthermore, we present a modification of the resonant phonon THz-QCL that allows the propagating electrons to resonantly emit two phonons per period. In this way, we effectively pin the electron density to the QCL geometry and prevent the electron distribution from heating up. Thereby, we effectively suppress non-radiative losses that we find at threshold in every second period of the original QCL design.

5.2 Comparison of theory with experiment

5.2.1 Introduction

The major purpose of this section is to compare theoretical results of our implementation of the NEGF formalism with experimental data for a typical four well resonant phonon THz-QCL. The nice agreement that we find in this section allows us in subsequent sections to analyze the transport mechanisms in this kind of QCL in more detail and to propose several design improvements.

Our results of different lead models show that the transport in such a THz-QCL can be modelled with calculations of a single or a few active QCL periods. We find excellent quantitative agreement of the calculated *I-V* characteristics with published experimental data up to and closely above threshold. This allows us to verify that the implemented scattering mechanisms are realistically implemented in our transport model. Our model also successfully predicts the emission frequency and the observed trends in the threshold current as a function of doping. We exemplify the mechanisms that lead to optical gain and that are relevant for the dependence of the threshold current on the doping density. Our results illustrate the heating of the QCL during pulsed mode operation. In agreement with experiment, we find a maximum operating temperature around 140 K.

All THz-QCLs considered in this section consist of 271 identical periods of GaAs and $Al_{.15}Ga_{.85}As$ layers of the widths (30) 92 (55) 80 (27) 66 (41) 155 Å, where the values in parentheses indicate the $Al_{.15}Ga_{.85}As$ barriers [165]. Only the widest well is doped. The only difference between the QCL structures studied in this section lies in the doping concentration of this well. The experimental heat sink temperature is 5 K. The QCLs are designed to utilize the depletion of the lower laser level by emission of LO-phonons [166]. We consider the QCL as an open quantum device with electrons propagating between the two reservoirs. We assume an efficient energy relaxation within the leads, so that the electrons have a Fermi distribution $f(E, \mu)$ therein. For reasons discussed in Sec. 5.2.5, we use a temperature of 40 K for both, the lattice temperature and the Fermi distribution of the lead electrons.

5.2.2 Assessment of single period calculations

Introduction

It is numerically futile to calculate the nonequilibrium Green's functions in the 271 identical periods of the present QCL structure. Therefore, it is an important result that the intrinsic transport properties of the active region of the present QCLs can be faithfully reproduced with the calculation of the Green's functions within a limited number of QCL period. We proof in this subsection that the transport in the present THz-QCL is mainly characterized within a single QCL period*. We show this by applying two different lead models on a single active period of the QCL. Both models agree in the predicted *I-V* characteristics and the optical gain with experimental data. We explain the physical origin of this agreement and point out the validity limits of single period calculations.

*Of course, this finding is only true if the quantum wells of the single explicitly calculated active period are given in the right order, i.e. the quantum well closest to the source is the injector the one closest to the drain is the collector. Thus all explicitly calculated quantum wells originate from the "same"period.

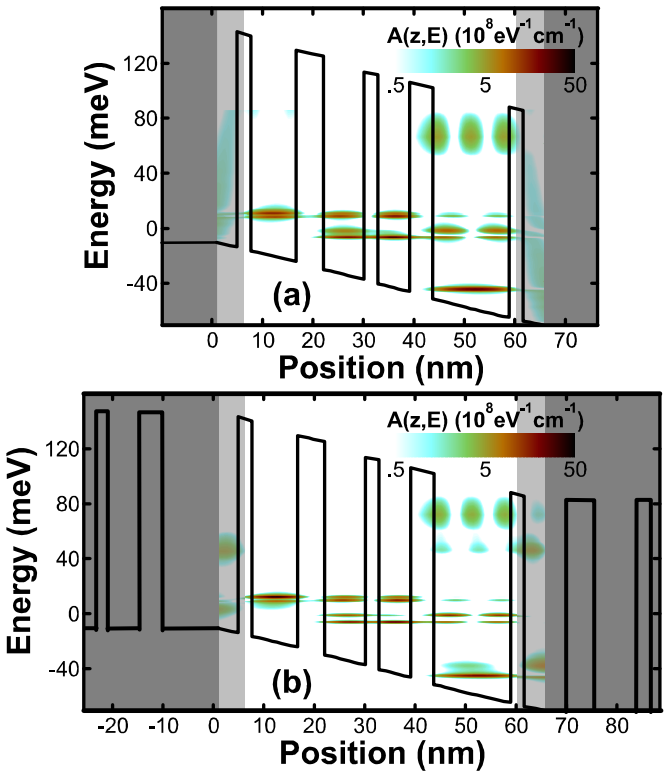

Figure 5.2.1: Contour plots of the energy resolved spectral function of the QCL of [165] as a function of position z and energy E. The sheet doping density is taken to be 1.9×10^{10} cm^{-2}. The solid lines indicate the self-consistent potential profile, the source-drain bias voltage is 50 mV per period. The zero in energy marks the chemical potential of the source. The shaded regions indicate the lead areas, including small transition regions. (a) Single period lead model. (b) Multiquantum well lead model.

Device states and state occupancy

In order to illustrate the rather small influence of neighboring periods in the four well THz-QCL design of [165], we apply both, the single period and the multiquantum well lead model on a single active period of the present QCL. We have already introduced both models in Sec. 3.6.2, but we emphasize that the lead electrons in the single period lead model enter the device as plane waves. Instead, the lead electrons of the multiquantum well lead model propagate in eigenstates of the field-free QCL and enter the device with a density of states that mimics the situation in a multi-period system more realistically.

Figures 5.2.1 (a) and (b) depict the conduction band profiles (solid lines) within the device, i.e. within a single active period of the THz-QCL of [165], as well as within the semi-infinite leads (grey-shaded regions) and the 6 nm wide transition zones (light grey-shaded regions). The doping of the widest quantum well in these figures is $n = 1.25 \times 10^{16}$ cm^{-3} and the applied bias voltage equals 50 mV per period. In the case depicted in Fig. 5.2.1 (a), we apply the single period lead model and attach two homogeneous semi-infinite GaAs leads to a single period of the active region of the QCL. The leads are doped with the doping density of the widest quantum well. In Fig. 5.2.1 (b), we show results of NEGF calculations with the multiquantum well lead model. Apart from being field-free, each of the two lead regions in the later model

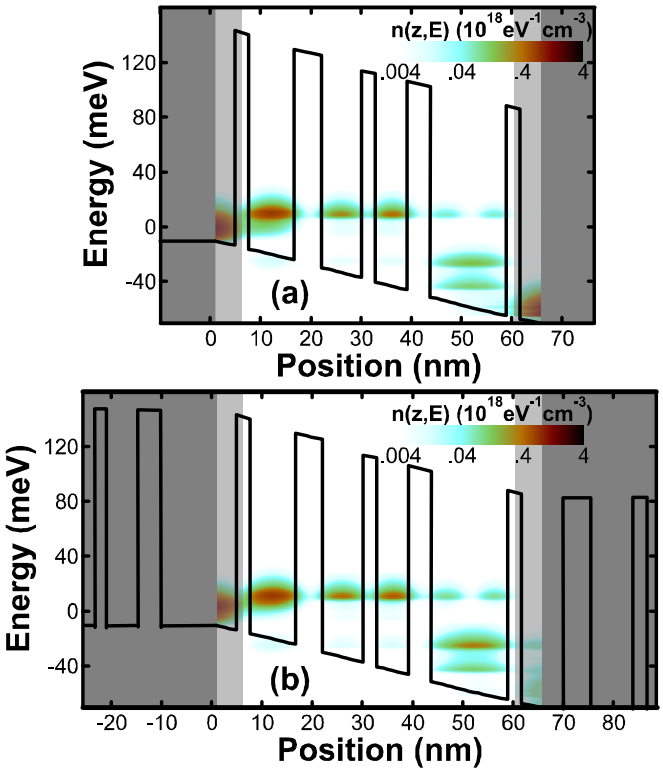

Figure 5.2.2: (Color online) Contour plots of the energy and spatially resolved density $n\,(z, E)$ of the QCL structure of Fig. 5.2.1. The solid lines indicate the self-consistent potential profile, the source-drain bias voltage is 50 mV per period. The zero in energy marks the chemical potential of the source. The shaded regions indicate the lead areas, including small transition regions. (a) Single periodic lead model. (b) Multi-quantum well lead model.

is an exact repetition of the appropriate half of the active zone and thus repeats the density of states and doping concentration of the active region. We find the potential profile deeper within the multiquantum well leads to have negligible influence on the device characteristics.

To get more insight into the difference between the two lead models, Figs. 5.2.1 (a) and (b) show contour plots of the energy and spatially resolved spectral density $A\left(z, z, k_{\|} = 0, E\right)$ (see Sec. 3.7.2) of the QCL. The maxima of the spectral function represent resonant states. Their finite width is caused by the incoherent scattering with phonons, impurities and rough interfaces and their coupling to the leads. In Fig. 5.2.1 (a), the large continuous spectral function in the transition zones near the lead/device boundary represents the continuous bulk-like density of states in the leads. By contrast, the spectral function the transition zones of Fig. 5.2.1 (b) shows two broad resonances that are caused by the tunneling processes through the confining potentials inside the leads. In spite of these differences in the lead density of states, the spectral function in the interior of the device - in particular between $z = 20$ nm and $z = 40$ nm - is very similar for both lead models. The reason for this finding lies in presence of the injector well for positions z between 7 nm and 16 nm. Any electron in the source has to pass the lowest injector state (at the energy $E \approx 10$ meV) and is thereby efficiently filtered. This filtering mechanism causes a comparable electron distribution in both lead models, as is shown in Figs. 5.2.2 (a) and (b). The Figs. 5.2.2 (a) and (b) depict contour plots of the energy and spatial resolved electron density $n\,(z, E)$ in the single period lead model (a) and the multiquantum well lead model (b)

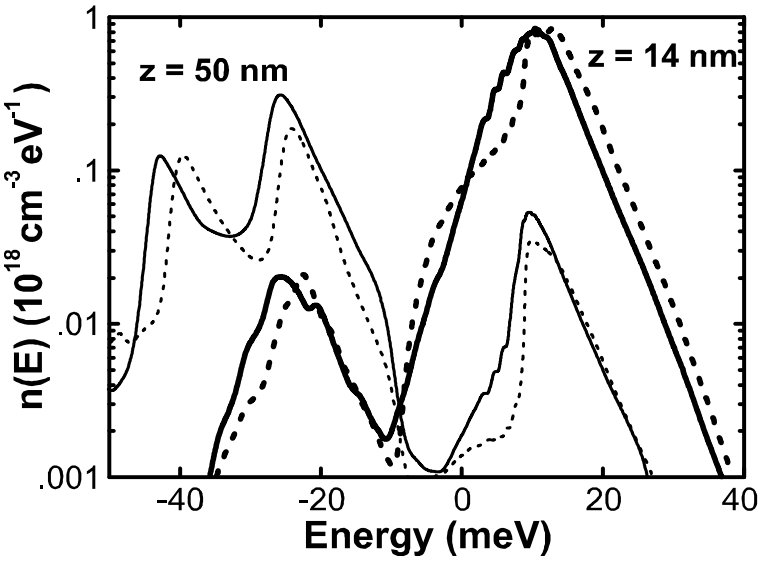

Figure 5.2.3: Cross section of the energy resolved density of the QCL shown in Fig. 5.2.1 in the leftmost quantum well (thick lines) and rightmost quantum well (thin lines). The results obtained with the single period lead model (dotted lines) agree well with the multiquantum well lead model (solid lines).

of the THz-QCL in Fig. 5.2.1. All physical observables depend on the lesser Green's function and consequently on the energy and spatially resolved carrier density $n(z, E)$ within the device. Thus, it is important that the difference of $n(z, E)$ of the two lead models is insignificant, as can be seen in Figs. 5.2.2 (a) and (b). This is shown in more detail in Fig. 5.2.3 that illustrates the density $n(z, E)$ of Figs. 5.2.2 at two different device positions, namely for $z = 14$ nm and $z = 50$ nm. According to this agreement, both models yield similar I-V characteristics and optical gain profiles in Figs. 5.2.4 (a) and (b), respectively. More importantly, the theoretical results of both models agree or lie closely to the experimental current and emission line depicted by the gray triangles and the gray line in Figs. 5.2.4 (a) and (b), respectively (see Sec. 5.2.3 for more details).

Limit of single period calculations

There are mainly two reasons why the transport problem in the cascade structure of the present QCL can be reduced to transport through a single period. First, the fact that even results of the single period lead model agree with experimental data illustrates the filtering capacity of the injector well. High barriers within each QCL period act as efficient energy filters so that the current does not depend critically on the density of states of the incoming carriers. The density of states within the leads has a higher influence on the transport within the device, if the number of filtering barriers is reduced.

The second reason why a single period is sufficient to predict transport in the total cascade structure lies in the low doping density. The state occupancy in the device is small enough so that Pauli blocking plays no role and the state occupation within the device does not affect the transition probability between the electronic states. Furthermore, the doping in most of the present QCLs is small enough that the Hartree potential is linear throughout the device. Thus, neither do details of the electron distributions in the leads play a significant role, nor do

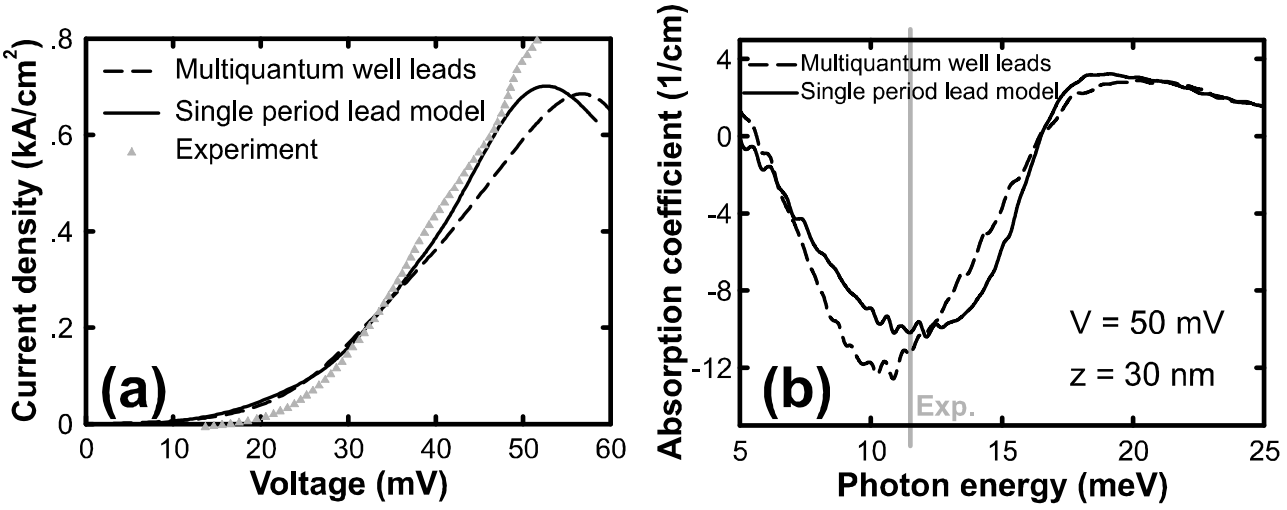

Figure 5.2.4: Comparison of NEGF calculations of the THz-QCL of Fig. 5.2.1 with the multi-quantum well lead model (dashed) and the single period lead model (solid). (a) Current density as a function of applied bias voltage per period. (b) Absorption coefficient as a function of photon energy in the center of the active region ($z = 30$ nm) at a bias voltage of 50 mV per period. The maximum of the experimental emission photon energy at 11.4 meV is indicated by the gray line.

electrostatic field domains exist in the cascade structure. However, the doping in the highest doped sample of Fig. 5.2.5 (i.e. the sheet doping density of 3.8×10^{10} cm^{-2}) represents the validity limit of the last condition. We find in Sec. 5.2.4 first deviations from a linear Hartree potential for this doping density. Furthermore, we show in Sec. 5.3.5 that higher order electron-electron scattering starts to play a significant role in the electron thermalization of this highest doped sample. Since we typically ignore this kind of scattering, we do not consider devices with higher doping densities.

5.2.3 Relevant scattering mechanisms

We emphasize that our implementation of the NEGF formalism on vertical transport in QCLs does not contain any fitting parameters. All parameters that enter our transport theory are device and material parameters that are (within a small range of experimental uncertainty) well known in literature. Therefore, it is an important check how well our theoretical results agree with experimental data of various QCLs.

Figure 5.2.5 gives a comparison of the measured [165] and calculated I-V characteristics of the QCL with different doping densities. As can be seen from these results, our model agrees excellently with the experimental data. This suggests that our treatment and inclusion of LO-phonon and acoustic phonon scattering, charged impurity and interface roughness scattering (see Sec. 3.5) and electron-electron scattering in the Hartree approximation captures the relevant physics of carrier transport in THz-QCLs.

In utilizing the phonon self-energies of Sec. 3.5, we apply the bulk phonon approximation which has been shown to be well justified for QCLs [60]. We also assume the phonons to remain at the lattice temperature of 40 K (see the discussion in Sec. 5.2.5). The material parameters are taken from [168]. We have assumed a Debye screening for the scattering with polar optical

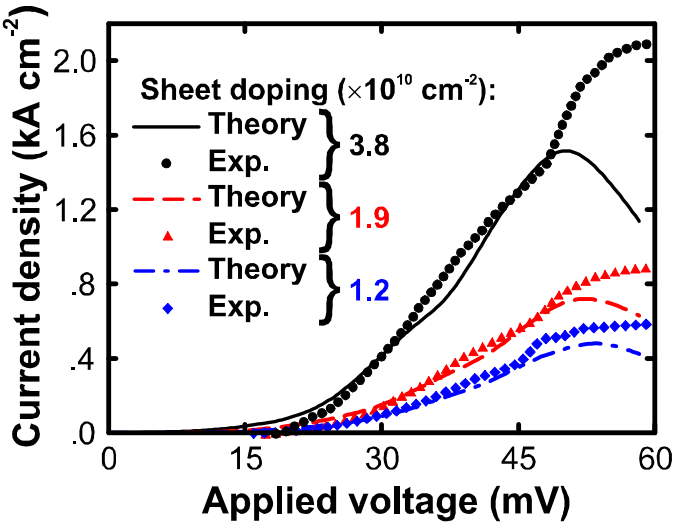

Figure 5.2.5: Experimental and calculated stationary current densities in units of kA cm^{-2} versus applied voltage per period in mV. The sheet doping densities are 3.8×10^{10} cm^{-2} (dots and solid line), 1.9×10^{10} cm^{-2} (triangles and dashed line), and 1.2×10^{10} cm^{-2} (diamonds and dash-dotted line), respectively.

phonons and charged impurities. We choose a Gaussian in-plane correlation for the interface roughness with a correlation length of $\lambda = 8$ nm [85, 89, 169] and roughness step height of $\delta z = 0.6$ nm which corresponds to a roughness of ± 1 monolayer in the growth direction and lies within typical experimental data [85, 89, 169, 170].

The higher order electron-electron scattering self-energy has not been included in these calculations; for a discussion of its effect, see Sec. 5.3.5. The calculated negative differential resistivity above the threshold bias, i.e. above 46 mV bias per period, originates from misaligned laser states. The experimental data also indicate misalignment effects, but they occur at higher current densities. The present theory ignores the coupling of the carriers to the laser field. This approximation may underestimate the current density above threshold. Larger bias voltages may also lead to hot electrons that are not fully captured by our lead models.

5.2.4 Threshold versus doping density

Introduction

The threshold current density, i.e. the current density at which light emission sets in, is of particular importance for the QCL performance, since it determines the thermal load during the laser operation. Experiments have shown that the threshold current density increases with higher doping density which has been explained with higher optical losses. In contrast, we show that the experimentally observed dependence of the threshold current on doping density can be solely explained with the QCL state alignment. For this purpose, we illustrate in detail the physical mechanisms that lead to occupation inversion and optical gain.

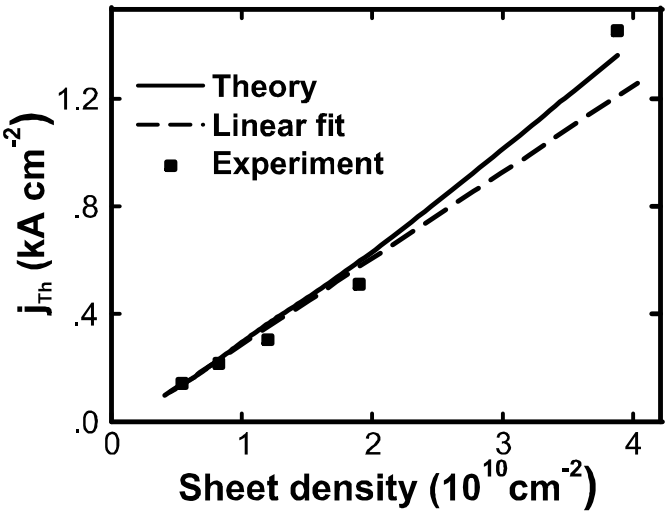

Figure 5.2.6: Comparison of measured and calculated threshold current density j_{Th} in units of kA cm^{-2} as a function of sheet density in units of 10^{10} cm^{-2}. The full line indicates the present theory, the squares are experimental data of Ref. [165]. A linear fit to the calculated data for low sheet densities (dashed line) illustrates the deviation from linearity at higher doping.

Amplitude gain and threshold current

The optical absorption coefficient is often defined with respect to the field intensity (α_I) rather than with respect to the field amplitude (α_A) [171]. In particular, in the gain regime of lasers one often refers to the power gain $-\alpha_I$. These quantities are related by $\alpha_I = 2\alpha_A$. We have derived in Sec. 3.3.3 the absorption coefficient with respect to the field amplitude and all results in this thesis actually show the smaller value α_A. The threshold current is usually defined as that current where the device averaged gain matches all external losses [172]. Since our calculations do not include external losses, we define the threshold current as that current where the device averaged gain* reaches transparency, i.e. $\alpha_A = 0$.

Our calculations yield a linear increase of the threshold current at low doping densities. For sheet densities above 2×10^{10} cm^{-2}, we obtain a slightly superlinear behavior. This trend has been observed experimentally for the presently studied THz-QCLs [165] as well as for similar structures [173]. As can be seen in Fig. 5.2.6, our NEGF calculations excellently reproduce the observed trend [165] in the threshold current as a function of the doping concentration, both for the linear as well as for the superlinear regime. The increase of the threshold current with doping has been assigned to optical losses due to free-carrier absorption [173, 174] and to a reduced upper state life time due to electron-phonon scattering [174]. However, simple model calculations have indicated that the free-carrier absorption cannot explain the slope in the threshold for low doping [122].

Occupation inversion in the linear regime

Our calculations show that the doping dependence of the threshold current is solely determined by changes in the level alignments. The mechanisms that are responsible for gain in the

*In calculating this spatial average, we leave out the areas close to the device boundaries that are influenced by the nonlocal scattering within the transition areas.

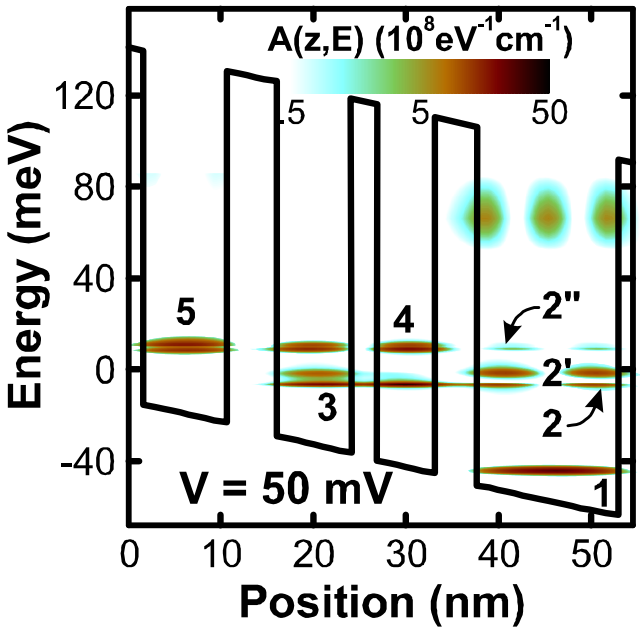

Figure 5.2.7: Contour plot of the spectral function $A(z, E)$ of the QCL with sheet doping density of 1.9×10^{10} cm^{-2}, in units of $10^8\,\mathrm{eV}^{-1}\,\mathrm{cm}^{-1}$, as a function of position z in nm and energy E in meV. The zero in energy marks the chemical potential of the source. The applied bias voltage is 50 mV per period. The solid line indicates the self-consistent potential profile. The spectral function is only shown within the energy interval from -70 to 110 meV. The labels number the relevant resonances that are discussed in the main text.

presently studied QCL structures are illustrated in figure 5.2.7. It depicts a contour plot of the energy and spatially resolved spectral function $A(z, E) = i\left[G^R(z, z, 0, E) - G^{R\dagger}(z, z, 0, E)\right]$ of a QCL with a sheet doping density of 1.9×10^{10} cm^{-2} for vanishing lateral momentum $k_\parallel = 0$ and a bias voltage of 50 mV per period. This voltage lies slightly above threshold. The maxima of the spectral function represent resonant states. Most noticeably, all states show a finite width and a fine structure that results from the coherent and incoherent coupling of all well states with one another. The upper laser level (labeled by #4) which is predominantly an antibonding state is aligned with the confined state #5 in the leftmost source-sided quantum well and therefore gets filled by resonant tunneling. The lower laser level #3 gets efficiently emptied by two mechanisms. First, the bonding state #3 is aligned with the states #2 and #2′ of the rightmost well which allows its coherent depletion by tunneling. Second, the energy difference between this state and the lowest resonance state (#1) matches approximately the energy of an LO-phonon (36 meV) which leads to an additional depletion by the resonant emission of LO-phonons. In the regime of low doping densities, the alignment conditions are unaffected by the carrier concentration. Therefore, the threshold voltage remains constant and the current depends linearly on the carrier density in this regime as can be deduced from figure 5.2.6.

Occupation inversion in the superlinear regime

The inhomogeneous spatial charge distribution at higher doping concentrations causes a nonlinear conduction band profile. There is a slightly positive space charge in the widest quantum well

that lowers its band edge including the states #1 and #2′ by a few meV. This effect improves the alignment of states #3 and #2′ with one another, leading to a superlinear enhancement of the current with doping density. This prediction is nicely confirmed by the experimental data, as shown in figure 5.2.6. Similar influence of the alignment conditions on the current density has been seen before in midinfrared QCLs [175, 176]. In addition, the improved alignment of the states #2′ and #3 at higher doping densities causes an enhanced anticrossing between these states and reduces the calculated peak gain energy by approximately 2 meV.

5.2.5 Heating of the QCL and temperature degradation

Introduction

It is known that the pulsed mode operation of typical THz-QCLs increases the lattice temperature. We discuss this heating with the comparison of experimental and theoretical *I-V* characteristics and find that the assumption of a lattice temperature of 35 K above the heat sink temperature - as suggested in [63] and [64] - nicely reproduces the experimental data. Furthermore, we present theoretical results of the optical gain at various temperatures. The theoretical results show a large decrease of the optical gain at lattice temperatures above 100 K. We find the optical gain for heat sink temperatures above 140 K to be smaller than typical external losses. This is in agreement with the maximum heat sink temperature at which the experimental QCL has shown optical gain.

Heating during pulsed model operation

The comparison between experiment and theory in Fig. 5.2.5 allows us to extract information about the heating of the device as a function of the bias voltage in the experiments. Propagating electrons in QCLs dissipate energy and cause the lattice temperature to deviate from the heat sink temperature of 5 K. Callebaut *et al.* [64] and Vitiello *et al.* [63] have shown that the lattice temperature increases in pulsed mode by approximately 20 K to 50 K above the heat sink temperature of 5 K, in spite of the 100 ns pulses that have been used in the experiments of [122]. Therefore, we have assumed a lattice temperature of 40 K throughout the device and including the leads, irrespective of the applied bias. At low bias, this assumption may slightly overestimate the device temperature. Indeed, the predicted current slightly overestimates the observed one for voltages below 25 mV per period (see Fig. 5.2.5) since higher temperatures facilitate the tunneling processes. At higher voltages, on the other hand, our model reproduces the measured current density up to threshold.

Maximum lasing temperature

It is a well-known issue that the light emission of THz-QCLs collapses if the QCLs are heated beyond a maximum temperature. The THz light emission of the experimental QCLs of [165] are limited to a maximum heat sink temperature of 140 K. In agreement with this observation, we find a drastic decrease of the calculated optical gain in these QCLs for lattice temperatures above 100 K. This is illustrated in Fig. 5.2.8 which shows the calculated optical absorption coefficient for the QCL in Fig. 5.2.7 in the center of the radiative quantum wells ($z = 27$ nm) for various lattice temperatures.The emission of the THz-QCL at a heat sink temperature of 140 K, i.e. a lattice temperature of 175 K (dash-dotted in Fig. 5.2.8), is a factor of 2 smaller than the emission of the same device but with a heat sink at 65 K (lattice temperature of 100 K,

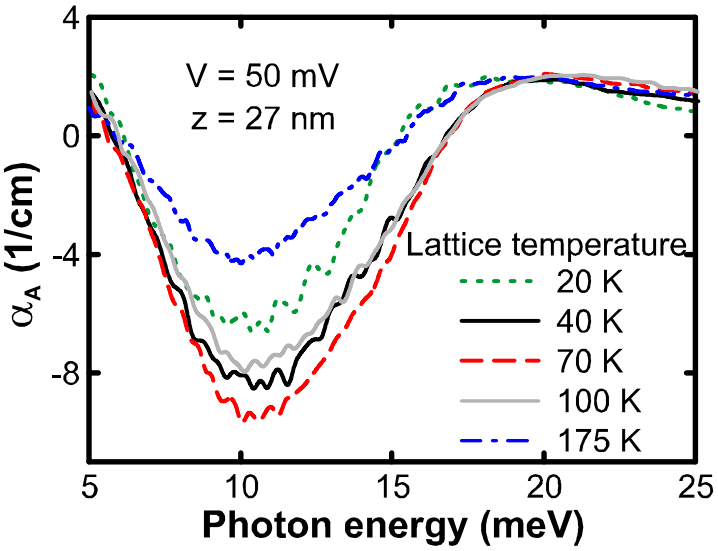

Figure 5.2.8: Calculated absorption coefficient α in the left of the active quantum wells (z = 27 nm) of the QCL in Fig. 5.2.7 as a function of the photon energy for different lattice temperatures. Please note that the heat sink temperature is approximately 35 K smaller than the assumed lattice temperature.

gray solid in Fig. 5.2.8). The calculated peak gain for a lattice temperature of 200 K remains lower than 3 cm^{-1} throughout the device, which is clearly smaller than typical external losses. Thus, no laser emission will set in at this temperature. We will see in Sec. 5.3.4 that thermal backfilling of electrons into the lower laser state as well as thermally activated emission of LO-phonons by electrons of the upper laser level is the origin for the temperature degradation of the QCL. There, we will also explain the increase of the optical gain with lattice temperatures up to 70 K which is shown in Fig. 5.2.8 for later reference.

5.3 Transport analysis in resonant phonon quantum cascade lasers

5.3.1 Introduction

We have found in Sec. 5.2 an excellent agreement of our calculations with the experimental data of [165]. This allows us to analyze the nature of charge transport in the GaAs/$Al_{.15}Ga_{.85}$As THz-QCL of [165] in great detail. Since this and very similar QCLs have been fabricated frequently, our findings are of a general interest. In addition, the results of this section are most valuable for proposing several design improvements in the subsequent section.

Since we treat the QCL as an open device, we are able to selectively turn off scattering mechanisms. Thus, we are able to identify the balance between coherent and incoherent transport in the present QCL. Furthermore, we uncover the relative importance of the individual scattering mechanisms for the electron transport and the optical gain. We find and explain that the scattering with LO-phonons only marginally changes the I-V characteristics. In contrast to suggestions in literature, we also show that the scattering at rough interfaces has a pronounced influence on the transport characteristics and optical gain. We perform NEGF calculations

of the present QCL at various lattice temperatures. Our results show that mainly thermal backfilling into the lower laser level and thermally activated phonon emission in the upper laser level cause the degradation of the QCL performance with temperature. It is common in literature to assume periodic boundary conditions for the transport in QCL periods. Since our model considers open quantum devices, we are able to check the validity of this assumption. We find the carrier distribution in present THz-QCLs to develop a periodicity that differs from the geometric periodicity of the QCL. We show that this discrepancy does not influence the *I-V* characteristics if the electron density in the QCL is small enough.

5.3.2 Coherent versus incoherent transport

Introduction

Transport calculations of mid-infrared QCLs [177] suggest that the contribution of coherent propagation to the charge transport in QCLs is insignificant compared to the efficient incoherent scattering. Furthermore, Monte-Carlo solutions of the semiclassical Boltzmann equation that neglect (coherent) correlation effects between laser states have successfully predicted charge transport in THz-QCLs [178]. Nevertheless, we show in this section that a general answer to the question whether the transport in THz-QCLs is mainly coherent or incoherent cannot be given, since the balance between both is sensitive to details of the device structure. It actually turns out that the four well resonant phonon THz-QCL of Fig. 5.2.5 is a very instructive example for the interplay of coherent and incoherent transport. We show that the nature of transport in this device is very sensitive to the applied bias voltage.

Effect of incoherent scattering

In spite of the previous findings for mid-infrared QCLs [177], we find that a rather large portion of the current in the resonant phonon THz-QCLs of [165] stems from coherent transport. This can be deduced from Fig. 5.3.1 as it shows different results for the current density of this THz-QCL with a sheet doping concentration of the widest QCL well of 1.9×10^{10} cm^{-2} and a lattice temperature of 40 K. The solid curve shows the most realistic calculation where phonon, impurity, interface roughness and electron-electron scattering in the Hartree approximation have been fully included. This curve equals the red dashed line in figure 5.2.5. The dashed curve in Fig. 5.3.1 shows the limiting case where all scattering self-energies have been artificially turned off ("ballistic regime"). Obviously, incoherent scattering enhances the current density in this QCL. in contrast, our calculations of the $n-i-n$ resistor in Fig. 4.2.5 yield a higher current in the ballistic situation. Both findings agree with results of M. Büttiker in [139] for transport in devices with various transmission and scattering probabilities. He has shown that incoherent scattering decreases the current in low resistive devices. Whereas the current in high resistive devices is increased by incoherent scattering [139].

Coherent regime

The two maxima of the ballistic current in Fig. 5.3.1 near 33 and 48 mV correspond to aligned laser states. At these voltages, electronic states are generated that extend across the entire QCL period. Such a delocalized state can be found in Fig. 5.3.2. This figure depicts a contour plot of the energy and spatially resolved spectral density $A\left(z, z, k_{\|}=0, E\right)$ within the THz-QCL of Fig. 5.3.1 at a bias voltage of 33 mV per period. At this bias voltage, the lowest state in the

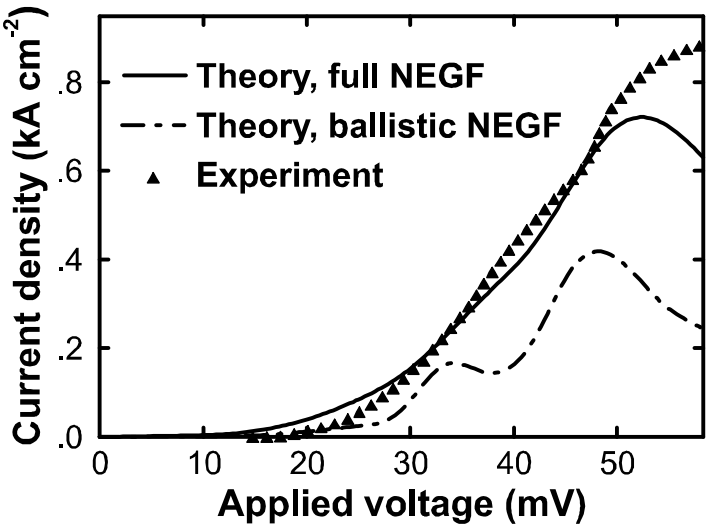

Figure 5.3.1: Experimental (triangles) and theoretically predicted (lines) I-V characteristics of the QCL of Fig. 5.2.4. Ballistic calculations (dash-dotted), i.e. NEGF calculations ignoring any incoherent scattering mechanism underestimate the current density. At the two ballistic resonances, however, a large portion of the realistic current is coherent.

injector well (labeled with #5) is aligned with the second state (#2′) of the rightmost quantum well, i.e. the collector well. This alignment generates a finite spectral function in the gap between the upper (#4) and the lower (#3) laser level. In this way, the spectral function at the energy $E = 12$ meV remains finite in every quantum well of the active period. Thus, electrons of this energy can coherently tunnel throughout the QCL period and maintain a maximum in the ballistic I-V characteristic.

Resonances in the current density caused by states that extend across the total QCL period are already known in literature. In the area of Monte-Carlo simulations of QCLs, anticrossing of laser states also lead to such highly delocalized states which eases the coherent multibarrier tunneling. In the Monte-Carlo formalism, however, the laser states are determined with a Hermitian Schrödinger equation which yields infinite state lifetime. Thus, when the alignment conditions of the above delocalized states are met, the corresponding resonance in the I-V characteristics predicted in the Monte-Carlo formalism is very large. In the Monte-Carlo literature, the resulting exaggerated peaks in the I-V characteristics are termed "parasitic current channels"which are typically omitted due to their artificial intensity [179]. It has been shown in [180] that a finite lifetime of the laser states reduces the height of the "parasitic"current peaks significantly. The finite lifetime of the electrons in the ballistic calculations of Fig. 5.3.1 originates from the finite probability for electrons to leave the device and thereby to "decay"into lead states. To be more precise, the Schrödinger equation that corresponds to our solution of the Dyson equation is non-Hermitian, irrespective whether incoherent scattering is implemented. Thus, we do not see artificial spikes in any I-V characteristics, including the ballistic one.

Incoherent regime

When the alignment conditions of Fig. 5.3.2 are not fulfilled, the completely delocalized state breaks apart and the ballistic I-V characteristic shows a negative differential resistivity. Such a situation is depicted in Fig. 5.2.7 as it shows the spectral function of the same QCL as shown

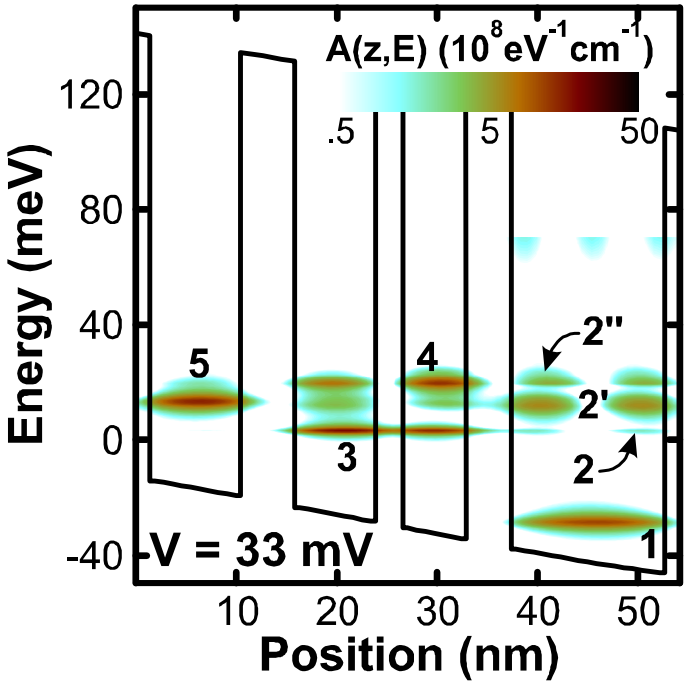

Figure 5.3.2: (Color online) Contour plot of the spectral function $A(z, E)$ of the QCL with sheet doping density of 1.9×10^{10} cm^{-2}, in units of 10^8 eV^{-1} cm^{-1}, as a function of position z in nm and energy E in meV. The zero in energy marks the chemical potential of the source. The applied bias voltage is 33 mV per period. The solid line indicates the self-consistent potential profile. The spectral function is only shown within the energy interval from -50 to 70 meV. The labels number the relevant resonances that are discussed in the main text.

in Fig. 5.3.2, but at an applied bias voltage of 50 mV per period. Here, the most prominent maxima of the spectral function separate into two groups of partly delocalized states: One group consists of the aligned injector (#5 in Fig. 5.2.7) and upper laser level (#4) and allows for the coherent propagation from the source sided device boundary to the center of the device. The second group of delocalized states is generated by the alignment of the lower laser level (#3) and the second state of the collector well (#2′) and eases the electronic propagation from the center of the device to its drain sided limit. Since the states of both groups are energetically separated, electronic transitions between them require for the dissipation of energy. Thus, at this bias voltage, the coherent propagation throughout the total QCL period is suppressed and the ballistic current is significantly smaller than results of calculations including incoherent scattering (see Fig. 5.3.1).

Coherent leakage in the incoherent regime

Nevertheless, the ballistic I-V characteristics in Fig. 5.3.1 shows a second resonance at 48 mV per period, i.e. close to the bias voltage of Fig. 5.2.7 and consequently in the middle of the incoherent transport regime. This resonance can be traced back to a coherent leakage of electrons from the upper laser level. As shown in Fig. 5.2.7, the upper laser level (#4) is not completely confined but leaks into the collector well to the right. Since both, the upper laser level as well as the second state of the collector well have a finite lifetime, they partly overlap and generate the small maxima of the spectral function labelled with #2″. Since #2″ lies at

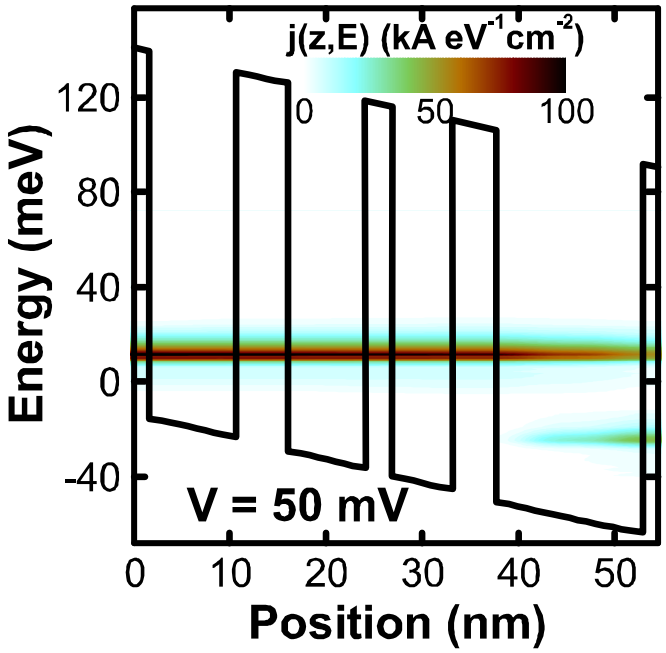

Figure 5.3.3: Conduction band profile (solid line) and contour plot of the energy and spatially resolved current density $j(z, E)$ of the QCL in Fig. 5.2.7. A large portion of the propagating electrons crosses the QCL period without dissipating energy.

the energy of the upper laser level *within* the collector well, the electronic tunneling out of the upper laser level is only slightly suppressed but not completely blocked. In order to further illustrate this result, Fig. 5.3.3 shows a contour plot of the energy and spatially resolved current density $j(z, E)$ (see Eq. (3.3.2)) in the situation of Fig. 5.2.7. The pronounced maximum of $j(z, E)$ in the energy windows from 0 and 30 meV extends over the entire QCL period. This implies that most of the electrons do not emit phonons until they reach the widest quantum well on the right hand side (around $z = 44$ nm). Figure 5.3.3 shows clearly that the amount of current carrying electrons at lower energies (about -25 meV) is rather small. In summary, we find that almost 50% of the realistic current originates in coherent multi-barrier tunneling. This is a somewhat surprising result, because the QCL is designed such that the resonant emission of LO-phonons is expected to dominate the transport in this regime. We will present in Sec. 5.4.2 a slightly modified design of this QCL that yields an improved suppression of this coherent leakage. Then, the ballistic current is reduced and the relative contribution of LO-scattering to the transport is enhanced.

Previous studies of mid-infrared QCLs [177] have suggested that the transport is predominantly incoherent. In typical mid-infrared QCLs, however, the average gap between confined laser states is much larger than in the present THz-QCLs. Consequently, the overlap of misaligned laser states which is essential for the coherent leakage at threshold is much smaller in typical mid-infrared QCLs than in the present THz-QCLs.

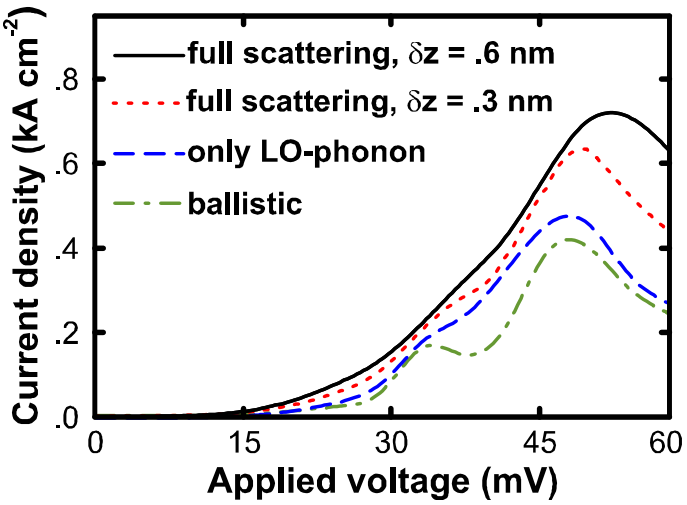

Figure 5.3.4: Calculated I-V characteristics of the QCL with a sheet doping density of 1.9×10^{10} cm^{-2}. The green dash-dotted line is a purely ballistic calculation without scattering self-energies. For the blue dashed line, polar optical phonon scattering has been included. All scattering mechanisms with a roughness step height of $\delta z = 0.6$ nm lead to the black solid curve. The red dotted curve differs from the black full line only by a reduced roughness step height of $\delta z = 0.3$ nm.

5.3.3 Comparison of scattering mechanisms

Introduction

Incoherent scattering mechanisms are known to be crucial for the transport characteristics of THz-QCLs [48, 158, 181]. It is therefore relevant to study the individual contributions of the various scattering mechanisms and analyze their relative importance. Although the present QCL structure is designed such that LO-phonons are resonantly emitted, we find the scattering with LO-phonons to have a surprisingly small influence on the current density. We show that the scattering with LO-phonons in the present QCL basically forks the current channel. In contrast, our results show that scattering at rough interfaces significantly increases the current density. We illustrate and discuss that the elastic interface roughness scattering efficiently reduces the occupation inversion. In agreement with experimental observations [170], we find that very rough interfaces can ruin the QCL performance. This finding is at variance with results of approximate scattering models in literature [150].

Influence of LO-phonons

In Fig. 5.3.4, we show several calculated I-V characteristics. The sheet doping concentration of the widest QCL well amounts to 1.9×10^{10} cm^{-2}. The solid curve shows the most realistic calculation where phonon, impurity, interface roughness and electron-electron scattering in the Hartree approximation have been fully included. This curve equals the dashed line in figure 5.2.5. The dash-dotted curve shows the limiting case where all scattering self-energies have been artificially turned off ("ballistic regime") and has already been discussed in Sec. 5.3.2.

The dashed curve in Fig. 5.3.4 shows the current where all scattering mechanisms but LO-phonon scattering have been neglected. The rather small increase of this current density

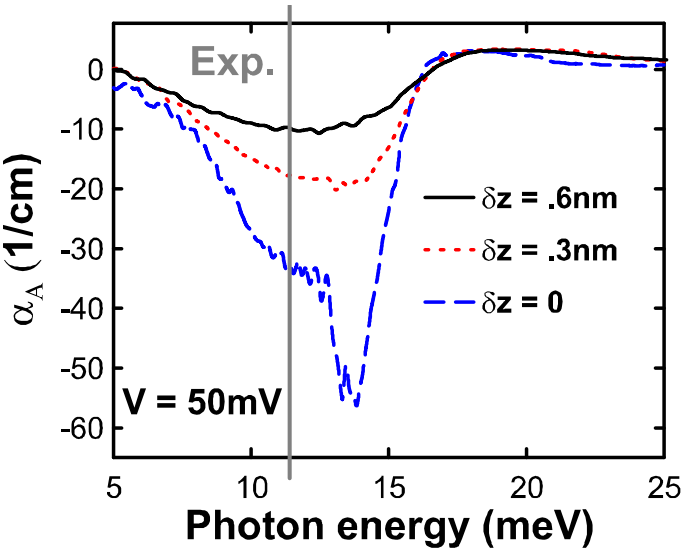

Figure 5.3.5: Calculated absorption coefficient $\alpha_A(z, E_{\text{Photon}})$ in the center of the QCL period at a bias of 50 mV for various roughness step heights in nm: $\delta z = 0.6$ nm (black solid), $\delta z = 0.3$ nm (red dotted) and $\delta z = 0$, i.e. smooth interfaces (blue dashed). The grey line marks the experimental photon emission energy.

compared to the ballistic results is due to three effects. First, the coherent leakage of the upper laser level into the collector well carries most of the current (see Sec. 5.3.2). Second, the lower laser level (#3 in Fig. 5.2.7) remains almost empty due the lack of a resonant state in the injector well at this energy. Since, in addition, the lower states #2 and #2′ are also almost empty, phonon emission mostly occurs between the upper laser level #4 and the lowest collector state #1. This process is not efficient since the energy separation between these levels amounts to approximately 50 meV and thus exceeds the optical phonon energy. There is, in addition, some optical phonon emission between state #2″ and #1 within the collector well, but this only forks the current channels and does not increase the current.

The isolated effect of charged impurity and acoustic phonon scattering is not shown in Fig. 5.3.4, because they have a small influence on the current density. By contrast, we find a marked influence of the interface roughness scattering which we now discuss in some detail.

Influence of rough interfaces

Figure 5.3.4 shows two I-V curves that are labeled by "full scattering". Both curves include the electron-electron scattering in the Hartree approximation as well as the scattering by phonons, impurities and rough interfaces. Yet, they differ in the assumed interface roughness step height δz. The in-plane roughness correlation length is assumed to be $\lambda = 8$ nm in both cases [85, 89, 169]. The value of $\delta z = 0.6$ nm corresponds to a roughness of ± 1 monolayer in the growth direction and lies within typical experimental data [85, 89, 169, 170]. We find a continuous increase of the current with interface roughness; the zero roughness case is shown by the dashed curve, and an intermediate value of $\delta z = 0.3$ nm is depicted as well .

Scattering by rough interfaces is an elastic scattering mechanism that randomizes the electron in-plane momentum $k_{\|}$ by an amount of λ^{-1}. This corresponds to an energy randomization of approximately 9 meV. Consequently, this scattering mechanism enables transitions of elec-

trons from the upper laser level (#4) to the collector states (#2, #2′) as can be deduced from figure 5.2.7. This effect significantly enhances the leakage current of electrons, because the density of the states #2 and #2′ are much larger than the one of #2″. In addition, this effect reduces the occupation inversion and the optical gain significantly, since the states #2 and #2′ are aligned with the lower laser state #3 close to threshold. This effect is shown in Fig. 5.3.5 that displays the calculated cross sections of the absorption coefficient α_A as a function of the photon energy E_{photon} in the center of the QCL in Fig. 5.2.7 ($z = 28$ nm), and for various roughness step heights δz. The predicted gain maximum of the calculation including rough interfaces with a roughness step height $\delta z = 0.6$ nm matches the measured emission energy of 11.4 meV well (see also Fig. 5.2.4 (a)). The gain is maximal for smooth interfaces and gets reduced by almost an order of magnitude by realistic interface roughness scattering. Thus, rough interfaces effectively suppress the formation of a laser which is in accord with experimental observations [170].

Our results seem at variance with previous NEGF findings of Nelander and Wacker for similar QCL structures [150]. These authors do not see a significant influence of rough interfaces on the current for a correlation length of $\lambda = 10$ nm and a step height $\delta z = 0.24$ nm. While their roughness model slightly differs from ours (exponential instead of Gaussian correlation), we have checked that this difference is insignificant and does not influence our results. In addition, these authors obtain a large effect due to charged impurity scattering. The discrepancies may be caused by the assumption of momentum independent scattering potentials in reference [150].

5.3.4 Temperature degradation

Introduction

The operation of state of the art THz-QCLs is still restricted to low temperatures*. In order to extend the operation temperatures, the degradation mechanisms of the laser output performance with temperature has to be analyzed. First, we show that the increase of optical gain and current with increasing lattice temperatures up to 70 K (i.e. heat sink temperatures up to 35 K) is based on an enhanced number of electrons that fulfill the resonant tunneling conditions. Due to the heating of the QCL, however, most of these low lattice temperatures lie beyond experimentally accessible areas. More importantly, however, we show that the thermal backfilling of electrons into the lower laser level and the thermally activated phonon emission of electrons of the upper laser level drastically decrease the optical gain with temperature.

Low temperature performance

We have found in Fig. 5.2.8 a maximum of the optical gain at a lattice temperature of 70 K. The significant increase of the peak gain for increasing lattice temperatures up to 70 K reflects the resonant tunneling aspect of the transport. At low temperatures and for a given bias voltage, only few electrons can resonantly tunnel through the QCL. Increasing the lattice temperature smears out the electron distribution so that more electrons can match the resonance condition. This also results in a higher occupation of the upper laser level and a larger optical gain. Accordingly, the device current density increases with temperatures up to 70 K, as can be seen in Fig. 5.3.6 for the single period and the multiquantum well lead model. Please note the a

*The recently developed room temperature THz-QCL [182] is based on two mid-infrared QCLs and intracavity difference-frequency

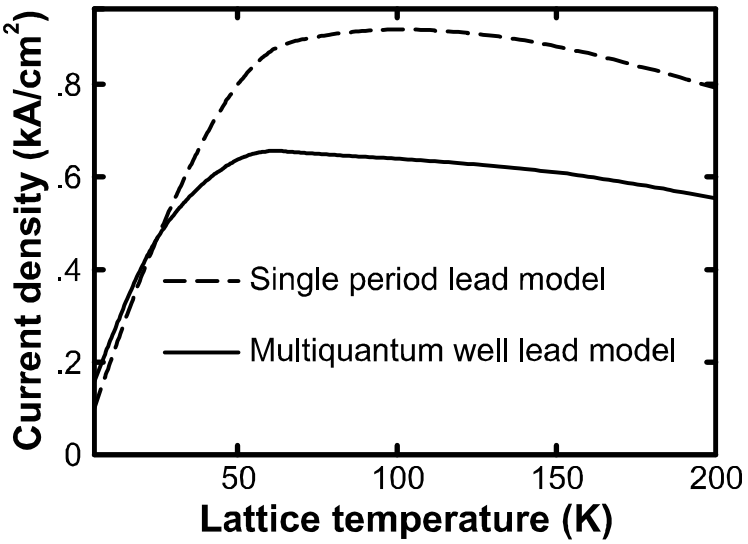

Figure 5.3.6: Current density of the QCL in Fig. 5.2.8 for two lead models (dashed line: single period, full line: multiquantum well) as a function of temperature. The bias voltage is set to 50 mV per period.

lattice temperature below approximately 35 K represents only a fictitious situation, because the heat sink temperature is typically 35 K lower than the lattice temperature (see the discussion in Sec. 5.2.5, [64], and [63])

High temperature performance

If we increase the temperature beyond 70 K, however, a increasing portion of the electrons is spread out energetically and lies predominantly off-resonance. The fact that the current is smaller for the multiquantum well lead model stems from the smaller density of states in the leads. Though, both models show a small decrease of the current density according to the off-resonant electrons. In experiments, however, the current density increases with the heat sink temperature. Since we do not see this in our calculations, this increase of the current most likely originates from an increased number of hot electrons that our lead models do not cover. Nevertheless, the drastic reduction of the calculated gain in Fig. 5.2.8 for lattice temperatures above 100 K cannot be explained with the small reduction of the current density in Fig. 5.3.6.

At temperatures above 100 K, the amount of electrons with high in-plane kinetic energies becomes significant. This can be seen in Fig. 5.3.7 (a) that shows the energy resolved electron density $n(z, E)$ in the injector well (labeled with I), the two active quantum wells (II and III) and the collector well (IV) of the four well THz-QCL of Fig. 5.3.6 at a temperature of 200 K. The subband energies are depicted in Fig. 5.3.7 (b) which shows the spatially integrated spectral function Eq. (3.7.6) of the same QCL. The dashed lines mark the subband energies of the lowest state in the QCL period ($E = 17.4$ meV) as well as the lower ($E = 55.5$ meV and $E = 60.9$ meV) and the upper laser levels ($E = 71.1$ meV and $E = 73.4$ meV). Electrons with more than 20 meV of kinetic energy above the subband minima can be found in the upper laser level (see Fig. 5.3.7 (a)). This kinetic energy suffices for electrons in the upper laser level to scatter into the lower laser level by emitting an optical phonon (thermally activated phonon emission). In addition, some electrons in the collector well (IV) can reach sufficiently high

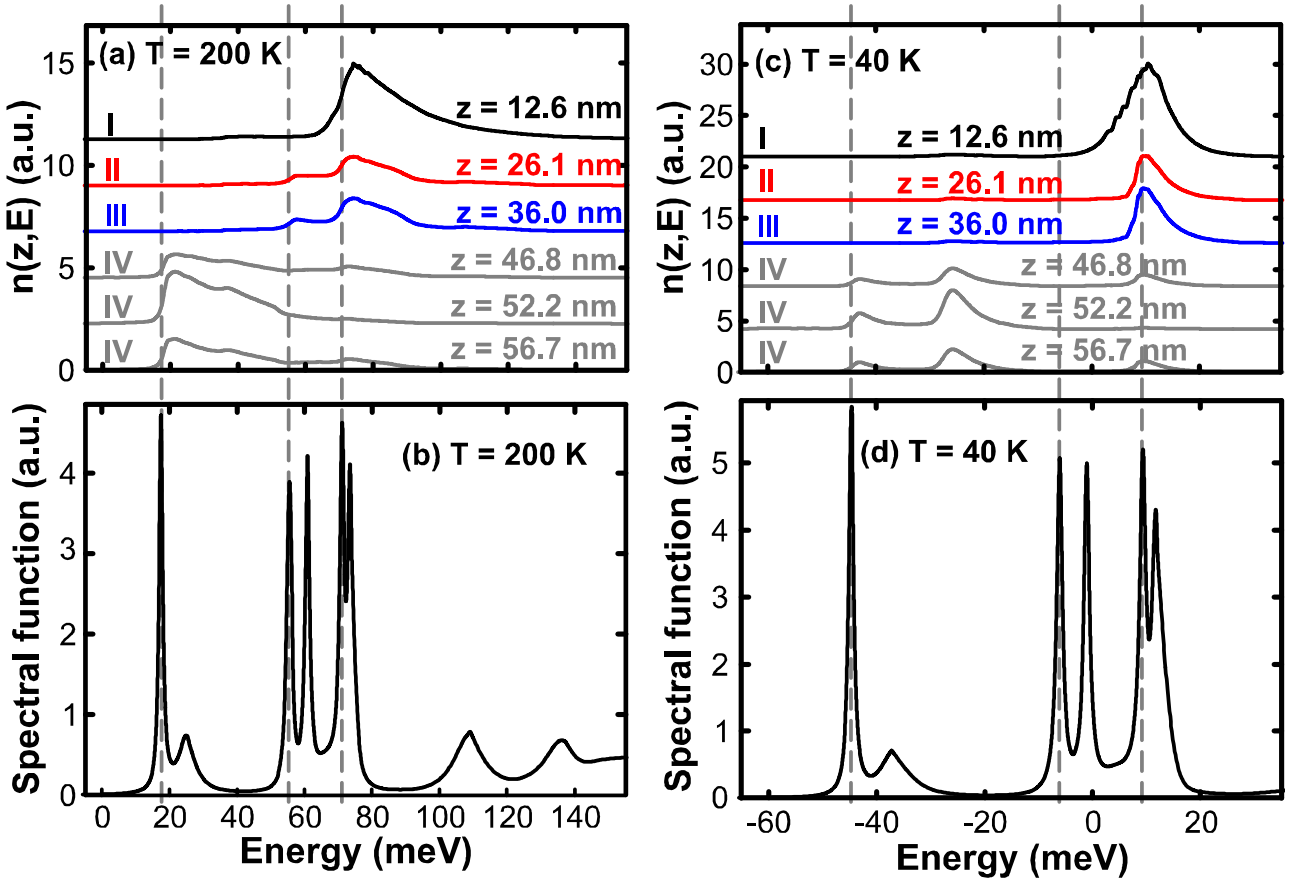

Figure 5.3.7: Energy resolved density at a bias of 50 mV per period at a lattice temperature of 200 K (a) and 40 K (c) for various spatial position in the QCL of Figs. 5.3.6 and 5.2.7. The Roman numbers denote the injector (I), the two active (II and III) and the collector well (IV). The peaks in the spatially integrated spectral function at 200 K (b) and 40 K (d) mark the energy of resonant states.

kinetic energies to fill the lower laser level. We find these mechanisms to reduce the occupation inversion and the optical gain.

We show for comparison the energy resolved density and the spectral function of this QCL at 40 K lattice temperature in Figs. 5.3.7 (c) and (d), respectively. It is easy to see that both mechanisms, the thermally activated phonon emission and the thermal backfilling are absent at this lower temperature.

Nelander and Wacker have shown in [150] that there is an additional effect that limits the optical gain, the broadening of the absorption and emission linewidth namely. Since we do not take vertex corrections into account (see Sec. 3.3.3), the emission lines in Fig. 5.2.8 do not show such a broadening.

5.3.5 Periodicity of quantum cascade structures

Introduction

We have exemplified in detail in Sec. 3.6 that our model does not *a priori* assumes periodic boundary conditions. To the best of our knowledge, all theoretical models in literature solve the

transport problems in quantum cascade lasers with periodic (or better field-periodic) boundary conditions. In this way, the considered solutions of the transport problem are limited on a small subset of the Hilbert space, namely the field-periodic one. We motivate the question in how far a QCL is periodic with a basic discussion of energy conservation. We present results of NEGF calculations that explicitly consider two QCL periods. Our results show that the transport in two adjacent periods of the present resonant phonon QCL indeed differs. However, when the doping and accordingly the electron density in the QCL is low enough, the nonperiodic effects do not significantly influence the (experimentally accessible) device observables. In contrast, the calculated *I-V* characteristics of NEGF calculations in a single and two QCL periods differ. We illustrate the origin of this discrepancy and discuss that higher order electon-electron interaction might become relevant at these higher electron densities.

How periodic is a QCL?

In a finite electric field, a periodic carrier distribution can only build up in a cascade structure if there is a sufficient amount of inelastic scattering that resets the carrier distribution in each injector well to the same set of values. For a doping density of 1.9×10^{10} cm^{-2}, we find a threshold voltage of 46 mV/period. Thus, the electrons have to dissipate 46 meV in each QCL period in order to maintain a periodic distribution. However, the emission of a single LO-phonon within one period dissipates only an energy of 36 meV. Consequently, the remaining 10 meV have to be dissipated by other processes. Possible candidates are higher order electron-electron (e-e) scattering or/and the emission of acoustic phonons. The emission rate of photons up to threshold is known to be very inefficient ($\tilde{}0.1$ μs^{-1}). We have seen above that scattering with acoustic phonons plays only a secondary role. Thus, the only plausible candidate appears to be the e-e scattering. As will be discussed below, however, even this scattering mechanism seems not capable of dissipating this amount of energy.

Low electron densities

In order to investigate the periodicity of the present QCL in more detail, we have performed elaborate calculations that take into account two full QCL periods explicitly as active open device, attached to multiquantum well leads as discussed in section 3.6.2. In this way, we do not assume an electronic carrier distribution that follows the QCL period *a priori*. We assume a sheet doping density of 1.9×10^{10} cm^{-2} and focus on the situation for an applied bias voltage of 52 mV per QCL period, i.e. just slightly above the threshold voltage. Our key finding is that carrier distributions build up that are commensurable with the geometric QCL period but with a *commensurability period that is larger than a single QCL period* and extends over two or even more QCL periods. This result implies that the number of emitted LO phonons is no longer strictly one per geometric QCL period as we are now going to show. Figure 5.3.8 (a) shows a contour plot of the energy and spatially resolved current density $j(z, E)$ as defined in Eq. (3.3.2). To better guide the eye, the conduction band profile of the device (solid line) is depicted as well. The spatially resolved current density is a quantity that vividly illustrates coherent transport as well as energy dissipation processes. If there is no energy dissipation, the contour plot of $j(z, E)$ would only show one or several horizontal (i.e. spatially constant) stripes that extend across the entire device. Any disruptions of these stripes, on the other hand, mark positions where LO phonon emission sets in. A sequence of three emitted LO-phonons can easily be identified in the figure. This result implies the resonant emission of three LO-phonons across two QCL periods and a net energy dissipation of $3 \times 36 = 108$ meV in the

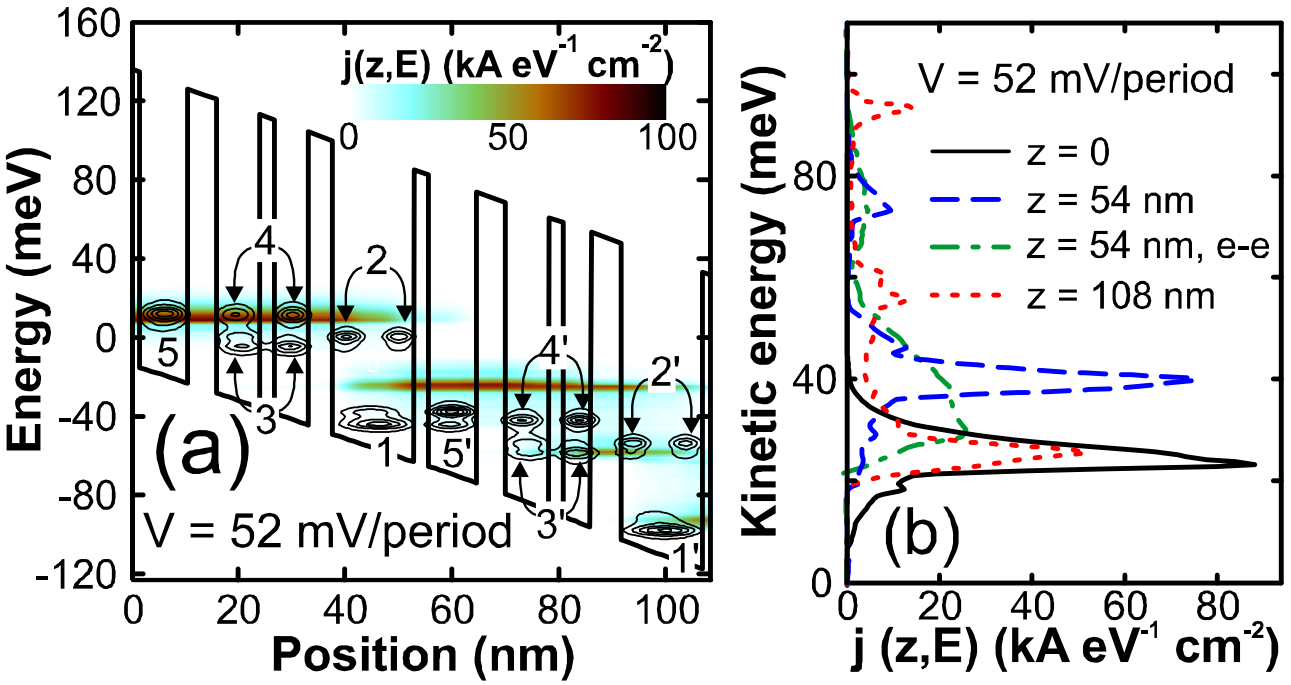

Figure 5.3.8: (a) Conduction band profile (solid line) and contour plot of the energy and spatially resolved current density $j(z,E)$ of the QCL with a sheet doping density of 1.9×10^{10} cm^{-2} at a voltage of 52 mV per period. The contour lines show the spectral function at vanishing in-plane momentum $A(z,E)$. The zero in energy marks the chemical potential of the source. Here, two QCL periods are explicitly taken into account. States of the first (second) period are labeled with numbers (primed numbers). (b) Cross section of the energy and spatially resolved current density in the leftmost ($z = 0$, black solid) barrier, the central barrier ($z = 54$ nm, blue dashed), and the rightmost ($z = 108$ nm, red dotted) device barrier of (a), respectively. The green dash-dotted line depicts $j(z,E)$ of a single-period calculation at $z = 54$ nm of the same QCL with higher order electron-electron scattering Eqs. (3.5.99) and (3.5.100) included.

device which differs from the voltage drop of $2 \times 52 = 104$ meV only by 4 meV which lies in the range of acoustic phonon energies. To illustrate this result in more detail, Fig. 5.3.8 (b) depicts cross sections of the spatially resolved current density at three prominent device positions: initial injection region ($z = 0$), end of first QCL period ($z = 54$ nm), and final collector region ($z = 108$ nm). Since the total current density is a conserved quantity, the area under each of the three curves is the same. For each curve, the energy is counted relative to the local conduction band edge. If the electronic carrier distribution were perfectly periodic in each QCL period, the three curves in Fig. 5.3.8 (b) would lie on top of each other. By contrast, the calculations show that the electrons have emitted only one LO-phonon (36 meV) at the end of the first period. The elastic and inelastic scattering mechanisms are not able to dissipate the remaining 16 meV within this QCL period. This is a consequence of the good state alignment that supports efficient coherent multibarrier tunneling as discussed in Sec. 5.3.2. Therefore, the electrons enter the second period with a higher energy which leads to the shift of the peak in $j(z,E)$ at $z = 54$ nm. This can be seen in Fig. 5.3.8 (a); the energy of the leftmost current stripe coincides with the injector state #5 and the upper laser state #4, whereas the following

current stripe lies above the corresponding states #5' and #4' of the second period. Thus, these propagating electrons of the second period are now able to emit an LO-phonon, ending up in and occupying the lower laser level #3'. This occupancy leads to the build-up of the current stripe near $z = 80$ nm in Fig. 5.3.8 (a) that is absent in the first period. The electrons can now tunnel resonantly from #3' into state #2' and scatter into the lowest collector state #1' by the emission of an additional LO-phonon. Near the end of the second QCL period, the electrons have accumulated enough energy to actually emit two LO-phonons. This resets the main portion of the carrier distribution almost completely to its original value, as shown by the dotted line in Fig. 5.3.8 (b). Since all electronic states have a finite width, the remaining small energy difference can be compensated by LA scattering. The smaller peaks in $j(z, E)$ at $z = 108$ nm reflect the ballistic portion of transport and lie exactly one and two LO phonon energies above the main peak. This process is repeated in the subsequent QCL periods such that we obtain a commensurable charge distribution with period two. A consequence of this incomplete carrier thermalization is a significant reduction in the occupation inversion and the optical gain in every second period. Concretely, we find a drop of approximately 65 % in the second period shown in Fig. 5.3.8. Since the detailed energy balance depends on the applied bias voltage, the carrier density and current distribution may even become incommensurable with the geometric periods.

In summary, we find that the carrier distribution in a THz-QCL does not simply follow the geometric periodicity of the structure but develops commensurable and conceivably even incommensurable distributions as a function of bias. The results of the calculation shown in Fig. 5.3.8 and discussed so far do not include higher-order e-e interactions. It is known in literature that the inelastic electron-electron interaction can thermalize the intrasubband electron distribution [183, 184]. In order to estimate whether the inelastic e-e scattering can relax the electrons and restore the periodicity of the carrier distribution to a single QCL period, we have calculated the Green's functions including the approximated self-energies of Eqs. (3.5.99) and (3.5.100). The scattering rates that result from this self-energy are comparable with those of the resonant emission of LO-phonons, in agreement with similar findings of Monte-Carlo simulations [95]. Nevertheless, we find the e-e interaction to be unable to thermalize the nonequilibrium subband distribution sufficiently strongly. This is illustrated by the green dash-dotted line in Fig. 5.3.8 (b) which depicts $j(z, E)$ in the last barrier of a single-period calculation, when the inelastic electron-electron scattering Eqs. (3.5.99) and (3.5.100) is included. This position equals the central barrier of a two-periods calculation ($z = 54$ nm). Compared with the calculation ignoring inelastic electron-electron scattering (blue dashed line in Fig. 5.3.8 (b)), this scattering indeed thermalizes parts of the electron distribution. However, the thermalization is too inefficient in order to reach the initial electron distribution given by the black line in Fig. 5.3.8 (b).

We would like to emphasize that the total current density is insensitive to these commensurability effects and therefore not a suitable observable for detecting them for the weak doping levels that are characteristic of THz-QCLs. This explains the good agreement in Fig. 5.2.5 between the experimental data and results we have obtained with a single-period model. It also explains the agreement of the I-V characteristics of the single-period model with results of two explicitly calculated QCL periods which is shown by the red lines and symbols in Fig. 5.3.9 for the doping density of 1.9×10^{10} cm^{-2}. The peaks in the integral current density in Fig. 5.3.8 (b) only reflect the energetic position and widths of the resonant states. For low doping levels, these positions are insensitive to small changes in the local carrier occupancies.

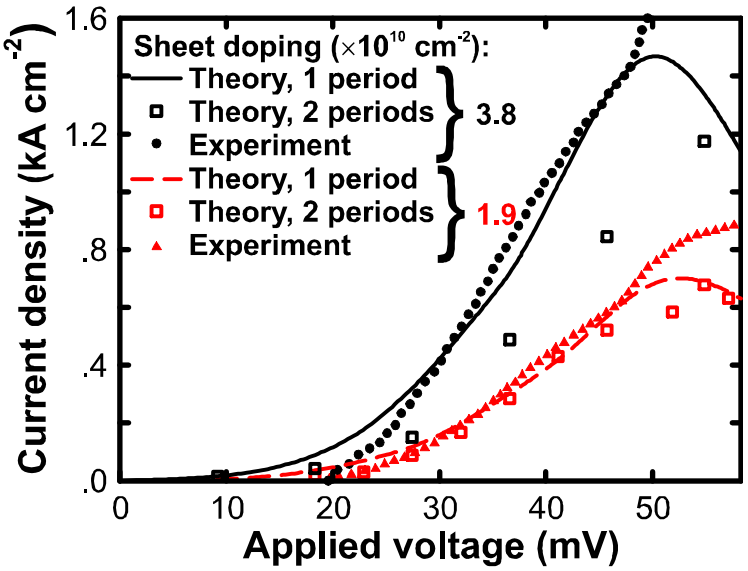

Figure 5.3.9: Current density as a function of applied bias voltage per period of the GaAs/$Al_{.15}Ga_{.85}As$ QCL at 40 K for the sheet doping density of 1.9×10^{10} cm^{-2} (red) and 3.8×10^{10} cm^{-2} (black). The results of NEGF calculations of a single period (lines) agree well with experiment (dots and triangles). When two periods (squares) are explicitly calculated, the theoretical results agree with experimental data only for the lower doped sample, whereas non-periodic electron densities influence the results of the higher doped device.

Higher electron densities

We have already seen in Sec. 5.2.4 that the Poisson potential at the higher doping density of 3.8×10^{10} cm^{-2} is affected by inhomogenously distributed charges. Accordingly, the Hartree potential of the QCL with a doping density of 3.8×10^{10} cm^{-2} deviates from an exact linear behavior as can be seen in Fig. 5.3.10 (a). The thick solid line in this figure shows the self-consistent determined conduction band profile of the QCL at the higher doping density. In order to guide the eye, the gray dotted line shows a linear potential drop of 56 mV per period and illustrates the deviation of the Hartree potential from linearity. Due to this nonlinearity, the resonant states (depicted as contour lines in Fig. 5.3.10 (a)) slightly differ in both periods. Therefore, the alignment conditions and the transmission probabilities of the two QCL periods differ and the I-V characteristics of two explicitly considered higher doped QCL periods differ from results of a single period (see black lines and symbols in Fig. 5.3.9). Figure 5.3.10 (b) depicts cross sections of the spatially resolved current density at the initial (solid, $z = 0$), the central (dashed, $z = 54$ nm) and the last device barrier (dotted, $z = 108$ nm). In contrast to the two-period results in the lower doped QCL (see Fig. 5.3.8 (b)), the energy resolved current density does not recover its energy distribution after two QCL periods. In addition, the two-period results in Fig. 5.3.9 deviate from the experimental data. For these reasons, we expect higher order electron-electron scattering to become important at a sheet doping density of 3.8×10^{10} cm^{-2}. However, single period calculations of higher doped QCLs including the approximate electron-electron scattering self-energies Eqs. (3.5.100) and (3.5.99) have only shown an incomplete thermalization, as is shown by the dash-dotted line in Fig. 5.3.10 (b). Nevertheless, this incomplete thermalization might be sufficient to restore the periodicity of the electron distribution well enough to yield a periodic Hartree potential. Unfortunately,

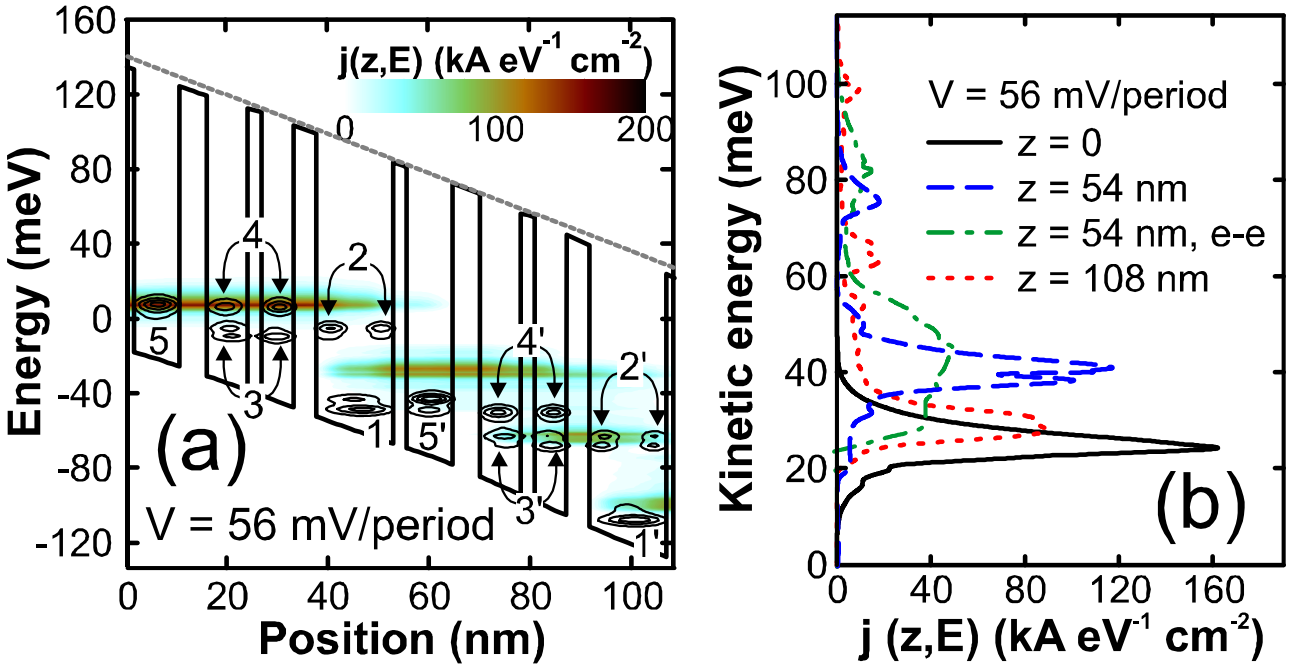

Figure 5.3.10: (a) Conduction band profile (thick line) and contour plot of the energy and spatially resolved current density j(z,E) of two periods of the QCL with a sheet doping density of 3.8×10^{10} cm^{-2} at a bias of 56 mV per period. The thin lines depict contour lines of the spectral function at vanishing in-plane momentum which represents resonant states. States of the first (second) period are labeled with numbers (primed numbers). The zero in energy marks the chemical potential of the source. The gray dotted line is given to illustrate the deviation of the conduction band from linear behaviour. (b) Cross section of the energy and spatially resolved current density of (a) in the leftmost (black solid) barrier, the central barrier (blue dashed), and the rightmost (red dotted) device barrier, respectively. The green dash-dotted line shows the energy resolved current density in the central barrier when inelastic electron-electron scattering in the static GW0 approximation is included.

the electron-electron scattering self-energies in Eqs. (3.5.100) and (3.5.99) are numerically too demanding to be implemented in two-period calculations. Thus, a revision of the electron-electron scattering self-energies is required in order to proof this effect. However, we have to leave this to future work.

5.4 Proposals of new and improved THz-QCLs

5.4.1 Introduction

We utilize the results of transport in resonant phonon THz-QCLs of the preceding sections in order to suggest several design improvements. We propose a change in the collector well width of the THz-QCL of Ref. [165] that efficiently blocks the coherent leakage of electrons out of the upper laser. We also demonstrate that the incoherent filling of the upper laser level by resonant emission of polar optical phonons as suggested by Yamanishi *et al.* [11] significantly improves the occupation inversion. We show that the probability of non-radiative transitions

between the laser levels can be significantly reduced when the optical transition is diagonal instead of direct. Based on the THz-QCL of Ref. [165] we propose a QCL design that yields diagonal optical transitions with a optical gain that is almost insensitive to scattering at rough interfaces. Finally, we suggest to add a quantum well to the active period of the QCL in [165] in order to thermalize the propagating electrons within each QCL period. In this way, the electron distribution is pinned to the QCL geometry and non-radiative transitions that we have found in Sec. 5.3.5 are suppressed.

5.4.2 How to reduce threshold current and to increase gain

Introduction

The reduction of the threshold current is of particular interest since it determines the thermal load of the active region during laser operation. We have shown in Sec. 5.3.2 that coherent multibarrier tunneling in the THz-QCL of Ref. [165] significantly contributes to the current density at threshold. On the one hand, this coherent tunneling is required to fill the upper laser level of this QCL (see Sec. 5.2.4). On the other hand, when electrons are less well confined in the upper laser level, their dwell time in this level is rather short and the light emission probability is small.

Therefore, we present in this section two QCL designs that suppress coherent current close to and above the threshold bias. First, we propose a QCL that is based on the THz-QCL of Ref. [165] with a modified collector well width. We show that this modification reduces the coherent leakage of electron of the upper laser level into the drain. Thereby the threshold current is significantly reduced, while the QCL still maintains an almost equal optical gain. Second, we present the "indirect pump"QCL design of Yamanishi *et al.*[11] that completely avoids coherent tunneling in and out of the upper laser level, but fills the upper laser level by resonant emission of LO-phonons. We illustrate and explain that this design yields a much larger optical gain than the THz-QCL of Ref. [165] although the doping density, the lattice temperature and the device materials are comparable in both QCLs.

Leakage into the drain

The coherent leakage of the resonant phonon QCL structure discussed in Sec. 5.3.2 has several adverse effects for the device performance. It enhances the current density close to threshold and causes a large number of electrons to tunnel out of the upper laser level without emitting photons. In order to suppress this leakage, the QCL should be designed in such a way that the upper laser level does not extend into the collector well ($\#2''$ in Fig. 5.2.7). The simplest way to achieve this goal is to broaden the collector well since this automatically misaligns the collector well states with the laser levels. Figure 5.4.1 shows the spectral function of the THz-QCL of Fig. 5.2.7 modified by a larger collector well width of 17.1 nm (instead of 15.3 nm in Fig. 5.2.7). With this design, the collector well states lie at lower energies and the spectral density in the collector well at the energy of the upper laser level becomes very small. Consequently, the maximum $\#2''$ of the spectral function $A(z, E)$ in the original design (see Fig. 5.2.7) is missing in the modified design (see Fig. 5.4.1). This modification reduces the current density around the threshold bias, as can be seen in Fig. 5.4.2 (a). Compared to the ballistic (dashed) and realistic (solid) I-Vcharacteristics of the original design (grey), the contribution of coherent tunneling to the threshold current in the modified design (black) is efficiently suppressed. Although the current density is reduced by this broadening of the collector well, our calculations show

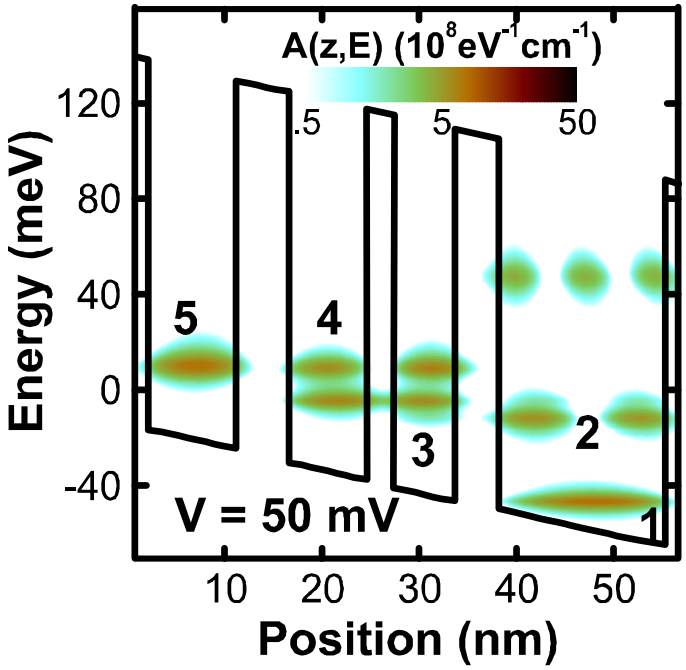

Figure 5.4.1: Contour plot of the spectral function $A(z, E)$ of the QCL of Fig. 5.2.7 modified by a broader collector well. The zero in energy marks the chemical potential of the source. The applied bias voltage is 50 mV per period. The solid line indicates the self-consistent potential profile. The spectral function is only shown within the energy interval from -70 to 80 meV. The labels number the resonances that have already been discussed in Sec. 5.2.4.

neither the peak gain energy nor the maximum value of the gain is changed. This can be seen in Fig. 5.4.2 (b), as it shows the optical absorption coefficient α in the center of the original (grey) and in the modified QCL (black) when incoherent scattering is included.

Leakage into the source

We have discussed in Sec. 5.2.4 that the upper laser level of the QCL of Fig. 5.2.7 gets filled by coherent tunneling of electrons from the source or source sided QCL period. Although this filling mechanism is efficient, it is based on the alignment of the injector state (#5 in Fig. 5.2.7) with the upper laser level (#4 in Fig. 5.2.7). This state alignment causes an anticrossing between the upper laser level and the injector state which has several adverse effects. First, the electrons are distributed in two energetically distinct laser levels. The thermal broadening in Fig. 5.2.7 smears out both laser levels. However, this splitting may cause an additional broadening of the optical gain. Second, the upper laser state is not completely confined in the area of the lower laser level (#4 in Fig. 5.2.7). In this way, the optical transition is partly diagonal and the emission probability is reduced. Finally, electrons in the upper laser level can leak into the source. Thus, a finite portion of the electrons get reflected by the confining barriers and may coherently leave the upper laser level towards the source.

One way to avoid the alignment of the upper laser level with the injector state, but still to guarantee an efficient filling of the upper laser level, has been introduced by Yamanishi *et al.* in [11], i.e. the "indirect pump"four level QCL. In order to illustrate this design, we consider a similar QCL consisting of the periodically repeated sequence of $Al_{.23}Ga_{.77}As$/GaAs layers of

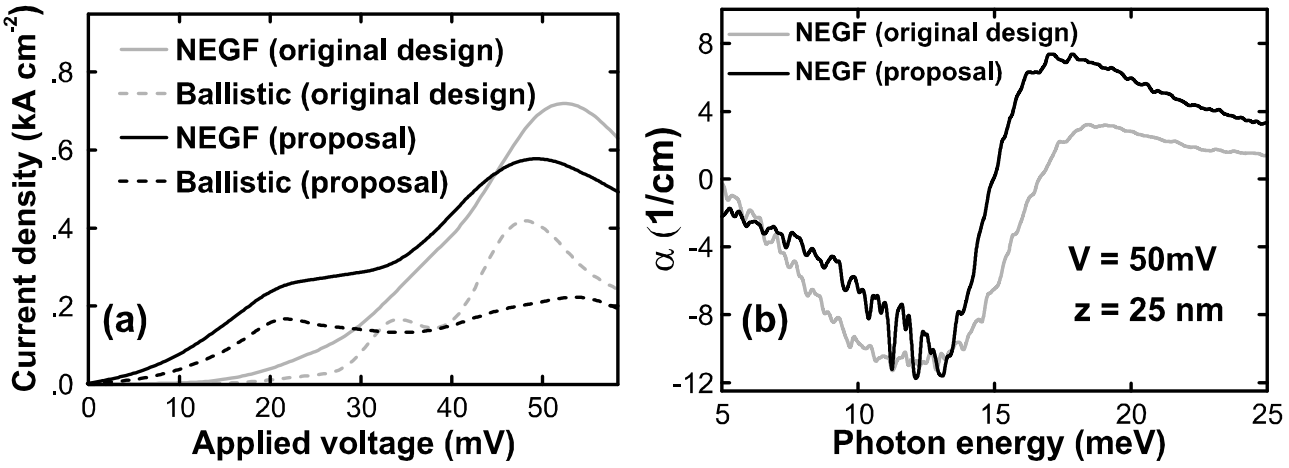

Figure 5.4.2: (a) Calculated IV-characteristics of the QCL of Fig. 5.2.7 with the original (grey) and the broader collector well (black). The broadening of the collector well suppresses the coherent transport (dashed) which simultaneously reduces the current when incoherent scattering is included (solid). (b) Calculated absorption coefficient $\alpha\left(z, E_{photon}\right)$ at $z = 25$ nm in the THz-QCL of Fig. 5.2.7 with the original (grey) and the broader (black) collector well. The peak gain energy is not affected by the broadening of the collector well.

the widths (18) 98 (27) 71 (27) 142 (9) 98 (36) 169 Å, where the numbers in parentheses denote $Al_{.23}Ga_{.77}As$ barriers and only the underlined well is doped with 1.2×10^{16} cm^{-3}. In order to simplify the comparison with the resonant phonon QCL of the previous sections, the device temperature of this four level QCL is set to 40 K. In contrast to the resonant phonon design of Fig. 5.2.7, this QCL design clearly separates the injector state and the upper laser level. This is illustrated in Fig. 5.4.3 which depicts the resonant laser states of this indirect pump QCL at a bias voltage of 109 mV per period by a contour plot of the spectral function at vanishing in-plane momentum. The energy difference of the upper laser state (#4) and the injector state (#5) equals 36 meV. Therefore, the upper laser level gets efficiently filled from the injector state by the resonant emission of LO-phonons. Furthermore, the upper laser level does not leak out of the two central quantum wells between $z = 28$ nm and $z = 52$ nm. In this way, electrons of the upper laser level of the indirect pump QCL are much better confined than in the upper laser level of the resonant phonon QCL of [165]. The mechanisms that deplete the lower laser level (#3) are the same as in the resonant phonon QCL of Fig. 5.2.7 (see Sec. 5.2.4). Therefore, due the better confinement of the upper laser level, we find a much higher occupation inversion compared to results of the resonant phonon design of [165]. This occupation inversion is illustrated in Fig. 5.4.4 (a) which shows a contour plot of the energy resolved density $n\left(z, E\right)$ of the "indirect pump"QCL at the bias of 109 mV per period and 40 K lattice temperature. In order to guide the eye where the resonant states lie, the contour lines in Fig. 5.4.4 depict maxima of the spectral function. Most of the electrons in the "indirect pump"QCL are "trapped"in the upper laser level and we find the absolute maximum of $n\left(z, E\right)$ in the upper laser level #4. In contrast, in the resonant phonon design of [165], the maxima of $n\left(z, E\right)$ in the injector and collector wells are larger than in the upper laser level (see Fig. 5.2.2 and Fig. 5.3.7 (c)).

Although the doping density in the indirect pump QCL is slightly smaller than in the resonant phonon design of [165], we find the maximum local optical gain of the indirect pump

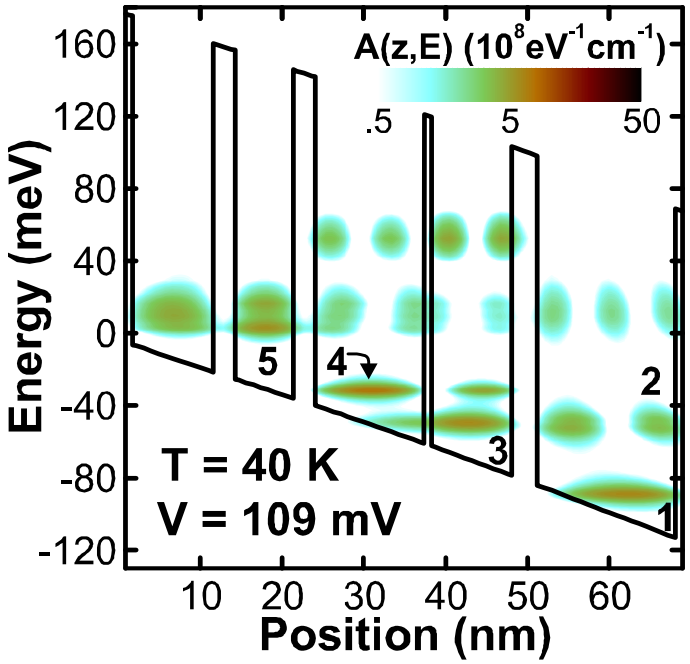

Figure 5.4.3: Calculated conduction band profile (solid) and contour plot of the spectral function at vanishing in-plane momentum $A(z, E)$ of the "indirect pump"QCL described in the text. The spectral function is shown in the relevant energy range betwenn -120 meV and 80 meV.

QCL in Fig. 5.4.4 (a) to reach 73 cm^{-1} and the averaged gain to be 14 cm^{-1}. This is significantly larger than the maximum local gain of 11 cm^{-1} and the averaged gain of 4 cm^{-1} of the resonant phonon QCL of [165] (see Fig. 5.2.8). Unfortunately, we find the thermally activated phonon emission (discussed in Sec. 5.3.4) to dramatically reduce the optical gain of the indirect pump QCL at higher lattice temperatures. This can be seen in Fig. 5.4.4 (b) which shows $n(z, E)$ at a lattice temperature of 200 K. At this temperature, the occupation of the upper and lower laser level is comparable. Thus, the maximum operating temperature is limited to similar temperatures as the resonant phonon design [185].

Apart from the better confinement of the upper laser level, there is a second feature of this design that yields a higher optical gain: The upper and lower laser states in Fig. 5.4.3 are not symmetrically located in both central quantum wells. Instead, the upper level #4 is rather concentrated in the left well, whereas the lower level #3 is rather centered in the right well. We will show in Sec. 5.4.3 that this spatial separation of the laser levels suppresses non-radiative laser transitions and thereby may lead to higher optical gain.

5.4.3 How to suppress nonradiative losses

Introduction

Kumar *et al.* have suggested in [186] that a reduction of the wavefunction overlap of the upper and lower laser level improves the QCL performance. When this spatial overlap is reduced, the optical transition becomes (spatially) diagonal which reduces the optical matrix element. However, this can be overcompensated by the reduction of non-radiative transitions from the upper into the lower laser level. This may, in total, result in higher optical gain and higher

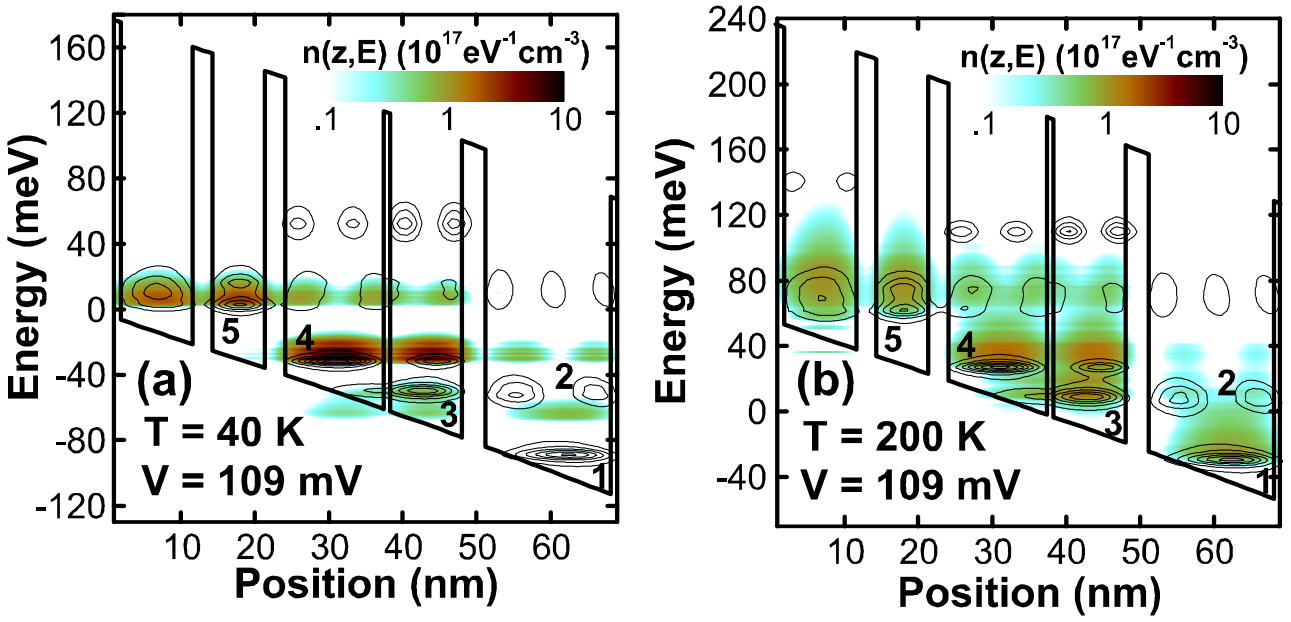

Figure 5.4.4: Calculated conduction band profile (thick line) and contour plot of the energy and spatially resolved electron density $n\,(z, E)$ in the "indirect pump"QCL at a bias voltage of 109 mV per period and a device temperature of (a) 40 K and (b) 200 K. The thin lines depict contour lines of the spectral function $A(z, E)$ at vanishing in-plane momentum. The zero in energy marks the chemical potential of the source.

maximum QCL temperatures.

In this section, we present a modification of the QCL of [165] that results in an "indirect pump"QCL (see Sec. 5.4.2) and more importantly diagonal laser transitions. We demonstrate that the small overlap of the upper and lower laser levels indeed reduces the probability of non-radiative transitions. In particular, we show that the scattering at rough interfaces has only a small influence on the optical gain - in very contrast to the large reduction of gain in the original QCL in Sec. 5.3.3. We find a peak gain in the modified design that is approximately a factor of 3 larger than in the original QCL of [165].

Design proposal

In order to confirm that diagonal transitions reduce non-radiative losses while still allowing for significant optical gain, we modify the laser transition of the QCL of [165] into a diagonal one. For this purpose, we replace the $Al_{.15}Ga_{.85}As$ barrier in the center of the two laser levels (between $z = 24$ nm and $z = 26.7$ nm in Fig. 5.2.7) with a GaAs layer of the same width. Thus, the modified QCL consists of periodically repeated GaAs/$Al_{.15}Ga_{.85}As$ layers of widths (30) 92 (55) 173 (41) 155 Å, where the values in parentheses indicate the $Al_{.15}Ga_{.85}As$ barriers and the widest well is still the only doped region. For a better comparison with the original design, we use the same device and material parameters. Therefore, we assume a lattice temperature of 40 K, we consider a sheet doping density of 1.2×10^{10} cm^{-2} in the widest well and we include roughness parameters $\lambda = 8$ nm and $\delta z = 0.6$ nm (see Sec. 3.5.5). The replacement of the barrier layer results in a three well design with the laser levels located in separate wells. This is illustrated by the solid line in Fig. 5.4.5 (a) which shows the self-consistently calculated

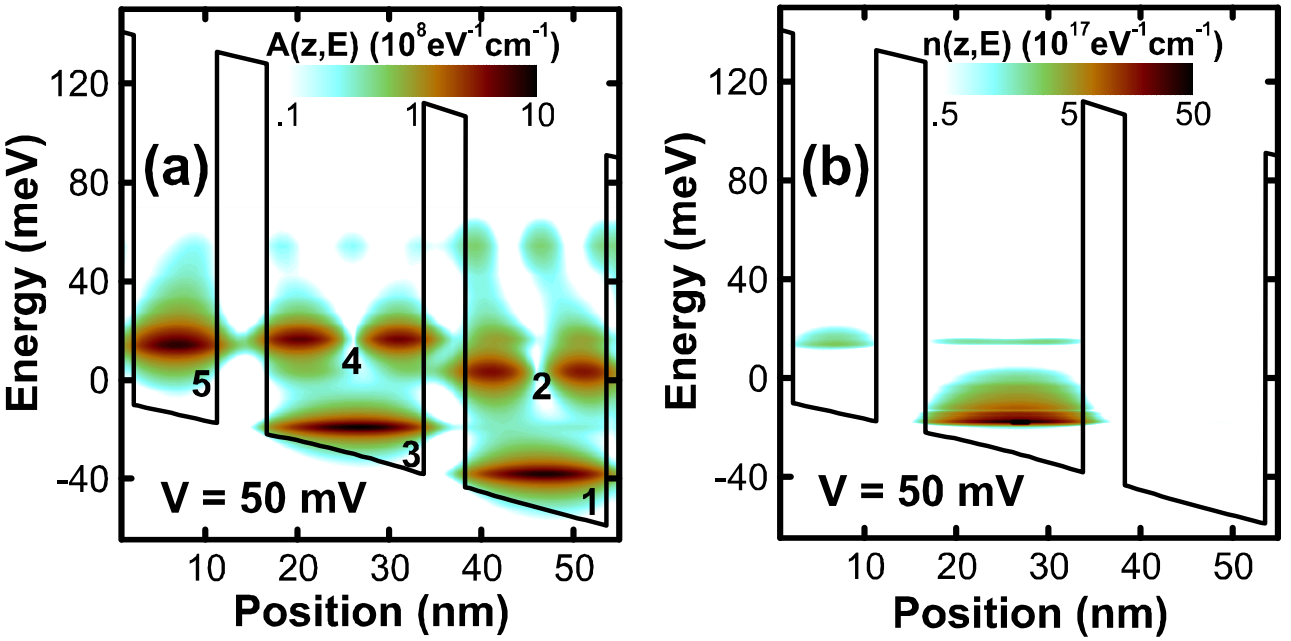

Figure 5.4.5: (a) Contour plot of the spectral function $A(z, E)$ and conduction band profile (solid line) of the proposed new QCL described in the main text. The zero in energy marks the chemical potential of the source. The applied bias voltage is 50 mV per period. The spectral function is only shown within the energy interval from -65 to 70 meV. The labels number the resonant states as discussed in the main text. (b) Contour plot of the energy and spatially resolved electron density $n(z, E)$ of the QCL in (a).

conduction band profile of the modified QCL at 50 mV per period. The contour shows the spectral function at vanishing in-plane momentum and depicts the (labeled) resonant states. Electrons from the injector state #5 tunnel resonantly into state #4. The upper laser level #3 gets filled by electrons of level #4 that resonantly emit a LO-phonon. Therefore, this design is an "indirect pump"QCL similar as the one discussed in Fig. 5.4.3. Accordingly, electrons in the upper laser level do hardly leak out of the central quantum well and are efficiently "trapped". This is shown by the contour plot in Fig. 5.4.5 (b) which shows the spatially and energy resolved electron density $n(z, E)$ in the QCL of (a). The maximum of $n(z, E)$ in the upper laser level #3 is clearly the highest in the total QCL period.

Diagonal transition and rough interfaces

There is only a small overlap of the upper laser level #3 with the lower laser level #1 at positions $z \geq 30$ nm. At these positions, the optical absorption coefficient $\alpha(z, E_{photon})$ becomes negative, as can be seen in the contour plot of Fig. 5.4.6 (a). Note that the potential profile (solid line) is only meant to guide the eye and is not on scale with the photon energy.

We recall that we have found in Sec. 5.3.3 for the original QCL design of [165] that scattering at rough interfaces efficiently reduces the occupation inversion and the optical gain. We have found in the original design a continuos decrease of the optical gain with increasing δz. In particular, we have seen in Fig. 5.3.5 that the interface roughness scattering reduces the optical gain in the original QCL by almost a factor of 10.

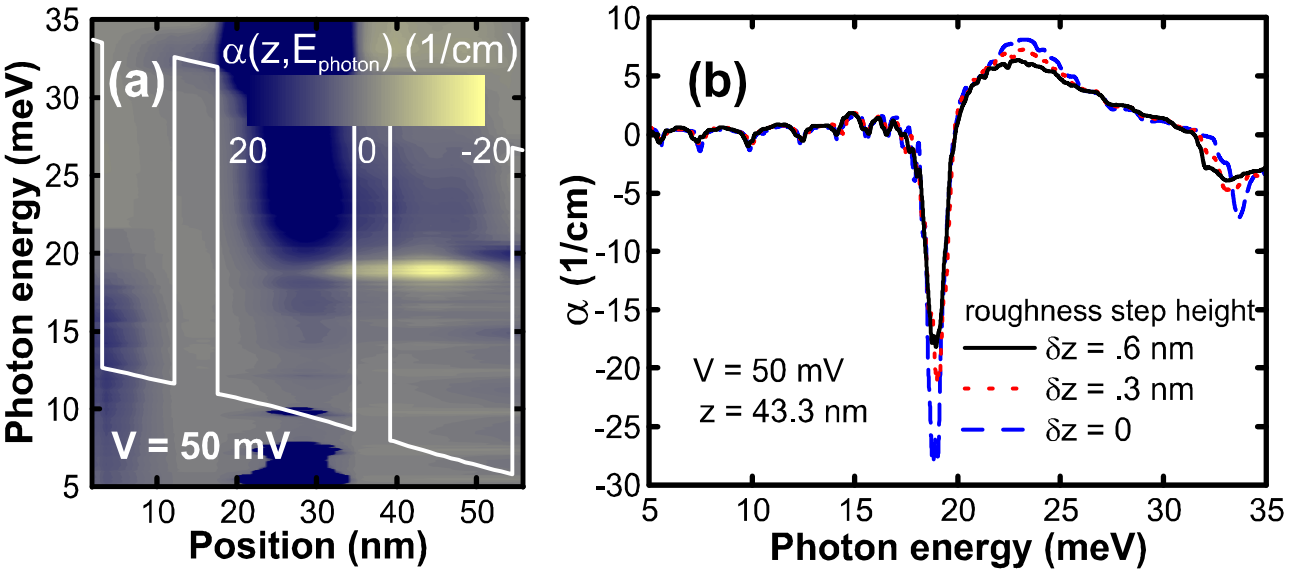

Figure 5.4.6: (a) Contour plot of the absorption coefficient $\alpha\,(z, E_{Photon})$ of the new proposed QCL in Fig. 5.4.5 as a function of position and photon energy. The potential profile (white line) is only meant to guide the eye. (b) Calculated absorption coefficient $\alpha\,(z, E_{photon})$ at $z = 43.3$ nm in the new proposed QCL with rough interfaces of different roughness step height δz. Due to the diagonality of the laser transition, calculations including realistic interfaces (solid) yield almost the same optical gain as calculations with realitively smooth (dotted) and perfect interfaces (dashed).

The small overlap of the upper and lower laser levels in the modified design, however, almost completely suppresses such non-radiative losses. This is illustrated in Fig. 5.4.6 (b) which shows cross sections of the optical absorption coefficient $\alpha\,(z, E_{photon})$ at $z = 43.3$ nm in the modified QCL at a voltage of 50 mV for various roughness stepheights δz. Obviously, the scattering at rough interfaces has only a marginal effect on the optical gain in the modified design. Most notably, the peak gain of a calculation of the modified design including a realistic step height of $\delta z = 0.6$ nm for the interface roughness is approximately a factor of 3 larger than in the original QCL.

5.4.4 How to improve stability at higher doping densities

Introduction

We have seen in Sec. 5.3.5 that the incompletely dissipated net gain of electronic energy in the QCL of [165] heats up the carrier distribution and allows non-radiative transitions from the upper into the lower laser level. In this section, we propose a modification of this QCL structure that guarantees a complete dissipation of the net energy gain at laser threshold. Thereby, we pin the electron distribution to the QCL periodicity. This has two positive effects: First, non-radiative transitions in subsequent periods are suppressed, since the electrons do not accumulate enough energy. Second, the alignment of the device states becomes more stable with respect to higher doping densities, because deviations from a periodic electron distribution are reduced and the conduction band profile is less distorded from the QCL periodicity.

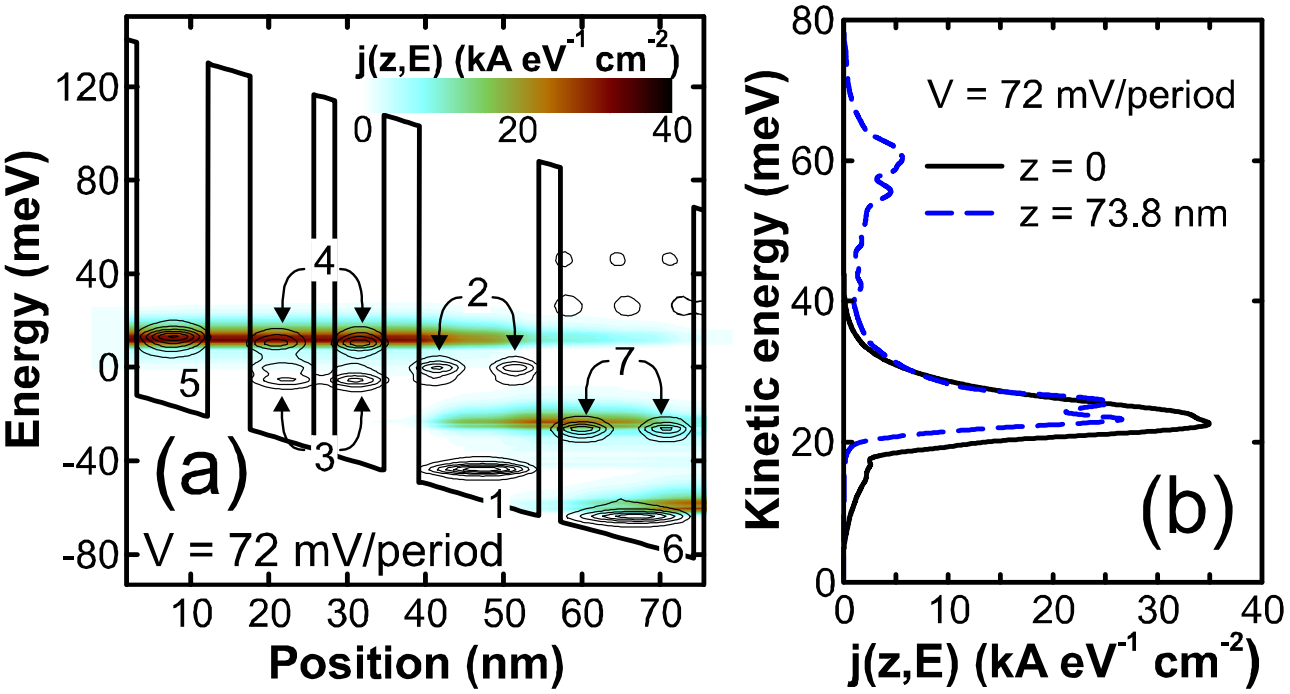

Figure 5.4.7: (a) Calculated conduction band profile (thick line) and contour plot of the energy and spatially resolved current density j(z,E) in a single period of the proposed new QCL design described in the main text. The thin lines depict contour lines of the spectral function $A(z, E)$ at vanishing in-plane momentum. The zero in energy marks the chemical potential of the source. (b) Cross section of the energy and spatially resolved current density of (a) in the leftmost (black solid) barrier, and the rightmost (blue dashed) device barrier, respectively. For each curve, the energy is counted relative to the respective local conduction band edge.

Design proposal

We augment each QCL period from [165] by two additional layers, a 3 nm $Al_{.15}Ga_{.85}As$ barrier, followed by a 17.1 nm wide GaAs quantum well namely. This leads to a threshold bias of ~72 mV per period which results in a potential drop that is commensurable with the energy of two LO-phonons. The purpose of these additional layers is to allow the electrons to dissipate the 16 meV of energy they have gain when they traverse a period of the original QCL of [165] biased with the same electric field (see discussion in Sec. 5.3.5). This is illustrated in more detail in the following.

Restoration of the QCL periodicity

Figure 5.4.7 (a) shows a contour plot of the energy and spatially resolved current density $j(z, E)$. Also shown in this figure are contour lines of the spectral function at vanishing in-plane momentum. Since we have only added one additional quantum well to the QCL period of [165], the electronic transport within the first four quantum wells (up to $z = 55$ nm in Fig. 5.4.7 (a)) agrees with the one discussed in detailed in Sec. 5.2.4 and Sec. 5.3.5.

We have shown in Sec. 5.3.5 that most electrons that arrive in state #1 have a surplus of 16 meV of kinetic energy in the in-plane motion. Their total energy is sufficient to resonantly enter the second state (#7) of the additional quantum well and to scatter into state #6 by

the resonant emission of a second LO-phonon. This can be seen in Fig. 5.4.7 (a) for positions $z \geq 70$ nm. Here, the dominant maximum of $j(z, E)$ coincides with the state #6. Thus, the main portion of the carrier distribution at the end of the period is reset to its original value. In this way, the electrons are almost completely thermalized within a single period and the electron distribution is pinned to the QCL periodicity. non-radiative transitions between the laser states of this and the following QCL period are thereby suppressed.

The thermalization is also illustrated in Fig. 5.4.7 (b) which shows cross sections of the energy resolved current density $j(z, E)$ of Fig. 5.4.7 (a) in the first and last barrier of the QCL period. Since the total current density is a conserved quantity, the area under each of the two curves is the same. If the electronic carrier distribution is the same in each QCL period, the two curves in Fig. 5.4.7 (b) lie on top of each other. Indeed, the main portion of the carrier distribution at the end of the period (dashed) is almost completely reset to its original value (solid). The smaller peak of $j(z, E)$ at $z = 73.8$ nm and $E = 60$ meV reflects the ballistic portion of transport and lies one LO-phonon energy above the main peak.

5.5 Conclusion

We have shown in this chapter that the stationary transport in low doped THz-QCLs can be modeled with NEGF calculations of a single QCL period with open boundary conditions. We have successfully reproduced the experimental *I-V* characteristics, the optical gain, the threshold current as a function of doping density, and the temperature degradation of a recently fabricated resonant phonon QCL. The agreement with experimental results allowed us to analyze the transport in THz-QCLs in great detail. Since we do not impose the commonly used periodic boundary conditions, we were able to selectively turn off scattering mechanisms. Thereby, we have unveiled significant coherent leakage of electrons out of the upper laser level. This leakage increases the threshold current and simultaneously reduces the occupation inversion. We have found an unexpectedly small influence of LO-phonon scattering on the *I-V* characteristics, but demonstrated a tremendous reduction of the optical gain with increasingly rough interfaces. This finding agrees with experimental results, but is at variance with results of approximate scattering models in literature. We have demonstrated that thermal backfilling of electrons into the lower laser level as well as the thermally activated emission of LO-phonons by electrons in the upper laser level effectively reduces the occupation inversion and determines the maximum operating laser temperature. Elaborate calculations of transport in two periods of the experimental QCL have shown that the electrons at the threshold bias leave every second period with a net gain of energy. This energy heats up the electron distribution and enables nonradiative transitions between the laser levels.

Our theoretical results for the fabricated QCL enable us to propose several QCL design improvements. We have shown how to suppress the coherent leakage out of the upper laser level. In this way, we have successfully reduced the threshold current, while the optical gain remained effectively unchanged. We have demonstrated that the upper laser level can be efficiently filled by resonant emission of LO-phonons, as suggested by Yamanishi *et al.* [11]. We have illustrated that this design efficiently confines electrons in the upper laser level which yields a very large occupation inversion. Furthermore, we have proposed a THz-QCL with diagonal optical transitions and very small spatial overlap of the laser states. Most importantly, the optical gain in this new design is almost insensitive to the interface roughness scattering. Finally, we have modified the experimental resonant phonon QCL such that the formation of

heated electrons is suppressed. Electrons in this new QCL leave each period with no gain of kinetic energy. In this way, these electrons faithfully follow the geometric QCL periodicity and nonradiative transitions between the laser states are suppressed.

Part III

Stationary spin transport in two- and three-dimensionsal nanodevices

In the preceding part of this thesis, we have applied the nonequilibrium Green's function formalism on the vertical electron transport in a single semiconductor conduction band in order to assess common approximations and to develop and evaluate new, numerically efficient methods in this formalism. In this last part of the thesis, we utilize our results of the vertical transport part and implement the NEGF formalism on the stationary transport in systems of higher complexity. In particular, we focus on the stationary, spin-resolved transport in two-dimensional electron and hole gases. The spin polarized transport (i.e. "spintronics") in semiconductor heterostructures has attracted great interest, in particular since Datta and Das have proposed the spin transistor [187]. Possible applications of spintronics include entangled spins for quantum computers [188], spin memory devices [189] and spin valves [190], etc. The recently observed spin-Hall effect [12, 13] is a promising candidate to generate spin polarized carriers in all-semiconductor, non-magnetic nanodevices. In particular, theoretical transport calculations of concrete devices [191, 192] have shown that the intrinsic spin-Hall effect can yield local spin polarizations up to 100 %.

However, all transport calculations in literature are based on envelope function approaches which are known to be plagued by artifacts in the context of the spin-orbit interaction [193]. For this reason, we apply the NEGF formalism on the spin-dependent envelope function approach as well as on an atomistic, microscopic relativistic tight-binding model. We compare results of the intrinsic spin-Hall effect of both models and find a good qualitative agreement. Thereby, we verify the common and numerically efficient approximation of a spin-orbit potential that is (for small applied bias voltages) linear in the momentum operator.

We derive a novel, numerically efficient scattering self-energy in the self-consistent Born approximation for the inelastic scattering of electrons with acoustic phonons. This allows us to clarify the phonon-mediated influence of the spin-Hall effect on the spin polarization of completely confined carriers. We find the spin polarization of carriers in the confined states of a quantum dot to be several orders of magnitude smaller than the polarization of propagating carriers. Thus, ballistic transport calculations that do not consider confined states are sufficient for the qualitative prediction of the spin polarization in all-semiconductor devices.

It is common in the area of spin-transport calculations to neglect the spin-orbit interaction within the semi-infinite leads. Accordingly, device proposals for efficient spin-polarizers often assume an inhomogeneous spin-orbit interaction strength which complicates the experimental realization. We extend the iterative algorithm for the lead surface Green's function introduced for the vertical transport calculations of this thesis to the case of the spin-orbit interaction in two- and three-dimensional devices. This allows us to verify that a *homogeneous* spin-orbit interaction strength is completely sufficient for large spin polarizations. We show that interferences of the propagating carriers can be utilized to generate spin polarizations that can - at specific device positions - almost reach 100 %. We propose two concrete all-semiconductor, non-magnetic spin polarizers. The spin polarization in these devices is entirely based on carrier interferences induced by the device geometry instead of inhomogeneous interaction constants.

Chapter 6

Method - atomistic and continuum models

6.1 Introduction

Most aspects of an implementation of the NEGF formalism on spin transport in two- and three-dimensional systems have already been discussed in detail in chapter 3. Since our methods in chapter 3 can be straightforwardly extended to the systems in this part of the thesis, we limit ourselves in this chapter on the relevant differences. Thus, we introduce the bases functions the Green's functions will be represented with. We discuss the implemented Hamilton operators and emphasize their approximate nature. In particular, the common implementation of the spin-orbit interaction potential for transport in two-dimensional electron and hole gases requires for a proof of validity. This motivates our implementation of microscopic NEGF calculations.

Incoherent scattering in NEGF calculations of two-dimensional systems can only rarely be found in literature [134, 194]. Typically, scattering is implemented in the Büttiker probe model [195–197] or as a random potential [198]. We explain that the Büttiker probe model is inappropriate to check whether the intrinsic spin-Hall effect of confined electrons and holes maintains a finite spin polarization. In contrast, a single calculation with a random potential gives only coherent transport results. Therefore, the modelling of incoherent scattering requires for a numerically demanding statistics of *many* random potentials. For these reasons, we derive a novel scattering self-energy in the self-consistent Born approximation for the inelastic scattering with longitudinal acoustic phonons. This derivation is based on our approximations in Sec. 3.5.3 and decouples the retarded and lesser Green's functions similar to our acoustic phonon self-energy in the vertical transport situation (see Sec. 3.5.3 for a detailed discussion). This decoupling is essential for a numerical feasible implementation of self-consistent inelastic scattering.

Since we want to answer several general questions on the intrinsic spin-Hall effect rather than to quantitatively predict experimental results, we do not solve the Poisson equation and limit the calculations to faintly doped devices at lattice temperatures up to 10 K. This eases our numerical implementation significantly, because the Green's functions may be discretized on a homogeneous grid and possible charge accumulations near the device boundaries need not to be screened self-consistently. However, we emphasize that the new methods introduced in sections 3.6 and 3.7 can be extended to more complex systems straightforwardly. Nevertheless, we extend the iterative solution scheme of the lead surface Green's functions of Sec. 3.7.4 to the two- and three-dimensional transport problems of this part of the thesis. Thereby, we introduce

a novel, numerically efficient method to include incoherent scattering and spin-orbit interaction in the lead density of states. This is essential to avoid artificial reflections at the lead/device boundaries, as we have discussed in detail in Sec. 4.2.2.

6.2 Fundamentals

6.2.1 Introduction

We introduce the basis functions and Hamilton operators for the implementation of the NEGF formalism in the two-dimensional envelope function and the three-dimensional microscopic tight binding model. We will use the later model in Sec. 7.2 for the proof that the common but approximate treatment of the spin-orbit interaction in the envelope function model gives qualitatively correct results. For later reference, we introduce the relative spin polarization in x, y and z.

6.2.2 Basis functions and Hamiltonian

Introduction

We adapt the nonequilibrium Green's function formalism on two-dimensional electron and hole gases in a spatial eigenfunctions representation. Laterally homogeneous zincblende heterostructures develop a splitting of the band edges with respect to the sign of the spin polarization that is close to the Γ-point linear in the in-plane momentum $k_{\|}$. We follow the common approach and implement a $k_{\|}$-linear spin-orbit Hamiltonian on the transport in *inhomogeneous* two-dimensional electron and hole gases. In order to verify the validity of this approximate Hamilton operator, we additionally implement the NEGF method in a microscopic tight binding representation for transport in two-dimensional GaAs devices. In this approach, we represent each individual atom with eight atomic orbitals. The spin-orbit interaction in the tight binding approach is represented by an intraatomic interaction and does not explicitly depend on the in-plane momentum $k_{\|}$.

Envelope function representation

All two-dimensional electron or hole gases in this thesis are considered to be completely confined in the lowest state ($\nu_0(z)$) of a quantum well grown in the z-direction. Therefore, the particle creation and annihilation operators can be written in the second quantization

$$\hat{\psi}(\vec{x},\sigma,t) = \sum_{\sigma,l,m} \psi_{l,m}(x,y,\sigma)\,\nu_0(z)\,\hat{a}_{\sigma lm0}(t)\,, \tag{6.2.1}$$

$$\hat{\psi}^{\dagger}(\vec{x},\sigma,t) = \sum_{\sigma,l,m} \psi^{*}_{l,m}(x,y,\sigma)\,\nu^{*}_0(z)\,\hat{a}^{\dagger}_{\sigma lm0}(t)\,. \tag{6.2.2}$$

The indices σ, l and m label the basis states in the spin space, the x- and y-dimension, respectively. Since no electron or hole is allowed to change the quantum well state, the z-component of the particle wavefunctions is obsolete and will be frequently dropped in the envelope function representation.

We use a product ansatz for the basis wave functions in the Heisenberg representation

$$\psi_{\hat{H}_0}(x,y,\sigma) = \varphi_{\hat{H}_0}(x)\,\phi_{\hat{H}_0}(y)\,|\sigma\rangle\,. \tag{6.2.3}$$

We represent the spin degree of freedom by the eigenfunctions of the spin operator in z-direction ($\sigma = \pm$)

$$\hat{S}_z\,|\pm\rangle = \pm\frac{\hbar}{2}\,|\pm\rangle\,. \tag{6.2.4}$$

In order to guarantee a high flexibility and accuracy of the modeled devices (similar to Sec. 3.2.2), we choose spatial eigenfunctions for the basis in the (x,y) plane

$$\hat{x}\varphi_{\hat{H}_0}(x') = x'\varphi_{\hat{H}_0}(x')\,, \tag{6.2.5}$$

$$\hat{y}\phi_{\hat{H}_0}(y') = y'\phi_{\hat{H}_0}(y')\,. \tag{6.2.6}$$

We discretize the spatial eigenfunctions on homogeneous grids with spacing Δ_x and Δ_y in the respective directions (see discussion in Sec. 3.2.2)

$$\varphi_{\hat{H}_0}(x) = \begin{cases} \sqrt{\Delta_x^{-1}}, \forall x \in [x-\Delta_x/2; x+\Delta_x/2] \\ 0,\ \text{elsewhere} \end{cases}\,, \tag{6.2.7}$$

$$\phi_{\hat{H}_0}(y) = \begin{cases} \sqrt{\Delta_y^{-1}}, \forall y \in [y-\Delta_y/2; y+\Delta_y/2] \\ 0,\ \text{elsewhere} \end{cases}\,. \tag{6.2.8}$$

Laterally homogeneous zincblende heterostructures or superlattices develop a $k_\parallel$-linear splitting of the spin-up and spin-down band edge energy state near the Brillouin center $k_\parallel = 0$ [199, 200]. This holds for any orbital nondegenerate band edge state. For [001] grown structures, this spin splitting depends on two parameters, namely the so-called bulk inversion asymmetry (BIA) coupling or Dresselhaus term α_{BIA} and the structure inversion asymmetry (SIA) or Rashba term α_{SIA} [193, 199, 200]. While the BIA term is always nonzero, the SIA term vanishes for D_{2d} symmetric structures. For structures grown along the [011] or [111] axes, on the other hand, the $k_\parallel$-linear spin-splitting depends only on a single parameter that can significantly differ from the two [001] constants. When we set the coordinate axes ($\vec{e}_x$, $\vec{e}_y$ and $\vec{e}_z$) parallel to the cubic axes of the crystal, this approximate spin splitting can be described with the effective Hamilton operator

$$\hat{H}_{SO} = \alpha_{BIA}\left(-k_x\boldsymbol{\sigma}_x + k_y\boldsymbol{\sigma}_y\right) + \alpha_{SIA}\left(k_y\boldsymbol{\sigma}_x - k_x\boldsymbol{\sigma}_y\right). \tag{6.2.9}$$

Hereby, the $\boldsymbol{\sigma}_i$ are the Pauli matrices and the z-component of the spin is perpendicular to the (x,y)-plain of the two-dimensional electron or hole gas. Matrices in the spin space are given in bold type.

For a heterostructure or quantum confined two-dimensional particle gases, this Hamiltonian Eq. (6.2.9) is then commonly transformed to an envelope function Hamiltonian in real space by augmenting it with a confining potential $V(x,y)$ and by replacing $k_x \to -i\nabla_x$, $k_y \to -i\nabla_y$, *independently of the crystal orientation of the growth axis and its microscopic symmetry.* This is numerically very efficient and we follow this approach for two band effective mass transport (EFT) calculations in two-dimensional nanodevices

$$\hat{H}_0 = -\frac{\hbar^2}{2m^*}\left(\nabla_x^2 + \nabla_y^2\right)\mathbf{1} + V(x,y)\,\mathbf{1} - i\alpha_{BIA}\left(-\nabla_x\boldsymbol{\sigma}_x + \nabla_y\boldsymbol{\sigma}_y\right) - i\alpha_{SIA}\left(\nabla_y\boldsymbol{\sigma}_x - \nabla_x\boldsymbol{\sigma}_y\right). \tag{6.2.10}$$

However, we also perform comparative microscopic tight binding calculations in order to validate this approach (see the next paragraph). Since Majewski and Vogl have shown from atomistic ab-initio and tight binding calculations that the Dresselhaus term dominates in spatially extended nanostructures [193], we will neglect the Rashba term in our EFT calculations presented in this thesis*.

Microscopic tight binding representation

In order to proof that the spin orbit Hamilton operator of Eq. (6.2.9) is valid in inhomogeneous two-dimensional electron and hole gases and transport calculations based on this operator give reliable qualitative results, we apply the NEGF method on a second model, namely an atomistic relativistic tight-binding model and compare the results of both models in Sec. 7.2. We apply the two-center approximation on the tight binding model and represent the electronic Hamiltonian in a Löwdin type basis set [201]

$$H_{l_1,m_1,l_2,m_2} = \left\langle l_1, m_1, \sigma_1, \vec{R}_1 | \hat{H} | l_2, m_2, \sigma_2, \vec{R}_2 \right\rangle . \tag{6.2.11}$$

Here, (l, m) labels the angular symmetry of the respective orbital, σ its spin orientation and $\vec{R}$ the atomic centers. We apply this model on GaAs devices. We represent eight orbitals of each Ga and As atom by the tesseral spherical harmonics with the spin quantized in the z-direction. Following the notation of Podolskiy and Vogl [202], these functions are (each of them with the spin oriented either + or −)

$$\begin{aligned} s &= \overline{Y}_{0,0}(\theta, \phi), \\ p_x &= \overline{Y}_{1,1}(\theta, \phi), \\ p_y &= \overline{Y}_{1,-1}(\theta, \phi), \\ p_z &= \overline{Y}_{1,0}(\theta, \phi). \end{aligned} \tag{6.2.12}$$

We use the empirical matrix elements of the electronic Hamiltonian of GaAs given in [203]. It is worth to note that the spin orbit coupling in the empiric tight binding method is a pure intra-atomic coupling potential (see Eqs. (34) and (35) in [202]). Therefore, the relativistic spin-orbit interaction in the tight binding method does not explicitly act on electrons tunneling between adjacent atoms. This is in very contrast to the envelope function theory in Eq. (6.2.10) which relates the spin orbit interaction intimately with the momentum of propagating electrons.

The numerical load of microscopic transport calculations limits our calculations to a sp^3-representation. It is known (see e.g. [204]) that this limited number of orbitals results in a band structure that deviates from the experimental finding. Nevertheless, our major concern is the validation of the envelope function Hamiltonian Eq. (6.2.10). Thus, we want to show the *qualitative* agreement of the envelop function model with the microscopic model. Quantitative comparisons require for sophisticated calculations that are (currently) beyond the capability of state of the art hardware.

*Comparative calculations of the Rashba and Dresselhaus term have shown that they yield spin polarizations of opposite sign and therefore compensate each other.

6.2.3 Extension of known observables

Introduction

Observables such as the charge current density and the charge density in the two-dimensional envelope function model can be straightforwardly derived from Eqs. (2.2.6) and (2.2.7) (see also Sec. 3.3.2). Since the purpose of this part of the thesis is to proof the applicability of the Hamilton operator of Eq. (6.2.10) and to propose efficient all-semiconductor spin polarizers, we will mainly focus on the local relative spin polarization $P_i(x,y)$ in the directions $i = x, y, z$, which we introduce here. Some studies in literature discuss the spin current as an instructive spin related "observable". Since the spin current is a nonconserved quantity however, we do not consider it in this thesis, but we refer to [205–207] for its discussion.

Envelope function model

We define the relative polarization of electrons or holes with respect to the spin-$\hat{S}_z$ operator by

$$P_z(x,y) = \frac{n^z_{+,+}(x,y) - n^z_{-,-}(x,y)}{n^z_{+,+}(x,y) + n^z_{-,-}(x,y)}. \tag{6.2.13}$$

Hereby, we have introduced the spin resolved electron/hole density and correlation at the grid point (x,y) by

$$n^z_{\pm,\pm}(x,y) = \frac{-i}{2\pi}\int \mathrm{d}E G^<(x,y,\pm;x,y,\pm,E). \tag{6.2.14}$$

The relative polarization in the remaining spin directions can be derived by rotations in spin space around the axis $\vec{e}$ by the angle α

$$\mathbf{R}_{\vec{e}}(\alpha) = \mathrm{e}^{-i\alpha\vec{e}\cdot\overleftrightarrow{\boldsymbol{\sigma}}/\hbar} = \cos(\alpha/2)\,\mathbf{1} - i\vec{e}\cdot\overleftrightarrow{\boldsymbol{\sigma}}\sin(\alpha/2), \tag{6.2.15}$$

when we write the local, spin dependent density as a matrix in bold type with the spin quantized in the z-direction

$$\mathbf{n}^z(x,y) = \begin{pmatrix} n^z_{+,+}(x,y) & n^z_{+,-}(x,y) \\ n^z_{-,+}(x,y) & n^z_{-,-}(x,y) \end{pmatrix}. \tag{6.2.16}$$

Here, we have combined the spin Pauli matrices into $\overleftrightarrow{\boldsymbol{\sigma}}$

$$\overleftrightarrow{\boldsymbol{\sigma}} = \begin{pmatrix} \boldsymbol{\sigma}_x \\ \boldsymbol{\sigma}_y \\ \boldsymbol{\sigma}_z \end{pmatrix}. \tag{6.2.17}$$

Thus, the spin dependent density for the quantization in x and y read

$$\mathbf{n}^x(x,y) = \mathbf{R}^{-1}_{\vec{e}_y}(\pi/2)\,\mathbf{n}^z(x,y)\,\mathbf{R}_{\vec{e}_y}(\pi/2), \tag{6.2.18}$$

$$\mathbf{n}^y(x,y) = \mathbf{R}^{-1}_{\vec{e}_x}(\pi/2)\,\mathbf{n}^z(x,y)\,\mathbf{R}_{\vec{e}_x}(\pi/2). \tag{6.2.19}$$

This gives us for the relative spin polarization in the directions x and y

$$P_x(x,y) = \frac{n^z_{+,-}(x,y) + n^z_{-,+}(x,y)}{n_{+,+}(x,y) + n^z_{-,-}(x,y)}, \tag{6.2.20}$$

$$P_y(x,y) = i\frac{n^z_{+,-}(x,y) - n^z_{-,+}(x,y)}{n^z_{+,+}(x,y) + n^z_{-,-}(x,y)}. \tag{6.2.21}$$

Energy resolved observables, such as the energy resolved density of Eq. (3.3.4) depend on too many coordinates to be illustrated with contour or line graphs. For this reason, we define a scalar energy resolved density by the integral of the energy and spatially resolved density over the total device

$$n\left(E\right) = -i \int_{\text{Device}} \mathrm{d}x\mathrm{d}y \left[G^{<}\left(x,y,+;x,y,+,E\right) + G^{<}\left(x,y,-;x,y,-,E\right)\right]. \tag{6.2.22}$$

Similarly, we define an absolute spin polarization in z-direction

$$\delta n_z\left(E\right) = \int_{\text{Device}} \mathrm{d}x\mathrm{d}y \left|\mathrm{Im}\, G^{<}\left(x,y,+;x,y,+,E\right) - \mathrm{Im}\, G^{<}\left(x,y,-;x,y,-,E\right)\right|. \tag{6.2.23}$$

Please note that the later function depicts at which energy the local spin polarizations are pronounced, irrespective of the polarization sign. Thus, when the symmetry of the device yields spin polarizations with a inversion center*, $\delta n_z\left(E\right)$ will be finite.

Microscopic tight binding

The relative spin polarization is a basis independent entity. However, we have to mention two differences between the microscopic and the envelope function model. First, the spin resolved electron density $n_{\pm,\pm}$ in the tight binding approach is given for every atom at position $\vec{R}$ as a sum over all atomic orbitals (l,m)

$$n_{\pm,\pm}\left(\vec{R}\right) = \frac{-i}{2\pi} \int \mathrm{d}E \sum_{l,m} G^{<}\left(l,m,\pm,\vec{R};l,m,\pm,\vec{R},E\right). \tag{6.2.24}$$

Second, the atoms are given for positions $\vec{R}$ on an unstrained (three-dimensional) zink-blende type lattice. In order to compare the microscopic results with the sheet density and sheet polarization of the envelope function model, we have to take cross sections of the observables in the tight binding representation in the center of the confining quantum well in the z-direction.

6.3 Novel scattering self-energy for acoustic phonons

6.3.1 Introduction and motivation

We have discussed in Sec. 4.3.2 that the neglect of energy dissipation may lead to artificial results. Unfortunately, the numerical implementation of incoherent scattering in terms of self-energies in two- and higher dimensional NEGF calculations is numerically very demanding. In particular, energy dissipation in NEGF calculations typically requires for a self-consistent solution of a system of four coupled partial differential equations (see the discussion in Sec. 4.3.3). In this case, two Green's functions and two self-energies (retarded and lesser) for various energies have to be kept in RAM, which most effectively limits the maximum number of spatial grid points. In addition, many self-energies represent spatially extended scattering events and are therefore non-diagonal in the spatial coordinates. As we have already discussed in Sec. 4.3.4, any non-diagonal entry in the self-energies increases the numerical load further.

*Changing the sign of the spin polarization with the spatial inversion.

One possible solution of this issue is to included energy dissipation in terms of the Büttiker probe model. In this model, neither the self-energies, nor the Green's functions have to be stored in RAM. There is also no need to solve the retarded and lesser Green's functions self-consistently.

The major purpose of the implementation of energy dissipation in this thesis, however, is to clarify whether confined electrons and holes in systems with a pronounced intrinsic spin-Hall effect maintain a significant spin polarization. The Büttiker probe model is inappropriate to answer this question, because in this model, confined states are filled with electrons and holes of unpolarized Büttiker probes. In reality, however, propagating electrons and holes are spin polarized due to the intrinsic spin-Hall effect and get occasionally "trapped"after the emission of a phonon. Thus, the open question is, whether they loose their spin polarization after they stop their propagation. In order to answer this question, we implement a scattering self-energy in the self-consistent Born approximation for the inelastic scattering with acoustic phonons. Thereby, we apply the approximations that we have introduced in Sec. 3.5.3, i.e. we assume an unscreened scattering with the acoustic phonons in the high temperature approximation and average the Green's functions within the limits of final energies. In this way, we get an efficient scattering self-energy in the self-consistent Born approximation. However, this type of scattering self-energy is only "correct"at temperatures above approximately 30 K (see Fig. 3.5.3). This is larger than the typical lattice temperatures at which the intrinsic spin Hall effect is observed. Therefore, we apply this inelastic scattering self-energy only to qualitatively analyze whether the intrinsic spin Hall effect polarizes completely confined electrons or holes (see Sec. 7.3). Since the second purpose of this part of the thesis is to demonstrate that the intrinsic spin Hall-effect can be utilized for efficient all-semiconductor spin polarizers and to propose efficient device designs, most of the two-dimensional transport in this thesis is calculated purely ballistically.

6.3.2 Derivation and approximations

We start with the general formula for the phonon scattering self-energy Eq. (2.4.8)

$$\begin{aligned} & \Sigma^{<}\left(\vec{x}_3,\vec{x}_4,E\right) \\ = & \frac{1}{(2\pi)^3}\int \mathrm{d}\vec{q}\left|U_q\right|^2 \mathrm{e}^{i\vec{q}\cdot\left(\vec{x}_3-\vec{x}_4\right)}\left[n_q G_0^{<}\left(\vec{x}_3,\vec{x}_4,E-\hbar\omega_q\right)+\left(1+n_q\right)G_0^{<}\left(\vec{x}_3,\vec{x}_4,E+\hbar\omega_q\right)\right]. \end{aligned}$$

Since we assume the electrons and holes to completely stay in the lowest confined quantum well state ($\nu_0(z)$), we can separate the z-dependence of the Green's functions

$$\begin{aligned} & \Sigma^{<}\left(\vec{x}_3,\vec{x}_4,E\right) \\ = & \frac{1}{(2\pi)^3}\int \mathrm{d}\vec{q}\left|U_q\right|^2 \mathrm{e}^{i\vec{q}\cdot\left(\vec{x}_3-\vec{x}_4\right)}\left[\nu_0^*\left(z_3\right)\nu_0\left(z_4\right)\right] \\ & \times\left[n_q G_0^{<}\left(\vec{x}_{\parallel,3},\vec{x}_{\parallel,4},E-\hbar\omega_q\right)+\left(1+n_q\right)G_0^{<}\left(\vec{x}_{\parallel,3},\vec{x}_{\parallel,4},E+\hbar\omega_q\right)\right]. \end{aligned} \tag{6.3.1}$$

We consider the unscreened scattering potential of Eq. (3.5.19) and a linear phonon dispersion ($\omega_q = v_s q$)

$$\begin{aligned} & \Sigma^{<}\left(\vec{x}_3,\vec{x}_4,E\right) \\ = & \frac{1}{(2\pi)^3}\frac{\hbar D^2}{2\rho v_s}\int \mathrm{d}\vec{q}q\mathrm{e}^{i\vec{q}\cdot\left(\vec{x}_3-\vec{x}_4\right)}\left[\nu_0^*\left(z_3\right)\nu_0\left(z_4\right)\right] \\ & \times\left[n_q G_0^{<}\left(\vec{x}_{\parallel,3},\vec{x}_{\parallel,4},E-\hbar v_s q\right)+\left(1+n_q\right)G_0^{<}\left(\vec{x}_{\parallel,3},\vec{x}_{\parallel,4},E+\hbar v_s q\right)\right]. \end{aligned} \tag{6.3.2}$$

Low temperature approximation

At very small temperatures, it is appropriate to assume the phonon number to vanish

$$n_q \approx 0. \tag{6.3.3}$$

Since the phonon momentum q does not cancel out in this approximation, we have to average the product of the Green's function and phonon momentum (compare Eq. (3.5.26))

$$\begin{aligned} qG^{R,<}\left(\vec{x}_{\parallel,1},\vec{x}_{\parallel,1},\tilde{E}\right) &\approx \frac{1}{2\hbar^2 v_s \omega_D}\int_{E-\hbar\omega_D}^{E+\hbar\omega_D} |E'-E|\, G^{R,<}\left(\vec{x}_{\parallel,1},\vec{x}_{\parallel,2},E'\right)\mathrm{d}E', \\ \forall \tilde{E} &\in [E-\hbar\omega_D, E+\hbar\omega_D]. \end{aligned} \tag{6.3.4}$$

Utilizing this approximation, we perform the q-integral in the self-energies and get

$$\Sigma^{<}\left(\vec{x}_3,\vec{x}_4,E\right) = \frac{D^2}{4\rho v_s^2 \hbar\omega_D}\left|\nu_0\left(z_3\right)\right|^2 \delta\left(\vec{x}_3-\vec{x}_4\right)\int_{E-\hbar\omega_D}^{E+\hbar\omega_D} |E'-E|\, G^{<}\left(\vec{x}_{\parallel,1},\vec{x}_{\parallel,2},E'\right)\mathrm{d}E'. \tag{6.3.5}$$

Similar to the results in Sec. 3.5.3, the retarded self-energy decouples from the lesser Green's function. Since the delta distribution in z-direction allows us to project the self-energy onto the two-dimensional system, we get for both self-energies

$$\Sigma^{R,<}\left(\vec{x}_{\parallel,3},\vec{x}_{\parallel,4},E\right) = \frac{D^2}{4\rho v_s^2 \hbar\omega_D L_z}\delta\left(\vec{x}_{\parallel,3}-\vec{x}_{\parallel,4}\right)\int_{E-\hbar\omega_D}^{E+\hbar\omega_D} |E'-E|\, G^{R,<}\left(\vec{x}_{\parallel,1},\vec{x}_{\parallel,2},E'\right)\mathrm{d}E'. \tag{6.3.6}$$

Here, L_z is the thickness of the quantum well that confines the two-dimensional electron or hole gas.

High temperature approximation

We have shown in Sec. 3.5.3 that at temperatures above approximately 30 K, the Bose distribution for acoustic phonons can be approximated by

$$n_q + 1 \approx n_q = \frac{1}{\exp\left(\hbar v_s q/k_B T\right)-1} \approx \frac{k_B T}{\hbar v_s q}.$$

In this case, the scattering self-energy simplifies to

$$\begin{aligned} \Sigma^{<}\left(\vec{x}_3,\vec{x}_4,E\right) &= \frac{1}{\left(2\pi\right)^3}\frac{D^2 k_B T}{2\rho v_s^2}\left[\nu_0^*\left(z_3\right)\nu_0\left(z_4\right)\right]\int \mathrm{d}\vec{q}\mathrm{e}^{i\vec{q}\cdot\left(\vec{x}_3-\vec{x}_4\right)} \\ &\quad\times\left[G_0^{<}\left(\vec{x}_{\parallel,3},\vec{x}_{\parallel,4},E-\hbar v_s q\right)+G_0^{<}\left(\vec{x}_{\parallel,3},\vec{x}_{\parallel,4},E+\hbar v_s q\right)\right]. \end{aligned} \tag{6.3.7}$$

Next, we approximate the Green's functions in this self-energy by their energy average (see Eq. (3.5.26)) in the interval $\tilde{E}\in[E-\hbar\omega_D, E+\hbar\omega_D]$

$$\tilde{G}^{</R}\left(\vec{x}_{\parallel,3},\vec{x}_{\parallel,4},\tilde{E}\right) = \frac{1}{2\hbar\omega_D}\int_{E-\hbar\omega_D}^{E+\hbar\omega_D} G^{</R}\left(\vec{x}_{\parallel,3},\vec{x}_{\parallel,4},E'\right)\mathrm{d}E',\ \forall\tilde{E}\in[E-\hbar\omega_D,E+\hbar\omega_D]. \tag{6.3.8}$$

Once again, this approximation decouples the retarded self-energy from the lesser Green's function

$$\Sigma^{<,R}\left(\vec{x}_3,\vec{x}_4,E\right)=\frac{D^2k_BT}{2\rho v_s^2\hbar\omega_D}\left|\nu_0\left(z_3\right)\right|^2\delta\left(\vec{x}_3-\vec{x}_4\right)\int_{E-\hbar\omega_D}^{E+\hbar\omega_D}G^{<,R}\left(\vec{x}_{\parallel,3},\vec{x}_{\parallel,4},E'\right)\mathrm{d}E'. \tag{6.3.9}$$

When we project the three-dimensional self-energy on the quantum well with thickness L_z, we finally get

$$\Sigma^{<,R}\left(\vec{x}_{\parallel,3},\vec{x}_{\parallel,4},E\right)=\frac{D^2k_BT}{2\rho v_s^2\hbar\omega_DL_z}\delta\left(\vec{x}_{\parallel,3}-\vec{x}_{\parallel,4}\right)\int_{E-\hbar\omega_D}^{E+\hbar\omega_D}G^{<,R}\left(\vec{x}_{\parallel,3},\vec{x}_{\parallel,4},E'\right)\mathrm{d}E'. \tag{6.3.10}$$

6.3.3 Limitations and conclusion

We have already mentioned that we implement the scattering self-energy Eq. (6.3.10) only to find out whether propagating electrons that enter a completely confined (quantum dot) state maintain a finite spin polarization within this state. Since the electrons are polarized when they propagate (due to the intrinsic spin Hall effect), the answer to this question is not trivial. This question cannot be unambiguously answered within the Büttiker probe model, since in this model, any completely confined state is only filled by electrons originating from the unpolarized artificial leads (see Sec. 4.3.6). In particular, a filling of confined states with spin polarized electrons of the continuum is only included when the scattering self-energy depends on the device Green's function. Of course, this is the case in a self-consistent Born calculation - in contrast to the Büttiker probe model.

However, we have to be aware of the approximate character of the self-energies given in Eqs. (6.3.6) and (6.3.10). First, in the low temperature approximation, no energy absorption should be possible, since the number of phonons is set to zero. In spite of this, we approximate the Green's function with a symmetric integral over the energies - including final energies that exceed the initial energy. We have to apply this approximation, in order to decouple the retarded self-energy from the lesser Green's function. Second, the applicability of the high temperature approximation is questionable, since the temperature of the two-dimensional devices considered in this thesis lie below 30 K, i.e. below the limit of validity for this approximation. Third, both approximations underestimate the occupation of a confined state in equilibrium, as illustrated in Fig. (3.5.5). For these reasons, we apply the scattering self-energy Eq. (6.3.10) only for a qualitative answer to the before mentioned question and calculate ballistic transport in two-dimensional devices otherwise.

6.4 Numerical details

6.4.1 Introduction

Due to the small required energy range the Green's functions have to be calculated in, we can discretize the Green's functions and self-energies on a homogeneous grid. Similar as in Sec. 3.7.4, we solve the surface Green's functions of the semi-infinite leads in an iterative manner. In this way, we include the spin-orbit interaction as well as incoherent scattering in the lead density of states, which is often neglected in literature. In addition, we introduce a novel damping potential that improves the convergency of the lead iterations. Finally, we implement a common technique in the tight binding model in order to efficiently model confining barrier materials while suppressing interface and surface states.

6.4.2 Comment on the energy discretization

We have introduced in Sec. 3.7.2 our method of an inhomogeneous discretization of the Green's function with respect to energy and in-plane momentum. Since we represent the Green's functions in two-dimensional systems with a spatial grid and in three-dimensional devices with the atomic orbitals, the only remaining entity to resolve is the total energy. When incoherent scattering is neglected and the carrier transport is mainly one-dimensional, the Green's functions diverge with $1/\sqrt{E - E_m}$, i.e. when the total energy E matches a (sub-) band edge E_m (see also the discussion in Sec. 3.2.3). The only mechanism that can broaden the divergence width and reduce the divergence height is incoherent scattering. Therefore, any discretization of the total carrier energy in a purely ballistic calculation has to avoid the energy of this divergence. Similar to our discussion in Sec. 3.2.3, any observable depends on the Green's functions integrated over energy. The observables are converged in the energy resolution, when the divergence at E_m is well enough resolved (see e.g. [119]).

All the devices in this part of the thesis are considered to contain electron or hole gases of low density. Furthermore, the device temperatures are always set lower or equal 10 K and the bias voltage never exceeds 20 mV. For these reasons, the energy range in which electrons or hole take part on transport is typically less than 20 meV. This energy range is small enough to be resolved with a linear but very dense energy grid. For more efficient and self-consistent calculations, however, the self-adaptive grid that we introduced in Sec. 3.7.2 can be straightforwardly applied.

6.4.3 Adaptation of open boundary conditions

General iterative leads

In both, the envelope and the tight binding NEGF calculations, we apply the iterative method of Sec. 3.7.4 for the calculation of the lead surface Green's function and contact self-energies. We extend the device Hamiltonian at the lead/device boundary into the lead regime and thereby include in the leads incoherent scattering as well as the spin-orbit interaction. In the case of the microscopic tight binding model, we periodically repeat the Hamiltonian of the device limiting unit cells into to the leads. Whereas in the envelope function model, the potential and effective mass at the device surface is homogeneously extended into the respective lead. We use a constant τ for the initial guess of the surface Green's function and the contact self-energy. Following the iterative scheme of Sec. 3.7.4, we calculate the Green's function in a finite section of the lead that is connected to this contact self-energy. The new lead Green's function is then used to recalculate the contact self-energy again. This procedure is iterated until the contact self-energies converge. In order to improve the convergence of the iterative calculation of the lead Green's functions, we add in the envelope function model and the microscopic tight binding model an artificial complex potential V_{art} to the diagonal of the inverse retarded Green's function of the leads. This potential depends only on the distance r to the interface between lead and device

$$\mathbf{V}_{art}(r) = (1+i)\,\eta \exp(\lambda r)\,\mathbf{1}. \tag{6.4.1}$$

The larger the distance to the actual device, the stronger are the electronic wave functions damped by this artificial potential. In this way, interferences that originate from the arbitrary constant τ are smoothly damped and the results in the device are completely independent of τ. Typical values for $\eta = 0.8$ eV and $\lambda = 0.2$ nm^{-1} require for approximately 250 iterations (or a sum length of 75 nm for the lead) to yield a well converged density in the device (relative change of subsequent iterations less than 0.1 %).

Since we do not solve the Poisson equation, we neglect the repulsive or attractive charge accumulations at the device boundaries (see Sec. 4.2.3). For this reason, we assume an equilibrium Fermi distributions in the source and drain leads and do not take finite current densities within the leads into account.

Surface and interface states in the tight binding model

Since we apply the microscopic tight binding model on a GaAs quantum wire, we have to implement a confining potential in all spatial directions perpendicular to the transport direction. In the envelope function theory, this confining potential can be implemented either by a large potential $V(x, y)$ in the Hamiltonian of Eq. (6.2.10) or by limiting the (x, y) grid on points within the wire. Unfortunately, this cannot be done straightforwardly in the tight binding model. It is well known in literature (see e.g. [208]) that considering only the atoms of the wire and leaving the orbitals of the surface atoms unsaturated leads to dangling bonds and to a finite density of states in the semiconductor band gap. Typically, these dangling bonds are saturated by Hydrogen atoms. Unfortunately, this kind of saturation increases the number of implemented atoms and correspondingly the numerical load significantly. Instead, we apply periodic boundary conditions perpendicular to the GaAs quantum wire and cover the wire with a material of higher band gap. In order to ensure well confined electrons, we use GaAs for the cover material and - similar to [209] - increase all orbital energies in the covering material by 0.6 eV compared to the values given in [203]. In this way, we model the confinement by AlAs barrier material, but avoid interface states at the AlAs/GaAs boundary that appear due to the small - numerically feasible - device length scales.

6.5 Conclusion

We have represented the nonequilibrium Green's functions in a two-band envelope function model. The commonly implemented spin-orbit Hamiltonian of this model is only an approximation of the band structure of laterally homogeneous zincblende heterostructures. In order to check the validity of this Hamiltonian in inhomogeneous systems in the subsequent chapter, we have also represented the Green's functions in a 16-band microscopic tight binding basis. We have explained the need of an inelastic scattering self-energy in the self-consistent Born approximation. For this reason, we have derived in detail a novel self-consistent scattering self-energy for the inelastic scattering with acoustic phonons. The symmetry of this self-energy allows for a numerically efficient solution of retarded and lesser Green's functions. We have specified several numerical details of our implementation and introduced a novel numerically efficient algorithm for the iterative solution of the surface Green's function in arbitrary semi-infinite leads. This method is capable to include incoherent scattering as well as the spin-orbit interaction in the lead density of states, which is essential for reflectionless lead/device boundaries.

Chapter 7

New results on spin polarization

7.1 Introduction

The spin-orbit interaction in two-dimensional zinc-blende semiconductors can generate spin currents perpendicular to a charge current even in the absence of applied magnetic fields. This phenomenon has been termed spin-Hall effect [13, 193, 194, 199, 200, 205–207, 210–214]. It may become a useful tool for creating spin polarized currents. In a perfect two-dimensional electron gas (2DEG) with no scattering (ballistic transport), the so-called intrinsic spin-Hall effect is nonzero only for laterally confined two-dimensional systems [194, 205–207, 210, 212]. In fact, some authors call this effect interface-induced [210] or mesoscopic [205, 206] spin-Hall effect. In this chapter, we will focus exclusively on such confined 2D systems. It has been shown recently and we confirm this finding that elastic or inelastic scattering dampens the spin-Hall effect, but does not change the picture qualitatively, in contrast to the situation in unconfined 2DEGs [194]. Unfortunately, all published theoretical predictions so far rely on the $k \cdot p$ envelope function theory (EFT). This method is known to be plagued by artefacts in the context of spin-orbit induced spin effects that are caused by the underlying continuum approach [193]. Therefore, we present both an atomistic, microscopic relativistic tight-binding analysis of the intrinsic spin-Hall effect in confined nanostructures as well as an EFT analysis of several device geometries in terms of the spin-dependent NEGF formalism. In particular, we show that the microscopic approach confirms important qualitative features of the spin-Hall effect that have been obtained previously within the EFT model [194, 205–207, 210, 212]. Furthermore, we demonstrate that carrier oscillations can be used to locally excite a very pronounced spin-Hall effect. In particular, we find an almost complete local spin polarization of holes propagating through coupled quantum dots. We confirm that efficient propagation is essential for a significant spin polarization. We show that the spin polarization of confined holes is negligible compared to the spin-Hall effect of propagating holes - irrespective of the phonon-mediated interaction between the continuum and confined states. This allows us to limit our considerations on numerically efficient *ballistic* NEGF calculations for the prediction of the spin polarization in efficient all-semiconductor, non-magnetic spin polarizers. We significantly simplify a known T-shaped three terminal device and proof its capability to polarize the spin of holes with respect to one lateral direction. In addition, we also propose a novel four terminal device that simultaneously polarizes the carrier spin in both lateral directions.

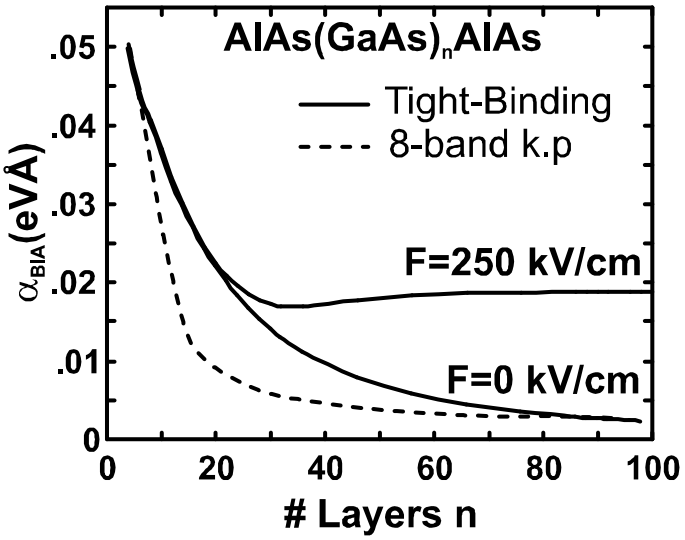

Figure 7.2.1: Calculated spin-splitting constant of the lowest conduction band in [001] GaAs multiquantum well with AlAs barriers, as a function of the number of GaAs atomic layers. Full curve shows the results of relativistic empirical tight-binding theory for electric fields F equal to 0 and 250 kV/cm, respectively. Dashed curve shows results of an 8-band k.p calculation which predicts a field-independent coupling. The data are taken from [215] with kind approval of P. Vogl.

7.2 New assessment of the envelope function approximation

7.2.1 Introduction

We illustrate significant discrepancies in band structure parameters resulting from envelope function and microscopic tight binding calculations in GaAs/AlGaAs heterostructures. Since it has not been checked in literature, the commonly implemented approximation to use two-band envelope function models for the intrinsic spin-Hall effect has to be verified. For this purpose, we calculate the electronic transport in a GaAs quantum wire in both models and compare the resulting relative spin polarizations. The predicted spin polarization of both models qualitatively agree in the spatial as well as momentum dependence. Quantitative comparisons, however, fail due to different band structure parameters. Nevertheless, our finding is an essential prerequisite for all qualitative predictions of the intrinsic spin-Hall effect in later sections, because the numerical load of NEGF calculations in the microscopic (TB) model prohibit the calculation of transport in more sophisticated devices.

7.2.2 Motivation - spin splitting constants

We have introduced in Sec. 6.2.2 a $k_{\|}$-linear spin-orbit interaction potential. The proportionality constants α_{BIA} and α_{SIA} in Eq. (6.2.10) depend crucially on the wave functions and their symmetry at interfaces. Therefore, it is not surprising that microscopic calculations yield significantly different results than a continuum approach such as $k \cdot p$ envelope function theory. This is illustrated for the lowest conduction subband of a [001] GaAs/AlGaAs heterostructure

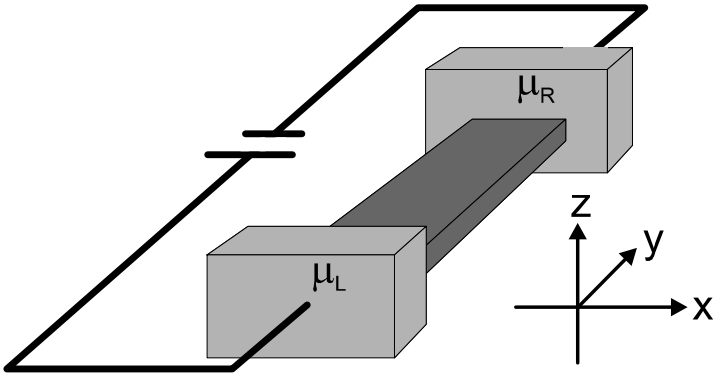

Figure 7.2.2: Schematic drawing of the coordinate system and device structure used in the present calculations, except for the multiterminal junction in Figs. 7.4.1 and 7.4.2.

in Fig. 7.2.1. In contrast to the predictions of a simple 8-band $k \cdot p$-theory, the BIA coupling depends strongly on the applied electric field. An atomistic approach such as a tight-binding model includes all spin-orbit effects to all orders in the wave vector. Microscopically, the spin-orbit interaction is an intra-atomic interaction between p- and d-states. In bulk $k \cdot p$-theory, on the other hand, the k-linear spin splitting near the conduction band edge is described by the effective, phenomenological 2×2 Hamiltonian that we have introduced in Eq. (6.2.9). This leads to the legitimate question whether the spin-orbit coupling and, in particular, the intrinsic spin-Hall effect can be described with the commonly implemented envelope function theory. We have therefore performed comparative tight-binding and envelope function (EFT) calculations for laterally confined 2DEGs, i.e. quantum wire structures.

7.2.3 Results for GaAs quantum wire

By applying a voltage to an open device such as depicted schematically in Fig. 7.2.2, we transfer orbital momentum and angular momentum to the two-dimensional system. Due to the spin-orbit interaction, this can induce not only a spatially inhomogeneous spin polarization, but also a total nonvanishing magnetic moment.

We calculate electronic transport in a laterally confined open GaAs electron system in a relativistic, 16-band sp^3 tight-binding (TB) NEGF model as well as in the continuous real-space EFT model of Eq. (6.2.10). In Figs. 7.2.3 (a) and (b), we compare the results of both approaches for the spin polarization in a system that laterally consists of 10×4 GaAs unit cells. This GaAs slab is confined by AlAs layers that are wrapped around the GaAs device and act as barrier material. Alternatively, we have also used bond-saturating H-atoms as barrier material. However, we found no qualitative difference between finite and infinite barriers and have therefore used AlAs barriers (modelled with a potential offset of 0.6 eV - see Sec. 6.4.3) for the results shown here. Longitudinally, i.e. along the y-axis, the TB as well as the EFT system is open and attached to homogeneous semi-infinite GaAs quantum wires of the same lateral properties as the device. The electrons within the lead quantum wires are given in equilibrium Fermi distributions. Technically and conceptually, this amounts to a ballistic NEGF calculation that has been widely implemented [194, 205–207, 210, 212]; however, the atomistic TB basis makes these calculations very demanding computationally. When we apply a bias voltage of 20 mV, the difference in the contact Fermi levels drives an electric current. The Fermi energy

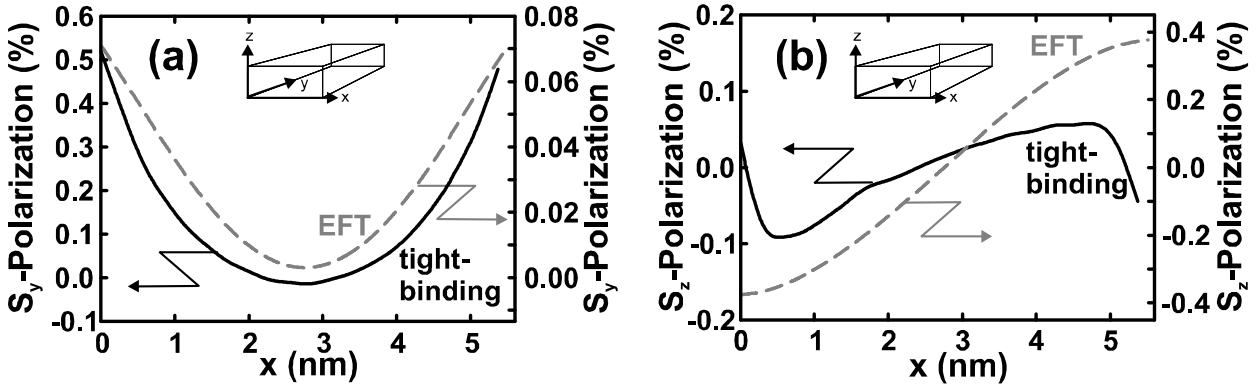

Figure 7.2.3: Calculated relative spin polarizations (a) $P_y(x)$ and (b) $P_z(x)$ in percent for an open quantum wire, attached to contacts in the y-direction, versus the lateral device coordinate x (cf. Fig. 7.2.2). The full curves have been obtained with a relativistic empirical tight-binding theory. The dashed lines are envelope function results.

in the left contact lies 20 meV above the lowest propagating mode and only the lowest mode gets occupied. The TB and EFT calculations cannot be compared *quantitatively* since the confinement potentials, the direction-dependent spin BIA-related constants, as well as effective masses are different. The key result, however, is that TB and EFT yield qualitatively similar and, particularly, nonzero spin polarizations $P_i(x), i = x, y, z$ as illustrated in Fig. 7.2.3. In both models, these polarizations vanish in equilibrium and increase approximately linearly with net electron momentum along the y-direction. This agreement indicates that the inclusion of spin-orbit interaction of higher order than linear in k (beyond Eq. (6.2.9)) for electrons and light holes in EFT calculations is not necessary (in agreement with findings in [216]). Both approaches yield a very small $P_x(x) \approx 0$. The vertical spin polarization $P_z(x)$ shows the characteristic accumulation of opposite spins near the edges of the sample [194, 205, 206, 210, 212], again in accord with previous EFT findings. The longitudinal component $P_y(x)$ adds up to a nonzero magnetization along the y-direction. We emphasize that this net longitudinal magnetization vanishes in TB if the device dimensions along x and z are equal, in accordance with four-current conservation [207]. The fact that the relation $P_y > P_z$ holds in TB but is reversed in EFT is a result of the sensitivity of this polarization on the spin-orbit coupling parameter. We note that in EFT, we find $P_z \propto \alpha_{BIA}^2$; $P_x, P_y \propto \alpha_{BIA}^3$.

7.2.4 Conclusion

Our results show that NEGF calculations in the envelope function approach qualitatively reproduce the spin polarization of microscopic tight binding NEGF calculations. In particular, both models, predict a k-linear increase of the polarization. The predicted shape of the polarization for different spin directions also qualitatively agrees in both models. In the light of the discrepancies between tight binding and 8-band* $k \cdot p$ band structure calculations, this results is remarkable. The absolute height of the spin polarization is, however, sensitive to details of the band structure. Therefore, a detailed calculation of the band structure parameters (effective mass, spin splitting constants α_{BIA} and α_{SIA}) for each individual device is mandatory for

*Note that these are still more sophisticated than the present 2-band envelope function calculations.

quantitative predictions which we leave to future work.

7.3 Intrinsic spin-Hall effect in resonant states?

7.3.1 Introduction

In this section, we show that the spin-orbit interaction in inhomogeneous two-dimensional systems is intimately related to derivatives of the retarded Green's function of propagating carriers. In particular, we illustrate in a double dot system that interferences and reflections of carriers can be used to generate very high or even complete local spin polarizations. We also show that external fields can be used to tune the carrier interferences and accordingly the spin polarization in the dots.

The spatial derivatives of Green's functions of confined carriers can be very large. However, we show that an efficient propagation is also an essential prerequisite for the spin-Hall effect. In particular, we find that the spin polarization of carriers confined in quantum dot states is insignificant compared to the spin-Hall effect on carriers in the state continuum. Even the self-consistent scattering of spin polarized carriers with acoustic phonons cannot significantly mediate the spin polarization into the confined dot states.

Since tight binding calculations predict that α_{BIA} is an order of magnitude larger for light hole states in tensile strained GaAs layers than for the lowest conduction band states [193], we consider in the following light holes and take $\alpha_{BIA} = 0.2$ eVÅ and the effective mass of $m^* = 0.11$ m_0.

7.3.2 Spin-orbit interaction in partly confined states

Introduction

The carrier momentum in inhomogeneous devices is not conserved. Therefore, the simple picture of a spin-orbit interaction that is proportional to the carrier momentum does not capture all relevant physics. We show that the spin-orbit interaction is directly related to the spatial derivative of the retarded Green's function. Partially reflecting barriers can be used to yield large spatial derivatives of the retarded Green's function. We illustrate with the example of light holes in a GaAs double dot systems that pronounced spin polarizations can be generated by interferences of propagating carriers.

Motivation - carrier oscillations

It is common to consider the intrinsic spin-Hall effect for electrons and holes that propagate in devices without significant obstacles (e.g. reflecting barriers). In such devices, the carriers mainly propagate in one-dimensional quantum wires and maintain the characteristic spin polarization in z-direction with opposite signs near the edges of the sample (see Sec. 7.2.3). Calculations of such devices yield relatively large spin polarizations (see also Sec. 7.4), but they do not contain confined or quasi confined carriers. Confined carriers are typically avoided, because the approximate spin-orbit interaction in Eq. (6.2.9) is proportional to the carrier momentum which suggests that any (even incomplete) confinement weakens the spin-orbit interaction. While the spin-orbit interaction and accordingly the intrinsic spin-Hall effect is indeed proportional to the carrier momentum in homogeneous quantum wires, this picture is not entirely

true in inhomogeneous devices: The momentum in inhomogeneous devices is not conserved. We have transformed Eq. (6.2.9) into the spatial representation which resulted in a spin-orbit interaction potential that is proportional to a spatial derivative (see Eq. (6.2.10)). When we consider the spin-orbit interaction as a small perturbation to the spin conserving Green's function $G^R_{\text{no SO}}$, we can expand the retarded Green's function into a series (omitting the variables for brevity) and neglect term higher than quadratic in α_{BIA}

$$\begin{aligned} G^R &= \left(G^{R-1}_{\text{no SO}} - i\alpha_{BIA}\left(-\boldsymbol{\sigma}_x\nabla_x + \boldsymbol{\sigma}_y\nabla_y\right)\right)^{-1} \\ &\approx G^R_{\text{no SO}} + i\alpha_{BIA}\left[\left(-\boldsymbol{\sigma}_x\nabla_x + \boldsymbol{\sigma}_y\nabla_y\right)G^R_{\text{no SO}}\right]G^R_{\text{no SO}} \\ &\quad -\alpha^2_{BIA}\left[\left(-\boldsymbol{\sigma}_x\nabla_x + \boldsymbol{\sigma}_y\nabla_y\right)G^R_{\text{no SO}}\left(-\boldsymbol{\sigma}_x\nabla_x + \boldsymbol{\sigma}_y\nabla_y\right)G^R_{\text{no SO}}\right]G^R_{\text{no SO}}. \end{aligned} \tag{7.3.1}$$

In the last equation, the spin-orbit interaction is proportional to spatial derivatives of the retarded Green's function. Obviously, confining barriers generate oscillations and accordingly a significant spin polarization. We demonstrate this fact with ballistic NEGF calculations of stationary hole transport in coupled quantum dots. We show that dot constellations that cause large interferences in the hole density yield very pronounced spin polarizations. In contrast, when the dot potential is tuned such that the local hole density of states is rather homogeneous, the spin polarization vanishes almost completely.

Spin polarization in double-dot systems

In Figs. 7.3.1 (a)-(f), we show results of ballistic transport calculations in the EFT model in a two dimensional GaAs light hole gas at 1 K lattice temperature. The hole gas is confined in two circular quantum dots of diameters of 60 nm and couples to spin-unpolarized leads (black rectangles) at the left and right sides of the figures, respectively. In Figs. 7.3.1 (a)-(c) we apply a bias voltage of 2 mV that drops directly at the source contact (see Fig. 7.3.1 (a)). In particular, the chemical potential of the source (left) equals 2 meV and the one of the drain (right) is 0, while the potential lies in between (see Figs. 7.3.1 (a) and (d)). In this way, holes propagate from the left to the right lead. The flat potential within the double dot causes the propagating charge state at low energies to couple predominantly to a binding combination of the two lowest dot states that extend over both quantum dots. This can be seen in Fig. 7.3.1 (b), as it shows the spectral function, integrated over energy

$$A\left(x,y\right) \equiv \int_{\Omega} \mathrm{d}E\left(G^R\left(x,y;x,y,E\right) - G^A\left(x,y;x,y,E\right)\right). \tag{7.3.2}$$

In Fig. 7.3.1 (b), we set the energy range $\Omega = [0, 3\text{ meV}]$, i.e. the total occupied energy range. Thus, Fig. 7.3.1 (b) shows the sum of all relevant squared hole wavefunctions in the device. The spin polarization $P_z\left(x,y\right)$ in Fig. 7.3.1 (c) shows the transverse asymmetry with respect to the x-axis that is typical [194, 205, 206, 210, 212] for the intrinsic spin-Hall effect (similar to Fig. 7.2.3 (b)). However, the hole gas maintains a pronounced spin polarization only in the centers of each quantum dot, where the spatial derivative of the hole density of states is high.

In order to demonstrate that carriers given in homogeneous spectral functions are not significantly spin polarized, we consider in Figs. 7.3.1 (d)-(f) the potential to drop linearly along the entire structure between source (left) and drain (right) contact. The spin polarization in the right dot vanishes effectively for two reasons: First, the asymmetry in the potential causes the low-lying propagating modes to couple primarily to the energetically separated charge state of the left dot (see Fig. 7.3.1 (e)). This mode faces a significant interference of the propagating

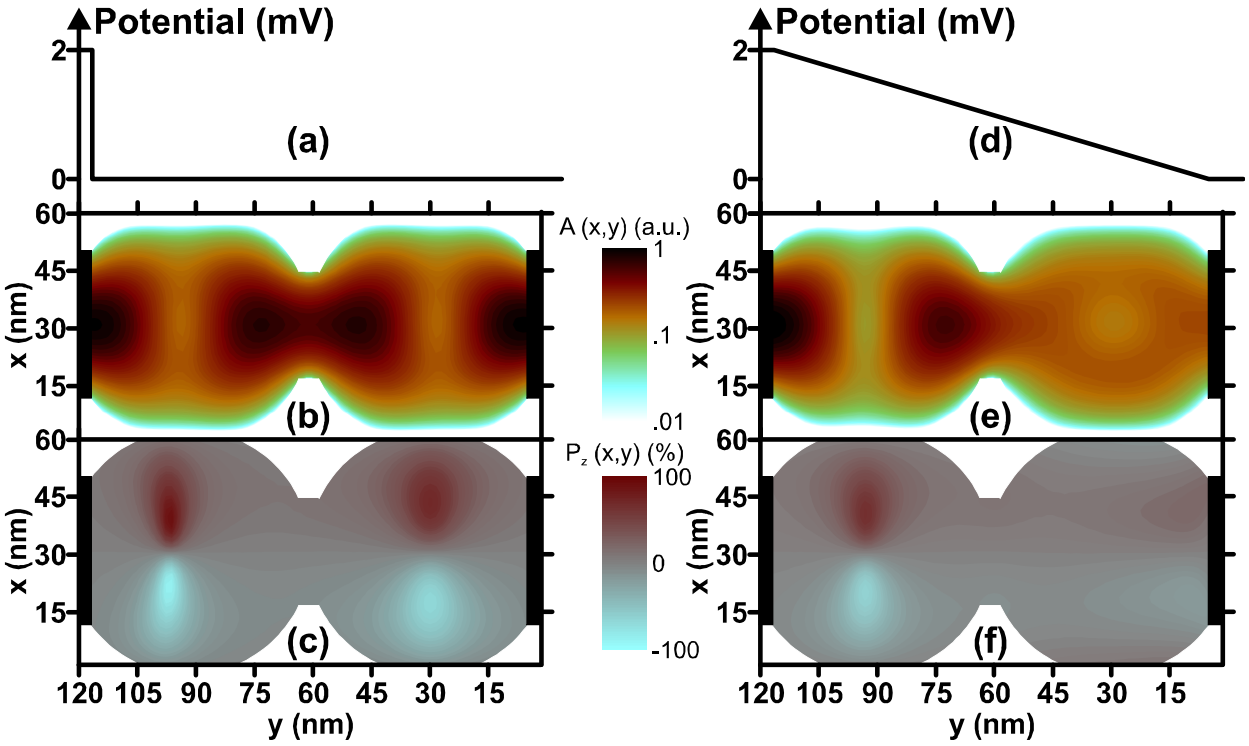

Figure 7.3.1: Valence band profiles (a) and (d) and contour graphs of the calculated spectral function $A(x, y)$ (b) and (e) and the relative spin polarizations $P_z(x, y)$ (c) and (f) in a biaxially tensile strained two-dimensional GaAs light hole gas for a laterally defined double dot geometry. The device is open and attached to a left and right spin-unpolarized contact, shown in black. The net charge current flows from the left towards the right gate. (a)-(c) applied bias of 2 mV drops immediately at the left contact. (d)-(f) Applied bias of 2 mV, but with linear potential drop across the entire device.

holes in the right dot which efficiently smears out the hole wave functions. In this way, spatial derivatives of the retarded Green's functions in Eq. (7.3.1) and simultaneously the spin polarizations are reduced. Second, the hole density of the right dot exceeds the one in the left by approximately a factor of 2. However, most of these holes originate from the drain lead and get reflected due to their small energy. Therefore, they do not propagate through the total device and are not spin-polarized by the intrinsic spin-Hall effect. In summary, the relative spin polarization P_z is nonzero mostly in the left dot (see Fig. 7.3.1 (f)). An additionally applied magnetic field has only a weak effect due to the large confinement of the carriers. We have applied a homogeneous vertical magnetic field of 2 T on the device, but have seen only negligible influence.

7.3.3 Spin-orbit interaction in completely confined states

Introduction

We have shown in the preceding section that obstacles, such as reflecting barriers, in the propagation path of spin carrying holes can yield very large spin polarizations. We add a limitation of this finding in this section: We show that a complete confinement of the carriers suppresses the

spin-Hall effect tremendously - even when originally spin-polarized carriers inelastically scatter into the confined states.

Motivation - phonon-mediated spin polarization?

We have already seen in Fig. 7.3.1 (f) that apart from a significant spatial derivative of the local hole density of states, a significant amount of *propagation*, i.e. a nonvanishing expectation value of the momenta in the spin-orbit interaction potential Eq. (6.2.9) is required to maintain a large spin polarization. Nevertheless, spatial derivatives of the Green's function of completely confined carriers are usually larger than those of propagating carriers. When propagating carriers are spin polarized by the intrinsic spin-Hall effect and scatter inelastically into completely confined states, the carriers in the confined states get to some degree involved into the propagation. Thus, it is a legitimate question whether the confined carriers in the presence of inelastic scattering are spin polarized or not. In order to answer this question, we consider stationary hole transport through a single quantum dot and implement the inelastic scattering with acoustic phonons in the self-consistent Born approximation (see Sec. 6.3). We emphasize that lower order scattering models, such as the Büttiker probe model (see Sec. 4.3.6), cannot consistently account for the polarization of holes that thermalize into the dot states.

Spin polarization in confined states

We consider light holes in a GaAs quantum wire of 35 nm width at a temperature of 10 K. Holes propagate in the x-direction between source and drain which are separated by 60 nm. The potential profile within the wire is constant in y-direction and reads in the propagation direction

$$V(x,y) = V_0 \left[\theta(x - x_1) - \theta(x - x_2)\right], \tag{7.3.3}$$

with the dot depth of $V_0 = -5$ meV, and the dot dimensions $x_1 = 12.5$ nm and $x_2 = 48.5$ nm (see dotted line in Figs. 7.3.2 (a) and (b)). We apply a bias voltage of 2 meV that we assume to drop completely within the source.

Coherently propagating light holes get reflected at the dot boundaries and build up an interference pattern. This pattern mainly follows the spatial shape of the third dot state which lies above the lead band edge. This is illustrated in Fig. 7.3.2 (a) which shows a contour plot of the sheet hole density that results from a ballistic NEGF calculation. Due to the missing energy dissipation, no holes relax into the lower lying dot states and the density in the area of the dot is rather small. Nevertheless, the efficient propagation and the pronounced density oscillations of the ballistic calculation yield large spin polarization in x- and z-direction, as can be seen in Figs. 7.3.3 (a) and (b).

In contrast, when inelastic scattering with longitudinal acoustic phonons is included, the holes dissipate energy and fill the first two dot states that lie below the band edge of the leads. This can be seen in Fig. 7.3.2 (b) which shows a contour plot of the hole density that results from a NEGF calculation of the same dot as in Fig. 7.3.2 (a) but with the scattering self-energies of Sec. 6.3 included. We find the shape of the relative spin polarizations $P_x(x,y)$ and $P_z(x,y)$ of the scattered NEGF calculation to agree with the ballistic results of Figs. 7.3.2 (a) and (b). However, the amplitudes of both polarizations in the scattered NEGF calculation are by approximately a factor of 3 smaller than the ballistic results. Most of this reduction originates from the fact that the holes confined in the two lower dot states are almost unpolarized.

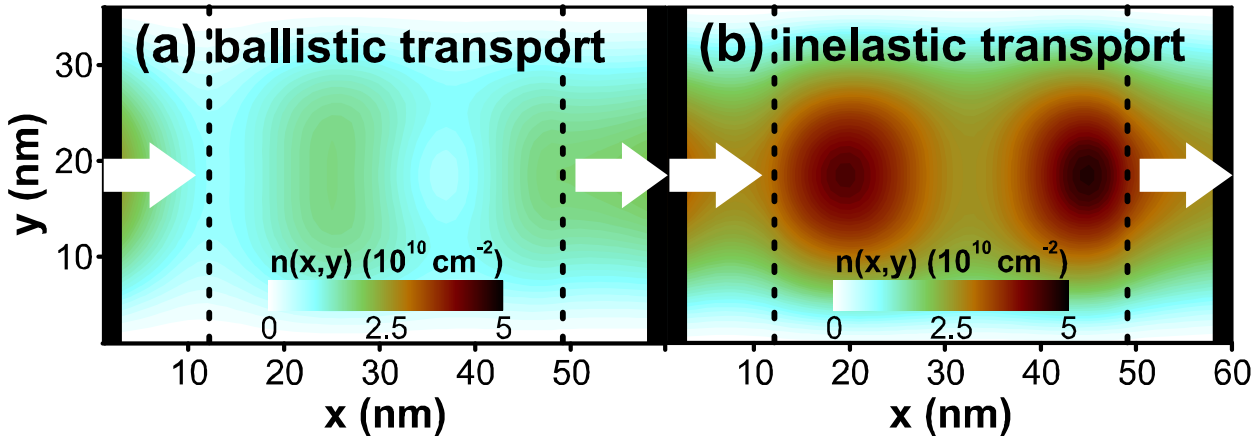

Figure 7.3.2: Comparison of results of a completely ballistic NEGF calculation (a) and a NEGF calculation including inelastic scattering with acoustic phonons (b). The contour plot shows the hole density of a 5 meV deep GaAs quantum dot in a 35 nm wide quantum wire at 10 K lattice temperature and 2 meV applied bias voltage. The extension of the dot in x-direction is 36 nm and is marked with dotted lines. The source (left) and drain (right) leads are depicted with black rectangles. The current flow is illustrated with white arrows.

Therefore, the relative polarization gets reduced according to the large unpolarized hole density in the lower dot states.

In order to illustrate this in more detail, Fig. 7.3.4 shows a comparison of the energy resolved density $n\,(E)$ of Eq. (6.2.22) (solid) and the energy resolved absolute spin polarization δn_z of Eq. (6.2.23) (dotted) that result from a ballistic calculation (red) and a NEGF calculation that includes acoustic phonons (black), respectively. The onset of $n\,(E)$ in the ballistic calculation at approximately $E = 1.9$ meV marks the band edge of the source and drain leads. Any dot state below this energy is exclusively filled by holes that have dissipated energy. Therefore, the first ($E = -1.9$ meV) and the second ($E = 1.1$ meV) dot states are only filled in the calculation including acoustic phonons. The broader maxima of $n\,(E)$ at $E = 5.6$ meV and $E = 8.6$ meV mark the third and forth dot state which lie in the continuum of propagating holes. Thus, the later two states can be seen in both calculations. The spin polarization $\delta n_z\,(E)$ of the two lower dot states in the calculation including phonons is much smaller than the polarization of the third state (note the logarithmic scale). It is worth to note that the polarization of the third dot state differs between the ballistic and scattered NEGF calculation only moderately. In particular, we find the phonon scattering to reduce the peak height of δn_z at $E = 5.6$ nm by approximately 30 %.

7.3.4 Conclusion

We have shown that the "straightforward"reflectionless propagation of carriers (as considered in Sec. 7.2.3) does not yield the largest possible spin polarizations. Instead, we have demonstrated that interferences and oscillations of the propagating carriers can support the spin polarization of the intrinsic spin-Hall effect significantly. In particular, we have shown that the local spin polarization of holes propagating through a coupled quantum dot system can almost reach 100 %. However, this result is sensitive to any external perturbation that influences the hole wave functions. Due to large confinement energies, completely confined carriers are typically

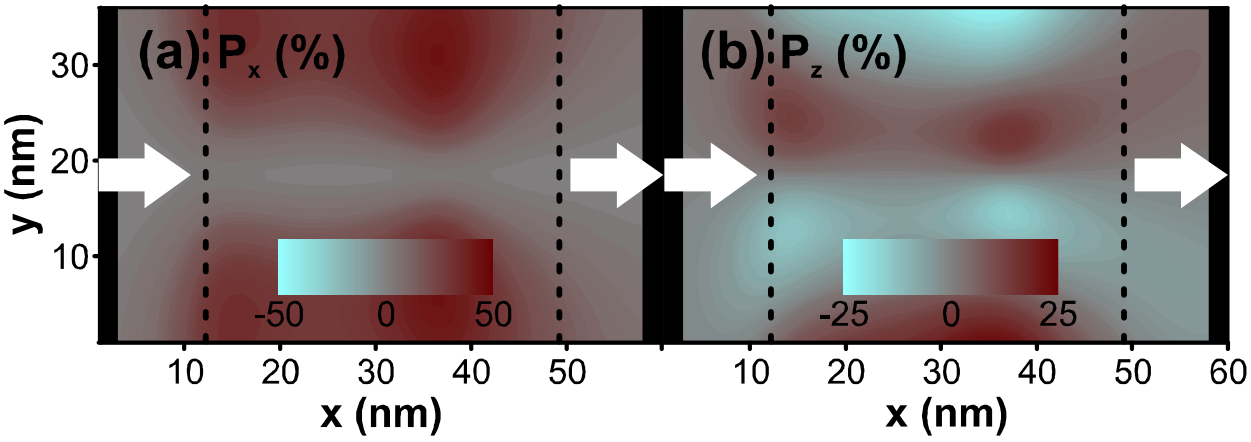

Figure 7.3.3: Contour plots of the relative spin polarisation in x-direction (a) and z-direction (b) of the ballistic quantum dot calculation in Fig. 7.3.2 (a).

less sensitive to the external perturbations than propagating ones. Unfortunately, the spin-orbit interaction requires for an efficient carrier propagation. Accordingly, we have found that carriers in completely confined dot states are effectively unpolarized. This is even the case, when propagating carriers get first spin-polarized by the intrinsic spin-Hall effect and then thermalize by the emission of acoustic phonons into the confined dot states. Nevertheless, these results show that ballistic NEGF calculations of the intrinsic spin-Hall effect are sufficient to qualitatively predict the spin polarization of all-semiconductor devices in Sec. 7.4.

7.4 Proposal of efficient all-semiconductor spin polarizers

7.4.1 Introduction

We have shown in the preceding section that interferences of carriers can be used to stimulate a large spin-Hall effect. Therefore, interferences in the presence of the spin-orbit interaction can be used to design efficient all-semiconductor spin polarizers. This is the purpose of this section. We first modify a known proposal of an efficient three terminal spin polarizer: We show that inhomogeneous spin-orbit interaction strengths are not required for an efficient spin-Hall effect in T-shaped devices. This is an important result, because it eases the experimental realization significantly. However, we show that the T-shaped device effectively polarizes the carrier spin with respect to one lateral direction. Therefore, we propose a novel four terminal device that acts as an efficient spin-polarizer simultaneously in both lateral directions.

All calculations in this sections are meant as qualitative predictions and therefore ignore incoherent scattering. Confined states beneath the band edges of the leads do not significantly contribute to the spin-Hall effect and are consequently neglected (see the discussion in Sec. 7.3).

7.4.2 Modification of a known T-shaped device

It has been shown in [191, 192] that amazingly large spin polarizations can be generated near contacts of T-shaped three terminal devices. In such a device, it is common to assume the

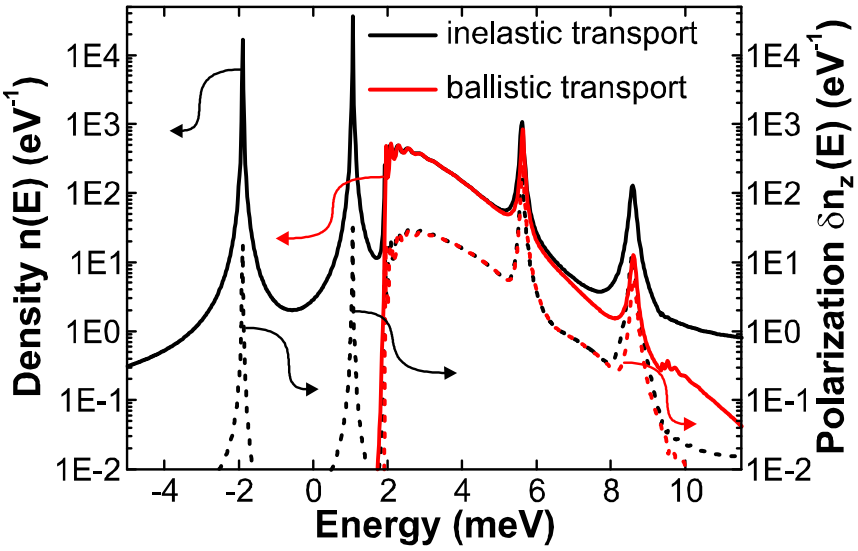

Figure 7.3.4: Comparison of a ballistic NEGF calculation (red) and a calculation including inelastic scattering with acoustic phonons (black). The solid lines depict the energy resolved hole density $n\,(E)$ and the dotted lines show the energy resolved absolute spin polarization $\delta n_z\,(E)$ in z-direction. Peaks mark the energy of resonant dot states and the onset at approximately 1.9 meV equals the energy of the lead band edge.

spin-orbit interaction strength α_{BIA} or α_{SIA} to be induced by the electrostatic field of gate electrodes (see also Fig. 7.2.1) which yields a finite spin-orbit interaction only in the center of the device. Since it is experimentally difficult to limit such electric fields on areas smaller than 30 nm, we propose a modification of this spin polarizer: we assume a constant spin-orbit interaction parameter $\alpha_{BIA} = 0.2$ eVÅ in the device as well as in the leads. We apply a bias voltage of 5 mV across the T-shaped device shown in Figs. 7.4.1 (a) and (b). The device temperature is set to 1 K and the potential within the device is constant, i.e. the applied bias drops within the source lead. We consider light holes of the effective mass $m^* = 0.11$ m$_0$ that propagate from the unpolarized upper source lead to the two lower unpolarized drain leads to the right and to the left. In Fig. 7.4.1 (a), we depict the coplanar spin polarization $P_y\,(x, y)$. At the two drain leads, $P_y\,(x, y)$ amounts to approximately 25 % and is positive on the lead at the right and left hand side, whereas the spin polarization is almost zero near the source lead. Thus, such a device acts as an efficient y-polarizer, provided that impurity and acoustic phonon scattering lengths exceed the sample dimensions. In Fig. 7.4.1 (b), we show the vertical spin polarization $P_z\,(x, y)$ for the same device. In this case, the spin polarizations have opposite sign at the two drain leads and varies along the contact from 50 % to 0. In summary, our results show that the hole interferences at the intersection of the two quantum wires of a T-shaped device are sufficient to generate very large spin polarizations. An inhomogeneous spin-orbit interaction is not required for an efficient all semiconductor spin-filter.

7.4.3 Novel four terminal device

The three terminal device of the preceding section acts as a spin polarizer for P_y and P_z. However, the polarization in z-direction is rather hard to use, because it varies strongly along the lead/device boundary. Therefore, the T-shaped device is an efficient spin polarizer for only

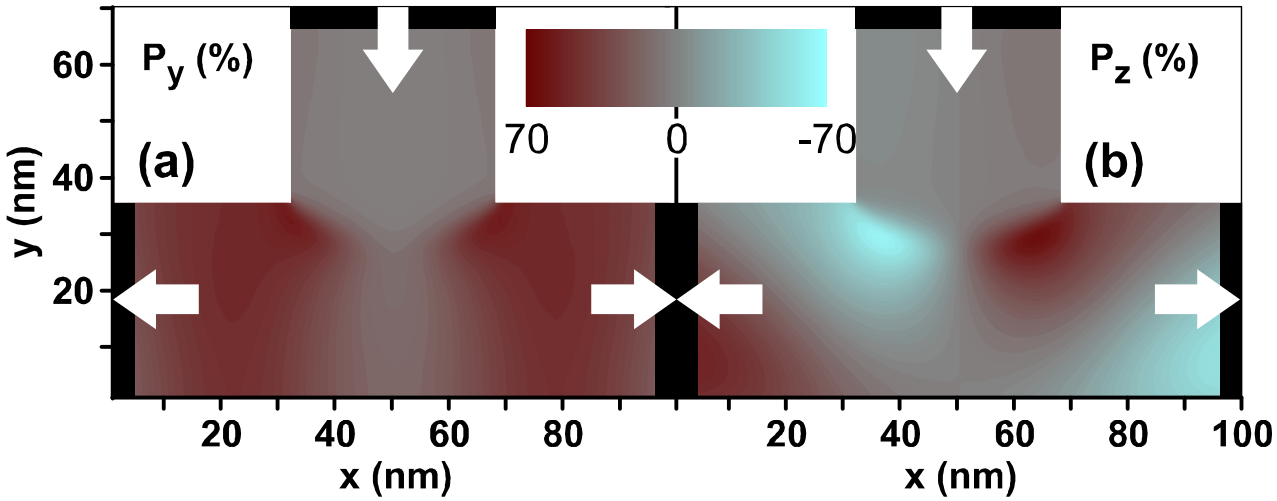

Figure 7.4.1: Contour graph of calculated relative spin polarizations (a) $P_y(x,y)$ and (b) $P_z(x,y)$ in a biaxially tensile strained two-dimensional GaAs light hole gas for a laterally defined three terminal device, as a function of the lateral dimension. The device is open and attached to spin-unpolarized contacts at the top and on the right hand and left hand side, respectively (shown in black). The net charge current flows from the top towards the side contacts and is indicated by the white arrows.

one spin direction.

In Figs. 7.4.2 (a) and (b), we propose a novel cross-shaped device that simultaneously acts as a y- and x-polarizer. This device consists of two 24 nm wide quantum wires that intersect perpendicularly in the center of the device. We apply a voltage of 3 meV between the upper and left unpolarized source leads and the lower and right unpolarized drain leads. We assume a device temperature of 10 K and consider the voltage to drop completely within the source leads. We assume light holes of the effective mass of $m^* = 0.11$ m_0 and a constant spin-orbit parameter $\alpha_{BIA} = 0.2$ eVÅ.

Unpolarized holes enter the device from the left and upper source lead. The interferences of the holes at the intersection of the quantum wires in the central device region yield an oscillating $P_x(x,y)$ in the lower branch (see Fig. 7.4.2 (a)) and an oscillating $P_y(x,y)$ in the right branch (see Fig. 7.4.2 (b)) of the device. The sign of the respective polarizations depend on the distance of the respective lead to the center of the device. More importantly, however, the holes enter each drain with a polarization that is approximately constant across the lead surface. In the configuration of Figs. 7.4.2 (a) and (b), the relative polarization in x- and y-direction at the right and lower lead varies between 9.8 and 11.3 %.

7.5 Conclusion

We have shown that the spin-Hall effect predicted by NEGF calculations in the envelope function approach qualitatively agrees with results of NEGF calculations in the microscopic tight binding model. In particular, both models agree in the general shape of the spin polarization as well as in the linear dependence on the propagation momentum. For this reason, we have been able to use the numerically efficient envelope function model for the qualitative prediction of

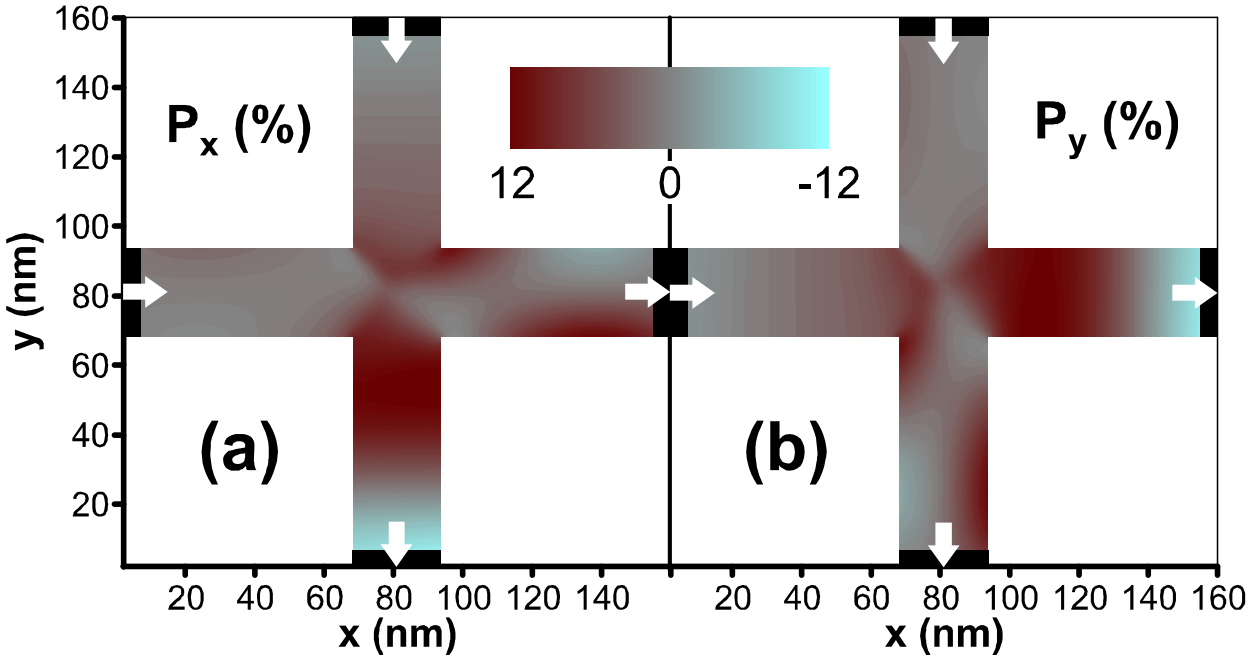

Figure 7.4.2: Contour graph of calculated relative spin polarizations (a) $P_y(x,y)$ and (b) $P_z(x,y)$ in a biaxially tensile strained two-dimensional GaAs light hole gas for a laterally defined four terminal device, as a function of the lateral dimensions. The device is open and attached to spin-unpolarized source (upper and left) and drain (lower and right) contacts, shown in black. The net charge current flows from the top and the left towards the right and the lower contacts and is indicated by the white arrows.

the spin-orbit interaction in more sophisticated devices such as quantum dots and intersecting quantum wires.

We have demonstrated that interferences and oscillations of propagating carriers can be utilized to generate very high spin polarizations. In this way, partially confined carriers can locally yield much larger spin polarizations than carriers that propagate without obstacles, in spite of the reduced current density. In particular, we have shown an almost complete local spin polarization of holes in a coupled quantum dot system. Still, an efficient propagation is essential for the intrinsic spin-Hall effect. Consequently, we have shown that carriers in completely confined states are effectively unpolarized - irrespective of their inelastic interaction with polarized carriers. For this reason, ballistic NEGF calculations that do not consider completely confined states are sufficient to qualitatively predict efficient all-semiconductor, non-magnetic spin polarizers. We have modified a T-shaped three terminal device given in literature and have shown that a *homogeneous* spin-orbit interaction strength is sufficient to yield a large spin polarization. This is an important modification, because such a homogeneous spin-orbit interaction simplifies the experimental fabrication significantly. However, the T-shaped device effectively polarizes the spin only in one lateral direction. Therefore, we have proposed a novel four terminal device that simultaneously polarizes the spin in both lateral directions.

Bibliography

[1] X. Michalet, F. F. Pinaud, L. A. Bentolola, J. M. Tsay, S. Doose, J. J. Li, G. Sundaresan, A. M. Wu, S. S. Gambhir, and S. Weiss, Science **307**, 538 (2005).

[2] P. Offermans, P. M. Koenraad, and J. H. Wolter, Phys. Rev. B **72**, 165332 (2005).

[3] C. Zhang, J. Xu, T. Zhu, F. Zhang, Z. Tan, and S. J. Schiff, Phys. Rev. B **80**, 035333 (2009).

[4] L. Wilson, Tech. Rep., International Technology Roadmap for Semiconductors (2008), URL `http://www.itrs.net/home.html`.

[5] L. P. Kadanoff and G. Baym, *Quantum Statistical Mechanics* (W. A. Benjamin, Inc., Menlo Park, California, 1962).

[6] H. Haug and A.-P. Jauho, *Quantum Kinetics in Transport and Optics of Semiconductors* (Springer, Berlin, 1996).

[7] S. Datta, *Electronic Transport in Mesoscopic Systems* (Cambridge University Press, Cambridge, 1995).

[8] E. M. Lifschitz and L. P. Pitajewski, *Lehrbuch der theoretischen Physik, Band X Physikalische Kinetik* (Akademie-Verlag, Berlin, 1983).

[9] A. L. Fetter and J. D. Walecka, *Quantum Theory of Many-Particle Systems* (McGraw-Hill Inc., New York, 1971).

[10] G. D. Mahan, *Many-Particle Physics* (Plenum Press, 1990).

[11] M. Yamanishi, T. Edamura, and H. Kan, Opt. Express **16**, 20748 (2008).

[12] Y. K. Kato, R. C. Myers, A. C. Gossard, and D. D. Awschalom, Science **306**, 1910 (2004).

[13] J. Wunderlich, B. Kaestner, J. Sinova, and T. Jungwirth, Phys. Rev. Lett. **94**, 047204 (2005).

[14] J. Schwinger, J. Math. Phys. **2**, 407 (1961).

[15] L. P. Keldysh, Sov. Phys. JETP **20**, 1018 (1965).

[16] E. Fick, *Einführung in die Grundlagen der Quantentheorie* (Aula Verlag, Wiesbaden, 1988).

[17] J. Rammer and H. Smith, Rev. Mod. Phys. **58**, 323 (1986).

[18] D. K. Ferry and C. Jacoboni, *Quantum Transport in Semiconductors* (Plenum Press, New York, 1992).

[19] P. Danielewicz, Ann. Phys. **152**, 239 (1984).

[20] D. Langreth and J. Wilkins, Phys. Rev. B **6**, 3189 (1972).

[21] D. K. Ferry and S. M. Goodnick, *Transport in Nanostructures* (Cambridge University Press, Cambridge, 1997).

[22] R. Lake, G. Klimeck, R. C. Bowen, and D. Jovanovic, J. Appl. Phys. **81**, 7845 (1997).

[23] H. Bruus and K. Flensberg, *Many-Body Quantum Theory in Condensed Matter Physics* (Oxford University Press, Oxford, 2004).

[24] W. Kohn and J. M. Luttinger, Phys. Rev. **108**, 590 (1957).

[25] Y. Xu, J.-S. Wang, W. Duan, B.-L. Gu, and B. Li, Phys. Rev. B **78**, 224303 (2008).

[26] M. Luisier, A. Schenk, and W. Fichtner, J. Appl. Phys. **100**, 043713 (2006).

[27] V. N. Do, P. Dollfus, and V. L. Nguyen, J. Appl. Phys. **100**, 093705 (2006).

[28] Z. Chen, J. Wang, B. Wang, and D. Y. Xing, Phys. Lett. A **334**, 436 (2005).

[29] Y. Ke, K. Xia, and H. Guo, Phys. Rev. Lett. **100**, 166805 (2008).

[30] A. Bulusu and D. G. Walker, Transaction of the ASME **129**, 492 (2007).

[31] T. Yamamoto and K. Watanabe, Phys. Rev. Lett. **96**, 255503 (2006).

[32] M. Lazzeri, S. Piscanec, F. Mauri, A. C. Ferrari, and J. Robertson, Phys. Rev. Lett. **95**, 236802 (2005).

[33] H. Li and X. Q. Zhang, Phys. Lett. A **372**, 4294 (2008).

[34] T. Sato, K. Shizu, T. Kuga, K. Tanaka, and H. Kaji, Chem. Phys. Lett. **458**, 152 (2008).

[35] P. Damle, A. W. Ghosh, and S. Datta, Chem. Phys. **281**, 171 (2002).

[36] J. R. Gao, J. N. Hovenier, Z. Q. Yang, J. J. A. Baselmans, A. Baryshev, M. Hajenius, T. M. Klapwijk, A. J. L. Adam, T. O. Klaassen, B. S. Williams, et al., Appl. Phys. Lett. **86**, 244104 (2005).

[37] H.-W. Hübers, S. G. Pavlov, H. Richter, A. D. Semenov, L. Mahler, A. Tredicucci, H. E. Beere, and D. A. Ritchie, Appl. Phys. Lett. **89**, 061115 (2006).

[38] A. W. M. Lee, Q. Qin, S. Kumar, B. S. Williams, Q. Hu, and J. L. Reno, Appl. Phys. Lett. **89**, 141125 (2006).

[39] P. Y. Yu and M. Cardona, *Fundamentals of Semiconductors* (Springer, 2001).

[40] N. Vukmirović, Z. Ikonić, D. Indjin, and P. Harrison, Phys. Rev. B **76**, 245313 (2007).

[41] S.-C. Lee, F. Banit, M. Woerner, and A. Wacker, Phys. Rev. B **73**, 245320 (2006).

[42] M. V. Fischetti, J. Appl. Phys. **83**, 270 (1998).

[43] R. Bertoncini and A.-P. Jauho, Phys. Rev. Lett. **68**, 2826 (1992).

[44] S. Hackenbuchner, Master's thesis, Technische Universität München (2002).

[45] S.-C. Lee and A. Wacker, Phys. Rev. B **66**, 245314 (2002).

[46] A. Wacker, phys. stat. sol. (c) **5**, 215 (2008).

[47] A. Haque and A. N. Khondker, Phys. Rev. B **49**, 14007 (1994).

[48] A. Wacker, Phys. Rev. B **66**, 085326 (2002).

[49] J. D. Jackson, *Classical Electrodynamics* (Wiley & Sons, 1999).

[50] F. Banit, S.-C. Lee, A. Knorr, and A. Wacker, Appl. Phys. Lett. **86**, 041108 (2005).

[51] H. Ehrenreich and M. H. Cohen, Phys. Rev. **115**, 786 (1959).

[52] O. Madelung, *Introduction to Solid-State Theory* (Springer, 1996).

[53] J. Lindhard, Kgl. Danske Videnskab. Selskab, Mat.-fys. **28**, 8 (1954).

[54] X. L. Lei, J. Phys. C **18**, L593 (1985).

[55] S.-C. Lee and I. Galbraith, Physica B **272**, 237 (1999).

[56] O. Bonno, J.-L. Thobel, and F. Dessenne, J. Appl. Phys. **97**, 043702 (2005).

[57] A. Gold and V. T. Dolgopolov, JETP Lett. **86**, 256 (2007).

[58] J. T. Lü and J. C. Cao, Appl. Phys. Lett. **89**, 211115 (2006).

[59] N. Mori and T. Ando, Phys. Rev. B **40**, 6175 (1989).

[60] X. Gao, D. Botez, and I. Knezevic, J. Appl. Phys. Lett. **103**, 073101 (2008).

[61] P. Lugli, C. Jacoboni, L. Reggiani, and P. Kocevar, Appl. Phys. Lett. **50**, 1251 (1987).

[62] B. K. Ridley, W. J. Schaff, and L. F. Eastman, J. Appl. Phys. **96**, 1499 (2004).

[63] M. S. Vitiello, G. Scarmacio, V. Spagnolo, B. S. Williams, S. Kumar, Q. Hu, and J. L. Reno, Appl. Phys. Lett. **86**, 111115 (2005).

[64] H. Callebaut, S. Kumar, Q. H. B. S. Williams, and J. L. Reno, Appl. Phys. Lett. **83**, 207 (2003).

[65] Y. Asai, Phys. Rev. B **78**, 045434 (2008).

[66] H. Fröhlich, Adv. Phys. **3**, 325 (1954).

[67] B. K. Ridley, *Quantum Processes in Semiconductors* (Oxford Science Publications, Oxford, 1982).

[68] S. M. Goodnick and P. Lugli, Phys. Rev. B **37**, 2578 (1988).

[69] A. Svizhenko and M. P. Anantram, Phys. Rev. B **72**, 085430 (2005).

[70] A. Wacker, Phys. Rep. **357**, 1 (2002).

[71] P. Lawaetz, Phys. Rev. **183**, 730 (1969).

[72] J. Bardeen and W. Shockley, Phys. Rev. **80**, 72 (1950).

[73] C. Kittel and C. Y. Fong, *Quantentheorie der Festkörper* (Oldenburg, 1988).

[74] C. Herring and E. Vogt, Phys. Rev. **101**, 944 (1956).

[75] C. Jacoboni and P. Lugli, *The Monte Carlo Method for Semiconductor Device Simulation* (Springer, Wien, 1989).

[76] C. Jacoboni and L. Reggiani, Rev. Mod. Phys. **55**, 645 (1983).

[77] P. Boguslawski and J. Mycielski, J. Phys. C: Solid State Phys. **10**, 2314 (1977).

[78] P. Boguslawski and J. Mycielski, J. Phys. C **13**, 1019 (1980).

[79] P. Vogl, Phys. Rev. B **13**, 694 (1976).

[80] H. Brooks, Phys Rev. **83**, 879 (1951).

[81] E. Conwell and V. F. Weisskopf, Phys. Rev. **77**, 388 (1950).

[82] J. B. Krieger and T. Meeks, Phys. Rev. B **8**, 2780 (1973).

[83] D. Chattopadhyay and H. J. Queisser, Rev. Mod. Phys. **53**, 745 (1981).

[84] T. Kubis, Master's thesis, Technische Universität München (2003).

[85] B. R. Nag, Semicond. Sci. Technol. **19**, 162 (2004).

[86] H. Sakaki, T. Noda, K. Hirakawa, M. Tanaka, and T. Matsusue, Appl. Phys. Lett. **51**, 1934 (1987).

[87] R. F. Schnabel, R. Zimmermann, D. Bimberg, H. Nickel, R. Lösch, and W. Schlapp, Phys. Rev. B **46**, 9873 (1992).

[88] P. Roblin, R. C. Potter, and A. Fathimulla, J. Appl. Phys. **79**, 2502 (1996).

[89] T. Unuma, M. Yoshita, T. Noda, H. Sakaki, and H. Akiyama, J. Appl. Phys. **93**, 1586 (2003).

[90] S. Yamakawa, H. Ueno, K. Taniguchi, C. Hamaguchi, K. Miyatsuji, K. Masaki, and U. Ravaioli, J. Appl. Phys. **79**, 911 (1996).

[91] G. H. Kruithof, T. M. Klapwijk, and S. Bakker, Phys. Rev. B **8**, 6642 (1991).

[92] K. S. Thygesen and A. Rubio, Phys. Rev. B **77**, 115333 (2008).

[93] U. von Barth and B. Holm, Phys. Rev. B **54**, 8411 (1996).

[94] B. Holm and U. von Barth, Phys. Rev. B **57**, 2108 (1998).

[95] M. Manenti, F. Compagnone, A. D. Carlo, and P. Lugli, J. Comput. Electron. **2**, 433 (2003).

[96] M. Paulsson and M. Brandbyge, Phys. Rev. B **76**, 115117 (2007).

[97] I. Knezevic, Phys. Rev. B **77**, 125301 (2008).

[98] T. Grange, R. Ferreira, and G. Bastard, Phys. Rev. B **76**, 241304(R) (2007).

[99] J. Taylor, H. Guo, and J. Wang, Phys Rev B **63**, 245407 (2001).

[100] D. Mamaluy, A. Mannargudi, D. Vasileska, M. Sabathil, and P. Vogl, Semicond. Sci. Technol. **19**, 118 (2004).

[101] I. Appelbaum, T. Wang, J. D. Joannopoulos, and V. Narayanamurti, Phys. Rev. B **69**, 165301 (2004).

[102] M. Pourfath, H. Kosina, and S. Selberherr, J. Comput. Electron. **5**, 155 (2006).

[103] A. Pecchia and A. D. Carlo, Rep. Prog. Phys. **67**, 1497 (2004).

[104] A. Svizhenko, M. P. Anantram, T. R. Govindan, B. Biegel, and R. Venugopal, J. Appl. Phys. **91**, 2343 (2002).

[105] T. Kubis, C. Yeh, and P. Vogl, J. Comput. Electron. **7**, 432 (2008).

[106] S. M. Sze and K. K. Ng, *Physics of Semiconductor Devices* (John Wiley & Sons, Inc., 2007).

[107] S. Hackenbuchner, Ph.D. thesis, Technische Universtät München (2002).

[108] M. Sabathil, S. Hackenbuchner, M. J. A., Z. G., and P. Vogl, J. Comput. Electron. **1**, 81 (2002).

[109] S. E. Laux, A. Kumar, and M. V. Fischetti, J. Appl. Phys. **95**, 5545 (2004).

[110] H. Takeda, N. Mori, and C. Hamaguchi, J. Comput. Electron. **2**, 119 (2003).

[111] S. Datta, Superlattices and Microstructures **28**, 253 (2000).

[112] W. R. Frensley, Rev. Mod. Phys. **62**, 745 (1990).

[113] W. Pötz, J. Appl. Phys. **86**, 2458 (1989).

[114] T. González and D. Pardo, Solid-State Electron. **39**, 555 (1996).

[115] W. Pötz, J. Appl. Phys. **71**, 2297 (1992).

[116] J. H. Oh, D. Ahn, Y. S. Yu, and S. W. Hwang, Phys. Rev. B **77**, 035313 (2008).

[117] T. Zibold, P. Vogl, and A. Bertoni, Phys. Rev. B **76**, 195301 (2007).

[118] R. Venugopal, Z. Ren, and M. Lundstrom, IEEE Trans. Nanotechnology **2**, 135 (2003).

[119] M. Sabathil, Ph.D. thesis, Technische Universität München (2004).

[120] Z. Ren, R. Venugopal, S. Datta, M. Lundstrom, D. Jovanović, and J. Fossum, IEDM Techn. Digest Intern. p. 715 (2000).

[121] M. V. Fischetti, Phys. Rev. B **59**, 4901 (1999).

[122] A. Benz, G. Fasching, A. M. Andrews, M. Martl, K. Unterrainer, T. Roch, W. Schrenk, S. Golka, and G. Strasser, Appl. Phys. Lett. **90**, 101107 (2007).

[123] G. D. Mahan, Phys. Rep. **145**, 251 (1987).

[124] M. P. L. Sancho, J. M. L. Sancho, and J. Rubio, J. Phys. F: Met. Phys. **14**, 1205 (1984).

[125] M. P. L. Sancho, J. M. L. Sancho, and J. Rubio, J. Phys. F: Met. Phys. **15**, 851 (1985).

[126] C. Strahberger, Ph.D. thesis, Technische Universität München (2001).

[127] C. Strahberger and P. Vogl, Phys. Rev. B **62**, 7289 (2000).

[128] C. Rivas and R. Lake, phys. stat. sol. (b) **239**, 94 (2003).

[129] S. Sanvito, C. J. Lambert, J. H. Jefferson, and A. M. Bratkovsky, Phys. Rev. B **59**, 11936 (1999).

[130] M. Luisier, Ph.D. thesis, Eidgenössische Technische Hochschule Zürich (2007).

[131] A. Trellakis, A. Galick, A. Pacelli, and U. Ravaioli, J. Appl. Phys. **81**, 7880 (1997).

[132] R. Venugopal, M. Paulsson, S. Goasguen, S. Datta, and M. Lundstrom, J. Appl. Phys. **93**, 5613 (2003).

[133] A. A. Yanik, G. Klimeck, and S. Datta, Phys. Rev. B **76**, 045213 (2007).

[134] R. Golizadeh-Mojarad and S. Datta, Phys. Rev. B **75**, 081301(R) (2007).

[135] Y.-S. Liu, H. Chen, X.-H. Fan, and X.-F. Yang, Phys. Rev. B **73**, 115310 (2006).

[136] S. Sato and N. Sano, J. Comput. Electron. **7**, 301 (2008).

[137] A. Pecchia, G. Romano, and A. D. Carlo, Phys. Rev. B **75**, 035401 (2007).

[138] P. S. Damle, Ph.D. thesis, Purdue University (2003).

[139] M. Büttiker, Phys. Rev. B **33**, 3020 (1986).

[140] S. Washburn and R. A. Webb, Rep. Prog. Phys. **55**, 1311 (1992).

[141] A. Dhar and D. Sen, Phys. Rev. B **73**, 085119 (2006).

[142] C. Weber, A. Wacker, and A. Knorr, Phys. Rev. B **79**, 165322 (2009).

[143] G. Klimeck, R. Lake, C. L. Fernando, R. C. Bowen, D. Blanks, M. Leng, T. Moise, Y. C. Kao, and W. R. Frensley, in *Proceedings of the International Conference on Quantum Devices and Circuits: Alexandria, Egypt 4-7 June 1996*, edited by K. Ismail, S. Bandyopadhyay, and J. P. Leburton (Alexandria, Egypt, 1996).

[144] S. Jin, Y. J. Park, and H. S. Min, J. Appl. Phys. **99**, 123719 (2006).

[145] Z. Ren, R. Venugopal, S. Goasguen, S. Datta, and M. Lundstrom, IEEE Trans. Electron. Dev. **50**, 1914 (2003).

[146] R. Venugopal, Z. Ren, S. Datta, M. S. Lundstrom, and D. Jovanovic, J. Appl. Phys. **92**, 3730 (2002).

[147] P. Greck, Master's thesis, Technische Universität München (2008).

[148] A. Wacker, A.-P. Jauho, S. Rott, A. Markus, P. Binder, and G. H. Döhler, Phys. Rev. Lett. **83**, 836 (1999).

[149] T. Schmielau and M. F. Pereira, phys. stat. sol. B **246**, 329 (2009).

[150] R. Nelander and A. Wacker, Appl. Phys. Lett. **92**, 081102 (2008).

[151] M. Lundstrom and Z. Ren, IEEE Trans. Electron. Dev. **49**, 133 (2002).

[152] S. Wang and N. Mingo, Phys. Rev. B **79**, 115316 (2009).

[153] B. H. Wu and J. C. Cao, Physica E **40**, 1319 (2008).

[154] P. Greck, private communication.

[155] R. C. Iotti and F. Rossi, phys. stat. sol. (b) **238**, 462 (2003).

[156] C. Weber, F. Banit, S. Butscher, A. Knorr, and A. Wacker, Appl. Phys. Lett. **89**, 091112 (2006).

[157] H. Willenberg, G. H. Döhler, and J. Faist, Phys. Rev. B **67**, 085315 (2003).

[158] C. Jirauschek, G. Scarpa, P. Lugli, M. Vitiello, and G. Scamarcio, J. Appl. Phys. **101**, 086109 (2007).

[159] F. Compagnone, A. D. Carlo, and P. Lugli, Appl. Phys. Lett. **80**, 920 (2002).

[160] X. Gao, D. Botez, and I. Knezevic, J. Appl. Phys. **101**, 063101 (2007).

[161] I. Savić, N. Vukmirović, Z. Ikonić, D. Indjin, R. W. Kelsall, P. Harrison, and V. Milanović, Phys. Rev. B **76**, 165310 (2007).

[162] S.-C. Lee and A. Wacker, Appl. Phys. Lett. **83**, 2506 (2003).

[163] N. Vukmirović, D. Indjin, Z. Ikonić, and P. Harrison, IEEE Photon. Technol. Lett. **20**, 129 (2008).

[164] X. Zheng, W. Chen, M. Stroscio, and L. F. Register, Phys. Rev. B **73**, 245304 (2006).

[165] A. M. Andrews, A. Benz, C. Deutsch, G. Fasching, K. Unterrainer, P. Klang, W. Schrenk, and G. Strasser, Mat. Sci and Eng. B **147**, 152 (2008).

[166] B. S. Williams, H. Callebaut, S. Kumar, Q. Hu, and J. L. Reno, Appl. Phys. Lett. **82**, 1015 (2002).

[167] S. Kumar, B. S. Williams, S. Kohen, and Q. Hu, Appl. Phys. Lett. **84**, 2494 (2004).

[168] e. b. O. M. Landolt-Börnstein, *Semiconductors: Intrinsic Properties of Group IV Elements and III-V, II-VI and I-VII Compounds* (Springer, Berlin, 1987).

[169] K. Leosson, J. R. Jensen, W. Langbein, and J. M. Hvam, Phys. Rev. B **61**, 10322 (2000).

[170] T. Roch, A. M. Andrew, G. Fasching, A. Benz, W. Schrenk, and K. Unterrainer, Cent. Eur. J. Phys. **5**, 244 (2007).

[171] A. E. Siegman, *Lasers* (University Science Books, Mill Valley, California, 1986).

[172] S. Kumar, B. S. Williams, and Q. Hu, J. Appl. Phys. **97**, 053106 (2005).

[173] L. Ajili, G. Scalari, M. Giovannini, N. Hoyler, and J. Faist, J. Appl. Phys. **100**, 043102 (2006).

[174] H. C. Liu, M. Wächter, D. Ban, Z. R. Wasilewski, M. Buchanan, G. C. Aers, J. C. Cao, S. L. Feng, B. S. Williams, and Q. Hu, Appl. Phys. Lett. **87**, 141102 (2005).

[175] S. L. Lu, L. Schrottke, S. W. Teitsworth, R. Hey, and H. Grahn, Phys. Rev. B **73**, 033311 (2006).

[176] V. D. Jovanović, D. Indjin, N. Vukmirović, Z. Ikonić, P. Harrison, E. H. Linfield, H. Page, X. Marcadet, C. Sirtori, C. Worrall, et al., Appl. Phys. Lett. **86**, 211117 (2005).

[177] R. C. Iotti and F. Rossi, Phys. Rev. Lett. **87**, 146603 (2001).

[178] C. Jirauschek and P. Lugli, J. Appl. Phys. **105**, 126102 (2009).

[179] H. Callebaut, S. Kumar, B. S. Williams, H. Qing, and J. L. Reno, Appl. Phys. Lett. **83**, 207 (2003).

[180] H. Callebaut and H. Qing, J. Appl. Phys. **98**, 104505 (2005).

[181] H. Callebaut, S. Kumar, B. S. Williams, Q. Hu, and J. L. Reno, Appl. Phys. Lett. **84**, 645 (2004).

[182] M. A. Belkin, F. Capasso, F. Xie, A. Belyanin, M. Fischer, A. Wittmann, and J. Faist, Appl. Phys. Lett. **92**, 201101 (2008).

[183] R. C. Iotti and F. Rossi, Appl. Phys. Lett. **78**, 2902 (2001).

[184] C. Jirauschek and P. Lugli, phys. stat. sol. (c) **5**, 221 (2008).

[185] H. Yasuda, T. Kubis, P. Vogl, N. Sekine, I. Hosako, and K. Hirakawa, Appl. Phys. Lett. **94**, 151109 (2009).

[186] S. Kumar, Q. Hu, and J. L. Reno, Appl. Phys. Lett. **94**, 131105 (2009).

[187] S. Datta and B. Das, Appl. Phys. Lett. **56**, 665 (1989).

[188] J. C. Egues, G. Burkard, and D. Loss, Phys. Rev. Lett. **89**, 176401 (2002).

[189] R. J. Young, S. J. Dewhurst, R. M. Stevenson, P. Atkinson, A. J. Bennet, M. B. Ward, K. Cooper, D. A. Ritchie, and A. J. Shields, New Journal of Physics **9**, 365 (2007).

[190] S. Gardelis, C. G. Smith, C. H. W. Barnes, E. H. Linfield, and D. A. Ritchie, Phys. Rev. B **60**, 7764 (1999).

[191] A. A. Kiselev and K. W. Kim, Appl. Phys. Lett. **78**, 775 (2001).

[192] M. Yamamoto, T. Ohtsuki, and B. Kramer, Phys. Rev. B **72**, 115321 (2005).

[193] J. A. Majewski and P. Vogl, in *Physics of Semiconductors*, edited by A. R. Long and J. H. Davies (Institute of Physics Publ., 2003), p. 305.

[194] R. Golizadeh-Mojarad and S. Datta, cond-mat/07030280 p. v2 (2007).

[195] H. Iwata, T. Matsuda, and T. Ohzone, Jpn. J. Appl. Phys. **45**, 4009 (2006).

[196] C. Ahn and M. Shin, IEEE Transactions on Nanotechnology **5**, 278 (2006).

[197] R. Venugopal, Ph.D. thesis, Purdue University (2003).

[198] B. K. Nikolić, S. Souma, L. P. Zârbo, and J. Sinova, Phys. Rev. Lett. **95**, 046601 (2005).

[199] E. L. Ivchenko, G. E. Pikus, and G. P. Skrebtsov, *Superlattices and Other Heterostructures: Symmetry and Optical Phenomena*, Springer Series in Solid-State Sciences (Springer, New York, 1997).

[200] P. Pfeffer, Phys. Rev. B **59**, 15902 (1999), and references therein.

[201] P.-O. Löwdin, J. Chem. Phys. **18**, 365 (1950).

[202] A. V. Podolskiy and P. Vogl, Phys. Rev. B **69**, 233101 (2004).

[203] P. Vogl, H. P. Hjalmarson, and J. D. Dow, J. Phys. Chem. Solids **44**, 365 (1983).

[204] J.-M. Jancu, R. Scholz, F. Beltram, and F. Bassani, Phys. Rev. B **57**, 6493 (1998).

[205] B. K. Nikolić, L. P. Zârbo, and S. Welack, Phys. Rev. B **72**, 075335 (2005).

[206] B. K. Nikolić, L. P. Zârbo, and S. Souma, Phys. Rev. B **73**, 075303 (2006).

[207] R. Shen, Y. Chen, Z. D. Wang, and D. Y. Xing, Phys. Rev. B **74**, 125313 (2006).

[208] G. W. Bryant and W. Jaskolski, J. Phys. Chem. B **109**, 19650 (2005).

[209] W. Jaskólski, M. Zieliński, G. W. Bryant, and J. Aizpurua, Phys. Rev. B **74**, 195339 (2006).

[210] K. Suzuki and S. Kurihara, cond-mat/0611013 p. v2 (2006).

[211] A. Khaetskii, Phys. Rev. Lett. **96**, 056602 (2006).

[212] K. Hattori and H. Okamoto, Phys. Rev. B **74**, 155321 (2006).

[213] J. Sinova, D. Culcer, Q. Niu, N. A. Sinitsyn, T. Jungwirth, and A. H. MacDonald, Phys. Rev. Lett. **92**, 126603 (2004).

[214] T. Kimura, Y. Otani, T. Sato, S. Takahashi, and S. Maekawa, Phys. Rev. Lett. **98**, 156601 (2007).

[215] P. Vogl, private communication.

[216] B. A. Bernevig and S.-C. Zhang, Phys. Rev. Lett. **95**, 016801 (2005).

[217] K. Königsberger, *Analysis 2* (Springer, 1997).

Appendix A

The cancelation of vacuum loops

We have already introduced in Eq. (2.3.6) the expansion terms of the Green's function up to linear order in the interaction potential W

$$
\begin{aligned}
&2\hbar^2 G\left(1;2\right) - 2\hbar^2 G_0\left(1;2\right) = \\
&\left\langle \hat{T}^\dagger \left(\int \mathrm{d3d4} \hat{\psi}^\dagger_{\hat{H}_0}\left(3\right) \hat{\psi}^\dagger_{\hat{H}_0}\left(4\right) W^*\left(3;4\right) \hat{\psi}_{\hat{H}_0}\left(4\right) \hat{\psi}_{\hat{H}_0}\left(3\right) \right) \hat{T} \left(\hat{\psi}_{\hat{H}_0}\left(1\right) \hat{\psi}^\dagger_{\hat{H}_0}\left(2\right) \right) \right\rangle \\
&- \left\langle \hat{T} \left(\hat{\psi}_{\hat{H}_0}\left(1\right) \hat{\psi}^\dagger_{\hat{H}_0}\left(2\right) \right) \hat{T} \left(\int \mathrm{d3d4} \hat{\psi}^\dagger_{\hat{H}_0}\left(3\right) \hat{\psi}^\dagger_{\hat{H}_0}\left(4\right) W\left(3;4\right) \hat{\psi}_{\hat{H}_0}\left(4\right) \hat{\psi}_{\hat{H}_0}\left(3\right) \right) \right\rangle .
\end{aligned}
$$

We abbreviate in the following the operator

$$
\hat{F} \equiv \int \mathrm{d3d4} \hat{\psi}^\dagger_{\hat{H}_0}\left(3\right) \hat{\psi}^\dagger_{\hat{H}_0}\left(4\right) W\left(3;4\right) \hat{\psi}_{\hat{H}_0}\left(4\right) \hat{\psi}_{\hat{H}_0}\left(3\right) . \tag{A.0.1}
$$

When we contract the operators $\hat{\psi}_{\hat{H}_0}\left(1\right)$ and $\hat{\psi}^\dagger_{\hat{H}_0}\left(2\right)$ of the right side of the last equation into the Green's function $G_0\left(1;2\right)$, the operators in $\hat{F}$ are contracted in disconnected diagrams [9] or vacuum loops [8]

$$
i\hbar \left\langle \hat{T}^\dagger \hat{F}^\dagger \right\rangle G_0\left(1;2\right) - i\hbar G_0\left(1;2\right) \left\langle \hat{T}\hat{F} \right\rangle = 0. \tag{A.0.2}
$$

These terms vanish exactly, since $\hat{F}$ is Hermitian and symmetric in the time coordinates t_3 and t_4. All other disconnected diagrams of odd order in W have the same structure as given in Eq. (A.0.2), but are multiplied by the factors ($n \in \mathbb{N}$)

$$
\left(-\frac{i}{\hbar} \hat{T}^\dagger \hat{F}^\dagger \right)^{2n} , \ \left(\frac{i}{\hbar} \hat{T}\hat{F} \right)^{2n} \tag{A.0.3}
$$

for the expansion of $\hat{S}_{C_1}$ and $\hat{S}_{C_2}$, respectively. In particular, they appear twice with opposite signs. Thus, it follows by complete induction that all vacuum loops of odd order in W vanish exactly.

It is straightforward to derive the lowest even order terms in W of the expansion of Eq. (2.3.5) that represent vacuum loops

$$
\left(-\frac{i}{\hbar} \hat{T}^\dagger \hat{F}^\dagger \right) G_0\left(1;2\right) \left(\frac{i}{\hbar} \hat{T}\hat{F} \right) + G_0\left(1;2\right) \frac{1}{2!} \left(\frac{i}{\hbar} \hat{T}\hat{F} \right)^2 + \frac{1}{2!} \left(-\frac{i}{\hbar} \hat{T}^\dagger \hat{F}^\dagger \right)^2 G_0\left(1;2\right) = 0. \tag{A.0.4}
$$

Obviously, these terms vanish exactly. Thus, we apply the argumentation of the odd terms in W also on the even terms and conclude that all disconnected diagrams of any order in W vanish exactly.

Appendix B

Fundamental relation between self-energies

We start with Eq. (2.2.10) and translate it into the notation of Lifschitz and Pitajewski

$$G^{--}(1;2)+G^{++}(1;2)-G^{-+}(1;2)-G^{+-}(1;2)=0. \tag{B.0.1}$$

Thus, when we apply the operator $\hat{G}^{-1}(1)$ on this equation, we get with the Langreth theorem (see Eq. (2.3.24))

$$\begin{aligned}
&\hat{G}^{-1}(1)\left[G^{--}(1;2)+G^{++}(1;2)-G^{-+}(1;2)-G^{+-}(1;2)\right]=\delta(1-2)-\delta(1-2)\\
&+\int \mathrm{d}3\left[\boldsymbol{\sigma}_z\boldsymbol{\Sigma}(1;3)\,\mathbf{G}(3;2)\right]^{--}+\int \mathrm{d}3\left[\boldsymbol{\sigma}_z\boldsymbol{\Sigma}(1;3)\,\mathbf{G}(3;2)\right]^{++}\\
&+\int \mathrm{d}3\left[\boldsymbol{\sigma}_z\boldsymbol{\Sigma}(1;3)\,\mathbf{G}(3;2)\right]^{-+}+\int \mathrm{d}3\left[\boldsymbol{\sigma}_z\boldsymbol{\Sigma}(1;3)\,\mathbf{G}(3;2)\right]^{+-}.
\end{aligned} \tag{B.0.2}$$

When we expand the terms on the right side, we get the condition

$$\begin{aligned}
0 \;=\;& \Sigma^{--}(1;3)\,G^{--}(3;2)+\Sigma^{-+}(1;3)\,G^{+-}(3;2)-\Sigma^{+-}(1;3)\,G^{-+}(3;2)\\
&-\Sigma^{++}(1;3)\,G^{++}(3;2)-\Sigma^{--}(1;3)\,G^{-+}(3;2)-\Sigma^{-+}(1;3)\,G^{++}(3;2)\\
&+\Sigma^{+-}(1;3)\,G^{--}(3;2)+\Sigma^{++}(1;3)\,G^{+-}(3;2).
\end{aligned} \tag{B.0.3}$$

We resort these terms and apply Eq. (2.2.10)

$$\begin{aligned}
0 \;=\;& \left[\Sigma^{--}(1;3)+\Sigma^{+-}(1;3)\right]\left[G^{--}(3;2)-G^{-+}(3;2)\right]\\
&+\left[\Sigma^{-+}(1;3)+\Sigma^{++}(1;3)\right]\left[G^{+-}(3;2)-G^{++}(3;2)\right]\\
=\;& \left[\Sigma^{--}(1;3)+\Sigma^{+-}(1;3)+\Sigma^{-+}(1;3)+\Sigma^{++}(1;3)\right]\left[G^{--}(3;2)-G^{-+}(3;2)\right]
\end{aligned} \tag{B.0.4}$$

This gives us the condition for the self-energies

$$\Sigma^{--}(1;3)+\Sigma^{++}(1;3)=-\Sigma^{-+}(1;3)-\Sigma^{+-}(1;3). \tag{B.0.5}$$

Appendix C

Calculation of the causal phonon self-energy Σ^{--}

C.1 Causal phonon Green's function D_0^{--}

The free causal phonon Green's function is defined by (see Eq. (2.2.2))

$$i\hbar D_0^{--}(\vec{q},\omega) = i\hbar \int \mathrm{d}(t_2-t_1)\, \mathrm{e}^{-i\omega(t_2-t_1)} \left[\theta(t_1-t_2)\, D_0^{+-}(\vec{q},t_1,t_2) + \theta(t_2-t_1)\, D_0^{-+}(\vec{q},t_1,t_2)\right]. \tag{C.1.1}$$

We set in the free phonon Green's functions D_0^{-+} and D_0^{+-} from Eq. (2.4.6) and get

$$\begin{aligned}
& i\hbar D_0^{--}(\vec{q},\omega) \\
= \;& \frac{1}{2\pi}\int \mathrm{d}\omega' \left[\mathrm{Pr}\left(i\frac{1}{\omega-\omega'}\right) + \pi\delta(\omega-\omega')\right](2\pi n_q \delta(-\omega'-\omega_q) + 2\pi(1+n_q)\,\delta(-\omega'+\omega_q)) \\
& + \frac{1}{2\pi}\int \mathrm{d}\omega' \left[\mathrm{Pr}\left(-i\frac{1}{\omega-\omega'}\right) + \pi\delta(\omega-\omega')\right](2\pi n_q \delta(\omega'-\omega_q) + 2\pi(1+n_q)\,\delta(\omega'+\omega_q)) \\
= \;& i\,\mathrm{Pr}\left(\frac{1}{\omega+\omega_q}\right) n_q + i\,\mathrm{Pr}\left(\frac{1}{\omega-\omega_q}\right)(1+n_q) + n_q\pi\delta(\omega+\omega_q) + (1+n_q)\,\pi\delta(\omega-\omega_q) \\
& - i\,\mathrm{Pr}\left(\frac{1}{\omega-\omega_q}\right) n_q - i\,\mathrm{Pr}\left(\frac{1}{\omega+\omega_q}\right)(1+n_q) + n_q\pi\delta(\omega-\omega_q) + (1+n_q)\,\pi\delta(\omega+\omega_q) \\
= \;& i\left[\mathrm{Pr}\left(\frac{1}{\omega-\omega_q}\right) - i\pi\delta(\omega-\omega_q)\right] - i\left[\mathrm{Pr}\left(\frac{1}{\omega+\omega_q}\right) - i\pi\delta(\omega+\omega_q)\right] \\
& + 2\pi(1+n_q)\,\delta(\omega+\omega_q) + 2\pi n_q\delta(\omega-\omega_q) \\
= \;& i\lim_{\varepsilon\to 0}\frac{1}{\omega-\omega_q+i\varepsilon} - i\lim_{\varepsilon\to 0}\frac{1}{\omega+\omega_q+i\varepsilon} + 2\pi(1+n_q)\,\delta(\omega+\omega_q) + 2\pi n_q\delta(\omega-\omega_q).
\end{aligned} \tag{C.1.2}$$

It is important to note that both ε-terms in the two denominators of the last line are positive imaginary. Unfortunately, results for these signs can differ in literature.

C.2 Causal phonon self-energy Σ^{--}

We simply use Eq. (C.1.2) and set it in the definition of the causal self-energy G^R, Eq. (2.2.11)

$$\begin{aligned}
& -i\Sigma^{--}\left(\vec{x}_1,\vec{x}_2,\omega\right) \\
= & \int \mathrm{d}\tau \mathrm{e}^{-i\omega\tau} iG^{--}\left(\vec{x}_1,\vec{x}_2,\tau\right) i\hbar D_0^{--}\left(\vec{x}_1,\vec{x}_2,\tau\right)\left(-iU\left(\vec{x}_1\right)\right)\left(-iU\left(\vec{x}_2\right)\right) \\
= & -\frac{i}{\left(2\pi\right)^4}\int \mathrm{d}\vec{q}\mathrm{d}\omega' \left|U_q\right|^2 \mathrm{e}^{i\vec{q}\cdot\left(\vec{x}_1-\vec{x}_2\right)} G^{--}\left(\vec{x}_1,\vec{x}_2,\omega-\omega'\right) \\
& \times\left[i\lim_{\varepsilon\to 0}\left(\omega'-\omega_q+i\varepsilon\right)^{-1} - i\lim_{\varepsilon\to 0}\left(\omega'+\omega_q+i\varepsilon\right)^{-1}\right. \\
& \left. +2\pi\left(1+n_q\right)\delta\left(\omega'+\omega_q\right)+2\pi n_q\delta\left(\omega'-\omega_q\right)\right]. \qquad \text{(C.2.1)}
\end{aligned}$$

In the last equation, the absolute value of the squared interaction potential is taken, instead of the U_q^2. In the case of real interaction potentials (as for the Fröhlich interaction), this does not matter. One example for a non-vanishing imaginary part of U_q is the deformation potential. In this case, the interaction potential is proportional to the spatial derivative acting on the phonon Green's function at the interaction position. Acting once at $\vec{x}_1$ and once at $\vec{x}_2$ on the function $\mathrm{e}^{i\vec{q}\cdot\left(\vec{x}_1-\vec{x}_2\right)}$, the self-energy contains a product of the type $i\vec{q}\cdot\left(-i\vec{q}\right)$ which is again a real scalar. Therefore, in any case of phonon interaction potentials we may use the latter result. Next, we set in the definition of the retarded self-energy G^R, Eq. (2.2.11)

$$\begin{aligned}
& -i\Sigma^{--}\left(\vec{x}_1,\vec{x}_2,\omega\right) \\
= & -\frac{i}{\left(2\pi\right)^4}\int \mathrm{d}\omega'\mathrm{d}\vec{q}\left|U_q\right|^2 \mathrm{e}^{i\vec{q}\cdot\left(\vec{x}_1-\vec{x}_2\right)}\left[G^R\left(\vec{x}_1,\vec{x}_2,\omega-\omega'\right)+G^{-+}\left(\vec{x}_1,\vec{x}_2,\omega-\omega'\right)\right] \\
& \times\left[i\lim_{\varepsilon\to 0}\left(\omega'-\omega_q+i\varepsilon\right)^{-1} - i\lim_{\varepsilon\to 0}\left(\omega'+\omega_q+i\varepsilon\right)^{-1}\right. \\
& \left. +2\pi\left(1+n_q\right)\delta\left(\omega'+\omega_q\right)+2\pi n_q\delta\left(\omega'-\omega_q\right)\right]. \qquad \text{(C.2.2)}
\end{aligned}$$

In contrast to G^{-+}, the retarded Green's function has only poles in the lower half of the complex plane. Here, the imaginary signs of the ε-terms in D_0^{--} become most important (see above),

because they allow us to utilize the residue theorem

$$
\begin{aligned}
& -i\Sigma^{--}\left(\vec{x}_1,\vec{x}_2,\omega\right) \\
= & -i\int\frac{\mathrm{d}\vec{q}}{\left(2\pi\right)^3}\left|U_q\right|^2\mathrm{e}^{i\vec{q}\cdot\left(\vec{x}_1-\vec{x}_2\right)}\left(-\mathrm{Res}_{-\omega_q-i\varepsilon}\frac{G^R\left(\vec{x}_1,\vec{x}_2,\omega-\omega'\right)}{\omega'+\omega_q+i\varepsilon}+\mathrm{Res}_{\omega_q-i\varepsilon}\frac{G^R\left(\vec{x}_1,\vec{x}_2,\omega-\omega'\right)}{\omega'-\omega_q+i\varepsilon}\right) \\
& +\int\frac{\mathrm{d}\omega'\mathrm{d}\vec{q}}{\left(2\pi\right)^4}\left|U_q\right|^2\mathrm{e}^{i\vec{q}\cdot\left(\vec{x}_1-\vec{x}_2\right)}G^{-+}\left(\vec{x}_1,\vec{x}_2,\omega-\omega'\right)\left(\lim_{\varepsilon\to0}\left(\omega'-\omega_q+i\varepsilon\right)-\lim_{\varepsilon\to0}\left(\omega'+\omega_q+i\varepsilon\right)^{-1}\right) \\
& -i\int\frac{\mathrm{d}\vec{q}}{\left(2\pi\right)^3}\left|U_q\right|^2\mathrm{e}^{i\vec{q}\cdot\left(\vec{x}_1-\vec{x}_2\right)}\left[G^R\left(\vec{x}_1,\vec{x}_2,\omega+\omega_q\right)\left(1+n_q\right)+G^{-+}\left(\vec{x}_1,\vec{x}_2,\omega+\omega_q\right)\left(1+n_q\right)\right. \\
& \left.+n_qG^R\left(\vec{x}_1,\vec{x}_2,\omega-\omega_q\right)+n_qG^{-+}\left(\vec{x}_1,\vec{x}_2,\omega-\omega_q\right)\right] \\
= & -\frac{i}{\left(2\pi\right)^3}\int\mathrm{d}\vec{q}\left|U_q\right|^2\mathrm{e}^{i\vec{q}\cdot\left(\vec{x}_1-\vec{x}_2\right)}\left(-G^R\left(\vec{x}_1,\vec{x}_2,\omega+\omega_q\right)+G^R\left(\vec{x}_1,\vec{x}_2,\omega-\omega_q\right)\right) \\
& -\frac{i}{\left(2\pi\right)^3}\int\mathrm{d}\omega'\mathrm{d}\vec{q}\left|U_q\right|^2\mathrm{e}^{i\vec{q}\cdot\left(\vec{x}_1-\vec{x}_2\right)}G^{-+}\left(\vec{x}_1,\vec{x}_2,\omega-\omega'\right) \\
& \times\left[\frac{i}{2\pi}\left(\mathrm{Pr}\left(\frac{1}{\omega'-\omega_q}\right)-i\pi\delta\left(\omega'-\omega_q\right)\right)-\frac{i}{2\pi}\left(\mathrm{Pr}\left(\frac{1}{\omega'+\omega_q}\right)-i\pi\delta\left(\omega'+\omega_q\right)\right)\right] \\
& -\frac{i}{\left(2\pi\right)^3}\int\mathrm{d}\vec{q}\left|U_q\right|^2\mathrm{e}^{i\vec{q}\cdot\left(\vec{x}_1-\vec{x}_2\right)}\left[G^R\left(\vec{x}_1,\vec{x}_2,\omega+\omega_q\right)\left(1+n_q\right)+G^{-+}\left(\vec{x}_1,\vec{x}_2,\omega+\omega_q\right)\left(1+n_q\right)\right. \\
& \left.+n_qG^R\left(\vec{x}_1,\vec{x}_2,\omega-\omega_q\right)+n_qG^{-+}\left(\vec{x}_1,\vec{x}_2,\omega-\omega_q\right)\right]. \qquad \text{(C.2.3)}
\end{aligned}
$$

Here, Pr denotes a principle value integral. We sum up the terms and get

$$
\begin{aligned}
& -i\Sigma^{--}\left(\vec{x}_1,\vec{x}_2,\omega\right) \\
= & \frac{1}{\left(2\pi\right)^4}\int\mathrm{d}\omega'\int\mathrm{d}\vec{q}\left|U_q\right|^2\mathrm{e}^{i\vec{q}\cdot\left(\vec{x}_1-\vec{x}_2\right)}G^{-+}\left(\vec{x}_1,\vec{x}_2,\omega-\omega'\right)\left[\mathrm{Pr}\left(\frac{1}{\omega'-\omega_q}\right)-\mathrm{Pr}\left(\frac{1}{\omega'+\omega_q}\right)\right] \\
& -\frac{i}{\left(2\pi\right)^3}\int\mathrm{d}\vec{q}\left|U_q\right|^2\mathrm{e}^{i\vec{q}\cdot\left(\vec{x}_1-\vec{x}_2\right)}\left(\frac{1}{2}G^{-+}\left(\vec{x}_1,\vec{x}_2,\omega-\omega_q\right)-\frac{1}{2}G^{-+}\left(\vec{x}_1,\vec{x}_2,\omega+\omega_q\right)\right) \\
& -\frac{i}{\left(2\pi\right)^3}\int\mathrm{d}\vec{q}\left|U_q\right|^2\mathrm{e}^{i\vec{q}\cdot\left(\vec{x}_1-\vec{x}_2\right)}\left[n_qG^R\left(\vec{x}_1,\vec{x}_2,\omega+\omega_q\right)+\left(n_q+1\right)G^R\left(\vec{x}_1,\vec{x}_2,\omega-\omega_q\right)\right. \\
& \left.+G^{-+}\left(\vec{x}_1,\vec{x}_2,\omega+\omega_q\right)\left(1+n_q\right)+n_qG^{-+}\left(\vec{x}_1,\vec{x}_2,\omega-\omega_q\right)\right]. \qquad \text{(C.2.4)}
\end{aligned}
$$

Appendix D

Linear response to an electrostatic perturbation

In the following, we derive the change of the retarded, advanced and lesser Green's functions due to an external electrostatic potential $\delta V(\vec{x})$. All the unperturbed Green's functions are considered to solve the Dyson and Keldysh equations of a homogeneous system in equilibrium. Therefore, we may utilize the equation

$$G^{<,R}(\vec{x}_1, \vec{x}_2, E) = G^{<,R}(\vec{x}_1 - \vec{x}_2, E). \tag{D.0.1}$$

D.1 Retarded and advanced response

The Dyson equation for the retarded Green's function in the stationary limit, i.e. in the energy domain reads

$$\begin{aligned} & \left[E\hat{1} - \hat{H}_0(\vec{x}_1, E) - \delta V(\vec{x}_1)\hat{1}\right]\left[G^R(\vec{x}_1, \vec{x}_2, E) + \delta G^R(\vec{x}_1, \vec{x}_2, E)\right] \\ = \; & \delta(\vec{x}_1 - \vec{x}_2) + \int \mathrm{d}\vec{x}_3 \left[\Sigma^R(\vec{x}_1, \vec{x}_3, E) + \delta\Sigma^R(\vec{x}_1, \vec{x}_3, E)\right] \times \\ & \left[G^R(\vec{x}_3, \vec{x}_2, E) + \delta G^R(\vec{x}_3, \vec{x}_2, E)\right]. \end{aligned} \tag{D.1.1}$$

The unperturbed retarded Green's function $G^R(\vec{x}_1, \vec{x}_2, E)$ solves the unperturbed Dyson equation and some parts of the upper equation cancel. When we in addition ignore terms of higher order than linear in the perturbation, we get

$$\begin{aligned} & \left[E\hat{1} - \hat{H}_0(\vec{x}_1, E)\right]\delta G^R(\vec{x}_1, \vec{x}_2, E) - \delta V(\vec{x}_1)\hat{1}G^R(\vec{x}_1, \vec{x}_2, E) \\ = \; & \int \mathrm{d}\vec{x}_3 \Sigma^R(\vec{x}_1, \vec{x}_3, E)\delta G^R(\vec{x}_3, \vec{x}_2, E) + \int \mathrm{d}\vec{x}_3 \delta\Sigma^R(\vec{x}_1, \vec{x}_3, E) G^R(\vec{x}_3, \vec{x}_2, E). \end{aligned} \tag{D.1.2}$$

The operator in parentheses on the left side of this equation can be summed with the unperturbed retarded self-energy $\Sigma^R(\vec{x}_1, \vec{x}_3, E)$ on the right side to the inverse retarded Green's function of the unperturbed system. Therefore, we get

$$\begin{aligned} \delta G^R(\vec{x}_1, \vec{x}_2, E) = & \int \mathrm{d}\vec{x}_3 G^R(\vec{x}_1, \vec{x}_3, E)\delta V(\vec{x}_3) G^R(\vec{x}_3, \vec{x}_2, E) \\ & + \int \mathrm{d}\vec{x}_3 \mathrm{d}\vec{x}_4 G^R(\vec{x}_1, \vec{x}_3, E)\delta\Sigma^R(\vec{x}_3, \vec{x}_4, E) G^R(\vec{x}_4, \vec{x}_2, E). \end{aligned} \tag{D.1.3}$$

In the stationary limit, the advanced Green's function equals the Hermitian conjugate of the retarded one

$$\begin{aligned}\delta G^A(\vec{x}_1,\vec{x}_2,E) &= \int \mathrm{d}\vec{x}_3 G^A(\vec{x}_1,\vec{x}_3,E)\,\delta V(\vec{x}_3)\,G^A(\vec{x}_3,\vec{x}_2,E)\\ &\quad+\int \mathrm{d}z_3\mathrm{d}z_4 G^A(\vec{x}_1,\vec{x}_3,E)\,\delta\Sigma^A(\vec{x}_3,\vec{x}_4,E)\,G^A(\vec{x}_4,\vec{x}_2,E)\,. \quad \text{(D.1.4)}\end{aligned}$$

D.2 Response of the correlation function

We use the Keldysh equation for the change of the lesser Green's function

$$\begin{aligned}&\delta G^<(\vec{x}_1,\vec{x}_2,E)\\ =&\int \mathrm{d}\vec{x}_3\mathrm{d}\vec{x}_4\left[G^R(\vec{x}_1,\vec{x}_3,E)+\delta G^R(\vec{x}_1,\vec{x}_3,E)\right]\left[\Sigma^<(\vec{x}_3,\vec{x}_4,E)+\delta\Sigma^<(\vec{x}_3,\vec{x}_4,E)\right]\\ &\times\left[G^A(\vec{x}_4,\vec{x}_2,E)+\delta G^A(\vec{x}_4,\vec{x}_2,E)\right]-G^<(\vec{x}_1,\vec{x}_2,E)\\ \approx&\int \mathrm{d}\vec{x}_3\mathrm{d}\vec{x}_4\delta G^R(\vec{x}_1,\vec{x}_3,E)\,\Sigma^<(\vec{x}_3,\vec{x}_4,E)\,G^A(\vec{x}_4,\vec{x}_2,E)\\ &+\int \mathrm{d}\vec{x}_3\mathrm{d}\vec{x}_4 G^R(z_1,z_3,E)\,\Sigma^<(\vec{x}_3,\vec{x}_4,E)\,\delta G^A(\vec{x}_4,\vec{x}_2,E)\\ &+\int \mathrm{d}\vec{x}_3\mathrm{d}\vec{x}_4 G^R(\vec{x}_1,\vec{x}_3,E)\,\delta\Sigma^<(\vec{x}_3,\vec{x}_4,E)\,G^A(\vec{x}_4,\vec{x}_2,E)\,. \quad \text{(D.2.1)}\end{aligned}$$

In the last equation, we have neglected terms of higher order in the perturbation than linear. When we additionally ignore the vertex corrections ($\delta\Sigma^{R,<}$) and set in the results for δG^R and δG^A of the preceding section, we get (omitting the energy variable E)

$$\begin{aligned}&\delta G^<(\vec{x}_1,\vec{x}_2)\\ \approx&\int \mathrm{d}\vec{x}_3\mathrm{d}\vec{x}_4\mathrm{d}\vec{x}_5 G^R(\vec{x}_1,\vec{x}_3)\,\delta V(\vec{x}_3)\,G^R(\vec{x}_3,\vec{x}_4)\,\Sigma^<(\vec{x}_4,\vec{x}_5)\,G^A(\vec{x}_5,\vec{x}_2)\\ &+\int \mathrm{d}\vec{x}_3\mathrm{d}\vec{x}_4\mathrm{d}\vec{x}_5 G^R(\vec{x}_1,\vec{x}_3)\,\Sigma^<(\vec{x}_3,\vec{x}_4)\,G^A(\vec{x}_4,\vec{x}_5)\,\delta V(\vec{x}_5)\,G^A(\vec{x}_5,\vec{x}_2)\,. \quad \text{(D.2.2)}\end{aligned}$$

We can simplify this result, when we utilize the Keldysh equation for the unperturbed lesser Green's function

$$\begin{aligned}&\delta G^<(\vec{x}_1,\vec{x}_2)\\ =&\int \mathrm{d}\vec{x}_3\left[G^R(\vec{x}_1,\vec{x}_3)\,\delta V(\vec{x}_3)\,G^<(\vec{x}_3,\vec{x}_2)+G^<(\vec{x}_1,\vec{x}_3)\,\delta V(\vec{x}_3)\,G^A(\vec{x}_3,\vec{x}_2)\right]. \quad \text{(D.2.3)}\end{aligned}$$

We introduce the difference coordinate $\vec{r}=\vec{x}_1-\vec{x}_2$. The unperturbed Green's functions and self-energies depend only on the relative distance of their propagation coordinates. We replace $\vec{x}_2$ with $\vec{x}_1-\vec{r}$ and get

$$\begin{aligned}&\delta G^<(\vec{x}_1,\vec{r})=\int \mathrm{d}\vec{x}_3\left[G^R(\vec{x}_1-\vec{x}_3)\,\delta V(\vec{x}_3)\,G^<(\vec{x}_3-\vec{x}_1+\vec{r})\right.\\ &\left.+G^<(\vec{x}_1-\vec{x}_3)\,\delta V(\vec{x}_3)\,G^A(\vec{x}_3-\vec{x}_1+\vec{r})\right]. \quad \text{(D.2.4)}\end{aligned}$$

Now, we Fourier transform with respect to $\vec{r}$

$$\begin{aligned}
&\delta G^{<}\left(\vec{x}_1,\vec{q}\right)=\int \mathrm{d}\vec{r}\mathrm{d}\vec{x}_3\mathrm{e}^{-i\vec{q}\cdot\vec{r}}\left[G^R\left(\vec{x}_1-\vec{x}_3\right)\delta V\left(\vec{x}_3\right)G^{<}\left(\vec{x}_3-\vec{x}_1+\vec{r}\right)\right.\\
&\left.+G^{<}\left(\vec{x}_1-\vec{x}_3\right)\delta V\left(\vec{x}_3\right)G^A\left(\vec{x}_3-\vec{x}_1+\vec{r}\right)\right]\\
=&\int \mathrm{d}\vec{x}_3\mathrm{e}^{i\vec{q}\cdot\left(\vec{x}_3-\vec{x}_1\right)}\left[G^R\left(\vec{x}_1-\vec{x}_3\right)\delta V\left(\vec{x}_3\right)G^{<}\left(\vec{q}\right)+G^{<}\left(\vec{x}_1-\vec{x}_3\right)\delta V\left(\vec{x}_3\right)G^A\left(\vec{q}\right)\right]\\
=&\frac{1}{\left(2\pi\right)^3}\int \mathrm{d}\vec{l}\mathrm{e}^{i\left(\vec{l}-\vec{q}\right)\cdot\vec{x}_1}\left[G^R\left(\vec{l}\right)\delta V\left(\vec{l}-\vec{q}\right)G^{<}\left(\vec{q}\right)\right.\\
&\left.+G^{<}\left(\vec{l}\right)\delta V\left(\vec{l}-\vec{q}\right)G^A\left(\vec{q}\right)\right].
\end{aligned}\tag{D.2.5}$$

When we additionally Fourier transform with respect to $\vec{x}_1$, we get

$$\begin{aligned}
&\delta G^{<}\left(\vec{Q},\vec{q}\right)\\
=&\frac{1}{\left(2\pi\right)^3}\int \mathrm{d}\vec{l}\mathrm{d}\vec{x}_1\mathrm{e}^{-i\left(\vec{Q}-\vec{l}+\vec{q}\right)\cdot\vec{x}_1}\left[G^R\left(\vec{l}\right)\delta V\left(\vec{l}-\vec{q}\right)G^{<}\left(\vec{q}\right)+G^{<}\left(\vec{l}\right)\delta V\left(\vec{l}-\vec{q}\right)G^A\left(\vec{q}\right)\right]\\
=&\int \mathrm{d}\vec{l}\delta\left(\vec{Q}-\vec{l}+\vec{q}\right)\left[G^R\left(\vec{l}\right)\delta V\left(\vec{l}-\vec{q}\right)G^{<}\left(\vec{q}\right)+G^{<}\left(\vec{l}\right)\delta V\left(\vec{l}-\vec{q}\right)G^A\left(\vec{q}\right)\right]\\
=&G^R\left(\vec{Q}+\vec{q}\right)\delta V\left(\vec{Q}\right)G^{<}\left(\vec{q}\right)+G^{<}\left(\vec{Q}+\vec{q}\right)\delta V\left(\vec{Q}\right)G^A\left(\vec{q}\right).
\end{aligned}\tag{D.2.6}$$

Appendix E

Linear response to a time dependent perturbation

Similar to the derivations given in Appendix D, we derive the change of the retarded and lesser Green's functions due to an external potential. The differences to the derivations in real space lie in some of the applied approximations as well as in the representation. We present both cases of linear response separately, because in this way, we believe the results are easier to understand.

E.1 Retarded and advanced response

We insert the perturbed retarded Green's function of a quasi one dimensional system into the Dyson equation Eq. (2.3.33)

$$\begin{aligned}
&\left(i\hbar\frac{\mathrm{d}}{\mathrm{d}t_1}+\frac{\mathrm{d}}{\mathrm{d}z_1}\frac{\hbar^2}{2m\left(z_1\right)}\frac{\mathrm{d}}{\mathrm{d}z_1}-\frac{\hbar^2k_\parallel^2}{2m\left(z_1\right)}\hat{1}-V\left(z_1\right)\hat{1}-\delta V\left(t_1\right)\hat{1}\right)\\
&\times\left[G^R\left(z_1,z_2,k_\parallel,t_1-t_2\right)+\delta G^R\left(z_1,z_2,k_\parallel,t_1,t_2\right)\right]\\
=\;&\delta\left(t_1-t_2\right)\delta\left(z_1-z_2\right)+\int\mathrm{d}z_3\mathrm{d}t_3\left[\Sigma^R\left(z_1,z_3,k_\parallel,t_1-t_3\right)+\delta\Sigma^R\left(z_1,z_3,k_\parallel,t_1,t_3\right)\right]\\
&\times\left[G^R\left(z_3,z_2,k_\parallel,t_3-t_2\right)+\delta G^R\left(z_3,z_2,k_\parallel,t_3,t_2\right)\right].
\end{aligned}\tag{E.1.1}$$

Since G^R already solves the Dyson equation, some terms cancel

$$\begin{aligned}
&\left(i\hbar\frac{\mathrm{d}}{\mathrm{d}t_1}+\frac{\mathrm{d}}{\mathrm{d}z_1}\frac{\hbar^2}{2m\left(z_1\right)}\frac{\mathrm{d}}{\mathrm{d}z_1}-\frac{\hbar^2k_\parallel^2}{2m\left(z_1\right)}\hat{1}-V\left(z_1\right)\hat{1}\right)\delta G^R\left(z_1,z_2,k_\parallel,t_1,t_2\right)\\
&-\delta V\left(t_1\right)G^R\left(z_1,z_2,k_\parallel,t_1-t_2\right)\\
\approx\;&\int\mathrm{d}z_3\mathrm{d}t_3\left[\Sigma^R\left(z_1,z_3,k_\parallel,t_1-t_3\right)\delta G^R\left(z_3,z_2,k_\parallel,t_3,t_2\right)\right.\\
&\left.+\delta\Sigma^R\left(z_1,z_3,k_\parallel,t_1,t_3\right)G^R\left(z_3,z_2,k_\parallel,t_3-t_2\right)\right].
\end{aligned}\tag{E.1.2}$$

Here, we have neglected the products of higher order than linear in the perturbation. The operators in Eq. (E.1.2) that are multiplied with δG^R constitute the unperturbed retarded Green's function G^R. If we abbreviate the matrix shape of the Green's functions and self-energies due to the spatial coordinates with bold type and omit the $k_\parallel$ argument for better

readability, we get for the perturbation of the retarded Green's function

$$\begin{aligned}
&\delta\mathbf{G}^R(t_1,t_2)\\
=&\int \mathrm{d}t_3\mathrm{d}t_4\mathbf{G}^R(t_1-t_3)\left[\delta(t_3-t_4)\mathbf{1}\delta V(t_3)+\delta\mathbf{\Sigma}^R(t_3,t_4)\right]\mathbf{G}^R(t_4-t_2)\\
=&\int \mathrm{d}t_4\mathbf{G}^R(t_1-t_4)\delta V(t_4)\mathbf{G}^R(t_4-t_2)\\
&+\int \mathrm{d}t_3\mathrm{d}t_4\mathbf{G}^R(t_1-t_3)\delta\mathbf{\Sigma}^R(t_3,t_4)\mathbf{G}^R(t_4-t_2).
\end{aligned}\tag{E.1.3}$$

Since we are looking for perturbing terms in the stationary case, we have to Fourier transform the last results ($\tau=t_1-t_2$)

$$\begin{aligned}
&\delta\mathbf{G}^R(\omega,E)\\
=&\int \mathrm{d}\tau\mathrm{d}t_1\mathrm{d}t_4\exp(iE\tau/\hbar)\exp(i\omega t_1)\mathbf{G}^R(t_1-t_4)\delta V(t_4)\mathbf{G}^R(t_4-t_2)\\
&+\int \mathrm{d}\tau\mathrm{d}t_1\mathrm{d}t_4\mathrm{d}t_3\exp(iE\tau/\hbar)\exp(i\omega t_1)\mathbf{G}^R(t_1-t_3)\delta\mathbf{\Sigma}^R(t_3,t_4)\mathbf{G}^R(t_4-t_2)
\end{aligned}\tag{E.1.4}$$

We replace the time t_2 with

$$t_2=\tau-t_1\tag{E.1.5}$$

and perform all integrals

$$\begin{aligned}
&\delta\mathbf{G}^R(\omega,E)\\
=&\int \mathrm{d}\tau\mathrm{d}t_1\mathrm{d}t_4\exp(i\omega t_1)\mathbf{G}^R(t_1-t_4)\delta V(t_4)\exp(iE\tau/\hbar)\mathbf{G}^R(\tau-t_1+t_4)\\
&+\int \mathrm{d}\tau\mathrm{d}t_1\mathrm{d}t_4\mathrm{d}t_3\exp(i\omega t_1)\mathbf{G}^R(t_1-t_3)\delta\mathbf{\Sigma}^R(t_3,t_4)\exp(iE\tau/\hbar)\mathbf{G}^R(\tau-t_1+t_4)\\
=&\int \mathrm{d}t_1\mathrm{d}t_4\exp(i\omega t_1)\exp(i(t_1-t_4)E/\hbar)\mathbf{G}^R(t_1-t_4)\delta V(t_4)\mathbf{G}^R(E)\\
&+\int \mathrm{d}t_1\mathrm{d}t_4\mathrm{d}t_3\exp(i\omega t_1)\exp(i(t_1-t_4)E/\hbar)\mathbf{G}^R(t_1-t_3)\delta\mathbf{\Sigma}^R(t_3,t_4)\mathbf{G}^R(E)\\
=&\int \mathrm{d}t_4\exp(-it_4E/\hbar)\exp(it_4(\omega+E/\hbar))\mathbf{G}^R(E+\hbar\omega)\delta V(t_4)\mathbf{G}^R(E)\\
&+\int \mathrm{d}t_4\mathrm{d}t_3\exp(-iEt_4/\hbar)\exp(i(E/\hbar+\omega)t_3)\mathbf{G}^R(E+\hbar\omega)\delta\mathbf{\Sigma}^R(t_3,t_4)\mathbf{G}^R(E)\\
=&\mathbf{G}^R(E+\hbar\omega)\delta V(\omega)\mathbf{G}^R(E)+\mathbf{G}^R(E+\hbar\omega)\delta\mathbf{\Sigma}^R(E+\hbar\omega,-E)\mathbf{G}^R(E).
\end{aligned}\tag{E.1.6}$$

Analogously (starting with Eq. (2.3.34)) we get for the advanced perturbation

$$\begin{aligned}
&\delta\mathbf{G}^A(t_1,t_2)\\
=&\int \mathrm{d}t_4\mathbf{G}^A(t_1-t_4)\delta V(t_4)\mathbf{G}^A(t_4-t_2)\\
&+\int \mathrm{d}t_3\mathrm{d}t_4\mathbf{G}^A(t_1-t_3)\delta\mathbf{\Sigma}^A(t_3,t_4)\mathbf{G}^A(t_4-t_2).
\end{aligned}\tag{E.1.7}$$

The Fourier transformed perturbation reads

$$\delta\mathbf{G}^A(\omega,E)=\mathbf{G}^A(E+\hbar\omega)\delta V(\omega)\mathbf{G}^A(E)+\mathbf{G}^A(E+\hbar\omega)\delta\mathbf{\Sigma}^A(E+\hbar\omega,-E)\mathbf{G}^A(E).\tag{E.1.8}$$

E.2 Perturbations of the lesser Green's function

We decompose the lesser Green's function in an unperturbed and a correction term and set the sum of both in the Keldysh equation (omitting the in-plane momentum and denoting the matrix shape due to the spatial coordinates with bold type)

$$\begin{aligned}
& \mathbf{G}^{<}(t_1-t_2)+\delta\mathbf{G}^{<}(t_1,t_2) \\
= & \int \mathrm{d}t_3\mathrm{d}t_4 \left[\mathbf{G}^{R}(t_1-t_3)+\delta\mathbf{G}^{R}(t_1,t_3)\right]\left[\mathbf{\Sigma}^{<}(t_3-t_4)+\delta\mathbf{\Sigma}^{<}(t_3,t_4)\right] \\
& \times\left[\mathbf{G}^{A}(t_4-t_2)+\delta\mathbf{G}^{A}(t_4,t_2)\right] \\
\approx & \int \mathrm{d}t_3\mathrm{d}t_4 \mathbf{G}^{R}(t_1-t_3)\,\mathbf{\Sigma}^{<}(t_3-t_4)\,\mathbf{G}^{A}(t_4-t_2) \\
& + \int \mathrm{d}t_3\mathrm{d}t_4 \delta\mathbf{G}^{R}(t_1,t_3)\,\mathbf{\Sigma}^{<}(t_3-t_4)\,\mathbf{G}^{A}(t_4-t_2) \\
& + \int \mathrm{d}t_3\mathrm{d}t_4 \mathbf{G}^{R}(t_1-t_3)\,\mathbf{\Sigma}^{<}(t_3-t_4)\,\delta\mathbf{G}^{A}(t_4,t_2) \\
& + \int \mathrm{d}t_3\mathrm{d}t_4 \mathbf{G}^{R}(t_1-t_3)\,\delta\mathbf{\Sigma}^{<}(t_3,t_4)\,\mathbf{G}^{A}(t_4-t_2)\,. \qquad \text{(E.2.1)}
\end{aligned}$$

Where we have neglected any terms of higher order in $\mathcal{E}(\omega)$ than linear. The lesser Green's function $\mathbf{G}^{<}(t_1-t_2)$ solves the Keldysh equation without the photonic field. Therefore we can simplify both sides of the last equation

$$\begin{aligned}
\delta\mathbf{G}^{<}(t_1,t_2) = & \int \mathrm{d}t_3\mathrm{d}t_4 \delta\mathbf{G}^{R}(t_1,t_3)\,\mathbf{\Sigma}^{<}(t_3-t_4)\,\mathbf{G}^{A}(t_4-t_2) \\
& + \int \mathrm{d}t_3\mathrm{d}t_4 \mathbf{G}^{R}(t_1,t_3)\,\mathbf{\Sigma}^{<}(t_3-t_4)\,\delta\mathbf{G}^{A}(t_4,t_2) \\
& + \int \mathrm{d}t_3\mathrm{d}t_4 \mathbf{G}^{R}(t_1,t_3)\,\delta\mathbf{\Sigma}^{<}(t_3,t_4)\,\mathbf{G}^{A}(t_4,t_2)\,. \qquad \text{(E.2.2)}
\end{aligned}$$

We set in the results of the last section and Fourier transform each term of the resulting sum. First, we transform the two terms containing δV

$$
\begin{aligned}
&\int \mathrm{d}\tau \mathrm{d}t_1 \mathrm{d}t_3 \mathrm{d}t_4 \mathrm{d}t_5 \mathrm{e}^{iE\frac{\tau}{\hbar}+i\omega t_1} \mathbf{G}^R(t_1-t_5)\,\delta V(t_5)\,\mathbf{G}^R(t_5-t_3)\,\mathbf{\Sigma}^<(t_3-t_4)\,\mathbf{G}^A(t_4+\tau-t_1)\\
&+\int \mathrm{d}\tau \mathrm{d}t_1 \mathrm{d}t_3 \mathrm{d}t_4 \mathrm{d}t_5 \mathrm{e}^{iE\frac{\tau}{\hbar}+i\omega t_1} \mathbf{G}^R(t_1-t_3)\,\mathbf{\Sigma}^<(t_3-t_4)\,\mathbf{G}^A(t_4-t_5)\,\delta V(t_5)\,\mathbf{G}^A(t_5-t_1+\tau)\\
=&\int \mathrm{d}t_1 \mathrm{d}t_3 \mathrm{d}t_4 \mathrm{d}t_5 \mathrm{e}^{iE(t_1-t_4)/\hbar}\mathrm{e}^{i\omega t_1} \mathbf{G}^R(t_1-t_5)\,\delta V(t_5)\,\mathbf{G}^R(t_5-t_3)\,\Sigma^<(t_3-t_4)\,\mathbf{G}^A(E)\\
&+\int \mathrm{d}t_1 \mathrm{d}t_3 \mathrm{d}t_4 \mathrm{d}t_5 \mathrm{e}^{iE(t_1-t_5)/\hbar}\mathrm{e}^{i\omega t_1} \mathbf{G}^R(t_1-t_3)\,\mathbf{\Sigma}^<(t_3-t_4)\,\mathbf{G}^A(t_4-t_5)\,\delta V(t_5)\,\mathbf{G}^A(E)\\
=&\int \mathrm{d}t_3 \mathrm{d}t_4 \mathrm{d}t_5 \mathrm{e}^{i(E/\hbar+\omega)t_5}\mathrm{e}^{-iEt_4/\hbar} \mathbf{G}^R(E+\hbar\omega)\,\delta V(t_5)\,\mathbf{G}^R(t_5-t_3)\,\Sigma^<(t_3-t_4)\,\mathbf{G}^A(E)\\
&+\int \mathrm{d}t_3 \mathrm{d}t_4 \mathrm{d}t_5 \mathrm{e}^{i(E/\hbar+\omega)t_3}\mathrm{e}^{-iEt_5/\hbar} \mathbf{G}^R(E+\hbar\omega)\,\mathbf{\Sigma}^<(t_3-t_4)\,\mathbf{G}^A(t_4-t_5)\,\delta V(t_5)\,\mathbf{G}^A(E)\\
=&\int \mathrm{d}t_3 \mathrm{d}t_5 \mathrm{e}^{i(E/\hbar+\omega)t_5}\mathrm{e}^{-iEt_3/\hbar} \mathbf{G}^R(E+\hbar\omega)\,\delta V(t_5)\,\mathbf{G}^R(t_5-t_3)\,\mathbf{\Sigma}^<(E)\,\mathbf{G}^A(E)\\
&+\int \mathrm{d}t_4 \mathrm{d}t_5 \mathrm{e}^{i(E/\hbar+\omega)t_4}\mathrm{e}^{-iEt_5/\hbar} \mathbf{G}^R(E+\hbar\omega)\,\mathbf{\Sigma}^<(E+\hbar\omega)\,\mathbf{G}^A(t_4-t_5)\,\delta V(t_5)\,\mathbf{G}^A(E)\\
=&\int \mathrm{d}t_5 \mathrm{e}^{i(E/\hbar+\omega)t_5}\mathrm{e}^{-iEt_5/\hbar} \mathbf{G}^R(E+\hbar\omega)\,\delta V(t_5)\,\mathbf{G}^R(E)\,\mathbf{\Sigma}^<(E)\,\mathbf{G}^A(E)\\
&+\int \mathrm{d}t_5 \mathrm{e}^{i(E/\hbar+\omega)t_5}\mathrm{e}^{-iEt_5/\hbar} \mathbf{G}^R(E+\hbar\omega)\,\mathbf{\Sigma}^<(E+\hbar\omega)\,\mathbf{G}^A(E+\hbar\omega)\,\delta V(t_5)\,\mathbf{G}^A(E)\\
=&\mathbf{G}^R(E+\hbar\omega)\,\delta V(\omega)\,\mathbf{G}^R(E)\,\mathbf{\Sigma}^<(E)\,\mathbf{G}^A(E)\\
&+\mathbf{G}^R(E+\hbar\omega)\,\mathbf{\Sigma}^<(E+\hbar\omega)\,\mathbf{G}^A(E+\hbar\omega)\,\delta V(\omega)\,\mathbf{G}^A(E)\\
=&\mathbf{G}^R(E+\hbar\omega)\,\delta V(\omega)\,\mathbf{G}^<(E)+\mathbf{G}^<(E+\hbar\omega)\,\delta V(\omega)\,\mathbf{G}^A(E)\,. \qquad \text{(E.2.3)}
\end{aligned}
$$

Then, we transform the remaining term that originates from $\delta\mathbf{\Sigma}^R$

$$
\begin{aligned}
&\int \mathrm{d}\tau \mathrm{d}t_1 \mathrm{d}t_3 \mathrm{d}t_4 \mathrm{d}t_5 \mathrm{d}t_6 \mathrm{e}^{iE\frac{\tau}{\hbar}+i\omega t_1} \mathbf{G}^R(t_1-t_5)\,\delta\mathbf{\Sigma}^R(t_5,t_6)\,\mathbf{G}^R(t_6-t_3)\,\mathbf{\Sigma}^<(t_3-t_4)\\
&\times\mathbf{G}^A(t_4+\tau-t_1)\\
=&\int \mathrm{d}t_1 \mathrm{d}t_3 \mathrm{d}t_4 \mathrm{d}t_5 \mathrm{d}t_6 \mathrm{e}^{i(\omega+E/\hbar)t_1}\mathrm{e}^{-iEt_4/\hbar} \mathbf{G}^R(t_1-t_5)\,\delta\mathbf{\Sigma}^R(t_5,t_6)\,\mathbf{G}^R(t_6-t_3)\\
&\times\mathbf{\Sigma}^<(t_3-t_4)\,\mathbf{G}^A(E)\\
=&\int \mathrm{d}t_3 \mathrm{d}t_5 \mathrm{d}t_6 \mathrm{e}^{i(\omega+E/\hbar)t_5}\mathrm{e}^{-iEt_3/\hbar} \mathbf{G}^R(E+\hbar\omega)\,\delta\mathbf{\Sigma}^R(t_5,t_6)\,\mathbf{G}^R(t_6-t_3)\,\mathbf{\Sigma}^<(E)\,\mathbf{G}^A(E)\\
=&\int \mathrm{d}t_5 \mathrm{d}t_6 \mathrm{e}^{i(\omega+E/\hbar)t_5}\mathrm{e}^{-iEt_6/\hbar} \mathbf{G}^R(E+\hbar\omega)\,\delta\mathbf{\Sigma}^R(t_5,t_6)\,\mathbf{G}^R(E)\,\mathbf{\Sigma}^<(E)\,\mathbf{G}^A(E)\\
=&\mathbf{G}^R(E+\hbar\omega)\,\delta\mathbf{\Sigma}^R(E+\hbar\omega,-E)\,\mathbf{G}^<(E)\,. \qquad \text{(E.2.4)}
\end{aligned}
$$

Analogously, the remaining term that originates from $\delta\mathbf{G}^A$ reads

$$\begin{aligned}
&\int \mathrm{d}\tau\mathrm{d}t_1\mathrm{d}t_3\mathrm{d}t_4\mathrm{d}t_5\mathrm{d}t_6 \exp\left(iE\tau/\hbar\right)\exp\left(i\omega t_1\right)\mathbf{G}^R\left(t_1-t_3\right)\boldsymbol{\Sigma}^<\left(t_3-t_4\right)\mathbf{G}^A\left(t_4-t_5\right)\\
&\times\delta\boldsymbol{\Sigma}^A\left(t_5,t_6\right)\mathbf{G}^A\left(t_6+\tau-t_1\right)\\
=&\int \mathrm{d}t_1\mathrm{d}t_3\mathrm{d}t_4\mathrm{d}t_5\mathrm{d}t_6 \exp\left(iE\left(t_1-t_6\right)/\hbar\right)\exp\left(i\omega t_1\right)\mathbf{G}^R\left(t_1-t_3\right)\boldsymbol{\Sigma}^<\left(t_3-t_4\right)\mathbf{G}^A\left(t_4-t_5\right)\\
&\times\delta\boldsymbol{\Sigma}^A\left(t_5,t_6\right)\mathbf{G}^A\left(E\right)\\
=&\int \mathrm{d}t_3\mathrm{d}t_4\mathrm{d}t_5 \exp\left(i\left(E/\hbar+\omega\right)t_3\right)\mathbf{G}^R\left(E+\hbar\omega\right)\boldsymbol{\Sigma}^<\left(t_3-t_4\right)\mathbf{G}^A\left(t_4-t_5\right)\\
&\times\delta\boldsymbol{\Sigma}^A\left(t_5,-E\right)\mathbf{G}^A\left(E\right)\\
=&\int \mathrm{d}t_4\mathrm{d}t_5 \exp\left(i\left(E/\hbar+\omega\right)t_4\right)\mathbf{G}^R\left(E+\hbar\omega\right)\boldsymbol{\Sigma}^<\left(E+\hbar\omega\right)\mathbf{G}^A\left(t_4-t_5\right)\delta\boldsymbol{\Sigma}^A\left(t_5,-E\right)\mathbf{G}^A\left(E\right)\\
=&\int \mathrm{d}t_5 \exp\left(i\left(E/\hbar+\omega\right)t_5\right)\mathbf{G}^R\left(E+\hbar\omega\right)\boldsymbol{\Sigma}^<\left(E+\hbar\omega\right)\mathbf{G}^A\left(E+\hbar\omega\right)\delta\boldsymbol{\Sigma}^A\left(t_5,-E\right)\mathbf{G}^A\left(E\right)\\
=&\mathbf{G}^R\left(E+\hbar\omega\right)\boldsymbol{\Sigma}^<\left(E+\hbar\omega\right)\mathbf{G}^A\left(E+\hbar\omega\right)\delta\boldsymbol{\Sigma}^A\left(E+\hbar\omega,-E\right)\mathbf{G}^A\left(E\right)\\
=&\mathbf{G}^<\left(E+\hbar\omega\right)\delta\boldsymbol{\Sigma}^A\left(E+\hbar\omega,-E\right)\mathbf{G}^A\left(E\right).
\end{aligned}\tag{E.2.5}$$

The last term is given by

$$\begin{aligned}
&\int \mathrm{d}\tau\mathrm{d}t_1\mathrm{d}t_3\mathrm{d}t_4 \exp\left(iE\tau/\hbar\right)\exp\left(i\omega t_1\right)\mathbf{G}^R\left(t_1-t_3\right)\delta\boldsymbol{\Sigma}^<\left(t_3,t_4\right)\mathbf{G}^A\left(t_4-t_1+\tau\right)\\
=&\int \mathrm{d}t_1\mathrm{d}t_3\mathrm{d}t_4 \exp\left(i\left(\omega+E/\hbar\right)t_1\right)\exp\left(-iEt_4/\hbar\right)\mathbf{G}^R\left(t_1-t_3\right)\delta\boldsymbol{\Sigma}^<\left(t_3,t_4\right)\mathbf{G}^A\left(E\right)\\
=&\int \mathrm{d}t_3\mathrm{d}t_4 \exp\left(i\left(\omega+E/\hbar\right)t_3\right)\exp\left(-iEt_4/\hbar\right)\mathbf{G}^R\left(E+\hbar\omega\right)\delta\boldsymbol{\Sigma}^<\left(t_3,t_4\right)\mathbf{G}^A\left(E\right)\\
=&\mathbf{G}^R\left(E+\hbar\omega\right)\delta\boldsymbol{\Sigma}^<\left(E+\hbar\omega,-E\right)\mathbf{G}^A\left(E\right).
\end{aligned}\tag{E.2.6}$$

In summary, the change of the lesser Green's function reads

$$\begin{aligned}
&\delta\mathbf{G}^<\left(\omega,E\right)\\
=&\mathbf{G}^R\left(E+\hbar\omega\right)\delta V\left(\omega\right)\mathbf{G}^<\left(E\right)+\mathbf{G}^<\left(E+\hbar\omega\right)\delta V\left(\omega\right)\mathbf{G}^A\left(E\right)\\
&+\mathbf{G}^R\left(E+\hbar\omega\right)\delta\boldsymbol{\Sigma}^R\left(E+\hbar\omega,-E\right)\mathbf{G}^<\left(E\right)+\mathbf{G}^<\left(E+\hbar\omega\right)\delta\boldsymbol{\Sigma}^A\left(E+\hbar\omega,-E\right)\mathbf{G}^A\left(E\right)\\
&+\mathbf{G}^R\left(E+\hbar\omega\right)\delta\boldsymbol{\Sigma}^<\left(E+\hbar\omega,-E\right)\mathbf{G}^A\left(E\right).
\end{aligned}\tag{E.2.7}$$

Appendix F

Phonon momentum in LO-phonon scattering

The exact solution of the integral in Eq. (3.5.9) introduces an extremely lengthy and error-prone expression. Since it matches nicely the exact solution (see Fig. 3.5.1), we carry out the approximated integral in Eq. (3.5.9) in the following. The first step is to replace the difference of the two propagation coordinates with its absolute value

$$\begin{aligned} & \int_{-\infty}^{\infty} \mathrm{d}q_z \frac{q_\parallel^2 + q_z^2}{\left[q_\parallel^2 + q_z^2 + \xi^{-2}\right]^2} \exp\left[iq_z\left(z_3 - z_4\right)\right] \\ = & \int_{-\infty}^{\infty} \mathrm{d}q_z \frac{q_\parallel^2 + q_z^2}{\left[q_\parallel^2 + q_z^2 + \xi^{-2}\right]^2} \exp\left(iq_z\left|z_3 - z_4\right|\right). \end{aligned} \tag{F.0.1}$$

This is trivial in the case of $z_3 > z_4$ and easy to see after a substitution ($q_z = -q_z'$) in the opposite situation. Given in the last formulation, this integral is already solved in literature (see e.g. [217])

$$\int_{-\infty}^{\infty} \mathrm{d}q_z \frac{q_\parallel^2 + q_z^2}{\left[q_\parallel^2 + q_z^2 + \xi^{-2}\right]^2} \exp\left(iq_z\left|z_3 - z_4\right|\right) = 2\pi i \sum_{\mathrm{Im}\, c>0} \mathrm{Res}_c \left(\frac{\left(q_\parallel^2 + q_z^2\right) \exp\left(iq_z\left|z_3 - z_4\right|\right)}{\left(q_\parallel^2 + q_z^2 + \xi^{-2}\right)^2} \right). \tag{F.0.2}$$

Here $\mathrm{Res}_c f$ is the residual of the function f at the point c. The denominator in the residual vanishes at two points

$$c_{1,2} = \pm i\sqrt{q_\parallel^2 + \xi^{-2}}, \tag{F.0.3}$$

where only c_1 has to be accounted for. At c_1, the integrand has a pole of second order, so that the residual reads:

$$\begin{aligned}
&\mathrm{Res}_{c_1}\left(\frac{\left(q_\parallel^2+q_z^2\right)\exp\left(iq_z\left|z_3-z_4\right|\right)}{\left(q_z-i\sqrt{q_\parallel^2+\xi^{-2}}\right)^2\left(q_z+i\sqrt{q_\parallel^2+\xi^{-2}}\right)^2}\right)\\
=\;&\frac{\mathrm{d}}{\mathrm{d}q_z}\left(\frac{q_\parallel^2+q_z^2}{\left(q_z+i\sqrt{q_\parallel^2+\xi^{-2}}\right)^2}\exp\left(iq_z\left|z_3-z_4\right|\right)\right)\Bigg|_{q_z=i\sqrt{q_\parallel^2+\xi^{-2}}}\\
=\;&\frac{i\left|z_1-z_2\right|\xi^{-2}}{4q_\parallel^2+4\xi^{-2}}\exp\left(-\sqrt{q_\parallel^2+\xi^{-2}}\left|z_3-z_4\right|\right)-\frac{i}{2\sqrt{q_\parallel^2+\xi^{-2}}}\exp\left(-\sqrt{q_\parallel^2+\xi^{-2}}\left|z_3-z_4\right|\right)\\
&+\frac{i\xi^{-2}}{4\sqrt{q_\parallel^2+\xi^{-2}}\left(q_\parallel^2+\xi^{-2}\right)}\exp\left(-\sqrt{q_\parallel^2+\xi^{-2}}\left|z_3-z_4\right|\right). \qquad \text{(F.0.4)}
\end{aligned}$$

Now we can summarize our results

$$\begin{aligned}
&\int_{-\infty}^{\infty}\mathrm{d}q_z\frac{q_\parallel^2+q_z^2}{\left(q_\parallel^2+q_z^2+\xi^{-2}\right)^2}\exp\left[iq_z\left(z_3-z_4\right)\right]\\
=\;&\frac{\pi\exp\left(-\sqrt{q_\parallel^2+\xi^{-2}}\left|z_1-z_2\right|\right)}{\sqrt{q_\parallel^2+\xi^{-2}}}\left(1-\frac{\xi^{-2}\left|z_1-z_2\right|}{2\sqrt{q_\parallel^2+\xi^{-2}}}-\frac{\xi^{-2}}{2\left(q_\parallel^2+\xi^{-2}\right)}\right). \qquad \text{(F.0.5)}
\end{aligned}$$

Appendix G

Lesser polarization in electron-electron interaction

In order to apply the GW_0-approximation, we replace the Green's functions in Eq. (3.5.92) with the free particle Green's functions of Eq. (2.3.43). Furthermore, we assume a bulk dispersion relation $\varepsilon\left(\vec{k}\right) = \hbar^2 k^2/2m^*$. Then, we get for the lesser polarization

$$\begin{aligned} iP_0^<\left(\vec{q},\omega\right) &= \frac{1}{\hbar^3}\frac{2}{(2\pi)^2}\int \mathrm{d}E\mathrm{d}\vec{Q}\left[1-f\left(\frac{\hbar^2Q^2}{2m^*},\mu\right)\right] f\left(\frac{\hbar^2\left|\vec{Q}+\vec{q}\right|^2}{2m^*},\mu\right) \\ &\quad \times\delta\left(E/\hbar+\omega-\frac{\hbar\left|\vec{Q}+\vec{q}\right|^2}{2m^*}\right)\delta\left(E/\hbar-\frac{\hbar Q^2}{2m^*}\right). \end{aligned} \tag{G.0.1}$$

We introduce spherical coordinates for the $\mathrm{d}\vec{Q}$ integral, and get

$$\begin{aligned} iP_0^<\left(\vec{q},\omega\right) &= \frac{m^*}{\pi\hbar^4}\int \mathrm{d}E\mathrm{d}Q\mathrm{d}\left(\cos\phi\right)\frac{Q^2}{\sqrt{2m^*E/\hbar^2}}\left[1-f\left(\frac{\hbar^2Q^2}{2m^*},\mu\right)\right] \\ &\quad \times f\left(\frac{\hbar^2\left|\vec{Q}+\vec{q}\right|^2}{2m^*},\mu\right)\delta\left(E/\hbar+\omega-\frac{\hbar\left(Q^2+q^2+2Qq\cos\phi\right)}{2m^*}\right) \\ &\quad \times\left[\delta\left(Q-\sqrt{2m^*E/\hbar^2}\right)+\delta\left(Q+\sqrt{2m^*E/\hbar^2}\right)\right]. \end{aligned} \tag{G.0.2}$$

We perform the $\mathrm{d}Q$ integral

$$\begin{aligned} &iP_0^<\left(\vec{q},\omega\right) = \frac{m^*}{\pi\hbar^4}\int \mathrm{d}E\mathrm{d}\left(\cos\phi\right)\sqrt{2m^*E/\hbar^2}\left[1-f\left(E,\mu\right)\right] \\ &\times\left[f\left(\left(E+\hbar^2q^2/2m^*+2\sqrt{\hbar^2E/2m^*}q\cos\phi\right),\mu\right)\right. \\ &\times\delta\left(\omega-\hbar q^2/2m^*-2\sqrt{E/2m^*}q\cos\phi\right)+f\left(\left(E+\hbar^2q^2/2m^*-2\sqrt{\hbar^2E/2m^*}q\cos\phi\right),\mu\right) \\ &\left.\delta\left(\omega-\hbar q^2/2m^*+2\sqrt{E/2m^*}q\cos\phi\right)\right]. \end{aligned} \tag{G.0.3}$$

Finally, we can evaluate the integral over $\mathrm{d}(\cos\phi)$ which cancels the last Dirac-δ and gives a simple formula

$$\begin{aligned}
& iP_0^{<}(\vec{q},\omega) \\
= \; & \frac{m^{*2}}{\pi\hbar^5 q}\int \mathrm{d}E\mathrm{d}(\cos\phi)\left[1-f(E,\mu)\right] \\
& \times\left[f\left(\left(E+\hbar^2q^2/2m^*+2\sqrt{\hbar^2E/2m^*}q\cos\phi\right),\mu\right)\delta\left(\cos\phi-\frac{m^*\omega}{\sqrt{2m^*E}q}+\frac{\hbar q^2}{2\sqrt{2m^*E}q}\right)\right. \\
& \left.+f\left(\left(E+\hbar^2q^2/2m^*-2\sqrt{\hbar^2E/2m^*}q\cos\phi\right),\mu\right)\delta\left(\cos\phi+\frac{m^*\omega}{\sqrt{2m^*E}q}-\frac{\hbar q^2}{2\sqrt{2m^*E}q}\right)\right] \\
= \; & \frac{2}{\pi}\frac{m^{*2}}{q\hbar^5}\int \mathrm{d}E\left(1-f(E,\mu)\right)f(E+\hbar\omega,\mu)\,. \qquad \text{(G.0.4)}
\end{aligned}$$

Appendix H

Publication list

- *Comparison between semiclassical and full quantum transport analysis of THz quantum cascade lasers*, A. Mátyas, T. Kubis, P. Lugli and C. Jirauschek, submitted to Physica E: Low-dimensional Systems and Nanostructures (2009)
- *How periodic are terahertz quantum cascade lasers?*, T. Kubis and P. Vogl, accepted for Journal of Physics: Conference Series (2009)
- *Carrier transport in THz quantum cascade lasers: Are Green's functions necessary?*, A. Mátyás, T. Kubis, P. Lugli and C. Jirauschek, accepted for Journal of Physics: Conference Series (2009)
- *Nonequilibrium Green's function calculation for four-level scheme terahertz quantum cascade lasers*, H. Yasuda, T. Kubis, P. Vogl, N. Sekine, I. Hosako and K. Hirakawa, Appl. Phys. Lett. **94**, 151109 (2009)
- *Predictive quantum theory of current and optical emission in quantum cascade lasers*, T. Kubis and P. Vogl, Proc. SPIE **7230**, 723019 (2009)
- *Predictive Quantum Theory of Current and Optical Gain in Quantum Cascade Lasers*, T. Kubis and P. Vogl, Laser Physics **19**, 762 (2009)
- *Theory of nonequilibrium quantum transport and energy dissipation in terahertz quantum cascade lasers*, T. Kubis, C. Yeh, P. Vogl, A. Benz, G. Fasching and C. Deutsch, Phys. Rev. B **79**, 195323 (2009)
- *Microscopic theory of spin-filtering in non-magnetic semiconductor nanostructures*, T. Kubis and P. Vogl, phys. stat. sol. (c) **5**, 290 (2008)
- *Non-equilibrium quantum transport theory: Current and gain in quantum cascade lasers*, T. Kubis, C. Yeh and P. Vogl, J. Comput. Electron. **7**, 432 (2008)
- *Quantum theory of transport and optical gain in quantum cascade lasers*, T. Kubis, C. Yeh and P. Vogl, phys. stat. sol. (c) **5**, 232 (2008)
- *Simulation of quantum cascade lasers - optimizing laser performance*, S. Birner, T. Kubis and P. Vogl, Photonik international **2**, 60 (2008)

- *Simulation zur Optimierung von Quantenkaskadenlasern*, S. Birner, T. Kubis and P. Vogl, Photonik 1/2008, 44 (2008)

- *nextnano: General Purpose 3-D Simulations*, S. Birner, T. Zibold, T. Andlauer, T. Kubis, M. Sabathil, A. Trellakis and P. Vogl, IEEE Transactions on Electron Devices **54**, 2137 (2007)

- *Self-consistent quantum transport theory: Applications and assessment of approximate models*, T. Kubis and P. Vogl, J. Comput. Electron. **6**, 183 (2007)

- *Self-consistent quantum transport theory of carrier capture in heterostructures*, Proceedings of the 14th International Conference on Nonequilibrium Carrier Dynamics in Semiconductors, T. Kubis, A. Trellakis and P. Vogl, edited by M. Saraniti and U. Ravaioli, Chicago, USA, July 25-19, 2005, Springer Proceedings in Physics, vol. 110, pp. 369-372

Acknowledgement

First of all, I have to thank Prof. Peter Vogl for the opportunity to work on the exciting field of quantum transport in semiconductor nanodevices. He offered me the freedom to choose nonequilibrium Green's functions for the description of the transport problems and helped me out of dead ends with fruitful discussions. In particular, the always up-to-date hard- and software which is a matter of course at his chair turned out to be vital for all the numerical results in my thesis.

The pleasant atmosphere at Prof. Vogl's chair is only possible thanks to the cooperativeness and collegiality of Dr. Matthias Sabathil, Dr. Jacek Majewski, Dr. Alexandros Trellakis, Dr. Reinhard Scholz, Dr. Tobias Zibold, Dr. Till Andlauer, Stefan Birner, Catherine Yeh, Christoph Schindler, Peter Greck, Thomas Eisfeller, Michael Bayer, Christian Ammann, Christian Uhl, Philip Weidmann, Linus Gisslen, and Martin Haeufel. Special thanks are indebted to our secretaries Liane Lindner and Veronika Enter which kept administrative trouble far off my every day work.

During the last years, I had the opportunity to enjoy several collaborations with experimental and electrical engineering groups. Thus, I also want to thank Dr. Andreas Wittmann, Dr. Christian Jirauschek, Alpár Mátyás, Dr. Gernot Fasching, Alexander Benz, Christoph Deutsch and Hiroaki Yasuda for their great work and all the fantastic things I have learned while working with them.

Most of all, however, I have to thank my mother and my brother for their endless patience and support they offered me during all the trouble of my thesis. Without their help, this thesis would have never been completed.